Wenjun Lu

Floe Ice – Sloping Structure Interactions

Thesis for the degree of Philosophiae Doctor

Trondheim, December 2014

Norwegian University of Science and Technology
Faculty of Engineering Science and Technology
Department of Civil and Transport Engineering

NTNU – Trondheim
Norwegian University of
Science and Technology

NTNU
Norwegian University of Science and Technology

Thesis for the degree of Philosophiae Doctor

Faculty of Engineering Science and Technology
Department of Civil and Transport Engineering

ISBN 978-82-326-0560-6 (printed ver.)
ISBN 978-82-326-0561-3 (electronic ver.)
ISSN 1503-8181

Doctoral theses at NTNU, 2014:324

Printed by NTNU-trykk

To my grandmother

Abstract

Several interaction processes can be identified during floe ice - sloping structure interactions. However, fierce processes around the waterline are the most conspicuous phenomena. These violent processes feature ice fracturing and the potential rotation of subsequent ice blocks. This thesis focuses primarily on the fracture of ice floes. The exact failure pattern of an ice floe is complicated by the actual ice conditions in which the sloping structure is positioned. Regarding the ice condition, we do not predefine it as a 'level ice' or a 'broken ice' field. Instead, considering an ice field composed of ice floes of varying sizes is a more realistic approach. Studying the interaction between an ice floe and a sloping structure (i.e., floe ice - sloping structure interactions) can yield more general results because an ice floe has a spatial scale that typically ranges from 10 m to 10 km. The ice floe can be large enough to be regarded as level ice or can be small enough to be treated as a member of a broken ice field.

Currently, Arctic exploration and exploitation are expanding into a relatively 'open' ice condition, within which, a knowledge gap exists regarding the fracture of a finite size ice floe in the context of ice-structure interactions. To advance our understanding, this thesis studied the following observed failure modes of a finite size ice floe within such an 'open' ice condition:

1) In-plane splitting failure;
2) Out-of-plane flexural failure; and
3) Competition between different failure modes in the context of ice - sloping structure interactions.

This thesis addresses influential factors, such as an ice floe's size, geometry, confinement, and ice-structure contact properties. In a decoupled manner, these different failure modes were studied primarily using the concept of fracture mechanics. The major contributions of this study are the following:

1) Analytical solutions for each failure mode were proposed for ice floes of varying sizes, which range over a large spatial scale (i.e., from approximately 1 m to 10 km); and
2) Each analytical solution within the established analytical framework was rigorously verified, either by numerical simulations, existing idealised analytical results, experimental measurements, or all of the above.

Theoretically, through derivations, implementations and validations of all these analytical solutions, many interesting results were obtained, such as the following:

1) The validity of using Linear Elastic Fracture Mechanics (LEFM) to study an ice floe's splitting failure on an engineering scale was confirmed;
2) An ice floe's confinement has a much more profound effect on increasing the force required to split an ice floe in comparison with the influence of floe geometry;
3) Three out-of-plane flexural failure scenarios were further conservatively identified and analytically studied; and
4) A floe size requirement (i.e., a square floe's size $L < 27(\text{ice thickness})^{3/4}$) was suggested for the radial-crack-initiation-controlled fracture of an ice floe.

From a practical point of view, with all these analytical solutions of failure modes at our disposal, we are thus able to construct a failure map that relates an ice floe's dominant failure mode to its geometry, relevant contact and material properties. In addition, these analytical formulae can be effectively incorporated with multi-body dynamic simulators to assess the performance of Arctic offshore structures in ice over large temporal and spatial scales.

In addition, as opposed to relatively 'open' ice conditions, we have also studied ice - sloping structure interaction in 'tight' ice conditions. One extreme interaction scenario within these ice conditions is when a large amount of ice rubble accumulates in front of a sloping structure. This scenario has long been recognised as one of the controlling design conditions and has previously been under thorough investigation.

In this thesis, a novel approach that combines both physical model tests (i.e., measured by tactile sensors and load cells) and a theoretical model was employed to study ice load's spatial and temporal variations on a sloping structure under the influence of rubble accumulation. The following results were found:

1) The presence of rubble accumulation increases the global ice resistance;
2) The maximum value of ice resistance occurs in a location below the waterline, which signifies the importance of the ice rotating process and rubble accumulation effect; and
3) The developed theoretical model, which was validated by both physical model tests and existing theoretical models, can serve as a preliminary tool to study ice load's temporal and spatial distribution under the influence of rubble accumulation.

As an extension, we also explored a seemingly promising numerical method's (i.e., the Cohesive Element Method (CEM)) applicability in studying ice - sloping structure interactions under the influence of rubble accumulation. Preliminary results demonstrate that there is still a substantial knowledge/computational gap in using this numerical method to simulate ice and sloping structure interactions in a three-dimensional setting.

The primary deliverable contributions of this thesis to the scientific and engineering community are the proposed analytical solutions and the framework for different failure modes under two different ice conditions. Such analytical treatment prepared us to simulate loads related to floe ice - sloping structure interactions, which are important for Arctic exploration and exploitation on large temporal and spatial scales.

Preface

This thesis is submitted to the Norwegian University of Science and Technology (NTNU) for partial fulfilment of the requirements for the degree of philosophiae doctor.

This doctoral work was performed at the Department of Civil and Transport Engineering, NTNU, Trondheim, with Professor Sveinung Løset as the main supervisor and with co-supervisors Associate Professor Raed Lubbad and Professor Knut Høyland.

A majority of the thesis was financed by the Research Council of Norway through project 200618/S60-PetroRisk and NTNU's Research Centre for *Sustainable Arctic Marine and Coastal Technology* (SAMCoT CRI). Additionally, the work related to ice rubble accumulation was partially supported by the European Community's 7th Framework Programme through the grant from the budget of the Integrated Infrastructure Initiative HYDRALAB-IV, Contract no. 261520. Furthermore, SAMCoT's academic and industrial partners also directly contributed to the finalisation of this doctoral thesis.

Acknowledgements

Looking back those 49 months I have spent on this thesis work, I am filled up with joy and gratitude. It has never been an easy hiking through this PhD journey irrespective of one's cleverness and diligence. Though driven by the fun part of intellectual challenges, I have also been constantly shadowed by psychological frustrations. However, I was fortunate enough to have the following person generously bestowing me great helps during this wonderful adventure.

The first person I have to thank is my main supervisor, Sveinung Løset, who is such a person full of positive energy and is always willing to support his students from all perspectives. First, you offered me the precious opportunity of being one of your students ever since my Master study in 2008. Within the followed-up PhD study from 2010, you continued to offer me countless opportunities, such as field expeditions to the Arctic, possibilities of meeting with and learning from world-renowned researchers, exposures to both domestic and international industrial needs, and collaborations with various parties. Most importantly, it was you who lighted up my face and pumped energy into my heart during those toughest days while I was suffering from negative feelings in life. Maybe as you have said, you are also taking energy from us and we are running a 'perpetual machine' here; but to me, this thesis would not be in existence without all the encouragements, beliefs, strength, guidance and knowledge you have granted to me.

The second person I would like to thank is my co-supervisor Raed Lubbad. If Sveinung is the steering wheel and gas pedal of a car, then you are the clutch and gearing system. I suppose I am your first PhD student. As an overly confident fresh MSc student, I was not fully cooperative in the very beginning. Moreover, repetitive revisions of papers discouraged me and brought about lots of self-doubts and negative feelings. A similar feeling can be found in the first usage of a clutch. Thinking back those days now, I feel all what I have been through is absolutely necessary. Gradually I learnt to settle down my heart and really spend time digging into the problem. Most importantly, you have guided me in different research problems, helped me in organising various ideas and also supplying me with new ideas. Afterwards, we geared up for the fruitful productions. I hope you have enjoyed the time within this research as much as I have done. For me, without all your guidance, constructive criticisms, suggestions and help, this thesis would not reach its current status.

The third person I want to thanks is my second co-supervisor, Knut Høyland. Your coordination regarding my involvement in the lab test in Hamburg Ship Model Basin is greatly acknowledged. Precious experiences and fruitful publications have been gained during this test. Moreover, your great help with the experiment is highly appreciated. More importantly, your inspiring courses regarding ice ridges and fracture of ice have largely influenced the focus of my doctoral study.

Then I want to thank our excellent supporters, Maria Azucena Gutierrez Gonzalez, Daniel Erland, Kjerstina Røhme, Elin Mette Tønset and Marit Skjåk-Bræk who are always there tirelessly helping me with all the administrative related issues and also

trying to sort out all the messes created by a ‘nerdy’ me. Your great help has made my life easier.

Afterwards, the first group of people I would like to thank are those great teachers from whom I have obtained the opportunities to eliminate those long-lasting theoretical puzzles and to enrich my knowledge. Most of them are the giants, upon whose shoulders this thesis stands. In chronological order of acquaintance, you are: Øivind Asgeir Arntsen, Tuomo Kärnä, Mauri Määttänen, Aleksey Marchenko, Andrei Metrikine, Jukka Tuhkuri, Devinder Sodhi, John Dempsey, Jaakko Heinonen, Erland Schulson, Kari Kolari and Andrew Palmer.

Then I would like to take the opportunity to thank all my collaborators, from whom I have learnt a lot and have obtained wonderful memories during the collaboration. You are, for field expedition: Stig Rune, Aleksey Shestov, Anatoly Sinitsyn, Ivan Metrikin, Marat Kashafutdinov, Andrei Tsarau, Renat Yumetov, Farzad Farid-Afshin; and for lab experiments: Nicolas Serré, Basile Bonnemaire, Karl-Ulrich Evers, Sergey Kulyakhtin, Oda Skogen Astrup, Henning Helgøy, Juliane Borge, and Trine Lundamo.

Special thanks go to all my colleagues and friends, with whose accompany and/or help, this journey becomes less difficult and less lonely. Apart from those collaborators mentioned above, you are (approximately in chronological order of acquaintance): Dongjie Xu, Juan Peng, Xiaohu Fan, Deyi Zhang, Xia Liu, Serene Tay Hui Xin, Trinh Dieu Huong, Yihan Xing, Felix Breitschädel, Woflgang Kempel, Ekaterina Kim, Marit Reiso, Kenneth Eik, Vegard Aksnes, Sergiy Sukhorukov, Anton Kulyakhtin, Christian Lønøy, Biao Su, Wenbin Dong, Li Zhou, Mayilvahanan Alagan Chella, Kai Wang, Wei Zhao, Lihao Zhao, Qingqing Pan, Marat Kashafutdinov, Lucie Strub-Klein, David Wrangborg, Ole-Christian Ekeberg, Qin Zhang, Sergey Kulyakhtin, Torodd Nord, Hayo Hendrikse, Arun Mulky Kamath, Hans Bihs, and Anna Pustogvar.

Last but not least, I want to thank my parents back in China. Your countless support is one of the great source powers which drives me forward; and I am really sorry for not being able to stay by your side for most of the time. I miss you so much!

Contents

Notations

A	crack length as shown in Fig. 3.5a;
L	size of an ice floe, e.g., if it is a rectangular ice floe, the size is its length; if it is a circular ice floe, the size is its diameter;
α	normalised crack length, i.e., $\alpha = A / L$;
α_0	initial normalised crack length;
α_i	consecutive normalised crack lengths, which was used to study radial crack propagation in Sections 3.1.2.1, $i = 1,2,3,\ldots\ldots$;
$\Delta\alpha$	crack size increment, which was used to study crack propagation in Section 3.1.2.1;
α_{cr}	critical normalised crack length at which the maximum ice splitting load is expected;
B	width of a rectangular ice floe;
β	normalised width of a rectangular ice floe, i.e., $\beta = B / L$;
b_x	body force induced by the inertia of an impacting ice floe;
$D = \frac{Eh^3}{12(1-\nu^2)}$	flexural rigidity of a plate;
E'	$E' = E$ for plane stress conditions, and $E' = E/(1-\nu^2)$ for plane strain conditions (where E is Young's modulus and ν is the Poisson's ratio);
$F_Y(A)$	ice splitting load of an ice floe with crack length A;
$F_{Z,radial,0}$	force required to initiate a radial crack;
$F_{Z,radial,1}(\alpha)$	force required to propagate a crack of a normalised length $\alpha = A / L$;
$F_{Z\_direct\_rotation}$	vertical force component leading to direct rotation of a small ice floe;
$F_{z\_radial/circumferential\_cracking}$	vertical force component leading to either radial or circumferential cracking of a finite size ice floe;
$F_{Z\_wedge\_bending}$	vertical force component leading to circumferential crack formation within a semi-infinite ice floe;
F_B	force required to break the incoming level ice;
F_R	force required to rotate the already broken ice block;
F_{srb}	static load induced by the rubble accumulation;
F_{PH}	ice pushing force induced by the friction between the accumulated rubble and the incoming intact level ice;
F_{totalH}	total horizontal ice loads measured by physical model #2 or calculated by the developed theoretical model on the sloping surface;
G_{Fm}	a new fracture energy input for the cohesive elements with the bulk elements' dissipation;
G_F	fracture energy of sea ice;
g	gravitational acceleration;
h	ice floe thickness;

$H(\alpha,0)$	weight function for the considered cracked body with a pair of force components acting at the crack mouth, as shown in Fig. 3.5a and c;
k	foundation modulus. For the fluid base, $k=\rho_w g$;
ρ_i	ice density;
ρ_w	fluid density;
K	normalised foundation modulus;
K_{IC}	fracture toughness of sea ice;
L_m	bulk elements' size;
ℓ	characteristic length of a floating ice floe under flexural deformation;
m	number of wedge beams formed during the failure of a semi-infinite ice floe;
n	ratio between the length of an ice floe to its characteristic length, i.e., $n=L/\ell$;
$p_{\text{ext}}(X)$	confinement on the boundary of an ice floe;
q_z	pressure obtained by evenly applying the vertical contact force within the corresponding contact area;
R	radius of the contact loading area, which is assumed as being a half circle;
$U(A,X,0)$	function defined by Eq. (3.6);
u_c	critical half Crack Opening Displacement (COD);
$W(\xi,\eta)$	normalised deflection of an ice floe at point (ξ,η) ;
$W_0(\alpha)$	normalised deflection of a cracked ice floe at point ($\xi=0,\eta=0$);
$w_{total}(\xi,\eta)$	deflection of an ice floe at point (ξ,η) ;
w_{flood}	maximum deflection under the condition of flooding on top of an ice floe;
γ_U	energy density of the bulk material to be dissipated during fracturing;
θ	angle between a crack path and the Y axis, as shown in Fig. 3.4;
σ_f	flexural strength of the ice [Pa];
$\sigma_M{}^0(n,R)$	Mises stress at point ($\xi=0,\eta=0$);
ξ_* and η_*	location where an equivalent point load (i.e., equivalent to the distributed pressure q_z within the contact area) is acting (see details in Appendix 2);
$\nabla^4(\,)=\frac{\partial^4}{\partial\xi^4}+2\frac{\partial^4}{\partial\xi^2\partial\eta^2}+\frac{\partial^4}{\partial\eta^4}$	biharmonic operator in the new coordinate system ξ, η, and z ;
$\delta(x)$	Dirac delta function. Its unit is the inverse of its argument.

Abbreviations

2D	Two-Dimensional
3D	Three-Dimensional
BCs	Boundary Conditions
CEM	Cohesive Element Method
COD	Crack Opening Displacement
CZM	Cohesive Zone Method
DEM	Discrete Element Method
FEM	Finite Element Method
FPZ	Fracture Process Zone
GPU	Graphic Processing Unit
HSVA	Hamburg Ship Model Basin
IB	Icebreaker
LC	Load Cell
LEFM	Linear Elastic Fracture Mechanics
MATLAB	Matrix Laboratory
MIZ	Marginal Ice Zone
NTNU	Norwegian University of Science and Technology
OATRC	Oden Arctic Technology Research Cruise
ODE	Ordinary Differential Equation
PDE	Partial Differential Equation
RITAS	Rubble Ice Transport around Arctic offshore Structures
SAMCoT	Sustainable Arctic Marine and Coastal Technology
SIF	Stress Intensity Factor
SMSC	Ship Model Simulation Centre
SSY	Small-Scale Yielding
WL	Waterline

Chapter 1 Introduction

1.1 Background and motivations

Due to the presence of rich natural resources in the Arctic (see Fig. 1.1a) and also the strategically important location of the Arctic (e.g., the Northern Sea Route shown in Fig. 1.1b), there has been a continuing interest in the study of ice loads on various types of man-made structures, which would be located within or transiting through Arctic waters.

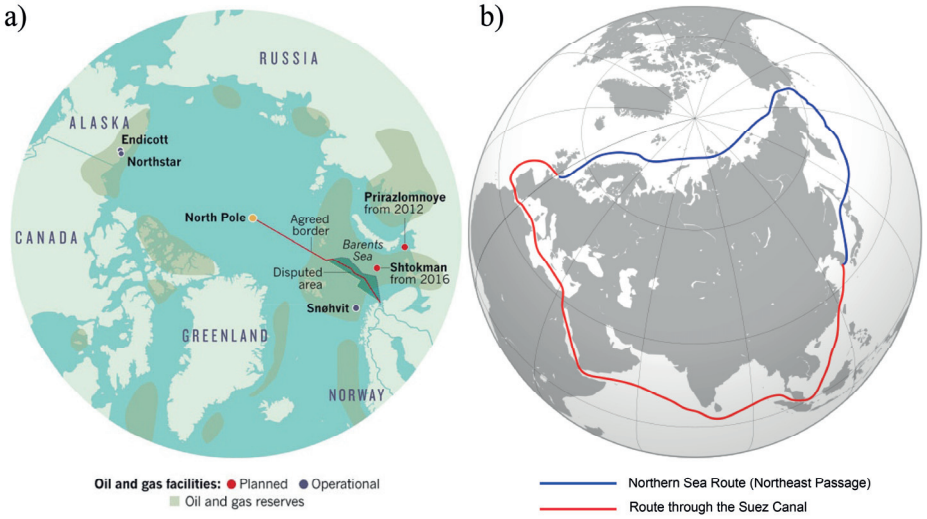

Fig. 1.1 a) a) Arctic oil and gas reserves and the 2010 Norwegian-Russian border agreement, which opened up the Barents Sea to oil companies (after (Schiermeier, 2012)); b) an overview of the reduced shipping distance through the Northern Sea Route (adapted from Wikipedia on the topic "Northern Sea Route").

In the context of ice - sloping structure interactions (i.e., a high loading rate), ice is generally considered to be a brittle material, strong in compression but relatively weak in tension. Therefore, sloping structures are the preferred geometric form to break incoming ice in a dominant bending failure mode (ISO/FDIS/19906, 2010). This thesis primarily focuses on ice loads on sloping structures (e.g., fixed or floating sloping structures and icebreakers).

A sloping structure deployed in Arctic waters may be exposed to a variety of ice features, which range from level ice, broken ice, rafted ice, ice ridges to icebergs. Depending on the encounter frequency, 'discrete events' (e.g., impact with ice ridges or icebergs) can be identified. Discrete events typically represent the design condition for Arctic structures (ISO/FDIS/19906, 2010). However, the work in the present thesis does not focus on these extreme events. Instead, this thesis focuses on a much more frequently encountered ice feature, i.e., an ice floe. An ice floe can be large enough to be considered as level ice or can be small enough to be treated as a member of a broken ice field. From an engineering application point of view, the interaction between a

sloping structure and an ice floe represents the most common ice - sloping structure interaction scenario. Understanding the failure pattern, failure processes and failure loads[1] of a single ice floe with varying sizes is of practical importance.

From a theoretical point of view, ice mechanics were studied and applied at different scales. As noted by Dempsey (2000), scales include the geophysical scale (e.g., the Arctic Basin), the floe scale (approximately 10 m ~ 10 km) and structural scales (approximately 10~100 m). Traditional ice-structure interaction studies have primarily been focused on the structural scale, whereas the incoming ice feature has often been idealised as a so-called 'level ice' condition, i.e., the study on the fracture of an ice floe is typically concentrated locally around the perimeter of the sloping structure that is in contact with virgin ice. Though challenging, there has always been a desire to bridge different scales together. Thanks to the advancement in computational power (particularly the advent and application of the Graphic Processing Unit (GPU) accelerated and physically based multi-body dynamic simulator in ice engineering (Konno, 2009; Konno and Mizuki, 2006; Konno et al., 2013; Konno et al., 2011; Lubbad and Løset, 2011; Metrikin et al., 2013; Metrikin and Løset, 2013; Yulmetov et al., 2014)), it seems to the author that the gap between the structural scale and floe scale can eventually be bridged. A numerical simulator that can cover both the structural and floe scales will undoubtedly better serve the current complicated field of Arctic offshore engineering research and development. For example, ice management is considered a promising technology for Arctic explorations. However, an ice management operation covers large temporal (i.e., several hours) and spatial (several kilometres) scales compared with those on the traditional structural scale. As a parallel development of the mentioned numerical simulator (Lubbad and Løset, 2011), this thesis is dedicated to the study of interactions between a sloping structure and an ice floe of varying sizes.

1.2 Observations

Observations made in the field/ice tank of a sloping structure interacting with an ice floe suggest that there are at least two important mechanisms that contribute to the total ice loads on a structure. These are the ice breaking process (i.e., by bending or splitting failure modes, as shown in Fig. 1.2a) and the subsequent rubble transportation process (see Fig. 1.2b). Between these two processes, this thesis primarily studies the ice breaking processes in different failure modes, which is generally termed as the 'fracture of an ice floe' in this study.

Apart from bending and splitting failure modes (see Fig. 1.2) during the fracturing of an ice floe, a closer look at the waterline indicates that newly broken ice blocks (typically wedge-shaped) need to be further rotated downwards, as shown in Fig. 1.3. This process is the so-called ice rotating process, for which there is an important, complex phenomenon called the 'ventilation and backfill effect', as illustrated in Fig. 1.3. This process can greatly influence the overall ice resistance (Lu et al., 2012b) and will be briefly covered in Appendix 4.

[1] A failure load is the force required to fail an ice feature in a certain failure mode.

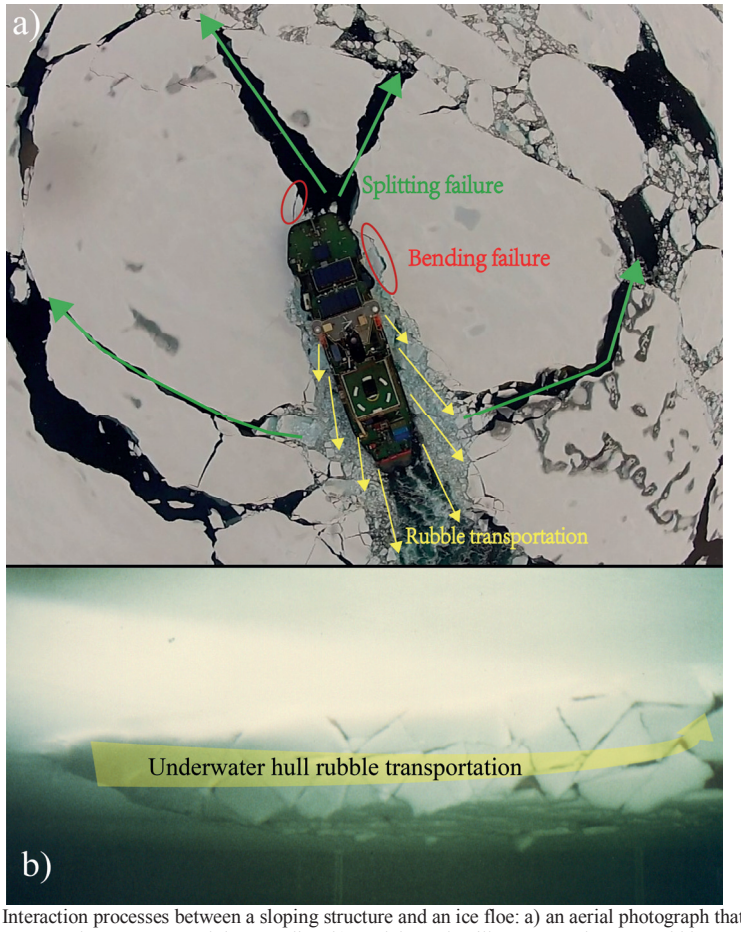

Fig. 1.2 Interaction processes between a sloping structure and an ice floe: a) an aerial photograph that illustrates the major processes that occur around the waterline: b) model test that illustrates underwater rubble transportation along the hull of an icebreaker (Valanto, 2001a).

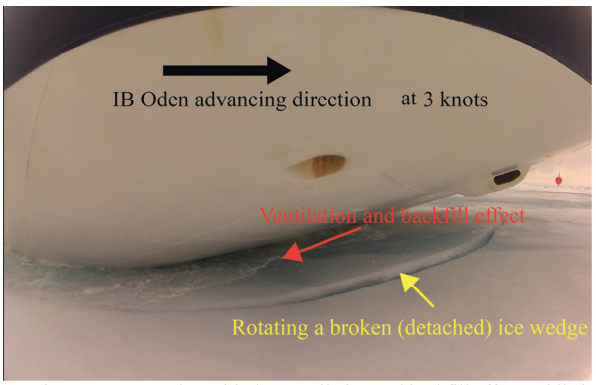

Fig. 1.3 The ice rotating process together with the 'ventilation and backfill effect' while icebreaker (IB) Oden advances within a large ice floe.

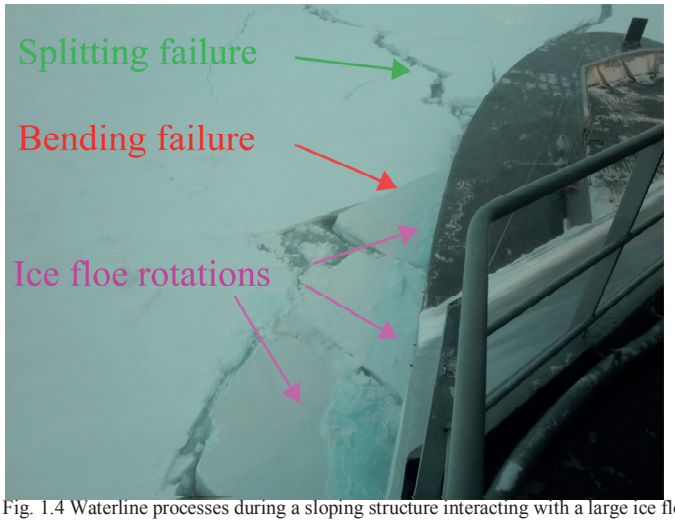

Fig. 1.4 Waterline processes during a sloping structure interacting with a large ice floe.

To summarise, as shown in Fig. 1.4, this thesis focuses on studying the fracture of an ice floe (by splitting or bending failures mode) and the rotation of ice blocks around the waterline.

1.3 Research context

The current research is primarily funded by the Research Council of Norway through the Research Centre SAMCoT, WP4-Floating structures in ice. Apart from conducting fundamental and applied researches, another concrete and important goal of SAMCoT-WP4 is to develop a numerical simulator that can simulate ice - sloping structure interactions that cover large temporal and spatial scales. The ideas and research methodologies are a continuation of previous work by Lubbad and Løset (2011). Upon the previously built foundation, three different though complementary studies were undertaken in parallel by different PhD students under SAMCoT. The ultimate goal of these fundamental studies is to construct the numerical simulator to ensure safe and economical exploration of the grand Arctic (see the satellite image in Fig. 1.5a).

Fig. 1.5a shows a satellite image that illustrates the spatial scale of a typical ice management operation. Different aspects of this problem were investigated by three different PhD candidates: MSc. Renat Yulmetov, who implemented the ice field and floe drift model with a GPU-accelerated and physically based modelling of multi-body dynamic simulator; the author of this thesis, who is in charge of studying the ice breaking and ice rotating process; and MSc. Andrei Tsarau, who focuses on the subsequent rubble transportation processes with an emphasis on the hydrodynamic effects.

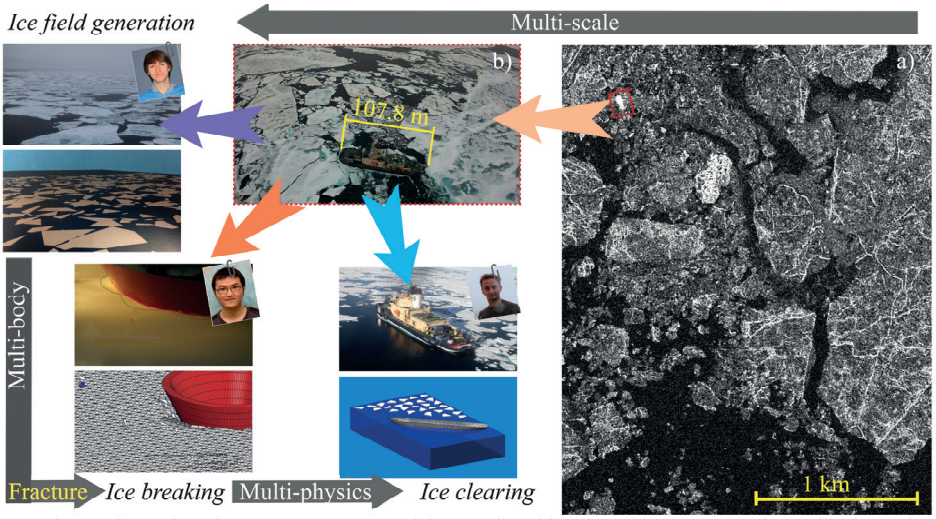

Fig. 1.5 Illustration of the research context and the overall multi-scale problem (note that the satellite image is provided by Statoil).

Within this context, the mission of this thesis is to study the fracture of ice floes and rotating of ice blocks by developing relevant analytical and numerical models.

1.4 Overall research questions

Based on the above descriptions, the following three mechanisms are considered in this thesis:

- Splitting failure of an ice floe;
- Bending failure of an ice floe;
- Ice floe rotation.

Based on these three observed mechanisms, the overall research questions of this thesis are the following:

- *In what type of conditions does an ice floe fail by splitting, bending or simply rotating?*

The ice loads experienced by a certain type of sloping structure is believed to be largely influenced by its pertinent failure mode. Therefore, it is critical to capture the salient failure modes of an ice floe. The dominant failure modes are influenced by structural properties (e.g., geometrical form and contact properties), interaction process (e.g., interaction speed), and characteristics of the ice features (particularly the size of the considered ice floe). Under this research question, this thesis quantified the influences of these different factors on the considered failure modes.

- *Given an ice floe's dominant failure modes (i.e., splitting, bending or rotation), how can their corresponding failure load be analytically and numerically calculated?*

This research question couples with the previous question. To determine which failure mode dominates in certain situations (e.g., contact properties, floe size and floe confinement), it is necessary to calculate the required force to induce different potential failure modes. Such a required force, according to Newton's third law, is the ice load that is exerted on the pertinent sloping structure.

Calculations of ice loads from different failure modes may arrive at different level of accuracies and complexities. Because the current research serves the development of a numerical simulator capable of conducting large spatial and temporal simulations, analytical solutions are preferred throughout the development. However, because analytical solutions are generally limited to idealised assumptions, numerical treatments were also sought in this thesis, as presented in Appendix 5.

- *How would other processes (e.g., rubble accumulation) influence the ice breaking and rotating processes?*

The current research studies the breaking of an ice floe and rotating of ice blocks. However, other mechanisms are equally important, e.g., rubble accumulations are often observed in a tight ice condition, while a sloping structure interacts with a large ice floe. We have therefore further studied the influences of ice rubble accumulation during level ice - wide sloping structure interactions, in which scenario, ice rubble clearing is minimal.

1.5 Research design

The research conducted in this thesis went through three different stages. Each stage was indispensable to the finalisation of the thesis. The first stage was primarily planned by the author's supervisors, i.e., Professor Sveinung Løset, Associate Professor Raed Lubbad and Professor Knut Høyland. The last two stages were primarily designed by the author under the guidance of those supervisors.

1.5.1 Defining the research problems

The thesis began with a blank page dated four years ago. In designing the research, the first challenge was to identify the research questions. The research questions briefly presented in Sections 1.2 and 1.4 were identified primarily through observations made during field expeditions. Professor Sveinung Løset and Associate Professor Raed Lubbad offered the author these valuable opportunities. In addition, industrial needs served as a driving impetus behind all the research questions. Furthermore, the research questions had to be of scientific value to advance the state-of-the-art knowledge. The incubation process of these research questions is illustrated in Fig. 1.6.

1.5.2 Conducting literature review

The literature review is a process of infiltrating and dismantling the observed problems, which helped the author to further refine the research questions and benefit from previously established theories and knowledge. Through the literature review, the observed overall problem, i.e., breaking of an ice floe and rotating of ice blocks around

the waterline, was further separated into three sub-problems, as shown in Fig. 1.7. The relevant terminologies will be introduced in Chapter 2.

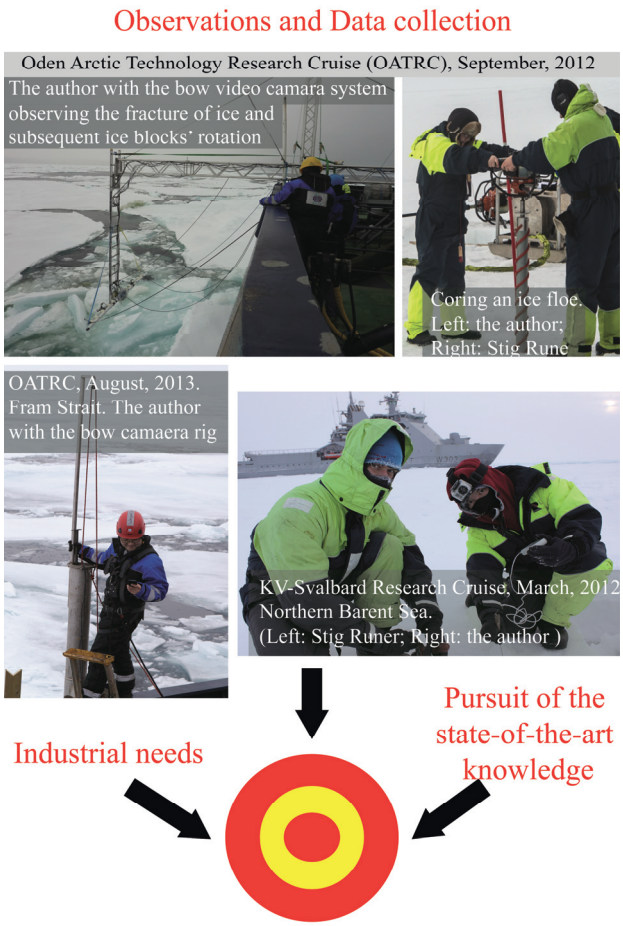

Fig. 1.6 Stage 1: Identifying the research problems.

1.5.3 Overall research methods

The final goal of this thesis is to deliver relevant and applicable methods, theories and models that can be readily used in ice loads calculations/estimations in pertinent ice conditions. While designing the research, three different approaches were adopted for each of the refined research question, which are methods based on experiments, numerical methods and analytical methods. The rationale here is that each research problem should be solved analytically, and each method should be validated by at least an additional method (see the number of darts on each target in Fig. 1.8). By doing so, mutual corroboration can be obtained for the developed methods. Furthermore, attacking the same problem using different approaches can shed light on the physical

processes from different perspectives and thus, enable an in-depth understanding to be obtained.

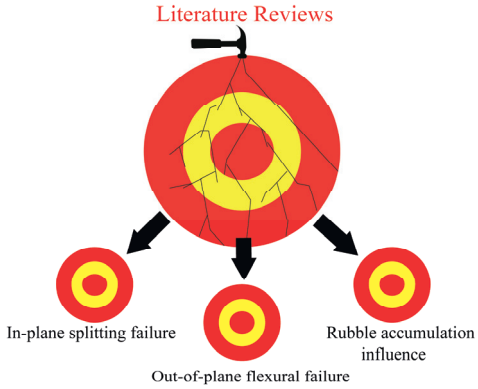

Fig. 1.7 Stage 2: Infiltrating into and dismantling of the original research question through relevant literature reviews.

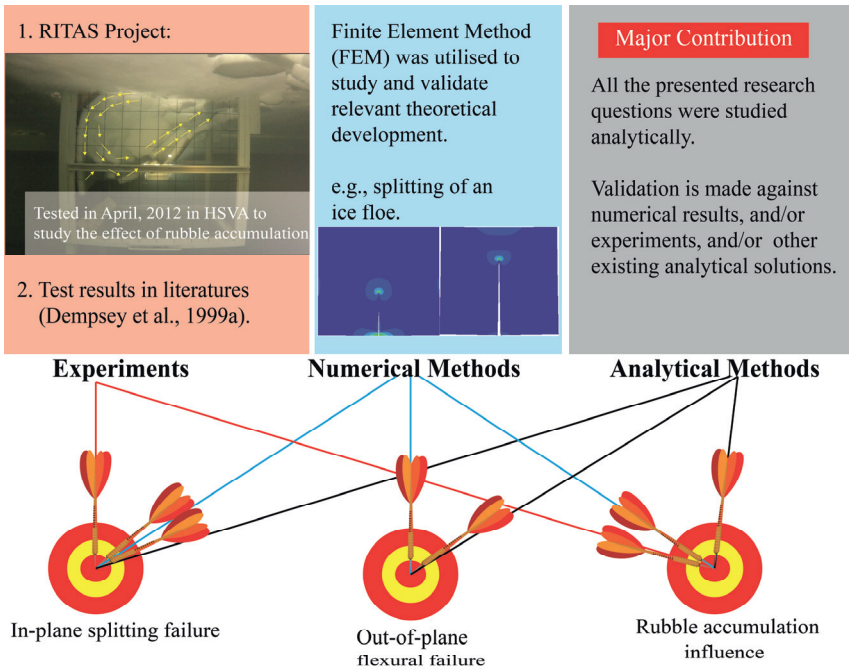

Fig. 1.8 Stage 3: Attacking the refined research problems with different research methods.

1.5.3.1 Experiments

The major experimental results reported in this thesis are based on the research project, Rubble Ice Transport around Arctic offshore Structures (RITAS). Through Professor Knut Høyland's coordination, the author participated in this research campaign in April,

2012 in Hamburg Ship Model Basin (HSVA), Germany. The measurements were used to validate the developed theoretical model to study the influence of rubble accumulation.

To study the splitting failure of an ice floe, the valuable experimental results by Dempsey et al., (1999a) were used for validation purposes.

Large amounts of valuable data were also collected during the research cruises mentioned in Fig. 1.6. However, these data were not explored in this thesis. Further exploitations of these data are to be conducted in follow-up studies.

1.5.3.2 Analytical studies

Readily applicable models are one of primary deliverables of the current thesis. Therefore, for each research question, analytical solutions were pursued (see Fig. 1.8). These different methods will be introduced in Chapter 3 and the relevant Appendices.

1.5.3.3 Numerical studies

Developed analytical models cannot always be validated by experimental measurements. Therefore, numerical models were also used to further substantiate the developed analytical methods. In this thesis, the primary numerical approach adopted is based on the versatile Finite Element Method (FEM).

1.6 List of Publications and author's contribution

The thesis comprises the author's major publications. Several additional publications are also listed here, though they are not included in this doctoral thesis.

1.6.1 Major publications

Paper **1**:
Lu, W., Lubbad, R. and Løset, S., (Accepted on November 12th, 2014). In-plane fracture of an ice floe: a theoretical study on the splitting failure mode. Cold Regions Science and Technology. DOI: *10.1016/j.coldregions.2014.11.007*.

Paper **2**:
Lu, W., Lubbad, R. and Løset, S., (submitted in July, 2014). Out-of-plane failure of an ice floe: radial-crack-initiation-controlled fracture. Cold Regions Science and Technology.

Paper **3**:
Lu, W., Lubbad, R. and Løset, S., (Submitted in September, 2014). Fracture of an ice floe: Local out-of-plane flexural failures versus Global in-plane splitting failure. Cold Regions Science and Technology.

Paper **4**:
Lu, W., Lubbad, R., Høyland, K. and Løset, S., 2014. Physical model and theoretical model study of level ice and wide sloping structure interactions. Cold Regions Science and Technology, 101: 40-72.

Paper **5**:
Lu, W., Lubbad, R. and Løset, S., 2014. Simulating ice - sloping structure interactions with the cohesive element method. Journal of Offshore Mechanics and Arctic Engineering, 136(3): 031501.

Paper **6**:
Lu, W., Serré, N., Høyland, K.V. and Evers, K.-U., 2013. Rubble Ice transport on Arctic Offshore Structures (RITAS), part IV Tactile sensor measurement of the level ice loads on inclined plate, Proceedings of the 22nd International Conference Port and Ocean Engineering under Arctic Conditions, Espoo, Finland.

1.6.2 Additional publications

The following additional publications were published during the doctoral study of the author. These publications have supporting roles in the major publications and are valuable for understanding the entire research picture. However, to be focused and concise in reporting the research work in this thesis, these research results are not included.

Interested readers are encouraged to consult these additional publications to obtain a complete picture of the relevant research conducted by the author during the period from July 2010 to August 2014.

Paper 1:
Lu, W., Høyland, K., Serré, N. and Evers, K.-U., 2014. Ice Load Measurement by Tactile Sensor in Model Scale Test in Relation to Rubble Ice Transport on Arctic Offshore Structures (RITAS). In: Hydralab (Editor), Proceedings of the HYDRALAB IV Joint User Meeting, Lisbon.

Paper 2:
Lu, W., Løset, S. and Lubbad, R., 2012. Simulating ice - sloping structure interactions with the cohesive element method, ASME 2012 31st International Conference on Ocean, Offshore and Arctic Engineering. American Society of Mechanical Engineers, Rio de Janeiro, Brazil, pp. 519-528.

Paper 3:
Metrikin, I., Lu, W., R., L., Løset, S. and Kashafutdinov, M., 2012. Numerical simulation of a floater in a broken-ice field: Part 1: Model description, Proceedings of the ASME 2012 31th International Conference on Ocean, Offshore and Arctic Engineering, Rio de Janeiro, Brazil.

Paper 4:
Serré, N., Lu, W., Høyland, K.V., Bonnemaire, B., Borge, J. and Evers, K.-U., 2013. Rubble Ice Transport on Arctic Offshore Structures (RITAS), part II: 2D scale-model study of the level ice action, Proceedings of the 22nd International Conference on Port and Ocean Engineering under Arctic Conditions, Espoo, Finland.

Paper 5:
Serré, N., Høyland, K.V., Lu, W., Bonnemaire, B. and Evers, K.-U., 2014. Rubble Ice Transport on Arctic Offshore Structures (RITAS), Scale Model Investigation of Level Ice Action. In: Hydralab (Editor), Proceedings of the HYDRALAB IV Joint User Meeting, Lisbon.

Paper 6:
Lu, W., Lubbad, R., Serré, N. and Løset, S., 2013. A theoretical model investigation of ice and wide sloping structure interactions, Proceedings of the 22nd International Conference on Port and Ocean Engineering under Arctic Conditions, Espoo, Finland.

Paper 7:
Lu, W., Løset, S. and Lubbad, R., 2012. Ventilation and backfill effect during ice-structure interactions. In: Li and Lu (Editors), The 21st IAHR International Symposium on Ice, Dalian, China, pp. 826-841.

Paper 8:
Lu, W., Lubbad, R., Løset, S. and Høyland, K.V., 2012. Cohesive zone method based simulations of ice wedge bending: a comparative study of element erosion, CEM, DEM and XFEM. In: Li and Lu (Editors), The 21st IAHR International Symposium on Ice, Dalian, China, pp. 920-938.

1.6.3 Authors' contributions and declaration of authorship

For all the major publications, the author was the first author who performed the pertinent derivations, calculations and verifications. The author also wrote the manuscripts of all the major publications.

For all the major publications, the co-author Lubbad helped the author in organising different ideas and also in supplying new ideas. Lubbad also reviewed each manuscript with constructive criticisms and suggestions. Because papers **2** and **3** are extensions of Lubbad's previous research work (Lubbad and Løset, 2011), he also supplied the author with relevant calculation scripts (i.e., MATLAB code for relevant analytical solutions (Nevel, 1961; Nevel, 1965)).

For all the major publications, the co-author Løset charted the overall research direction. In addition, Løset is also responsible for creating a unique study environment for the author, for example, inviting well-known professors to tutor the author, sending the author to field expeditions, and bringing in industrial inputs. Furthermore, Løset was actively involved in all the major discussions of each paper's research. He also greatly contributed to the proofreading of each manuscript.

For the major publication of Paper **4**, the co-author Høyland is responsible for initiating and inviting the author to conduct relevant tests at HSVA, Hamburg, Germany. Høyland contributed greatly to performing the tests together with the author.

For other publications, if the author is the first author, all calculations and verifications were conducted by the author; and the full manuscript was also written by the author. However, if the author is not the first author, then only a supportive role was played in these publications, e.g., only part of the paper was conducted by the author.

1.7 Thesis Structure

This thesis is written in a 'mini-monograph' fashion, i.e., important research methodologies and most of the interesting research results are presented from Chapter 1 to Chapter 5. These chapters as a whole can stand alone. Readers can gain a systematic understanding of the important studies reported in this thesis by reading the first five chapters only. Earnest and thorough readers are directed to specified papers listed in the Appendices for detailed information, e.g., detailed derivations, literature reviews, and additional reasoning behind assumptions.

The overall structure of the thesis is as follows.

Chapter 1 presents an overview of the research context and the overall research questions based on field observations, industrial needs and the pursuit to advance our knowledge. Afterwards, Chapter 2 discusses the state-of-the-art knowledge within relevant research topics. In addition, these detailed literature reviews break down the observed overall research questions into detailed, physically based research questions. Thereafter, Chapter 3 presents the major methods that were used to answer each of the refined research questions. Key resultant formulae are given with detailed derivations in the relevant Appendices. Based on these methodologies and assumptions, Chapter 4 presents the major research results in a selective manner. Lastly, this mini-monograph ends with a conclusion in Chapter 5, in which all the refined questions raised in Chapter 2 are addressed.

Chapter 2 State-of-the-art and refined research questions

The overall research questions that were defined in Chapter 1 were primarily based on field/lab observations and engineering application needs. To make any further theoretical advancement in these questions, it is of great importance to fit them into their corresponding physical and theoretical frameworks such that we attempt to stand on previous giants' shoulders. This chapter is therefore dedicated to literature reviews and to further refining pertinent research questions based on former researchers' work.

2.1 Basics regarding ice - sloping structure interactions

In this section, we briefly outline basic knowledge regarding ice - sloping structure interactions. Readers who are familiar with this can proceed directly to Section 2.2. Following already established terminologies, this thesis is concerned with two types of ice features, i.e., level ice and broken ice. Definitions of these two ice features are given in ISO/FDIS/19906 (2010) as follows:

Level ice:
Level ice is a region of ice with relatively uniform thickness; also called *sheet ice* (ISO/FDIS/19906, 2010, p. 6).

Broken ice:
Broken ice is loose ice, which consists of small floes that are broken up as a result of natural processes or active or passive intervention (ISO/FDIS/19906, 2010, p. 2).

One ambiguity can be found in the definition of these two terminologies, i.e., how large must a region be to be considered level ice? Or how small must floes be to be viewed as broken ice? As mentioned previously, the Arctic is typically composed of ice floes of varying sizes. Some ice floes can be extremely large (e.g., on the order of kilometres) and can be regarded as level ice; and some other floes can be so small (e.g., on the order of metres) that can be treated as a member of a broken ice field. However, there is a gap in defining the boundary of these two ice features. Nevertheless, numerous excellent studies have been conducted under these two highly idealised ice conditions, which are briefly presented in this section.

First, this thesis presents the interaction between level ice and sloping structures. Compared with a broken ice field, interactions with level ice have been under extensive study for different types of sloping structures (i.e., Arctic offshore structures or ice-going ships) in history.

2.1.1 Level ice - ship interactions

Regarding level ice - ship interactions, previous researchers, e.g.,(Kämäräinen, 2007; Kotras et al., 1983; Lindqvist, 1989; Naegle, 1980), have identified at least three major

interaction phases and several ice load components that can be studied separately. For example, the level ice - ship interaction processes were depicted by Kotras (1983), as shown in Fig. 2.1. Fig. 2.1a, b and c denote the so-called ice breaking phase, in which crushing failure of ice occurs at the initial contact followed by bending (or flexural) failure of the intact ice sheet into wedge-shaped broken ice blocks. Fig. 2.1c and d denote the ice rotating process involving the 'ventilation' effect (i.e., no water flooding on top of the rotating ice piece, which creates huge pressure differences above and below the rotating ice blocks). As a new interaction circle begins, the last plot in Fig. 2.1e implicitly illustrates that ice rubbles sliding along the ship hull signifies the rubble transportation process.

Along with this depiction, Valanto (2001b) quantified the comparative contribution of different force components, as shown in Fig. 2.2, using primarily this author's numerical simulations together with experimental measurements. These force components are either self-explained or their meanings can be consulted in the original literature. It should be noted that the results plotted in Fig. 2.2 are primarily for level ice - ship interactions, which reside in a high-speed interaction regime. For fixed or floating Arctic offshore structures, the relative speed between the incoming ice and the sloping structure is expected to be rather slow in the range around the ice drifting speed. To familiarise the reader of the ice drifting speed, Table 1 cites several recent measurements conducted by MSc. Renat Yulmetov (see in Fig. 1.5).

Table 1 Recent ice floe drifting speed measurements

Ice floe drift speed	Location	Mean [m/s]	Maximum [m/s]
(Yulmetov et al., 2013a)	Greenland Sea	0.1	1.13
(Yulmetov et al., 2013b)	north-western Barents Sea	0.38	1.5

With these ice drifting speed numbers in mind, the shaded area in Fig. 2.2 is approximately the interested region for level ice and fixed or floating offshore structure interactions. Within the shaded area, several force components identified by Valanto (2001) are expected to be absent or insignificant (e.g., ice floe slamming at the end of an ice rotating phase). In this thesis, we highlight the potential largest three force components. i.e., the ice loads due to the ice-breaking phase (i.e., labelled as 'dynamic bending and acceleration' in Fig. 2.2), the ice loads due to the ice rotating phase (i.e., labelled as 'ice floe rotation' in Fig. 2.2), and the rubble transportation phase (i.e., labelled as 'ice sliding phase' in Fig. 2.2).

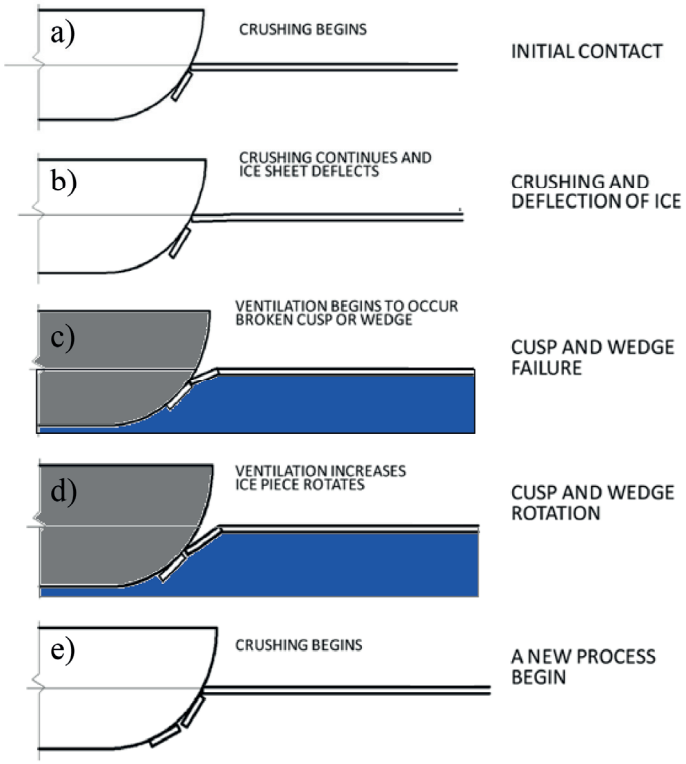

Fig. 2.1 Level ice and ship interaction processes (after Kotras (1983)).

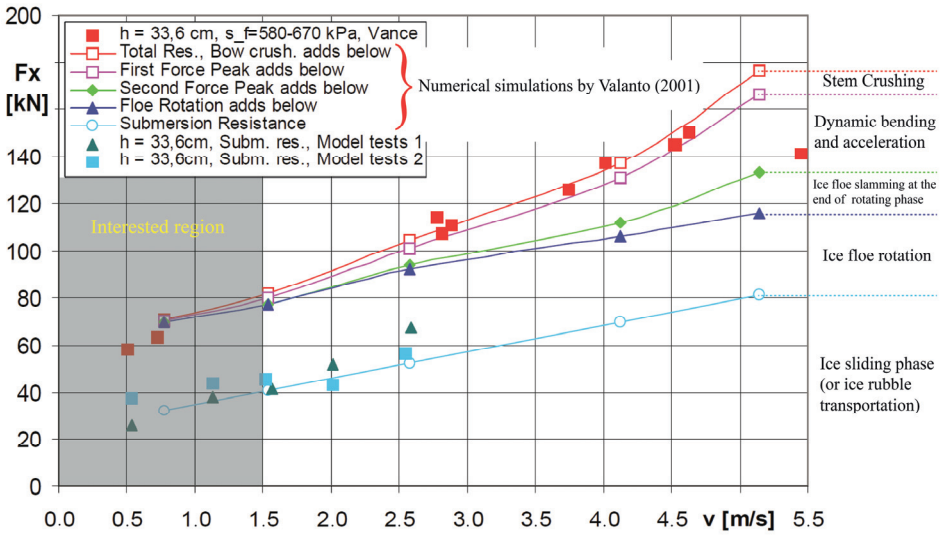

Fig. 2.2 Comparative contributions of different load components versus interaction speed (after Valanto (2001)).

2.1.2 Level ice - sloping offshore structure interactions

In terms of level ice interacting with a sloping offshore structure, ISO/FDIS/19906 (2010) illustrates this 'complicated process' in Fig. 2.3 with an example of an upward sloping conical structure. A vast literature source exists that proposes various calculation methods for all of these force components (detailed literature review can be further explored in Appendix 4).

As an analogy to the level ice - ship interaction research introduced in Section 2.1.1, the plots can also be categorised into the ice breaking phase shown in Fig. 2.3a, ice rotating phase shown in Fig. 2.3b, and rubble transportation phase shown in Fig. 2.3c, d and e. At this point, one might wonder why we generalised both the level ice - ship interaction and the level ice - sloping offshore structure interaction processes into these three different phases. It is simply because that unique physical process occurs within these three different phases. From a mechanical point of view, for the ice breaking phase, the major physical process is fracturing of the incoming ice. Ice material can be treated as purely elastic; for the ice rotating phase, depending on the interaction speed, rather fierce fluid-structure interaction scenarios occur (an ice piece can either be treated as an elastic body or a rigid body depending its actual size); for the rubble transportation process, it is primarily a multi-body interaction system, and each single ice rubble can be treated as a rigid body; or the entire rubble volume could even be ideally approximated as a continuum (e.g., (Serré, 2011; Serré and Liferov, 2010)).

Among these three different phases, this thesis covers the first two phases, which were introduced in Chapter 1. Special focus has been put on studying the fracturing of an ice floe.

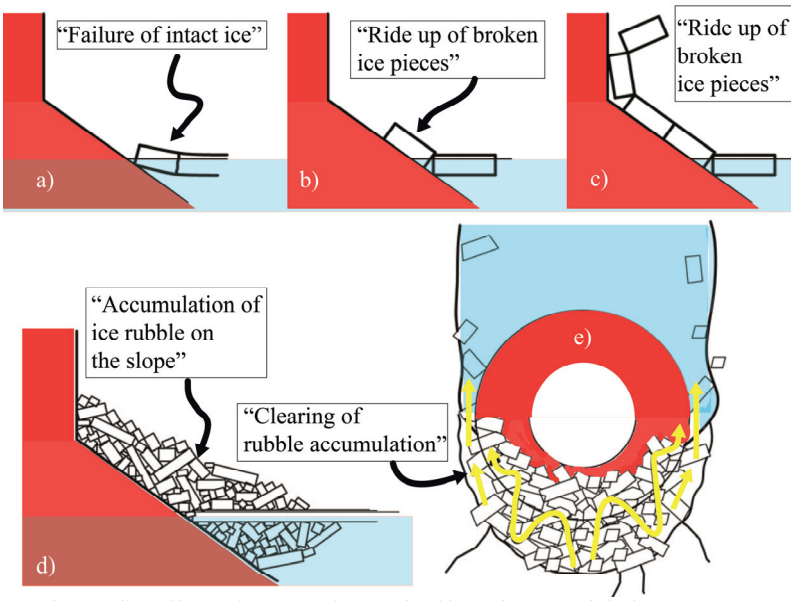

Fig. 2.3 The complicated interaction process between level ice and an upward sloping structure summarised in ISO/FDIS/19906 (2010) (after Fig. A.8-9 of ISO/FDIS/19906 (2010)).

2.1.3 Broken ice - structure interactions

Broken ice - structure interactions are not as well studied compared with that in the level ice condition. One reason is that apart from material properties, there are more parameters involved in describing a broken ice field, e.g., floe size, geometry, ice concentration, ice thickness and ice pressure. For level ice, apart from material properties, ice thickness is generally sufficient for ice loads calculations. Another reason is that a broken ice field typically leads to lower ice loads compared with those in a level ice condition. However, level ice is just a theoretical simplification; the actual Arctic generally consists of discontinuous features, such as ice ridges, leads or ice floes of varying sizes, which form a broken ice field. A typical broken ice field in nature can be found in the Marginal Ice Zone (MIZ), which stretches approximately 100 km from the ice edge (Weeks, 2010), where ice floes are primarily broken off by gravity waves (see Fig. 2.4).

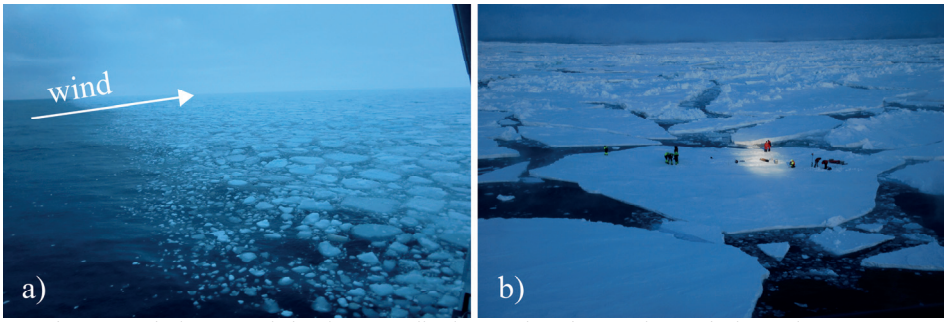

Fig. 2.4 Marginal Ice Zone during the KV-Svalbard Research Cruise, March, 2012 in the Northern Barents Sea: a) a sharp transition between open water and MIZ with short waves and small ice floes (less than 1 m); b) MIZ with long waves and large ice floes (approximately 100 m across).

Studying broken ice - structure interactions are of significant practical values. First, a great portion of a structure's service time is within broken ice fields (e.g., see Fig. 2.5a). It is beneficial to gain an understanding about a structure's most frequent loading condition.

Second, nowadays, the concept of floating Arctic offshore structures has become extremely attractive as opposed to traditional fixed Arctic offshore structures[2]. This interest is driven by the desire to perform Arctic exploration and exploitation in deeper Arctic waters (i.e., deeper than 100 m (Hamilton, 2011; Riska and Coche, 2013)) and also, the various flexibilities floating structures offer (e.g., disconnection in the face of extreme ice features). However, due to the limitation of mooring lines and dynamic positioning (DP) systems, a floating system is typically supported with ice management operations (Palmer and Croasdale, 2013), e.g., the floating structure, Kulluk, in the Canadian Beaufort Sea (see Fig. 2.5b). The goal of an ice management operation is to create a relatively 'open' ice condition that consists of small ice floes with low

[2] e.g., Molikpaq (a fixed caisson type structure) in Beaufort Sea was operating in a water depth of 21~45 m.

concentration. Therefore, ice loads calculations within a broken ice field become increasingly important.

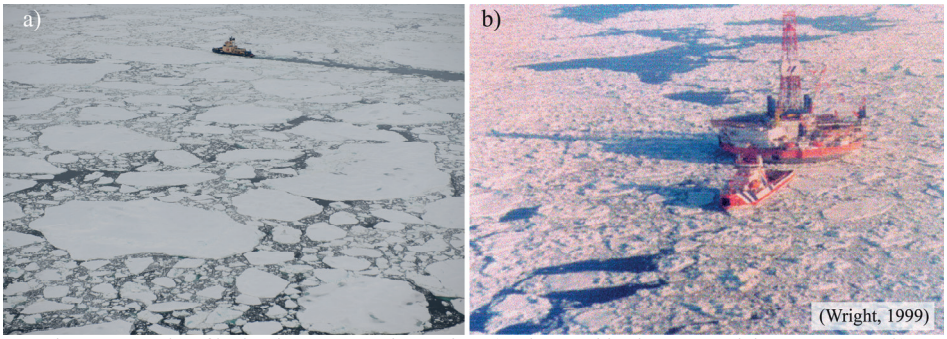

Fig. 2.5 Examples of broken ice - structure interactions a) Oden transiting in Fram Strait in August, 2012; b) Ice management operation generating a broken ice field for the protected vessel, i.e., Kulluk (after (Wright, 1999)).

However, ice loads calculations for a sloping structure within a broken ice field are still in its preliminary stage and are considered only for highly idealised scenarios. One of the most simple approaches is to idealise a broken ice field as level ice according to the *equivalent ice thickness* concept (Keinonen, 1996). Then, all the previously developed methods for level ice conditions can be applied by modifying the thickness information. However, as cited by Riska and Coche (2013), a separate study has shown that this concept only gives a better result for ship transit calculations (though a higher transit speed can be predicted) than for ice loads estimations.

Another highly idealised approach assumes that there are no ice floe fractures that occur during the interaction. i.e., the assumed broken ice field is composed of 'non-breakable floes'. The terminology, 'non-breakable floes', was first explicitly introduced by Lubbad and Løset (2011) and represents ice floes that are small enough that no further ice breaking occurs. These small non-breakable floes can be produced naturally due to environmental driving forces (e.g., small disk-shaped floes in a marginal ice zone, as shown in Fig. 2.4a), can be produced by an aggressive ice management operation, or most commonly, they can be ice rubbles broken off from the initial intact ice floe.

Significantly different approaches have been used to treat these non-breakable floes. One approach treats the ensemble of these non-breakable floes as a continuum, and relevant material models are applied to describe the overall behaviour of these floes, e.g., small ice floes produced by aggressive ice management has been treated by Croasdale et al. (2009) as a continuum (i.e., a stationary wedge) that interacts with the neighbouring ice environment and structure. A broken ice field has been numerically described as a continuum with a varying thickness with a Eulerian-Lagrangian formulation by Sayed and co-authors (Sayed and Barker, 2011; Sayed et al., 2014; Sayed et al., 2012; Sayed et al., 1995). The other approach treats each single ice floe distinctively based on theories of multi-body systems, e.g., Discrete Element Method (DEM) has been used to simulate the rubble accumulation process (Paavilainen et al., 2010; Paavilainen et al., 2006; Paavilainen et al., 2011) and to simulate structures' operation in a broken ice field (Hansen and Løset, 1999a; Hansen and Løset, 1999b;

Løset, 1994a; Løset, 1994b; Richard and Mckenna, 2013). Additionally, a physical engine - based, multi-body dynamic simulator (Lubbad and Løset, 2011) has been used to capture the rubble transportation phase, as illustrated in Fig. 1.2b.

In summary, within the context of ice-structure interactions, fracture of finite size ice floes has not been directly treated in open literature.

2.2 Fracturing of ice floes during floe ice - sloping structure interactions

In terms of fracturing of an ice floe, from the perspective of 'ice - sloping structure interactions', previous studies have implicitly assumed two extreme scenarios, i.e., a sloping structure interacting with breakable floes and non-breakable floes (introduced in Section 2.1.3). These two extreme scenarios were assumed to be the basic building blocks for the often assumed ice conditions.

2.2.1 Breakable floes idealised as level ice

"Breakable floes" are floes that can be further broken down by the sloping structure. The pertinent floe is generally assumed as level ice that suffers from minimal boundary effects. Under this assumption, an ice floe continuously fails in the bending failure mode. The flexural failure of level ice has been extensively studied in history with various analytical and numerical methods and also with a series of experiments.

Based on observations, the ultimate flexural failure of level ice is featured by producing wedge-shaped broken ice blocks, which has fostered the development of solutions to wedge plates/beams on an elastic foundation. For example, Nevel's (1958; 1961) analytical solution regarding an infinite wedge beam on an elastic foundation was widely applied in calculating the ice breaking load for level ice - sloping structure (i.e., ships and offshore structures) interactions (Kotras et al., 1983; Lubbad and Løset, 2011; Milano, 1972; Nevel, 1992). Sawamura et al. (2008; 2010) numerically tabulated the results of an infinite ice wedge's flexural failure, which were used for level ice - ship interaction simulations. Empirical formulae (e.g., Kashtelian's work) used to estimate an ice wedge's flexural failure were used by Su et al. (2010) and Liu et al. (2010) to construct numerical tools to study level ice - ship interactions.

However, to reproduce the fracturing process of an ice floe, complicated material models have been implemented and solved with various numerical methods, e.g., the cohesive zone method (CZM) in combination with the finite element method (FEM), which has been used to simulate the fracture of level ice interacting with a sloping structure in 2D (Kolari et al., 2009; Paavilainen et al., 2009) and 3D (Konuk et al., 2009; Lu et al., 2012a).

2.2.2 Implementations of ice - sloping structure interactions

Ice loads calculations for the previously outlined ice - sloping structure interactions can be developed to reach different levels of complexities and accuracies. Three categorises can be identified:

- A purely analytical approach: e.g., analytical solutions for level ice and sloping structure interactions (Croasdale and Cammaert, 1994; Lindqvist, 1989; Ralston, 1977; Ralston, 1980) and broken ice field interaction with offshore structures (Croasdale et al., 2009). These analytical solutions typically involve a large number of assumptions, though are effectively suitable for generating a sizeable result pool for probabilistic analysis for the design stage;
- A purely numerical approach: earnest ice material modelling based on the finite element method (FEM) that accounts for the fracturing of ice floes and the discrete element method (DEM), which accounts for the rubble transportation process (further literature exploration will be presented in Appendix 4);
- A hybrid approach with both analytical and numerical implementations, e.g., the numerical simulators developed by Liu et al. (2010) and Su et al. (2010) used empirical formulae to calculate the ice breaking and rubble transportation phases, where a numerical approach was adopted to detect contact between the ship hull with an intact ice sheet.

Under the umbrella of the hybrid approach, we focus on the physical engine - based, multi-body dynamic simulator, which is the major service target of the studies conducted in this thesis. The physical engine - based, multi-body dynamic simulator combines the advantages of both the analytical and numerical approaches. Analytically, fractures of ice floes are predicted and calculated by Nevel's (1961) solutions with reasonable assumptions (see the local wedge bending failure in Fig. 2.6). Numerically, the subsequent rubble transportation is simulated with the physical engine - based multi-body dynamic simulator. Compared with the traditional analytical approach (e.g., (Croasdale and Cammaert, 1994) and (Ralston, 1980)), though it is not as efficient, it can offer ice load histories instead of just a single design ice load. Compared with detailed numerical simulations based on FEM and/or DEM, though it cannot yield local ice pressure distributions around the structure and cannot reflect a more flexible ice failure patterns, it is computationally effective due to its analytical nature in treating the fracture of ice floes. Such computational effectiveness enables us to simulate an ice - sloping structure interaction event on unprecedented temporal and spatial scales. The screenshot in Fig. 2.6 of the simulation (Lubbad and Løset, 2011) exemplifies the spatial scale this simulator is capable of.

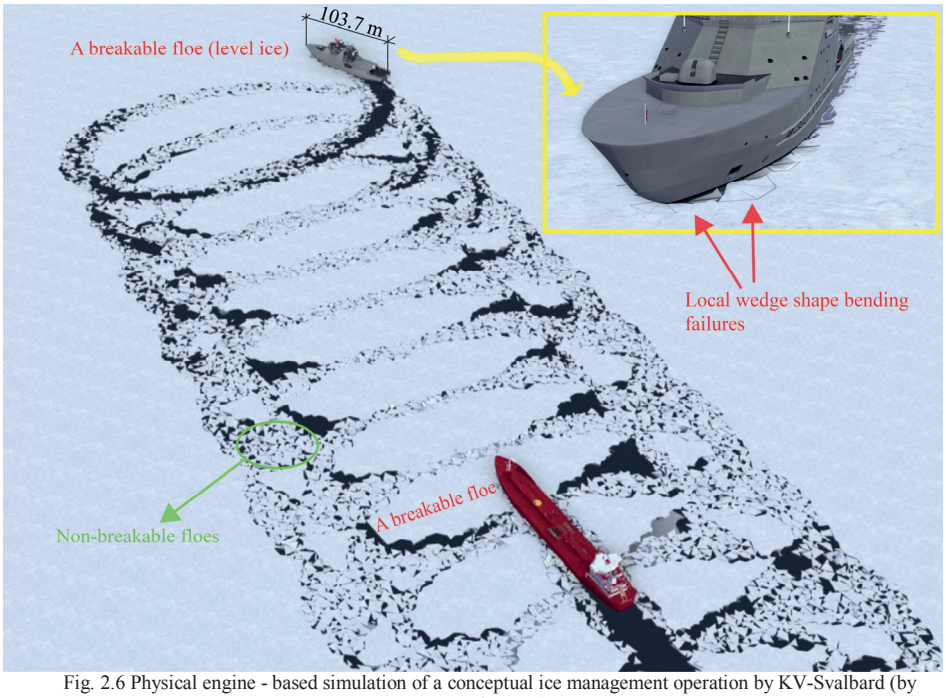

Fig. 2.6 Physical engine - based simulation of a conceptual ice management operation by KV-Svalbard (by courtesy of SMSC).

2.3 Fracture of ice floes: knowledge gaps

Standing on the foredeck of an icebreaker sailing in the Arctic, one can easily be amazed by the rather large-scale, violent scenes and scary noises from fracturing ice floes. People (researchers and engineers) often talked about 'fractures of ice'. However, in regard to most engineering applications with the presence of ice fracturing process (e.g., ice - sloping structure interactions), researchers/engineers seldom use the knowledge of fracture mechanics. In common practice (e.g., (API_RP2, 1995; ISO/FDIS/19906, 2010)), different failure modes are assigned to the ice feature; thereafter, corresponding material strength based theories are used to calculate the ultimate failure of the considered ice feature, i.e., cracks are not considered directly. To a certain extent, this makes sense because ice is a rather brittle material in the context of ice - sloping structure interactions. In addition, these strength theory based calculations are mainly targeting failure modes that occur locally around the structure (i.e., within the structural scale of 10~100 m). Within such a local scale, those predefined failure modes are mostly controlled by crack initiation, e.g., formation of circumferential cracks in local bending failure mode.

However, one ambition of this thesis is attempting to link the fracture of ice floes from the structural scale to the floe scale (approximately 10 m ~ 10 km) to support the development of the aforementioned numerical simulator. In Section 2.2, we presented the state-of-the-art regarding the fracture of an ice floe from the perspective of 'ice - sloping structure interactions'. One can immediately see that the fracture of an ice floe

has been treated with fairly simplified analytical/empirical methods by several researchers using the hybrid approach, i.e., the local bending failures of level ice were typically assumed to be the dominant failure mode. This assumption might be true for the so-called level ice condition. However, 'level ice' is a theoretical simplification rather than representing the actual Arctic ice conditions. Arctic sea ice is generally composed of discontinuous features such as ice ridges, leads and ice floes of various sizes (see the satellite image in Fig. 1.5a), which form a broken ice field. Certain ice floes can be idealised as level ice, whereas other floes' failure modes are significantly affected by the boundaries due to their limited sizes. Furthermore, most of the recent Arctic offshore structures are designed with the support of ice management, i.e., these structures are most likely working in a broken ice field (e.g., Fig. 2.6) in which a breakable ice floe is of a finite size. There is no readily available method to calculate fracture of an ice floe of finite size.

Lubbad and Løset's (2011) implementation (see Fig. 2.7) is suitable for a large ice floe, which can be idealised as level ice. However, as the encountered ice floe's size is reduced, e.g., in an ice management operation, as shown in Fig. 2.7, the dominant failure modes of an ice floe of a finite size are largely influenced by its free boundaries. As has already been introduced in Section 1.2, the splitting failure mode has been frequently observed when an icebreaker interacts with an ice floe that is of limited size. Moreover, we need to know the influences of the free boundaries on the local bending failure of a finite-sized ice floe, i.e., what is the size requirement for an ice floe that can be treated as level ice such that Nevel's (1958; 1961) analytical solution becomes valid.

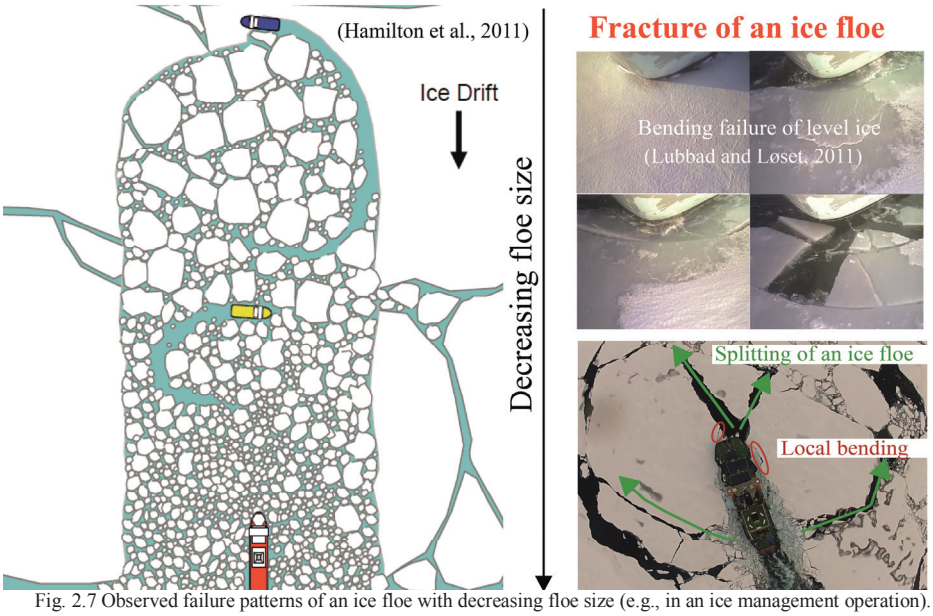

Fig. 2.7 Observed failure patterns of an ice floe with decreasing floe size (e.g., in an ice management operation).

In summary, there is a knowledge gap regarding the quantification of the border between a breakable and non-breakable floe. Moreover, within the breakable floe regime, how the floe boundaries influence the possible failure patterns, i.e., splitting and bending failure mode, is unknown. These knowledge gaps will be dealt with using approaches based on fracture mechanics. Different cracks' initiation and propagation are studied to yield a more convincing quantified border among different failure modes.

2.4 Fractures of ice floes: refined research questions

To quantify the border between a breakable and non-breakable floe and also the borders among different possible failure modes for breakable floes of varying sizes, all of these different scenarios must be identified and studied. This thesis adopted a decoupled manner to identify and study all these different scenarios separately. Based on the developed theoretical frameworks, the competitions and borders among all these scenarios can therefore be quantified.

2.4.1 In-plane fracture of an ice floe: splitting failure mode

According to field experience, the splitting failure mode has been frequently observed while a sloping structure (i.e., an icebreaker) interacts with a finite size ice floe with little confinement. This failure mode has also been observed and studied by different methods in history (a thorough literature review is presented in Appendix 1). However, these studies were not specially targeting the application of 'ice - sloping structure interactions'. In the current thesis, splitting failure of an ice floe is defined as a Mode I in-plane fracture of an ice floe by a pair of laterally opposing force components that are induced by the contact between the sloping structure and the ice floe (see Fig. 2.8).

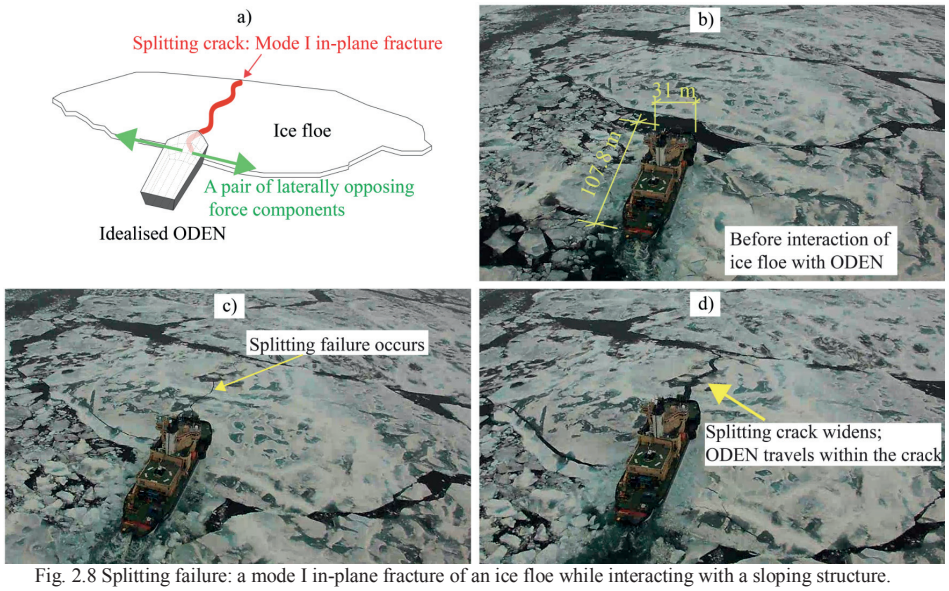

Fig. 2.8 Splitting failure: a mode I in-plane fracture of an ice floe while interacting with a sloping structure.

Based on previous studies, basic fracture mechanics theories and also intuitive observations, it is presumed that the size of an ice floe, its confinement, and the contact properties (e.g., contact geometry that leads to that pair of laterally opposing force components) are key elements that determine the occurrence of the splitting failure mode. Thereafter, the refined research questions are as follows:

1) Among all the previously developed theoretical approaches, what are their respective advantages and disadvantages while being applied to the current 'floe ice - sloping structure interaction' scenario?
2) What is the maximum load required to propagate a splitting crack through the entire body of an ice floe?
3) What is the influence of ice floe size and confinement in reference to Question #2?
4) Are we able to establish an analytical framework that can be conveniently implemented in the development of future numerical simulators?

2.4.2 Out-of-plane flexural failure of an ice floe

For a sloping structure, apart from the splitting failure mode, the local bending failure of an ice floe has long been considered a dominant failure mode. However, in treating this type of failure mode, the traditional idealisation of the two building blocks, 1) the local bending failure of breakable 'level ice' and 2) non-breakable floes as presented in Section 2.2, are questionable when applied to ice floes of finite size.

In history, the bending failure of an ice floe of varying size can benefit from the rich literature regarding the 'bearing capacity of an ice floe'. In essence, both scenarios can be perceived as an out-of-plane flexural failure of a thin plate on a Winkler-type elastic foundation. Based on a thorough literature review regarding the bearing capacity of an ice floe presented in Appendices 2 and 3, we identified three different out-of-plane flexural failure scenarios of an ice floe depending on its physical size, which are plotted in Fig. 2.9. To be more general herein, we cease to use the terminology of 'bending failure mode'. Instead, we shift to a more general jargon: *out-of-plane flexural-type failure* of an ice floe in the context of 'ice - sloping structure interactions'.

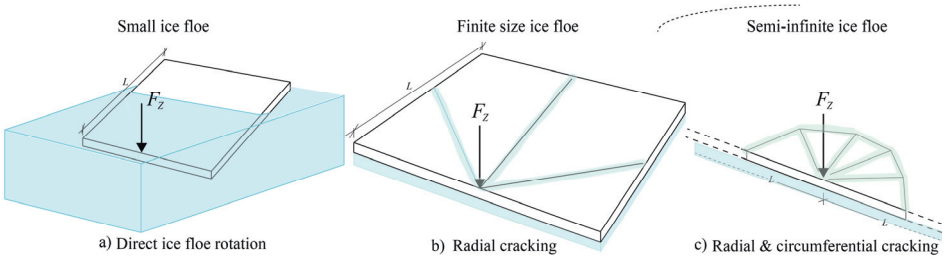

Fig. 2.9 Out-of-plane flexural failure scenarios of an ice floe of varying size.

It is well accepted in the research community that the flexural failure of an infinite thin plate on a Winkler-type elastic foundation involves the initiation of radial cracks and

subsequent circumferential crack formations. The same observation has also been made for level ice - sloping structure interactions. This scenario is illustrated in Fig. 2.9c, where the considered level ice is assumed as a semi-infinite ice floe. However, as the size of the ice floe reduces further, the free boundaries of an ice floe begin to influence the overall failure pattern. According to the bearing capacity tests conducted by Sodhi (1997), it was found that only radial cracks formed for a finite size ice floe with free boundaries. This scenario is illustrated in Fig. 2.9b. Lastly, it can be well imagined that a fairly small ice floe can simply be rotated without any material failure, as shown in Fig. 2.9a. Though no fracture is involved in this scenario, it is still treated as a type of 'out-of-plane flexural failures' because its occurrence often leads to a reduced vertical contact force F_Z.

Based on the identified three scenarios, the refined research questions surface as follows:

1) For a finite size ice floe, how do we quantify radial crack initiation and propagation separately?
2) Based on the quantification on Question #1, from an engineering application point of view, are we able to justify if the failure of a finite size ice floe is controlled by radial crack initiation or controlled by propagation?
3) Are we able to propose readily applicable analytical formulas for the three failure scenarios in Fig. 2.9?
4) What are the size borders among different failure scenarios in Fig. 2.9? e.g., how large should an ice floe be to be treated as level ice (i.e., a semi-infinite ice floe)?

2.4.3 Competition of different failure modes

In a relatively open ice field, i.e., a broken ice field with low ice concentration, there appears to be a competing mechanism between in-plane splitting failure and out-of-plane flexural failure. Both Fig. 1.2a and Fig. 2.8 illustrate this, i.e., the presence of the splitting failure mode alleviates the continuous local bending failure mode, and the structure can travel within the 'lead' created by the splitting crack.

These two failure modes are studied separately with varying floe sizes and contact properties. For application purposes, it is crucial to capture the dominant failure modes during the interaction to obtain a reasonable calculation of the ice load. To determine which failure mode dominates at certain conditions, such a competing mechanism must be quantified. With all the refined research questions in Sections 2.4.1 and 2.4.2 answered, we can therefore create a failure map that identifies the dominant failure mode with the given information (e.g., floes size, ice thickness, ice pressure, and contact properties).

2.5 Influences of rubble accumulation

Research questions raised in Section 2.4 focused primarily on the fracture of an ice floe. The main application of the study is a broken ice field composed of ice floes of varying

sizes. The competing mechanism mentioned in Section 2.4.3 is expected to occur only in a relatively open ice condition. However, in addition to this, it is also interesting and practically important to consider relatively 'tight' ice conditions, e.g., a large ice floe and a pressurised ice field. As the confinement over an ice floe's boundary increases, splitting failure is suppressed and continuous local bending failure begins to dominate.

The continuous local bending failure process generates a large amount of ice rubbles. In Section 2.1, the importance of rubble transportation in contributing to the global ice resistance was highlighted. Depending on the amount of ice rubbles and also the geometry of the sloping structure (e.g., wide or narrow sloping structure), the generated ice rubbles can either be effectively cleared or accumulated around the sloping structure. This thesis considers an extreme scenario: rubble accumulation without clearing. This topic has been pursued throughout history by experiments (Timco, 1991), numerical methods (Paavilainen and Tuhkuri, 2013; Paavilainen et al., 2010; Paavilainen et al., 2011) and analytical methods (Croasdale and Cammaert, 1994; Frederking and Timco, 1985; Ralston, 1980).

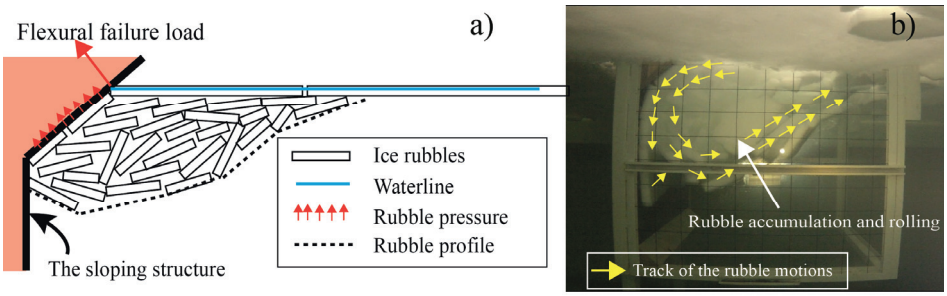

Fig. 2.10 2D model illustrating the ice - sloping structure interaction under the influences of rubble accumulation: a) theoretical model; b) physical model test.

In the current thesis, we developed a theoretical model composed of a series of analytical solutions to reconstruct different ice force components' temporal and spatial variations under the influence of rubble accumulation (see Fig. 2.10). The following refined questions will be addressed:

1) What and how much is rubble accumulation's effects on ice breaking and the rotating phase, respectively?
2) What are the spatial and temporal distributions of different force components on a sloping structure?

In addition, this thesis also explored the applicability of a numerical approach, the Cohesive Element Method (CEM), in simulating ice - sloping structure interactions with the presence of rubble accumulation (see Fig. 2.11). This method is promising in a sense that the fracture and fragmentation of ice can be simulated following the Cohesive Zone Method (CZM). However, the greatest challenge of this method is its convergence issue. This thesis evaluated the effectiveness of different numerical remedies that can be introduced to CEM-based simulations.

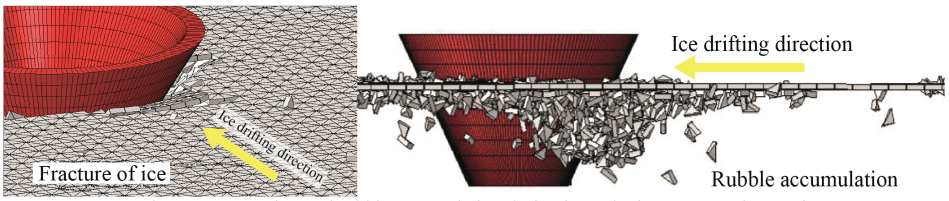

Fig. 2.11 Fracturing and rubble accumulation during ice - sloping structure interactions.

2.6 Detailed research contents and structure

The refined research questions raised in the previous sections were addressed in a systematic manner, as shown in Fig. 2.12.

During the floe ice - sloping structure interactions, this thesis studied two different failure modes: 'in-plane splitting failure (detailed study is presented in Appendix 1)' and 'out-of-plane flexural failure'. The out-of-plane flexural failure mode depends largely on the floe size. Three different scenarios were identified in Section 2.4.2 (a more detailed literature review is presented in Appendix 2). All three scenarios were studied and are described in Appendix 2 and Appendix 3.

After constructing the theoretical/numerical tools to evaluate different failure modes, this thesis quantified the competition between the in-plane and out-of-plane failure modes of an ice floe. A detailed study of this is presented in Appendix 3.

After studying the fracture of an ice floe with major application in a relatively open ice condition, the second part of the thesis shifts to a more severe ice condition, i.e., a 'tight' ice condition with dominant local bending failure and rubble accumulation. This condition is studied through a combination of a theoretical model analysis and physical model tests in Appendix 4. In addition, a numerical investigation towards a seemingly promising numerical method, i.e., the cohesive element method (CEM), was further explored in Appendix 5 to identify the influence of rubble accumulation during floe ice - sloping structure interactions.

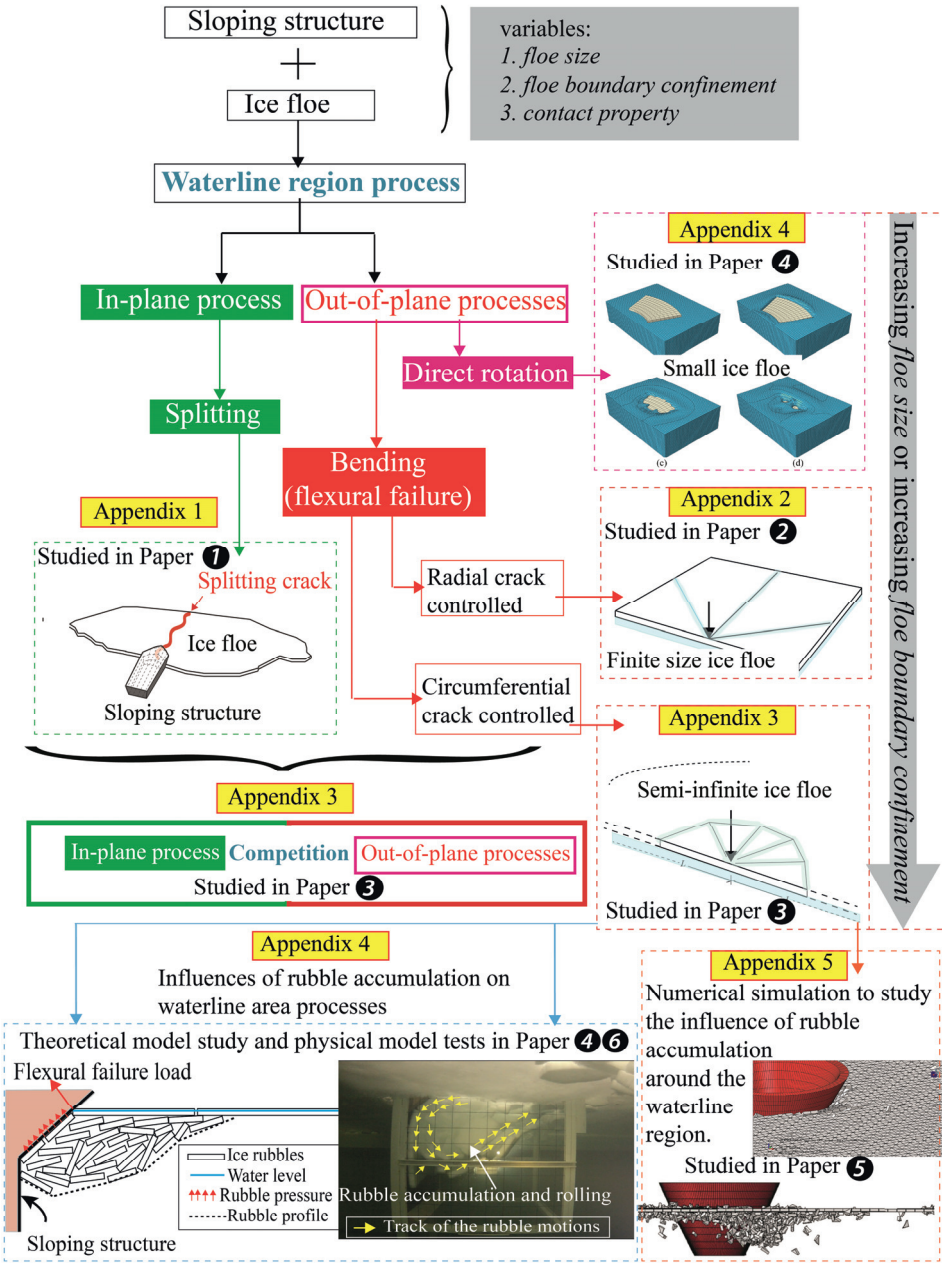

Fig. 2.12 Detailed research content and research structures.

Chapter 3 Methodologies

This thesis addresses primarily the fracture of an ice floe during its interaction with a sloping structure. Chapter 2 refined the initial research questions and sketched out the overall research structure. Those refined research questions were addressed individually by different methods. This chapter presents the key methods and fundamental assumptions that were used to determine the answers to each of the refined research questions.

3.1 Holistic model for the fracture of an ice floe

As a sloping structure (e.g., an icebreaker) impacts with an ice floe, as shown in Fig. 3.1(1) to (2), complicated stress field forms within the contact area. However, from a global perspective, three different contact force components can be isolated along with the global coordinate system (see Fig. 3.1(3)). These are a vertical force component F_Z, which leads to a potential out-of-plane flexural failure, a pair of horizontal loads F_Y, which lead to a potential in-plane splitting failure, and another in-plane force component F_X, which increases the compression within the ice floe. In reality, the actual failure patterns and failure loads are jointly affected by all these global force components and also the local stress field. As a simplification, this thesis decoupled all of these global force components and studied them separately.

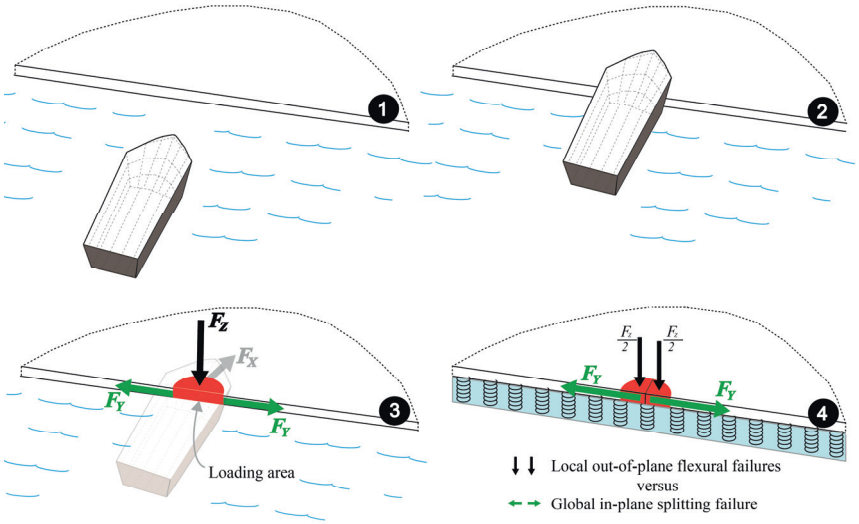

Fig. 3.1 Simplified global contact force and an ice floe's subsequent failures.

This thesis focuses on the force components F_Z and F_Y, which are considered the direct source for the dominant out-of-plane failure and in-plane failure separately. Their respective analytical solutions are pursued in this thesis; and highlights are also given to their potential competitions, as shown in Fig. 3.1(4).

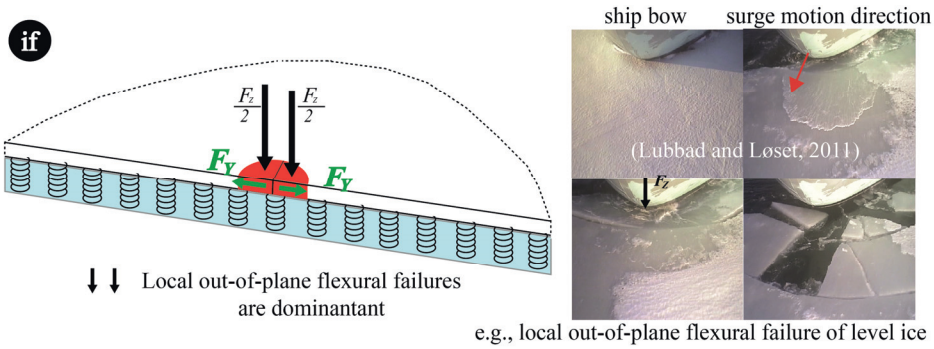

Fig. 3.2 Dominant local out-of-plane flexural failure.

If a sloping structure is interacting with a relatively large ice floe (e.g., level ice), an ice floe's lateral boundary confinement is significant or if the contact between the structure and the ice floe leads to a fairly large vertical force component, then the ice floe's dominant failure mode is expected to be a local out-of-plane flexural-type failure, as shown in Fig. 3.2. On the contrary, for a relatively small ice floe, a floe with limited/no lateral confinement or the contact property induces a large horizontal splitting load pair, the ice floe's dominant failure mode is expected to be a splitting failure mode, as shown in Fig. 3.3.

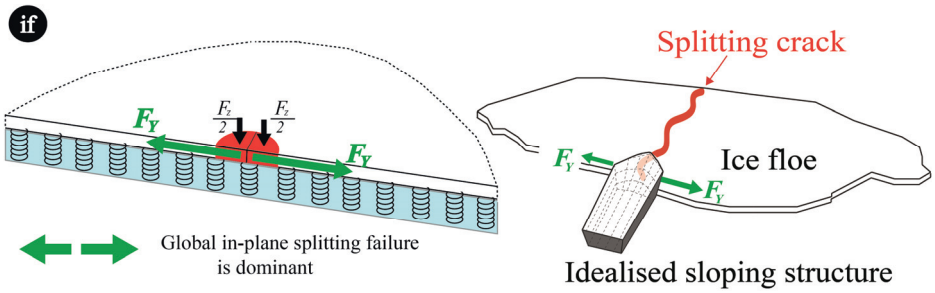

Fig. 3.3 Dominant global in-plane splitting failure.

This thesis is interested in studying the competition between these two dominant failure modes at the initial floe ice - sloping structure contact (see Fig. 3.1(4)), i.e., we are attempting to analytically and quantitatively answer the question: for which situation do the different failure modes occur? Because a decoupled approach was used, we will separately study these different failure modes with different methods and assumptions, which are presented in the following sections.

3.1.1 In-plane splitting failure mode: methods and assumptions

This section presents the methods and assumptions that were used to study the in-plane splitting failure of an ice floe (see Fig. 3.3). In the contact zone, besides the force component F_Y, all the other force components in Fig. 3.1(3) are neglected. The

theoretical model is thus reduced to the plots shown in Fig. 3.4 with the defined global coordinate system. In addition, two basic floe geometries (i.e., rectangular and circular ice floes, as shown in Fig. 3.4) are exemplified to demonstrate the calculation methods.

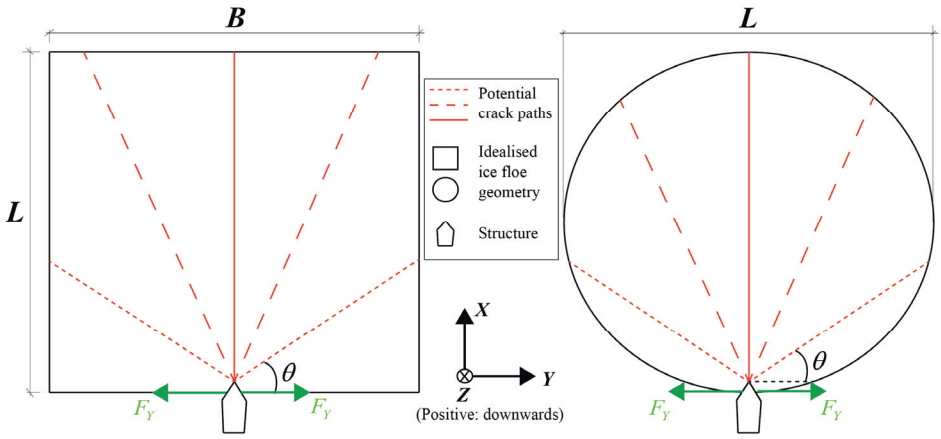

Fig. 3.4 Idealised theoretical model to study splitting failure of an ice floe with two basic geometries.

In reality, ice floes can be of arbitrary geometric shapes. The actual contact between a sloping structure and an ice floe further complicates this problem, and there are a number of relevant ice material parameters (e.g., temperature and brine volume) that influences the splitting process. Before presenting the detailed methods that were used, the following general assumptions were made:

- A static approach was adopted to analyse the splitting failure of an ice floe, i.e., the potential dynamic effect (e.g., stress wave propagation) within the ice floe is neglected;
- Two different approaches (i.e., plastic limit theory - based analysis and an approach based on fracture mechanics, see Fig. 3.5) were adopted to calculate the ice splitting load i.e., F_Y. These two approaches were assumed to be applicable for different scenarios, which will be introduced;
- The worst scenario, i.e., a head-on collision, is assumed following previous studies (Bhat, 1988). Therefore, the floe ice - sloping structure contact can be simplified to a certain extent, e.g., only a pair of equally opposite force components F_Y is considered in this contact scenario.

In addition, several specific assumptions are made for different methods, which will be subsequently presented.

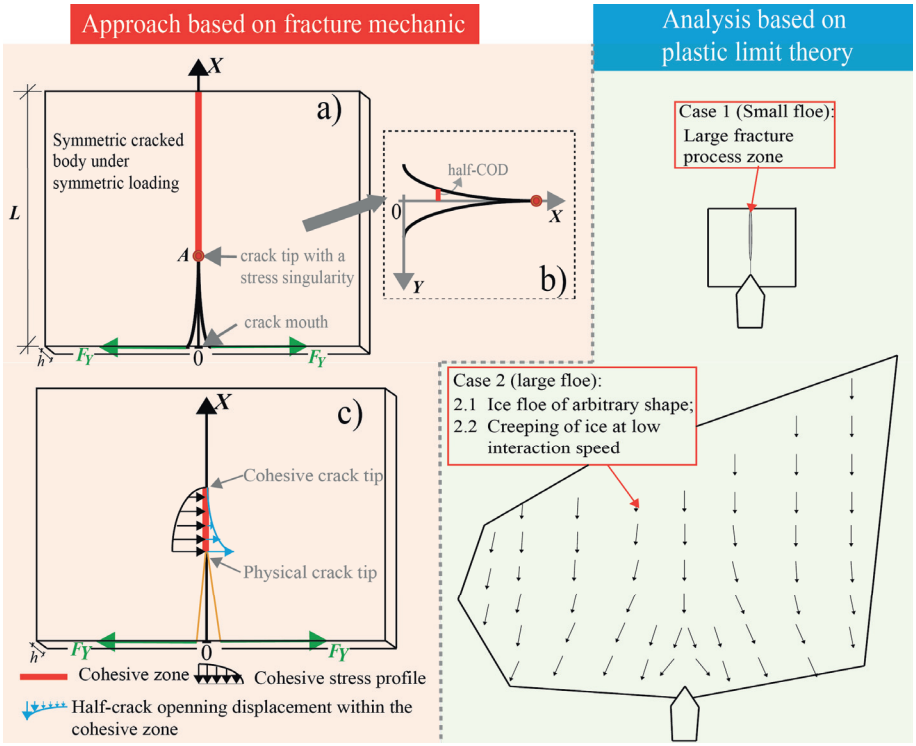

Fig. 3.5 Two approaches to calculate the ice splitting load F_Y.

3.1.1.1 Approach based on fracture mechanics

The approach based on fracture mechanics (see left side of Fig. 3.5) is the primary method that was studied in this thesis. Notably, the weight function method (Bueckner, 1970; Rice, 1972) can effectively calculate the Stress Intensity Factor (SIF) under different symmetric loadings on an elastic body and is therefore an ideal tool to study the influence of confinement on the boundaries of an ice floe. Additionally, it is beneficial to study the potential cohesive stress's contribution to the overall SIF. The principle of the weight function method brings additional assumptions that are necessary for our pursuit of analytical solutions in this section.

- In addition to the previous head-on collision assumption, the ice floe under consideration is assumed to be a symmetric body over the crack;
- It is further assumed that within such a symmetric body, the crack propagates in a self-similar manner;
- It was also assumed that the splitting crack propagates in a stable manner with varying crack lengths. This is questionable in the context of ice-structure interactions, i.e., a crack tends to propagate within ice in an uncontrolled manner partly due to the uncontrolled contact force between the structure and ice floe. However, by this assumption, we are able to construct the relationship between a

critical splitting load F_Y versus a given crack length, which enables us to determine the maximum load that is required to propagate a crack through an ice floe.

Before the study, it was unclear if Linear Elastic Fracture Mechanics (LEFM) is applicable for the current engineering application. Therefore, two different fracture mechanics-based methods were adopted: 1) LEFM (see Fig. 3.5a and b) and 2) the Cohesive Zone Method (CZM, a type of nonlinear fracture mechanics method, see Fig. 3.5c). These two methods shall be referred to as 'LEFM + weight function method' and 'CZM + weight function method' for brevity.

It is worth noting that the applicability of Linear Elastic Fracture Mechanics (LEFM) demands a Small-Scale Yielding (SSY) condition at the crack tip (see Fig. 3.5b). Mulmule and Dempsey (2000) proposed a size requirement (see Eq. (3.1)) for applying LEFM. Such a size requirement shall again be studied by the Cohesive Zone Method (CZM) as follows.

$$L \geq 12 l_{ch} \tag{3.1}$$

where l_{ch} is a characteristic length according to the CZM and is defined in Eq. (3.2).

$$l_{ch} = \frac{G_F E'}{\sigma_f{}^2} \tag{3.2}$$

in which,

E' $E' = E$ for plane stress conditions, and $E' = E/(1-\nu^2)$ for plane strain conditions (where E is Young's modulus and ν is the Poisson's ratio) [Pa]; and

σ_f is the flexural strength of the ice [Pa].

For the CZM, based on the 'viscoelastic fictitious crack model' developed and applied in previous studies (Dempsey et al., 1999a; Mulmule and Dempsey, 1998; Mulmule and Dempsey, 1999; Mulmule and Dempsey, 2000), a simplified version is implemented in the current study with the following additional assumptions:

- It is further assumed that the bulk material behaves elastically (i.e., no creeping effect within the bulk material);
- In addition, though a bilinear 'Traction and Separation Law (TSL)' has been derived in previous studies based on field tests (Dempsey et al., 1999a; Dempsey et al., 1999b), a linear TSL is further assumed in this study. Such a simplification enables us to reduce the initial CZM-based analysis into an effective eigenvalue analysis (please refer to Appendix 1 for detailed derivations and formulations).

Eventually, the following formulae were derived to calculate the ice splitting load F_Y:

Method #1: LEFM + weight function method:

$$\frac{F_Y(\alpha)}{hK_{IC}\sqrt{L}} = \frac{1}{H(\alpha,0)} \tag{3.3}$$

in which,

$F_Y(\alpha)$ is the ice splitting load with a normalised crack length $\alpha = A/L$;
A is the crack length, as shown in Fig. 3.5a;
h is the ice floe thickness;
K_{IC} is the fracture toughness of sea ice;
$H(\alpha,0)$ is a weight function for the cracked body with the splitting load acting at the crack mouth, as shown in Fig. 3.5a and c.

Eq. (3.3) explicitly illustrates that the ice splitting load $F_Y(\alpha)$ is scaled with the square root of the floe size $\sqrt{L}$, i.e., $F_Y(\alpha) \propto \sqrt{L}$. In terms of the influence of the confinement, assuming an ice floe is under the influence of symmetric confinement along its boundaries, the ice splitting load can be calculate using Eq. (3.4).

$$\frac{F_Y(\alpha)}{hK_{IC}\sqrt{L}} = \frac{1}{H(\alpha,0)}[1+\frac{\int_0^A p_{\text{ext}}(X)H(A,X)\,\mathrm{d}X}{K_{IC}}] \tag{3.4}$$

As shown in Eq. (3.4), there is an additional term $\int_0^A p_{\text{ext}}(X)H(A,X)\,\mathrm{d}X / K_{IC}$, which represents an additional stress intensity factor introduced by the confinement $p_{\text{ext}}(X)$ (note that a positive value represents compression). This terms must be overcome by increasing the ice splitting load $F_Y(\alpha)$.

Method #2: CZM + weight function method:

$$F_Y(A) = (u_c E' h)\frac{\int_B^A \sigma_{\text{coh}}(X)\,\mathrm{d}X}{\int_B^A \sigma_{\text{coh}}(X)U(A,X,0)\,\mathrm{d}X} \tag{3.5}$$

in which,

$F_Y(A)$ is the ice splitting load of an ice floe with crack length A;
u_c is the critical half Crack Opening Displacement (COD);
$U(A,X,0)$ is a function defined by Eq. (3.6).

$$U(A,X,S) = \int_{\max(X,S)}^{A} H(a,X)H(a,S)\,\mathrm{d}a \tag{3.6}$$

Eq. (3.5) is not written in a normalised form as that in Eq. (3.4) because it has a nonlinear size effect influenced by the cohesive stress distribution $\sigma_{\text{coh}}(X)$, which is the eigenvector of $U(A,X,0)$; it can be obtained by solving an eigenvalue problem (detailed derivation and formulations can be found in Appendix 1).

3.1.1.2 Analysis based on plastic limit theory

As a complementary approach to obtain analytical solutions to the ice floe's splitting failure, the plastic limit theory (Chen and Han, 1988) was also implemented for the current engineering application. This method is primarily used for two different cases because analytical solutions become difficult for the method based on fracture mechanics: 1) when the ice floe is too small and becomes comparable to the size of the cohesive zone (see Case 1 on the right side of Fig. 3.5), then the plastic limit analysis can serve as a simplified alternative to approximate the ice splitting load F_Y; 2) for irregular ice floe geometries or if the interaction speed is insignificant[3], the plastic limit analysis can serve as a convenient alternative to extract the upper limit of F_Y for engineering application purposes.

While implementing the plastic limit theories, the already established anisotropic parabolic yield function (Ralston, 1981; Reinicke and Ralston, 1977) can be used. Because this method is a complementary tool, detailed formulations are not presented herein. Following the interaction scenario, as illustrated in Fig. 3.4, relevant derivations and formulae were developed in Appendix 1 together with explicit formulae to calculate the relevant material constants.

3.1.2 Out-of-plane flexural failure: methods and assumptions

After studying the splitting failure mode, this section focuses on the out-of-plane flexural failure of an ice floe as depicted in Fig. 3.2. Under the predominant vertical force F_Z shown in Fig. 3.2, Fig. 2.9 illustrate that three different scenarios can be expected for a nearly square-shaped ice floe.

Among these three different failure modes, the major focus is on the second scenario, i.e., out-of-plane flexural failure of a finite size ice floe, simply because it has rarely been studied. According to the study of the bearing capacity of an infinite and semi-infinite ice floe, it is well accepted by the research community that the force in the vertical direction (i.e., $Z-$direction) required to initiate radial cracks is much less than that for the formation of circumferential cracks. Furthermore, Sodhi's (1997) test shed light on such a rarely studied failure scenario: radial cracking of an ice floe with free edges. Therefore, it is of theoretical interest to identify the floe size, smaller than which, an ice floe fails by forming only radial cracks. There is a practical interest for such a failure mode. In an ice management operation, the question regarding the target floe size to be produced downstream where the protected vessel/structure is located often arises. The study on the size requirement for radial cracking-type failure would give a mechanically preferred answer to this practical question.

[3] Unfortunately, we are unable to quantify what is 'insignificant' under this context. It is well accepted that a uniaxial compression strain rate below 10^{-3} leads to ductile behaviour of ice material (e.g., (Duval and Schulson, 2009)). However, this strain rate is difficult to be related to the interaction speed between a structure and an ice floe, which is primarily because the presence of non-simultaneous contact (Sanderson, 1988). This case is only presented here for theoretical completeness purposes.

Radial cracking of an ice floe was explored in a two-step approach. First, this thesis studied the radial crack initiation and propagation within a square-shaped ice floe. Based on the study, this thesis constructed the theoretical framework to identify the so-called 'radial-crack-initiation-controlled fracture of an ice floe' and its pertinent size requirement (presented in Section 3.1.2.1; details in Appendix 2). Second, the obtained results regarding the square-shaped ice floe are further extended to finite size rectangular ice floes with arbitrary width-to-length ratios; and analytical solutions are pursued for this type of failure mode, i.e., out-of-plane flexural failure of a finite size ice floe (presented in Section 3.1.2.2; details in Appendix 3).

3.1.2.1 Theoretical and numerical study of radial crack initiation and propagation within a square ice floe

In both cases, the considered ice floe is assumed to be a thin plate on a Winkler-type elastic foundation. Similar theoretical models were used to study radial crack initiation and propagation in Fig. 3.6a and b, respectively.

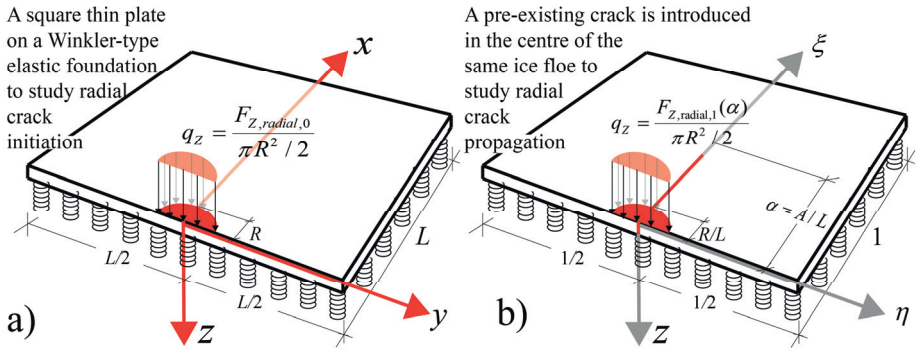

Fig. 3.6 Two theoretical models used to study: a) radial initiation and b) radial crack propagation.

Fig. 3.6a represents the radial crack initiation problem, where the crack initiation froce $F_{Z,radial,0}$ is assumed to be evenly applied within the half circular area as pressure q_z. The radial crack propagation problem illustrated in Fig. 3.6b is essentially the same model as in Fig. 3.6a, except that a pre-existing crack is introduced to study the required force $F_{Z,radial,1}(\alpha)$ to propagate a crack with varying lengths A. In addition, the following assumptions were made for the current theoretical study:

- The thin plate theory was assumed to be valid herein. According to the estimation of a floating ice floe's characteristic length[4] ℓ by Gold (1971) and also the thin plate theory requirement (Ventsel and Krauthammer, 2001), the current study is approximately suitable for ice floes with thicknesses less than 3.32 m;
- The considered ice floe is composed of homogeneous isotropic linear elastic ice material. Further discussions regarding such 'bold' assumptions are presented in

[4] Detailed formulation is presented in Eq. (3.10)

Appendix 2. However, for the current application, such a 'bold' assumption is reasonable for anisotropic columnar ice material;
- It is further assumed that the principle of superposition can be applied to the current problem;
- Any dynamic effect from the ice floe or from the fluid foundation is neglected. It is cautioned here that this assumption can be rather crude at high interaction speed as the hydrodynamic effect becomes important (Dempsey and Zhao, 1993; Lu et al., 2012b; Lubbad et al., 2008);
- In addition, only the flexural-type failure is considered in this study. Other types of out-of-plane failures, i.e., shear plug (ISO/FDIS/19906, 2010, p. 251), are not considered.

For the radial crack propagation study, several additional assumptions were made:
- It is assumed that LEFM is applicable to the current problem;
- The minimum length of the pre-existing crack is assumed to be $\alpha_0 = R/L$ (see Fig. 3.7b and c);
- Similar to the assumption made in Section 3.1.1.1, a stable radial crack propagation scenario is assumed. Though this is generally not the case for ice material (DeFranco and Dempsey, 1994), this assumption enables us to extract the maximum force required to sustain a radial crack at given length. Additionally, the radial crack is assumed to propagate in a self-similar manner.

Based on the above assumptions and the selected mathematical model shown in Fig. 3.6, the controlling Partial Differential Equations (PDE) of a plate bending problem can be formulated. Notably, in both problems, a normalisation procedure is implemented to simplify the following numerical models and to obtain universal results. The original PDE is normalised over the physical length L of the ice floe. Before the normalisation procedure, Fig. 3.6a illustrates the original size of the ice floe ($L \times L$) and the loading area (i.e., half circular area with radius R) in an x, y, and z coordinate system. Fig. 3.6b exemplifies the post-normalisation problem with the new coordinates, $\xi = x/L$, $\eta = y/L$, and z.

After the normalisation procedure, the control PDE of the two problems were formulated into non-dimensional form in Eq. (3.7).

$$\nabla^4 W(\xi,\eta) + KW(\xi,\eta) = \delta(\xi - \xi_*)\delta(\eta - \eta_*) \tag{3.7}$$

in which,

ξ_* and η_* are the location where an equivalent point load (i.e., equivalent to the distributed pressure q_z within the contact area) is acting (see details in Appendix 2);

$\nabla^4(\,) = \frac{\partial^4}{\partial\xi^4} + 2\frac{\partial^4}{\partial\xi^2\partial\eta^2} + \frac{\partial^4}{\partial\eta^4}$ is the biharmonic operator in the new coordinate system ξ, η, and z;

$\delta(x)$ is the Dirac delta function. Its unit is the inverse of its argument.

Particularly, a normalised deflection $W(\xi,\eta)$ and a normalised foundation modulus K are defined in Eqs. (3.8) and (3.9), respectively.

$$W(\xi,\eta)=\frac{w_{total}(\xi,\eta)D}{F_Z L^2} \tag{3.8}$$

$$K=\frac{kL^4}{D} \tag{3.9}$$

in which,

$w_{total}(\xi,\eta)$ is the deflection of an ice floe at point (ξ,η);

$D=\frac{Eh^3}{12(1-\nu^2)}$ is the flexural rigidity of a plate;

There are two length scales within Eq. (3.7). One is the physical length of the ice floe L, and the other is the characteristic length ℓ as defined in Eq. (3.10). These two length scales were incorporated into the normalised foundation modulus K. Here, it is convenient to define a coefficient number n in Eq. (3.11), which denotes the ratio of floe size and characteristic length.

$$\ell=\sqrt[4]{\frac{D}{k}} \tag{3.10}$$

in which,

k is the foundation modulus. For the fluid base, $k=\rho_w g$, with ρ_w and g being the fluid density and gravitational acceleration, respectively.

$$n=\frac{L}{\ell}=\sqrt[4]{K} \tag{3.11}$$

Solutions of Eq. (3.7) were studied numerically with FEM simulations by assigning different boundary conditions. Two different numerical set-ups are illustrated in Fig. 3.7, among which, Fig. 3.7a was used to study radial crack initiation; and Fig. 3.7b and c were used to study radial crack propagations. Symmetric boundary conditions (i.e., the yellow line) were implemented to improve computational efficiency. Additionally, fairly dense meshes were implemented in the loading area and the location of the crack tip. Fig. 3.7 demonstrates the biased mesh pattern.

The numerical set-up was implemented with Python script and calculated by ABAQUS 6.13/STANDARD solver. For the radial crack initiation problem shown in Fig. 3.7a, the major variable is the normalised foundation modulus K, which reflects the physical size of an ice floe. For the radial crack propagation problem, an additional variable must be studied, i.e., the relative radial crack length α_i. Fig. 3.7b and c demonstrate two simulations with the crack length changing from α_1 to α_2 with an exaggerated

increment of $\Delta\alpha$. The actual crack length varies from $\alpha = \alpha_0$ to $\alpha = 0.8$ (i.e., 80% of the floe size) with a small crack increment. Using an energy approach (Irwin, 1956), the corresponding radial crack propagation load $F_{Z,\text{radial},1}(\alpha)$ can be numerically calculated (see a detailed formulation in Appendix 2).

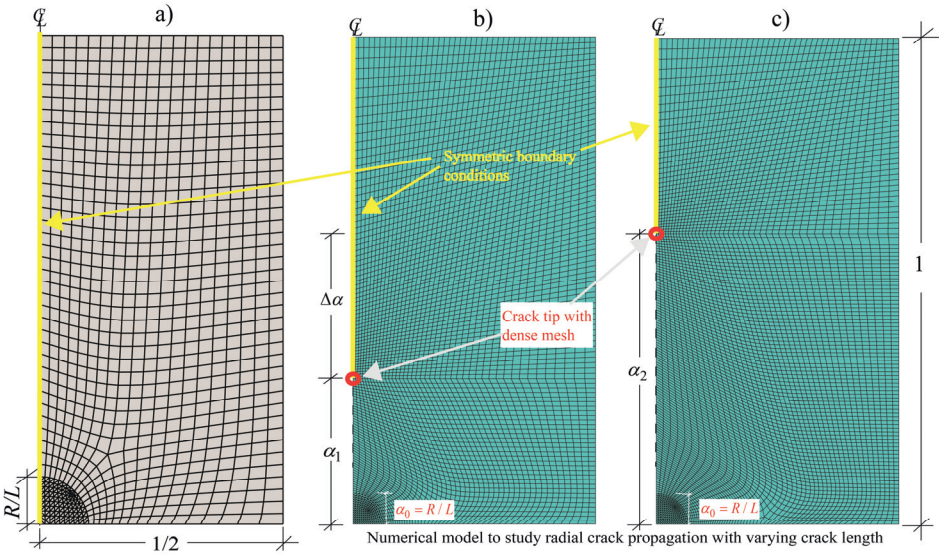

Fig. 3.7 Two different numerical set-ups to study: a) radial crack initiation; and b) and c) radial crack propagation with varying crack lengths.

Before calculating the results of the radial crack initiation load $F_{Z,radial,0}$ and propagation load $F_{Z,\text{radial},1}(\alpha)$, relevant benchmark tests were conducted to verify the validity of the numerical set-ups in Fig. 3.7. Using the knowledge of calculating $F_{Z,radial,0}$ and $F_{Z,\text{radial},1}(\alpha)$, we were able to distinguish radial-crack-initiation-controlled fracture of ice floes of varying sizes. Relevant benchmark test and the analysis results will be presented in Chapter 4.

3.1.2.2 Analytical solutions of out-of-plane failures of a rectangular ice floe

Numerical studies conducted in Section 3.1.2.1 enable us to identify square-shaped ice floes whose failure is largely influenced by its boundaries. Radial-crack-initiation-controlled fracture is one of such type (see Fig. 2.9b). The crack can 'feel' the free boundaries and propagate through the entire body of an ice floe before any circumferential crack forms. As an extension of the numerical studies in Section 3.1.2.1, this section strives to obtain analytical solutions to calculate the failure load of arbitrary rectangular ice floes, whose failure is significantly influenced by their free boundaries.

Based on the study in Section 3.1.2.1, it is found that (to be presented in Chapter 4) for a square-shaped ice floe whose physical size $L \le 2\ell$, its failure is controlled by radial

crack initiation. In this section, this finding for a square-shaped ice floe is extended to a rectangular ice floe with arbitrary width-to-length ratios, i.e., wide and long ice floes shown in Fig. 3.8b and c. In both scenarios, either the width or the length of the considered floe is less than 2ℓ and their respective failure is highly influenced by their free boundaries. Wide ice floes with lengths less than 2ℓ and long ice floes with widths less than 2ℓ are assumed to fail at radial crack initiations and circumferential crack initiations, respectively. Analytical solution towards the out-of-plane flexural failure of a finite size ice floe (i.e., with either length or width less than 2ℓ) are pursued in this section.

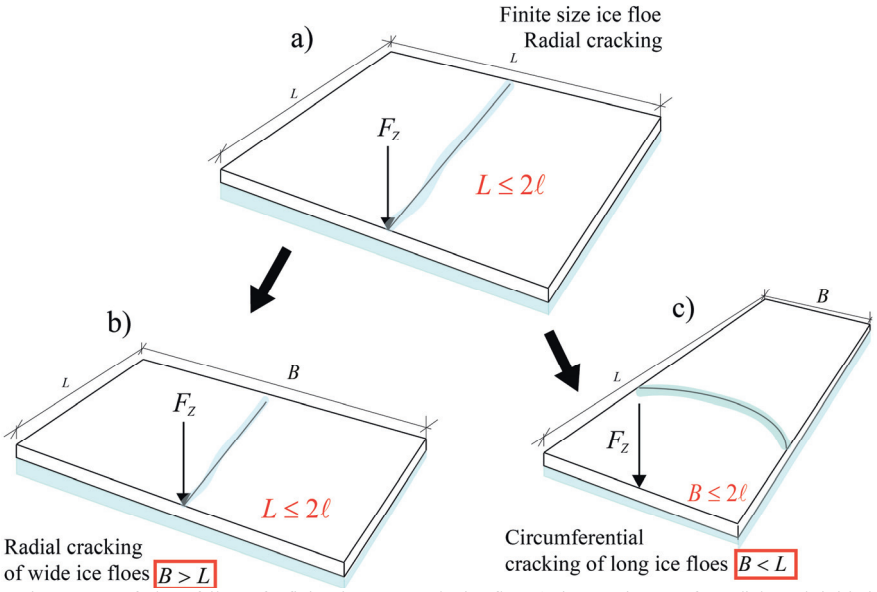

Fig. 3.8 Out-of-plane failure of a finite size rectangular ice floe: a) size requirement for radial-crack-initiation controlled fracture of a square-shaped ice floe; b) radial cracking of a wide ice floe; and c) circumferential cracking of a long ice floe.

A recently published methodology (Li et al., 2013) was used in the current study to determine the failure scenarios of a rectangular ice floe in Fig. 3.8. The same theoretical model shown in Fig. 3.6a, i.e., a thin plate on a Winkler-type elastic foundation, was assumed, though with a different coordinate system, as shown in Fig. 3.9. In addition, for simplicity, this study considers a concentrated load F_z acting at a location $x = x_0, y = y_0$. The same normalisation procedure as described in Section 3.1.2.1 was implemented to transform the original coordinate system x, y, and z in Fig. 3.9 into $\xi = x/L$, $\eta = y/L$, $\beta = B/L$, and z, as shown in Fig. 3.10a.

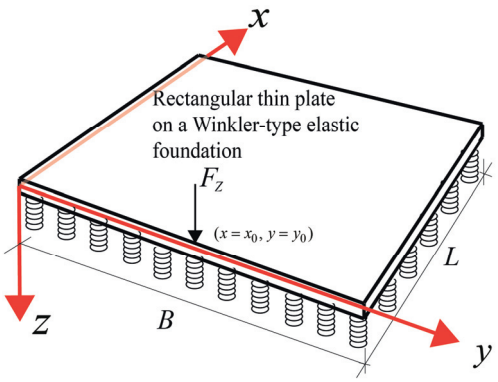

Fig. 3.9 Theoretical model to obtain an analytical solution of a rectangular plate under a concentrated load.

The analytical solution offered by the literature (Li et al., 2013) consists of the plate bending theory with a symplectic elasticity approach (Yao et al., 2009) and a superposition procedure. The solutions of three different boundary conditions on a rectangular plate were summed to yield the final free boundary conditions (see Fig. 3.10b, c, and d), which are the following:

1) All four boundaries of the rectangular plate are slidingly clamped, i.e., after the deformation, the slope and the shear force is 0 along all four boundaries. Corresponding formulae for the boundary conditions can be found in Appendix 3;
2) Gradually, the first two opposite sides (i.e., $\eta = 0,$ and $\eta = \beta$) of the rectangular plate is applied with a rotation angle, which can nullify the moment build-up in boundary condition (BC) 1;
3) Afterwards, the last two opposite sides (i.e., $\xi = 0,$ and $\xi = 1$) were also applied with the corresponding rotation angle to nullify their moment induced by boundary condition (BC) 1.

The eventual solutions (i.e., Fig. 3.10a) is superposed by the three solutions with different boundary conditions. The detailed formulation from an application point of view can be found in Appendix 3, and the detailed derivations can be found in the original literature (Li et al., 2013).

This method results in fairly accurate analytical solutions to the plate's flexural deflection W in Eq. (3.12).

$$W = W_1 + W_2 + W_3 \tag{3.12}$$

where $W_1, W_2,$ and W_3 are the solutions to the problems with three different boundary conditions of Fig. 3.10b, c, and d, respectively. Their explicit expression can be found in the original literature (Li et al., 2013).

However, difficulties arise in the stress calculations by this method. At first, the stress under a concentrated load is predicted as infinite by this analytical solution; in addition,

this method's stress calculation accuracy reduces when applied to small ice floes (i.e., a plate with a relatively small foundation modulus). Therefore, a pragmatic idealisation was eventually made in applying this analytical solution:

- The failure of an ice floe is assumed to be displacement controlled instead of material-strength controlled. An ice floe is assumed to fail once its maximum displacement (occurring beneath the loading point) exceeds the freeboard $w_{flood} = (1-\rho_i/\rho_w)h$ of an ice floe. This is a fairly conservative assumption to obtain the critical vertical force $F_{z\_radial/circumferential\_cracking}$ required to fracture an ice floe.

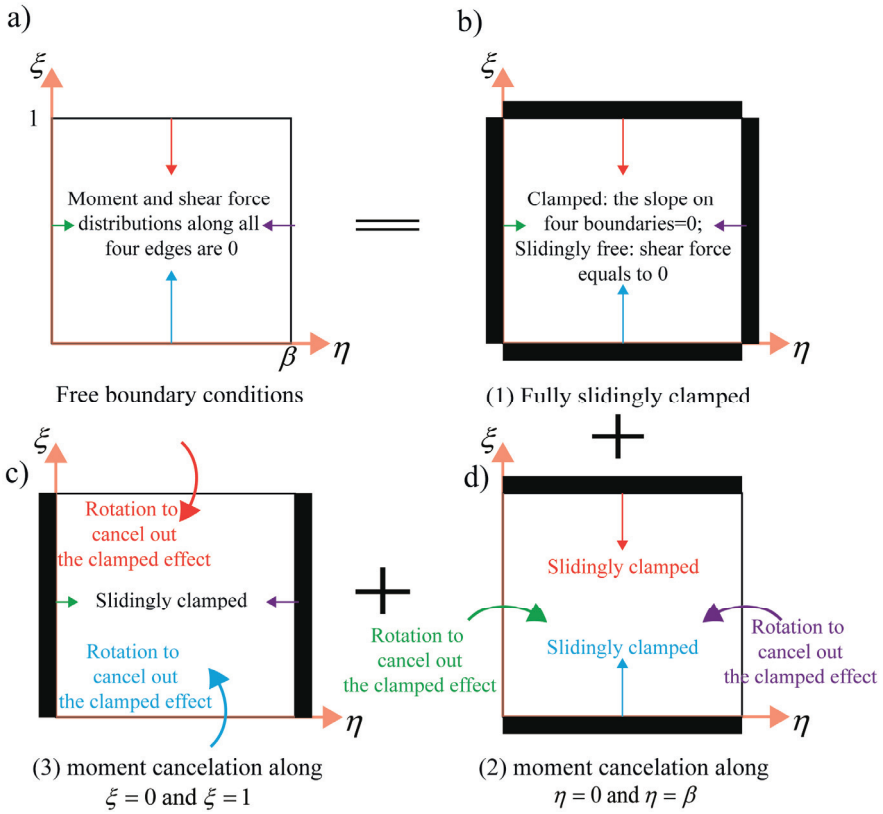

Fig. 3.10 Superstitions of three different boundary conditions to obtain analytical solutions of a free-floating rectangular ice floe.

Recalling the definition of the normalised deflection W in Eq. (3.8), replacing the maximum deflection w_{flood} in this equation, the following Eq. (3.13) can be obtained.

$$W = \frac{w_{flood} D}{F_{z\_radial/circumferential\_cracking} L^2} = \frac{D}{F_{z\_radial/circumferential\_cracking} L^2}(1-\frac{\rho_i}{\rho_w})h \qquad (3.13)$$

where ρ_i is the ice density. With the symplectic approach, W is analytically solvable with Eq. (3.12). Thus, the critical force for the failure pattern in Fig. 3.8b and c can be conservatively derived in Eq. (3.14), based on the assumed maximum deflection criterion.

$$F_{z\_radial/circumferential\_cracking} = \frac{D}{WL^2}(1-\frac{\rho_i}{\rho_w})h \tag{3.14}$$

In addition, all the assumptions that have been made to study radial crack initiation in Section 3.1.2.1 were also used herein.

Afterwards, additional analytical solutions to solve the direct rotation of a small ice floe in Fig. 2.9a and circumferential crack formation within a semi-infinite ice floe in Fig. 2.9c are studied in the following.

3.1.2.3 Direct rotation and circumferential crack formation

With regard to the analytical formulae to calculate the direct rotation of a small ice floe in Fig. 2.9a and the circumferential crack formation within a semi-infinite ice floe in Fig. 2.9c, no further contribution was made in this thesis. This thesis has simply compiled and adopted previous research results.

In Section 3.1.2.2, a displacement controlled method was used to determine the failure of an ice floe in Fig. 2.9b. For the direct rotation of an ice floe, the same freeboard displacement controlled (see Fig. 3.11) must be used by definition (i.e., no material failures). The formulation here for the direction rotation is considered to be a situation in which thin plate theories are not applicable. In this sense, the size of an ice floe that fails at direct rotation is approximately $L \leq \ell$. For such a small ice floe, simplified analytical solution can be obtained by using previously available knowledge, particularly relevant theories regarding a 'beam on elastic foundation' (Hetényi, 1946). The following assumptions are made to apply the relevant theories:

- The current problem can be described by the two-dimensional (2D) theory of a finite beam on a Winkler-type elastic foundation (Hetényi, 1946);
- To apply short beam theory, it is assumed that the width $B \leq \ell$, such that the deflection in the width direction can be neglected, and a 2D treatment is applicable. The case when $B > \ell$ will be studied with the theory introduced in Section 3.1.2.2 and with Eq. (3.14);
- It is assumed that once the freeboard is below the waterline, the required rotation force $F_{Z\_direct\_rotation}$ begins to decrease. The potential ventilation effect, which increases the ice rotating load (Lu et al., 2014b; Lu et al., 2013; Valanto, 2001b), is not considered herein.

Based on the above assumptions and floe size consideration, short beam theory (Hetényi, 1946, p. 46) can be applied here to further neglect the flexural deformation of the considered ice floe. In a previous study regarding the 'ice rotating phase' in

reference (Lu et al., 2014b), the same short beam theory was applied under similar assumptions. Based on similar derivations, Eq. (3.15) is obtained to calculate the vertical force $F_{Z\_direct\_rotation}$ that leads to the direct rotation of a small ice floe.

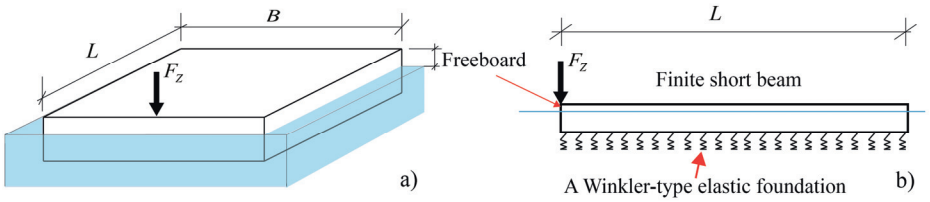

Fig. 3.11 Theoretical model for the direct rotation of a small ice floe.

$$F_{Z\_direct\_rotation} = \frac{1}{4} w_{flood} \rho_w g B L = (1 - \frac{\rho_i}{\rho_w}) \frac{h}{4} \rho_w g B L \tag{3.15}$$

In terms of the circumferential crack formation, following previous studies and applications, it is simply assumed that a semi-infinite ice floe is composed of several equally sized wedge beams. Thus the analytical solutions of Nevel (Nevel, 1958; Nevel, 1961) can be applied. However, a simplified version is adopted in the current analysis, which is an approximate formula given by Eq. (3.16) (according to equation (1) in Nevel (1972)).

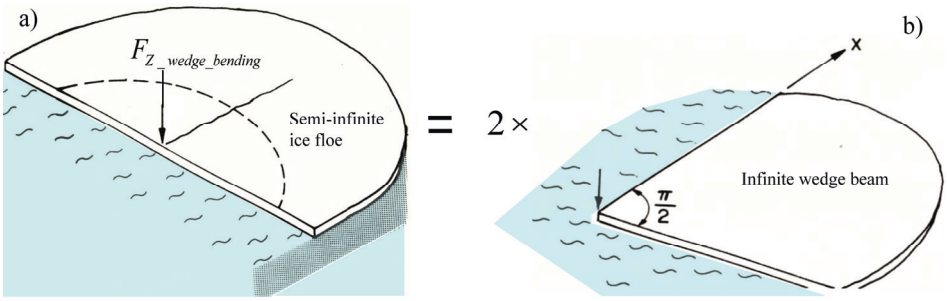

Fig. 3.12 Failure of a semi-infinite ice floe by forming two independent 'infinite wedge beams' (after Kerr (1976))

$$F_{Z\_wedge\_bending} = \frac{2m}{6} \tan(\frac{\pi}{2m}) \sigma_f h^2 [1.05 + 2.0(\frac{R}{\ell}) + 0.50(\frac{R}{\ell})^3] \tag{3.16}$$

where m is the number of wedge beams produced within a semi-infinite ice floe while a circumferential crack forms. Note here that the coefficient $(2m/6)\tan(\pi/(2m))$ is a monotonically decreasing function and converges to the value $(\pi/6)$ as $m \to \infty$. According to the out-of-plane flexural failure pattern description regarding a semi-infinite ice floe (Kerr, 1976) (see Fig. 3.12a or referring to the literature review in Appendix 2), m exhibits a small value. To be conservative and also to be consistent with the experimental description according to Kerr (1976), $m = 2$ is assumed in Eq.

(3.16) and illustrated in Fig. 3.12b. Thus, the following Eq. (3.17) is obtained to conveniently calculate the critical vertical force $F_{Z\_wedge\_bending}$ to initiate circumferential cracks in a semi-infinite ice floe, as shown in Fig. 3.12.

$$F_{Z\_wedge\_bending} = \frac{2}{3}\sigma_f h^2 [1.05 + 2.0(\frac{R}{\ell}) + 0.50(\frac{R}{\ell})^3] \tag{3.17}$$

3.1.3 Competition between different failure modes

In the preceding sections, the relevant formulae to calculate the ice splitting load F_Y were presented in Eqs. (3.3) to (3.5), and the different vertical force components $F_{Z\_direct\_rotation}$, $F_{z\_radial/circumferential\_cracking}$, and $F_{Z\_wedge\_bending}$ were presented in Eqs. (3.15), (3.14) and (3.17) that correspond to the failure scenarios in Fig. 2.9a, b, and c, respectively. Thereafter, key formulae were further validated using either numerical results, experimental measurements or both. The verification shall be presented in Chapter 4. After the verification process, these formulae are used to quantify the competition and identify the boundaries among different failure modes, which is the focus of this section.

The rationale behind 'quantifying the competition' is rather straightforward. After the corresponding failure loads of different failure modes are calculated, this thesis assumes that an ice floe will fail with the smallest failure load, i.e., the failure mode is determined by the smallest value of F_Y and various comparable vertical force components ($F_{Z\_direct\_rotation}$, $F_{z\_radial/circumferential\_cracking}$, and $F_{Z\_wedge\_bending}$).

However, it should be noted that the ice splitting load F_Y acts in the horizontal direction, whereas the vertical force components act in the Z-direction. To ensure these different force components can be compared, contact properties should be introduced. The contact property between an ice floe and a sloping structure is largely idealised in this thesis. Firstly, we neglect the complicated stress field within the loading area, as shown in Fig. 3.1(3). Instead, only the force components in the global coordinate direction are considered. Secondly, the subsequent failure mode of an ice floe is assumed to be independently influenced by their corresponding force component, i.e., these force components are decoupled. Lastly, these different force components (i.e., F_Y and F_Z) are related through simple load ratio relationships. Contact force decomposition in different directions (i.e., X, Y, and Z) depends largely on the contact geometry. For generality purposes, without delving into contact mechanics to analyse the stress distribution within the contact zone for specific structure geometries, we circumvent this problem by assuming a series of deterministic load ratios (i.e., β_{XY}, β_{XZ}, and β_{YZ}) in different directions, as shown in Eq. (3.18).

$$\begin{aligned}\beta_{YX} &= \frac{F_Y}{F_X};\\ \beta_{XZ} &= \frac{F_X}{F_Z};\\ \beta_{YZ} &= \beta_{YX}\beta_{XZ} = \frac{F_Y}{F_Z};\end{aligned} \tag{3.18}$$

where the definitions of different force components are shown in Fig. 3.1. The load ratios can be theoretically extracted for a given contact scenario based on contact mechanics or simple geometric overlapping analysis (Lubbad and Løset, 2011; Su et al., 2010). However, this is beyond the scope of the current thesis. As a further simplification and for quantitative comparison purpose, we simply chose $\beta_{YZ} = 0.5$ in most of the quantitative comparison results, which will be presented in Section 4.1.4. However, it is worth mentioning that such specific simplifications do not violate the generality of the developed theory.

3.2 Level ice - wide sloping structure interactions with rubble accumulation

After studying fracturing of an ice floe in Section 3.1, the 'floe ice - sloping structure interaction' is further studied in a 'tight' ice condition by incorporating the effect from rubble accumulation. This topic is studied in a 2D setting (i.e., a wide sloping structure) by two parallel approaches, namely, a physical model study and a theoretical model study.

3.2.1 Theoretical model development

Based on previous studies (referring to the state-of-the-art review in Section 2.1) and also based on field and laboratory tests observations (see the literature review in Appendix 4), the interaction mechanism between level ice and a wide sloping structure under the influence of rubble accumulation is proposed, as shown in Fig. 3.13. Two sequential procedures were identified in this interaction mechanism, i.e., the ice breaking procedure in Fig. 3.13a and the ice rotating procedure in Fig. 3.13b.

Depending on the amount of rubble accumulation, the two procedures were further refined. For the ice breaking procedure shown in Fig. 3.13a with little rubble accumulation, the incoming level ice fails directly against the sloping structure, which is termed as the 'Phase 1 ice breaking process' in Fig. 3.13(1). However, as more rubble accumulates in front of the structure, it is possible that the incoming ice fails against the packed rubble; this is termed as the Phase 2 ice breaking process in Fig. 3.13(4).

In terms of the ice rotating process, it has been noticed in field observation (see Appendix 4) that possible secondary ice breaking can occur, which has also been confirmed theoretically (Lu et al., 2013) by considering the influence of rubble accumulations. Therefore, the possibility of secondary ice breaking is also included in the current theoretical model development, as shown in Fig. 3.13(3).

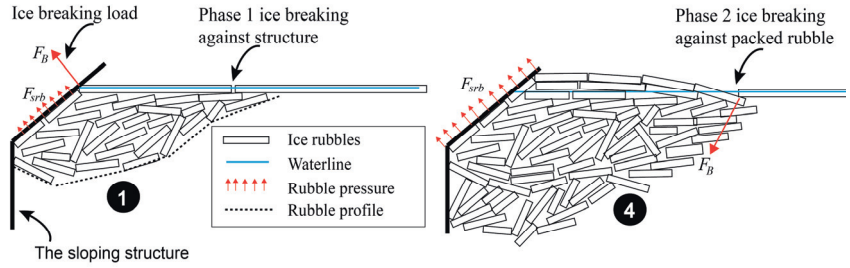

a) Ice breaking procedure, Phase 1(left) and Phase 2 (right)

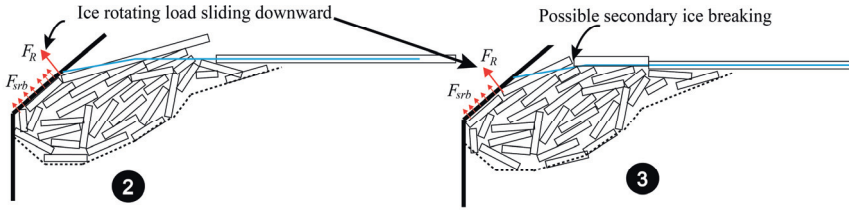

b) Ice rotating procedure, initial rotation(left) and rotation with secondary breaking (right)

Fig. 3.13 The proposed interaction mechanism between level ice and a wide sloping structure under the influence of rubble accumulation.

Based on the assumed interaction mechanism in Fig. 3.13, the theoretical model is constructed in the time domain in Fig. 3.14. This theoretical model is composed of three different modules, namely the ice breaking module, ice rotating module and rubble accumulation module. Fig. 3.14 illustrates the inputs and outputs of this theoretical model together with its temporal construction method, i.e., the ice breaking module and ice rotating module is activated consecutively together with an increasing rubble accumulation volume as different modules' boundary conditions.

While developing analytical formulae to each module, the following theoretical assumptions were made:

- The ice breaking module is calculated by the theory of semi-infinite beam on a Winkler-type elastic foundation;
- The ice rotating module is formulated by assuming the rotating ice block as a short beam on a Winkler-type elastic foundation. In addition, to account for the limited ventilation effect, an elastic-plastic foundation is assumed during the ice rotating formulation;
- A continuum approach was used to analyse the effect of the accumulated ice rubble;
- With the theoretical plots in Fig. 3.13, the physical meanings and the spatial variations of three different force components are illustrated, which are the following: the ice breaking load F_B is the force required to break the incoming level ice and is located near the waterline where the direct ice-structure contact occurs; the ice rotating load F_R is the force required to rotate the already broken

ice block and is further transferred downwards (see Fig. 3.13b) below the waterline; and the rubble accumulation load F_{srb}, which serves as the boundary condition (i.e., external load) for the previous two different modules;

- In addition to the three force components, it is further assumed that there is a force component F_{PH} that acts in the horizontal direction, as shown in Fig. 3.15. This force component is responsible for the rolling motion of ice rubbles observed in the tests.

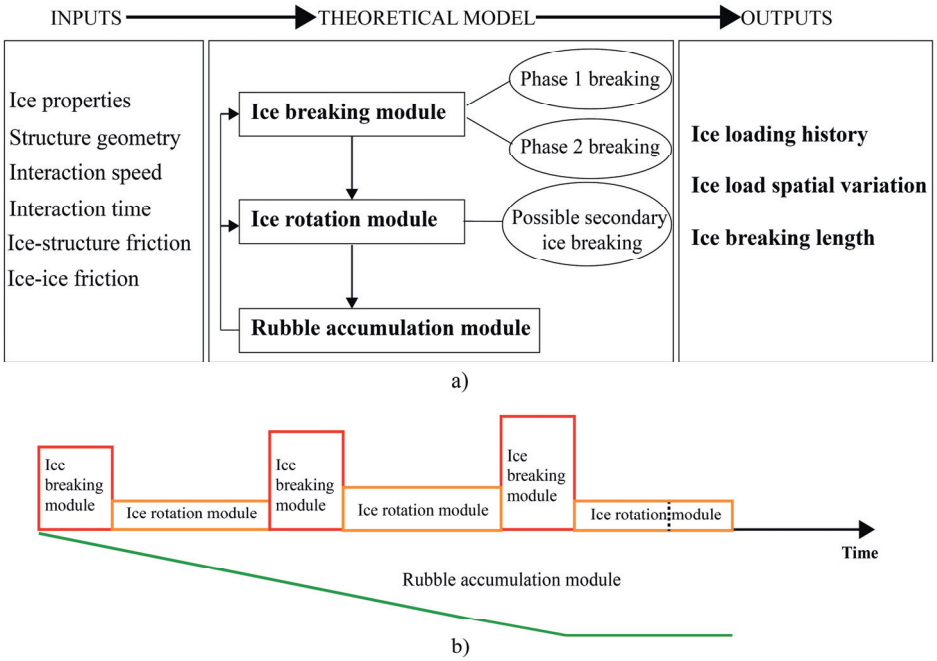

Fig. 3.14 Overall structure and its time domain development for the theoretical model.

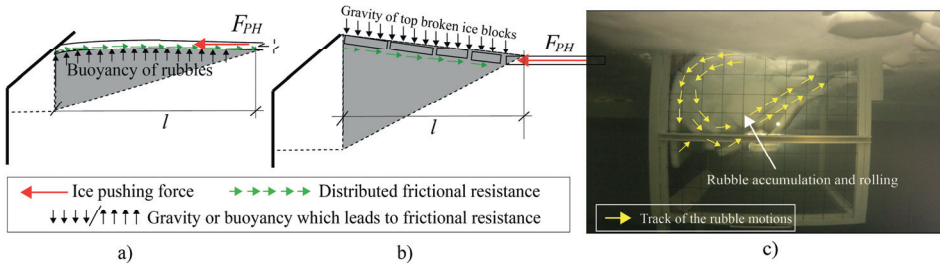

Fig. 3.15 Ice rubble pushing force component.

In total, four force components are calculated in the developed theoretical model. However, as shown in Fig. 3.13, these forces act in different directions. To ensure all of these force components are comparable, they were further projected in the horizontal direction (i.e., the intact level ice's moving direction) as F_{BH}, F_{RH}, F_{srbH}, and F_{PH} based on simple static mechanics. Adding up all these force components, the total horizontal

ice loads on a sloping structure can be obtained. Particularly, it should be noted that the spatial and temporal distributions of each force component were calculated. Thus, each force component varies with both time t and vertical coordinate Z.

3.2.2 Physical model test

Two different physical model tests were conducted in this study. One physical model (i.e., Physical model #1) used a tactile sensor to measure the force distribution on a sloping surface, as shown in Fig. 3.16. The tactile sensor consisted of a matrix of sensels capable of converting pressure into voltage signals recorded by the connected computer. The sensor has a rather high spatial resolution, i.e., each sensel is approximately $3.56\ \text{mm} \times 7.56\ \text{mm}$. The details of the historic use of tactile sensors and their applications in ice engineering are presented in a separate paper (Lu et al., 2014a).

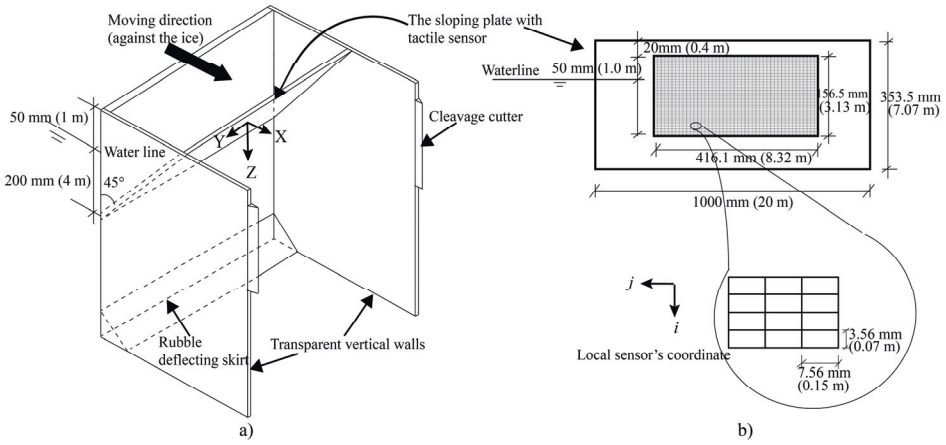

Fig. 3.16 Physical model #1, which uses a tactile sensor (model-scale sizes are given with their intended full-scale size in the bracket).

One should be cautious here because the tactile sensor's calibration used in the current study appears to be problematic when measuring the peak ice load. Therefore, the ice loads measured by the load cells in Physical model #2 is used for further validation of the theoretical model.

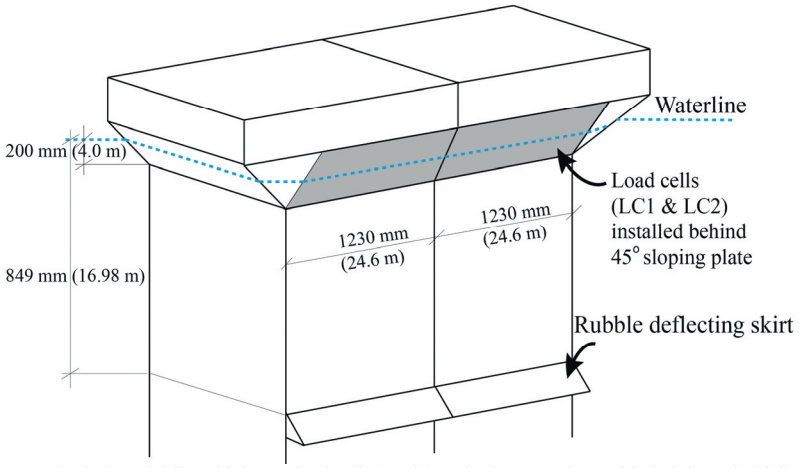

Fig. 3.17 Physical model #2, which uses load cells (model-scale sizes are given with their intended full-scale size in the bracket).

The measurements made by both the tactile sensor and load cells are to be compared with the theoretical predictions developed according to Fig. 3.14.

3.3 Remedies towards CEM's application

Section 3.2 studied the 'level ice - wide sloping structure interactions' using theoretical and physical models. As an additional tool, one promising numerical method, the Cohesive Element Method (CEM), is further explored in this section. This method is capable of simulating the fracturing and fragmentation of a solid and fits well into the FEM formulation. The method has been considered a potentially ideal tool to study ice-structure interactions (Konuk et al., 2009). However, this method suffers from a convergence issue, i.e., the calculation results vary with mesh refinement. In this study, several remedies are proposed to alleviate the observed convergence issue, based on which, further evaluation on CEM's merits in simulating ice - sloping structure interactions are conducted.

The numerical set-up shown in Fig. 3.18 was implemented in ABAQUS 6.12/EXPLICIT with MATLAB scripts. This numerical set-up is a replicate of the corresponding physical model test in Fig. 3.19. Because it is rather computationally exhaustive to run a large amount of CEM-based simulations, an ice floe with dimensions of $50\ \text{m} \times 50\ \text{m}$ with fixed boundaries was assumed.

The mesh of the ice floe in Fig. 3.18 is specially treated, as shown in Fig. 3.20, by inserting cohesive elements everywhere to simulate multiple cracks propagating, branching, fragmenting and interacting. However, this strategy was found to be too ambitious because the calculation results depend on the mesh size.

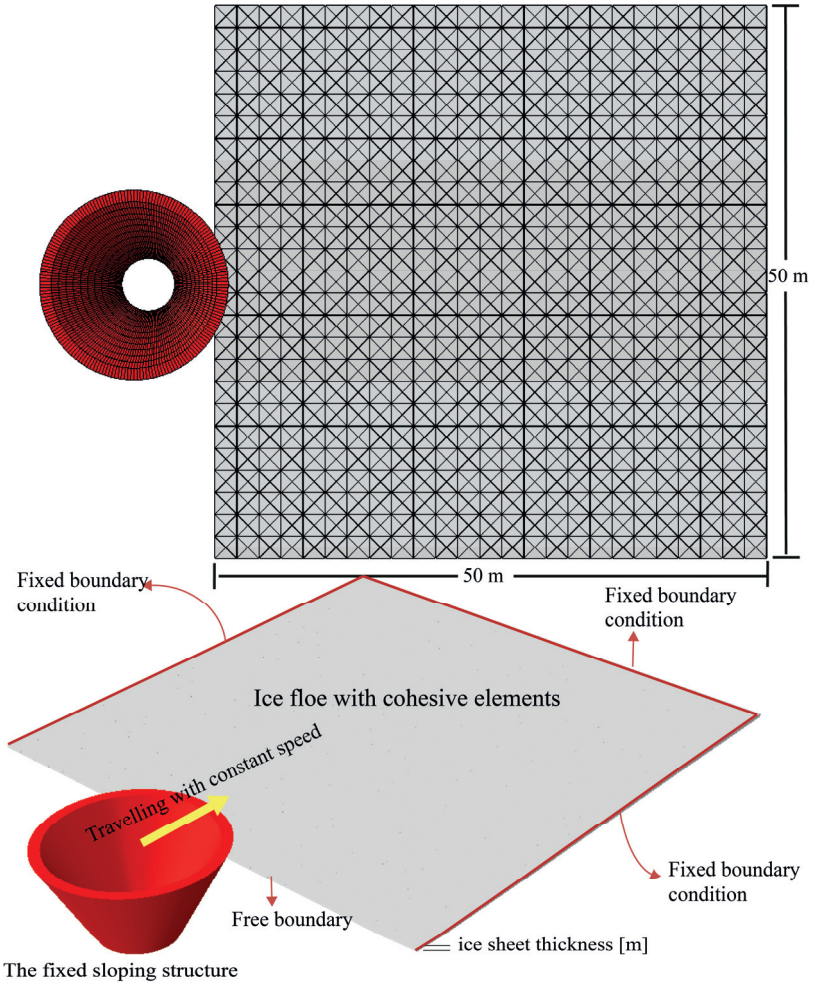

Fig. 3.18 Numerical set-up to test different remedies for the CEM-based simulation (the size is in full scale, and the waterline diameter of the sloping structure is 13.6 m).

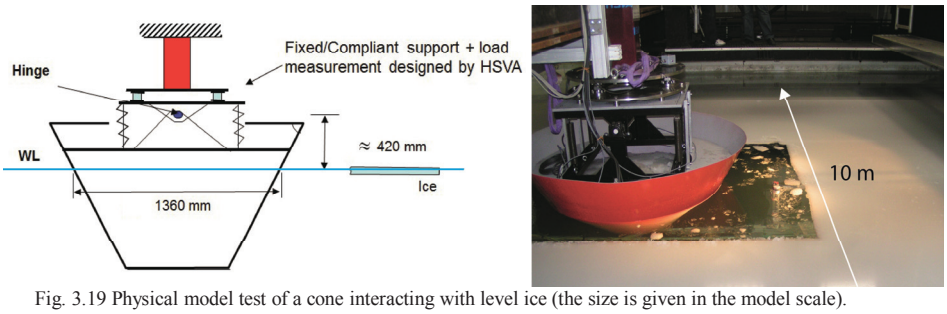

Fig. 3.19 Physical model test of a cone interacting with level ice (the size is given in the model scale).

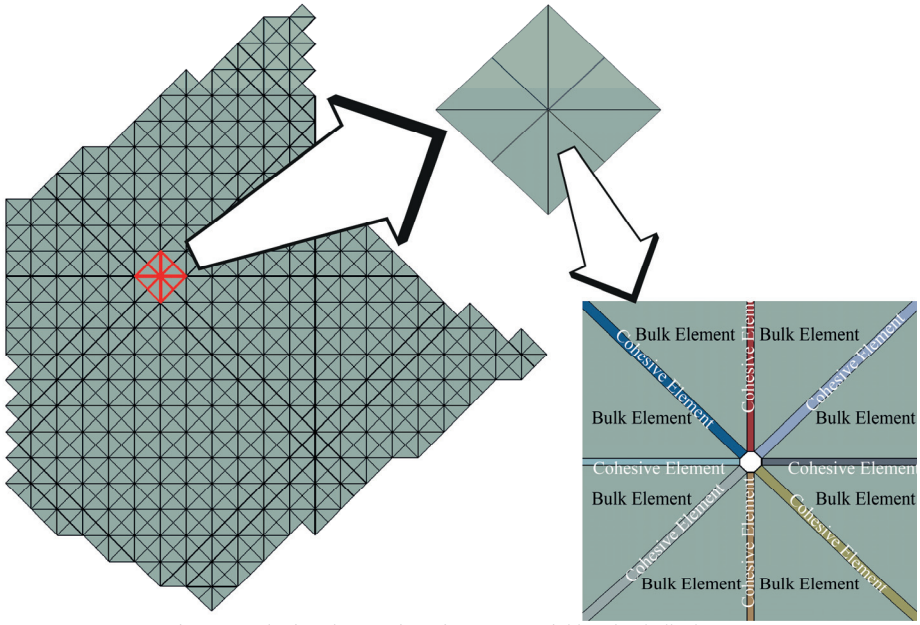

Fig. 3.20 Cohesive elements insertion among neighbouring bulk elements.

To alleviate the mesh size dependency, through relevant studies in other materials (a detailed literature review is presented in Appendix 5), the following remedies are proposed:

3.3.1 Remedy #1: Introducing fracture energy randomisation

It has been assumed that the fracture energy within an ice floe follows a stationary random Gaussian field distribution. The ice material's fracture energy distributions were implemented in the numerical model with 3 different correlation lengths shown in Fig. 3.21 to Fig. 3.23.

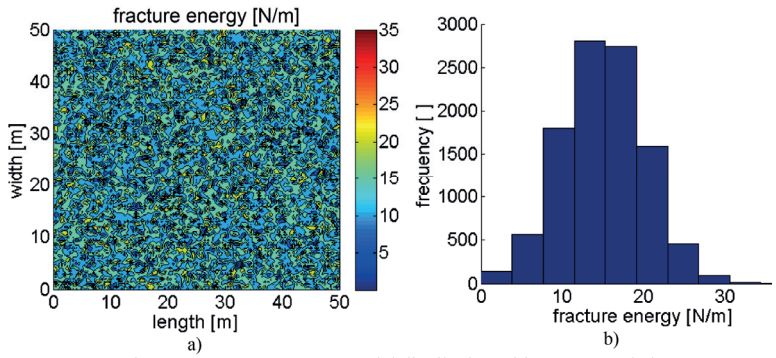

Fig. 3.21 Fracture energy's spatial distribution with a 0-m correlation.

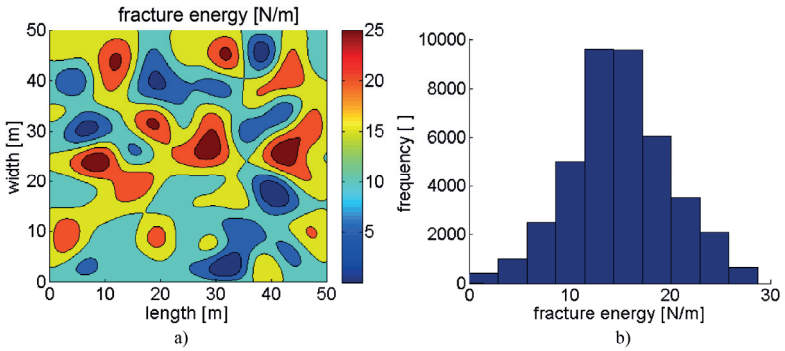

Fig. 3.22 Fracture energy's spatial distribution with a 1-m correlation.

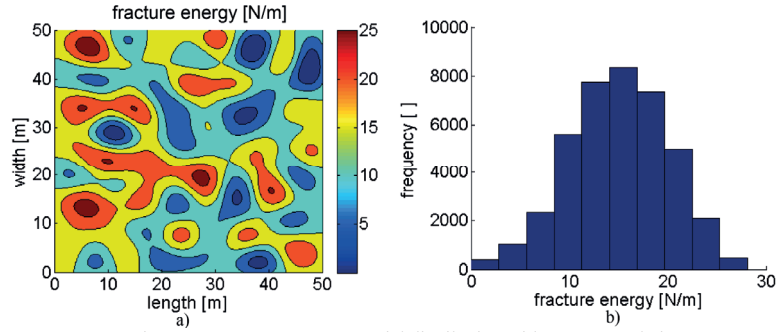

Fig. 3.23 Fracture energy's spatial distribution with a 5-m correlation.

With a randomised fracture energy field, it is anticipated that the fracture can be localised and therefore, not be too heavily influenced by the mesh size.

3.3.2 Remedy #2: Introducing bulk material's energy dissipation

The second remedy approach involves introducing additional bulk elements' energy dissipation into the cohesive element, which is illustrated in Fig. 3.24. The new fracture energy input for cohesive elements now becomes the following and is shown in Eq. (3.19).

$$G_{Fm} = G_F + L_m \gamma_U \tag{3.19}$$

in which,

G_{Fm} is a new fracture energy input for the cohesive elements with the bulk elements' dissipation;

G_F is the fracture energy of sea ice and is taken as 15 N/m according to the measurements and theoretical study in previous literatures (Dempsey et al., 1999a; Mulmule and Dempsey, 1998; Mulmule and Dempsey, 1999);

L_m is the size of the bulk elements;

γ_U is the energy density of the bulk material to be dissipated during fracturing.

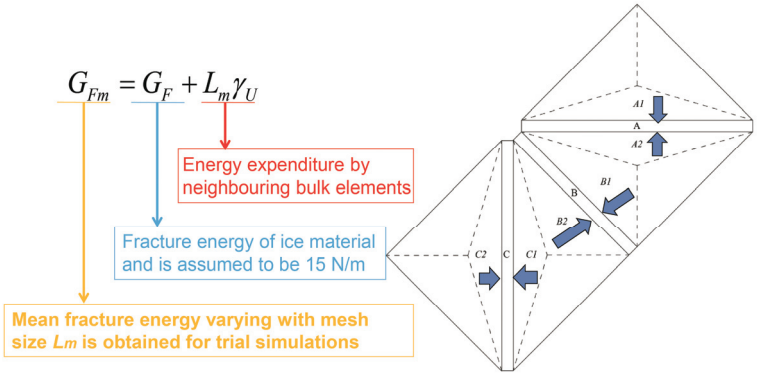

Fig. 3.24 Additional bulk elements' energy allocations.

The efficiency of these remedies is examined by comparing the simulation results with a varying mesh size implementation; and the simulation results are further compared with the results obtained in the physical model tests (in Fig. 3.19).

Chapter 4 Results and discussions

Different methods and assumptions were adopted while addressing each of the refined research questions. As illustrated in Fig. 1.8, the analytical solution to each problem is pursued together with additional corroborations from either numerical solutions, experimental measurements, or both. Therefore, most of the results presented in this chapter are primarily validations of the developed methods (in Chapter 3). In addition, based on the verified methods, new findings from relevant studies are presented and discussed in this chapter in a selective manner, i.e., only the most interesting results are presented. For detailed results and discussions, one can refer to the publications in the Appendices.

4.1 Fracture of an ice floe

In this section, the implemented methods to study the in-plane splitting failure and out-of-plane flexural failure of an ice floe were validated. These verified methods were further used to study the influences of different parameters, particularly the influence of floe sizes.

4.1.1 In-plane splitting failure: verifications and parametric studies

Two different methods were proposed to study the splitting failure of an ice floe, which are the method based on fracture mechanics, which is the primary method, and also the analysis based on plastic limit theory, which serves as a complementary tool. Their implementations are verified in this section, where the major focus is on the method based on fracture mechanics.

4.1.1.1 Validation against field experiments

First, these two approaches were validated against the only ice splitting experiments available in open literature (Dempsey et al., 1999a), as shown in Fig. 4.1. In this figure, the normalised ice splitting load $F_Y/(hL)$ in the vertical axis is plotted against the floe size L in the horizontal axis. Within this figure, the proposed size requirement for the applicability of LEFM is also illustrated (Mulmule and Dempsey, 2000).

The following observations from Fig. 4.1 can be made:

- The results obtained using the 'CZM + weight function' method agree well with most of the experimental results, including those in the laboratory-scale range;
- The 'LEFM + weight function' method can only approximate the test results well when the floe size is large enough, such as those in the field scale (e.g., larger than the recommended size $12l_{ch}$);
- At the laboratory scale, the 'LEFM + weight function' method yields an ice splitting load that exceeds the prediction from plastic upper limit theory (i.e., strength theory). The plastic upper limit method and plastic lower limit method

could be applied at the laboratory scale to level off the increasing value of $F_Y/(Lh)$ calculated by LEFM theory;

- The plastic upper limit method and plastic lower limit method are fairly conservative when applied at the field scale.

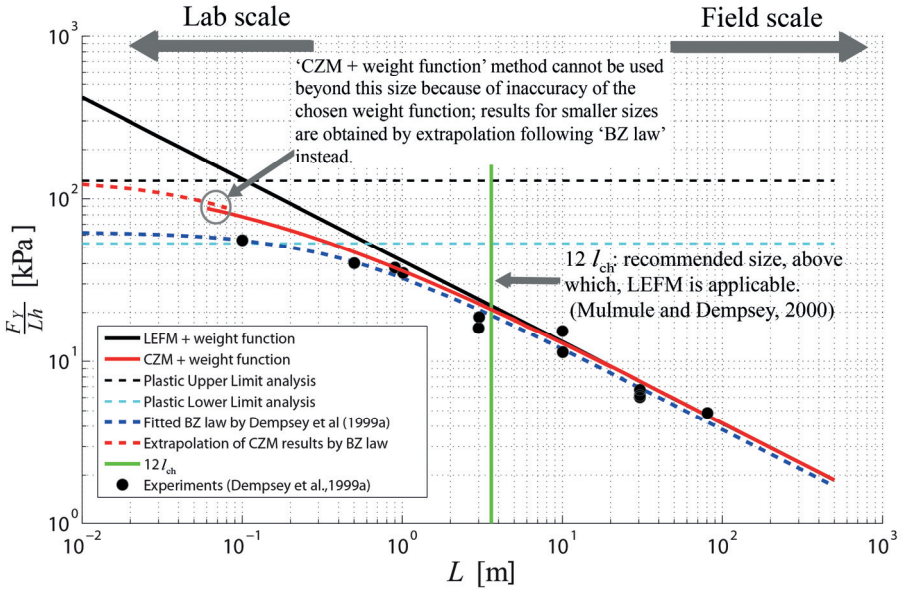

Fig. 4.1 Splitting load for a square ice floe with an edge crack ($A/L = 0.3$): comparison of the results obtained using different methods with test data.

4.1.1.2 Validation against available analytical solutions

Afterwards, the principal method, i.e., the method based on fracture mechanics, is further validated against previous known analytical solutions for a special case, i.e., the splitting force of a semi-infinite ice floe, which is plotted in Fig. 4.2 with the normalised ice splitting load $F_Y/(hK_{IC})$ in the vertical axis over the crack length A in the horizontal axis. Here, K_{IC} is the fracture toughness of sea ice.

Because the Fracture Process Zone (FPZ) is infinitesimally small in comparison with the size of a semi-infinite ice floe, based on theory, the results calculated according to CZM should reduce to the results based on LEFM. The comparisons made in Fig. 4.2 confirmed this. Both the 'LEFM + weight function' and the 'CZM + weight function' methods, when applied to the semi-infinite ice floe case, had identical results as those in a previous publication (Palmer et al., 1983).

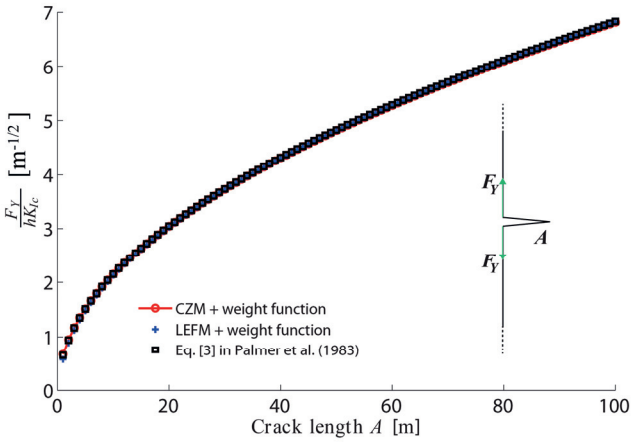

Fig. 4.2 Comparison of the ice splitting loads obtained using different methods for a semi-infinite ice floe.

4.1.1.3 Validation against numerical solutions (FEM): splitting of square and circular ice floes

FEM-based numerical simulation results are available in the literature for a square ice floe (Bhat, 1988) and a circular floe (Bhat et al., 1991). The current implemented methods were further validated against these numerical solutions in Fig. 4.3. Note that a field-scale (see Fig. 4.1) floe size was deliberately chosen to calculate the results using the 'CZM + weight function method'.

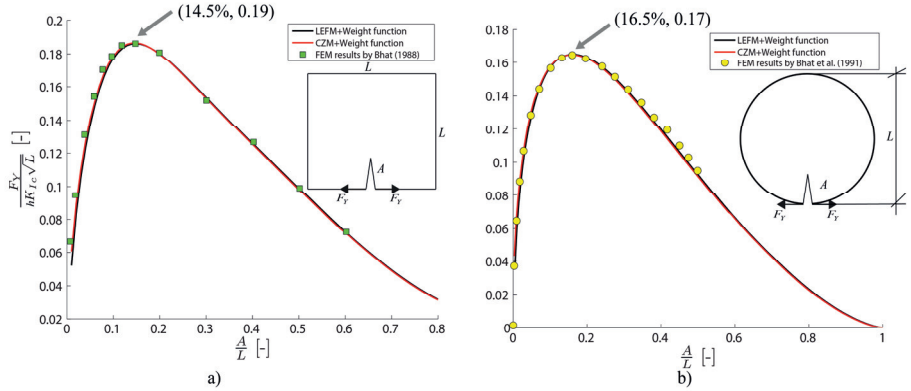

Fig. 4.3 Ice splitting load for a) an edge-cracked square and b) a circular ice floe with varying crack lengths.

Fig. 4.3 shows that the normalised ice splitting load for both floe shapes increase initially, while the crack reaches certain length (i.e., $A = 14.5\%L$ for a square ice floe; and $A = 16.5\%L$ for a circular ice floe), the force begins to decrease to maintain a balance between the crack-driving force and the crack resistance. Due to the nature of ice-structure interactions, the load history for splitting cracks' extension would not behave as that is shown in Fig. 4.3. In reality, while the ice splitting load increases beyond the

peak points shown in Fig. 4.3, the subsequent crack propagates catastrophically. For engineering applications, regarding how much force is required to split an ice floe, it is sufficient to account for only the maximum values in Eq. (4.1).

$$\begin{aligned} F_Y &= 0.19 h K_{Ic} \sqrt{L} && \text{for a square ice floe with critical crack length } \alpha_{cr} = A/L = 14.5\% \\ F_Y &= 0.17 h K_{Ic} \sqrt{L} && \text{for a circular ice floe with critical crack length } \alpha_{cr} = A/L = 16.5\% \end{aligned} \tag{4.1}$$

4.1.1.4 Parametric studies on the ice floe geometry, confinement or inertial effect

Favourable agreements were attained in the previous validations. Afterwards, the developed theoretical model was further explored to study different parameters, such as the influences of floe geometry (see Fig. 4.4) and the influences of confinement or the inertial effect (see Fig. 4.6).

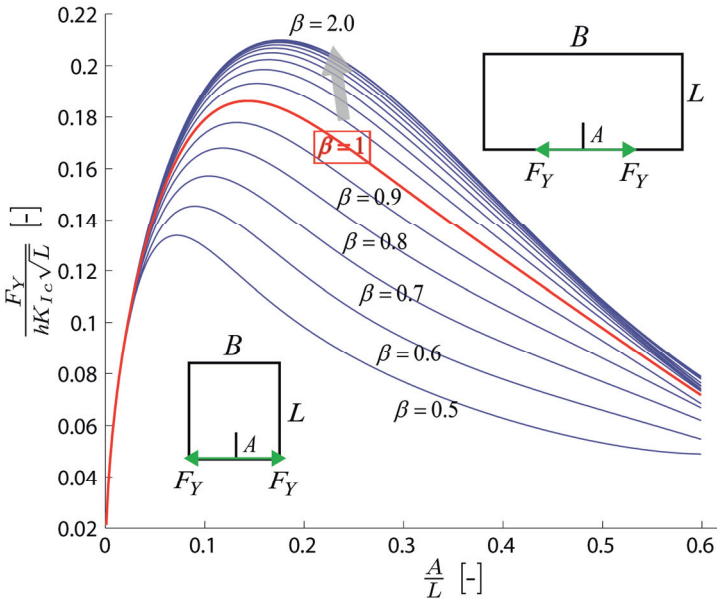

Fig. 4.4 Splitting load for a rectangular ice floe for a varying width-to-length ratio.

Fig. 4.4 illustrates a diminishing influence from the width to length ratio $\beta = B/L$ on the normalised ice splitting load, e.g., the results of $\beta > 1$ converge to the results of $\beta = 2$.

On the contrary, the effect of confinement demonstrates a more profound effect on increasing the ice splitting load. Eq. (3.4) was used to quantify the effect of a special type of confinement, i.e., an impacting inertia-induced confinement of the floe (see Fig. 4.5c).

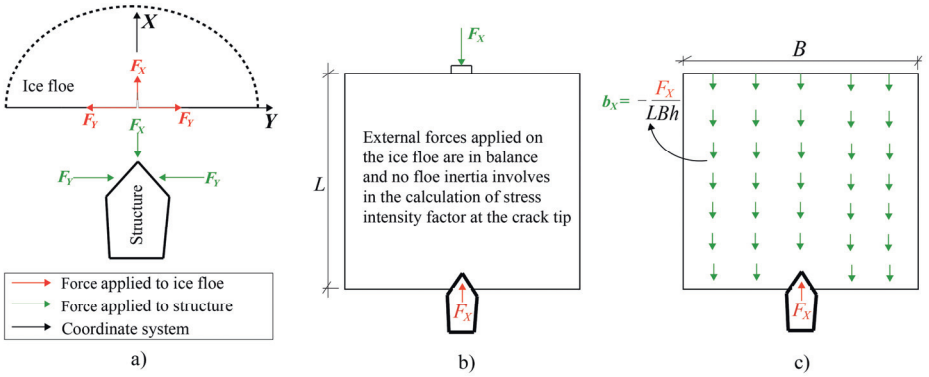

Fig. 4.5 Illustration of different force components and two different interaction processes: a) definition of force components in the coordinate system; b) structure rams into a stationary ice feature; c) a moving ice feature impacts the structure.

Regarding the floe ice - sloping structure interactions, the ice load actions and reactions are illustrated in Fig. 4.5a. The load ratio β_{YX} is defined by Eq. (3.18).

Among the interactions, two extreme scenarios can be identified. One is that the inertia of an ice floe can be neglected, as shown in Fig. 4.5b, e.g., the sloping structure rams into an ice floe, which is effectively stopped by a neighbouring ice floe (Eq. (3.3) applicable); another scenario involves a large inertia within the ice floe, e.g., an ice floe impacting the sloping structure. This inertia can be expressed as a body force $b_x = -F_X / hL^2$ for a square ice floe (Bhat, 1988). This body force introduces a special confinement for a crack. Dempsey et al. (1994) used the solution of Timoshenko and Goodier (1951) and Little (1973) to approximate the confinement's pressure profile $p_{ext}(x')$, as described in Eq. (4.2).

$$p_{ext}(x') = -\frac{F_X}{\pi h}\frac{\delta(x')}{L} + \frac{2}{\pi}\frac{F_X}{hL}\left(\frac{1}{2} - x'\right)\left\{\frac{1/2}{1/2 - x'} + \left(3 - \frac{3\pi}{4}\right) + \left(\frac{\pi}{2} - 1\right)\left[4\left(\frac{1}{2} - x'\right)^2 - \frac{3}{5}\right]\right\} \quad (4.2)$$

The magnitude of confinement in Eq. (4.2) is reflected by the value of F_X. A large F_X indicates a large inertial effect and hence, a large confinement on the central splitting crack. To explicitly express this confinement effect, a parameter $\beta_{confinement}$ is defined by Eq. (4.3).

$$\beta_{confinement} = F_X / F_Y = 1/\beta_{YZ} \quad (4.3)$$

Inserting Eqs. (4.2) and (4.3) back into Eq. (3.4), the ice splitting load under the influence of confinement $\beta_{confinement}$ is illustrated in Fig. 4.6 together with the FEM results of Bhat (1988).

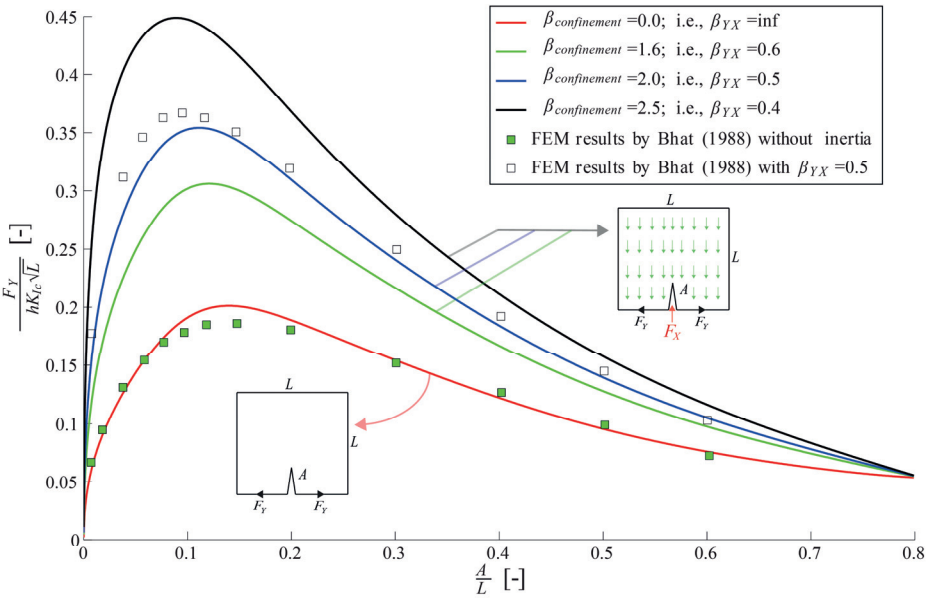

Fig. 4.6 Ice splitting load under inertial-induced confinement for a square ice floe.

Fig. 4.6 shows that the theoretical prediction by Eq. (3.4) agrees well with the FEM results by Bhat (1988). In addition, comparing Fig. 4.4 with Fig. 4.6, the plots also demonstrate that the confinement has a much more profound effect on increasing the ice splitting load.

4.1.2 Radial-crack-initiation controlled fracture

Given the geometry and size of an ice floe and the loading area at the contact, with the normalised PDE in Eq. (3.7), the interesting results, i.e., the radial crack initiation load $F_{Z,\text{radial},0}$ and propagation load $F_{Z,\text{radial},1}$, can be derived in non-dimensional form in Eqs. (4.4) and (4.5), respectively.

$$\frac{F_{Z,\text{radial},0}(n,R)}{\sigma_f h^2} = \frac{1}{{\sigma_M}^0(n,R)} \tag{4.4}$$

in which,

$\sigma_M{}^0(n,R)$ is the Mises stress at point ($\xi=0,\eta=0$), which is dependent on floe size (i.e., reflected by the coefficient n) and the loading area size (i.e., reflected by the loading radius R).

$$\frac{F_{Z,\text{radial},1}(n,R)}{\sigma_f h^2} = \left(\frac{k}{108}\right)^{\frac{1}{8}} \frac{\sqrt{G_F}}{\sigma_f} \left(\frac{E}{1-\upsilon^2}\right)^{\frac{3}{8}} \frac{h^{-3/8}}{\sqrt{n\dfrac{dW_0(n,R)}{d\alpha}}} \tag{4.5}$$

in which,

$W_0(n,R)$ is the normalised deflection of a cracked ice floe at point ($\xi = 0, \eta = 0$).

Therefore, the original pursuit of determining $F_{Z,\text{radial},0}$ and $F_{Z,\text{radial},1}$ was shifted into solving ${\sigma_M}^0(n,R)$ and $dW_0(\alpha)/d\alpha$ with numerical models of Fig. 3.7a and Fig. 3.7b and c, respectively. The relevant results are presented as follows.

4.1.2.1 Results and discussions for radial crack initiation

First, the Mises stress from the simulation of Fig. 3.7a are presented in Fig. 4.7 with a prescribed loading area $R = 0.2\ell$ and a varying floe size, i.e., $n = 1, 2, 3, \ldots\ldots, 9$. It is clear from these plots that when an ice floe is relatively small (e.g., $n \le 7$), the stress distribution is influenced by its boundaries, whereas the stress is primarily concentrated within a small portion of a large ice floe (e.g., $n \ge 8$).

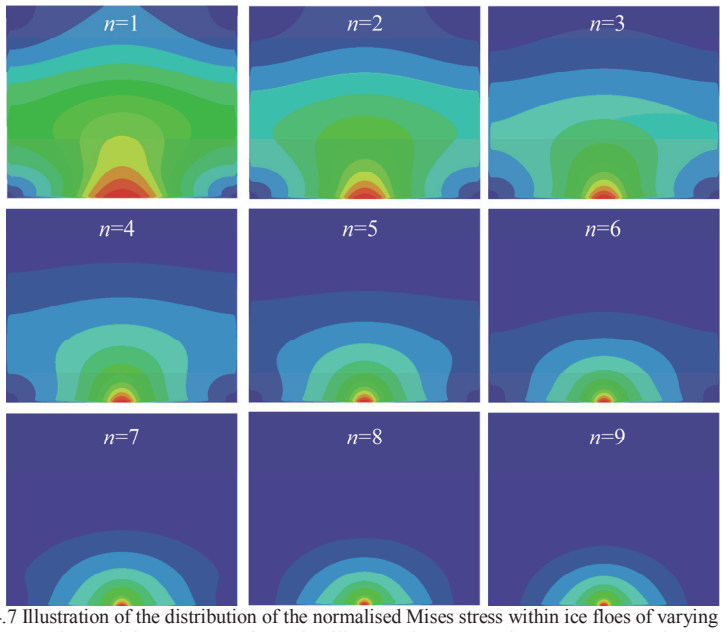

Fig. 4.7 Illustration of the distribution of the normalised Mises stress within ice floes of varying sizes with $R = 0.2\ell$ (note that a rainbow spectrum is used to illustrate the comparative stress values, where red and violet correspond to the maximum and minimum values; the Mises stress in the figure should only be understood as comparative values within each subplot).

Furthermore, the quantitative results of Eq. (4.4) are presented in Fig. 4.8 with three prescribed loading area sizes ($R = 0.05\ell$, 0.1ℓ, and 0.2ℓ). It is interesting to note in Fig. 4.8 that when $L \le 4\ell$, the normalised radial crack initiation load is larger than that

predicted by the semi-infinite ice floe solutions. This result is thought to be due to the effect of the free boundaries. For a small ice floe, in addition to the energy required to induce sufficient flexural deformation, another type of deformation (e.g., rigid body rotation) is also presented because of the free boundaries. Therefore, more energy, in comparison with a semi-infinite ice floe, is required to initiate the radial crack. In practice, this means that using Nevel's (1965) or Lubbad and Løset's (2011) solutions for radial crack initiation calculations is not always conservative.

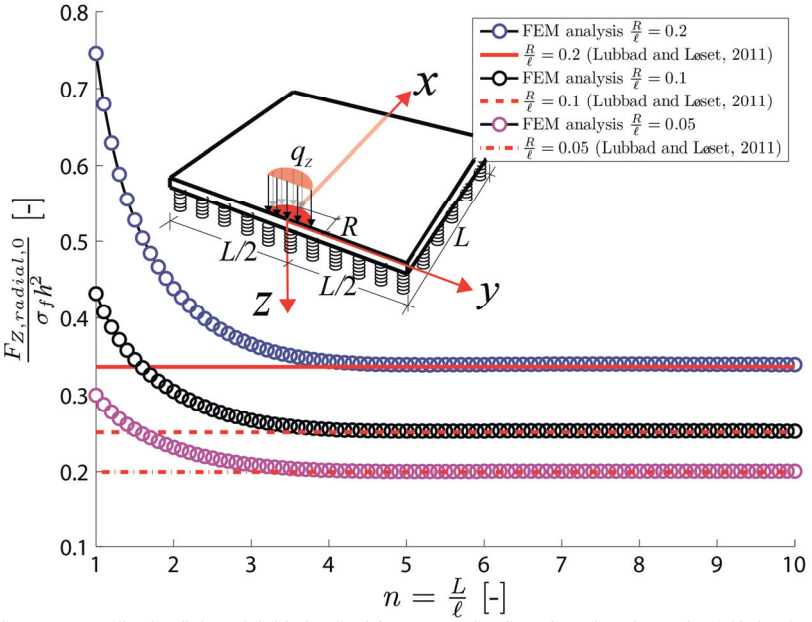

Fig. 4.8 Normalised radial crack initiation load for a square ice floe of varying size under half-circular edge loading.

With respect to the maximum deflection of an ice floe presented in Fig. 4.9, the size of the loading area appears to have a relatively minor effect on the normalised deflection value. Because large deflections are found for smaller ice floes, we further analysed the possibility of flooding on top of an ice floe before radial crack initiation. The results show that using typical ice material properties, a radial crack initiates much earlier than any inundation could occur over the freeboard of an ice floe.

As the floe size increases, e.g., $n \geq 4$ or $L \geq 4\ell$, the numerical results converged to the analytical solutions predicted by Lubbad and Løset (2011) for semi-infinite ice floe. In addition, a similar numerical set-up to Fig. 3.7a was implemented with a rectangular loading area to validate against Nevel's (1965) analytical solutions for large floes (presented in Appendix 2). A similar converging trend was also obtained. Thus, both validations signify the correctness of the derivations and numerical set-ups to study radial crack initiation.

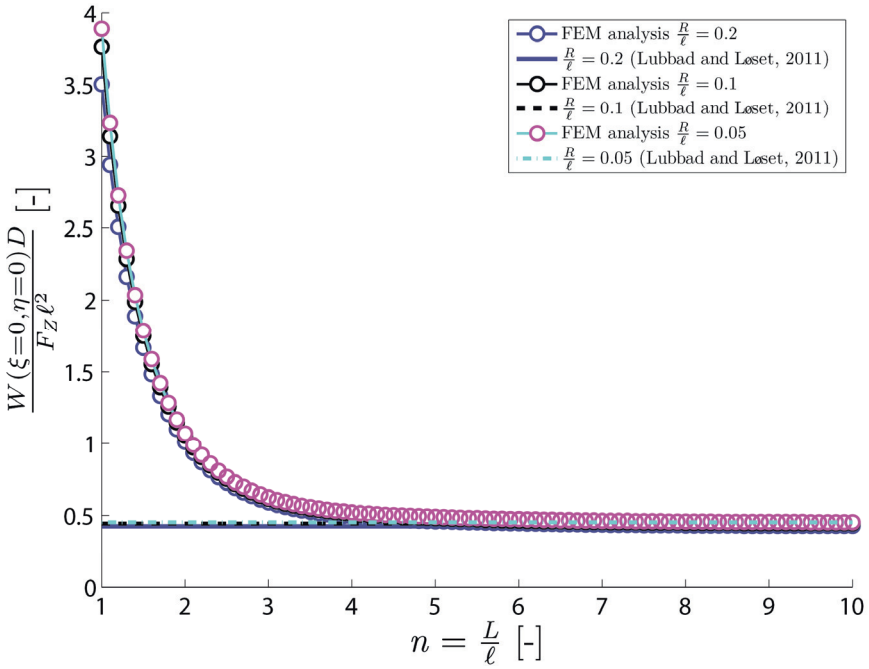

Fig. 4.9 Normalised maximum deflection at ($\xi = 0, \eta = 0$) for a square ice floe of varying size under a half-circular edge loading.

4.1.2.2 Results and discussions for radial crack propagation

4.1.2.2.1 A benchmark test on the splitting failure

Before presenting the results of radial crack propagation studies, a benchmark test was conducted. The same energy approach (Irwin, 1956) was adopted together with a similar numerical set-up to study the splitting of a square ice floe (see details in Appendix 2), where analytical solutions were available. The visual illustration of the simulation is presented in Fig. 4.10, in which the stress concentrations always occurred at the crack tip.

Afterwards, the normalised ice splitting load $F_Y/(hK_{IC}\sqrt{L})$ is plotted versus the normalised crack length α, which is shown in Fig. 4.11 together with the analytical solutions (Lu et al., (submitted in March 2014)) and previous FEM results (Bhat, 1988). Though the numerical model used in Fig. 3.7b and c is not a special-purpose scheme to calculate a fracture mechanics problem [5], favourable agreements in Fig. 4.11 substantiated our further use of the same methodologies to study the radial crack propagation problem within an ice floe.

[5] Special-purpose programs are those specially designed to address cracks and determine the Stress Intensity Factor (SIF) directly (Bažant and Planas, 1998).

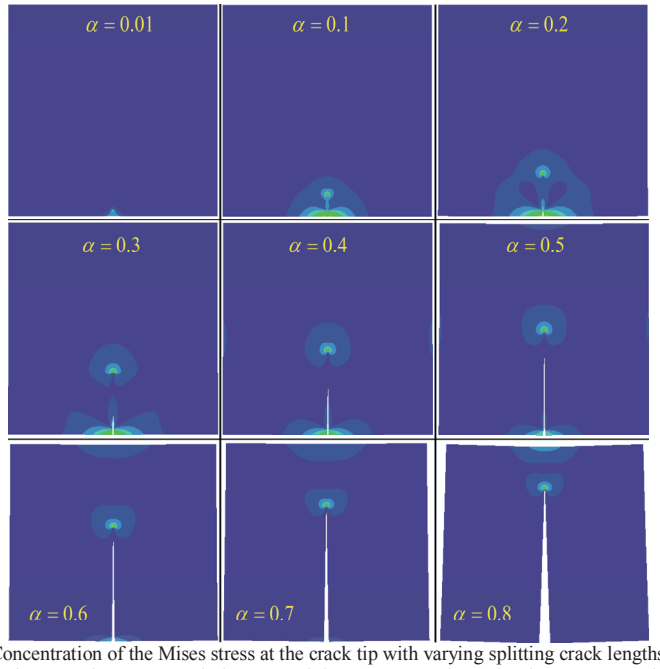

Fig. 4.10 Concentration of the Mises stress at the crack tip with varying splitting crack lengths (note that the crack opening displacement is exaggerated; the same rainbow spectrum shown in Fig. 4.7 was used; the Mises stress in these plots should only be understood as comparative values).

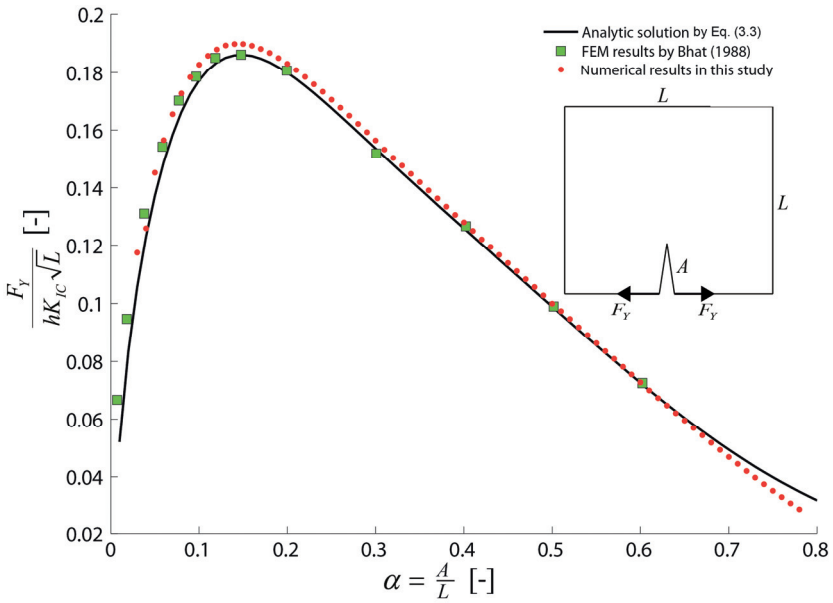

Fig. 4.11 Benchmark comparison of the current numerical scheme with the analytical solution.

4.1.2.2.2 Radial crack propagation

First, the visual illustration of the Mises stress distribution within a cracked ice floe is illustrated in Fig. 4.12 with varying floe sizes (i.e., $n = 1, 4,$ and 8) and crack lengths (i.e., $\alpha = \alpha_0, 0.3, 0.6,$ and 0.8) with $R = 0.2\ell$ as an example. Fig. 4.12 demonstrates that stress concentration does not always occur at the radial crack tip. Depending on the floe size, for a small ice floe (e.g., $n = 1$ in Fig. 4.12), stress appears to concentrate at the crack tip; however, for a large size ice floe (e.g., $n = 8$ in Fig. 4.12), the stress concentration tends to occur at the location where a circumferential crack will develop. The latter case implies that further increasing the load $F_{Z,\text{radial},1}$ shall initiate a circumferential crack instead of propagating the existing radial crack.

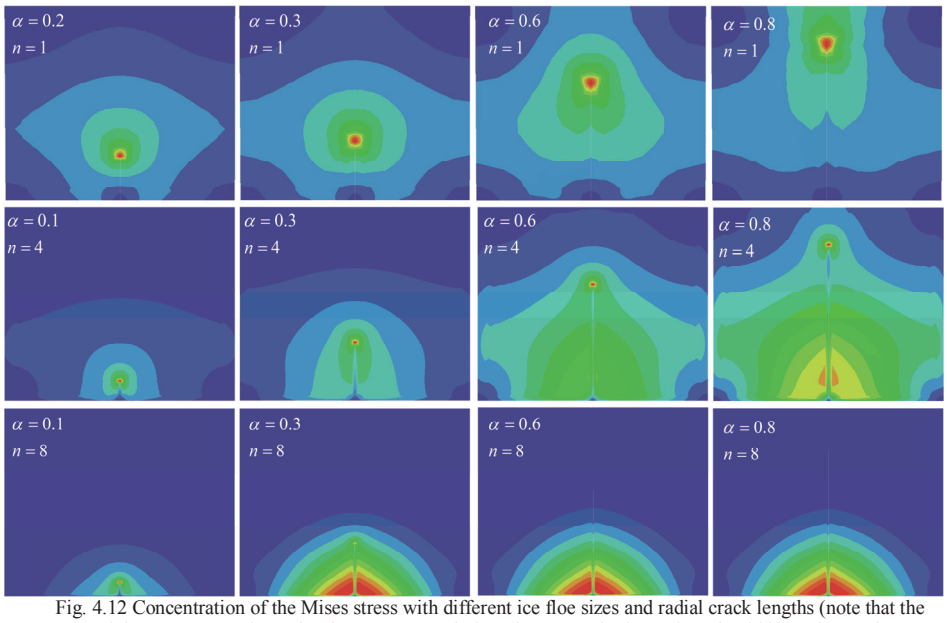

Fig. 4.12 Concentration of the Mises stress with different ice floe sizes and radial crack lengths (note that the same rainbow spectrum shown in Fig. 4.7 was used; the Mises stress in these plots should be understood as comparative values) (with $R = 0.2\ell$).

Based on the numerical set-up, the key quantitative results $dW_0(\alpha)/d\alpha$ in Eq. (4.5) are presented in Fig. 4.13 with prescribed loading area sizes ($R = 0.05\ell,\ 0.1\ell,$ and 0.2ℓ).

Following the definition in Eq. (4.5), without including any material properties and thickness information, Fig. 4.13 represents the non-dimensional radial crack propagation load versus crack length for different ice floe sizes. For a small ice floe (e.g., $n \le 3$), less force is required to propagate the radial crack. For a large ice floe (e.g., $n \ge 5$), an increasingly larger force is required to propagate the radial crack. In particular, the curves with $n = 7$ and $n = 8$ were truncated at approximately $\alpha = 30\% \sim 40\%$ in all of the subplots of Fig. 4.13 because the deflection curves $W_0(\alpha \ge 30\% \sim 40\%)$ flattened for large ice floes, and their numerical derivatives lose meaning by dividing nearly zero values.

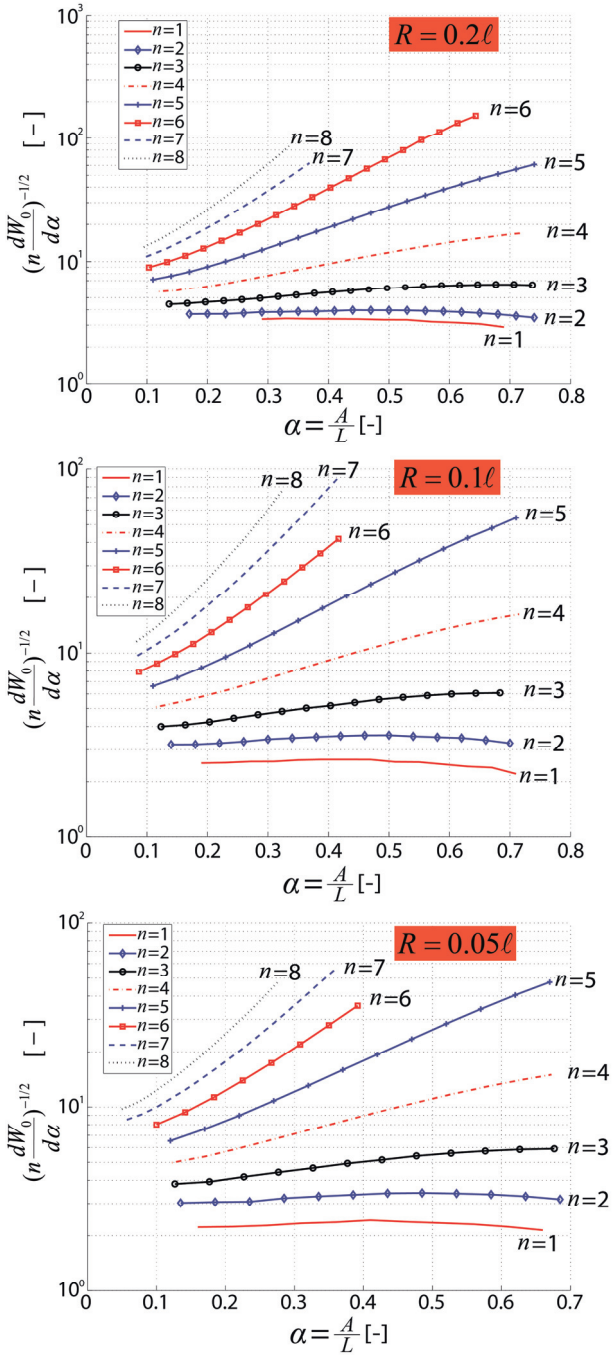

Fig. 4.13 Derivative of maximum deflections of a cracked ice floe with varying sizes (note that the Y-axis is on a logarithmic scale).

4.1.2.2.3 Radial-crack-initiation-controlled fracture

With both $F_{Z,\text{radial},0}$ and $F_{Z,\text{radial},1}$ calculated for various floe sizes and crack lengths, it is therefore possible to determine the maximum radial crack length that can be propagated under radial crack initiation load alone. This competition can be quantified as follows: for an arbitrary relative crack length α in the range $[R/L, 1]$ and for a varying floe size expressed by n, three different cases can be defined as in Eq. (4.6)

Within these three different scenarios, we conservatively confine our interests in the first scenario: i.e., radial-crack-initiation-controlled fracture. The other two scenarios can be conservatively treated as the fracture of a semi-infinite ice floe in Fig. 2.9c.

$$\begin{cases} \dfrac{F_{Z,\text{radial},0}(n)}{\sigma_f t^2} > \dfrac{F_{Z,\text{radial},1}(n,\alpha)}{\sigma_f t^2} \rightarrow \alpha_{\max} = 1 & \text{Radial-crack-initiation-controlled fracture;} \\ \dfrac{F_{Z,\text{radial},0}(n)}{\sigma_f t^2} = \dfrac{F_{Z,\text{radial},1}(n,\alpha)}{\sigma_f t^2} \rightarrow \alpha_{\max} & \text{maximum radial crack length under radial crack initiation load;} \\ \dfrac{F_{Z,\text{radial},0}(n)}{\sigma_f t^2} < \dfrac{F_{Z,\text{radial},1}(n,\alpha)}{\sigma_f t^2} \rightarrow \alpha_{\max} = 0 & \text{Radial crack initiation load cannot extend radial crack.} \end{cases} \quad (4.6)$$

Nevertheless, by assigning typical ice material properties (details can be found in Appendix 2) to Eqs. (4.4) and (4.5) and inserting them into Eq. (4.6), the corresponding maximum radial crack length under the influence of radial crack initiation load can be plotted in Fig. 4.14. Because of the piecewise equation defined in Eq. (4.6), these curves are not smooth. Nevertheless, the left column of Fig. 4.14 shows that when $G_F = 1\,\text{N/m}$, for any ice floe with size $L \le 3\ell$ and with a thickness found in most engineering application ranges (e.g., $t \ge 0.3\,\text{m}$), the radial crack initiation load is large enough to propagate a radial crack through the entire floe body. In contrast, when $G_F = 15\,\text{N/m}$, in the right column of Fig. 4.14, such a size requirement is $L \le 2\ell$. In total, both columns in Fig. 4.14 demonstrate that when $L \le 2\ell$ and using typical ice material properties[6], a nearly square-shaped ice floe can fail at radial crack initiation. Fig. 4.14 also shows that a larger loading area tends to propagate longer radial cracks. However, such a difference is minor and would not influence the aforementioned general observation. Collectively, we are therefore able to conclude that for a nearly square ice floe smaller than 2ℓ, the floe can be treated as a finite size floe whose failure is controlled by radial crack initiation; otherwise, the floe can be conservatively treated as a semi-infinite ice floe.

In practice, depending on the exact material properties and ice thickness, the same comparison shown in Fig. 4.14 can be used to quantify the optimum floe size in the downstream of an ice management operation. If fracturing of ice floes is unavoidable for the protected vessel downstream, ensuring that most of the ice floes fail by radial-crack-initiation-controlled fracture can largely reduce its overall ice load.

[6] Typical ice material properties that were employed for the calculation of Fig. 4.14 include: $\sigma_f = 550\,\text{kPa}$; $E = 5.5\,\text{GPa}$; $\rho_i = 920\,\text{kg/m}^3$; $\rho_w = 1020\,\text{kg/m}^3$; $\nu = 0.3$.

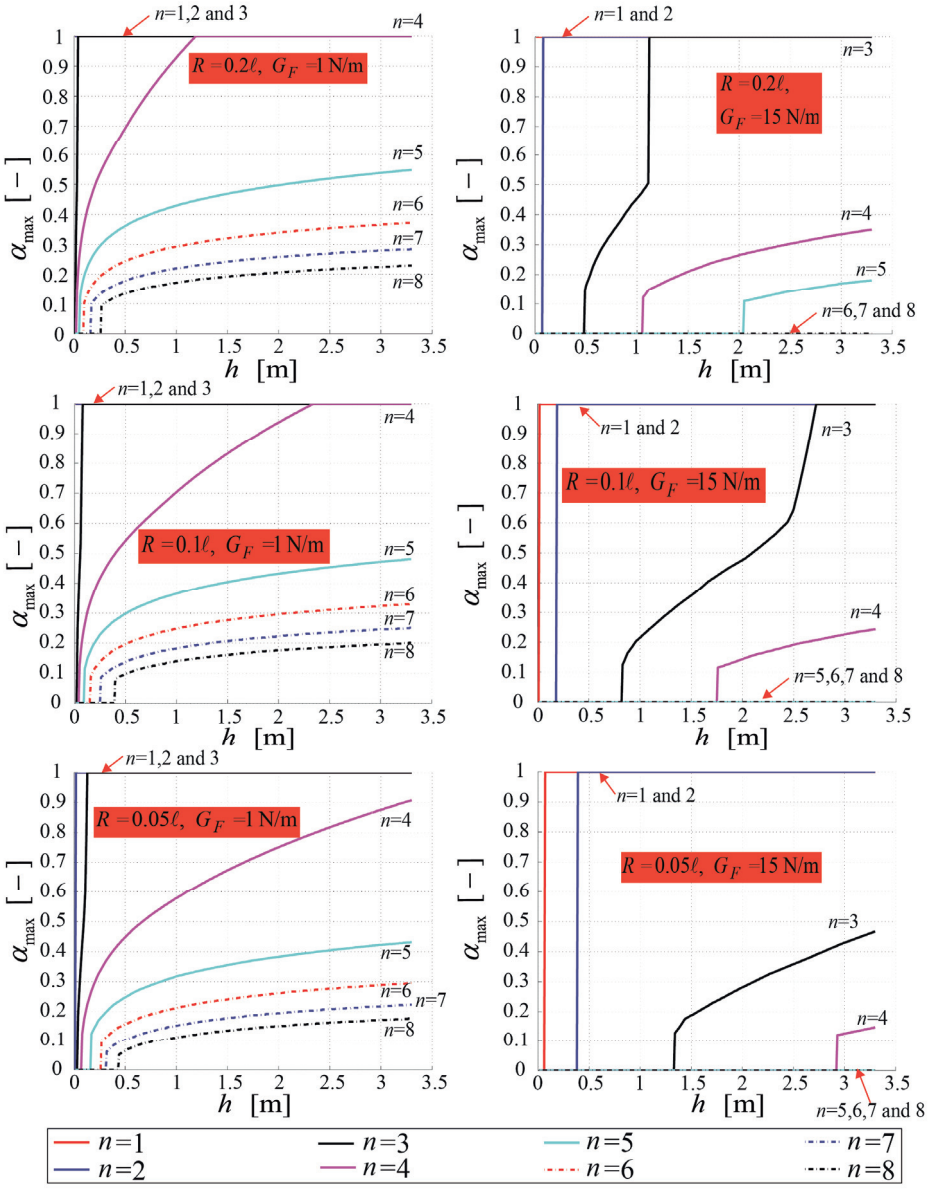

Fig. 4.14 Maximum radial crack length induced by the radial crack initiation load.

4.1.3 Analytical solutions of out-of-plane failures of an ice floe

In the previous section, numerical results regarding radial crack initiation and propagation and their competition were presented. One important finding is that for a square ice floe smaller than 2ℓ, the floe's failure is radial-crack-initiation controlled. As

a step further, this section presents results based on the symplectic approach to analytically study the failure of an arbitrary rectangular ice floe in Fig. 3.8.

First, the analytical solution based on the symplectic approach is used to calculate the overall deflection of a square ice floe with dimensions of $2\ell \times 2\ell$ under a concentrated load at point ($\xi = 0, \eta = 0$). The deflection is visualised in Fig. 4.15b, within which, two curves were selected for validation, where curve '1' (i.e., $\xi = 0$) has a curvature that determines the initiation of a radial crack, and curve '2' (i.e., $\eta = 0$) has a curvature that implies a circumferential crack initiation. Afterwards, the same numerical model shown in Fig. 3.7a was implemented to calculate the same ice floe's deflection along these two curves (see Fig. 4.15a). Because a concentrated load introduces numerical difficulties, it was converted into a distributed pressure in the numerical model within a small half-circular area with a radius of $R = 0.01\ell$ (shown in Fig. 4.15a).

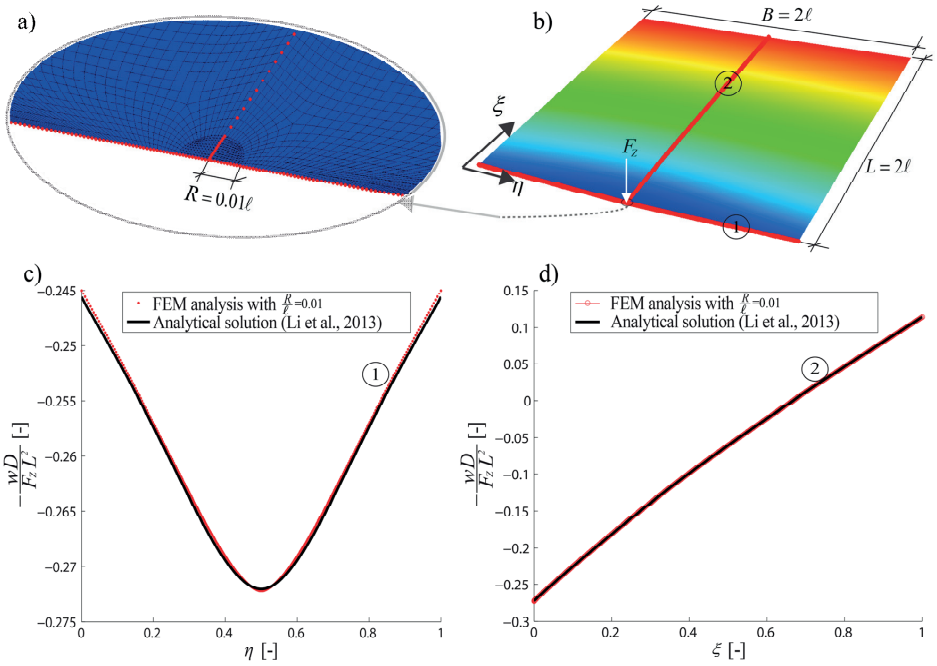

Fig. 4.15 Validation of the symplectic-based solution against the FEM results: a) mesh pattern for the FEM; b) analytical solution; c) comparison of the deflection at $\xi = 0$; d) comparison of the deflection at $\eta = 0$.

The normalised deflections of these two curves are compared in Fig. 4.15c and d. The excellent agreement verifies the correct implementation of the symplectic approach to analytically calculate the deflection of an ice floe under a concentrated load. This method is further extended to study the failure of an arbitrary rectangular ice floe, as shown in Fig. 3.8.

Fig. 4.16 illustrates the comparison of the maximum normalised deflection between the numerical results and the analytical solutions for long and wide ice floes, respectively.

Satisfactory agreement is achieved for a rectangular ice floe with various width-to-length ratios.

The calculated defection W in Fig. 4.16 can be inserted into Eq. (3.14) to obtain the critical vertical force $F_{z\_radial/circumferential\_cracking}$ for the out-of-plane flexural failure of a finite rectangular ice floe. The rectangular ice floes considered in Fig. 4.16 are floes with its width or length in the range of ℓ and 2ℓ; the other side varies with different width-to-length ratios. According to the assumptions discussed in Section 3.1.2.2, long ice floes in Fig. 3.8c and wide ice floes in Fig. 3.8b will fail at circumferential and radial crack initiation, respectively. Note that this assumption is approximate as neither crack initiation nor propagation has been substantially investigated for arbitrary rectangular ice floes. While calculating the critical failure load $F_{z\_radial/circumferential\_cracking}$, a conservative displacement-controlled criterion was adopted. In Appendix 2, a comparative study of the critical stress criterion and critical deflection criterion on a square-shaped ice floe was performed. Based on the stress criterion, radial crack initiation occurs prior to the occurrence of the critical deflection. Similarly, for a beam-like ice floe (e.g., long ice floe in Fig. 4.16a), previous studies of a beam on a Winkler-type elastic foundation also show that flexural failure occurs much earlier than the inundation of the considered ice floe (Lubbad et al., 2008). In summary, for both potential failure modes in Fig. 3.8, a displacement controlled failure criterion is proposed and validated for various width-to-length ratios in Fig. 4.16.

Fig. 4.16 also shows that the results begin to converge for long/wide floes with width-to-length ratios smaller/larger than certain values (e.g., $\beta \le 0.2$ and $\beta \ge 5$ for long rectangular floes and wide rectangular floes, respectively).

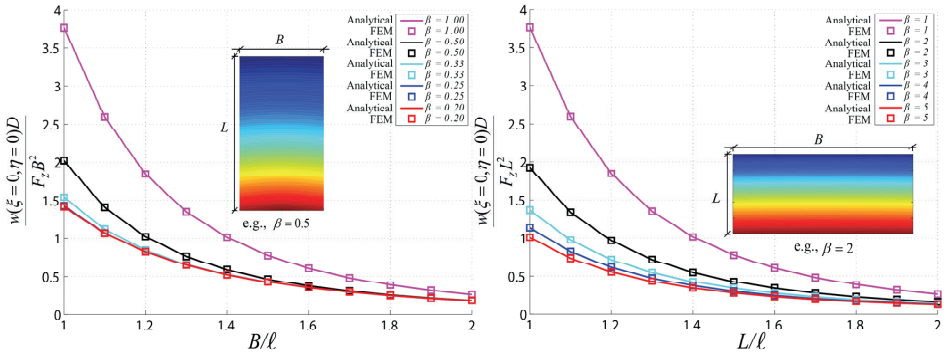

Fig. 4.16 Validation of the symplectic-based solution against FEM results for ice floes with different aspect ratios.

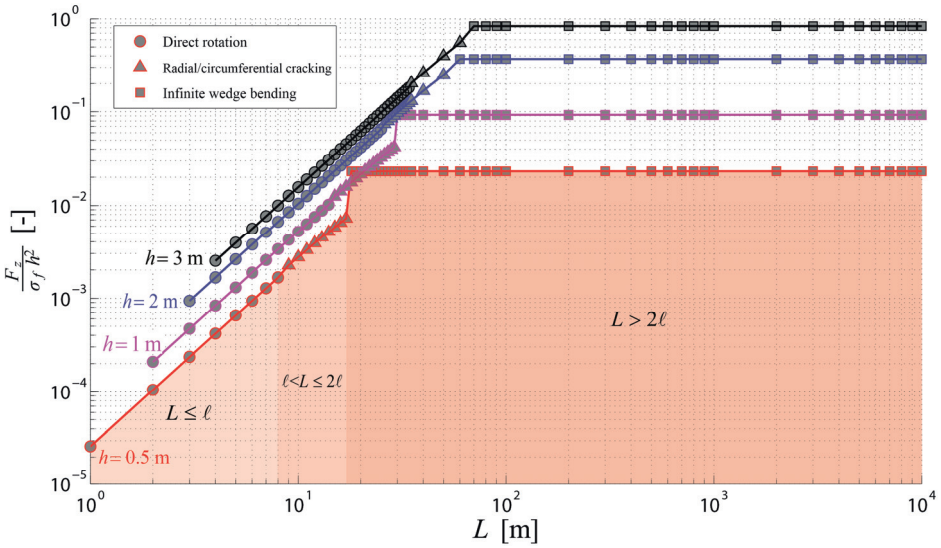

Fig. 4.17 Different out-of-plane flexural failure scenarios according to floe size and ice thickness (note that the calculation was made for a square ice floe).

After verifying the symplectic approach, Eqs. (3.14), (3.15) and (3.17) can therefore be used to quantitatively illustrate different failure scenarios' (see Fig. 2.9) critical vertical forces' variation with floe sizes. Fig. 4.17 illustrates the normalised vertical force $F_Z/(\sigma_f h^2)$ and the corresponding failure scenario for square ice floes with sizes varying from approximately 1 m to 10 km. Four curves are plotted in Fig. 4.17, which represent different ice thicknesses. Within each curve, three sections can be identified: 1) direct rotation of a small ice floe with $L \le \ell$; 2) radial cracking of a square ice floe with size $\ell < L \le 2\ell$; and 3) failure of semi-infinite ice floes ($L > 2\ell$) which is manifested as infinite ice wedges' independent bending failure. As an example, different sections were coloured for the case with an ice thickness of $h = 0.5$ m. Because different failure criteria have been assumed for these three failure scenarios, a non-smooth transition is identified between the failure scenario of radial cracking for a finite size ice floe and infinite wedge bending for a semi-infinite ice floe.

4.1.4 Competitions between flexural and splitting failure modes

According to the simplified contact properties assumed in Section 3.1.3 with Eq. (3.18), all of the developed formulae for different failure modes can therefore be plotted in a single figure to quantify the competition. An example of such competition is plotted in Fig. 4.18 with square ice floes of varying sizes with a contact property $\beta_{YZ} = 0.5$.

As stated in Section 3.1.3, the failure mode is determined by the smaller failure load. Therefore, with all the floe sizes considered, the dominant failure mode that yields a lower failure load (i.e., normalised value of $\beta_{YZ}F_Z/(Lh)$ or $F_Y/(Lh)$) can be identified.

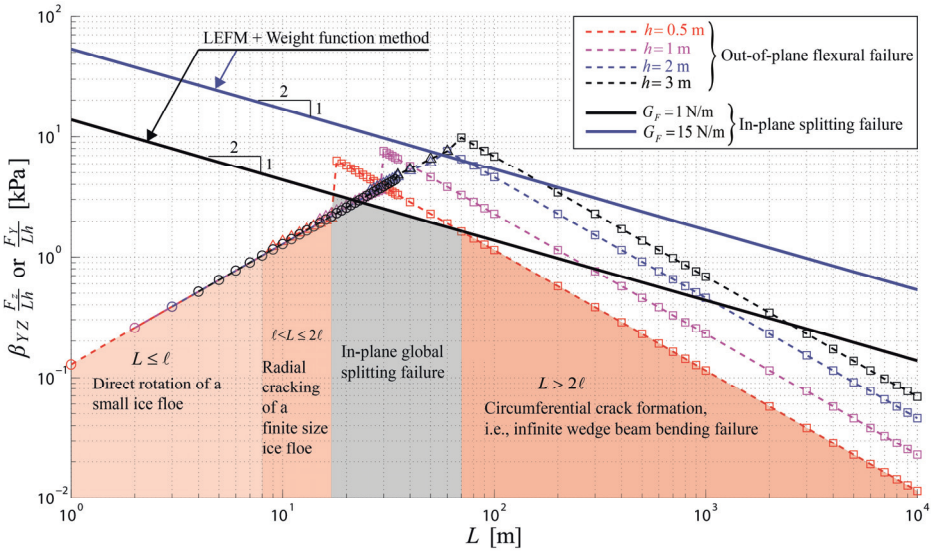

Fig. 4.18 Competition between different failure modes for a square ice floe of varying sizes and ice thicknesses ($\beta_{YZ} = 0.5$).

As discussed in Section 4.1.1.1, the 'LEFM + weight function' method is applicable for most field-scale engineering applications. Therefore, for the normalised ice splitting load $F_Y/(Lh)$, this method was used for the current comparison. In Fig. 4.18, two solid curves (with a slope 1:2) that represent the normalised ice splitting load versus floe size are plotted. These two curves were calculated with different fracture energy inputs. The lower black solid curve was calculated with fracture energy $G_F = 1$ N/m, which was based on laboratory tests (e.g., (Schulson and Duval, 2009)), and the upper blue solid curve was calculated with a fracture energy of $G_F = 15$ N/m, which was based on field measurements (Dempsey et al., 1999a). There are still controversies regarding the fracture energy of sea ice. Advocators behind these two values criticise each other for either using an inappropriately subsized test sample in the laboratory to obtain $G_F = 1$ N/m or using a loading rate that is too slow, such that the creep effect was falsely introduced within the large test sample to obtain $G_F = 15$ N/m. It is not the intention of this thesis to test the validity of these two numbers due to limited amount of test data. However, in using the field test data, Mulmule and Dempsey (1998,1999) did account for the creeping effect (at least in the bulk material) by applying the viscoelastic fictitious crack model. This model treats the secondary creeping effect in the bulk material (not inside the FPZ) by a viscoelastic model, i.e., the fracture energy that is back-calculated by their algorithm based on their test data is supposed to be influenced by the creeping effect of ice to a much lesser extent. From an engineering application point of view, we present both results here and leave it to the readers' judgment to choose appropriately for their specific applications;

In addition, the same four curves that represent the out-of-plane flexural failures with different ice thicknesses $h = 0.5, 1, 2,$ and 3 m in Fig. 4.17 are re-plotted in Fig. 4.18 by

multiplying the load ratio β_{YZ} (for comparison purposes). As an example of reading Fig. 4.18, the intersections between the black solid curve with $G_F = 1$ N/m and the red dashed curve with $h = 0.5$ m are highlighted to show the dominant failure patterns depending on floe size. In addition, the intersection between the splitting failure curve with the semi-infinite ice floe's wedge bending curves can determine the size requirement for an ice floe to be considered level ice (i.e., dominated by local bending failure) at the initial contact. Using the black solid curve with $G_F = 1$ N/m as an example, it contains intersections with wedge bending failure curves at floe sizes of 70 m, 300 m, 1.1 km, and 2.5 km for ice thicknesses of $h = 0.5, 1, 2,$ and 3 m, respectively, i.e., a larger floe size is required for a thicker ice floe to be considered level ice.

Moreover, with all these available formulae (i.e., Eqs. (3.14), (3.15) and (3.17); and Eqs. (3.3) and (3.4)), a failure map can be created mainly based on the geometric information of ice thickness h and floe size L (see Fig. 4.19). Typical material properties (listed the figure) were used to plot the failure map. Though the quantification made in both Fig. 4.18 and Fig. 4.19 are only for specific material property inputs and contact properties (i.e., $\beta_{YZ} = 0.5$), the same formulae can be used to determine the actual failure mode of a certain sized ice floe with the same methodology. For example, the influence of confinement can be accounted for by introducing the confinement pressure $p_{ext}(X)$ in Eq. (3.4), and a different contact scenario can simply be involved by modifying the value of β_{YZ} in the comparison process, as demonstrated herein.

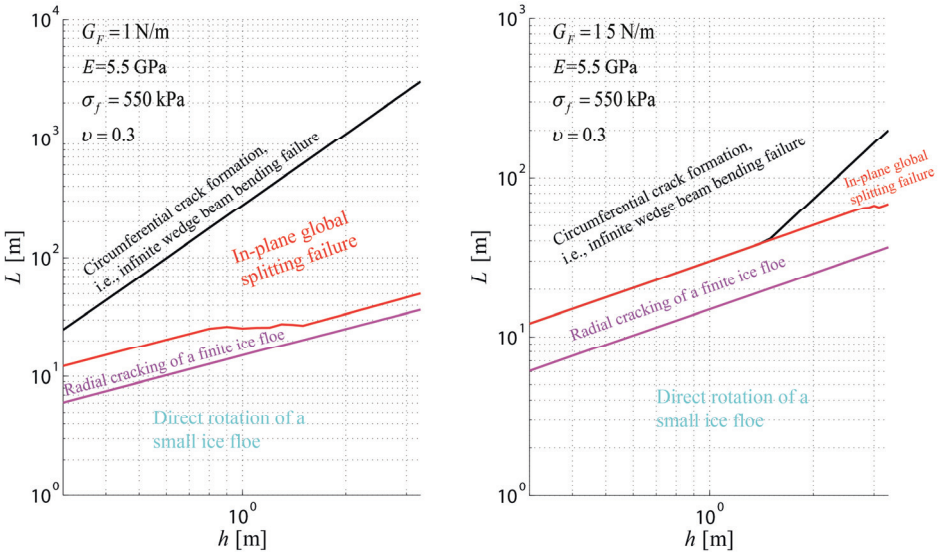

Fig. 4.19 Failure maps of a free square ice floe interacting with a sloping structure with $\beta_{YZ} = 0.5$.

4.2 Influences of rubble accumulations

The results of the physical and theoretical model study on the rubble accumulation's effect on ice loads are presented in this section. In addition, the results from exploring different remedies to apply CEM are also presented.

4.2.1 Physical model and theoretical model studies

First, the tactile sensor measurements are shown in Fig. 4.20. Fig. 4.20a illustrates the approximate location of the installed tactile sensor together with the waterline. Fig. 4.20b illustrates one group of the measured ice load's spatial distribution and its temporal development following the sequence from *1* to *6*. In addition, the approximate location of the waterline (i.e., the blue plane) and the intact level ice (i.e., the shaded solid) are also illustrated.

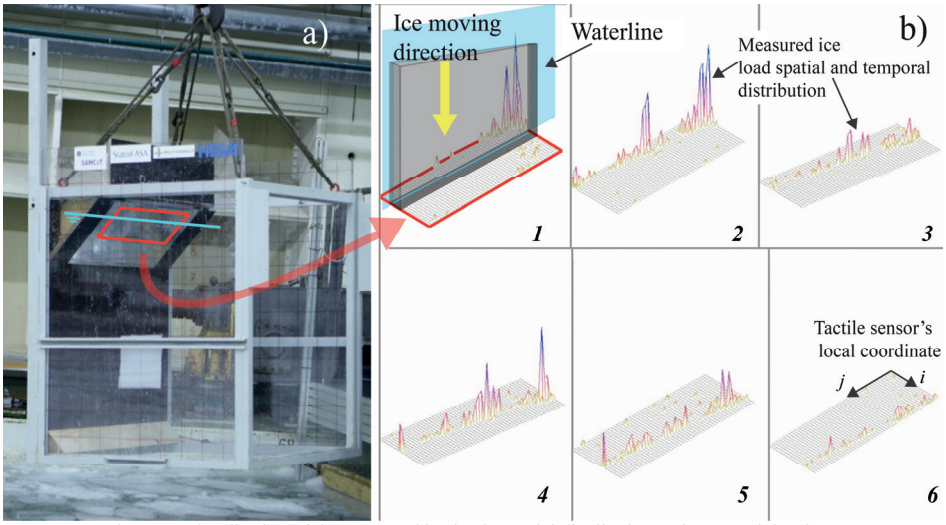

Fig. 4.20 Visualisation of the measured ice load's spatial distribution and temporal development.

Fig. 4.20 shows that the ice load does not diminish instantly below the waterline. Instead, the ice load travels further downwards at a smaller but comparable magnitude. This visual perception is further quantified in Fig. 4.21.

Each local sensel's measurement is summed along the j direction (see Fig. 4.20 or Fig. 3.16 for the local coordinate of the tactile sensor). Afterwards, the summed load is averaged in the time domain to obtain $\overline{F_H(z,t)}$, as shown in Fig. 4.21. Detailed formulae to calculate $\overline{F_H(z,t)}$ are presented in Appendix 4. Fig. 4.21 also illustrates the location of the intact level ice within the shaded area. The comparison is made between the tactile sensor's measurements and the developed theoretical model's prediction. In general, the current theoretical model's predictions regarding the mean ice load's spatial distribution are in agreement with the measurements (i.e., the results agree well with each other in terms of both load magnitude and spatial variation). However, differences do exist

between the results from the theoretical model and physical model tests. First, the theoretical model fails to predict any load above the shaded area (i.e., the thickness region of the un-deformed level ice), which is due to the simplification that the rubble sail's effect was not considered. Second, a further observation in the detailed differences in each test exposed further limitation of the developed theoretical model, such as the following:

- The dynamic effect is neglected, which lead to potential errors in Test #2210;
- It appears questionable to use the current theoretical model for rather thick ice (e.g., 1.22 m in Test #4210) because complications arise when the incoming ice is relatively thick.

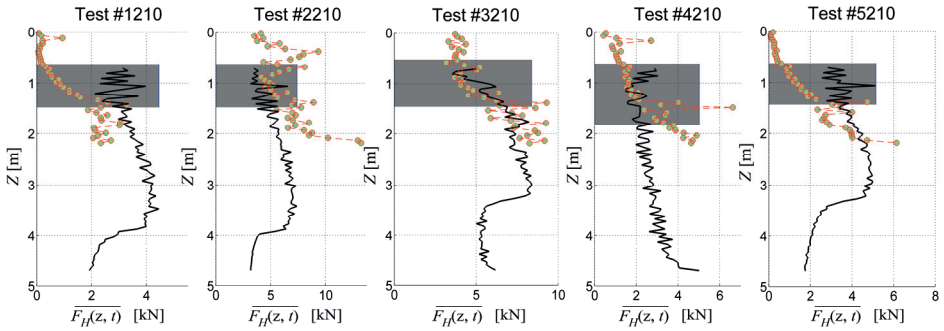

Fig. 4.21 Spatial variation of the mean ice loads (theoretical prediction: solid line; measurements: circles with dashed line).

Despite these differences, the developed theoretical model is further compared with the measurements by the load cells in a similar test set-up (see Fig. 3.17). The comparison consists of the global horizontal load F_{totalH} measured by the load cells and calculated by the theoretical model. The load history comparison illustrated in Fig. 4.22 is for test #3140. The results demonstrate that, in general, the theoretical model predicts less frequent ice loading events than that of the measurements. Such a discrepancy might be due to the 2D assumption of the theoretical model, which rules out the possibility of non-simultaneous ice breakings. During the entire interaction process, the load trends (i.e., the smoothed load histories), load magnitude, and cyclic pattern of the load appear to have been captured by the theoretical model. Similar satisfactory comparisons can also be found for other tests. The comparisons made here further validate the ability of the developed theoretical model to capture the ice load history (including the maximum ice load).

Afterwards, the developed theoretical model is further compared with other existing analytical/empirical models to predict the level ice loads on a sloping structure (see Fig. 4.23). These include the analytical model to calculate level ice and sloping structure interactions in the Phase 1 ice breaking process (see Fig. 3.13(1)) by Croasdale and Cammaert (1994), the 2D ridge building line load recommended by Croasdale (2012) and Comfort et al. (1998), respectively, and the secant formula adopted by Paavilainen and Tuhkuri (2013). In general, the current theoretical model predicts a similar global ice load compared with that of the existing models.

In summary, based on all the validation against physical model tests' results and other existing models, it is fair to say that the developed theoretical model is capable of predicting reasonable spatial and temporal distributions of level ice loads on a sloping structure under the influence of rubble accumulation.

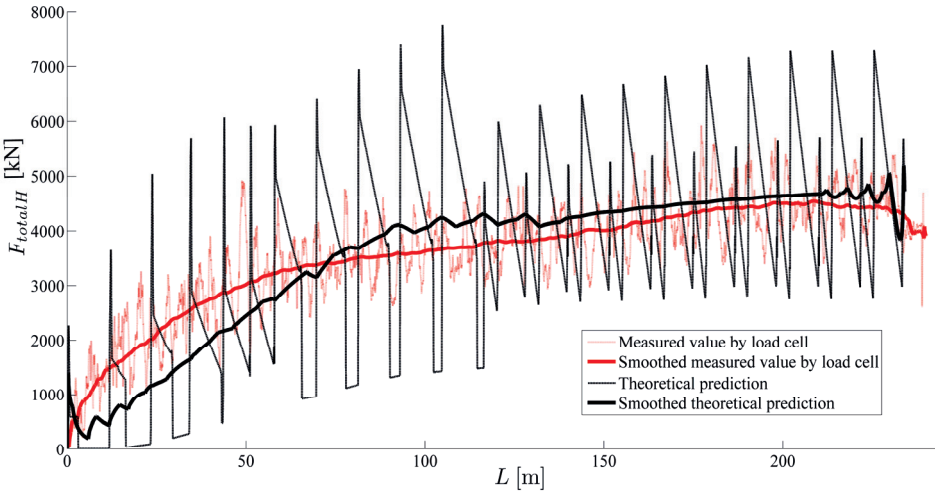

Fig. 4.22 Global load comparison between the theoretical model and load cells for test #3140.

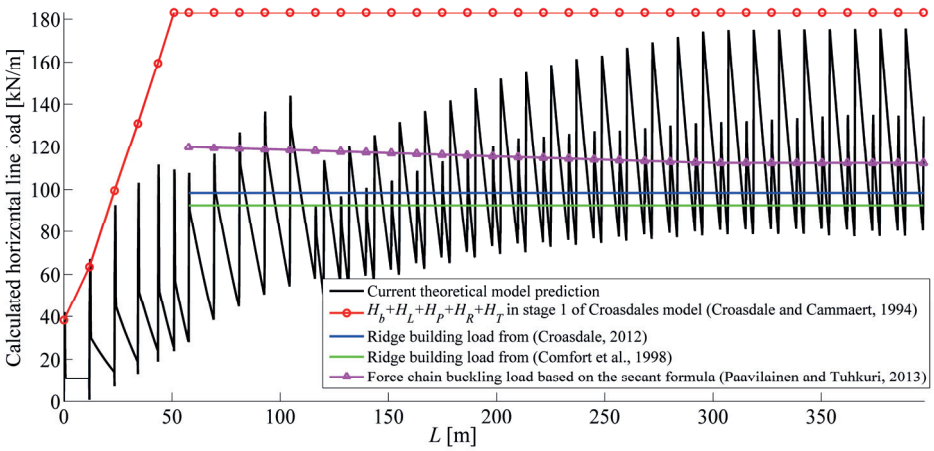

Fig. 4.23 Total load history of test #3210 in comparison with other existing theoretical models.

Thereafter, with the verified theoretical model, different force components can be studied separately to quantify the influences of rubble accumulations. Based on the global ice load's trend in Fig. 4.22 and Fig. 4.23, it can be observed that the rubble accumulation process increases the global ice load and eventually levels off on the so-called ridge building load. The ice load's spatial distribution illustrated in Fig. 4.21

signifies the importance of large $\overline{F_H(z,t)}$ values below the un-deformed level ice region (i.e., the shaded area). Considering the fact that ice breaking load occurs primarily around the waterline, it is considered that these comparable force components were further transferred downwards by the ice rotating process, as shown in Fig. 4.20b.

4.2.2 Trial simulations with remedies to the CEM

With the remedies introduced in Sections 3.3.1 and 3.3.2, the numerical set-up in Fig. 3.18 is solved with ABAQUS/EXPLICIT. A visual comparison between the numerical simulation and physical model test is shown in Fig. 4.24. The bending failure of the incoming level ice is reproduced numerically to a certain extent. However, one can still observe that the crack path in the numerical simulation is largely influenced by the mesh patterns (i.e., cracks only form along the boundaries of bulk elements).

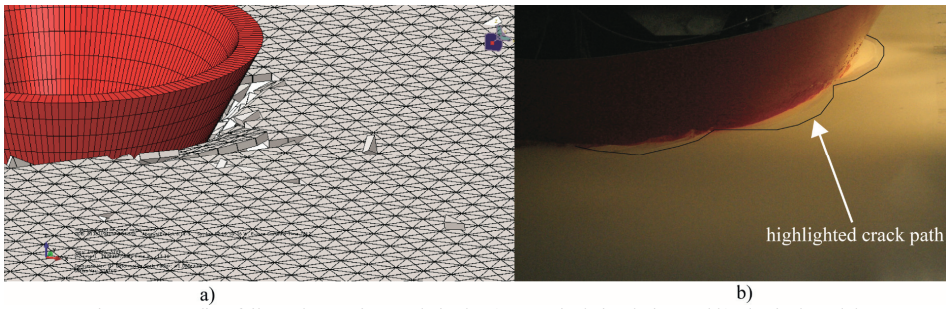

a) b)

Fig. 4.24 Bending failure observation made in the a) numerical simulation and b) physical model test.

To verify the effectiveness of different remedy methods, the global mean horizontal load of each simulation is extracted and plotted versus the inverse of mesh size in Fig. 4.25. These methods include the following: 1) implementing an ice sheet with homogenous material properties; 2) introducing a fracture energy variation into the concerned ice sheet, as shown from Fig. 3.21 to Fig. 3.23; and 3) introducing bulk elements' dissipation into the cohesive element, as shown in Fig. 3.24. The calculated results were compared with the physical model measurements and numerical simulations by Lubbad and Løset (2011).

The mean global horizontal ice load histories simulated by different mesh sizes are compared in Fig. 4.25. It was found that, strictly speaking, all the previously proposed methods failed to ensure mesh objectivity. The mean ice resistance increases with mesh refinement. Comparatively, the method that considers bulk energy dissipation gives relatively less mesh-dependent results, particularly from mesh sizes of 1 m to 2.5 m. This result can be interpreted by the experimental observation shown in Fig. 4.26a, which was produced in the test by reversing the cone structure for a short distance at the end of the test. Then, the broken ice rubble surfaced. Fig. 4.26a shows that ice fails on different scales even under the dominant local bending failure. There are relatively large ice rubbles produced primarily by the local bending failure mode. In addition, there are large amounts of ice flakes that are supposedly produced by crushing and other cracking processes (i.e., micro-cracking, shearing, etc.). Crushing failure in the current study was

accounted for by a perfect-plastic material property of the bulk elements. However, other energy dissipations from micro-cracking processes should also be considered. The bulk energy dissipation included in the fracture energy is one such alternative. However, Fig. 4.25 also shows that the introduction of a randomized fracture energy field appears to have little effect on alleviating the mesh dependency.

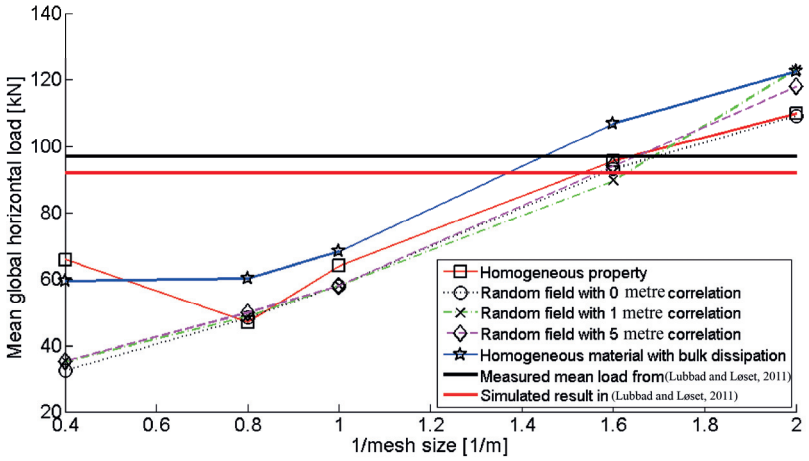

Fig. 4.25 Mesh dependency of the mean horizontal load.

The measured data were scaled up from ice tank (HSVA) tests, and the simulation results obtained by Lubbad and Løset (2011) are also illustrated in Fig. 4.25. Although the calculation results are mesh dependent, it can be observed that a mesh size (0.625 m) that is approximately twice the ice thickness (0.33 m) gives a relatively good estimation of the measured data. The reason behind this might be that choosing a mesh size that is close to the typical rubble length tends to approximate the global ice resistance well. This speculation is based on the observation that the typical rubble length in the radial direction is approximately two to three times the ice thickness (see Fig. 4.26b). Using a mesh size that can reproduce the dominant failure pattern yields closer results to the measurements.

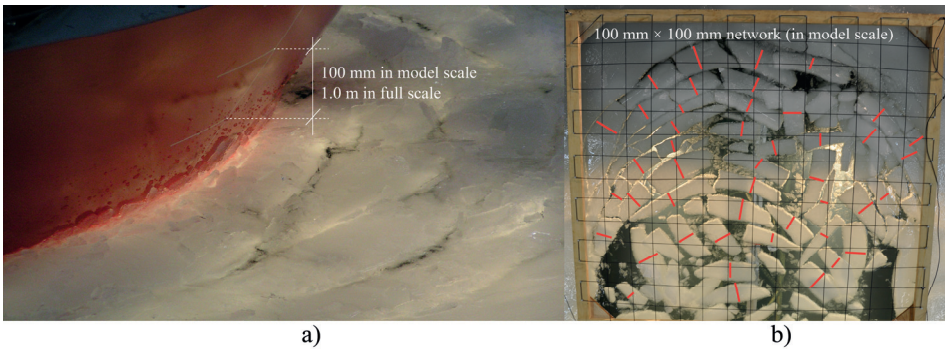

Fig. 4.26 a) Ice breaking patterns; and b) ice breaking length in the radial direction (note that the radial direction of the ice breaking length is labelled in red, and the ice thickness at model-scale is 33 mm).

Based on the previous discussions, a preliminary simulation (the simulation based on the consideration of bulk energy dissipation and a mesh size of 0.625 m) is further scrutinised. First, the simulated time history is compared with the measurements in Fig. 4.27. It can be observed that both the simulation and measurements produce similar results, particularly the load frequency.

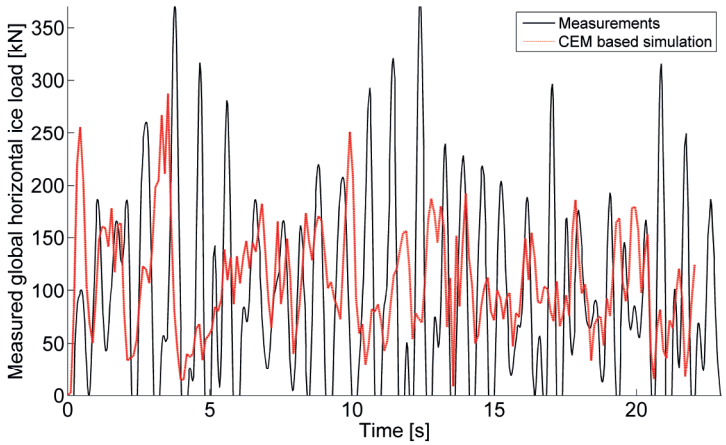

Fig. 4.27 Comparison of the ice load history.

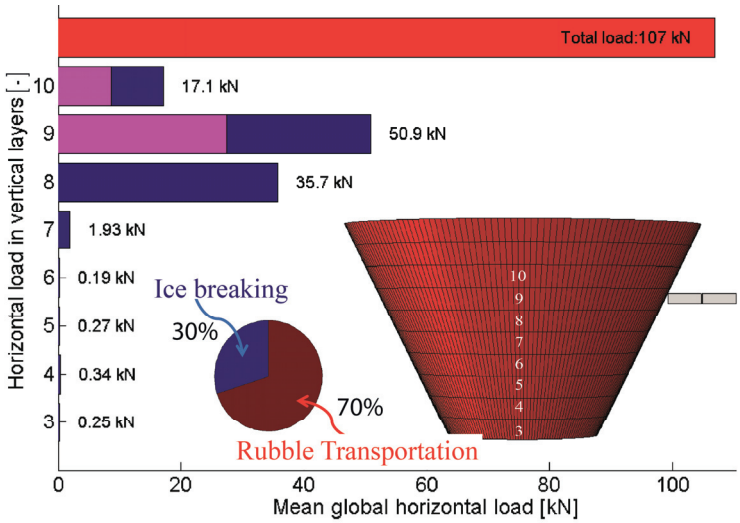

Fig. 4.28 Mean horizontal load in different integration layers (mesh size: 0.625 m).

Next, the ice load history was separated into those due to ice breaking and those due to rubble accumulation. To extract the ice breaking load and rubble accumulation load separately, along the vertical direction of the structure, several equally spaced layers were defined (as shown in Fig. 4.28). The mean horizontal loads, which are the

integrated contact pressure in the respective layers, are also shown in Fig. 4.28. While extracting the ice breaking load, only the loading impulses around the waterline are assumed as the ice breaking load. After extracting these load impulses, the remaining loads are considered to be the result of rubble accumulation. According to this load separation method, the ice breaking load covers 30% of the global load, which agrees with the result in (Lubbad and Løset, 2011), in which the ice breaking module contributes only 25% of the global ice resistance. This result signifies the importance of the rubble accumulation on the global ice resistance.

Chapter 5 Conclusions

This thesis focuses on studying the interaction between an ice floe (within a scale of 10 m to 10 km) and a sloping structure. Attention was given to the fracture of an ice floe and subsequent rotation of the ice blocks. An ice floe can be large enough to be idealised as a level ice field whose failure is dominated by the local bending failure mode around the perimeter of a sloping structure in contact with virgin ice or an ice floe can be of finite size, where its failure is influenced by its free boundaries. Practically relevant scenarios under these two cases were studied.

At first, the failures of an ice floe under the influence of free boundaries were studied. This is a more general approach to studying ice load on a sloping structure because an ice field in the Arctic cannot always be idealised as a level ice condition as most previous researchers or engineering practitioners did. The practical application of the studies made here is for the operation of Arctic offshore structures in a relatively 'open' ice condition, e.g., a broken ice field. The fracture of an ice floe in such an ice condition has rarely been studied in history within the context of ice-structure interactions. However, relevant studies have been conducted in other closely related areas, e.g., fracture toughness tests of sea ice and bearing capacity of ice covers. Knowledge was transferred from these areas to an idealised 'floe ice - sloping structure' interaction scenario. Specifically, both the in-plane splitting failure and out-of-plane flexural failures of a finite size ice floe were studied in a decoupled manner. Relevant theoretical formulae were proposed, implemented and validated. In the end, we drew the following conclusions corresponding to the research questions described in Section 2.4:

1) Regarding the global in-plane splitting failure mode

- An analytical framework was established based on both fracture mechanics and plastic limit theory analysis to calculate the ice splitting load (i.e., the force required to split an ice floe);
- Serving as a primary tool, the fracture mechanic based approach was explored under the method of Linear Elastic Fracture Mechanics (LEFM) and Cohesive Zone Method (CZM, i.e., a type of nonlinear fracture mechanics). These methods were successfully validated against available experimental data, numerical simulation results and idealised analytical solutions;
- Upon successful implementation of the approaches based on fracture mechanics, it was found that for sea ice, solutions by LEFM are sufficient for most engineering-scale applications. However, when extrapolating lab-scale results to field-scale, caution should be made for the applicability of LEFM; in this case, CZM can serve as a potential tool that bridges the lab scale with the field scale;
- The influences of floe size, geometry and confinement on ice splitting load were quantified with the derived formulae. The results show that for most engineering applications, the ice splitting load is scaled with $(\text{floe size})^{1/2}$; the geometry has a lesser effect on the ice splitting load compared with the effect of boundary confinement, e.g., for a rectangular ice floe, the ice splitting load begins to converge and ceases to increase when the width-to-length ratio is $\beta \geq 2$;

however, the special confinement induced by the floe inertia demonstrates that a confinement can 'effectively' increase the ice splitting load;

- As noted by previous researchers, ice floes in summer Arctic waters tend to appear in nearly circular shapes, whereas a nearly rectangular shape can be expected in winter Arctic waters. This to say, most of the ice floes can be idealised as the base case problems (i.e., rectangular and circular ice floes) that were studied in this thesis. In this sense, the maximum ice splitting loads are given in Eq. (4.1) and Fig. 4.4. Notably, in all cases, the maximum ice splitting load corresponds to a critical crack length that is less than 20% of the floe size;
- For an ice floe that has a highly irregular geometry, the proposed fracture mechanics based approach can become analytically difficult. Then, the plastic limit theory can serve as a simplified analytical alternative to yield a conservative estimation of the ice splitting load.

2) Regarding the local out-of-plane flexural failure mode

- Based on literature reviews and field observations, depending on the size of an ice floe, we conservatively identified three different scenarios of the out-of-plane flexural failure mode of an ice floe: 1) direct rotation of a small ice floe; 2) radial cracking of a finite size ice floe; and 3) circumferential crack formation within a semi-infinite ice floe;
- The theoretical development was focused on the radial cracking of a square-shaped ice floe. A normalisation procedure and simplified numerical models were used to study the radial crack initiation and propagation, respectively. These numerical models were successfully validated against idealised analytical solutions and related benchmark tests;
- Based on the quantified competition between radial crack initiation and propagation, it was found that for typical ice material properties, the failure of a nearly square-shaped ice floe is radial-crack-initiation controlled once its physical size L is smaller than 2ℓ (note that ℓ is the characteristic length of a floating ice floe; its detailed formulation is given in Eq. (3.10), and it can also be approximated as $\ell = 13.5(\text{ice thickness})^{3/4}$, according to previous studies);
- Radial-crack-initiation-controlled fracture of a finite ice floe implies a reduced ice load on a sloping structure compared with continuous local bending failure of a semi-infinite ice floe. The above size requirement (i.e., $L < 2\ell$ or $L < 27(\text{ice thickness})^{3/4}$) for radial cracking failure of an ice floe thus conveys a practical suggestion to an ice management operation, i.e., producing ice floes smaller than 2ℓ downstream of an ice management operation is mechanically preferred to reduce ice load on the protected vessel;
- The identified size region in which radial-crack-initiation-controlled fracture occurs for a nearly square-shaped ice was further extended to arbitrary rectangular ice floes with varying width-to-length ratios. These rectangular ice floes are assumed to fail by forming only radial or circumferential cracks (i.e., radial or circumferential cracking of finite rectangular ice floes). In addition, the analytical solution was obtained for this type of failure scenario based on a

symplectic approach. The analytical solution was successfully implemented and verified by FEM-based numerical calculations;

- Based on previous studies and relevant assumptions, analytical formulae were proposed for the identified three failure scenarios in their respective size region, i.e., 1) theories regarding a short beam on an elastic foundation to calculate the direct rotation of a small ice floe (i.e., $L \leq \ell$); 2) a symplectic approach to analytically calculate the radial/circumferential cracking of a finite size ice floe (i.e., $\ell < L \leq 2\ell$); and 3) theories on an infinite wedge beam on an elastic foundation to calculate the failure of a semi-infinite ice floe (i.e., $L > 2\ell$).

3) Regarding the competition between different failure modes

- With all the analytical formulae at our disposal, the failure load for different failure scenarios across a floe size scale ranging from approximately 1 m to 10 km can thus be constructed. Therefore, in the context of floe ice - sloping structure interactions, the force required to fail an ice floe at the structural scale and floe scale is theoretically bridged;
- The competition among different failure modes can therefore be quantified. It was found that the fracture energy of sea ice, ice thickness, contact properties and confinement greatly influence the failure mode of an ice floe;
- As a demonstration to quantify such competition, with a reasonably assumed contact property of $\beta_{YZ} = 0.5$ (note that this coefficient is defined in Eq. (3.18), which signifies a ratio between the horizontal and vertical ice load due to the ice-structure contact force's decomposition) and further assuming a fracture energy of sea ice as 1 N/m with typical ice material properties, it was found that a nearly square-shaped ice floe should be larger than 70 m, 300 m, 1.1 km, and 2.5 km for ice thicknesses $h = 0.5, 1, 2, \text{and } 3$ m, respectively, to be considered level ice. This analysing procedure can be easily applied to other contact or confinement scenarios;
- Similarly, a failure map can be constructed based on all the developed formulae for different failure modes. All these analytical formulae can be implemented in the multi-body dynamic simulator developed at SAMCoT to numerically model a series of ice floe failure events that cover large temporal and spatial scales.

After studying the major interaction processes, i.e., fracture of an ice floe, in a relatively 'open' ice condition, we proceed to a relatively 'tight' ice condition. In such an ice condition, the interaction processes primarily exhibit local bending failure of incoming intact ice and also the subsequent ice rotating process. Particularly, we chose to study a relatively extreme scenario, i.e., level ice - wide sloping structure interactions under the influence of rubble accumulation. This extreme scenario was studied by physical model tests and a theoretical model, which is capable of predicting ice load's spatial and temporal variations. The followings are the major conclusions in this study.

- Both tactile sensor's measurements and the theoretical model's predictions demonstrate that rubble accumulation increases the global ice resistance up until the ridge building load;

- Satisfactory agreement was obtained between the theoretical model and physical model tests' measurement when the interaction speed is low (i.e., approximately 0.2 m/s) and when the ice thickness is less than 1 m;
- The largest mean ice load typically occurs below the un-deformed level ice's thickness region. This arrangement indicates the importance of the rubble accumulation load and ice rotating load when considering the largest mean ice load;
- Compared with other two-dimensional theories (i.e., the ridge building load), the current theoretical model yields relatively conservative but similar predictions regarding the maximum ice load. However, the validity of the physical model tests and, accordingly, the theoretical model's application in the context of full scale requires further more rigorous validations;
- Based on the physical model's measured results, the currently developed theoretical model can serve as a preliminary yet useful prediction and investigation tool to harvest the spatial and temporal variations of ice load on a sloping structure under the influence of rubble accumulation.

Afterwards, a potentially promising numerical tool, the Cohesive Element Method (CEM) was further explored to study ice load's distribution under the influences of rubble accumulation. However, in this task, the key contribution is to evaluate different remedies for this method. The results show that there is still a substantial knowledge/computational gap before we can confidently use this seemingly promising method, which is capable of simulating the fracture and fragmentation process.

Ice load calculations can be delivered at different levels of complexities and accuracies. It is critically important to use the appropriate method to address problems at the correct scale. Throughout this entire thesis, developing the concerned failure modes' load calculation methods were the key theoretical contributions; organising all these formulae together to create a failure map and to construct ice load's temporal and spatial variations are the key applied contributions. The practical problem we now face in the Arctic waters entails large temporal and spatial scale operations. Most of the developed tools in this thesis, due to their analytical nature, can be incorporated with a multi-body dynamic simulator to further study the Arctic research problems on large temporal and spatial scales.

References

API_RP2, 1995. Recommended Practice for Planning, Designing, and Constructing Structures and Pipelines for Arctic Conditions. American Petroleum Institute.

Bažant, Z.P. and Planas, J., 1998. Fracture and size effect in concrete and other quasibrittle materials. CRC.

Bhat, S.U., 1988. Analysis for splitting of ice floes during summer impact. Cold Regions Science and Technology, 15(1): 53-63.

Bhat, S.U., Choi, S.K., Wierzbicki, T. and Karr, D.G., 1991. Failure analysis of impacting ice floes. Journal of Offshore Mechanics and Arctic Engineering, 113: 171.

Bueckner, H.F., 1970. Novel principle for the computation of stress intensity factors. Zeitschrift fuer Angewandte Mathematik & Mechanik, 50(9).

Chen, W.F. and Han, D.J., 1988. Plasticity for structural engineers. Springer-Verlag (New York).

Comfort, G., Singh, S. and Dinovitzer, A., 1998. Limit-force ice loads and their significance to offshore structures in the Beaufort Sea. International Journal of Offshore and Polar Engineering, 8(1).

Croasdale, K.R., 2012. Ice rubbling and ice interaction with offshore facilities. Cold Regions Science and Technology, 76–77(0): 37-43.

Croasdale, K.R., Bruce, J.R. and Liferov, P., 2009. Sea ice loads due to managed ice, Proceedings of the 20th International Conference on Port and Ocean Engineering under Arctic Conditions (POAC'09), Luleå, Sweden, pp. 139.

Croasdale, K.R. and Cammaert, A.B., 1994. An improved method for the calculation of ice loads on sloping structures in first-year ice. Power Technology and Engineering (formerly Hydrotechnical Construction), 28(3): 174-179.

DeFranco, S.J. and Dempsey, J.P., 1994. Crack propagation and fracture resistance in saline ice. Journal of Glaciology, 40(136): 451-462.

Dempsey, J.P., 2000. Research trends in ice mechanics. International Journal of Solids and Structures, 37(1-2): 131-153.

Dempsey, J.P., Adamson, R.M. and Mulmule, S.V., 1999a. Scale effects on the in-situ tensile strength and fracture of ice. Part II: First-year sea ice at Resolute, NWT. International journal of fracture, 95(1): 347-366.

Dempsey, J.P., DeFranco, S.J., Adamson, R.M. and Mulmule, S.V., 1999b. Scale effects on the in-situ tensile strength and fracture of ice Part I: Large grained freshwater ice at Spray Lakes Reservoir, Alberta. International journal of fracture, 95(1): 325-345.

Dempsey, J.P., DeFranco, S.J., Blanchet, D. and Prodanovic, A., 1994. Mechanisms of fracture of sea ice. Hydrotechnical Construction, 28(3): 164-168.

Dempsey, J.P. and Zhao, Z.G., 1993. Elastohydrodynamic response of an ice sheet to forced sub-surface uplift. Journal of the Mechanics and Physics of Solids, 41(3): 487-506.

Frederking, R.M.W. and Timco, G.W., 1985. Quantitative analysis of ice sheet failure against an inclined plane. J. Energy Resour. Technol.;(United States), 107(3).

Gold, L.W., 1971. Use of ice covers for transportation. Canadian Geotechnical Journal, 8(2): 170-181.

Hamilton, J.M., 2011. The Challenges of Deep-Water Arctic Development. International Journal of Offshore and Polar Engineering, 21(4): 241-247.

Hansen, E.H. and Løset, S., 1999a. Modelling floating offshore units moored in broken ice: comparing simulations with ice tank tests. Cold Regions Science and Technology, 29(2): 107-119.

Hansen, E.H. and Løset, S., 1999b. Modelling floating offshore units moored in broken ice: model description. Cold Regions Science and Technology, 29(2): 97-106.

Hetényi, M., 1946. Beams on elastic foundation, 1. University of Michigan Press Ann Arbor, Michigan, USA.

Irwin, G.R., 1956. Onset of fast crack propagation in High Strength Steel and Aluminum Alloys, Sagamore Research Conference Proceedings, pp. 289-305.

ISO/FDIS/19906, 2010. Petroleum and natural gas industries - Arctic offshore structures,International Standard, International Standardization organization, Geneva, Switzerland,.

Kämäräinen, J., 2007. Theoretical Investigation on the Effect of Fluid Flow Between the Hull of a Ship and Ice Floes on Ice Resistance in Level Ice. Helsinki University of Technology, Department of Mechanical Engineering, Laboratory for Mechanics of Materials, Helsinki, Finland.

Keinonen, A., 1996. Icebreaker characteristics synthesis-Icebreaker Performance Models, Seakeeping, Icebreaker Escort, Transport Canada.

Kerr, A.D., 1976. The bearing capacity of floating ice plates subjected to static or quasi-static loads. Journal of Glaciology, 17: 229-268.

Kolari, K., Kuutti, J. and Kurkela, J., 2009. Fe-Simulation of Continuous Ice Failure Based on Model Update Technique, Proceedings of the 20th International Conference on Port and Ocean Engineering under Arctic Conditions, Luleå, Sweden.

Konno, A., 2009. Resistance Evaluation of Ship Navigation in Brash Ice Channels, Proceedings of the 20th International Conference on Port and Ocean Engineering under Arctic Conditions, Luleå, Sweden.

Konno, A. and Mizuki, T., 2006. Numerical Simulation of Pre-Sawn Ice Test of Model Icebreaker Using Physically based Modelling, Proceedings oh the 18th IAHR International Symposium on Ice, Sapporo, Japan, pp. 17-23.

Konno, A., Nakane, A. and Knamori, S., 2013. Validation of Numerical Estimation of Brash Ice Channel Resistance with Model Test Proceedings of the 22nd International Conference on Port and Ocean Engineering under Arctic Conditions, Espoo, Finland.

Konno, A., Saitoh, O. and Watanabe, Y., 2011. Numerical Investigation of Effect of Channel Condition against Ship Resistance in Brash Ice Channels, Proceedings of the 21st International Conference on Port and Ocean Engineering under Arctic Conditions, Montréal, Canada.

Konuk, I., Gürtner, A. and Yu, S., 2009. A Cohesive Element Framework for Dynamic Ice-Structure Interaction Problems—Part I: Review and Formulation, Proceedings of the ASME 2009 28th International Conference on Ocean, Offshore and Arctic Engineering. ASME, Honolulu, Hawaii, USA, pp. 1-9.

Kotras, T.V., Baird, A.V. and Naegle, J.N., 1983. Predicting Ship Performance in Level Ice. Transactions - Society of Naval Architects and Marine Engineers, Volume 91, 1983. SNAME, New York, NY, USA, pp. 329-349.

Li, R., Zhong, Y. and Li, M., 2013. Analytic bending solutions of free rectangular thin plates resting on elastic foundations by a new symplectic superposition method. Proceedings of the Royal Society A: Mathematical, Physical and Engineering Science, 469(2153): 20120681.

Lindqvist, G., 1989. A straightforward method for calculation of ice resistance of ships, Proceedings of POAC 1989, pp. 722-735.

Little, R.W., 1973. Elasticity. Prentice-Hall Englewood Cliffs, New Jersey.

Liu, J., Lau, M. and Williams, F.M., 2010. Mathematical modeling of ice-hull interaction for ship maneuvering in ice simulations.

Løset, S., 1994a. Discrete element modelling of a broken ice field — Part I: model development. Cold Regions Science and Technology, 22(4): 339-347.

Løset, S., 1994b. Discrete element modelling of a broken ice field — Part II: simulation of ice loads on a boom. Cold Regions Science and Technology, 22(4): 349-360.

Lu, W., Høyland, K., Serré, N. and Evers, K.-U., 2014a. Ice Load Measurement by Tactile Sensor in Model Scale Test in Relation to Rubble Ice Transport on Arctic Offshore Structures (RITAS). In: Hydralab (Editor), Proceedings of the HYDRALAB IV Joint User Meeting, Lisbon.

Lu, W., Løset, S. and Lubbad, R., 2012a. Simulating ice-sloping structure interactions with the cohesive element method, ASME 2012 31st International Conference on Ocean, Offshore and Arctic Engineering. American Society of Mechanical Engineers, Rio de Janeiro, Brazil, pp. 519-528.

Lu, W., Løset, S. and Lubbad, R., 2012b. Ventilation and backfill effect during ice-structure interactions. In: Li and Lu (Editors), The 21st IAHR International Symposium on Ice, Dalian, China, pp. 826-841.

Lu, W., Lubbad, R., Høyland, K. and Løset, S., 2014b. Physical model and theoretical model study of level ice and wide sloping structure interactions. Cold Regions Science and Technology, 101: 40-72.

Lu, W., Lubbad, R. and Løset, S., (submitted in March 2014). In-plane fracture of an ice floe: a theoretical study on the splitting failure mode. Cold Regions Science and Technology.

Lu, W., Lubbad, R., Serré, N. and Løset, S., 2013. A theoretical model investigation of ice and wide sloping structure interactions, Proceedings of the 22nd International Conference on Port and Ocean Engineering under Arctic Conditions, Espoo, Finland, pp. 1-14.

Lubbad, R. and Løset, S., 2011. A numerical model for real-time simulation of ship-ice interaction. Cold Regions Science and Technology, 65(2): 111-127.

Lubbad, R., Moe, G. and Løset, S., 2008. Static and Dynamic Interaction of Floating Wedge-Shaped Ice Beams and Sloping Structures. 19th IAHR Internatioanl Symposium on Ice: 179-189.

Metrikin, I., Kerkeni, S., Jochmann, P. and Løset, S., 2013. Experimental and Numerical Investigation of Dynamic Positioning in Level Ice, ASME 2013 32nd International Conference on Ocean, Offshore and Arctic Engineering. American Society of Mechanical Engineers, pp. V006T07A019-V006T07A019.

Metrikin, I. and Løset, S., 2013. Non-Smooth 3D Discrete Element Simulation of a Drillship in Discontinuous Ice, Proceedings of the 22nd International Conference on Port and Ocean Engineering under Arctic Conditions, Espoo, Finland.

Milano, V.R., 1972. Ship resistance to continuous motion in ice, Stevens Institute of Technology.
Mulmule, S.V. and Dempsey, J.P., 1998. A viscoelastic fictitious crack model for the fracture of sea ice. Mechanics of Time-dependent Materials, 1(4): 331-356.
Mulmule, S.V. and Dempsey, J.P., 1999. Scale effects on sea ice fracture. Mechanics of Cohesive frictional Materials, 4(6): 505-524.
Mulmule, S.V. and Dempsey, J.P., 2000. LEFM size requirements for the fracture testing of sea ice. International journal of fracture, 102(1): 85-98.
Naegle, J.N., 1980. Ice-Resistance Prediction and Motion Simulation For Ships Operating in The Continuous Mode of Icebreaking, The University of Michigan, Michigan.
Nevel, D.E., 1958. The theory of a narrow infinite wedge on an elastic foundation, U. S. Army Snow Ice and Permafrost Research Establishment, Corps of Engineering.
Nevel, D.E., 1961. The narrow free infinite wedge on an elastic foundation, DTIC Document.
Nevel, D.E., 1965. A semi-infinite plate on an elastic foundation, DTIC Document.
Nevel, D.E., 1972. The ultimate failure of a floating ice sheet, International Association for Hydraulic Research, Ice Symposium, pp. 17-22.
Nevel, D.E., 1992. Ice forces on cones from floes, IAHR Symposium, 11th, pp. 1391-1404.
Paavilainen, J. and Tuhkuri, J., 2013. Pressure distributions and force chains during simulated ice rubbling against sloped structures. Cold Regions Science and Technology, 85(0): 157-174.
Paavilainen, J., Tuhkuri, J. and Polojarvi, A., 2010. Rubble pile formation against an inclined structure analysis of simulation results. IAHR International Symposium on Ice: 1-11.
Paavilainen, J., Tuhkuri, J. and Polojärvi, A., 2006. Discrete element simulation of ice pile-up against an inclined structure. Proceedings of the 18th International Symposium on Ice, IAHR, 2: 177-184.
Paavilainen, J., Tuhkuri, J. and Polojärvi, A., 2009. 2D combined finite-discrete element method to model multi-fracture of beam structures. Engineering Computations, 26(6): 578-598.
Paavilainen, J., Tuhkuri, J. and Polojärvi, A., 2011. 2D numerical simulations of ice rubble formation process against an inclined structure. Cold Regions Science and Technology, 68(1–2): 20-34.
Palmer, A.C. and Croasdale, K.R., 2013. Arctic Offshore Engineering. World Scientific.
Palmer, A.C., Goodman, D.J., Ashby, M.F., Evans, A.G., Hutchinson, J.W. and Ponter, A.R.S., 1983. Fracture and its role in determining ice forces on offshore structures. Annals of glaciology, 4: 216-221.
Ralston, T.D., 1977. Ice force design considerations for conical offshore structures, Proceedings of the 4th International Conference on Port and Ocean Engineering under Arctic Conditions, Newfoundland Memorial University, Canada, pp. 12.
Ralston, T.D., 1980. Plastic limit analysis of sheet ice loads on conical structures. Physics and Mechanics of Ice, Springer-Verlag, New York, USA: 289-308.
Ralston, T.D., 1981. Plastic limit analysis of ice splitting failure. Proc. 6th POAC, Quebec, 1: 205-215.

Reinicke, K.M. and Ralston, T.D., 1977. Plastic limit analysis with an anisotropic, parabolic yield function, International Journal of Rock Mechanics and Mining Sciences & Geomechanics Abstracts. Elsevier, pp. 147-162.

Rice, J.R., 1972. Some remarks on elastic crack-tip stress fields. International Journal of Solids and Structures, 8(6): 751-758.

Richard, M. and Mckenna, R., 2013. Factors Influencing Managed Sea Ice Loads, Proceedings of the 22nd International Conference on Port and Ocean Engineering under Arctic Conditions, Espoo, Finland.

Riska, K. and Coche, E., 2013. Station Keeping in Ice - Challenges and Possibilities, Proceedings of the 22nd International Conference on Port and Ocean Engineering under Arctic Conditions, Espoo, Finland.

Sanderson, T.J.O., 1988. Ice mechanics and risks to offshore structures.

Sawamura, J., Riska, K. and Moan, T., 2008. Finite Element Analysis of Fluid-Ice Interaction during Ice Bending, 19th IAHR International Symposium on Ice, Vancouver, British Columbia, Canada, pp. 239-250.

Sawamura, J., Tachibana, T., Tsuchiya, H. and Osawa, N., 2010. Numericial Investigation for the Bending Failure of Wedge-Shaped Floating Ice, 20th IAHR International Symposium on Ice, Lahti, Finland.

Sayed, M. and Barker, A., 2011. Numerical Simulations of Ice Interaction with a Moored Structure, OTC Arctic Technology Conference.

Sayed, M., Kubat, I., Wright, B. and Millan, J., 2014. Numerical Simulations of Ice Forces on Moored and Thruster-Assisted Drillships, OTC Arctic Technology Conference. Offshore Technology Conference.

Sayed, M., Kubat, I.K. and Wright, B., 2012. Numerical Simulations of ice forces on the Kulluk: the role of ice confinement ice pressure and ice management, OTC Arctic Technology Conference. Offshore Technology Conference.

Sayed, M., Neralla, V. and Savage, S., 1995. Yield conditions of an assembly of discrete ice floes, Proceedings of 5th International Offshore and Polar Engineering Conference (ISOPE), pp. 330-335.

Schiermeier, Q., 2012. The great Arctic oil race begins. Nature, 482(7383): 13-14.

Schulson, E.M. and Duval, P., 2009. Creep and fracture of ice, 1. Cambridge University Press, Cambridge, 190-211 pp.

Serré, N., 2011. Numerical modelling of ice ridge keel action on subsea structures. Cold Regions Science and Technology, 67(3): 107-119.

Serré, N. and Liferov, P., 2010. Loads from ice ridge keels-experimental vs. numerical vs. analytical, 20th IAHR International Symposium on Ice, Lahti, Finland.

Sodhi, D.S., 1997. Vertical penetration of floating ice sheets. International Journal of Solids and Structures, 35(31-32): 4275-4294.

Su, B., Riska, K. and Moan, T., 2010. A numerical method for the prediction of ship performance in level ice. Cold Regions Science and Technology, 60(3): 177-188.

Timco, G.W., 1991. The vertical pressure distribution on structures subjected to rubble forming ice, 11th International Conference on Port and Ocean Engineering under Arctic Conditions, St.John's, Canada, pp. 185-197.

Timoshenko, S.P. and Goodier, J.N., 1951. Theory of elasticity. New York, McGraw-Hill, 5: 500.

Valanto, P., 2001a. On the cause and distribution of resistance forces on ship hulls moving in level ice, Proceedings of the 18th International Conference on Port and Ocean Engineering under Arctic Conditions, Ottawa, Ontario, Canada, pp. 803-816.

Valanto, P., 2001b. The resistance of ships in level ice. SNAME, 109: 53-83.

Ventsel, E. and Krauthammer, T., 2001. Thin plates and shells: theory: analysis, and applications. CRC press, New York.

Weeks, W.F., 2010. On sea ice. University of Alaska Press.

Wright, B., 1999. Evaluation of full scale data for moored vessel stationkeeping in pack ice. PERD/CHC Report: 26-200.

Yao, W.A., Zhong, W.X. and Lim, C.W., 2009. Symplectic elasticity. World Scientific.

Yulmetov, R., Løset, S. and Eik, K.J., 2013a. Analysis of Drift of Sea Ice and Icebergs in the Greenland Sea, The proceedings of the 22nd International Conference on Port and Ocean Engineering under Arctic Conditions, Espoo, Finland.

Yulmetov, R., Løset, S. and Lubbad, R., 2014. An Effective Numerical Method for Generation of Broken Ice Fields, Consisting of a Large Number of Polygon-Shaped Distinct Floes, Proceedings of the 22nd IAHR International Symposium on Ice, Singapore.

Yulmetov, R., Marchenko, A. and Løset, S., 2013b. Ice drift and sea current analysis in the northwestern Barents Sea, The proceedings of the 22nd International Conference on Port and Ocean Engineering under Arctic Conditions, Espoo, Finland.

Appendix 1 In-plane splitting failure of an ice floe

This appendix includes the paper accepted in Journal of Cold Regions Science and Technology (see below).

- Lu, W., Lubbad, R. and Løset, S., (Accepted on November 12th, 2014). In-plane fracture of an ice floe: a theoretical study on the splitting failure mode. Cold Regions Science and Technology. DOI: *10.1016/j.coldregions.2014.11.007*.

Appendix I

In-plane fracture of an ice floe: a theoretical study on the splitting failure mode

Wenjun Lu[1] **Raed Lubbad** **Sveinung Løset**

Sustainable Arctic Marine and Coastal Technology (SAMCoT), Centre for Research-based Innovation (CRI)

Norwegian University of Science and Technology (NTNU), Trondheim, Norway

[1] Corresponding author
E-mail address: wenjun.lu@ntnu.no (Wenjun Lu)

Abstract

In practical offshore structure/icebreaker designs, it is critical to capture the salient failure modes of the ice feature. The dominant failure modes are influenced by the structural properties, interaction process, and characteristics of the ice features. For an ice feature of finite size with relatively small lateral confinement, splitting failure has been frequently observed during ice-structure interactions. In literature, the splitting failure of an ice floe has been studied using several different methods, ranging from strength theory to methods based on fracture mechanics. One contribution of this paper is that these various methods are compiled and evaluated collectively. Another contribution of this paper is the construction of an analytical framework to obtain solutions for the splitting process of an ice floe upon serious considerations of relevant fundamental theories. The framework developed for its calculations is presented but not limited these two base cases (i.e., rectangular and circular ice floes). Specifically, because of the complexity of the splitting failure scenario (particularly the ice floe geometry) and our pursuit of analytical solutions, within the presented framework, two different approaches have been proposed: the fracture mechanics approach and plasticity theory approach. All of the employed methods are validated against data from previous field tests or numerical results. Recommendations and discussion were presented for each of these methods' respective application range. It was found that most of the floe sizes under engineering interests can be accurately described by linear elastic fracture mechanics. The cohesive zone method, which is one type of the nonlinear fracture mechanics based approaches, is found to be potentially applicable in extrapolating laboratory-scale measurements to the field scale. Worth mentioning, the weight function method was effectively used to calculate the fracture properties of an ice floe under various symmetric loading conditions (e.g., boundary confinement). The boundary confinement can easily prevent splitting failure or increase the ice splitting load. As one type of the lateral confinement, the inertia-induced body force, is also studied and compared with previous numerical results. Comparatively, the plasticity theory based approach (i.e., the plastic upper/lower limit theory) enables us to effectively attain a conservative estimation of the ice splitting load in an analytical form. It can serve as a supplementary tool to the fracture mechanics based approach.

Keywords:

Ice structure interactions

Fracture of an ice floe

Splitting failure mode

Weight function method

Cohesive zone method

Plastic limit analysis

1 Introduction

'Level ice' is rather a theoretical simplification of the real ice conditions in the Arctic seas. A typical ice field in the Arctic is far from continuous. During the interaction between ice and structures (e.g., icebreakers, fixed and floating offshore structures), it has been frequently observed that an ice floe, with little lateral confinement, fails in the splitting failure mode. The splitting failure of ice is believed to be a load-releasing mechanism. Its occurrence lowers the global ice resistance in comparison to other continuous failure modes. However, it is not yet entirely clear in what conditions the splitting failure could take place. Presumably, the size of the ice floe, the lateral confinement, and the ice-structure contact conditions (e.g., the structural geometry, aspect ratio, and indentation rate) are believed to play significant roles in this process.

As one of the important failure modes, splitting failure of an ice floe has been observed and studied in different literatures. Experimentally, during indentation tests (Timco, 1987), the splitting of an ice floe was observed and termed as 'radial cracks' and little information was provided on the size, geometry, and lateral confinement of the ice floe because this work primarily focuses on the effects of the indentation rate and aspect ratio. Sodhi et al. (1993) conducted indentation tests with unconfined rectangular floes of varying sizes and indentation speeds. These authors found that at low interaction speeds (i.e., 0.2-8 mm/s), a micro-cracked region appeared in front of the flat indenter, and the ice floe split, whereas at high interaction speeds (i.e., higher than 100 mm/s), the ice failed in spalling. In the field, accelerometers have been installed on ice floes, and the resulting data were used to back-calculate the impact force on Hans Island (Danielewicz et al., 1983). Grape and Schulson (1992) studied the effects of lateral confinement on the indentation pressure and failure patterns. These authors visually illustrated that at low lateral confinement (e.g., 0.6 MPa), a large crack ran through the ice plate, whereas at high confinement (e.g., 1.8 MPa), the large crack was supressed and the ice failed locally in an out-of-plane manner (i.e., across the ice grain columns). The aforementioned tests were not directly dedicated to studying the splitting failure mode. Their findings on the splitting or quasi-splitting failure modes came out as a 'by-product' of the main test goals (i.e., indentation tests or impact loads). Therefore, most of the test results, when applied to splitting problems, were obscured by uncertainties, especially the contact between the structure and the ice floe. Dempsey et al. (1999a) later conducted a series of splitting tests to measure the scale-invariant fracture toughness of sea ice. These tests were conducted using simple geometries (i.e., square ice plates ranging up to an unprecedented size of 80 m), and the corresponding analysis that was based on nonlinear fracture mechanics (NLFM) is highly regarded.

Theoretically, in the context of an 'intermediate sized (undefined)' ice floe interacting with bridge piers, splitting failure has been documented by Michel (1978) as a shear or tension cracking. Ralston (1981) studied the splitting of an ice floe based on plastic upper limit theory. The two aforementioned approaches come under the umbrella of the so-called 'strength theory', which is based on the assumption that the concerned body is flawless, i.e., the material strength is not size dependent (Bažant, 2005). Palmer et al. (1983) promoted the application of fracture mechanics to calculate the ice load. These authors also derived a formula to calculate the ice splitting load for a semi-infinite ice sheet using linear elastic fracture mechanics (LEFM). Later, Bhat (1988) and Bhat et al. (1991) studied ice floe splitting using finite element method (FEM) based on LEFM. Separately, these authors investigated rectangular and circular ice floes (in

separate studies) with different contact conditions[2]. These studies were associated with the summer impacts of ice floes against Hans Island (Danielewicz et al., 1983). Hence, the inertial effect of the floe on the stress intensity factor (SIF) was included. For a similar scenario, Dempsey et al. (1994) utilised the weight function method based on LEFM to extract the stress intensity factor for a square ice plate. Later, based on the field splitting experiments (Dempsey et al., 1999a), the cohesive zone method (CZM), which is a theory based on NLFM, and the weight function method were employed to study the fracture of an ice floe (Dempsey et al., 1999a; Dempsey et al., 1999b; Mulmule and Dempsey, 1997; Mulmule and Dempsey, 1998; Mulmule and Dempsey, 1999).

The literature review above demonstrates that different terminologies have been used to describe the global failure of a large ice floe. The term 'splitting' is widely used in the literature (e.g., (API_RP2, 1995; Bhat, 1988; Bhat et al., 1991; Dempsey et al., 1994; ISO/FDIS/19906, 2010; Løset et al., 2006; Michel, 1978; Ralston, 1981)). However, in several studies, a large crack is termed a 'radial crack' (e.g., (Hallam, 1986; Palmer et al., 1983; Sanderson, 1988; Timco, 1987)). In this paper, we adopt the term 'splitting failure' to describe the global failure of a large ice floe under a 'lateral' ice splitting load (i.e., a Mode I fracture process). Intuitively and also based on previous relevant studies, we assume that the floe size, its lateral confinement, and the contact conditions (e.g., the structural geometry, aspect ratio, and indentation rate) are the primary factors that affect the occurrence of splitting failure. Without resort to specific contact geometry and its other possible failure modes, the aim of this paper is to quantify the effect of the floe size and its lateral confinement specifically on the splitting failure process. The quantifications are within the context of 'ice and sloping structure interactions'. Therefore, the crack initiation process is discussed only qualitatively. A vast amount of knowledge exists in the literature 'implicitly' studying the fracture initiation process during ice and sloping structure interactions. The primary focus of this paper is the crack propagation process and the required ice splitting load. However, a comprehensive study of the interaction between an ice floe and sloping structures should include at least two main failure mechanisms, i.e., the local bending failure and global splitting failure of an ice floe. We focus on splitting failure in this paper. The competition between the local failure and global failure is presented in a separate paper.

This paper consists of four major parts. In the first part, the splitting failure scenario is described. Corresponding idealisations and simplifications are presented. In the second part, analytical methods are described to calculate the ice splitting load and verified using existing test data and numerical results. In the third part, the effects of the size and lateral confinement of the ice floe on the ice splitting load are studied separately. In the fourth part, the developed framework and different influence factors are discussed, and finally, conclusions are drawn from the theoretical studies.

2 Fracture of an ice floe: global splitting failure

Sloping structures are favoured in icy waters due to their capability in causing bending failure of the incoming ice. However, besides the bending failure mode, global splitting failures have also been frequently observed in the field (see Fig. 1 and Fig. 2). A splitting crack in an ice floe

[2] This is studied by varying the ratio of the splitting load F_Y to the ice load F_X, the definitions of which are given in Section 2.2.

can easily travel a distance that is over one order of magnitude larger than the structural size (Bhat et al., 1991).

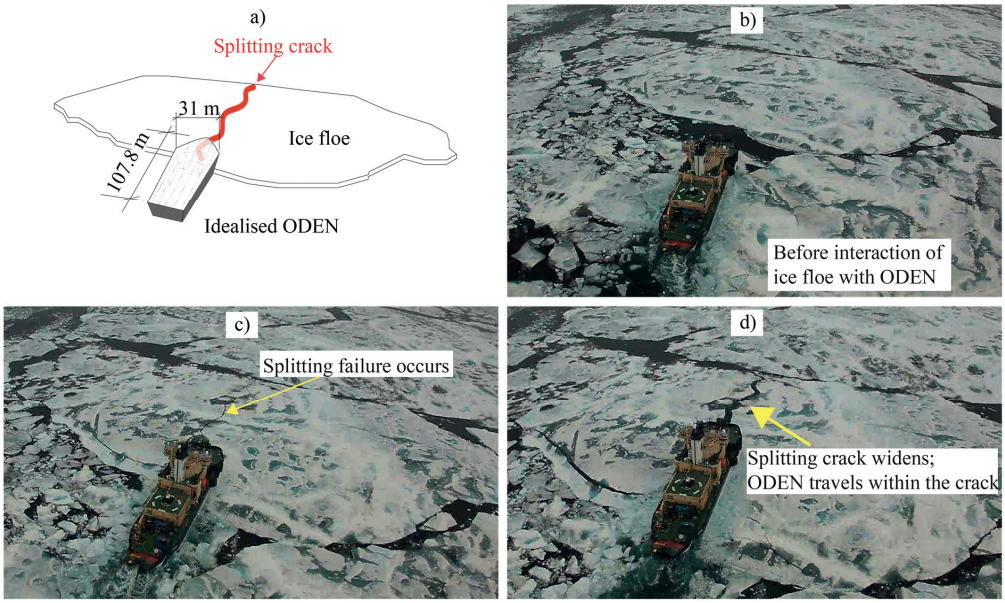

Fig. 1 Global splitting of an ice floe while interacting with ODEN in the Greenland Sea (August, 2013): a) highlight of the interaction process; b) before the interaction; c) splitting crack appears; d) ODEN travels within the splitting crack.

Second-year ice floes are often encountered in the Greenland Sea between eastern Greenland and Svalbard in the summertime, forming a broken ice field. The ice floes are typically 30-120 m across (Sanderson, 1988). Splitting failures were observed frequently during the voyage of the icebreaker ODEN (Lubbad et al., 2012; Lubbad et al., 2013). In the wintertime, in the same Arctic waters, though first-year sea ice forms a relatively uniform and continuous ice field, as long as the boundary confinement is not significant, splitting failures may also frequently take place. This is frequently documented by the video camera system installed on the bow of KV Svalbard (see Fig. 2) on a voyage to the Northern Greenland Sea (Lubbad, 2012). Once splitting failure occurs, continuous local bending failure ceases to develop. The icebreaker can therefore travel within the 'leads' created by the splitting failure (see Fig. 1d). Thus, splitting failure is believed to act as a load-releasing mechanism, in comparison to continuous local failures.

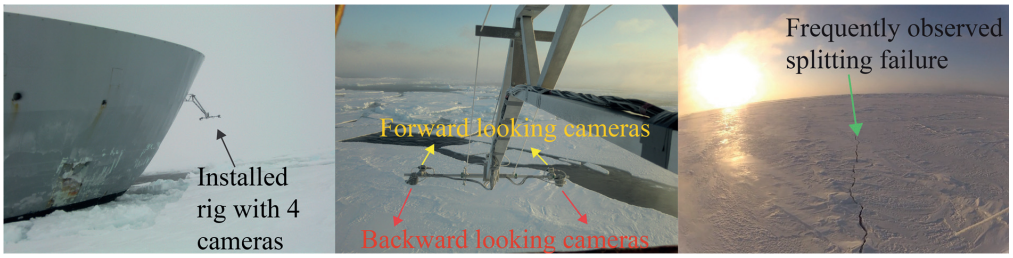

Fig. 2 Video camera system onboard KV Svalbard and frequently observed splitting failure of a large ice floe (March, 2012).

2.1 Idealised ice floe splitting

The complexity of the interaction processes necessitates the formulation of an idealised yet realistic model for the interaction upon which the theories are to be developed.

2.1.1 Crack initiation

Fig. 3 presents the idealised initial interaction process between a sloping structure and an ice floe.

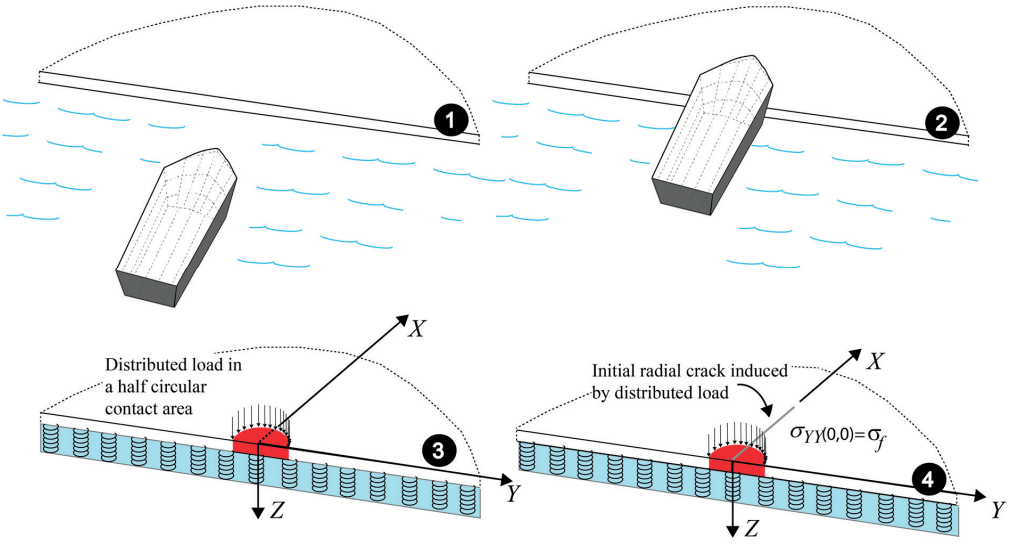

Fig. 3 Idealised crack initiation process.

Let us first consider an icebreaker/offshore structure that is entering into or being impacted by an ice floe, as shown in Fig. 3 (1) to (2). The ice floe is modelled as a linear elastic plate resting on a Winkler foundation. The contact between the sloping structure and ice is difficult to describe accurately (see the discussion in Section 2.2). In general, this contact leads to a vertical load component. A concentrated vertical load component acting on the edge of a semi-infinite ice floe will first initiate a radial crack[3] perpendicular to the free boundary, as solved by Westergaard in 1923 (Nevel, 1965). A more representative contact than a concentrated point load can be modelled by distributing the point load over an area, as shown in Fig. 3(3). Lubbad and Løset (2011) assumed that the contact area was a half circle and obtained an expression for $\sigma_{YY}(0,0)$ by superposition (the coordinate system is shown in Fig. 3(3)). Equating $\sigma_{YY}(0,0)$ with the flexural strength of ice σ_f yields the criterion for crack initiation (see Fig. 3 (4)).

[3] The radial crack before the circumferential crack in the local bending failure should be distinguished from the splitting failure. First, they occur on different length scales; second, the radial crack is mainly induced by a vertical load component (out-of-plane), whereas the splitting failure considered in this paper is induced by a pair of horizontal loads (in-plane opening).

2.1.2 Crack propagation

The primary focus of this paper is the propagation of a splitting crack. Depending on the geometry of the sloping structure in contact with the ice floe (i.e., the contact geometry), a pair of splitting loads F_Y may develop after crack initiation by the vertical contact load in the Z direction (see F_Y in Fig. 4). In principle, the crack paths are not known a priori. Therefore, several symmetric possibilities are plotted in Fig. 4 with one independent variable, i.e., the crack angle θ. The focus of this paper is to calculate the ice splitting load F_Y under various conditions by different approaches.

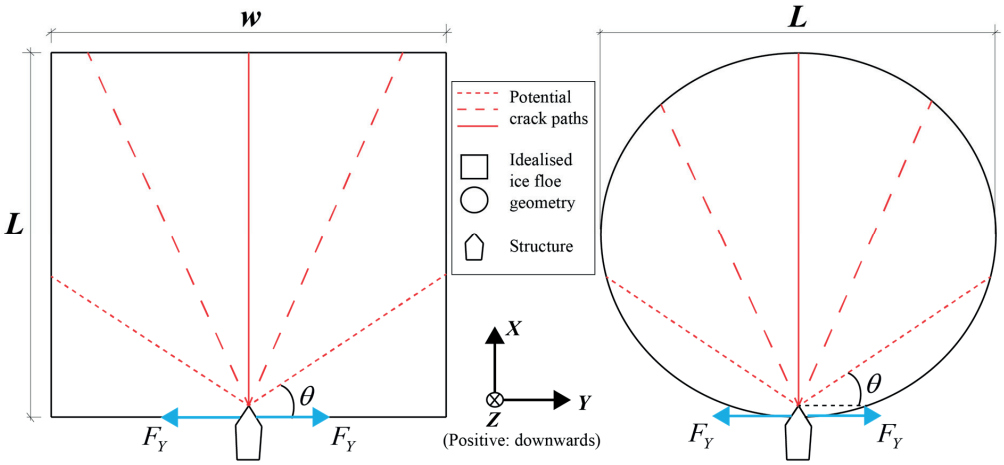

Fig. 4 Two base cases for the theoretical model: bird's eye view of the interaction between a structure and ice floe (from symmetry considerations, the centre of the structure is assumed to be a mirror-line for both cracks).

Fig. 4 illustrates the two cases for symmetric ice floes with head-on contact with the structure. The developed framework (which combines fracture mechanics and plasticity-based theory) is anticipated to work for various geometries under various lateral confinements. The cases in Fig. 4 are used herein as bases cases to demonstrate the capabilities of the presented framework.

2.2 Simplifying assumptions

Splitting failure of an ice floe is influenced by a set of parameters that range from ice material properties to structural properties. It is difficult to study all of these parameters in detail in a single paper. In this section, we qualitatively describe all of the parameters that we believe to be significant together with the assumptions used in the current formulations.

- **Temperature, brine volume, grain size, and loading rate**

These parameters primarily control the strength of the ice considered. Extensive experimental studies (in both the laboratory and field) and theoretical studies have demonstrated the effect of these parameters on the tensile and compressive strength of ice and its corresponding failure patterns (i.e., brittle or ductile failure). These parameters play an important role in the construction of the yield surface for the ice considered, which will be described in Section 3.2

(i.e., plasticity-based theory). Based on the presented framework to calculate the ice splitting load F_Y, it is straightforward to study the influence of these parameters on the splitting failure of an ice floe. Interested readers can refer to any text book or literature in relation to ice mechanics (e.g., (Michel, 1978; Sanderson, 1988; Schulson and Duval, 2009; Timco and Weeks, 2010; Weeks, 2010) to quantify the corresponding influence of these parameters.

- **Size, geometry, and lateral confinement of ice floes**

The size, geometry, and lateral confinement (or ice concentration) of ice floes are site specific. These parameters are important on-going research topics (e.g., (Rothrock and Thorndike, 1984). However, it is not our intention to attach our analysis to any specific site. Without loss of generality, we assume that the aforementioned data are known inputs to the theoretical model. One of the primary objectives in this study is to quantify the influence of the floe size and lateral confinement on the splitting load. The quantification scheme is presented with two base cases (i.e., rectangular and circular ice floes), as shown in Fig. 4. The developed formulas and framework can be easily generalised to other geometries under various lateral confinements.

- **Contact considerations**

The contact conditions significantly affect the dominant failure modes and magnitude of the corresponding failure load. In this paper, we focus primarily on the splitting failure mode and do not consider other possible failure modes (e.g., local bending failure). The effect of contact is considered from two different perspectives.

First, the occurrence of splitting can be primarily attributed to the load in the lateral direction (i.e., the Y direction in Fig. 5). The decomposition of the load into different directions (i.e., the X and Y directions) depends largely on the contact geometry and interaction process. For generality, we do not use contact mechanics to analyse the stress distribution within the contact zone for specific structural geometries; instead, we follow the same treatment that has been used in previous studies (Bhat, 1988; Bhat et al., 1991; Dempsey et al., 1994; Sodhi et al., 1993) and circumvent the exact contact problem by assuming one load ratio (i.e., β_{YX}), as in Eq. (1).

$$\beta_{YX} = \frac{F_Y}{F_X} \tag{1}$$

where the different load components are defined in Fig. 5a.

Second, two different situations can be identified (see Fig. 5b and c) depending on how much inertia force is induced within the ice floe during the contact. The inertial effect of the ice floe further influences the stress intensity at the crack tip. Here we present two extreme cases in which the inertial effect can and cannot be neglected respectively. Fig. 5b represents a structure ramming into an ice feature which is 'stopped' by adjacent floes. In this situation, the inertial effects of ice floe on the splitting process can be neglected. On the other hand, Fig. 5c illustrates an ice floe impacting onto a structure and the splitting process is influenced by the inertial effect of the ice floe. This inertial effect has been modelled in the literature using a distributed body force b_X (as shown in Fig. 5c) (Bhat, 1988; Bhat et al., 1991; Dempsey et al., 1994). These two different situations (i.e., Fig. 5b and c) are supposed be treated differently.

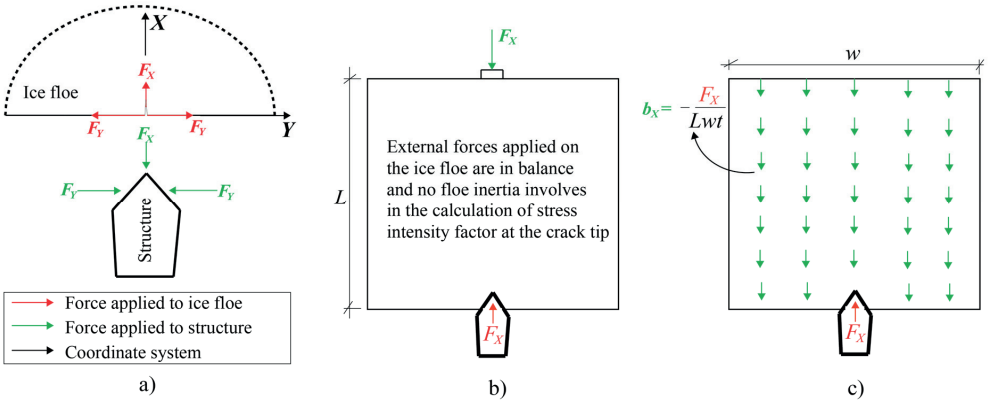

Fig. 5 Illustration of different load components and two different interaction processes: a) definition of load components in the coordinate system; b) structure rams into ice feature which is 'stopped' by adjacent floes; c) ice feature impacts onto the structure.

Meanwhile, we present the notation used throughout the entire paper below.

For the structure (the load components are shown in green in Fig. 5):

- The ice resistance is denoted by F_X: it is the total ice load in the opposite X- direction as shown in Fig. 5

For the ice floe (the load components are shown in red in Fig. 5):

- The ice splitting load is denoted by F_Y and consists of a pair of loads of equal magnitude acting in opposite directions.

A primary objective of this study is to calculate the ice splitting load F_Y.

3 Global ice splitting load calculations

Two different approaches were adopted to analyse the splitting failure of an ice floe. The motivation behind using two different approaches is due to the complexity of the interactions (e.g., the contact geometries, interaction speed, and fracture properties[4] of the ice floes). These two approaches have their respective advantages and application ranges. The different methods for splitting failure are presented individually below. Because only the ice splitting load F_Y is considered in this section, the base cases in Fig. 4 is further idealised in Fig. 6 with ice splitting load only.

[4] i.e., the size of the fracture process zone (FPZ) and the applicability of LEFM (which will be discussed later)

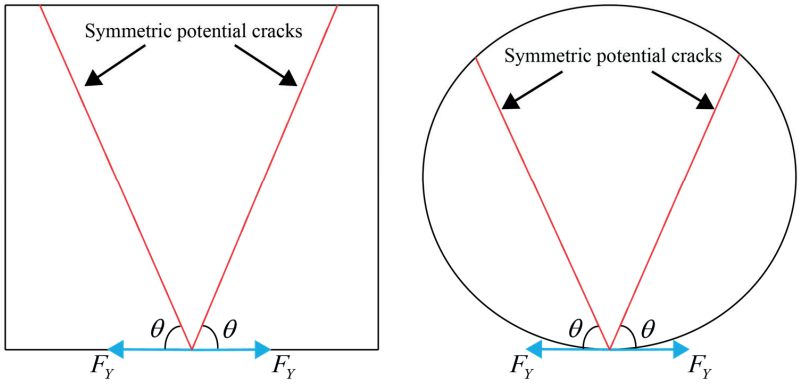

Fig. 6 Free-body diagram of the splitting of an ice floe (base cases: rectangular ice floe (left) and circular ice floe (right)).

3.1 Fracture mechanics approach

While interacting with structures, ice typically fails in a brittle manner. A realistic description of ice splitting failure should be based on fracture mechanics to account for the behaviour of the fracture process zone (FPZ). To study the fracture properties of an ice floe under various symmetric loading conditions (e.g., the ice splitting load, symmetric lateral confinement), a powerful tool known as the weight function method has been adopted herein. However, the adoption of weight function method is limited by several restrictions:

- The geometry of the ice floe is symmetric.
- The crack path is symmetric.
- The loading condition on the ice floe is symmetric. This restriction requires the lateral confinement of the concerned ice floe to be symmetric and a head-on contact between the structure and ice floe (otherwise an asymmetric loading condition develops).

One way of addressing these restrictions calls for a numerical approach (e.g., calculating stress intensity factor or J-integral with FEM). However, we prefer to use an analytical approach to solve this problem. This study also serves to support the development of a numerical simulator (Lubbad and Løset, 2011; Metrikin et al., 2012), which requires almost completely analytical algorithms for the failure mode so that the simulation can be applied to processes over large temporal and spatial ranges. Therefore, the analytical approach is highly regarded in this paper even under all these restrictions. From a practical perspective, a different yet conservative approach (i.e., a plastic limit analysis) is presented in Section 3.2 as a supplementary approach for interaction scenarios free from these restrictions.

Depending on the size of the FPZ, we can further distinguish between problems that can be solved using LEFM theory and those that cannot. It is therefore of interest for us to delineate the boundary between the applicability of LEFM and NLFM for the current ice floe splitting problem. Mulmule and Dempsey (2000) identified this boundary in a different context, i.e., to determine the validity of ice fracture toughness tests in relation to test sample's size. These authors recommended that the size of the concerned body should satisfy $L \geq 12 l_{ch}$ and $L \geq 200d$ for LEFM to be valid. The grain size is denoted by d, and l_{ch} is a characteristic length defined in Eq. (2).

$$l_{\text{ch}} = \frac{JE'}{\sigma_t^2} \tag{2}$$

where the variables above are defined as follows:

J is the fracture energy of the ice considered [N/m];

E' $E' = E$ for a plane stress condition, and $E' = E/(1-\nu^2)$ for a plane strain condition (where E is Young's modulus and ν is the Poisson ratio) [Pa]; and

σ_t is the tensile strength of ice [Pa].

We discuss whether the same criterion should be applied to the current engineering application of splitting failure of an ice floe in a later section.

In this paper, the weight function method, which is independent of external loadings, is adopted to calculate the stress intensity factor. The CZM is used to model nonlinear behaviour in the FPZ. These methods are described below.

3.1.1 Weight function method

Bueckner (1970) and Rice (1972) developed the weight function method for a symmetrically loaded linear elastic body (e.g., Fig. 7). Given the weight function $H(A,x)$ of a cracked body, the pertinent stress intensity factor $K(A)$ can be expressed by Eq. (3) under different types of symmetric loadings $\sigma(x)$. For engineering applications, we assume in this paper the existence of a unique weight function $H(A,x)$ for a given symmetrically cracked body (e.g., Fig. 7a).

$$K(A) = \int_0^A \sigma(x) H(A,x) dx \tag{3}$$

where A is the length of the initial crack (see Fig. 7a); and $\sigma(x)$ is the stress profile on the crack face (e.g., $\sigma(x) = F_Y / t\delta(x)$ describes[5] the ice splitting load at the crack mouth with a delta function and t is the thickness of the ice floe, as shown in Fig. 7a).

Dempsey et al. (1994) first used the weight function method to calculate the stress intensity factor for the splitting of rectangular ice floes. Dempsey et al. (1995) derived a weight function for a reverse-tapered plate to study the crack stability of this particular geometry. The advantage of using a weight function is that the stress intensity factors under various symmetric loading conditions are reduced to an integral, as in Eq. (3), as long as the weight function is known. Thus, we avoid using FEM to calculate the stress intensity factor, as was done by Bhat (1988) and Bhat et al. (1991). Weight functions are only provided for a limited number of idealised and symmetric geometries in handbooks (e.g., (Wu and Carlsson, 1991), (Fett and Munz, 1997)). If the desired weight function is not available in the literature, then the Petroski-Achenbach method (1978) can be utilised to obtain a general form of the weight function. With known boundary conditions for the crack opening displacement (COD) profile (see Fig. 7b), the weight

[5] Note here that the unit of $\delta(x)$ is $[\text{m}^{-1}]$, which makes the definition of stress profile $\sigma(x) = F_Y / t\delta(x)$ having a unit of [pa].

function can be determined either analytically or numerically (i.e., using FEM and least-squares interpolation) (e.g., (Dempsey et al., 1995; Dempsey et al., 1994; Tsai and Ma, 1989; Wu, 1984; Wu, 1991; Wu and Carlsson, 1983)).

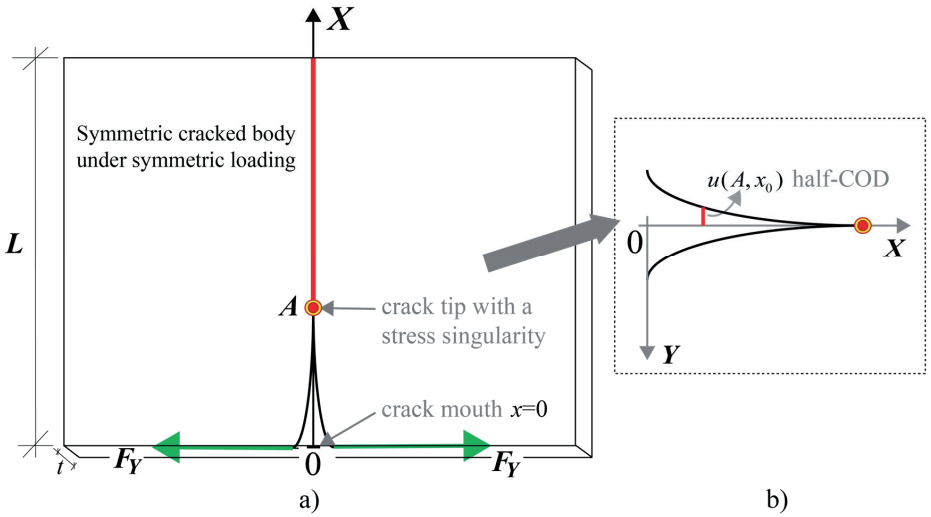

Fig. 7 a) Symmetrically cracked body under an edge splitting load; b) detailed crack face information.

3.1.2 Using linear elastic fracture mechanics in conjunction with the weight function method

The fracture process of a cracked body is accurately described by LEFM as long as the inelastic zone at the crack tip (see Fig. 7) is sufficiently small compared to the size of the respective body and ligament.

For the concerned base cases in Fig. 6, as will be proven in Section 3.2, the splitting crack propagates in a self-similar manner (i.e., $\theta = 90^{\circ}$, and the crack path overlaps with the centre line of symmetry). The weight function method and Eq. (3) are applied to a cracked body with an external ice splitting load $\sigma(x) = F_Y(A,x)/t\delta(x)$: equating the stress intensity factor to the fracture toughness K_{IC} yields the critical ice splitting load given in Eq. (4).

$$\frac{F_Y(A)}{t} = \frac{K_{IC}}{H(A,0)} \tag{4}$$

If the boundary confinement or ice floe inertial effects cause an additional external stress profile $p_{ext}(x)$ to develop along the crack face, the ice splitting load can be derived similarly as in Eq. (3) to yield Eq. (5). The crack closure effect of $p_{ext}(x)$ results from the boundary confinement; thus, the second term on the right side of Eq. (5) increases the ice splitting load above that predicted by Eq. (4).

$$\frac{F_Y(A)}{t} = \frac{1}{H(A,0)}[K_{IC} + \int_0^A p_{ext}(x)H(A,x)dx] \tag{5}$$

Eqs. (4) and (5) represent methods that will be referred to as the 'LEFM + weight function' method in the forthcoming calculations and discussion.

3.1.3 Incorporating the weight function method into the cohesive zone method

The underlying assumption in LEFM is that small-scale yielding (SSY) occurs at the crack tip relative to the size of the cracked body. The bulk material is treated as linearly elastic outside this non-elastic zone. However, sea ice has a fairly large grain size compared to metal and exhibits a creep effect at the relatively high working temperature near its melting point; thus, special attention is demanded in terms of the applicability of LEFM (Mulmule and Dempsey, 2000). In the CZM (Hillerborg et al., 1976), the nonlinear material behaviour (i.e., strain softening behaviour) is generalised into a line-like (for a 2D problem) FPZ in front of the physical crack tip B (see Fig. 8). Within the FPZ (i.e., line BA in Fig. 8), the material follows a traction and separation law (TSL). The presence of this FPZ cancels out the stress singularity at the cohesive crack tip A.

Fig. 8 presents the cracked body described above for the problem under consideration. The ice splitting load F_Y at the crack mouth and cohesive stress $\sigma_{coh}(x)$ within the FPZ produce the corresponding stress intensity factors $K_F(A)$ and $K_\sigma(A)$ at the cohesive crack tip and the half-CODs $u_F(A,x)$ and $u_\sigma(A,x)$ along the crack face. According to the cohesive zone theory, these quantities are related by Eqs. (6) and (7).

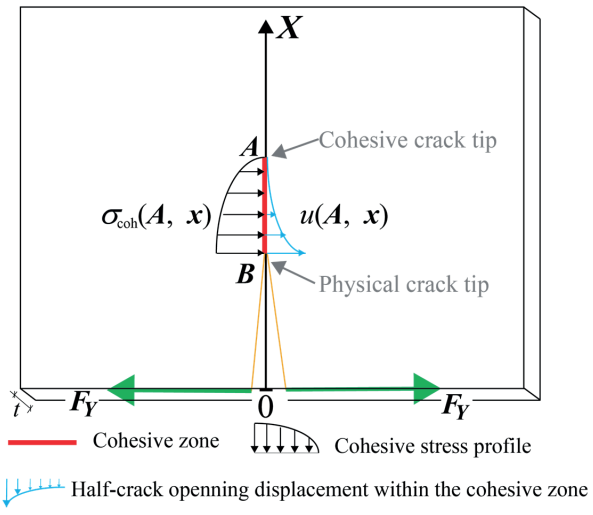

Fig. 8 Schematic of the CZM (only half of the symmetric cohesive stress and displacement profile are shown).

$$K_F(A) + K_\sigma(A) = 0 \tag{6}$$

$$u(A,x) = u_F(A,x) + u_\sigma(A,x) \tag{7}$$

The cohesive stress $\sigma_{\text{coh}}(x)$ can be related to the half-COD following the TSL:

$$\sigma_{\text{coh}}(x) = f(2 \cdot u(A,x)) \tag{8}.$$

The TSL is considered a material property, and its construction is essential to the application of this method. A series of large-scale field experiments were conducted to measure the fracture properties of ice (Dempsey et al., 1999a; Dempsey et al., 1999b). Based on the measurements, the viscoelastic fictitious crack model was developed in order to back-calculate the TSL for sea ice (Mulmule and Dempsey, 1997; Mulmule and Dempsey, 1998; Mulmule and Dempsey, 1999). These results led to the proposition of a convex-shaped TSL. However, a linear softening TSL is typically adopted in numerical applications for simplicity (Lu et al., 2014; Lu et al., 2012; Paavilainen et al., 2009).

We distinguish between the viscoelastic fictitious crack method and 'CZM + weight function' method developed here. First, in the viscoelastic fictitious crack model, the surrounding bulk material is treated as a creeping material that is described by a viscoelastic model. In an ice splitting problem, the largest splitting load is of primary interest. Moreover, the splitting failure usually takes place in a fast and uncontrolled manner. Thus, the creeping behaviour of the bulk material is not accounted for in the 'CZM + weight function' method. Second, the frequently applied linear softening TSL is adopted in this study instead of a nonlinear convex-shaped TSL. Therefore, Eq. (8) can be explicitly written as follows:

$$\sigma_{\text{coh}}(x) = \sigma_t\left(1 - \frac{u(A,x)}{u_c}\right) \quad \text{or} \quad u(A,x) = \left(1 - \frac{\sigma_{\text{coh}}(x)}{\sigma_t}\right)u_c \tag{9},$$

where

u_c is the critical separation (i.e., a critical half-COD) based on the CZM.

We used Eqs. (6), (7), and (9) as well as a series of derivations in Appendix A to obtain the following eigen equation:

$$\lambda\sigma(x) = \int_B^A \sigma(s)U(A,x,s)ds \tag{10}$$

where

$\lambda = l_{ch}$ is the eigenvalue of the equation above and

$U(A,x,s)$ following the definition in equation (6) of Wang and Dempsey (2011), it is presented as follows:

$$U(A,x,s) = \int_{\max(x,s)}^{A} H(a,x)H(a,s)da \qquad \text{A repetition of Eq. (28) in Appendix A}$$

The maximum eigenvalue corresponds to the peak ice splitting load (Wang and Dempsey, 2011). Use the corresponding eigenvector $\sigma(x)$ to multiply both sides of Eq. (9) yields the peak ice splitting load $F_Y(A,0)$, as shown in Eq. (11) (see the detailed derivations in Appendix A).

$$F_Y(A,0) = (u_c E' t)\frac{\int_B^A \sigma_{\text{coh}}(x)dx}{\int_B^A \sigma_{\text{coh}}(x)U(A,x,0)dx} \tag{11}$$

Eqs. (10) and (11) above considerably simplify the calculations of the ice splitting load using the linear softening TSL. The key steps are to construct $U(A,x,s)$ using Eq. (28) and to solve Eqs. (10) and (11).

In this section, we have presented two methods for calculating the stress intensity factor for a symmetrically cracked body. These methods are the 'LEFM + weight function' method (given by Eqs. (4) and (5)) and the 'CZM + weight function' method (given by Eqs. (10) and (11)). Both of these methods require a known weight function for the ice floe. The analytical application of these two methods is restricted to situations in which the geometry of the considered ice floe is symmetric; the crack propagates in a self-similar manner; and a head-on contact scenario is required. Plastic limit theory is introduced below to circumvent these restrictions.

3.2 Plastic limit theory approach

Plastic limit analysis is extensively employed in the limit analysis of engineering structures to determine the upper and lower bounds on the collapse load of a structure. Both plastic upper limit theory and plastic lower limit theory are employed in the current study.

3.2.1 Plastic upper limit analysis

The basic tenet in plastic upper limit analysis is that for a reasonably assumed admissible velocity field, equating the rate of work performed by the external load to the internal rate of energy dissipation yields an external load that is not less than the actual collapse load (Chen and Han, 1988). The application of this theory to problems related to ice engineering is not new. This theory has been applied to the analysis of indentation problems (Karr, 1988; Karr and Das, 1983; Karr et al., 1989; Ralston, 1978; Reinicke, 1980; Reinicke and Remer, 1978); to derive formulas for level ice and sloping structure interactions (ISO/FDIS/19906, 2010; Ralston, 1977a; Ralston, 1980); to analyse ice sheets' bearing capacities (Sodhi, 1995); and to analyse current splitting problems (Bhat et al., 1991; Ralston, 1981). However, ice is not a strictly plastic material. Ice is a nonlinear creeping material that exhibits behaviour between viscous Newtonian flow and pure plastic yielding (Sanderson, 1988). This theory is applied in ice engineering for various reasons. In this study, the primary motivation for using this theory is to analyse the splitting load stems from two different cases (see Fig. 9)

In Case 1, when the structure is interacting with a small ice floe (which will be discussed later), the size of the nonlinear FPZ at the crack tip becomes comparable to that of the ice floe. Thereby falsifying the underlying assumption in LEFM (i.e., small-scale yielding at the crack tip) (Anderson, 2005). NLFM methods, such as the aforementioned CZM, should be applied in

these situations. However, as a simple alternative, the plastic upper limit theory fits rather properly for such a small sized ice floe. It also offers a conservative solution from an engineering perspective.

In Case 2, in the first situation (i.e., 2.1 in Fig. 9), an analytical approach typically cannot be used to obtain the stress intensity factor for an arbitrary ice floe geometry because of the limitations discussed in the previous section. To avoid numerical approaches, plastic limit analysis can serve as an expedient first step to obtain an analytical estimate of the splitting load for arbitrary geometries. For theoretical completeness, we consider a minor situation (i.e., 2.2 in Fig. 9) that is not strictly a splitting problem. Instead of fast cracking, the ice floe starts to creep around the structure either because of wind, current drag or pushed by adjacent floes. Plastic limit analysis could be used to approximate the creeping effect in this problem because of the potentially low interaction speed involved.

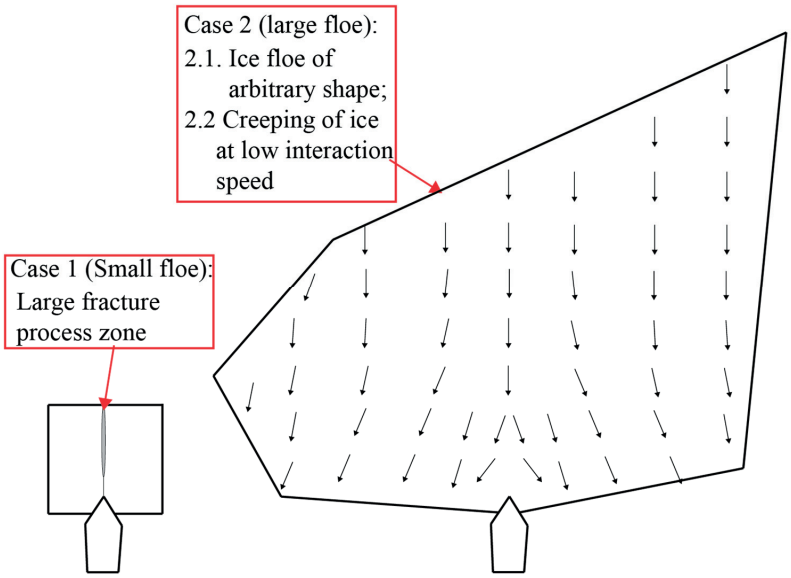

Fig. 9 Situations for which plastic upper limit analysis is applicable.

The following three-step procedure is recommended to extract the ice splitting load using plastic upper limit theory.

Step 1: Construction of the yield surface and calculating the energy dissipation rate

Sea ice is typically composed of a granular layer on top followed by a transition layer with columnar ice below (Weeks and Ackley, 1982). Plastic upper limit theory will be exemplified by the S2 first-year sea ice (i.e., columnar ice with its c-axis randomly oriented in the horizontal XY plane), which is prevalent in nature (see Fig. 10). Plasticity theory and a large number of experimental tests have been used to formulate different yield functions for S2 ice (e.g.,

(Derradji-Aouat, 2003) and review works by Matskevitch (1994), Sand and Fransson (2006) and Sand (2008)).

Because of the columnar S2 ice's anisotropic material behaviour; and it is sensitive to hydrostatic pressure; and there is a large difference between the compressive and tensile strength, a parabolic yield function was proposed by Reinicke and Ralston (1977) as in Eq. (12).

$$\begin{aligned} f(\sigma_{ij}) = a_1[(\sigma_{22}-\sigma_{33})^2+(\sigma_{33}-\sigma_{11})^2]+a_3(\sigma_{11}-\sigma_{22})^2 \\ +a_4[{\sigma_{23}}^2+{\sigma_{31}}^2]+a_6{\sigma_{12}}^2 \\ +a_7[\sigma_{11}+\sigma_{22}]+a_9\sigma_{33}-1=0 \end{aligned} \quad (12),$$

where

$f(\sigma_{ij})$ is a parabolic yield function for columnar S2 sea ice;

σ_{ij} are the stress components in different directions, ($i=1,2,3$; $j=1,2,3$); the 1, 2, and 3 directions correspond to the $X, Y,$ and Z directions in Fig. 10

a_i $i=1,3,4,6,7,9$ are material constants that depend on the properties of the ice considered (e.g., the temperature, brine volume, grain size, and loading rate). $a_6=2(a_1+2a_3)$, and a_4 vanishes for plain strain or plane stress problems. Therefore independent material constants are a_i with $i=1,3,7,9$

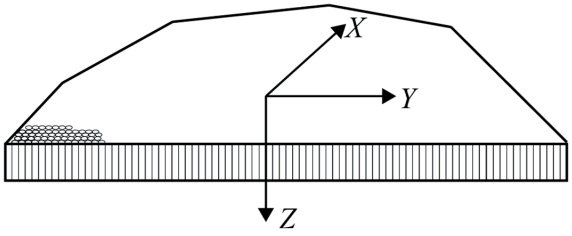

Fig. 10 Schematic of columnar structure of S2 sea ice showing the coordinate system for a portion of the floating ice floe (Z corresponds to the direction of gravity).

Later, a potential velocity discontinuity is considered (e.g., a crack) in the continuum body, where the velocity components are shown in Fig. 11. Drucker's postulate and the normality rule can be used with the obtained yield function to derive the energy dissipation rate D_A for a reference volume within the velocity discontinuity field. In a plane stress situation, the energy dissipation rate D_A was derived by Prodanovic (1978) and reported in several publications (Ralston, 1981; Reinicke, 1980; Reinicke and Ralston, 1977). This expression for D_A is given in Eq. (13).

To formulate Eq. (13), it is critical to obtain values for the material constants a_i $(i=1,3,7,9)$. In Appendix B, we present two methods (i.e., an indirect estimate and direct curve fitting method) to derive values for these material constants. These material constants can vary considerably

depending on the ice conditions (e.g., the temperature, brine volume, and loading rate). We also studied the properties of Eq. (13) in detail for two groups of material constants (i.e., material constants under high- and low-strain-rate loadings). In both situations, the importance of the tensile velocity component (i.e., δv_n) in minimising the value of D_A is highlighted. That is, in splitting failure, the material particles in the respective ice floe tend to fail in a tensile manner.

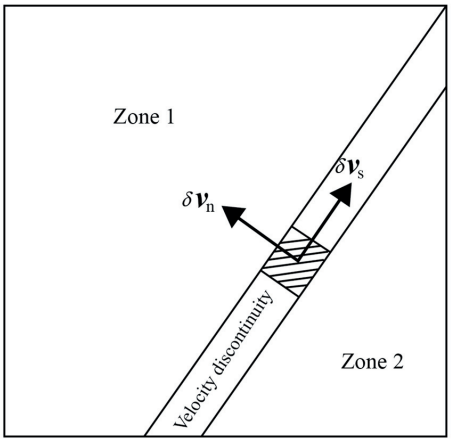

Fig. 11 Definition of velocity discontinuity.

$$D_A = \frac{1}{2a_1}\left[\sqrt{\frac{(a_7^2 + 2a_1)}{a_6}}\sqrt{4(a_1 + a_3)(\delta v_n)^2 + 2a_1(\delta v_s)^2} - a_7 \delta v_n\right] \tag{13}$$

In the equation above,

δv_n, and δv_s are the velocity components normal to (i.e., tensile) and parallel to (i.e., shearing) the velocity discontinuity (see Fig. 11), [m/s].

Step 2: Searching for crack paths by minimising the overall energy dissipation

Once the energy dissipation rate is known, the plastic upper limit theory can be used to derive Eq. (14), which relates the work power of the external splitting load to the internal dissipation rate for the base cases in Fig. 6.

$$\begin{aligned} 2F_Y \delta v_Y = {} & 2t\int_A^{L_{crack}(\text{geometry,size},\theta)} D_A(\delta v_{Yn}(x',\theta), \delta v_{Ys}(x',\theta))dx' \\ & + 2t\int_A^{L_{crack}(\text{geometry,size},\theta)} [p_{\text{ext,n}}(x',\theta)\delta v_{Yn}(x',\theta) + p_{\text{ext,s}}(x',\theta)\delta v_{Ys}(x',\theta)]dx' \end{aligned} \tag{14}$$

where the notation used is defined in Fig. 12, i.e.,

2 the loadings on a symmetric ice floe are symmetric: thus, all of the dissipation terms are multiplied by 2;

δv_Y	is a virtual velocity component in the ice splitting direction, [m/s];
δv_{Yn} and δv_{Ys}	are the δv_Y -induced velocity components normal to (i.e., tensile) and parallel to (i.e., shearing) the velocity discontinuity [m/s], which are given explicitly in Eq. (40) in Appendix B;
x'	is a local coordinate along the crack path, [m];
A	is the length of the initial radial crack (see Fig. 3 (3)), where $A = 0$ denotes a crack free body, [m];
$L_{\text{crack}}(\text{geometry, size}, \theta)$	is the length of the crack as a function of the ice floe geometry, floe size, and crack angle θ (see Fig. 4), [m];
$p_{\text{ext,n}}(x', \theta)$ and $p_{\text{ext,s}}(x', \theta)$	are the additional stresses along the crack in the normal and shearing directions, respectively, which are caused by the possible lateral confinement of the ice floe or any other external loadings, [Pa].

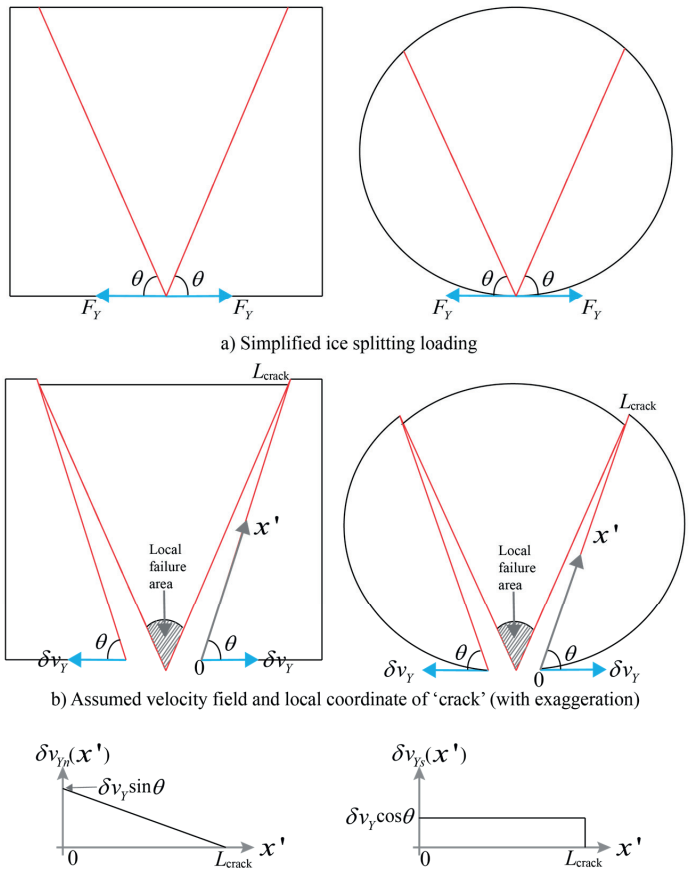

Fig. 12 Assumptions used to calculate the 'crack' paths that dissipate the lowest amount of energy (rectangular ice floe (left) and circular ice floe (right)).

According to Eq. (14), with a given geometry, the unknown crack path $L_{\text{crack}}(\text{geometry, size}, \theta)$ can be obtained by minimising the ice splitting load F_Y through varying the crack angle θ. Thus, the corresponding ice splitting load F_Y is obtained. Eq. (14) can easily be generalised to

other ice floe geometries and loading conditions as long as the principle of plastic upper limit theory is obeyed (i.e., the external work and internal plastic energy dissipation are balanced).

Step 3: Calculation and further simplifications of the ice splitting load

The aforementioned two steps can be used to derive analytical expressions for the ice splitting load for the base cases shown in Fig. 12. As for an ice floe of arbitrary shape, simple numerical integration and optimisation methods can be employed to calculate the crack path and ice splitting load. For circular and square ice floes and rectangular ice floes with $\beta \geq 1$, the general findings given above can be used to derive the ice splitting load, which is given in Eq. (15). The detailed derivation can be found in Appendix B.

$$\frac{F_{Y\_\text{plastic\_upper\_limit}}}{Lt} = \int_{A/L}^{1} \bar{D}_A(\alpha) d\alpha = \frac{\int_a^1 [(1-\alpha)] d\alpha}{2a_1} [\sqrt{\frac{(a_7^2 + 2a_1)}{a_6}} \sqrt{4(a_1 + a_3)} - a_7] \tag{15}$$

Similarly, Eq. (15) can be generalised to include the effect of lateral confinement using the principle of plastic upper limit analysis. Here, an example with evenly distributed lateral confinement is presented. We assume that the external confinement is evenly distributed in the direction of the thickness t and can be expressed as a combination of two components, i.e., a normal component $p_{\text{ext,n}}(x', \theta)$ and shear component $p_{\text{ext,s}}(x', \theta)$ along the postulated crack (velocity jump). For a rectangular ice floe that is confined uniformly and laterally along its boundary, i.e., $p_{\text{ext}}(x') = p_{\text{ext,n}}$ only, Eq. (14) can therefore be reduced to Eq. (16).

$$\frac{F_{Y\_\text{plastic\_upper\_limit}}}{Lt} = \frac{1}{2} \sqrt{\frac{(a_7^2 + 2a_1)(a_1 + a_3)}{a_1^2 a_6}} - \frac{a_7}{4a_1} + \frac{p_{\text{ext,n}}}{2} \tag{16}$$

3.2.2 Case studies based on plastic upper limit analysis

In this section, we present some general findings that are obtained by performing the above recommended calculations based on two sets of rather different material constants. The detailed calculations consistently follow the recommendations in a stepwise manner and are described in detail in Appendix B. The calculations are conducted on the two base cases in Fig. 12 and it is found that:

- The material constants significantly affect the ice splitting load. In general, larger yield surface increases the ice splitting load (see Fig. 20 and Fig. 22 in Appendix B).
- The formulated energy dissipation rate (i.e., Eq. (13)) tends to dissipate less energy in the normal direction (i.e., δv_n) than in the parallel direction, because ice fails more easily in the tensile direction (see Fig. 21 in Appendix B).
- Analysing the preferred crack paths indicates that both the circular and square ice floes favour a direct crack path with $\theta = 90^o$ (see Fig. 22 in Appendix B).
- In an extended analysis of arbitrary rectangular ice floes, the direct crack path (i.e., $\theta = 90^o$) is preferred for both sets of material constants, while whereas the width-to-length ratio $\beta = w / L$ is larger than 1 (see Fig. 4 and Fig. 23).

3.2.3 Plastic lower limit analysis

In contrast to plastic upper limit analysis, plastic lower limit analysis yields a lower bound of the collapse load of a structure (e.g., an ice floe). It requires the construction of an admissible stress field. Based on this theorem, a lower bound can be obtained. However, it is worth pointing out that this lower bound is under the continuum mechanics theory. It is not a lower bound as opposed to the value calculated by fracture mechanics approach. The detailed theoretical development and proof for this analysis can be found in Chen and Han (1988).

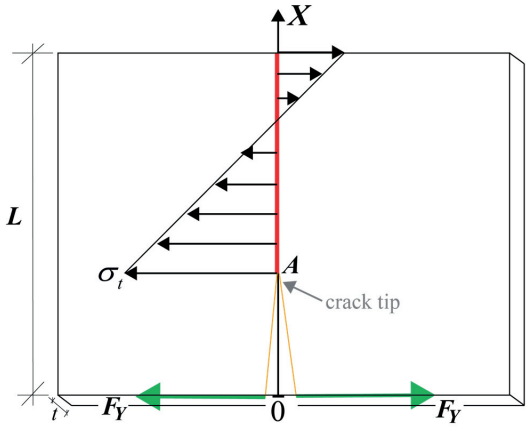

Fig. 13 Schematic of the assumed stress field for the splitting of an ice floe (note that the ice floe's geometry can be arbitrary).

Fig. 13 presents the corresponding admissible stress field that is assumed within the velocity discontinuity. The tensile stress at the crack tip A has attained its maximum value (i.e., tensile strength σ_t). Force and moment balances are used to derive a lower bound of the ice splitting load for an arbitrary geometry, which is given in Eq. (17). Note here that a same equation (before rearrangement) has been utilised by (Dempsey et al., 1999a) to define a nominal strength for the considered ice floe.

$$\frac{F_{Y\_\text{plastic\_lower\_limit}}}{Lt} = \frac{\sigma_t}{2L}\frac{(L-A)^2}{(2L+A)} \tag{17}$$

4 Validation of the ice splitting load calculations

In Sections 3.1 and 3.2, formulas for the ice splitting load were derived using two different approaches. In this section, these methods are validated against both experimental results and known solutions.

4.1 Validation against experimental data

To the authors' knowledge, the only experiments that have been performed to date specifically on the splitting of an ice floe were conducted by Dempsey et al. (1999a). In these experiments, a series of cracked square ice floes of varying sizes (i.e., 0.3 to 80 m) were split by a

hydraulically driven flatjack. Known load-displacement information and relevant crack opening displacement histories were used to study the effect of the size of the ice floe on the fracture properties (e.g., the fracture toughness, TSL for ice, and evolution of the FPZ). Here, we assume that these fracture properties are given (see Table 3). The objective is to calculate the ice splitting load using the developed methods for comparison with the measurements of Dempsey et al. (1999a). The general test conditions and ice properties are summarised in Table 1.

Table 1 Test conditions and geometries of Dempsey et al. (1999a)

Temperature	$T = -15^{o}$	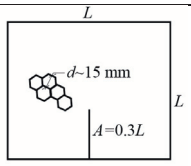
Salinity	$S = 5‰$	
Loading rate	$\dot{K}_I = 200\ \text{kPa}\sqrt{\text{m}}/\text{s}$	
Ice thickness	$t = 1.8$ m	

4.1.1 Calculation of the ice splitting load using plastic limit analysis

- Plastic upper limit analysis

In order to calculate the material constants for the plastic upper limit analysis, it is of importance to study the ice properties during the test. However, no multi-axial tests for the ice samples have been reported. Based on the test conditions in Table 1, the material constants are indirectly approximated (see Appendix B).

First, the brine volume $v_b = 19$ [ppt] is calculated using Eq. (35) in Appendix B for a given salinity and temperature. This leads to a tensile strength of $\sigma_{t1} = 639$ kPa based on Eq. (36). However, the tested ice has a fairly large grain size ($d \sim 15\text{mm}$). The tensile strength generally decreases with increasing grain size (Schulson and Duval, 2009). Using the Orowan formula (i.e., Eq. (10.1) in Schulson and Duval (2009)) (which should only be applied to granular ice) yields $\sigma_{t2} = 425$ kPa for an ice sample with a grain size of 15 mm. This result is less than the previous σ_{t1} value. The exact tensile strength is expected to lie within this range. Mulmule and Dempsey (1999) used a low-strain-rate compressive test to estimate the tensile strength at 0.5 MPa. As measurements are not available, the aforementioned estimates and analysis are used to adopt the same value of $\sigma_t = 0.5$ MPa for this test.

Next, for the uniaxial compressive strength, it depends strongly on the loading rate in a uniaxial compressive test. However, the loading rate in tests by Dempsey et al. (1999a) is expressed as the rate of change in the stress intensity factor $\dot{K}_I$ (see Table 1). Due to the stress singularity at the crack tip, we can hardly relate this rate to the material's compressive loading rate. Therefore, we assume that the loading rate of the flatjack is equivalent to the loading rate of the concerned material particles in the cracked body. From Fig. 6 in Mulmule and Dempsey (1999), the loading rate of the flatjack can be calculated as 0.41 kPa/s for Test SQ7 (i.e., $30\text{m}\times 30\text{m}$). In LEFM, the stress intensity factor is related to the external loading (i.e., $K_I \propto \sigma_{ext}\sqrt{L}$). That is, to maintain a constant rate of change in the stress intensity factor $\dot{K}_I$, the loading rate of the flatjack should be inversely proportional to the square root of the size of the ice floe (i.e., fast loading should be performed for a small ice floe and vice versa). The fastest loading rate in this test is expected to be applied to the smallest ice floe tested (0.5 m). Thus, we obtain the loading rate $\dot{\sigma}_{test\_05} = \dot{\sigma}_{test\_30}\sqrt{30/0.5} = 3.18$ kPa/s. For a plane stress scenario with a Young's modulus of

$E = 3.1$ GPa, based on the calculation in Table II of Mulmule and Dempsey (1999), the strain rate for the 0.5 m square test could be calculated as $\dot{\varepsilon} = 1.0258 \times 10^{-6} \text{s}^{-1}$. Using Eq. (37) in Appendix B, the known brine volume, and the loading rate, the largest compressive strength in this test series is calculated to be $\sigma_c = 1.31$ MPa.

Using the procedures described above, we obtain the approximate values of $\sigma_t = 0.5$ MPa and $\sigma_c = 1.31$ MPa. The loading rate is rather slow; therefore, it is reasonable to approximate the Frederking type A and B stresses as $\sigma_{psA} = 5\sigma_c$ and $\sigma_{psB} = 1\sigma_c$, respectively (see the discussion in Appendix B). Eq. (38) in Appendix B is used to calculate the material constants given in Table 2.

Table 2 Material constants approximated for the tests of Dempsey et al. (1999b)

a_1 [MPa^{-2}]	a_3 [MPa^{-2}]	a_6 [MPa^{-2}]	a_7 [MPa^{-1}]	a_9 [MPa^{-1}]
0.2044	1.3223	5.6980	1.2366	-0.5356

Using the material constants given above and $a = A/L = 0.3$ for the initial crack size in Eq. (15) yields the following upper limit for the splitting of the ice floe under consideration:

$$\frac{F_{Y\_\text{plastic\_upper\_limit}}}{Lt} = 122.61 \text{ kPa}.$$

- Plastic lower limit analysis

Using the known value of $\sigma_t = 0.5$ MPa, a lower limit on the splitting load for the ice floe under consideration is calculated via Eq. (17) as follows:

$$\frac{F_{Y\_\text{plastic\_lower\_limit}}}{Lt} = 53.26 \text{ kPa}.$$

4.1.2 Calculation of the ice splitting load by fracture mechanics

We combine both LEFM and the CZM with the weight function method to calculate the ice splitting load for edge-cracked square ice floes of different sizes, as given in Table 1. Additional inputs for the required calculations are listed in Table 3.

Table 3 Inputs to the 'LEFM/CEM + weight function' method

Inputs	Comments
$J = 15$ [J/ m^2]	Fracture energy value is backcalculated using the 'viscoelastic fictitious crack model' (Mulmule and Dempsey, 1998) based on the same experiments' measurements
$E = 5$ [GPa]	This value is not specified for different tests, but an average value is from Table II of Mulmule and Dempsey (1999)
$\frac{F_{Y\_\text{test}}}{Lt} = \frac{1000}{9.3878}\sigma_n^t$ [kN]	Test results in (Dempsey et al., 1999a) are presented in a particularly defined form of nominal strength σ_n^t [MPa]. With $A/L = 0.3$, it leads to the current form for comparison purposes
$12l_{\text{ch}} = 12JE/\sigma_t^2 = 3.6$ [m]	Recommended size, which signifies the minimum size for the applicability of LEFM (Mulmule and Dempsey, 2000)

The weight function for a square body with an edge crack is taken from Tsai and Ma (1989). The calculation results obtained using the different methods and the measurements are illustrated in Fig. 14.

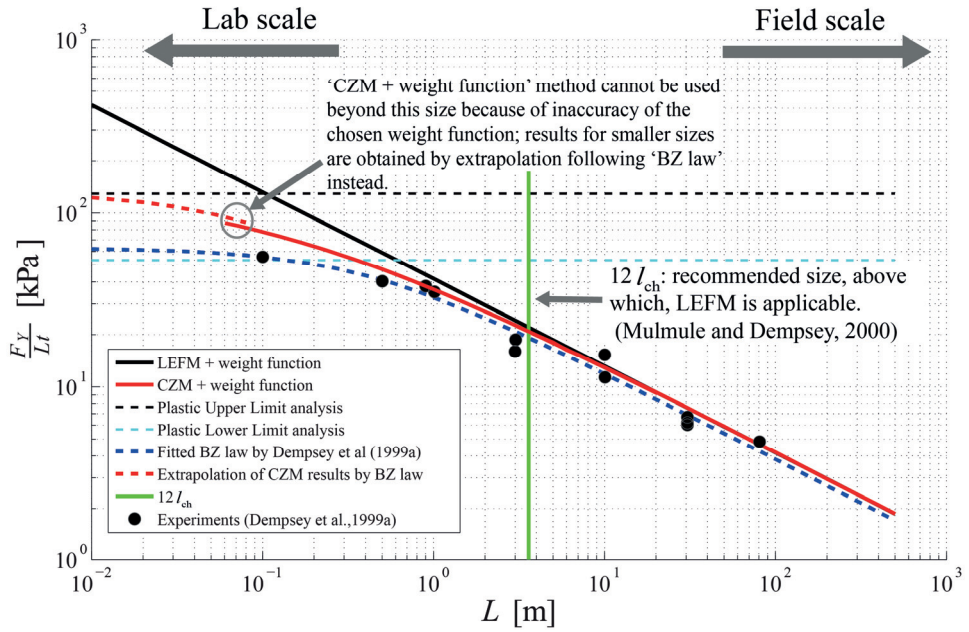

Fig. 14 Splitting load for a square ice plate with an edge crack ($A/L=0.3$): comparison of results obtained using different methods with test data.

The following observations can be made from Fig. 14.

- The results obtained using the 'CZM + weight function' method agree well with most of the experimental results, including those in the laboratory-scale range.
- The 'LEFM + weight function' method only approximates the test results when the size of the test sample is large enough as in field scale (e.g., larger than the recommended size $12l_{ch}$).
- At the laboratory scale, the 'LEFM + weight function' method predicts an ice splitting load that exceeds the prediction from plastic upper limit theory (i.e., strength theory). The plastic upper limit method and plastic lower limit method could be applied at the laboratory scale to level off the increasing value of $F_Y/(Lt)$ calculated by LEFM theory.

4.2 Validation against analytical solutions for the splitting of a semi-infinite ice sheet

Eshelby (1975) deduced analytical solution towards the SIF for an edge crack in a semi-infinite plane with concentrated loads at the crack mouth. Later, Palmer et al. (1983) rearranged the

formula and applied it to the calculation of ice splitting load of a semi-infinite ice sheet. For completeness and as an illustration, the weight function for a semi-infinite plate $H_{\text{r\_semi}}(A,x)$ is shown in Eq. (18) (deduced from Section 8.3a of (Tada et al., 2000)).

$$H_{\text{r\_semi}}(A,x)=\frac{2}{\sqrt{(\pi A[1-(\frac{x}{A})^2])}}[1.3-0.3\left(\frac{x}{A}\right)^{5/4}] \tag{18}$$

In the 'CZM + weight function' method, Eq. (18) is substituted into Eqs. (10) and (11), and the eigenvalue problem is solved to obtain the ice splitting load. In the 'LEFM + weight function' method, Eq. (18) is substituted into Eq. (4) to obtain the ice splitting load. The results of these two methods are plotted in Fig. 15 and compared to the analytical solutions given by Eq. [3] in Palmer et al. (1983).

Because a semi-infinite ice sheet is large relative to its FPZ, the CZM solutions should coincide with those obtained using LEFM, in principle. Indeed, favourable agreement is obtained using these three methods, as shown in Fig. 15.

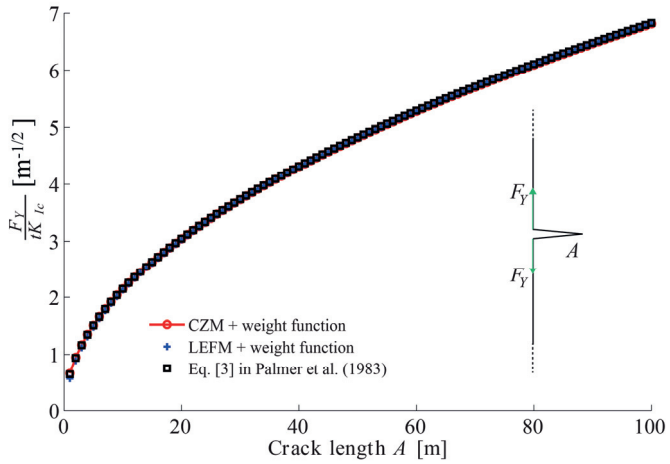

Fig. 15 **Comparison of the ice splitting loads obtained using different methods for a semi-infinite ice sheet.**

4.3 Validation against numerical solutions (FEM): splitting of square and circular ice floes

Use of the weight function method to obtain the ice splitting load for a semi-infinite ice sheet may appear to be redundant in the previous comparison for a semi-infinite ice sheet. However, the weight function method offers the advantage of being independent of the loading profile such that almost closed-form solutions can be obtained for the stress intensity factor and thus the ice splitting load (Dempsey et al., 1994). For the 'CZM + weight function' method, depending on the complexity of the weight function, simple numerical approaches typically need to be used to integrate Eq. (28) and solve the eigenvalue problem of Eq. (10). In the 'LEFM + weight function' method, a closed-form solution to Eq. (4) is available as long as a

closed form weight function is available. In either case, the stress intensity factor need not be calculated using a FEM routine.

Bhat (1988) and Bhat et al. (1991) analysed the ice splitting load for both rectangular and circular ice floes using FEM. These FEM results are compared against the theoretical solutions obtained using the 'CZM + weight function' method (i.e., Eq. (10) and (11)) and the 'LEFM + weight function' method (i.e., Eq. (4)). The weight function of an edge-cracked rectangular ice floe is taken from Tsai and Ma[6] (1989), whereas that for the circular ice floe is taken from Wu and Carlsson (1991).

Fig. 16 illustrates that the developed approach and respective formulas predict the ice splitting load fairly well compared to previous FEM simulations. The comparison is made at the field scale. We deliberately use an ice floe size L that is considerably larger than $12l_{ch}$ in the inputs. Therefore, very few discrepancies can be observed between the results of the 'LEFM + weight function' method and 'CZM + weight function' method. Due to the nature of the ice-structure interaction process, the load history for the crack propagation would not behave as in Fig. 16. In reality, while the ice splitting load is increasing beyond the peak points shown in Fig. 16, the consequent crack would propagate catastrophically. The stable crack increases to only 14.5% and 16.5% of the size of the body in the two base cases presented above. Thus, we focus on the maximum ice splitting load for which complete splitting failure would occur. Eq. (19) is used to predict the ice splitting load for the respective geometry. The same results and similar recommendations can also be found in Bhat (1988) and Bhat et al. (1991) respectively.

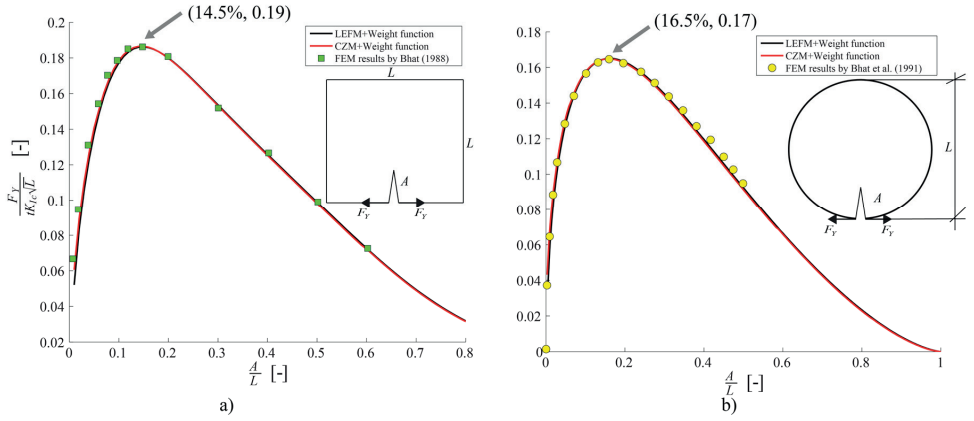

Fig. 16 Splitting load history for a) an edge-cracked square and b)7 a circular ice floe.

$$\begin{aligned} F_Y &= 0.19tK_{Ic}\sqrt{L} && \text{for a square ice plate with critical crack length } \alpha_{cr} = A/L = 14.5\% \\ F_Y &= 0.17tK_{Ic}\sqrt{L} && \text{for a circular ice plate with critical crack length } \alpha_{cr} = A/L = 16.5\% \end{aligned} \tag{19}$$

[6] As pointed out by one of the reviewers, this weight function is only accurate for $0 < A/L < 0.5$ and $0.5 < \beta < 2.0$.

[7] In Bhat et al. (1991)'s original paper, the FEM results were provided as a continuous curve. This continuous curve was digitised into a series of dots to present the discrete nature of the FEM analysis.

5 Ice floe geometry, lateral confinement, and inertia

In Section 4, the developed framework was validated against existing test data and numerical results. A particularly important observation from Fig. 14 is that most floe sizes of engineering interest can be well characterised by the LEFM method. Therefore, only the 'LEFM + weight function' method is employed in the following discussion.

5.1 Ice floe geometries

In Section 4, two base cases (i.e., square and circular ice floes, as shown in Fig. 6) were used to illustrate that the maximum splitting loads F_Y in Eq. (19) are close for these two different geometries. In this section, we extend the analysis of the square ice floe to rectangular ice floes. The ratio of the width w to length L is defined in Eq. (20), and the ice splitting load history for a rectangular floe is illustrated in Fig. 17.

$$\beta = \frac{w}{L} \tag{20}$$

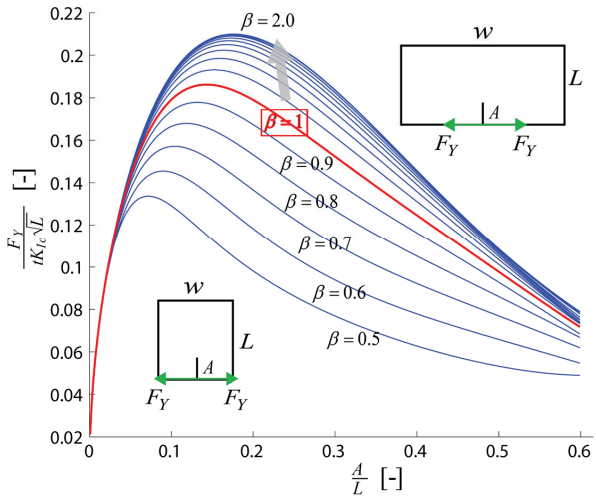

Fig. 17 Splitting history for a rectangular ice floe for a varying width-to-length ratio.

The maximum ice splitting loads for different β values in Fig. 17 are extracted and plotted in Fig. 18 and compared to indentation test data obtained by Sodhi et al. (1993). Fig. 18 is a qualitative comparison between the experimental and theoretical results. The data measured in Sodhi et al.'s (1993) test were indentation pressures in the X direction. These data are multiplied by the indentation area to yield the corresponding values for F_X (see Fig. 5a). These data are then further projected in the Y direction using Eq. (1), for which β_{YX} is unknown. From visual examination of the results, $\beta_{YX} = 0.07$ is chosen to plot Fig. 18. This β_{YX} value is rather low because a flat indenter was pushed into the ice. Thus, the validity of this value should be

further evaluated. However, irrespective of the potentially quantitatively inaccurate manipulations that produced Fig. 18, the major message here is that the ice splitting load tends to level off beyond $w/L \geq 2$.

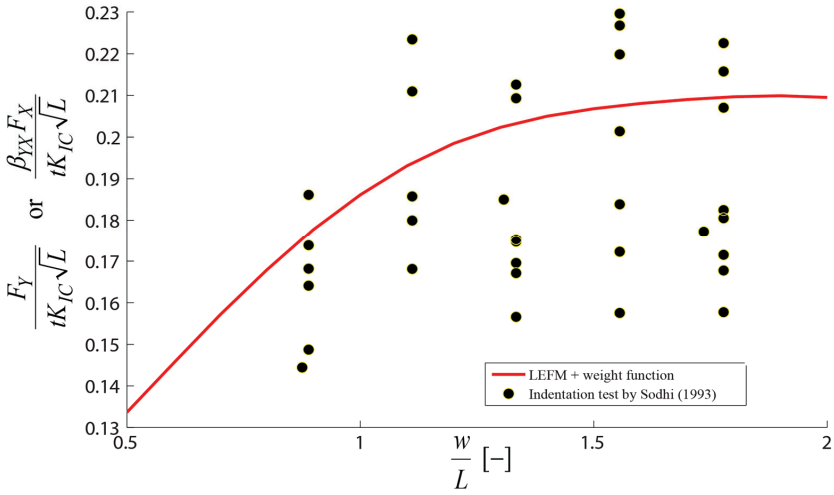

Fig. 18 Qualitative comparison of maximum ice splitting loads for a rectangular ice floe with various width-to-length ratios ($\beta_{YX} = 0.07$ is used to fit the theoretical prediction to the test data).

5.2 Ice floe confinement during splitting

In this section, we investigate the effect of lateral confinement on the ice splitting load. In Section 3.1.2, Eq. (5) was derived for the ice splitting load in the presence of a symmetric lateral confinement pressure $p_{\text{ext}}(x)$. For the nondimensionalised arguments $a = A/L$ and $x' = x/L$, the weight function becomes $H(A,x) = \frac{H(a,x')}{\sqrt{L}}$, and Eq. (5) becomes Eq. (21).

$$\frac{F_Y(a,0)}{t} = \frac{\sqrt{L}}{H(a,0)}\left[K_{IC} + \int_0^a p_{\text{ext}}(x')\frac{H(a,x')}{\sqrt{L}}Ldx'\right] \tag{21}$$

Without losing generality, it is convenient to assume a general form as expressed in Eq. (22).

$$p_{\text{ext}}(x') = \frac{\beta_{confine}F_Y(a,0)}{Lt}f(x') \tag{22}$$

where

$f(x')$ is a normalised function with $0 \leq x' \leq 1$ characterising the lateral confinement profile; depending on the external confinement, it can be an ensemble of discrete values or polynomials and is normalised by $\frac{\beta_{confine}F_Y(a,0)}{Lt}$ from $p_{\text{ext}}(x')$;

$\beta_{confine} F_Y(a,0)$ can be considered the largest absolute value of the boundary confinement; and

$\beta_{confine}$ is a ratio factor that expresses the relative magnitude of the maximum confinement value.

Substituting Eq. (22) into Eq. (21) yields Eq. (23) for the nondimensionalised ice splitting load under the effect of lateral confinement.

$$\frac{F_Y(a,0)}{K_{IC} t\sqrt{L}} = \frac{1}{H(a,0) - \beta_{confine}\int_0^a f(x')H(a,x')dx'} \tag{23}$$

With $\beta_{confine} = 0$, Eq. (23) is reduced to Eq. (4); otherwise with $\beta_{confine} > 0$, a larger ice splitting load F_Y can be encountered. In the next section, a special confinement that is introduced by the floe inertia is studied with the general deviation made herein.

5.3 Inertia of an ice floe

As discussed in Section 2.2, the inertia of an ice floe as it impacts a structure (see Fig. 5c) affects the value of the stress intensity factor. As a benchmark study on Eq. (23), recalling that the inertia of an impacting floe could be expressed as a body force $b_x = -F_X / L^2 t$ for a square ice floe (Bhat, 1988). This body force introduces a stress distribution at the central line of the ice floe. In this context, the stress distribution can be interpreted as a lateral confinement pressure profile. Dempsey et al. (1994) used the solution of Timoshenko and Goodier (1951) and Little (1973) to approximate the stress profile at the centre of a rectangular plate. For the readers' convenience, this stress/confinement profile is re-stated in Eq. (24) for the current application to a square ice floe.

$$p_{ext}(x') = -\frac{F_X}{\pi t}\frac{\delta(x')}{L} + \frac{2}{\pi}\frac{F_X}{Lt}\left(\frac{1}{2} - x'\right)\left\{\frac{1/2}{1/2 - x'} + \left(3 - \frac{3\pi}{4}\right) + \left(\frac{\pi}{2} - 1\right)\left[4\left(\frac{1}{2} - x'\right)^2 - \frac{3}{5}\right]\right\} \tag{24}$$

Using the formula in Eq. (22) and recalling Eq. (1) results in the following rearrangements:

$$f(x') = -\frac{\delta(x')}{\pi} + \frac{2}{\pi}\left(\frac{1}{2} - x'\right)\left\{\frac{1/2}{1/2 - x'} + \left(3 - \frac{3\pi}{4}\right) + \left(\frac{\pi}{2} - 1\right)\left[4\left(\frac{1}{2} - x'\right)^2 - \frac{3}{5}\right]\right\}$$

$$\beta_{confine} F_Y(a,0) = F_X(a,0)$$

$$\beta_{confine} = 1/\beta_{YX}$$

Substituting the expressions above into Eq. (23) yields the ice splitting load under inertial-induced confinement, as illustrated in Fig. 19. The results obtained using Eq. (23) are compared with those obtained using FEM from Bhat (1988). Favourable agreement between these two sets of results verifies the accuracy of Eq. (23). To test the effect of the weight functions developed in different studies, the comparison in Fig. 19 is based on the weight function for a square plate that was used in Mulmule and Dempsey (1998), which was derived using a framework established by Dempsey et al. (1995).

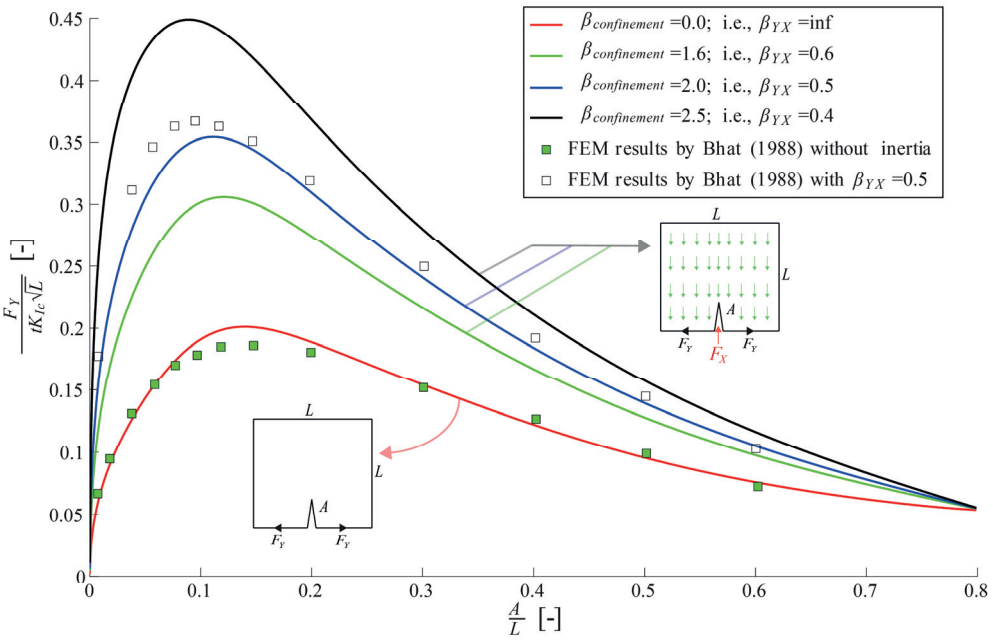

Fig. 19 Ice splitting load under inertial-induced lateral confinement for a square ice floe.

6 Discussion

In this section, the results from the previous analysis of the effect of floe size and its lateral confinement on the ice splitting load are discussed.

6.1 Discussion of the validation results

Three sets of validations were conducted in Section 4. All of the validation tests further confirm the validity of the developed framework to calculate the ice splitting load F_Y, especially the approach based on fracture mechanics.

Fig. 14, Fig. 15, and Fig. 16 all illustrate that for a sufficiently large ice floe, the results obtained from the LEFM-based approach (e.g., the 'LEFM + weight function' method) and the CZM coincide with each other. That is, the 'LEFM + weight function' method can be used to accurately estimate the ice splitting load for large ice floes.

Additionally, Fig. 14 further shows that:

- The $12l_{ch}$ value can serve as a satisfactory criterion beyond which LEFM is applicable. From an engineering perspective, ice splitting phenomena are mainly of interest at the field scale (i.e., sizes above 3 m), where LEFM is sufficiently accurate.

- At the laboratory scale, plastic upper limit theory predicts an ice splitting load that is twice as large as that predicted by plastic lower limit theory. However, the lower bound is a better approximation to the measured value. This result can be attributed to the rather brittle nature of ice during splitting failure, which can hardly be described by plasticity-based theory. However, plastic limit analysis should not be discarded because of the large discrepancy in the comparative analysis presented above. As no analytical fracture analysis is available in this case, the plastic limit analysis provides an effective upper bound of the ice splitting load.
- Based on Fig. 14, in order to extrapolate the laboratory-scale measurements to the field scale, it should follow a nonlinear trend. This nonlinear trend could be constructed using the 'CZM + weight function' method as long as a sufficiently accurate weight function is available (e.g., the weight function for a circular ice floe). However, as shown in Fig. 14, an accurate weight function is typically not available, as it is tedious to obtain and requires truncation approximations. The Bažant size effect law (i.e., the BZ law) could be applied as an alternative to extrapolate the results obtained between or among plastic limit analysis, LEFM, and the 'CZM + weight function' methods. This alternative approach is illustrated as a red dashed curve, which is obtained by extrapolating the results obtained using the 'CZM + weight function' method to asymptotically approximate the results obtained from plastic upper limit analysis following the Bažant size effect law (Bažant, 2005).

6.2 Discussion on ice floe geometry, lateral confinement, and inertial effects

Two base cases involving rectangular and circular ice floe geometries are studied in this paper. Fig. 16, Fig. 17, and Fig. 18 illustrate that comparable results are obtained for both geometries for the maximum ice splitting load. As long as there are no ice floe inertial effects, the maximum ice splitting load for a head-on contact between the structure and an ice floe does not vary considerably with the floe geometry, e.g., Fig. 18 illustrates that the maximum ice splitting load for the rectangular ice floe increases from $0.13tK_{IC}\sqrt{L}$ at low width-to-length ratios (i.e., 0.5) to $0.22tK_{IC}\sqrt{L}$ and then levels off at high width-to-length ratios (i.e., $\beta \geq 2$). Using Eq. (19) for different geometries, such as those shown in Fig. 16, yield fairly similar maximum ice splitting loads. The floe geometry has a less significant effect on the ice splitting load than the lateral confinement (which will be discussed later).

In the field, complex geometries are typically encountered, not strictly rectangular or circular shapes. However, the floe geometry resembles the base cases to a certain extent. For example, Rothrock and Thorndike (1984) noted that the ice floes in the summer are 'somewhat rounded in shape'. This is due to mechanical abrasion at the edges of the floes. For such situations, the circular ice floe assumption could be a good analytical approximation. In other situations, such as in Fig. 1, the irregular ice floe could be idealised as a rectangular ice floe. The plastic limit theory analysis that was developed in Section 3.2 could serve as an alternative analytical approach for highly irregular ice floe geometries.

Regarding lateral confinement and inertial effects on the ice splitting load, the 'LEFM + weight function' method was used to derive Eq. (23) to account for the effect of symmetric lateral confinement on an ice floe. Eq. (23) presents the advantages of using the weight function method. Any given symmetric lateral confinement $\sigma_{ext}(x')$ can be restructured into the form given in Eq. (22), which can then be used to calculate the stress intensity factor rather conveniently. The inertial effect, as a special case of confinement, is studied and compared with

the numerical results in Fig. 19. The favourable comparison confirms the validity of Eq. (23) and the treatment of the inertial-induced body force given by Eq. (24).

Higher lateral confinement generally produces higher ice splitting loads, and large width-to-length ratios also lead to slightly higher ice splitting loads. However, another important observation can be made by comparing the lateral confinement effects in Fig. 19 against the geometrical effects shown in Fig. 16, Fig. 17, and Fig. 18. This comparison illustrates that lateral confinement effects are more effective than geometrical effects in increasing the corresponding ice splitting load. That is, increasing the width-to-length ratio of a rectangular ice floe can only increase the maximum ice splitting load to a plateau of $0.21tK_{IC}\sqrt{L}$; whereas an increase in lateral confinement can significantly increase the corresponding maximum ice splitting load, e.g., Fig. 19 demonstrates the inertial effect, as a special type of confinement, increases the ice splitting load from $0.19tK_{Ic}\sqrt{L}$ without confinement (i.e., $\beta_{confinement}=0$) to $0.45tK_{Ic}\sqrt{L}$ while the confinement is large (i.e., $\beta_{confinement}=0.45$).

7 Conclusions

In this study, two different approaches are used to address the complexity of global splitting failure in an ice floe and obtain analytical solutions. One approach is based on fracture mechanics and the other approach is based on plastic limit analysis. In the fracture mechanics approach, a 'LEFM + weight function' method and 'CZM + weight function' method are used. Both methods are formulated and compared with available data from previous tests and numerical solutions. The following conclusions can be drawn from the favourable comparisons and the preceding discussion:

- The weight function method provides an effective solution to derive the stress intensity factor for describing symmetric loadings on a symmetrically cracked body.
- For the splitting problem considered here, floe sizes of engineering interest (e.g., $L \geq 12l_{ch}$) can typically be accurately described by LEFM. As an example, if the size of a geometrically similar ice floe increases 2 times, the corresponding ice splitting load would increase $\sqrt{2}$ times.
- The CZM can describe the fracture process while the concerned ice sample is small (e.g., at the laboratory scale). The CZM is a useful methodology for considering nonlinearities within the FPZ. Additionally, the 'CZM + weight function' can serve as a potential tool to extrapolate the laboratory scale measurements to the field scale using fracture mechanics.
- The applicability of the analytical formulas developed using fracture mechanics to calculate the ice splitting load should not be underrated because of the inherent restrictions in the assumptions used to derive these formulas. Practical problems may be reduced to one of the base cases considered in this paper. All of the theoretical development for the base cases can serve as benchmark tests to verify the various numerical approaches.
- Different geometries have been studied for the base cases, illustrating that geometry has only a slight effect on the maximum ice splitting load for a head-on contact scenario without floe inertial effects. Specifically, for a square ice floe, the maximum ice splitting load is calculated as $0.19tK_{Ic}\sqrt{L}$; whereas this value is $0.17tK_{Ic}\sqrt{L}$ for a

circular ice floe. Moreover, for rectangular ice floes with varying width-to-length ratios, the maximum ice splitting load increases from $0.13tK_{IC}\sqrt{L}$ at low width-to-length ratios (i.e., 0.5) to $0.21tK_{IC}\sqrt{L}$ and then levels off at high width-to-length ratios (i.e., $\beta \geq 2$). In all cases, the critical crack length is less than 20% of the size of the ice floe considered.

- In general, for an ice floe with an increasing lateral confinement, a corresponding increase can be found in the maximum ice splitting load. Such an increase in the maximum ice splitting load is more significant than geometric effect (e.g., by increasing a rectangular floe's width-to-length ratio). For example, while consider the inertial effect as a particular type of confinement, the maximum ice splitting load increases from $0.19tK_{Ic}\sqrt{L}$ without confinement (i.e., $\beta_{confinement} = 0$) to $0.45tK_{Ic}\sqrt{L}$ while the confinement is large (i.e., $\beta_{confinement} = 0.45$).
- An analysis of different symmetric lateral confinement profiles indicates that confinement in which most of the load components are closer to the edge crack can effectively increase the ice splitting load, i.e., prevent the development of splitting failure.

Because of the complexity of the splitting failure scenario (particularly the ice floe geometry) and our pursuit of analytical solutions, as an alternative approach, plastic limit analysis has been introduced as a supplementary tool to the fracture-mechanics-based approach described above. Plastic limit analysis can be effectively used to determine an analytical upper bound of the ice splitting load (e.g., see the comparison in Fig. 14). The results from the plastic lower limit analysis result are closer to the measured data at the laboratory scale, illustrating the brittle nature of the splitting failure. A parabolic yield function was developed based on two sets of different material constants and thoroughly analysed. The following conclusions are drawn from the results obtained using plastic limit theory (which do not contradict the results obtained using fracture-mechanics-based theory).

- In the splitting failure mode, the material particles within the ice floe are prone to be failed in a tensile mode to minimise the energy dissipation rate, i.e., the crack tends to propagate in an opening mode. This result, which is based on plasticity theory, is in accordance with one of the assumptions made in the fracture-mechanics-based approach, i.e., the splitting failure is considered to be a Mode I fracture (opening mode).
- The material constants significantly affect the ice splitting load. In general, larger yield surface increases the ice splitting load. However, in conjunction with the previous conclusion, the uniaxial tensile strength has a more profound impact on the estimated ice splitting load obtained using plastic upper/lower limit theory. This result can be exemplified by the plastic lower limit formula in Eq. (17).
- In Appendix B, the preferred crack path in a rectangular ice floe is investigated for a series of different width-to-length ratios $\beta = w/L$. Regardless of the material constants used, more than 85.4% of the rectangular ice floes split directly with a crack angle $\theta = 90^{o}$. This result obtained from using plasticity-based-theory also agrees with one of the assumptions used in the fracture-mechanics-based approach, i.e., the splitting crack propagates in a self-similar manner.
- The analytical formulas used to calculate the ice splitting load using plastic limit theory should not be underrated because of their conservative nature. These formulas can effectively serve as tools for making initial estimates of the ice splitting load for various ice floe geometries, contact scenarios (i.e., head-on collisions or others), and boundary confinements.

Acknowledgement

The authors would like to thank the Norwegian Research Council through the project 200618/S60-PetroRisk and the SAMCoT CRI for financial support. The authors are grateful for the interesting knowledge learned from and discussion with Professor John Dempsey and Dr. Devinder Sodhi. In addition, valuable discussions with Phd student Marat Kashafutdinov are highly appreciated.

Appendix A Derivation of ice splitting load using eigenvalue analysis

In this section, formulas to calculate the ice splitting load F_Y are derived following the procedures given in the original studies of Li and Bažant (1994) and Li and Liang (1993). Similar derivations can also be found in studies by Bažant and Planas (1998) and Wang and Dempsey (2011). Compared to these previous studies, the present derivation features a specific application (i.e., splitting failure in an ice floe); thus, detailed derivations are provided along with a physical interpretation.

The weight function method is used, i.e., Eq. (3) is substituted into Eq. (6) to obtain

$$\int_0^A \frac{F_Y(A,0)}{t}\delta(x)H(A,x)dx - \int_0^A \sigma_{\text{coh}}(x)H(A,x)dx = 0 \tag{25}.$$

Using the weight function method (i.e., Eq. (3)), the half-COD can be written as

$$u(A,x) = \frac{1}{E'}\int_0^A K(a)H(a,x)da = \frac{1}{E'}\int_0^A\int_0^A \sigma(s)H(a,s)\mathrm{d}sH(a,x)da \tag{26}.$$

Rearranging Eq. (26) yields Eq. (27),

$$u(A,x) = \frac{1}{E'}\int_0^A \sigma(s)U(A,x,s)ds \tag{27},$$

where the function $U(A,x,s)$ is defined in Eq. (28). This function represents the crack opening displacement at a location x for a cracked body with a crack length A under a unit load acting at a location s.

$$U(A,x,s) = \int_{\max(x,s)}^A H(a,x)H(a,s)da \tag{28}$$

$H(a,x)$=0 with $x \geq a$ (i.e., a unit load acting at $x \geq a$ results in a zero stress intensity factor at the crack tip a (Bažant and Planas, 1998)); therefore, the lower integration limit is given by $\max(x,s)$ in Eq. (28).

Substituting the right-hand side of Eq. (9) into the left-hand side of Eq. (7), and replacing the right-hand side of Eq. (7) with Eq. (27) yields Eq. (29).

$$(1-\frac{\sigma_{\text{coh}}(x)}{\sigma_t})u_c = \frac{1}{E'}[\frac{F_Y(A,0)}{t}U(A,x,0) - \int_B^A \sigma_{\text{coh}}(s)U(A,x,s)ds] \tag{29}$$

Using the Leibniz integral rule to take variations over A for Eq. (29) yields

$$-\frac{u_c}{\sigma_t}\delta\sigma(x)_{\text{coh}} = \frac{1}{E'}\frac{\delta F_Y(A,0)}{t}U(A,x,0) + \frac{1}{E'}\frac{F_Y(A,0)}{t}\delta U(A,x,0) - \frac{1}{E'}[\frac{\delta A}{\delta A}\sigma_{\text{coh}}(A)U(A,x,A) - \frac{\delta B}{\delta A}\sigma_{\text{coh}}(B)U(A,x,B) + \int_B^A \delta\sigma(s)_{\text{coh}}U(A,x,s)ds + \int_B^A \sigma_{\text{coh}}(s)\delta U(A,x,s)ds] \quad (30).$$

By definition, at the peak value of the ice splitting load, $\delta F_Y(A,0) = 0$ (Bažant and Planas, 1998). Therefore, the first term on the right-hand side of Eq. (30) vanishes.

The third term on the right-hand side of Eq. (30) results from the upper limit of the integration. Using the symmetric definition given in Eq. (28), the following manipulation could be used to equate $U(A,x,A)$ with $U(A,A,x)$: the physical interpretation of this term is the crack opening displacement at the crack tip A under a unit point load acting at a position x. The crack opening displacement at the cohesive crack tip is 0 by definition.

$$\begin{aligned} U(A,x,A) &= \int_{\max(x,A)}^{A} H(a,x)H(a,A)da \\ &= \int_{A}^{A} H(a,A)H(a,x)da \\ &= U(A,A,x) \\ &= 0 \end{aligned}$$

The fourth term on the right-hand side of Eq. (30) also vanishes. The physical crack length B is known; therefore, any virtual increase in the cohesive crack tip A leads to $\frac{\delta B}{\delta A} = 0$.

For the second and sixth terms on the right-hand side of Eq. (30), the value of $\delta U(A,x,0)$ should be determined using Leibniz's integral rule.

$$\frac{\partial U(A,x,s)}{\partial A} = \frac{\partial}{\partial A}[\int_{\max(x,s)}^{A} H(a,x)H(a,s)da] = H(A,x)H(A,s)$$

The aforementioned operation results in the summation of the second and sixth terms in Eq. (30) cancelling each other by virtue of Eq. (6), as given below.

$$\begin{aligned} \frac{F_Y(A,0)}{t}\delta U(A,x,0) - \int_B^A \sigma_{\text{coh}}(s)\delta U(A,x,s)ds &= \frac{F_Y(A,0)}{t}H(A,x)H(A,0) - \int_B^A \sigma_{\text{coh}}(s)H(A,x)H(A,s)ds \\ &= H(A,x)[\frac{F_Y(A,0)}{t}H(A,0) - \int_B^A \sigma_{\text{coh}}(s)H(A,s)ds] \\ &= H(A,x)[K_F(A) + K_\sigma(A)] \\ &= 0 \end{aligned}$$

The aforementioned simplifications can be used to reduce Eq. (30) to Eq. (31).

$$\delta\sigma_{\text{coh}}(x) = \frac{\sigma_t}{u_c E'}[\int_B^A \delta\sigma_{\text{coh}}(s)U(A,x,s)ds] \quad (31)$$

Replacing $\delta\sigma_{\text{coh}}(x)$ with a proportional cohesive stress profile $\sigma(x)$ and using the fracture energy $J=\sigma_t u_c$ (where u_c is the critical half-crack opening displacement) yields Eq. (10).

Solving the eigenvalue problem in Eq. (10) yields the eigenvector $\sigma(x)$, which is the stress profile in the cohesive zone. The next step is to use these solutions to retrieve the peak splitting load $F_Y(A,0)$.

Recall that for linear softening, the cohesive stress can be given by the left side of Eq. (9). Multiplying both sides of this equation with the obtained eigenvector $\sigma(x)$ and integrating the result over the cohesive zone (i.e., $B\to A$ yields Eq. (32).

$$\int_B^A \sigma(x)\sigma_{\text{coh}}(x)dx=\sigma_t\int_B^A \sigma(x)dx-\frac{\sigma_t}{u_c}\int_B^A \sigma(x)u(x)dx \tag{32}$$

Eqs. (7) and (27) can be used to explicitly express $u(x)$ in Eq. (32) as follows:

$$u(x)=\frac{1}{E'}[\frac{F_Y(A,0)}{t}U(A,x,0)-\int_B^A \sigma(s)U(A,x,s)ds] \tag{33}$$

Substituting Eq. (33) into Eq. (32) yields

$$\begin{aligned}\int_B^A \sigma(x)\sigma_{\text{coh}}(x)dx&=\sigma_t\int_B^A \sigma(x)dx-\frac{1}{E'}\frac{\sigma_t}{u_c}\int_B^A \sigma(x)[\frac{F_Y(A,0)}{t}U(A,x,0)-\int_B^A \sigma(s)U(A,x,s)\,\mathrm{d}\,s]dx\\&=\sigma_t\int_B^A \sigma(x)dx\\&-\frac{1}{E'}\frac{\sigma_t}{u_c}\int_B^A \sigma(x)[\frac{F_Y(A,0)}{t}U(A,x,0)]dx\\&+\frac{1}{E'}\frac{\sigma_t}{u_c}\int_B^A \sigma(x)\int_B^A \sigma(s)U(A,x,s)dsdx\end{aligned} \tag{34}$$

Using Eq. (10), the third term on the right side of Eq. (34) can be transformed as follows (note that $J=\sigma_t u_c$), which cancels out the left side of Eq. (34)

$$\frac{1}{E'}\frac{\sigma_t}{u_c}\int_B^A \sigma(x)\int_B^A \sigma(s)U(A,x,s)dsdx=\frac{\lambda}{E'}\frac{\sigma_t}{u_c}\int_B^A \sigma(x)\sigma_{\text{coh}}(x)dx=\int_B^A \sigma(x)\sigma_{\text{coh}}(x)dx$$

Straightforward manipulations on the remaining first and second terms on the right side of Eq. (34) yield Eq. (11).

Appendix B Using plastic upper limit theory to calculate the ice splitting load

Using the framework developed in Section 3.2.1 as a supplement to Section 3.1, the following important topics are discussed in detail in this Appendix.

- Recommended methods for determining the material constants in the parabolic yield function
- Demonstrating the properties of the chosen energy dissipation rate D_A in Eq. (13)
- Identifying the preferred crack path for the base case geometries
- Deriving the ice splitting load given by Eq. (15)

Two different material failure envelopes are studied herein: the failure envelopes under low- and high-strain-rate loading. We investigate the geometries of the base cases shown in Fig. 6.

Step 1: Constructing the yield surface and calculating the energy dissipation rate

➢ Indirect estimation of the material constants

Extensive multi-axial tests typically have to be performed to construct the yield surface for a site-specific ice condition. However, this information is often scarce and difficult to obtain. Following the framework developed by Chen and Han (1988), it is necessary to obtain at least the correct information of on the uniaxial compressive strength σ_c, uniaxial tensile strength σ_t, and Frederking type A and type B plane-strain strengths[8] (i.e., σ_{psA} and σ_{psB}, respectively). If no uniaxial strength tests are available, the following empirical formulas can be used to derive the strength of first-year sea ice.

- **Tensile strength is primarily sensitive to the porosity and grain size of ice**

For a known salinity and temperature, the brine volume of ice can be expressed as follows (taken from (Sanderson, 1988), p.14):

$$v_b = 0.001S(0.53 - \frac{49.2}{T}) \tag{35}$$

where

v_b is the brine volume [-];
S is the salinity [ppt];
T is the temperature, which is typically negative [°C].

[8] These terms are defined in Sanderson (1988), p. 87 or Timco and Frederking's papers (1984, 1986).

The tensile strength is largely affected by the ice porosity. Assuming a gas-free ice material, we can equate the ice porosity to its brine volume. This assumption is realistic at low temperatures, e.g., Richter-Menge and Jones (1993) found no difference between the brine volume and porosity at temperatures below -3 °C . The tensile strength σ_t can be related to the porosity (or brine volume v_b in units of [ppt]), as in Eq. (36) (taken from equation (10) of (Timco and Weeks, 2010)).

$$\sigma_t = 4.278 v_b^{-0.6455} \qquad (r^2 = 0.72) \tag{36}$$

where

σ_t is the uniaxial tensile strength of the considered ice sample [MPa];
v_b is used to approximate the porosity in units of [ppt]; and
r^2 represents the goodness of fit to the experimental data.

- **Uniaxial compressive strength is primarily sensitive to the loading rate**

The unconfined compressive strength σ_c [MPa] is largely influenced by the strain rate $\dot{\varepsilon}$ [s^{-1}]. These two variables are related to each other by Eq. (37) (Timco and Weeks, 2010).

$$\sigma_c = 37 \dot{\varepsilon}^{0.22} \left(1 - \sqrt{\frac{v_b}{270}}\right) \tag{37}$$

Depending on the loading rate, a range of 2 to 5 is recommended for the ratio of σ_{psA} / σ_c, whereas σ_{psB} remains almost the same as σ_c (Sanderson, 1988). For known $\sigma_c, \sigma_t, \sigma_{psA}$, and σ_{psB}, the material constants can be calculated using Eq. (38), which is derived by following the same methodologies as presented by Ralston (1977b).

$$\begin{aligned} a_1 &= \frac{1}{2}\frac{\sigma_c - \sigma_t}{\sigma_{psA}\sigma_c\sigma_t} + \frac{1}{\sigma_c\sigma_t} \pm \frac{\sqrt{(\sigma_{psA} - \sigma_c)(\sigma_{psA} + \sigma_t)}}{\sigma_{psA}\sigma_c\sigma_t} \\ a_7 &= \frac{\sigma_c - \sigma_t}{\sigma_c\sigma_t} \\ a_3 &= \frac{a_7\sigma_c + 1}{\sigma_c^2} - a_1 \end{aligned} \tag{38}$$

- Direct curve fitting to derive the material constants

However, if extensive multi-axial tests data are available, deriving the material constants becomes a curve-fitting problem. Here, we present two sets of experimental data. These data are the failure envelopes constructed using data from Timco and Frederking's tests (1984, 1986), which were conducted under a fairly slow loading rate (i.e., the strain rate was 2×10^{-4} s^{-1}). The multi-axial test data under a high loading rate were compiled by Schulson et al. (2006). The important test conditions for these two datasets are summarised in Table 4.

Table 4 Test conditions for the compiled data under both low- and high-strain-rate loading conditions

Literature source	d [mm]	T [°C]	Porosity	$\dot{\varepsilon}$ [s^{-1}]	Ice conditions
(Timco and Frederking, 1986); multi-axial compressive strength test		-2	4.1%	2×10^{-4}	Sea ice sampled in late May 1984 in northern Labrador, Canada
(Iliescu and Schulson, 2004); multi-axial compressive strength test	4-8	-10		4.5×10^{-3}	Fresh-water ice
(Schulson et al., 2006); multi-axial compressive strength test	3.9 ± 0.4	-10	4%	1.5×10^{-2}	Sea ice sampled in April in the Beaufort Sea, 300 km north of Prudhoe Bay
(Richter-Menge and Jones, 1993); tensile strength test	4.1	-10	2.2%	1.0×10^{-3}	Sea ice sampled in April 1986 in Beaufort Sea, 160 km north of Barter Island

Table 4 illustrates that the test data are comparable because the major conditions of the ice samples were similar. Although the tests conducted by Timco and Frederking (1986) under a low loading rate were performed at a different temperature, the final test data were extrapolated and reported at -10 °C . For different ice conditions (e.g., different grain sizes, porosities, and temperatures), the relevant formulas (e.g., Eqs. (35), (36), and (37)) can be used to extrapolate these data to the ice conditions of interest. These test data can be used to determine the material constants given in Table 5 based on curve fitting shown in Fig. 20.

Fig. 20 illustrates that the failure envelope under high-strain-rate loading is larger than its counterpart under low-strain-rate loading. This result agrees with the test results (Schulson and Duval, 2009). However, curve fitting cannot fit all of the test points while maintaining an elliptic yield function in the $\sigma_{11}-\sigma_{22}$ space. It is difficult to obtain a universal yield function that satisfies all of the different types of loading conditions (Vinogradov, 1987). In the current ice splitting problem, the tension and shearing processes are the dominant processes in the ice material. Therefore, it is reasonable to calibrate the intended yield function to fit the 'tension-tension', 'tension-compression', and 'compression-tension' quadrants. Following this principle, a conservative curve fit (which is shown in red) in Fig. 20 was used for the test data in all quadrants except the 'compression-compression' quadrant.

Table 5 Material constants at different loading rates

Columnar sea ice, -10 °C	a_1 [MPa^{-2}]	a_3 [MPa^{-2}]	a_7 [MPa^{-1}]	a_9 [MPa^{-1}]
(Schulson et al., 2006): high loading rate	0.0033	0.2467	1.0500	-0.03
(Timco and Frederking, 1986): low loading rate	0.04	0.43	0.78	0.74

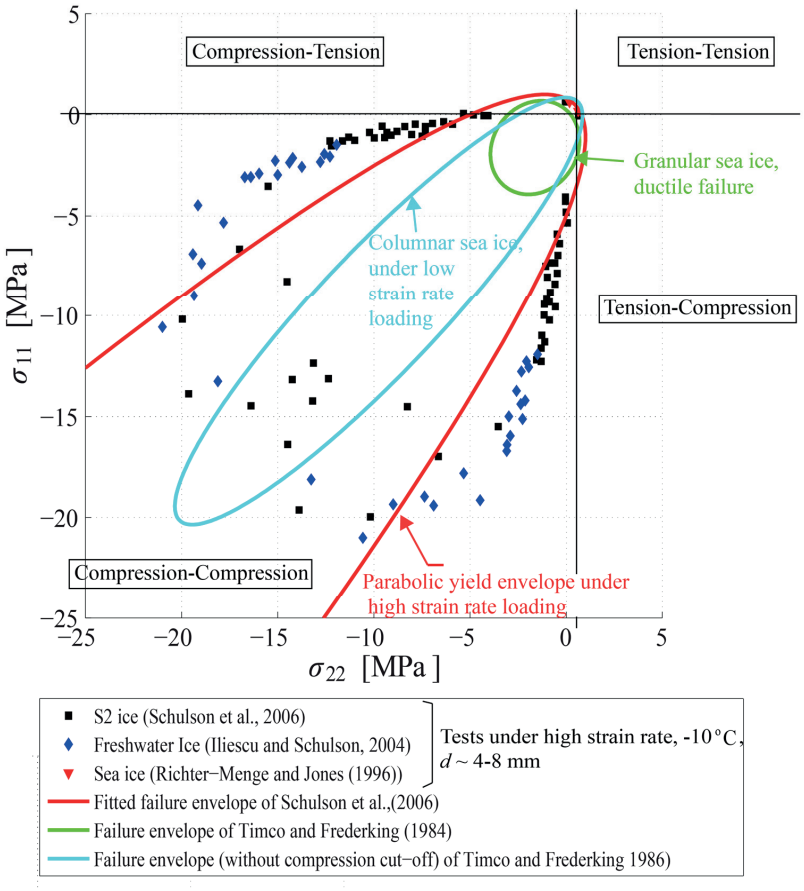

Fig. 20 Multi-axial test results and fitted curve (the test data by Timco and Frederking (1984, 1986) are not shown: only the analytical failure envelopes are shown; d is the grain size; and σ_{11} and σ_{22} correspond to the principal stresses in the X and Y directions, respectively).

The known material constants given in Table 5 and the energy dissipation rate D_A in Eq. (13) can be studied using various combinations of the normal and shear velocities to shed light on their respective resistance to crack propagation. That is, the relative contributions from the shear and normal velocity components (i.e., δv_n and δv_s) to the total energy dissipation rate are weighted using the contour plot shown in Fig. 21. This figure presents each of the energy dissipation rate contours for both the high- and low-strain-rate loading failure envelopes. Assuming a unit velocity jump $\delta v = 1 = \sqrt[2]{\delta v_n^2 + \delta v_s^2}$ along the curve of $\sqrt[2]{\delta v_n^2 + \delta v_s^2} = 1$, minimum values can be identified for both the high-strain-rate loading failure (i.e., the red circle on the dark solid curve) and low-strain-rate loading failure (i.e., the yellow circle on the dark dashed curve). In particular, the minimum energy dissipation of the high-strain-rate loading case occurs at $\delta v_n = 1$ and $\delta v_s = 0$, whereas the minimum energy dissipation locus for the low-strain-rate loading case occurs at $\delta v_n = 0.58$ and $\delta v_s = 0.81$ (i.e., $\arctan(\delta v_s / \delta v_n) = 54.6^\circ$). That is, the high-strain-rate loading condition favours pure tensile failure, whereas failure under the more slowly

loaded condition requires a particular combination of the shear and normal velocity components to reach the minimum energy dissipation. This result agrees with the ice material properties, i.e., a higher compressive strength is observed for the high-strain-rate loading failure envelope than the low-strain-rate loading failure envelope (see Fig. 20). The shear stress of a continuum can be manifested as half of the uniaxial compressive stress slanted 45° to the uniaxial direction (Irgens, 2008). However, this discussion is based on the assumption that ice is a continuum to which classic continuum mechanics, including plasticity theories, can be applied.

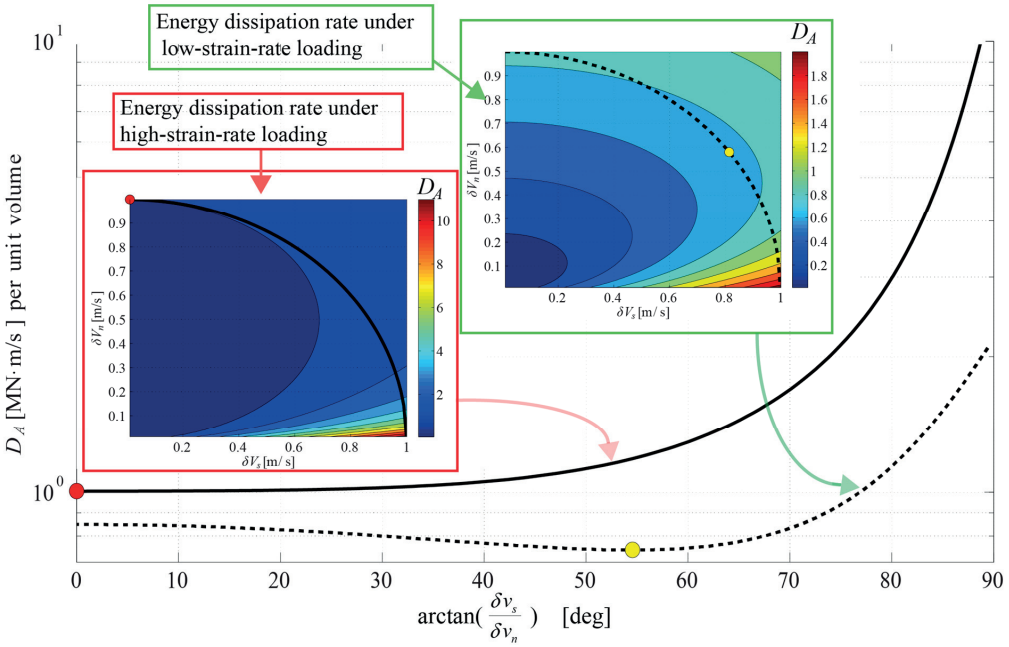

Fig. 21 Energy dissipation rate in the shear and normal directions for high-strain-rate loading (in red) and low-strain-rate loading (in green) for ice failure envelopes; the Y-axis in this plot is shown on a log scale to highlight small-scale variations in the energy dissipation rate.

Step 2: Searching for crack paths by minimising the overall energy dissipation

The simplified geometry in Fig. 12 can be used to explicitly express the crack path $L_{\text{crack}}(\text{geometry}, \text{size}, \theta)$ in Eq. (14), as given by Eq. (39).

$$L_{\text{crack}} = L\sin\theta \qquad \text{for a circular ice floe}$$

$$L_{\text{crack}} = \begin{cases} \dfrac{w}{2\cos\theta} & (0 \le \theta < \arctan(\dfrac{2L}{w})) \\ \dfrac{L}{\sin\theta} & (\arctan(\dfrac{2L}{w}) \le \theta \le 90^{\circ}) \end{cases} \qquad \text{for a rectangular ice floe} \tag{39}$$

The velocity profile in the local coordinate x' (see Fig. 12) can be expressed by Eq. (40).

$$\delta v_{Yn}(x',\theta) = \delta v_Y \sin\theta(1-\frac{x'}{L_{\text{crack}}})$$
$$\delta v_{Ys}(x',\theta) = \delta v_Y \cos\theta \tag{40}$$

Eqs. (40) and (13) can be combined to obtain a new expression for D_A, which is given by Eq. (41).

$$D_A = \frac{\delta v_Y}{2a_1}[\sqrt{\frac{(a_7^2+2a_1)}{a_6}}\sqrt{4(a_1+a_3)\sin^2\theta(1-\frac{x'}{L_{\text{crack}}})^2+2a_1\cos^2\theta}-a_7\sin\theta(1-\frac{x'}{L_{\text{crack}}})] \tag{41}$$

Assuming that $\alpha = \frac{x'}{L_{\text{crack}}}$, $a = \frac{A}{L_{\text{crack}}}$ and substituting Eq. (41) into Eq. (14), the following ice splitting load is obtained:

$$F_Y = \frac{L_{\text{crack}}t}{2a_1}\int_a^1[\sqrt{\frac{(a_7^2+2a_1)}{a_6}}\sqrt{4(a_1+a_3)\sin^2\theta(1-\alpha)^2+2a_1\cos^2\theta}-a_7\sin\theta(1-\alpha)]d\alpha \tag{42}.$$

We adopt the following notation (after cancelling out the velocity term) in Eq. (43) to further simplify Eq. (42):

$$\int_a^1 \bar{D}_A(\alpha,\theta)d\alpha = \frac{1}{2a_1}\int_a^1[\sqrt{\frac{(a_7^2+2a_1)}{a_6}}\sqrt{4(a_1+a_3)\sin^2\theta(1-\alpha)^2+2a_1\cos^2\theta}-a_7\sin\theta(1-\alpha)]d\alpha \tag{43}$$

The notation provided above can be used to re-cast Eq. (42) for the general case into equations that are specific to the base cases shown in Fig. 6, i.e., Eq. (44) for a circular ice floe and Eq. (45) for a rectangular ice floe.

$$\frac{F_Y}{Lt} = \sin\theta\int_a^1 \bar{D}_A(\alpha,\theta)d\alpha \tag{44}$$

$$\frac{F_Y}{Lt} = \begin{cases} \frac{\beta}{2\cos\theta}\int_a^1 \bar{D}_A(\alpha,\theta)d\alpha & (0 \le \theta < \arctan(\frac{2L}{w}), \beta = \frac{w}{L}) \\ \frac{1}{\sin\theta}\int_a^1 \bar{D}_A(\alpha,\theta)d\alpha & (\arctan(\frac{2L}{w}) \le \theta \le 90^o) \end{cases} \tag{45}$$

Eqs. (44) and (45) can be used to search for the crack path that minimises the ice splitting load. The corresponding value obtained for $F_Y/(Lt)$ for varying angle θ is shown in Fig. 22 and Fig. 23. The results and findings are presented below.

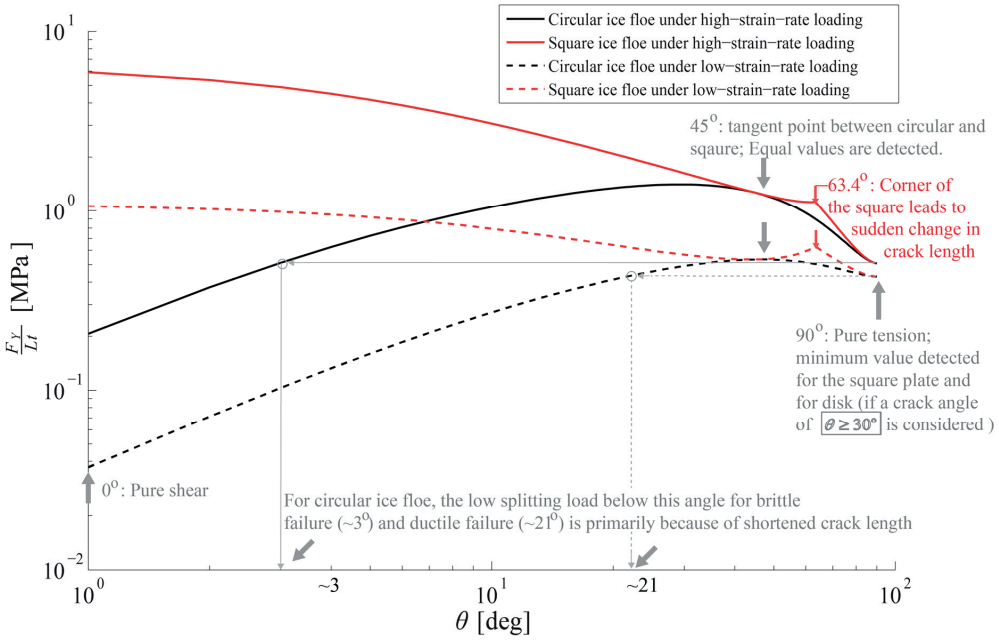

Fig. 22 Ice splitting load for square and circular ice floes with varying crack angles and loading rates: this plot is constructed using a log-log scale to highlight small-scale variations in the load.

Fig. 23 illustrates the required splitting load versus the crack angle θ for circular and rectangular ice floes. We highlight the following results from the figure.

- The ice splitting load under high-strain-rate loading is larger than that under low-strain-rate loading. This result corresponds with the size of the failure envelope shown in Fig. 20.
- For the square ice floe (i.e., $L = w$, see Fig. 4), the ice splitting load F_Y reaches its minimum value if the crack propagates directly through the ice floe (i.e., $\theta = 90^o$).
- For the circular ice floe, the dark solid and dashed curves in Fig. 22 illustrate that the ice splitting load attains its minimum value at $\theta = 0^o$. This result is obtained simply because L_{crack} is shortest at this crack angle. However, for practical reasons, it is reasonable to consider splitting failure as cracks for which $\theta \geq 30^o$. Otherwise, the theory will be limited to the analysis of the breakage of an insignificant chunk of the ice floe. Using this assumption (i.e., splitting occurs at $\theta \geq 30^o$) for the circular ice floe, we arrive at the similar conclusion that the crack tends to propagate directly forward with $\theta = 90^o$.

The crack path of a rectangular ice floe is further studied in terms of the width-to-length ratio, which is defined as $\beta = w / L$. Based on the derived Eq.(45), the ice splitting load versus the crack angle is illustrated by Fig. 23. The calculation results based on both the high-strain-rate loading failure envelope (left) and low-strain-rate loading failure envelope (right) illustrate that the direct crack (i.e., $\theta = 90^o$) is preferred for most β values. The red curves delineate the boundary between the two zones, i.e., zone 1 with two slanted cracks (i.e., $\theta < 90^o$) and zone 2

with one direct crack (i.e., $\theta = 90^{o}$). The derivations lead to the following quantitative observations.

Within the considered width-to-length ratio range (i.e., $0.2 \le \beta \le 5$, beyond which bending failure theory can dominate the current theory), the rectangular ice floe tends to fail by a direct crack. More specifically, assuming that β is uniformly distributed over the range given above, nearly $(5-0.5)/(5-0.2) = 93.75\%$ of the rectangular ice floe tends to fail with a crack angle $\theta = 90^{o}$ for fast loading. When the ice floe is loaded more slowly, a relatively smaller but still significant portion of the ice floes, $(5-0.9)/(5-0.2) = 85.42\%$, is dominated by the direct crack.

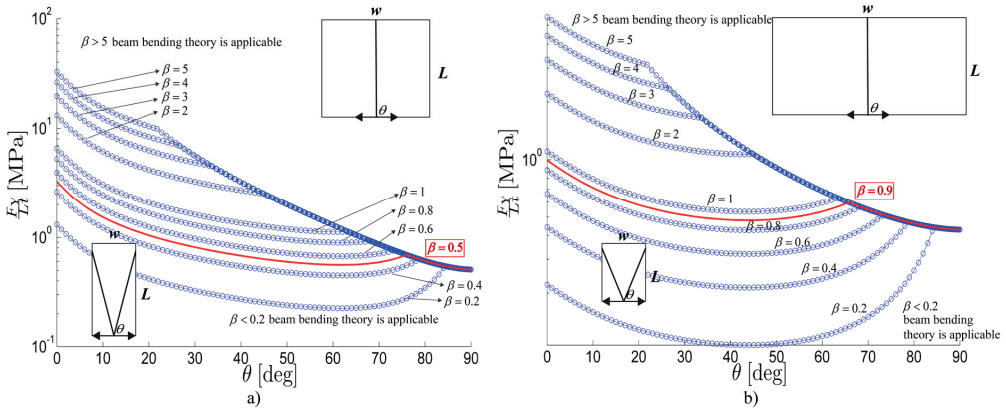

Fig. 23 Ice splitting load versus crack paths for different width-to-length ratios for a rectangular ice floe based on a) a high-strain-rate loading failure envelope and b) a low-strain-rate loading failure envelope; the Y axis is plotted on a log scale.

Step 3: Calculation and further simplification of the ice splitting load

The known energy dissipation rate and preferred crack path can be used to calculate the ice splitting load for the rectangular and circular ice floes by setting $\theta = 90^{o}$ in Eqs. (44) and (45). Thus, Eq. (15) is obtained as follows:

$$\frac{F_{Y\_plastic\_upper\_limit}}{Lt} = \frac{\int_a^1 [(1-\alpha)]d\alpha}{2a_1}\left[\sqrt{\frac{(a_7^2+2a_1)}{a_6}}\sqrt{4(a_1+a_3)}-a_7\right] \qquad \text{A repetition of Eq. (15).}$$

References

Anderson, T.L., 2005. Fracture mechanics: fundamentals and applications. CRC press.

API_RP2, 1995. Recommended Practice for Planning, Designing, and Constructing Structures and Pipelines for Arctic Conditions. American Petroleum Institute.

Bažant, Z.P., 2005. Scaling of structural strength. Butterworth-Heinemann.

Bažant, Z.P. and Planas, J., 1998. Fracture and size effect in concrete and other quasibrittle materials. CRC.

Bhat, S.U., 1988. Analysis for splitting of ice floes during summer impact. Cold Regions Science and Technology, 15(1): 53-63.

Bhat, S.U., Choi, S.K., Wierzbicki, T. and Karr, D.G., 1991. Failure analysis of impacting ice floes. Journal of Offshore Mechanics and Arctic Engineering, 113: 171.

Bueckner, H.F., 1970. Novel principle for the computation of stress intensity factors. Zeitschrift fuer Angewandte Mathematik & Mechanik, 50(9).

Chen, W.F. and Han, D.J., 1988. Plasticity for structural engineers. Springer-Verlag (New York).

Danielewicz, B.W., Metge, M. and Dunwoody, A.B., 1983. On estimating large scale ice forces from deceleration of ice floes, The seventh international conference on port and ocean engineering under arctic conditions, Espoo, pp. 537-546.

Dempsey, J.P., Adamson, R.M. and DeFranco, S.J., 1995. Fracture analysis of base-edge-cracked reverse-tapered plates. International journal of fracture, 69(4): 281-294.

Dempsey, J.P., Adamson, R.M. and Mulmule, S.V., 1999a. Scale effects on the in-situ tensile strength and fracture of ice. Part II: First-year sea ice at Resolute, NWT. International journal of fracture, 95(1): 347-366.

Dempsey, J.P., DeFranco, S.J., Adamson, R.M. and Mulmule, S.V., 1999b. Scale effects on the in-situ tensile strength and fracture of ice Part I: Large grained freshwater ice at Spray Lakes Reservoir, Alberta. International journal of fracture, 95(1): 325-345.

Dempsey, J.P., DeFranco, S.J., Blanchet, D. and Prodanovic, A., 1994. Mechanisms of fracture of sea ice. Hydrotechnical Construction, 28(3): 164-168.

Derradji-Aouat, A., 2003. Multi-surface failure criterion for saline ice in the brittle regime. Cold Regions Science and Technology, 36(1-3): 47-70.

Eshelby, J.D., 1975. The calculation of energy release rates. Prospects of fracture mechanics, 69-84.

Fett, T. and Munz, D., 1997. Stress intensity factors and weight functions. Computational Mechanics Publications Southampton.

Grape, J.A. and Schulson, E.M., 1992. Effect of confining stress on brittle indentation failure of columnar ice, The Second International Offshore and Polar Engineering Conference. International Society of Offshore and Polar Engineers.

Hallam, S., 1986. The role of fracture in limiting ice forces, Proc. of the IAHR symposium on ice, Iowa City, Iowa, pp. 287-319.

Hillerborg, A., Modeer, M. and Petersson, P.E., 1976. Analysis of crack formation and crack growth in concrete by means of fracture mechanics and finite elements. Cement and concrete research, 6(6): 773-781.

Iliescu, D. and Schulson, E.M., 2004. The brittle compressive failure of fresh-water columnar ice loaded biaxially. Acta Materialia, 52(20): 5723-5735.

Irgens, F., 2008. Continuum mechanics. Springer Verlag, Berlin Heidelberg.

ISO/FDIS/19906, 2010. Petroleum and natural gas industries - Arctic offshore structures,International Standard, International Standardization organization, Geneva, Switzerland,.

Karr, D.G., 1988. Three-Dimensional Analysis of Ice Sheet Indentation: Lower-Bound Solutions. Journal of Offshore Mechanics and Arctic Engineering, 110(1): 81-86.

Karr, D.G. and Das, S.C., 1983. Limit Analysis of Ice Sheet Indentation. Journal of Energy Resources Technology, 105(3): 352-355.

Karr, D.G., Watson, J.C. and HooFatt, M., 1989. Three-Dimensional Analysis of Ice Sheet Indentation: Limit Analysis Solutions. Journal of Offshore Mechanics and Arctic Engineering, 111(1): 63-69.

Li, Y.N. and Bažant, Z.P., 1994. Eigenvalue analysis of size effect for cohesive crack model. International journal of fracture, 66(3): 213-226.

Li, Y.N. and Liang, R.Y., 1993. The theory of the boundary eigenvalue problem in the cohesive crack model and its application. Journal of the Mechanics and Physics of Solids, 41(2): 331-350.

Little, R.W., 1973. Elasticity. Prentice-Hall Englewood Cliffs, New Jersey.

Lu, W., Lubbad, R. and Løset, S., 2014. Simulating ice-sloping structure interactions with the cohesive element method. Journal of Ocean, Offshore and Arctic Engineering.

Lu, W., Lubbad, R., Løset, S. and Høyland, K.V., 2012. Cohesive zone method based simulations of ice wedge bending: a comparative study of element erosion, CEM, DEM and XFEM. In: Li and Lu (Editors), The 21st IAHR International Symposium on Ice, Dalian, China, pp. 920-938.
Lubbad, R., 2012. Data report: KV-Svalbard Survey 2012, Faculty of Engineering Science and Technology (IVT), NTNU, Trondheim.
Lubbad, R., Loset, S. and Lu, W., 2012. Oden Arctic Technology Research Cruise 2012: Data report Part I, SAMCoT report, Norwegian University of Science and Technology, Trondheim.
Lubbad, R. and Løset, S., 2011. A numerical model for real-time simulation of ship-ice interaction. Cold Regions Science and Technology: 1-17.
Lubbad, R., Raaij, E.V., Løset, S. and Eik, K.J., 2013. Oden Arctic Technology Rsearch Cruise 2012, Proceedings of the 22nd International Conference on Port and Ocean Engineering under Arctic Conditions, Espoo, Finland.
Løset, S., Shkhinek, K., Gudmestad, O. and Høyland, K., 2006. Actions from Ice on Arctic Offshore and Coastal Structures, Krasnodar, St Petersburg, Russia, 137-148 pp.
Matskevitch, D.G., 1994. The Ice Strength Criteria and Their Role in Ice Load Determination, IAHR Ice Symposium pp. 784-796.
Metrikin, I., Lu, W., R., L., Løset, S. and Kashafutdinov, M., 2012. Numerical simulation of a floater in a broken-ice field: Part 1: Model description, Proceedings of the ASME 2012 31th International Conference on Ocean, Offshore and Arctic Engineering, Rio de Janeiro, Brazil.
Michel, B., 1978. Ice mechanics. LES PRESSES DE L'UNIVERSITE LAVAL, Quebec, 499 pp.
Mulmule, S.V. and Dempsey, J.P., 1997. Stress-separation curves for saline ice using fictitious crack model. Journal of engineering mechanics, 123: 870.
Mulmule, S.V. and Dempsey, J.P., 1998. A viscoelastic fictitious crack model for the fracture of sea ice. Mechanics of Time-dependent Materials, 1(4): 331-356.
Mulmule, S.V. and Dempsey, J.P., 1999. Scale effects on sea ice fracture. Mechanics of Cohesive frictional Materials, 4(6): 505-524.
Mulmule, S.V. and Dempsey, J.P., 2000. LEFM size requirements for the fracture testing of sea ice. International journal of fracture, 102(1): 85-98.
Nevel, D.E., 1965. A semi-infinite plate on an elastic foundation, U. S. Army Snow Ice and Permafrost Research Establishment, Corps of Engineering.
Paavilainen, J., Tuhkuri, J. and Polojärvi, A., 2009. 2D combined finite-discrete element method to model multi-fracture of beam structures. Engineering Computations, 26(6): 578-598.
Palmer, A.C., Goodman, D.J., Ashby, M.F., Evans, A.G., Hutchinson, J.W. and Ponter, A.R.S., 1983. Fracture and its role in determining ice forces on offshore structures. Annals of glaciology, 4: 216-221.
Petroski, H.J. and Achenbach, J.D., 1978. Computation of the weight function from a stress intensity factor. Engineering Fracture Mechanics, 10(2): 257-266.
Prodanovic, A., 1978. Two-Dimensional Limit Analysis of Ice Failure Described by a Quadratic Yield Function, 15th SES Meeting, University of Floarida, Gainesville, Florida, USA.
Ralston, T.D., 1977a. Ice force design considerations for conical offshore structures, Proceedings of the 4th International Conference on Port and Ocean Engineering under Arctic Conditions, Newfoundland Memorial University, Canada, pp. 12.
Ralston, T.D., 1977b. Yield and plastic deformation in ice crushing failure, ICSI/AIDJEX Symposium on Sea Ice--Processes and Models, Seattle, Washington.
Ralston, T.D., 1978. An analysis of ice sheet indentation, Fourth International Symposium on Ice Problems, pp. 13-31.
Ralston, T.D., 1980. Plastic limit analysis of sheet ice loads on conical structures. Physics and Mechanics of Ice, Springer-Verlag, New York, USA: 289-308.
Ralston, T.D., 1981. Plastic limit analysis of ice splitting failure. Proc. 6th POAC, Quebec, 1: 205-215.
Reinicke, K.M., 1980. Analytical approach for the determination of ice forces using plasticity theory, Physics and Mechanics of Ice. Springer, pp. 325-341.
Reinicke, K.M. and Ralston, T.D., 1977. Plastic limit analysis with an anisotropic, parabolic yield function, International Journal of Rock Mechanics and Mining Sciences & Geomechanics Abstracts. Elsevier, pp. 147-162.
Reinicke, K.M. and Remer, R., 1978. A procedure for the determination of ice forces-illustrated for polycrystalline ice, Proceedings of IAHR Symposium on Ice, pp. 217-238.
Rice, J.R., 1972. Some remarks on elastic crack-tip stress fields. International Journal of Solids and Structures, 8(6): 751-758.
Richter-Menge, J.A. and Jones, K.F., 1993. The tensile strength of first-year sea ice. Journal of Glaciology, 39: 609-618.

Rothrock, D.A. and Thorndike, A.S., 1984. Measuring the sea ice floe size distribution. Journal of Geophysical Research: Oceans (1978–2012), 89(C4): 6477-6486.
Sand, B., 2008. Nonlinear finite element simulations of ice forces on offshore structures. Doctoral thesis Thesis, Luleå University of Technology, Luleå.
Sand, B. and Fransson, L., 2006. Nonlinear finite element simulations of ice sheet forces on conical structures, 25th International Conference on Offshore Mechanics and Arctic Engineering. ASME Press, Hamburg, Germany.
Sanderson, T.J.O., 1988. Ice mechanics and risks to offshore structures.
Schulson, E.M. and Duval, P., 2009. Creep and fracture of ice, 1. Cambridge University Press, Cambridge, 190-211 pp.
Schulson, E.M., Fortt, A.L., Iliescu, D. and Renshaw, C.E., 2006. Failure envelope of first-year Arctic sea ice: The role of friction in compressive fracture. Journal of Geophysical Research: Oceans, 111(C11): C11S25.
Sodhi, D.S., 1995. Breakthrough loads of floating ice sheets. Journal of cold regions engineering, 9: 4.
Sodhi, D.S., Chin, S.N. and Stanley, J.M., 1993. Indentation and splitting of freshwater ice floes. AMD, 163: 165-175.
Tada, H., Paris, P.C. and Irwin, G.R., 2000. The stress analysis of cracks handbook, 130. ASME press New York.
Timco, G.W., 1987. Indentation and penetration of edge-loaded freshwater ice sheets in the brittle range. Journal of Offshore Mechanics and Arctic Engineering, 109(3): 287-294.
Timco, G.W. and Frederking, R.M.W., 1984. An investigation of the failure envelope of granular/discontinuous-columnar sea ice. Cold Regions Science and Technology, 9(1): 17-27.
Timco, G.W. and Frederking, R.M.W., 1986. Confined compression tests: Outlining the failure envelope of columnar sea ice. Cold Regions Science and Technology, 12(1): 13-28.
Timco, G.W. and Weeks, W.F., 2010. A review of the engineering properties of sea ice. Cold Regions Science and Technology, 60(2): 107-129.
Timoshenko, S.P. and Goodier, J.N., 1951. Theory of elasticity. New York, McGraw-Hill, 5: 500.
Tsai, C.H. and Ma, C.C., 1989. Weight functions for cracks in finite rectangular plates. International journal of fracture, 40(1): 43-63.
Vinogradov, A., 1987. Constitutive Modeling of Ice, Proceedings of the 6th International Offshore Mechanics and Arctic Engineering Symposium, pp. 181-188.
Wang, S. and Dempsey, J.P., 2011. A cohesive edge crack. Engineering Fracture Mechanics, 78(7): 1353-1373.
Weeks, W.F., 2010. On sea ice. University of Alaska Press.
Weeks, W.F. and Ackley, S.F., 1982. The growth, structure, and properties of sea ice, DTIC Document.
Wu, X.R., 1984. Approximate weight functions for center and edge cracks in finite bodies. Engineering Fracture Mechanics, 20(1): 35-49.
Wu, X.R., 1991. The arbitrarily loaded single-edge cracked circular disc; accurate weight function solutions. International journal of fracture, 49(4): 239-256.
Wu, X.R. and Carlsson, J., 1983. The generalised weight function method for crack problems with mixed boundary conditions. Journal of the Mechanics and Physics of Solids, 31(6): 485-497.
Wu, X.R. and Carlsson, J., 1991. Weight functions and stress intensity factor solutions. Pergamon.

Appendix 2 Out-of-plane flexural failure of an ice floe

This appendix includes the paper submitted to Journal of Cold Regions Science and Technology (see below). By the time the thesis is submitted, the paper is under review.

- Lu, W., Lubbad, R. and Løset, S., (submitted in July, 2014). Out-of-plane failure of an ice floe: radial-crack-initiation-controlled fracture. Cold Regions Science and Technology.

Appendix II

Out-of-plane failure of an ice floe: radial-crack-initiation-controlled fracture

Wenjun Lu[1] **Raed Lubbad** **Sveinung Løset**

Sustainable Arctic Marine and Coastal Technology (SAMCoT), Centre for Research-based Innovation (CRI)

Norwegian University of Science and Technology (NTNU), Trondheim, Norway

[1] Corresponding author: wenjun.lu@ntnu.no

Abstract

Out-of-plane failure of an ice floe has been studied extensively over the past several decades for different application purposes (e.g., an ice cover's bearing capacity for transportation; bending failure of level ice interacting with a sloping structure). Notably, most of the previous studies have idealised the considered ice floe as an infinite or semi-infinite thin plate resting on a Winkler-type elastic foundation. However, a typical ice field in the Arctic is far from continuous. Furthermore, recent Arctic offshore structures have usually been designed with support from ice management; i.e., these sloping structures are most often operating in a broken ice field and are interacting with ice floes of finite sizes. Bearing this loading environment in mind, this paper starts with the question 'What are the physical processes behind the failure of a finite size ice floe interacting with a sloping structure, and what will the failure pattern look like?' Based on an in-depth literature review in relation to out-of-plane failures of infinite and semi-infinite ice floes, depending on the floe sizes, we propose a conservative classification of an ice floe's out-of-plane failures under an edge load, i.e., 1) finite size ice floes that are broken at radial crack initiation and 2) a semi-infinite ice floe that is broken by sequentially forming radial and circumferential cracks. Between these two scenarios, we focused our study on 'radial-crack-initiation-controlled fracture' of a finite size ice floe. Specifically, we are trying to answer the following question: 'how small/large should an ice floe be to be treated as a finite size/semi-infinite ice floe?' Based on a series of assumptions, radial crack initiation and propagation within a square ice floe were theoretically formulated and numerically studied. The respective loads to initiate and propagate a radial crack have been extracted and compared to quantify the required size smaller than which an ice floe would fail at radial crack initiation. For typical ice material properties, it is found that a nearly square shaped ice floe can fail at crack initiation if its physical size is smaller than approximately $27\times(\text{ice thickness})^{3/4}$. On the theoretical side, this paper contributes to the derivation of non-dimensional formulae to study radial crack initiation and propagation. Additionally, simplified yet effective numerical models to study radial crack initiation and propagation within an ice floe were proposed and validated. On the practical side, the research methodologies and conclusions presented herein shed light on the possibility of a more economic design for an Arctic offshore structure whose major operating environment is filled with finite size ice floes. In addition, because the 'radial-crack-initiation-controlled fracture' of an ice floe means a much smaller ice load (i.e., compared with continuous circumferential type bending failure within a level ice environment) on a sloping structure, it is recommended, from a mechanically preferred point of view, that floes with sizes smaller than $27\times(\text{ice thickness})^{3/4}$ should be produced in the downstream of an ice management operation.

Keywords:

Sloping structure

Broken ice

Ice management

Radial crack

Fracture

1 Introduction

Out-of-plane failure of an ice floe has been an important research topic for decades. There are two main driving forces/applications behind this research. The first research application focuses on estimating the bearing capacity of ice covers for engineering applications such as transportation on ice roads, landing of air craft on a floating ice cover, and an ice cover serving as a construction platform. (Masterson, 2009). Numerous excellent studies have been conducted within this field. In this research context, the purpose is to use the ice cover and ensure its integrity. An ice cover is usually assumed to be an 'infinite' thin plate on a Winkler-type elastic foundation. Relevant experimental and theoretical studies can be found in early literature reviews (e.g., (Ashton, 1986; Kerr, 1976; Langhorne et al., 1999; Michel, 1978; Sodhi, 1995; Squire et al., 1996)).

The second research applications are related to the design and operation of sloping structures (e.g., icebreakers, fixed and floating offshore structures) in ice infested waters. This is the main focus of this paper. Sloping Arctic offshore structures and the bow of ice breakers are preferred geometric forms in ice-infested waters because such sloping geometries introduce a vertical load component that is exerted on the edge of an ice floe at contact. This vertical load component enables the incoming ice floe to fail in a predominant bending failure mode. Such bending failure mode can be considered a type of out-of-plane failure. Converse to the ice cover's bearing capacity problem, the purpose of the second research application is to understand how much ice load is exerted on the concerned sloping structure, and the purpose is to enable the designed structure to effectively break ice floes.

Comparing the 'ice-sloping structure interaction problem' with the 'ice cover's bearing capacity problem', many similarities regarding the ice floe's failure processes and failure pattern can be observed (Kerr, 1976). In both cases, a two stage fracture of an ice floe was observed and theoretically analysed. The first stage is the so-called radial cracking of the ice floe (i.e., radial cracks emanating from the vertically loaded area); the second stage is the formation of circumferential cracks some distance away from the vertically loaded area. It is generally accepted that the closest circumferential crack's formation corresponds to the maximum ice load on a sloping structure (or to the breakthrough/loss of the bearing capacity of an ice cover). Therefore, it is the circumferential crack's formation that is most studied during ice and sloping structure interactions. As an example, this is also one of the reasons that theories such as a two-dimensional beam on an elastic foundation are widely applied to analyse the failure of an ice sheet interacting with a sloping structure (e.g., (Croasdale and Cammaert, 1994; Lu, 2010; Lu et al., 2014; Mayne, 2007; Shkhinek and Uvarova, 2001)). Furthermore, for a more advanced three-dimensional theory, in view of the eventual breakthrough of an ice cover involving the formation of circumferential cracks, Nevel (1958; 1961) obtained analytical solutions for the failure of an infinite ice wedge beam on an elastic foundation. The solution then finds application in the calculations of ice breaking loads for various types of sloping structures (Kotras et al., 1983; Lubbad and Løset, 2011; Milano, 1972; Nevel, 1992).

It should be noted that all of the above-mentioned studies assumed that the considered ice floe is either infinite or semi-infinite or in the so-called 'level ice' condition. However, 'level ice' is rather a theoretical simplification. A typical ice field in the Arctic is far from continuous. Furthermore, recent Arctic offshore structures have usually been designed with support from ice management; i.e., these sloping structures are often operating in a broken ice field. Therefore, they are interacting with ice floes with finite size instead of those with infinite boundaries.

What would the failure pattern be like for a finite size ice floe interacting with a sloping structure? Based on previous theoretical studies and experimental observations, this paper attempted to propose a conservative classification of an ice floe's out-of-plane failure pattern depending on its geometric size: 1) finite size ice floes that fail at radial crack initiation and 2) semi-infinite ice floes that fail by sequentially forming radial and circumferential cracks. Focus has been directed towards the theoretical analysis of radial-crack-initiation-controlled fracture of an ice floe with finite size. Although radial-crack-initiation-controlled fracture of an ice floe does not necessarily lead to the critical design load in comparison to continuous failures within a level ice condition, an understanding of such a physical process is of practical importance. For example, 1) pertinent theoretical analysis can help capture a finite size ice floe's correct failure patterns, failure process and failure loads, which is beneficial to achieving a more economic structural design in its dominant operating ice conditions (e.g., if a broken ice field is its most frequently encountered loading environment); and 2) because radial-crack-initiation-controlled failure of an ice floe leads to a largely reduced[2] ice load compared with continuous circumferential cracking, an intuitive suggestion for ice management operation would be to manage the initially large ice floes into smaller sizes such that their prevailing failure patterns (if they fail) are controlled by radial crack initiation.

Driven by the above mentioned potential applications, we idealised the original problem as a finite size ice floe under an edge load[3]. Based on this idealised model, we separately studied radial crack initiation and propagation within an ice floe of varying size. During theoretical studies, the focus has been on deriving non-dimensional formulae such that generalised results can be obtained. Based on the derived formulae, simple but effective numerical models have been established to calculate the corresponding non-dimensional load to initiate and propagate a radial crack. Using the known radial crack initiation and propagation load, we are thus able to set a quantified floe size boundary between those that can be conservatively treated as semi-infinite ice floes and those whose fracture is controlled by radial crack initiation.

By implementing and validating the above briefly described approach, the main objectives of this paper include the following: 1) establishment of a verified methodology to study radial crack initiation and propagation within a finite size ice floe; 2) for typical ice material properties, recommendation of a physical size smaller than which an ice floe would fail at radial crack initiation. In the long term, the developed theories and formulations are to be implemented in a numerical simulator (Lubbad and Løset, 2011) to effectively calculate the global ice load and to test different ice management strategies in an ice field composed of ice floes of varying sizes.

2 Problem description and assumptions

In this paper, we focus on the out-of-plane failure of an ice floe under an edge load. In the context of a sloping structure interacting with an ice floe, the complete problem description is shown in Fig. 1. We consider the initial contact between a sloping structure and an ice floe (Fig. 1(1) and (2)). After isolating the loading area (Fig. 1(3)) where a complicated stress state exists, four load components can be expected in three different directions. These are a pair of splitting load components in the Y direction causing the in-plane failure of an ice floe; a load component in the vertical Z direction leading to the out-of-plane failure of an ice floe; and a load component in the X direction increasing the in-plane compressive stress within the ice floe. An

[2] For example, for a semi-infinite ice floe, only approximately 60% of the eventual breakthrough load is needed to initiate the first radial crack. Detailed information will be presented in Section 2.1.1 in relation to Eq. (3).
[3] More details of this model will be presented in Sections 2.2 and 3.1.

ice floe's eventual failure patterns and failure process are jointly affected by all of these load components. However, we neglect the interactions among these load components and study them separately; in other words, we decouple the in-plane and out-of-plane problems. The ice splitting load F_Y (i.e., the in-plane load pair required to propagate a global splitting crack through an ice floe) has been studied in a separate paper (Lu et al., (Accepted on November 12th 2014)). In this paper, we focus on the study of F_Z, under which the out-of-plane bending failure of an ice floe is induced. To be more representative of the actual contact between a sloping structure and an ice floe, we assume that this vertical load component is evenly distributed within a half circle, as shown in Fig. 1(4).

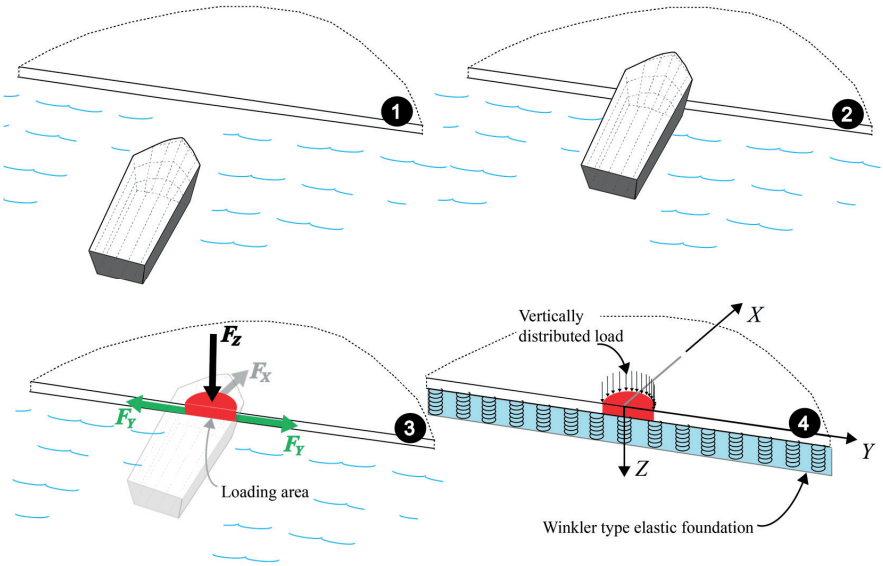

Fig. 1 Overall problem description.

In this study, the ice floe is considered to be a thin plate resting on a Winkler-type elastic foundation (Fig. 1(4)). As mentioned, out-of-plane bending failure of ice involves two different types of cracks: 1) radial cracks emanating from the loading area and 2) circumferential cracks, which usually correspond to the eventual breakthrough of the ice cover. It is convenient for us to define different load symbols as follows for later use.

$F_{Z,\text{radial},0}$: Maximum load required to initiate the radial crack in an ice floe.

$F_{Z,\text{radial},l}$: Load required to propagate a radial crack, which is a variable of the radial crack length.

$F_{Z,\text{circum},0}$: Maximum load required to initiate the circumferential crack in an ice floe.

$F_{Z,\text{break\_through}}$: Breakthrough load corresponding to the eventual out-of-plane bending failure of an ice floe.

$F^{\text{test}}_{Z,\text{break\_through}}$: Measured breakthrough load corresponding to the eventual out-of-plane bending failure of an ice floe.

2.1 Failure pattern of ice floes with varying sizes

To theoretically identify the failure patterns and failure process of a finite size ice floe with the simplified interaction scenario shown in Fig. 1(4), we first present a literature review on relevant studies for infinite and semi-infinite ice floes.

2.1.1 Radial crack initiation, propagation and eventual failure of semi-infinite/infinite ice floes

From a fracture mechanics point of view, the failure process of an ice floe includes radial crack initiation, propagation and the corresponding eventual failure with circumferential cracks. The characteristics of these cracks are described in the following for infinite and semi-infinite ice floes separately.

1. An infinite ice floe

For an infinite ice floe, extensive analytical, numerical and experimental work has been conducted to determine its bearing capacity. Ashton (1986) summarised a detailed description of the failure process of an infinite ice cover. Two types of cracks are of interest here, i.e., the initially formed radial cracks and the final formation of circumferential cracks.

- Radial crack initiation load $F_{Z,\text{radial},0,\text{inf}}$ within an infinite ice floe

Radial crack initiation corresponds to the 'first crack condition' in determining the bearing capacity of an ice cover in relevant codes (API_RP2, 1995; ISO/FDIS/19906, 2010). Solutions to the radial crack initiation load $F_{Z,\text{radial},0,\text{inf}}$ in an infinite ice floe have been achieved for a concentrated load (Hertz, 1884) and a distributed load over a circular area (Wyman, 1950). Based on Panfilov's (1960) experiment, Kerr (1976) showed an important relationship, given in Eq. (1) (note that originally from Eq. (73) of Kerr (1976)).

$$F_{Z,\text{break\_through,inf}}^{\text{test}} \approx 2F_{Z,\text{radial},0,\text{inf}} \tag{1}$$

Eq. (1) signifies that the load required to initiate radial cracks in an infinite ice floe is much less than the final breakthrough load $F_{Z,\text{break\_through,inf}}^{\text{test}}$.

- Radial crack propagation and eventual out-of-plane failure of an infinite ice floe

Regarding the study of radial crack propagation, two different assumptions have previously been made. The first attempt ignored the possible crack closure effect within radial cracks (Bažant and Li, 1993; Bažant and Li, 1994; Li and Bažant, 1994). A later improvement was made to include the crack closure effect within the radial cracks (Bažant, 2002; Bažant, 2005; Bažant and Kim, 1998a; Bažant and Kim, 1998b; Dempsey et al., 1995; Sodhi, 1996). Irrespective of the presence of crack closure within radial cracks, all of the above-mentioned research agreed that the breakthrough of an ice cover corresponds to the formation of a circumferential crack, $F_{Z,\text{circum},0}$. This means that the following relationship holds.

$$F_{Z,\text{break\_through,inf}}^{\text{test}} = F_{Z,\text{circum},0,\text{inf}} \tag{2}$$

2. A semi-infinite ice floe

For a semi-infinite ice floe, based on field observations, Kerr (1976) described the failure mechanism as follows: "*first a radial crack forms, which starts under the load and propagates normal to the free boundary. This is followed by the formation of a circumferential crack that causes final failure*" (p. 242). In the same paper, a further elaboration of Panfilov's (1960) experiment on a semi-infinite ice floe was added by Kerr (1976) as follows: "*first, the formation of a crack, which emanates under the load and is normal to the free boundary; then the formation of a circumferential crack at which the two wedges break off"* (p. 258). This is a similar observation as for the breakthrough of an infinite ice floe, but there are fewer radial cracks present (e.g., Sodhi (1997) observed approximately 20~30 radial cracks for 'infinite[4]' ice floes in basin tests). Fewer radial cracks were also noted by Nevel (1992) for the scenario in which a sloping conical structure interacts with level ice (i.e., 2~3 radial cracks).

- Radial crack initiation load $F_{Z,\text{radial},0,\text{semi}}$ within a semi-infinite ice floe

Analytical solutions regarding the radial crack initiation load $F_{Z,\text{radial},0,\text{semi}}$ for a semi-infinite ice floe can be found in Westergaard (1926) and Kerr and Kwak (1993) for a concentrated load; in Nevel (1965) for a distributed load over a rectangular area; and in Lubbad and Løset (2011) for a distributed load over a half circular area. Similarly, the radial crack initiation load $F_{Z,\text{radial},0,\text{semi}}$ for a semi-infinite ice floe does not correspond to the final breakthrough load. This is also verified by Panfilov's (1960) experiment, and Kerr (1976) quantified such a difference in Eq. (3) (note that originally from Eq. (77) of Kerr (1976)).

$$F^{\text{test}}_{Z,\text{break\_through},\text{semi}} \approx 1.6 F_{Z,\text{radial},0,\text{semi}} \tag{3}$$

- Radial crack propagation and eventual out-of-plane failure of a semi-infinite ice floe

To the authors' knowledge, radial crack propagation within a semi-infinite ice floe is not well studied in the available literature. Following similar observations and the same methodologies for the bearing capacity of an infinite ice floe, it is usually assumed that the eventual out-of-plane failure of a semi-infinite ice floe corresponds to the simultaneous failure of several independent infinite wedge beams (Kotras et al., 1983; Lubbad and Løset, 2011; Milano, 1972; Nevel, 1992) in a half plane; i.e., circumferential crack initiation dominates the eventual failure.

2.1.2 Failure patterns and processes of a finite size ice floe

In Section 2.1.1, failure patterns and processes for an infinite and a semi-infinite ice floe have been presented together with relevant studies. However, the intuitive words 'infinite' and 'semi-infinite' are only theoretical simplifications. To apply the pertinent theories to a sloping structure interacting with an ice floe with a certain physical length L, two important questions should be addressed: first, under a vertical edge loading, how large does an ice floe need to be so that theoretical simplification to a semi-infinite ice floe becomes feasible; and second, if the boundaries of a finite size ice floe should otherwise be considered, what are the failure patterns and processes?

[4] In Sodhi's (1997) tests, fixed boundaries along the ice sheet were utilised to mimic an 'infinite' ice floe.

To the authors' knowledge, the only experiment regarding the bearing capacity of a finite size ice floe was conducted by Sodhi (1997). 'Finite size' ice floes can be understood as floes with free edges in Sodhi's test. The test results (e.g., cracking pattern) were largely influenced by these free boundaries. During Sodhi's (1997) test, it was observed that for an ice floe with free edges, several radial cracks (i.e., 5~7) were formed under the loading area and propagated directly through the whole ice floe, reaching its free boundaries. No circumferential cracks developed in those tests.

Based on the previous literature review, the following generalisations can be drawn:

- Out-of-plane failure of an ice floe, whether large or small, involves the initiation and propagation of radial cracks. However, fewer radial cracks are expected for a smaller size ice floe.
- According to Eqs. (1) and (3), the load required to initiate radial cracks is much less than the load required to initiate a circumferential crack.
- According to Sodhi's (1997) experiment, it is possible for a finite size ice floe to fail purely in radial cracking without a circumferential crack.

The above literature reviews imply that for an ice floe smaller than a certain size, while interacting with a sloping structure, its failure may only be controlled by radial crack initiation without forming circumferential cracks. The corresponding ice load can thereby be largely reduced. An important task of this paper is to quantify this size requirement and its corresponding failure load. According to the literature review in Section 2.1.1, out-of-plane failure of a finite size ice floe is not well studied. This is summarised in Table 1.

Table 1 The status of previous research in relation to the out-of-plane failure of an ice floe

Literature review	Radial crack initiation	Radial crack propagation	Circumferential crack initiation
Finite size ice floe	Not studied	Not studied	Not studied
Semi-infinite ice floe	Studied	Not studied	Studied

2.2 Problem definitions

Sodhi (1996) showed that for an infinite ice floe, there is a maximum distance (i.e., two times the characteristic length) beyond which radial cracks can no longer propagate, irrespective of the magnitude of the vertical load. Instead, further increasing the vertical load leads to the initiation of a circumferential crack and, thus, the breakthrough of an ice floe. Under this consideration, depending on the size of an ice floe, we conservatively define two different scenarios of the failure patterns of a finite size ice floe.

Scenario #1: Radial-crack-initiation-controlled fracture

For an ice floe of a certain finite size, the developed radial cracks can 'feel' its boundary and thereby propagate directly through the whole body of the floe without forming circumferential cracks. Under this scenario, the breakthrough load can either be radial-crack-initiation controlled or radial-crack-propagation controlled. However, to be conservative, in this paper, a 'finite size' ice floe is defined as an ice floe that fails at radial crack initiation (i.e., radial-crack-initiation-controlled fracture). Mathematically, this is reflected by Eq. (4). In this scenario, only radial cracking occurs, as in Fig. 2a.

$$F_{Z,\text{break\_through}} = F_{Z,\text{radial},0} \geq F_{Z,\text{radial},1} \tag{4}$$

As described in the following studies, for an edge loaded ice floe, the radial crack propagation load $F_{Z,\text{radial},1}$ increases exponentially with increasing radial crack length and soon give way to the formation of a circumferential crack. That is, it is reasonable and convenient to neglect the situation in which $F_{Z,\text{break\_through}} = F_{Z,\text{radial},1} \geq F_{Z,\text{radial},0}$ and to group this situation in Scenario #2.

Scenario #2: Out-of-plane failure of a semi-infinite ice floe

With increasing ice floe size, if the radial crack initiation load $F_{Z,\text{radial},0}$ is not large enough to propagate a radial crack to its free boundary (i.e., $F_{Z,\text{radial},0} < F_{Z,\text{radial},1}$), we assume that we are in a situation of a semi-infinite ice floe; i.e., out-of-plane failure is controlled by circumferential crack initiation in a semi-infinite ice floe, as in Fig. 2b. Mathematically, this is reflected by Eq. (5).

$$F_{Z,\text{break\_through}} = F_{Z,\text{circum},0,\text{semi}} \tag{5}$$

Eq. (5) is also a conservative classification. The possible scenario of circumferential crack initiation in a finite size ice floe is ignored; i.e., we do not calculate $F_{Z,\text{circum},0,\text{finite}}$, which is assumed be smaller than $F_{Z,\text{circum},0,\text{semi}}$ because of the alleviation of the crack closure effect (i.e., less confinement).

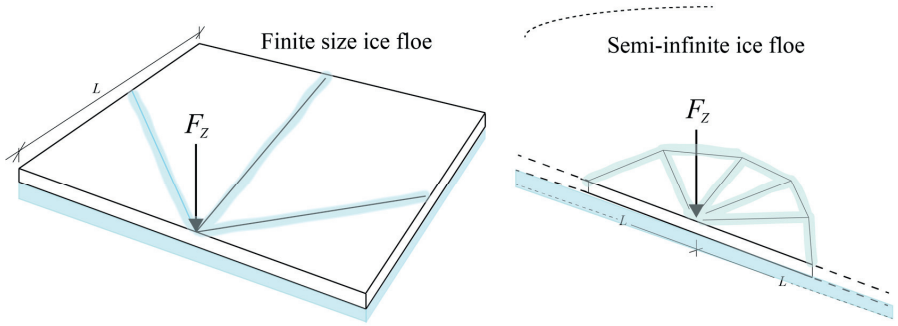

Fig. 2 Two defined scenarios: out-of-plane failure of a) a finite size ice floe; b) a semi-infinite ice floe.

Based on the problem definitions given in Fig. 2, the major focus of this paper in comparison with Table 1 are summarised in Table 2.

Table 2 Contributions made in this paper in relation to out-of-plane bending failures of an ice floe

Scenario #	Radial crack initiation	Radial crack propagation	Circumferential crack initiation
1. Finite size ice floe	Studied herein	Studied herein	Grouped into Scenario #2
2. Semi-infinite ice floe	No further contribution	No further contribution	No further contribution

2.3 General assumptions

For the problem of concern (i.e., Scenario #1), radial crack initiation and propagation are studied separately. Before embarking on the specific mathematical model of each scenario, several general assumptions are made here.

- The application context of the current theoretical development is a sloping structure interacting with a finite size ice floe. We assume that the interaction process can be idealised as in Fig. 1(4); i.e., other contact force components are neglected, and the boundaries of the ice floe are assumed to be free.
- During the interaction between a sloping structure and a finite size ice floe, it is possible that only the limit force or limit moment criteria is controlling the interaction scenario; i.e., the size of the ice floe or the driving force of the ice floe is so small that the floe can simply be pushed aside by the structure without any fracturing process (i.e., the limit stress criterion). For the current analysis, we assume that there is sufficient driving force or that the floe size is large enough that the contact force F_Z (as in Fig. 1(3)) can always initiate a fracturing process within the considered ice floe. The developed theory, together with other limiting mechanisms (i.e., the limit force and limit moment), will be treated in a separate paper using the multi-body dynamic simulator (Lubbad and Løset, 2011).
- We assume that the theory of a thin plate resting on a Winkler-type elastic foundation applies to the current problem, as in Fig. 1(4). For the thin plate theory to be valid, it is generally required that the ratio between the characteristic length (defined by Eq. (7) in a later section) and the thickness $\ell / t \geq 10$ (Ventsel and Krauthammer, 2001). Considering that the characteristic length of sea ice ℓ can be approximated as $\ell = 13.5t^{3/4}$ (Gold, 1971), we can obtain an approximate thickness range within which our developed theory applies, i.e., $t \leq 3.32$ m . As an example, in terms of the ice thickness in the Beaufort Sea, a bimodal distribution has been proposed by Wadhams and Horne (1980). The Probability Density Function (PDF) exhibits one frequency peak at approximately 1 m (most likely for first-year ice) and another frequency peak at approximately 3.1 m (most likely for multi-year ice) (Sanderson, 1988) . To a certain extent, this demonstrates that $t \leq 3.32$ m covers a large portion of the ice thickness range from an engineering application point of view.
- It is assumed that ice floes respond elastically without any creep effect. This means that the loading rate is sufficiently high that any non-elastic deformation does not have enough time to evolve. Because ice has a relatively large Young's modulus (Schulson and Duval, 2009), purely elastic behaviour also means that its deformation before crack initiation is so small that the principle of superposition applies to the current problem.
- We also assume that the considered ice floe is homogeneous. This is usually not true because a temperature profile exists along the thickness direction of an ice floe (Kerr, 1976; Kerr, 1996; Kerr and Palmer, 1972; Michel, 1978; Squire et al., 1996). This profile in turn influences the ice floe's mechanical behaviour through its thickness. Finely grained granular ice is expected on the upper surface of an ice floe where the circumferential crack initiates, whereas a rather porous and weak ice layer is expected at the bottom of an ice floe (i.e., the ice-water interface) where radial cracks are initiated. For simplicity and to be conservative, we do not further differentiate tensile strengths in the upper and lower layers of an ice floe. Assuming the ice floe to be a homogenous material, we treat the initiation of radial and circumferential cracks 'equally' using the same criteria.
- We also assume that the material behaviour within the considered ice floe is isotropic. For first-year sea ice, the major part is composed of columnar ice exhibiting certain anisotropy in its mechanical behaviours (Sanderson, 1988). The work by Carter and

Michel (1971) (as cited in Duval and Schulson, (2009), p. 222) showed that the tensile strength of columnar ice is 25% stronger along its column than perpendicular to it. However, considering that both the radial and circumferential cracks are initiated perpendicular to the column direction, it is reasonable to assume an isotropic material behaviour herein.

- Although a high loading rate is assumed, for simplicity, we do not consider any dynamic response from the ice cover; moreover, we also neglect any hydrodynamic effects from the fluid base. The fluid is simply treated as a Winkler-type elastic foundation. However, it should be noted that the hydrodynamic effect from the fluid base can be rather significant (Dempsey and Zhao, 1993; Lu et al., 2012; Lubbad et al., 2008).
- In this study, we focus on the flexural type out-of-plane failure of an ice floe. Other out-of-plane failure modes are not considered, such as 'shear plug' (ISO/FDIS/19906, 2010, p. 251), which Sodhi (1995) described as a failure close to the perimeter of the loading area by shearing or punching in an infinite ice floe. Such 'shear plug' failure is largely influenced by the size of the loading area. For example, for an infinite ice floe, shear plug occurs when the loading radius $R \le 1.14t$ (Sodhi, 1995). With regard to an ice floe under an edge load, we do not further investigate the possibility of such 'shear plug' failure. Instead, we assume that the considered ice floe fails in flexure, and we deterministically studied three different loading radiuses ($R = 0.05\ell,\ 0.1\ell,$ and 0.2ℓ) to show the general trend of the loading area's influences.
- In addition, for simplicity, we have also assumed the geometry of the ice floe to be a square shape. However, it should be noted that all of the following theoretical derivations (i.e., the non-dimensionalisation process) are also applicable to other geometries. Furthermore, Hamilton et al. (2011) noted that ice floes in the downstream of ice management are usually produced with an aspect ratio of 1:1. This implies that the assumption of an ice floe having a square shape is practically appropriate in the current considered applications.

3 Methodologies

Referring to Table 2, two different mathematical models are utilised to study radial crack initiation and radial crack propagation within a finite size ice floe.

3.1 Radial crack initiation within a finite size ice floe

Studying radial crack initiation within a semi-infinite ice floe is just a special case compared with that within a finite size ice floe. Based on assumptions made in Section 2.3, this problem is converted to a thin plate on an elastic foundation under an evenly distributed edge pressure within a half circular area, as illustrated in Fig. 3.

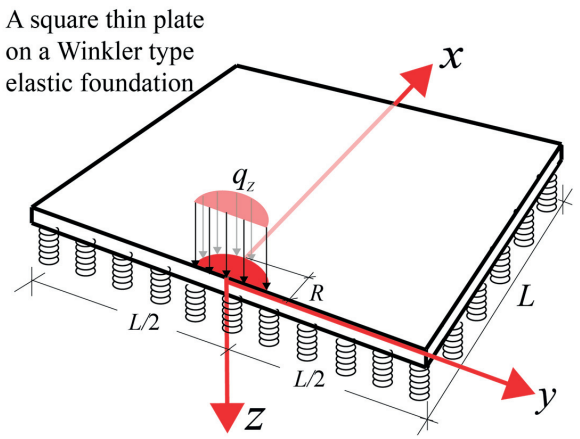

Fig. 3 Illustration of the model utilised to study radial crack initiation.

To the authors' knowledge, no analytical closed-form solutions exist to calculate the deflection and stress distribution of a finite plate with free edges under an evenly distributed edge pressure within a half circular area. Therefore, a numerical approach is adopted in this study. However, to obtain universal results, a non-dimensionalisation of the original problem is formulated before the numerical set-up is introduced.

3.1.1 Formulations of radial crack initiation

Following Kirchhoff's plate bending theory, the formulation of a thin plate under a concentrated load $q_Z dx_0 dy_0$ is expressed in Eq. (6) (Nevel, 1965; Timoshenko et al., 1959; Ventsel and Krauthammer, 2001).

$$D\nabla^4(w) + kw = q_Z dx_0 dy_0 \delta(x - x_0)\delta(y - y_0) \tag{6}$$

where

$q_Z = \frac{F_Z}{\pi R^2 / 2}$ and its magnitude is the pressure evenly distributed within a half circular area $S = \pi R^2 / 2$ with a radius of R, unit: [Pa];

$w(x, y, x_0, y_0)$ is the transverse deflection at point (x, y) of the plate in the $z-$direction under a lateral concentrated load $q_Z dx_0 dy_0$ acting at point (x_0, y_0), unit: [m];

$D = \frac{Et^3}{12(1-\nu^2)}$ is the flexural rigidity of the plate with symbols explained below, unit: [Nm];

E is Young's modulus of ice, unit: [Pa];

t is the thickness of the ice floe, unit: [m];

ν is the Poisson ratio, unit: [-];

$\nabla^4(\,) = \frac{\partial^4}{\partial x^4} + 2\frac{\partial^4}{\partial x^2 \partial y^2} + \frac{\partial^4}{\partial y^4}$ is the biharmonic operator;

k is the foundation modulus. For the fluid base, $k = \rho_w g$, with ρ_w and g being the fluid density and gravitational acceleration, respectively, unit: [Pa/m];

$\delta(x)$ is the Dirac delta function. Its unit is the inverse of its argument.

For a finite size ice floe, there are two length scales within Eq. (6). One is the characteristic length ℓ (defined in Eq. (7)), and the other one is its physical length L. To explicitly illustrate the influence of the physical length L on the calculated results, Eq. (6) is normalised by introducing $\xi = x/L$, $\xi_0 = x_0/L$, $\eta = y/L$, $\eta_0 = y_0/L$, and $S_0 = \pi(R/L)^2/2 = S/L^2$ and noting that $\delta((\xi - \xi_o)\cdot L) = \delta(\xi - \xi_o)/L$. After several manipulations, Eq. (6) is transformed into Eq. (8), with a length unit (e.g., [m]) on both sides.

$$\ell = \sqrt[4]{\frac{D}{k}} \tag{7}$$

$$\nabla^4 w(\xi,\eta,\xi_0,\eta_0) + \frac{kL^4}{D} w(\xi,\eta,\xi_0,\eta_0) = \frac{q_Z L^4}{D} d\xi_0 d\eta_0 \delta(\xi - \xi_0)\delta(\eta - \eta_0) \tag{8}$$

Note here that the new biharmonic operator reads $\nabla^4(\,) = \frac{\partial^4}{\partial\xi^4} + 2\frac{\partial^4}{\partial\xi^2\partial\eta^2} + \frac{\partial^4}{\partial\eta^4}$. Observing the linear PDE of Eq. (8), for a given boundary condition, the solution of $w(\xi,\eta,\xi_0,\eta_0)$ is functionally dependent, as given in Eq. (9).

$$w(\xi,\eta,\xi_0,\eta_0) = f_0(\frac{kL^4}{D}, \xi, \eta, \xi_0, \eta_0)\frac{q_Z L^4}{D} d\xi_0 d\eta_0 \tag{9}$$

in which the function $f_0(\frac{kL^4}{D}, \xi, \eta, \xi_0, \eta_0)$ is the influence surface that has the following physical meaning: it is the deflection at point (ξ, η) of the considered plate (i.e., with a normalised foundation modulus kL^4/D) under a unit concentrated load acting at point (ξ_0, η_0). To calculate the overall deflection $w_{total}(\xi,\eta)$ under an evenly distributed edge pressure q_Z over a normalised half circular area S_0, the principle of superposition can be utilised to sum up Eq. (9), as given in Eq. (10).

$$\begin{aligned} w_{total}(\xi,\eta) &= \sum_{(\xi_i,\eta_j)\in S_0} w(\xi,\eta,\xi_i,\eta_j) \\ &= \sum_{(\xi_i,\eta_j)\in S_0} f_0(\frac{kL^4}{D}, \xi, \eta, \xi_i, \eta_j)\frac{q_Z L^4}{D} d\xi_i d\eta_j \\ &= \iint_{S_0} f_0(\frac{kL^4}{D}, \xi, \eta, \xi_0, \eta_0)\frac{q_Z L^4}{D} d\xi_0 d\eta_0 \end{aligned} \tag{10}$$

By Maxwell's reciprocal law, we have $f_0(\frac{kL^4}{D}, \xi, \eta, \xi_0, \eta_0) = f_0(\frac{kL^4}{D}, \xi_0, \eta_0, \xi, \eta)$, which means the deflection at point (ξ_0, η_0) by a unit load acting at location (ξ, η) for the considered plate (i.e., influence surface=deflection surface). Accordingly, the integration in Eq. (10) can be simplified as Eq. (11).

$$
\begin{aligned}
w_{total}(\xi,\eta) &= \iint_{S_0} f_0(\frac{kL^4}{D}, \xi_0, \eta_0, \xi, \eta)\frac{q_Z L^4}{D} d\xi_0 d\eta_0 \\
&= \frac{q_Z L^4}{D} f_0(\frac{kL^4}{D}, \xi_*, \eta_*, \xi, \eta\ ) S_0 \\
&= \frac{F_Z(\xi_*, \eta_*)L^2}{D} f_0(\frac{kL^4}{D}, \xi, \eta, \xi_*, \eta_*)
\end{aligned}
\tag{11}
$$

in which (ξ_*, η_*) is located at the centroid of the deflection surface $f_0(\frac{kL^4}{D}, \xi_0, \eta_0, \xi, \eta)$ over an area S_0. Eq. (11) highlights the deflection equivalence at point (ξ, η) for a plate under an edge pressure q_Z over an area S and a concentrated force F_Z acting at the centroid (ξ_*, η_*) of its corresponding deflection surface. Based on the derivations in Eqs. (10) and (11), an equivalent PDE for the deflection of a plate under a distributed pressure q_Z over an area S can be written as Eq. (12).

$$
\nabla^4 w_{total}(\xi,\eta) + \frac{kL^4}{D} w_{total}(\xi,\eta) = \frac{F_Z L^2}{D}\delta(\xi-\xi_*)\delta(\eta-\eta_*) \tag{12}
$$

Further introducing the non-dimensional deflection $W(\xi,\eta)$ and normalised foundation modulus K, as in Eqs. (13) and (14), respectively, the above Eq. (12) can be further simplified as Eq. (15) (i.e., both sides have been non-dimensionalised).

$$
W(\xi,\eta) = \frac{w_{total}(\xi,\eta)D}{F_Z L^2} \tag{13}
$$

$$
K = \frac{kL^4}{D} \tag{14}
$$

$$
\nabla^4 W(\xi,\eta) + KW(\xi,\eta) = \delta(\xi-\xi_*)\delta(\eta-\eta_*) \tag{15}
$$

The values of (ξ_*, η_*) in Eq. (15) depend on $\iint_{S_0} f_0(K, \xi_0, \eta_0, \xi, \eta) d\xi_0 d\eta_0$; i.e., for a given boundary condition, the values of (ξ_*, η_*) depend on S_0, K and (ξ, η). For the current paper, we are not interested in the exact values of (ξ_*, η_*). Instead, we are most interested in the non-dimensional deflection in Eq. (13) and the PDE form of Eq. (15). The relationship between the overall defection $w_{total}(\xi,\eta)$ and the total vertical force F_Z is established via Eq. (13); the normalised foundation modulus K is an important parameter for Eq. (15). It represents the size of the considered ice floe. For example, if we define a parameter n denoting the ratio between the ice floe's physical length L and its characteristic length ℓ, the relationship given in Eq. (16) can be obtained.

$$
n = \frac{L}{\ell} = \sqrt[4]{K} \tag{16}
$$

Eq. (15) largely simplifies the original problem for a finite size ice floe under an evenly distributed edge pressure over a half circular area. For a given loading area S, we simply need to vary the value of n (or K); the corresponding calculated deflections are universal (i.e., in non-dimensional form) for various combinations of flexural rigidity D and actual loading F_Z. In other words, for two different ice floes with different flexural rigidity D under an edge pressure such as that shown in Fig. 3 (i.e., the same S but with different magnitudes of F_Z), as

long as the value n in these two cases is the same, the solutions of Eq. (15) are the same. Upon knowing their normalised deflection, their respective physical deflections can be easily back calculated from Eq. (13), depending on their respective flexural rigidity D, physical size L and overall load magnitude F_Z.

Among all of the results, the maximum stress is the most interesting because it denotes the inception of radial crack initiation. The moment in the x and y directions can be calculated as in Eq. (17).

$$\begin{aligned} M_{xx} &= -D[\frac{\partial^2}{\partial x^2} w_{total}(\xi,\eta) + v\frac{\partial^2}{\partial y^2} w_{total}(\xi,\eta)] \\ M_{yy} &= -D[\frac{\partial^2}{\partial y^2} w_{total}(\xi,\eta) + v\frac{\partial^2}{\partial x^2} w_{total}(\xi,\eta)] \\ M_{xy} &= -D(1-v)\frac{\partial^2}{\partial x \partial y} w_{total}(\xi,\eta) \end{aligned} \tag{17}$$

Introducing the same non-dimensionalisation over the physical length L and utilising the relationship in Eq. (13), Eq. (17) can be transformed into Eq. (18).

$$\begin{aligned} M_{\xi\xi} &= -F_Z[\frac{\partial^2}{\partial \xi^2} W(\xi,\eta) + v\frac{\partial^2}{\partial \eta^2} W(\xi,\eta)] \\ M_{\eta\eta} &= -F_Z[\frac{\partial^2}{\partial \eta^2} W(\xi,\eta) + v\frac{\partial^2}{\partial \xi^2} W(\xi,\eta)] \\ M_{\xi\eta} &= -F_Z(1-v)\frac{\partial^2}{\partial \xi \partial \eta} W(\xi,\eta) \end{aligned} \tag{18}$$

The corresponding maximum stress is assumed to be at the lower surface of the ice floe and can be written in the form of Eq. (19) (note that a positive value represents that the material particle is in tension).

$$\sigma_{\xi\xi} = \frac{6M_{\xi\xi}}{t^2}; \qquad \sigma_{\eta\eta} = \frac{6M_{\eta\eta}}{t^2}; \qquad \sigma_{\xi\eta} = \frac{6M_{\xi\eta}}{t^2} \tag{19}$$

The ice floe is thus in a multi-axial stress state. To determine the initiation of a radial crack, we assume here that the Mises yield criteria (Irgens, 2008) can be utilised to evaluate the ice material's tensile failure under a multi-axial stress state. However, no further plastic flow within the ice is allowed. Once the Mises stress reaches its yield criteria (i.e., flexural strength σ_f), radial crack initiation starts. Therefore, inserting Eqs. (18) and (19) into the definition of the Mises stress or equivalent stress σ_M, Eq. (20) can be derived with the function f, explicitly expressed in Eq. (21).

$$\begin{aligned} \sigma_M &= (\sigma_{\xi\xi}{}^2 + \sigma_{\eta\eta}{}^2 - \sigma_{\xi\xi}\sigma_{\eta\eta} + 3\sigma_{\xi\eta}{}^2)^{1/2} \\ &= \frac{6F_Z}{t^2} f(K, S_0) \end{aligned} \tag{20}$$

where

$$f^2 = [\frac{\partial^2}{\partial \xi^2} W(\xi,\eta) + v\frac{\partial^2}{\partial \eta^2} W(\xi,\eta)]^2 + [\frac{\partial^2}{\partial \eta^2} W(\xi,\eta) + v\frac{\partial^2}{\partial \xi^2} W(\xi,\eta)]^2 - [\frac{\partial^2}{\partial \xi^2} W(\xi,\eta) + v\frac{\partial^2}{\partial \eta^2} W(\xi,\eta)][\frac{\partial^2}{\partial \eta^2} W(\xi,\eta) + v\frac{\partial^2}{\partial \xi^2} W(\xi,\eta)] + 3(1-v)^2 \frac{\partial^2}{\partial \xi \partial \eta} W(\xi,\eta)^2 \quad (21)$$

For a given relative loading area S_0, the result of f in Eq. (21) depends on the solutions of Eq. (15); i.e., it depends only on the value of n (or K). To focus on the physical length L 's effect in this study, we deterministically studied three different loading area radiuses, i.e., $R = 0.05\ell,\ 0.1\ell,$ and 0.2ℓ. These values are approximately 0.5~3 times the ice thickness.

According to Eq. (20), we further define a normalised stress ${\sigma_M}^0$ as in Eq. (22).

$${\sigma_M}^0(K,S_0) = \frac{\sigma_M t^2}{F_Z} = 6f(K,S_0) \quad (22)$$

The normalised stress ${\sigma_M}^0$ on the LHS of Eq. (22) is independent of the load magnitude F_Z (note that σ_M and F_Z are proportional to each other). It is purely a function of the non-dimensional values K and S_0. Therefore, for a given relative loading area S_0 and for any arbitrary loading F_Z, together with its consequential maximum Mises stress σ_M, within an ice floe's elastic deformation range, the relationship in Eq. (22) holds. That is, assuming that radial crack initiation occurs when the maximum Mises stress reaches its flexural strength σ_f, the following relationship in Eq. (23) can be established.

$${\sigma_M}^0(K,S_0) = \frac{\sigma_M t^2}{F_Z} = \frac{\sigma_f t^2}{F_{Z,\text{radial},0}(K,S_0)} \quad (23)$$

Rearranging Eq. (23), we are thus able to establish the criteria for radial crack initiation within a plate, as given in Eq. (24).

$$\frac{F_{Z,\text{radial},0}(K,S_0)}{\sigma_f t^2} = \frac{1}{{\sigma_M}^0(K,S_0)} \quad (24)$$

Accordingly, the calculation for the radial crack initiation load has been simplified into calculating the normalised maximum 'Mises stress', defined in Eq. (22), under the loading case and boundary conditions stated in Fig. 3. To the authors' knowledge, no analytical solutions exist for such a loading case and boundary conditions in the available literature. As an alternative, the Finite Element Method (FEM) is employed to determine the value of ${\sigma_M}^0$ under different n values.

3.1.2 Numerical set-up to study radial crack initiation

The solution of Eq. (15) is achieved using the Finite Element Method (FEM) in this paper. Based on the formulation in Eqs. (13), (14) and (23), a numerical model with a normalised length scale, as in Fig. 4, is employed to calculate the normalised Mises stress in Eq. (23) under an arbitrary combination of F_Z and t. For square ice floes of different sizes, the normalised foundation $K = n^4$ is the only varied input. Detailed considerations for various inputs

implemented in the numerical models are discussed in Appendix A. The overall model description and implementation are introduced herein.

A Python script is implemented to set up a numerical model within ABAQUS/Standard, as in Fig. 4a, for the considered problem in Fig. 3. Symmetric boundary conditions, as in Eq. (25), have been implemented at the centre line (i.e., *CL*) to improve its numerical efficiency. Other boundaries are set free. The built-in elastic foundation implementation within ABAQUS/Standard has been utilised with varying K to calculate the results of square ice floes of different sizes.

$$\begin{aligned} u(\eta = 0) &= 0 \\ v(\eta = 0) &= 0 \\ \theta_{ZZ}(\eta = 0) &= 0 \end{aligned} \tag{25}$$

where u and v are translational displacements in the ξ (or x) and η (or y) directions and θ_{ZZ} is the rotational displacement around the Z axis (Fig. 3).

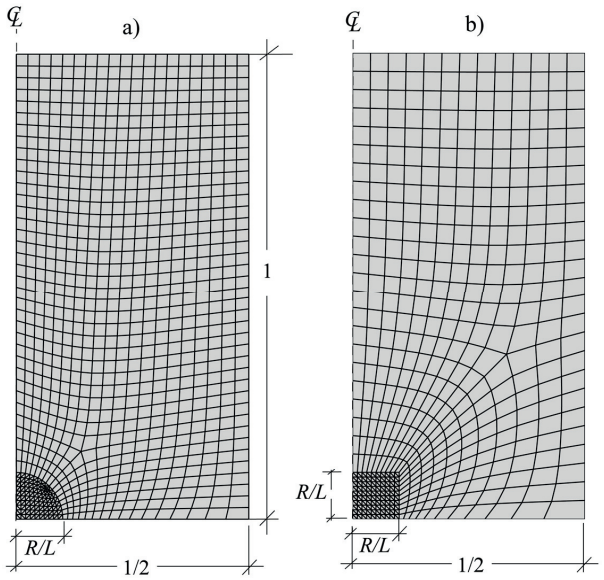

Fig. 4 a) Numerical set-up for crack initiation study; b) a benchmark test set-up against Nevel (1965) (N.B.: the actual mesh is much denser than shown in this figure).

In addition, a similar numerical set-up, but with a rectangular loading area, is implemented, as in Fig. 4b. This serves as a benchmark test against Nevel's (1965) analytical solution to further confirm the validity of the current numerical model.

The maximum Mises stress output of each simulation (i.e., with different elastic foundation moduli) is extracted and converted to the normalised Mises stress $\sigma_M{}^0(K, S_0)$ according to the middle term of Eq. (23).

The normalised length 1 is implemented, as in Fig. 4. For our problem of concern in Fig. 4a, the radius of the loading area R is deterministically assumed to be 5%, 10% and 20% of the

characteristic length (i.e., $R = 0.05\ell$, 0.1ℓ, and 0.2ℓ); for the benchmark test in Fig. 4b, the rectangular loading area has a corresponding size of width ($2 \times R / L$ in the y direction[5]) and length (R / L in the x direction). The size of R is deterministically assumed to be $R = 0.1\ell$ and 0.2ℓ for the benchmark test, the tabulated results of which can be found in APPENDIX A of Nevel (1965).

In each simulation, depending on the different values of L, the densely meshed loading area is scaled accordingly (as shown in Fig. 4). In all calculations, a biased mesh is adopted to further improve its efficiency. Because the maximum stress is expected within the loading area, a rather dense mesh is implemented within the loading area (see Fig. 4). Based on a series of calculations with different n (or K) values, the function $F_{Z,\text{radial},0}(n)/(\sigma_f t^2)$ in Eq. (24) can be established.

3.2 Radial crack propagation within a finite size ice floe

Following the study in Section 3.1, radial crack propagation is studied in this section with a pre-existing crack within the loading area. Specifically, we study the variation of the radial crack propagation load $F_{Z,\text{radial},1}(\alpha)$ with the normalised radial crack length α, as shown in Fig. 5. In addition to the general assumptions stated in Section 2.3, some other important assumptions are included in this study as follows:

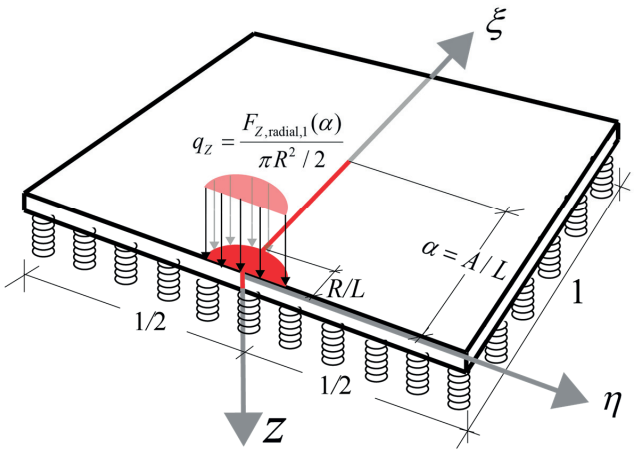

Fig. 5 Radial crack propagation within a square thin plate on a Winkler-type elastic foundation.

- It is assumed that Linear Elastic Fracture Mechanics (LEFM) is applicable to this problem; i.e., the Griffith criterion applies herein (Anderson, 2005). However, it should be noted that the large grain size and creep effect of ice material would introduce additional energy consumption at the crack tip apart from the energy needed to create new surfaces, thus setting a size requirement for the applicability of LEFM to the ice fracturing problem (Mulmule and Dempsey, 2000). Therefore, Mulmule and Dempsey (2000) proposed a size requirement (i.e., $L \geq 3\,\text{m}$ or $L \geq 200d$, d is the grain size) for

[5] Only half of the width is shown in the symmetric plot of Fig. 4.

the applicability of LEFM. For the current considered problem, the ice floe has a size of $L = n\ell \approx 13.5nt^{3/4}$. For $n \geq 1$, when the ice thickness $t \geq 0.14\,\text{m}$, this condition is theoretically satisfied. Accordingly, for most floe sizes encountered in engineering applications, the proposed criterion by Mulmule and Dempsey (2000) can be fulfilled. Therefore, it is reasonable to assume the applicability of LEFM to the current problem.

- The applicability of LEFM also calls for a sufficiently large ligament size. In this paper, we studied the radial crack propagation loads corresponding to varying crack lengths. However, accurate theoretical formulations and numerical calculations are implemented only up to a maximum crack size that is 80% of the floe size; i.e., the ligament is always larger than $0.2L$. For the crack propagation load to propagate a crack beyond $0.8L$, we simply adopt an extrapolation approach. Uncertainties and inaccuracies reside in such an extrapolation. However, it will not impair the overall accuracy of our analysis because radial crack propagation loads with crack lengths larger than $0.8L$ are either too large or too small to have any sensible influence on our classification of semi-infinite or finite size ice floes.
- In all classical fracture mechanics related analyses, there is always a pre-existing crack (Anderson, 2005). In this radial crack propagation study, we assume the starting radial crack length to be $\alpha_0 = R/L$; i.e., for all floe sizes considered, the radial crack initiation load can always propagate the radial crack to a distance of R (the boundary of the half-circular loading area).
- We assume that the crack driving energy is always in balance with the crack resistance energy; i.e., the radial crack always propagates in a stable manner. This is not true in reality because crack in ice usually propagates in a uncontrolled manner (DeFranco and Dempsey, 1994). However, assuming such a balanced state allows us to theoretically study the relationship between the radial crack propagation load and the radial crack length, i.e., how $F_{Z,\text{radial},1}(\alpha)$ varies with different crack length α.
- It is assumed that there is only one radial crack; multi-crack propagation and interactions are not considered in this paper. Moreover, this crack propagates in a self-similar manner, as in Fig. 5.
- Possible crack closure effect within the radial crack is neglected. The crack closure effect (or wedging effect, dome effect) has been mentioned and treated in previous literature for an infinite ice floe (Bažant, 2002; Bažant and Kim, 1998a; Bažant and Kim, 1998b; Kerr, 1976; Sodhi, 1995; Sodhi, 1996; Sodhi, 1997) and for a clamped circular plate (Dempsey et al., 1995). The presence of the radial crack closure effect would increase $F_{Z,\text{radial},1}(\alpha)$. However, for a finite size ice floe, it is reasonable to neglect the crack closure effect because the in-plane confinement is supposed to be small.

3.2.1 Formulation of radial crack propagation problem

For a thin plate on an elastic foundation under an edge loading, as in Fig. 5, the driving force behind the radial crack propagation is from the total moment created by the downward acting (i.e., positive Z - direction) force $F_{Z,\text{radial},1}$ and the corresponding upward acting (i.e., negative Z - direction) fluid reaction force. To solve this problem, we first focus on calculating the corresponding energy release rate G_f for a given crack length A. Irwin's (1956) energy approach is adopted to solve this Griffith like fracture. Considering the fluid base and the elastic plate as one system, its potential energy Π is defined in Eq. (26).

$$\Pi = U - T \tag{26}$$

where U is the strain energy and the elastic foundation's stored elastic energy and T is the work done by the external force, i.e., the evenly distributed edge pressure with a magnitude of $q_Z = F_{Z,\text{radial},1} / (\pi R^2 / 2)$. Assuming that for a given crack length A, q_Z is a constant, we are in a 'load controlled' scenario. Therefore, we can express T as Eq. (27).

$$T(A) = \iint_S \sum_{(x_i, y_j) \in S} w(x_i, y_i, x, y, A) q_Z dxdy \tag{27}$$

where the physical meaning of $w(x, y, x_i, y_i, A)$ is the same as that defined in Eq. (6), but a new variable A (the radial crack's physical length) is introduced into the solution. Following the first row of Eq. (10) and Maxwell's reciprocal law, we can also define $w_{total}(x, y, A) = \sum_{(x_i, y_j) \in S} w(x_i, y_i, x, y, A)$. Moreover, because we have assumed that it is a linear elastic system (both the plate and elastic foundation), we can express U as Eq. (28).

$$U(A) = \frac{1}{2} T(A) = \frac{q_Z}{2} \iint_S w_{total}(x, y, A) dxdy \tag{28}$$

For a square thin plate with a given radial crack length under an evenly distributed edge pressure within a half circular area, we further define a corresponding average deflection $w_0(A)$ under the loading area as Eq. (29).

$$w_0(A) = \frac{\iint_S w_{total}(x, y, A) dxdy}{S} \tag{29}$$

Using the definition in Eq. (29), Eqs. (27) and (28) can be rewritten as Eq. (30), which has a more straightforward physical meaning (i.e., work=force$\times$ displacement).

$$\begin{aligned} T(A) &= F_{Z,\text{radial},1} w_0(A) \\ U(A) &= \frac{1}{2} F_{Z,\text{radial},1} w_0(A) \end{aligned} \tag{30}$$

Accordingly, the potential energy can be calculated using Eq. (31).

$$\Pi = -\frac{1}{2} F_{Z,\text{radial},1} w_0(A) \tag{31}$$

According to Irwin (1956), the energy release rate G_f can be calculated with Eq. (32).

$$G_f = -\frac{1}{t} \frac{d\Pi}{dA} = \frac{F_{Z,\text{radial},1}}{2t} \frac{dw_0(A)}{dA} \tag{32}$$

Recalling the definition of the normalised deformation $W(\xi, \eta)$ in Eq. (13), the same normalisation procedure as in Section 3.1.1 with $\alpha = A / L$ can be utilised to simplify $w_0(A)$ in Eq. (29) to Eq. (33).

$$W_0(\alpha) = \frac{w_0(\alpha) D}{F_{Z,\text{radial},1} L^2} \tag{33}$$

Solving $w_0(\alpha)$ from Eq. (33) and inserting it into Eq. (32) leads to Eq. (34).

$$G_f = \frac{F_{Z,\text{radial},1}^2 L^2}{2tD} \frac{dW_0(\alpha)}{d\alpha} \frac{d\alpha}{dA} = \frac{F_{Z,\text{radial},1}^2 L}{2tD} \frac{dW_0(\alpha)}{d\alpha} \tag{34}$$

Expressing the flexural rigidity D explicitly and utilising Eq. (16), Eq. (34) can be rearranged as Eq. (35). A detailed derivation is made in Appendix B.

$$\frac{F_{Z,\text{radial},1}}{t^2} = \left(\frac{k}{108}\right)^{\frac{1}{8}} \sqrt{G_f} \left(\frac{E}{1-\upsilon^2}\right)^{\frac{3}{8}} \frac{t^{-3/8}}{\sqrt{n \frac{dW_0(\alpha)}{d\alpha}}} \tag{35}$$

A similar expression for an infinite ice floe can be found in Bažant (1992a). Differently, the derivation in Eq. (35) features a parameter n that has been introduced to reflect the effect of finite floe sizes. Note that Bažant (1992a) normalised an infinite plate with the characteristic length ℓ. If we follow the same normalisation as Bažant (1992a), i.e., assigning our normalisation length $L = \ell$ leads to $n = 1$, Eq. (35) thus reduces to the derived Eq. [21] in Bažant (1992a). This signifies the correctness of the above derivations.

To compare the results of radial crack initiation and propagation, Eq. (35) is rearranged according to Eq. (24) into Eq. (36).

$$\frac{F_{Z,\text{radial},1}}{\sigma_f t^2} = \left(\frac{k}{108}\right)^{\frac{1}{8}} \frac{\sqrt{G_f}}{\sigma_f} \left(\frac{E}{1-\upsilon^2}\right)^{\frac{3}{8}} \frac{t^{-3/8}}{\sqrt{n \frac{dW_0(\alpha)}{d\alpha}}} \tag{36}$$

The RHS of Eq. (36) can be further separated into three different components as $C_0 C_1 t^{-3/8}$. The first component $C_0 = \left(\frac{k}{108}\right)^{\frac{1}{8}} \frac{\sqrt{G_f}}{\sigma_f} \left(\frac{E}{1-\upsilon^2}\right)^{\frac{3}{8}}$ depends purely on ice material properties; the second component $C_1 = 1/\sqrt{n \frac{dW_0(\alpha)}{d\alpha}}$ is a non-dimensionalised value that depends on the relative crack size α and ice floe size $n = L/\ell$. If the nominal strength of ice is defined as the LHS of Eq. (36), the third component demonstrates that the radial crack resistance of a plate on a Winkler-type elastic foundation is scaled by the ice thickness to a power of $-3/8$. The task now is to calculate the non-dimensional value of C_1. A similar numerical set-up is adopted and described in the next section.

3.2.2 Numerical set-up to study radial crack propagation

To calculate C_1, a similar numerical set-up as in Fig. 4 is introduced in Fig. 6. In the new numerical set-up, a 'crack' is introduced in the centre line (i.e., *CL*). Only the region with the uncracked area (in yellow colour) is assigned symmetric boundary conditions, as in Eq. (25). The 'cracked' region in the centre line is set free.

To accurately capture the loading area's average deflection $w_0(A)$, a rather dense mesh has been assigned within the loading area, as in Fig. 6. It is also expected that a rather large stress gradient exists around the crack tip. Therefore, a dense mesh is also implemented around the crack tip. However, the current numerical set-up is not a special-purpose scheme to calculate a fracture mechanics problem. Special purpose programs are those specially designed to address cracks and determine the Stress Intensity Factor (SIF) directly (Bažant and Planas, 1998). The numerical set-up in Fig. 6 is purely an elasticity problem with different boundary conditions

such that the term C_1 can be numerically approximated from an energy point of view. Its rigorousness and accuracy is tested in Section 4.2.1 in a benchmark study for which analytical solutions are available.

A Python script has been implemented to construct the corresponding biased mesh with different crack lengths α. All of the other geometries not shown are the same as those in Fig. 4. In terms of the material properties, loading magnitude and mesh size considerations, the same inputs as those in Table A. 1 have been implemented. For each crack length α_i, we extract the corresponding normalised average displacement $W_0(\alpha_i)$ within the loading area according to Eq. (33). With exaggeration, Fig. 6 illustrates two successive crack lengths and their corresponding boundary conditions and loading area. Using a series of α_i and $W_0(\alpha_i)$ values calculated by FEM, 'Richardson's extrapolation (Yang et al. (2005), p. 211)' has been implemented to calculate the derivative of $dW_0(\alpha)/d\alpha$ with an truncation error of $O(\Delta\alpha^4)$.

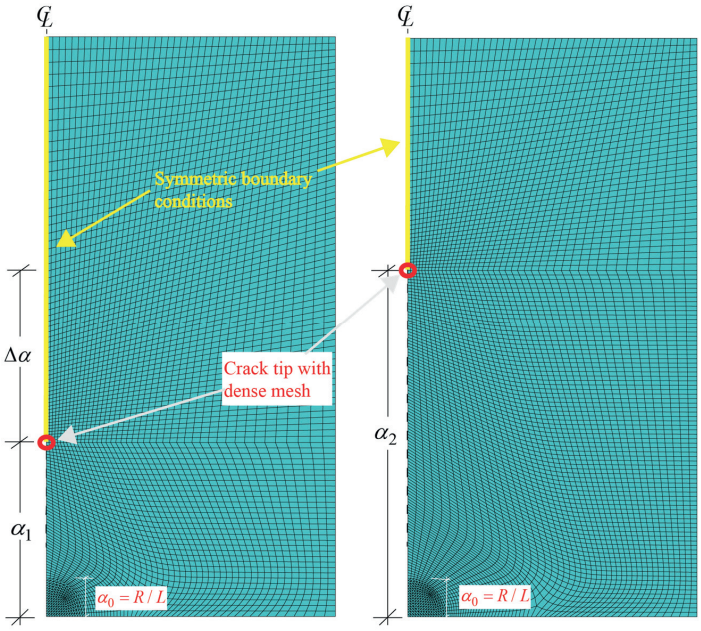

Fig. 6 Numerical set-up to study radial crack propagation (note that the actual mesh in the calculation is much denser and the step $\Delta\alpha$ is much smaller than those shown in the figure; the ice floe's physical size in this figure is 3ℓ).

4 Results

This section presents the results of radial crack initiation and propagation based on the methodologies introduced in Section 3.

4.1 Results for radial crack initiation within a finite size ice floe

Based on the methodology described in Section 3.1, a square ice floe under an evenly distributed edge pressure over a half circular area ($R = 0.05\ell$, 0.1ℓ, and 0.2ℓ) is calculated in this section. The primary results are the RHS of Eq. (24). According to the numerical set-up in

Fig. 4, we have calculated the normalised Mises stress $\sigma_M{}^0(n)$'s distribution within an ice floe of varying size. As an intuitive example (i.e., with loading radius $R = 0.2\ell$) showing an ice floe's boundary influences, Fig. 7 illustrates the comparative stress field with varying floe sizes. It should be noted that the colour bar values in these nine subplots are not consistent. That is, the same red colour in subplot ($n = 1$) does not have the same value in subplot ($n = 2$). The normalised Mises stress colour spectrum should only be understood as comparative values within each subplot in Fig. 7.

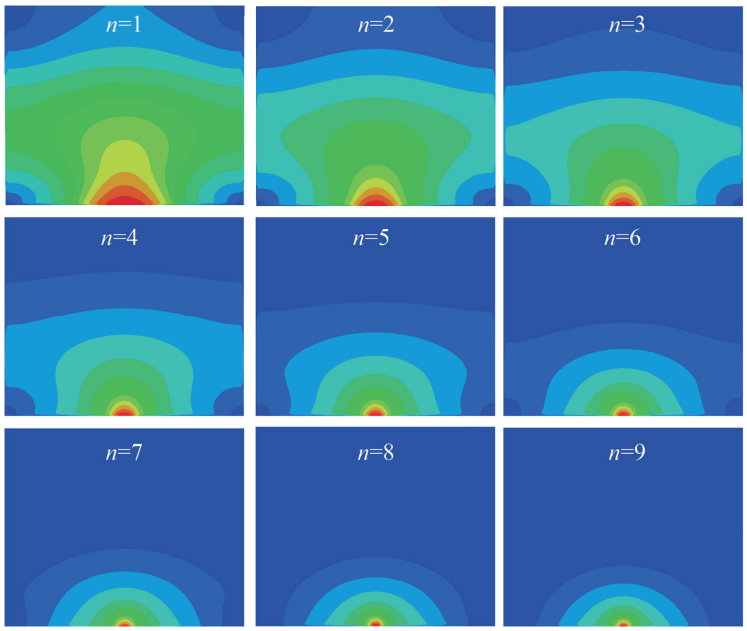

Fig. 7 Illustration of the distribution of the normalised Mises stress within ice floes of varying sizes with $R = 0.2\ell$ (note that a rainbow spectrum is utilised to illustrate the comparative stress values, with red and violet corresponding to the maximum and minimum values; the Mises stress in the figure should only be understood as comparative values within each subplot).

For the benchmark problem in Fig. 4b, the same stress distributions as in Fig. 7 were observed. Moreover, based on Eq. (24), we calculated the normalised radial crack initiation load for square ice floes of different sizes. For this purpose, a quantitative validation was made against analytical solutions of Nevel (1965), as in Fig. 8. Nevel's (1965) solutions are presented as tabulated results[6] in the paper's APPENDIX A with a Poisson ratio equal to 1/3.

Following this rather satisfactory benchmark validation, the same procedures were implemented for the numerical model in Fig. 4a. The normalised radial crack initiation load in this loading scenario (i.e., within a half circular area) is presented in Fig. 9.

[6] As an example, to make the results comparable, we have chosen $\mu = 0.2$ and $v = 0.4$ in Figure. 4 of Nevel (1965) according to its own notation (corresponding to $R = 0.2\ell$ in Fig. 4b of the current paper). Based on the second table in APPENDIX A, this leads to $M_x / P = 0.4639$ and, accordingly, $6P/(\sigma_x t^2) = 1/0.4639$. This eventually leads to $P_f/(\sigma_f t^2) = 1/0.4639/6 = 0.3593$, as in Fig. 9 of the current paper (i.e., the red solid horizontal line).

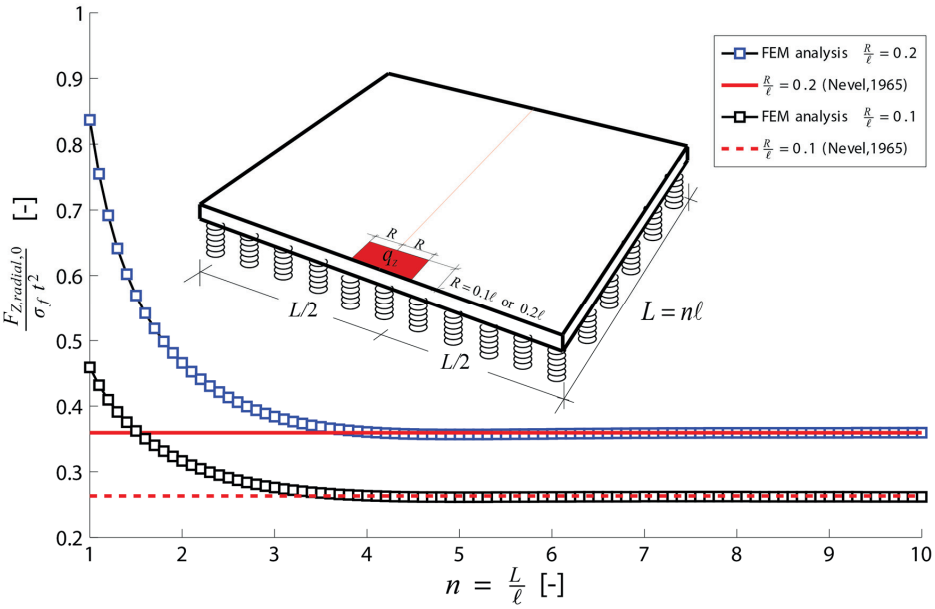

Fig. 8 Benchmark validation of the normalised radial crack initiation load for a square ice floe of varying size under a rectangular edge loading area.

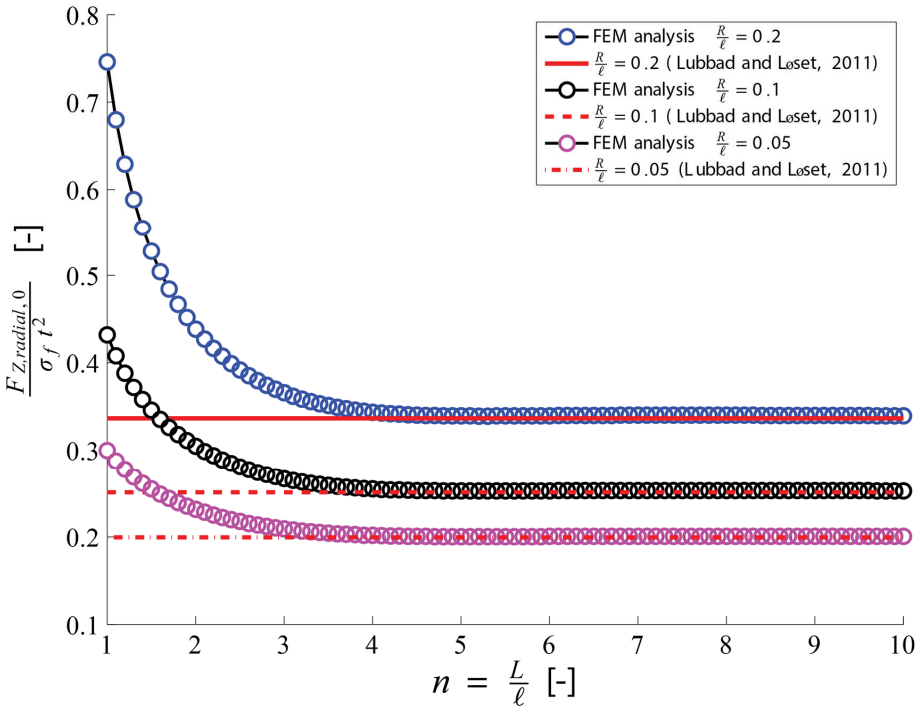

Fig. 9 Normalised radial crack initiation load for a square ice floe of varying size under half circular edge loading.

In addition to the normalised radial cracking load, the normalised deflection at point $\xi = 0, \eta = 0$ is presented in Fig. 10.

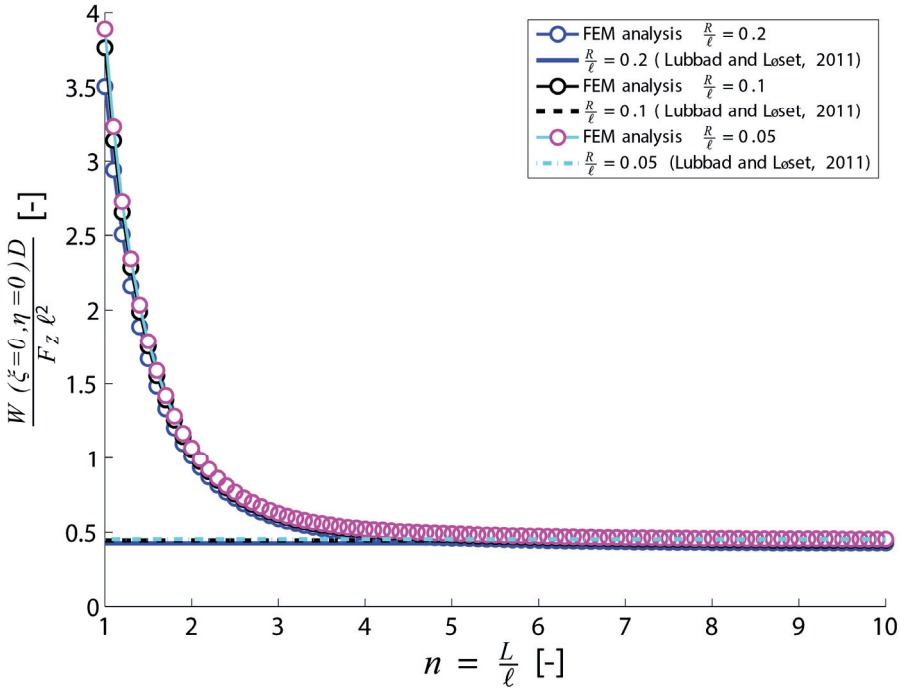

Fig. 10 Normalised deflection at ($\xi = 0, \eta = 0$) for a square ice floe of varying size under half circular edge loading.

4.2 Results for crack propagation within a finite size ice floe

The basic non-dimensional formula to handle radial crack propagation within a finite size ice floe was derived in Eq. (35). The key solution to this formula is $1/\sqrt{n\frac{dW_0(\alpha)}{d\alpha}}$. Before directly presenting the results according to the numerical set-up in Section 3.2.2, we first present a benchmark validation for the ice floe splitting problem in which analytical solutions are available.

4.2.1 Benchmark test for the splitting crack propagation within a finite size ice floe

The fundamental theory to derive Eq. (32) in Section 3.2.1 is applicable to any other loading/deformation scenario as long as the body under consideration is linear elastic. As a benchmark test, we consider an in-plane splitting problem, as shown in Fig. 11a: a square ice floe with an existing crack A being opened by a pair of splitting forces F_Y. The conjugate

deformation to each of the splitting loads is denoted as $u_0(A)$. Following the same methodology to derive Eq. (32), the splitting fracture problem in Fig. 11a can be derived as Eq. (37)[7].

$$G_f = -\frac{1}{t}\frac{d\prod}{dA} = 2\frac{F_Y}{2t}\frac{du_0(A)}{dA} \tag{37}$$

Here, it is convenient to introduce the non-dimensional compliance function given in Eq. (38) .

$$C(A) = \frac{u_0(A)E}{(F_Y/t)} \tag{38}$$

Introducing $\alpha = A/L$ and further considering the relationship in Eq. (39), Eq. (37) can be transformed into Eq. (40).

$$K_I = \sqrt{G_f E} \tag{39}$$

$$K_I = -\frac{1}{t}\frac{d\prod}{dA} = \frac{F_Y}{\sqrt{L}t}\sqrt{\frac{dC(\alpha)}{d\alpha}} \tag{40}$$

Equating the Stress Intensity Factor (SIF) with the fracture toughness $K_I = K_{Ic}$, the critical splitting load can be derived as Eq. (41) according to Eq. (40).

$$\frac{F_Y}{tK_{IC}\sqrt{L}} = 1/\sqrt{\frac{dC(\alpha)}{d\alpha}} \tag{41}$$

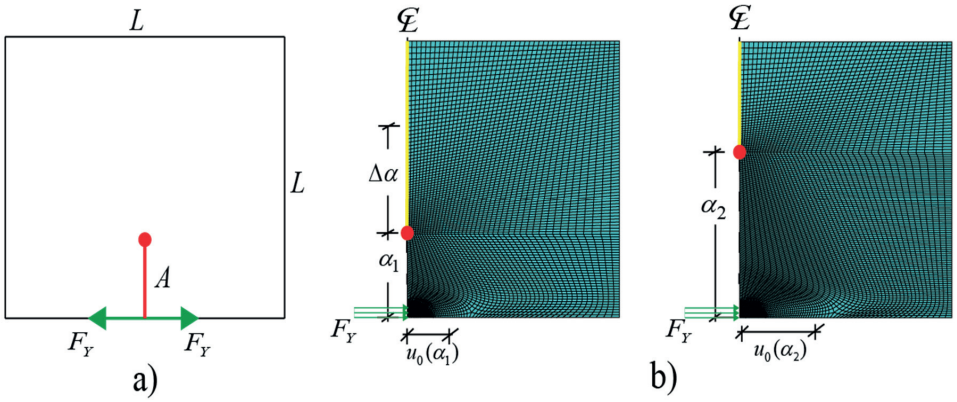

Fig. 11 Splitting of an ice floe: a) problem formulation; b) numerical set-up.

Similarly, it is the derivative of the normalised compliance function $dC(\alpha)/d\alpha$ that should be calculated in Eq. (41). As a benchmark test, we tested a similar numerical set-up for the radial crack propagation as that in Fig. 6. This is illustrated in Fig. 11, in which we adopted the same meshing style, same boundary conditions and same element type, except that the external loading is changed from F_Z in Fig. 5 to F_Y in Fig. 11b. Note here that instead of using a concentrated load as in Fig. 11a, which poses certain numerical difficulties, we have evenly

[7] Note here that the additional coefficient '2' in the RHS of Eq. (37) is because there is a pair of F_Y contributing to the potential energy through external work.

distributed F_Y within an infinitesimally small area near the crack mouth, as in Fig. 11b. A similar Python script is implemented to advance the crack tip during the calculation, as shown in Fig. 11. Afterwards, a series of α_i and $u_0(\alpha_i)$ is available. $u_0(\alpha_i)$ is further non-dimensionalised as $C(\alpha_i)$ according to Eq. (38). Eventually, the same 'Richardson's extrapolation (Yang et al. (2005), p. 211)' is employed to calculate the derivative of $dC(\alpha)/d\alpha$. Accordingly, Eq. (41) is solved.

The splitting process with varying relative crack length α, together with the stress concentration, is illustrated in Fig. 12. Correspondingly, the normalised splitting load (i.e., LHS of Eq. (41)) is compared with LEFM analytical solutions (Dempsey et al., 1994; Lu et al., (Accepted on November 12th 2014)) for the same problem in Fig. 13. Although an approximate numerical scheme has been utilised, the same numerical set-up (except the external loading) appears to reasonably capture the splitting crack's propagation with its corresponding splitting load.

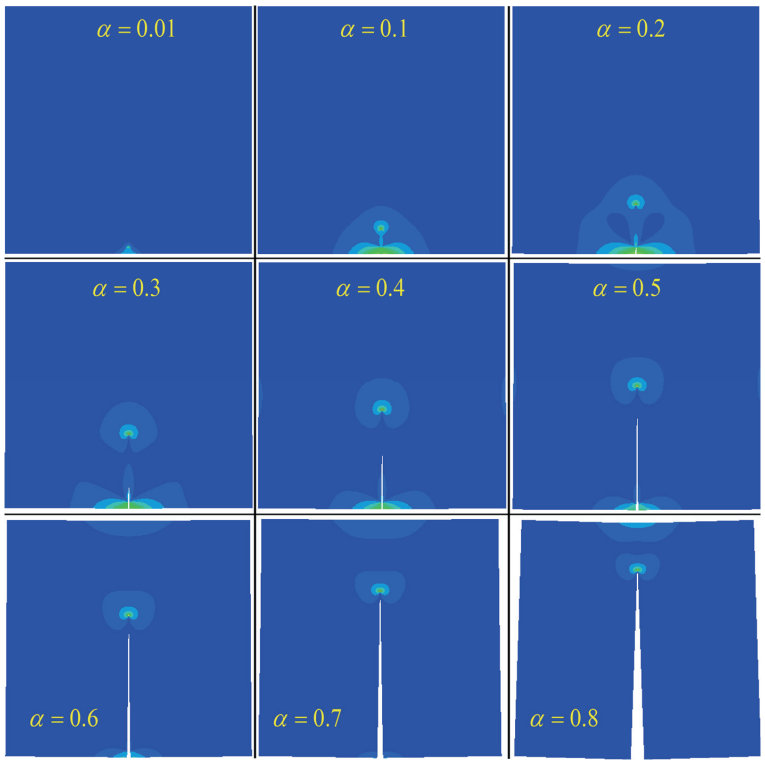

Fig. 12 Concentration of the Mises stress at the crack tip with varying splitting crack length (note that the crack opening displacement is exaggerated; the same rainbow spectrum as in Fig. 7 has been utilised; the Mises stress in these plots should only be understood as comparative values).

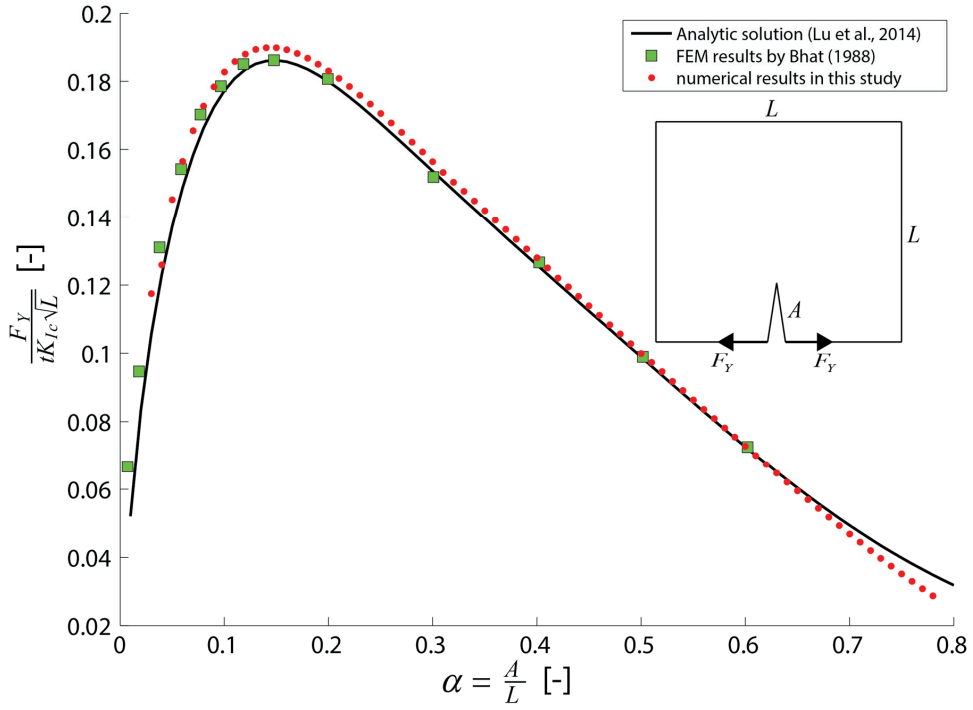

Fig. 13 Benchmark comparison of the current numerical scheme with the analytical solution.

4.2.2 Results for radial crack propagation within a finite size ice floe

Before presenting the quantitative results of C_1 within Eq. (36), we took the loading radius $R = 0.2\ell$ as an example and visualised the stress concentrations within a radially cracked ice floe of varying size and crack length. Similar inputs as in Table A. 1 were utilised with the numerical set-up in Fig. 6. The calculated Mises stress is illustrated for three groups of ice floe sizes with different radial crack lengths in Fig. 14. These Mises stresses should only be understood as comparative values that visualise the location of the maximum stress (stress concentration).

In addition, based on the derivations in Section 3.2.1 and FEM calculation results, the normalised average deformation $W_0(\alpha)$ (as defined by Eq. (33)) within the loading area is illustrated in Fig. 15. Eight different floe sizes with varying crack lengths were calculated. A huge difference in the vertical deformation was calculated for different floe sizes. Therefore, the presented curves in Fig. 15 were scaled with constant numbers such that different curves could be fitted in the same figure. It is, however, the trend (i.e., $dW_0(\alpha)/d\alpha$) of these curve that is most interesting.

Based on the calculated $W_0(\alpha)$ versus α, 'Richardson's extrapolation (Yang et al. (2005), p. 211)' is employed to calculate $dW_0(\alpha)/d\alpha$. Therefore, $C_1 = (n\frac{dW_0(\alpha)}{d\alpha})^{-1/2}$ within Eq. (36) is illustrated in Fig. 16. The results in are universal for the corresponding loading area S, as in Fig. 5. Additional

parameters that relate geometric and material information can be included, together with the results in Fig. 5, according to Eq. (36), such that the radial crack propagation load is calculated.

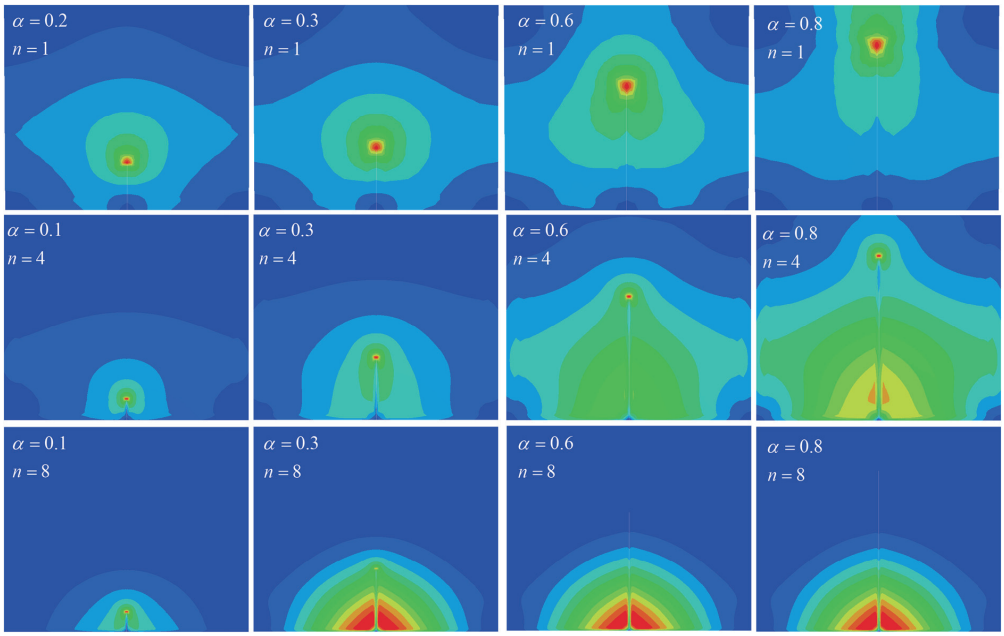

Fig. 14 Concentration of the Mises stress with different ice floe sizes and radial crack lengths (N.B., the same rainbow spectrum as in Fig. 7 has been utilised; the Mises stress in these plots should be understood as comparative values) (with $R = 0.2\ell$).

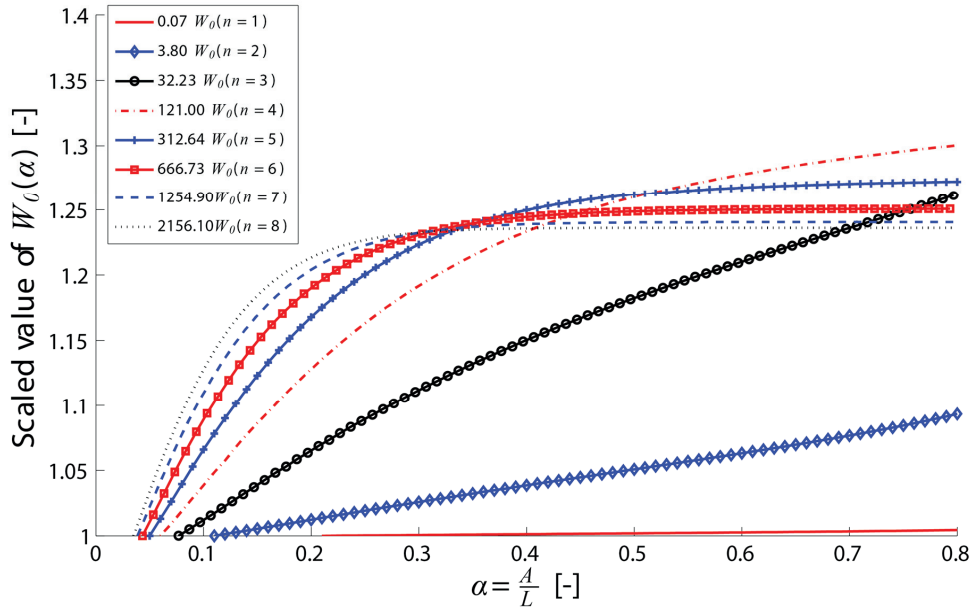

Fig. 15 Scaled value of average normalised deformation $W_0(\alpha)$ within the loading area with varying ice floe sizes and crack lengths ($R = 0.2\ell$).

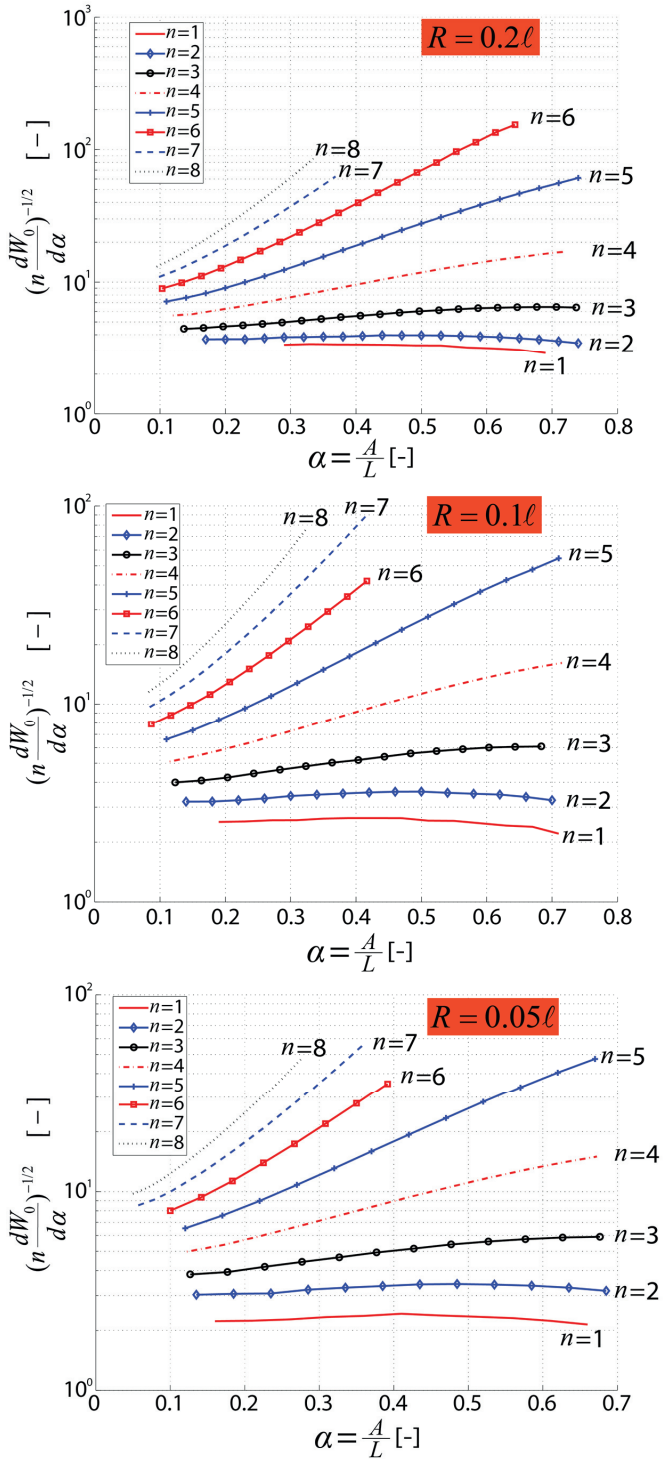

Fig. 16 C_1 for radial crack propagation with varying ice floe sizes (note that the Y axis is in logarithmic scale).

4.3 Competition between radial crack initiation and propagation

The results of radial crack initiation and propagation have been presented separately in Sections 4.1 and 4.2. The main focus of this paper is to study the radial-crack-initiation-controlled fracture of an ice floe. Therefore, these two separate loads have to be compared, and the boundaries between Scenarios #1 and #2 in Fig. 2 should be quantified.

Formulae to calculate radial crack initiation and propagation were presented in the same format in Eqs. (24) and (36). Moreover, the corresponding key unknowns were calculated and presented in previous sections (i.e., $1/\sigma_M^0$ for the radial crack initiation problem, and C_1 for the radial crack propagation problem). Now, it is possible to quantify such competition and identify radial-crack-initiation-controlled fracture. The criterion for radial-crack-initiation-controlled fracture was presented in Eq. (4). Following the formula derivations in Sections 3.1.1 and 3.2.1, we further define the following piecewise criterion in Eq. (42) to study the maximum radial crack extension induced by a radial crack initiation load. For an arbitrary relative crack length α in the range $[R/L,1]$ and for a varying floe size expressed by n, three different cases can be expected, as shown in Eq. (42).

$$\begin{cases} \dfrac{F_{Z,\text{radial},0}(n)}{\sigma_f t^2} > \dfrac{F_{Z,\text{radial},1}(n,\alpha)}{\sigma_f t^2} \rightarrow \alpha_{\max} = 1 & \text{Radial crack initiation controlled fracture;} \\ \dfrac{F_{Z,\text{radial},0}(n)}{\sigma_f t^2} = \dfrac{F_{Z,\text{radial},1}(n,\alpha)}{\sigma_f t^2} \rightarrow \alpha_{\max} & \text{maximum radial crack length under radial crack initiation load;} \\ \dfrac{F_{Z,\text{radial},0}(n)}{\sigma_f t^2} < \dfrac{F_{Z,\text{radial},1}(n,\alpha)}{\sigma_f t^2} \rightarrow \alpha_{\max} = R/L & \text{Radial crack initiation load cannot extend radial crack.} \end{cases} \quad (42)$$

Corresponding to Eq. (42), a conceptual illustration is made in Fig. 17 to further interpret the relationship between these loads in different cases sequentially following Eq. (42).

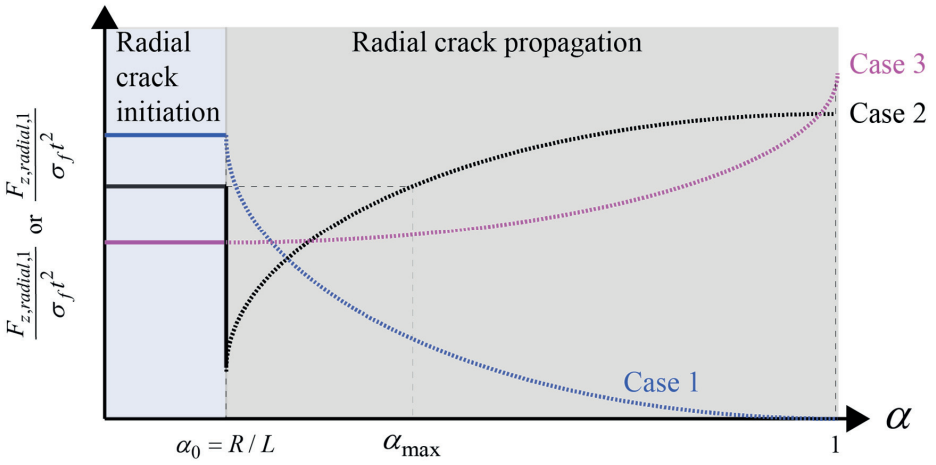

Fig. 17 Conceptual illustration of three different cases comparing the radial crack initiation load and the radial crack propagation load.

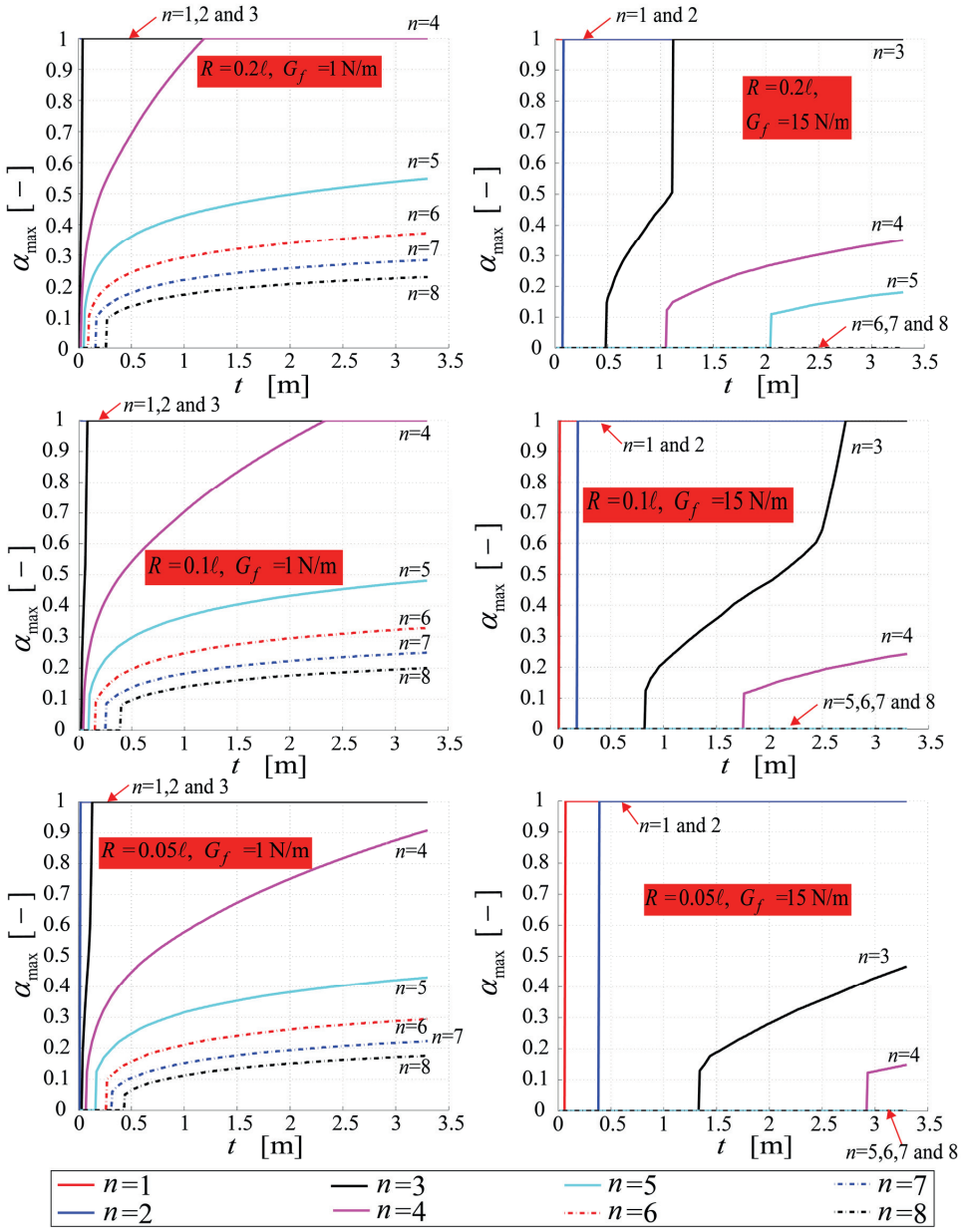

Fig. 18 Maximum radial crack length induced by the radial crack initiation load.

In Eq. (42), the value of the normalised radial crack initiation load $F_{Z,\text{radial},0}(n)/(\sigma_f t^2)$ is numerically calculated and presented in Fig. 9. For the value of the normalised radial crack propagation load $F_{Z,\text{radial},1}(n,\alpha)/(\sigma_f t^2)$, further calculations are needed to include material

properties and ice thickness information. In addition, the value of C_1 has only been formulated and calculated within the crack length $\alpha \in [R/L, 0.8]$. As an approximation, data extrapolation has been implemented in Fig. 16 to ensure that all curves cover a range of $\alpha \in [R/L, 1]$.

The results calculated according to Eq. (42) are presented in Fig. 18. Notably, while calculating $F_{Z,\text{radial},1}(n,\alpha)/(\sigma_f t^2)$ (defined in Eq. (36)), among all of the undetermined values, there exist controversies regarding the exact value of the energy release rate (or fracture energy) G_f for sea ice. Also, the ice thickness t introduces significant variability in the calculated results of $F_{Z,\text{radial},1}(n,\alpha)/(\sigma_f t^2)$. Therefore, we present in Fig. 18 two groups of comparisons with two different G_f values, and the major variable (i.e., horizontal axis) is chosen to be the ice thickness. Plots in the left column of Fig. 18 have taken $G_f = 1\,\text{N/m}$ according to laboratory experiments, e.g., (Schulson and Duval, 2009); the right column in Fig. 18 features the fracture energy $G_f = 15\,\text{N/m}$ according to field measurements (Adamson et al., 1995; Dempsey et al., 1999a; Dempsey et al., 1999b). Other commonly encountered and accepted material properties are listed in Table A. 1.

5 Discussions

Results for both radial crack initiation and propagation were presented in Section 4. A further discussion of these calculated results is presented in this section. The focus is placed on how the floe size influences radial crack initiation and propagation. Collectively, we attempt to answer the question proposed in the beginning of this paper: "how small/large should an ice floe be to be treated as a finite size/semi-infinite ice floe?"

5.1 Discussion about radial crack initiation within a finite size ice floe

Fig. 7 illustrates the distribution of the normalised Mises stress σ_M^0 (as defined in Eq. (23)) within an ice floe of varying size. It is obvious from these plots that when an ice floe is relatively small (e.g., $n \le 7$), the stress distribution is influenced by its boundaries, whereas the stress mainly concentrate in a small portion of a large ice floe (e.g., $n \ge 8$).

The benchmark comparison with Nevel's (1965) solution in Fig. 8 demonstrates that the normalised radial crack initiation load decreases rapidly towards the solutions of a semi-infinite plate when the floe size $L \ge 4\ell$. When a square floe's size $L \ge 9\ell$, the solution for a finite ice floe with free boundaries has already appeared to converge to the solution of a semi-infinite ice floe. This signifies the correctness of the employed numerical model in Fig. 4b. Based on the satisfactory validation, the numerical model in Fig. 4a was utilised to study our loading scenario of interest (i.e., edge loading within a half circular area, as in Fig. 3). The calculated results were illustrated, together with analytical solutions by Lubbad and Løset (2011), in Fig. 9. The same trend as the radial crack initiation load converging to semi-infinite plate solutions was also observed in Fig. 9. In practice, this implies that for a (nearly) square ice floe whose physical size is more than 9 times its characteristic length ℓ, it can be treated as a semi-infinite ice floe, for which relevant solutions for radial crack initiation apply.

Moreover, for all of the considered loading sizes ($R = 0.05\ell, 0.1\ell,$ and 0.2ℓ), it is interesting to note in Fig. 9 that when $L \le 4\ell$, the normalised radial crack initiation load is larger than that predicted by the semi-infinite ice floe solution. This is considered to be due to the effect of the free boundaries. For a small size ice floe, in addition to the energy needed to arouse sufficient flexural deformation, another type of deformation (e.g., rigid body rotation) is also present because of the free boundaries. This is further confirmed by the deflection study presented in Fig. 10; i.e., a larger deflection is expected for smaller ice floes. Therefore, more energy, in comparison with a semi-infinite ice floe, is needed to initiate the radial crack. In practice, this means that using Nevel's (1965) or Lubbad and Løset's (2011) solutions for radial crack initiation calculations is not always conservative.

With respected to the maximum deflection of an ice floe presented in Fig. 10, the size of the loading area appears to have a relatively minor effect on the normalised deflection value. Because large deflections are found for smaller ice floe, we further analysed the possibility of flooding on top of an ice floe before the radial crack initiation. We introduced a known coefficient $c_f = W(\xi = 0, \eta = 0)D/(F_Z \ell^2)$, as plotted in Fig. 10. By assuming that a vertical load $F_{Z,flooding}$ will lead to the flooding of an ice floe, the following relationship in Eq. (43) can be established.

$$c_f(n) = \frac{W(\xi = 0, \eta = 0)D}{F_Z \ell^2} = \frac{W_{flooding}(\xi = 0, \eta = 0)D}{F_{Z,flooding} \ell^2} \tag{43}$$

in which $W_{flooding}(\xi = 0, \eta = 0) = (1 - \rho_i / \rho_w)t$ is the freeboard of an ice floe. The normalised form of $F_{Z,flooding}$ can therefore be expressed as Eq. (44).

$$\frac{F_{Z,flooding}}{\sigma_f t^2} = \frac{(1 - \rho_i / \rho_w)}{\sigma_f c_f \ell^2} \frac{Et^2}{12(1 - \nu^2)} \tag{44}$$

With typical material properties, as in Table A. 1, we calculated $F_{Z,flooding}/(\sigma_f t^2)$ and compared it with the normalised radial crack initiation load in Fig. 19. The general trend shows that a smaller and thinner ice floe needs a lower load to have a deflection larger than its freeboard. However, based on elastic analysis, for the floe sizes and thicknesses of engineering application interests, Fig. 19 shows that the critical radial crack initiation load was reached much earlier than any flooding can occur. Because no flooding occurs before radial crack initiation, the adopted Winkler elastic foundation theory is thus substantiated in the current elastic analysis.

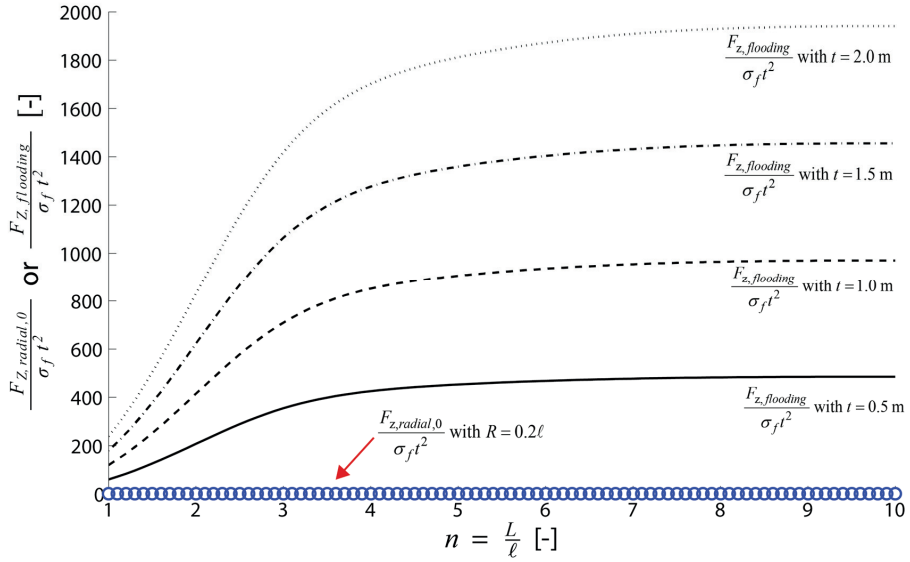

Fig. 19 Radial crack initiation load versus load that can introduce flooding on top of an ice floe.

5.2 Discussion about radial crack propagation within a finite size ice floe

For the problem of concern, based on Irwin's (1956) energy release rate approach, the radial cracking/ice splitting problem has been transformed into calculating the derivative of a non-dimensional deformation/compliance function over the crack length (see Eqs. (36) and (41), respectively).

In the benchmark test of the splitting of a square ice floe shown in Fig. 12, stress concentration always occurs at the crack tip with varying crack length. Fig. 13 further quantified that the normalised ice splitting load first increases with crack length. Afterwards, it reduces dramatically with crack length to maintain a balance between crack driven force and resistance. Most importantly, by comparison with analytical solutions, the favourable agreement in Fig. 13 corroborates the similar numerical set-up in Fig. 6 with which radial crack propagation is to be studied.

For radial crack propagation, the comparative Mises stress's visualisation shown in Fig. 14 (with $R = 0.2\ell$ as an example) demonstrates that stress concentration does not always occur at the radial crack tip. Depending on the floe size, for a small size ice floe (e.g., $n = 1$ in Fig. 14), stress appears to concentrate at the crack tip; however, for a large size ice floe (e.g., $n = 8$ in Fig. 14), stress concentration tends to occur at the location where a circumferential crack is to be developed. The latter case implies that further increasing the load $F_{Z,\text{radial},1}$ shall initiate a circumferential crack instead of propagating the existing radial crack.

The above visual observation is further quantified in Fig. 15 by the average normalised deflection under the loading area. To better interpret Fig. 15, by referring to the definition of $W_0(\alpha)$ in Eq. (33), we assume that $F_{Z,\text{radial},1}$ is fixed in all simulations (though it does not necessarily need to be a constant). Thus, the radial propagation in Fig. 15 is load controlled. For any crack increment under the load controlled situation, an increase in deflection (i.e., $dW_0(\alpha)$) represents

the energy available to propagate the corresponding radial crack. For a small size ice floe (e.g., $n \le 3$ in Fig. 15), $W_0(\alpha)$ is monotonically and rapidly increasing with radial crack extension. This implies that sufficient energy is available to propagate the crack. In contrast, for a large size ice floe (e.g., $n \ge 5$ in Fig. 15), $dW_0(\alpha)$ obviously decreases with increasing radial crack length, particularly after the radial crack is over 30% of the floe size. The energy available to propagate the radial crack, under the load controlled scenario, thus decreases dramatically with radial crack extension. In this situation, to further maintain sufficient energy to propagate the radial crack, the load $F_{Z,\text{radial},1}$ should not be fixed and should instead be increased. However, $F_{Z,\text{radial},1}$ cannot be increased arbitrarily. It is highly possible that $F_{Z,\text{radial},1}$ reaches the magnitude required to initiate a circumferential crack (i.e., $F_{Z,\text{circum},0} = F_{Z,\text{radial},1}$), and therefore, the radial crack ceases to propagate and gives way to circumferential crack formation.

Without including any material properties and thickness information, Fig. 16 presents, in a way, the non-dimensional radial crack propagation load versus crack length for different size ice floes. A similar trend to that discussed above is shown here. For a small size ice floe (e.g., $n \le 3$ Fig. 16), less load is needed to propagate the radial crack. For a large size ice floe (e.g., $n \ge 5$ Fig. 16), similar to that discussed above, an increasing load is needed to propagate the radial crack. Particularly, the curves with $n = 7$ and $n = 8$ were truncated at approximately $\alpha = 30\% \sim 40\%$ in all of the subplots in Fig. 16. This is because the deflection curves, as in Fig. 15, flattened off for a large size ice floe and their numerical derivatives lost meaning by dividing nearly zero values.

Furthermore, note that in Fig. 16, the Y axis is in logarithmic scale. This implies that the load required to further propagate the radial crack increases exponentially. In view of this exponential increasing trend, and considering the fact that the circumferential crack initiation load (or breakthrough load) is only several times larger than the radial crack initiation load (see empirical formulae presented in Eqs. (1) and (3)), it is reasonable to assume that the radial propagation load will soon give way to circumferential crack initiation. This is also the main reason that we conservatively categorised the out-of-plane bending failure of an ice floe into Scenario #1, which is controlled by radial crack initiation (see Fig. 2a), and Scenario #2, which is controlled by circumferential crack initiation (see Fig. 2b); i.e., radial-crack-propagation-controlled fracture has been conservatively grouped into Scenario #2.

5.3 Discussion about radial-crack-initiation-controlled fracture

The calculated results in Fig. 18 show how long the radial crack can propagate once radial crack initiation starts. Because of the piecewise equation defined in Eq. (42), these curves are not smooth enough. Nevertheless, the left column of Fig. 18 shows that when $G_f = 1\ \text{N/m}$, for any floe with size $L \le 3\ell$ and with a thickness in most engineering application ranges (e.g., $t \ge 0.3\ \text{m}$), the radial crack initiation load is large enough to propagate the radial crack through the whole floe body. In contrast, when $G_f = 15\ \text{N/m}$, in the right column of Fig. 18, such size requirement is $L \le 2\ell$. In total, both columns in Fig. 18 demonstrate that when $L \le 2\ell$, for the typical ice material properties listed in Table A. 1, a nearly square shaped ice floe can fail at radial crack initiation. Fig. 18 also shows that a larger loading area tends to propagate longer radial cracks. However, such a difference is minor and would not influence the above general observation. Collectively, we are therefore able to draw a conclusion that for a nearly square ice floe smaller than 2ℓ, it can be treated as a finite size floe whose failure is controlled by radial crack initiation; otherwise, it can be conservatively treated as a semi-infinite ice floe.

In practice, depending on the exact material properties and ice thickness, the same comparison as in Fig. 18 can be utilised to quantify the optimum floe size in the downstream of ice management. If fracturing of ice floes is unavoidable for the protected vessel downstream, ensuring that most of the ice floes fail by radial-crack-initiation-controlled fracture can largely reduce its overall ice load.

Note also that the characteristic length ℓ is largely influenced by the ice thickness. Thicker ice means that there are larger ice floes (recalling the empirical relationship $\ell = 13.5t^{3/4}$) whose failure is controlled by radial crack initiation. In practice, this means that during ice management, it is possible to generate larger size ice floes downstream if thicker ice is encountered. The detailed quantification could be made according to the comparison made in Fig. 18. As a crude estimation without considering ice concentration and ice pressure, for typical ice material properties, it is reasonable to say that if managing most ice floes with a size $L \le 2\ell = 27t^{3/4}$, a much smaller ice breaking load can be expected for the protected structure. As an example, for a 2-metre-thick ice floe, managing it into an ensemble of ice floes with sizes less than 45 metres would be a mechanically preferred approach. According to the theoretical analysis in this paper, these floes can fail at radial crack initiation. Such a floe size requirement appears to be a reasonable estimation according to the 'floe size versus ice thickness' studies in the relevant ice management literature (Hamilton et al., 2011; Keinonen, 2008; Keinonen et al., 2007). In addition, corroboration can also be found in ice management practice. e.g., the ice management tests reported by Keinonen et al. (2006) in relation to a coring operation in the Central Polar Pack showed that two icebreakers (i.e., ODEN and Sovetskiy Soyuz) successfully managed the 2-metre-thick ice into floes with an average size of approximately 10~20 m and maximum floe sizes of 20~40 m; in the meantime, the protected vessel (i.e., Vidar Viking) was also recorded to have successfully 'split' ice floes of approximately 30~40 m in diameter.

5.4 Discussion about the size effect in radial crack propagation

Another trend that can be observed, particularly from Fig. 18, is that the maximum radial crack is inversely proportional to the ice thickness t; i.e., longer radial crack extension is expected at crack initiation for thicker ice. This is mainly because of Eq. (36), where the radial propagation load $F_{Z,\text{radial},1}/(\sigma_f t^2)$ is scaled with $t^{-3/8}$, while the value of $F_{Z,\text{radial},0}/\sigma_f t^2$ is independent of the ice thickness.

The same size effect was previously derived by Bažant (1992a; 1992b) while studying an infinitely large ice floe's fracture due to thermal effects or due to a concentrated load's penetration. Further interpretation of this peculiar $-3/8$ power scaling number was made by Li and Bažant (1994). This is because, according to classical LEFM, the nominal strength (defined as $\text{critical load}/(\text{characteristic length})^2$ (Bažant, 2005)) is scaled with $(\text{characteristic length})^{-1/2}$ (e.g., in Eq. (41), $F_Y/L^2 \propto L^{-1/2}$). Li and Bažant (1994) argued that ice thickness is a third dimension (Z – direction) for the radial crack propagation problem in Fig. 5, but it is formulated as a two-dimensional problem in the $x-y$ plane. Therefore, the ice thickness t should not be viewed as a characteristic length, and there is no violation of the classical scaling of $\text{norminal strength} \propto (\text{characteristic length})^{-1/2}$.

It should be noted that there is a fundamental assumption behind the derivation of Eq. (35) in this paper and its counterpart Eq. [21] in Bažant (1992a); i.e., the radial crack closure effect has been neglected. After including the crack closure effect, Bažant (2002) managed to derive that an infinite ice floe's nominal strength corresponding to its breakthrough is proportional to

$(\text{ice thickness})^{-1/2}$, as in Eq. [18] of Bažant (2002). As opposed to the fracture mechanics approach, Sodhi (1995; 1997) considered the crack closure effect by assuming 'plastic hinges' developed within radial cracks, and the theory of plastic upper limit (Chen and Han, 1988) has been employed to study the breakthrough of an ice cover. A thoughtful discussion regarding the scale effect was presented by Dempsey et al. (2000) without a general agreement among the participants. However, the inherent conflicts and criticisms within the crack closure effect do not influence our current study. This is because we are interested in the fracture of a 'finite' size ice floe, and less confinement (closure effect) is expected within the considered radial crack. Therefore, our derivation of Eq. (35) has a sound physically based assumption. Nevertheless, further experimental validation is needed to ensure Eq. (35)'s correctness in practice.

5.5 Discussion of the methodology and its limitations

One major contribution of this paper is the adopted methodology, based on which we have studied radial crack initiation and propagation within a finite size ice floe. Specifically, we have derived non-dimensional Eqs. (24) and (35), based on which rather simple but effective numerical set-ups were proposed and validated. The limitations of our quantitative comparisons appeared to be limited to special cases, such as a square shaped ice floe with deterministic loading radiuses $R = 0.2\ell, 0.1\ell$ and 0.05ℓ. In addition, our quantitative conclusions seem to be further confined by 'typical ice material properties', as in Table A. 1.

However, the derivations of Eqs. (24) and (35) are universal for arbitrary ice floe shapes. In addition, the proposed and validated numerical set-up is applicable for an arbitrary symmetric geometry under various types of symmetric loading; i.e., the proposed methodology can easily be extended to other ice floe geometry and loading cases.

6 Conclusion

Out-of-plane failure of an ice floe has been studied extensively for decades. However, previous studies are based primarily on a theoretical idealisation of treating the concerned ice floe as either an infinite or semi-infinite thin plate on a Winkler-type elastic foundation. A literature review shows that a knowledge gap exists in terms of the failure of a finite size ice floe. Theoretically, the failure of a finite size ice floe is a more general scenario. Practically, a typical ice field in the Arctic is far from continuous, and recent Arctic offshore structures are usually supported by ice management. Therefore, the failure pattern, failure process and failure load of a finite size ice floe interacting with a sloping structure is of practical importance. Based on a detailed literature review relating to previous studies on out-of-plane failure of infinite and semi-infinite ice floes, we conservatively categorised two different scenarios under which a finite size ice floe would fail: Scenario #1: floes that fail at radial crack initiation, and Scenario #2: floes that can be treated as semi-infinite ice floes.

To quantify the boundary between these two scenarios, a complete methodology was proposed and presented sequentially in this paper. This methodology involves the non-dimensionalisation of controlled PDEs and establishing simple but effective numerical models. Using the proposed methodology, we studied radial crack initiation and propagation separately. The extracted radial crack initiation and propagation loads were compared to determine our scenario of interest: radial-crack-initiation-controlled fracture.

Recalling the main objectives of this paper, based on our studies and calculated results, the following conclusions can be drawn.

1) Regarding establishment of a verified methodology to study radial crack initiation and propagation within a finite size ice floe:
   - Non-dimensional Eq. (24), together with its numerical calculation set-up described in Section 3.1.2, was validated against Nevel's (1965) and Lubbad and Løset's (2011) solutions. Its main results, presented in Fig. 9, can be used to estimate the radial crack initiation load for similar loading cases (i.e., a nearly square shaped ice floe and a loading area with radius $R = 0.2\ell, 0.1\ell$ and 0.05ℓ).
   - Irwin's (1956) energy approach was adopted to derive the radial crack propagation load, as in Eq. (35), in a non-dimensional form together with its numerical calculation set-up described in Section 3.2.2. As a benchmark test, a similar problem (i.e., in-plane splitting of an ice floe) with the same energy-approach based derivation and with a similar numerical set-up was validated against analytical solutions. The results verified the correctness of Eq. (35) and its numerical set-up for studying radial crack propagations.
   - With two different particularly assumed loading scenarios (i.e., rectangular and half-circular loading areas), we studied the physical size effect on radial crack initiation and propagation loads. For a square ice floe with physical length $L \geq 9\ell$, its radial crack initiation load has already converged to that of a semi-infinite ice plate solution (e.g., (Nevel, 1965) and (Lubbad and Løset, 2011)) . It was also found that during radial crack propagation, stress concentration does not always occur at the radial crack tip. As an ice floe's physical size increases (e.g., $L \geq 4\ell$), stress concentration starts to occur at the location where a circumferential crack would initiate.
   - For other more general floe geometry and loading conditions, the same non-dimensional Eqs. (24) and (35), in combination with newly adapted numerical set-ups, can be utilised to study radial crack initiation and propagation within a finite size ice floe.

2) Regarding the floe size requirement for radial-crack-initiation-controlled fracture:
   - For typical ice material properties (e.g., those listed in Table A. 1), a square ice floe with its physical length $L \leq 2\ell$ tends to fail at radial crack initiation under an edge load.
   - Considering that radial-crack-initiation-controlled fracture of an ice floe required less effort (i.e., a smaller ice load exerted on a sloping structure) compared with continuous circumferential crack formations, from a mechanically preferred point of view and without considering floe concentration and its confinement, it is suggested to produce ice floes of size $L \leq 2\ell \approx 27t^{3/4}$ downstream of an ice management operation to reduce the possible ice breaking load on the protected vessel.

Acknowledgements

The authors would like to thank the Norwegian Research Council through the project 200618/S60-PetroRisk and the SAMCoT CRI for financial support. The authors are grateful for the interesting knowledge learned from and fruitful discussions with Professor John Dempsey

and Dr. Devinder Sodhi. In addition, valuable discussions with PhD student Marat Kashafutdinov are highly appreciated.

Appendix A Inputs for numerical calculations with FEM

For a particular problem applying FEM analysis, it is generally required to set up the exact geometric size, material properties, boundary conditions and loading amplitudes. In the current paper, we have derived non-dimensional formulae such that the intended FEM calculation results are non-dimensional values independent of exact geometric size, material properties, and loading amplitude. However, a numerical calculation requires numbers. Here, we present the input numbers we have utilised in all of the FEM analyses.

Table A. 1 Inputs for FEM analysis of radial crack initiation (Fig. 4) and propagation (Fig. 6)

Input value	Description
$t = 0.01$	We choose this value simply for numerical accuracy reasons (e.g., Hibbitt et al. (2013) propose that accurate numerical results regarding thin plate bending can be achieved with a plate thickness $t \le \ell/15$; for the chosen value 0.01, this condition can be fulfilled several times better).
$k = \rho_w g = 1025 \times 9.81 = 10055.25$	This is the physical elastic foundation modulus.
$E = 5.5 \times 10^9$ Pa, $\nu = 0.3$	This leads to the flexural rigidity $D = 503.663$ and $\ell = 0.4731$ according to Eq. (6) and the definition of D in Eq. (6).
$K = n^4$	According to Eqs. (16), this is the major input controlling the size of an ice floe.
$\Delta l_{\max}/5 = \Delta l_{\min} = \ell/100$	$\Delta l_{\max}$ and $\Delta l_{\min}$ represent the maximum and minimum mesh sizes in Fig. 4 and Fig. 6. After several numerical trials, the numerical results (i.e., maximum Mises stress) converge with the minimum mesh size $\Delta l_{\min}$, which is smaller than $\ell/50$. Here, we choose an even smaller mesh size that equals $\ell/100$ to ensure the convergence, which is confirmed in both Figs. 8 and 9.
$F_Z = 1$	According to the middle term of Eq. (23), the load magnitude can be an arbitrary value; we consistently choose $F_Z = 1$ in all numerical calculations.
$\sigma_f = 550$ kPa	Flexural strength of considered ice.
$\rho_i = 920$ kg/m^3	Ice density.

For the benchmark test in Fig. 11b, we have inputted the same material properties as in Table A. 1. Because there is only one length scale L in the problem of Fig. 11, we have taken the biased mesh as $\Delta l_{\max}/5 = \Delta l_{\min} = L/1000$. In addition, according to Eq. (38), we have employed $F_Y = 1$ as a numerical input, and this value allows for an easier calculation of the corresponding $C(\alpha)$ from the calculated $u_0(\alpha)$.

Appendix B Derivations of the size effect of a finite size ice floe's bending problem

The derivation of Eq. (35) is presented herein. Similar derivations can be found in the literature for an infinite ice floe (Bažant, 1992a; Bažant, 1992b). For the finite size ice floe bending problem, after normalising the controlling Partial Differential Equation (PDE in Eq. (6)) by its physical length L and after a series of derivations in the paper, we arrive at Eq. (34), which is repeated in Eq. (45).

$$G_f = \frac{F_{Z,\text{radial},1}^2 L}{2tD} \frac{dW_0(\alpha)}{d\alpha} \tag{45}$$

We can equivalently introduce the characteristic length ℓ to normalise Eq. (45), as in Eq. (46).

$$G_f = \frac{F_{Z,\text{radial},1}^2}{2tD} \frac{dW_0(\alpha)}{d\alpha} \frac{L}{\ell} \ell \tag{46}$$

In Eq. (46), by replacing $L/\ell = n$ and explicitly expressing ℓ according to Eq. (7), we can obtain Eq. (47).

$$G_f = \frac{nF_{Z,\text{radial},1}^2}{2tD} \frac{dW_0(\alpha)}{d\alpha} \frac{D^{1/4}}{k^{1/4}} = \frac{nF_{Z,\text{radial},1}^2}{2t} \frac{dW_0(\alpha)}{d\alpha} \frac{1}{k^{1/4}} \frac{1}{D^{3/4}} \tag{47}$$

Replacing $D = Et^3/[12(1-\nu^2)]$ in Eq. (47), we can obtain Eq. (48).

$$\begin{aligned} G_f &= \frac{nF_{Z,\text{radial},1}^2}{2t} \frac{dW_0(\alpha)}{d\alpha} \frac{1}{k^{1/4}} [\frac{12(1-\nu^2)}{E}]^{3/4} \frac{1}{t^{9/4}} \\ &= \frac{12^{3/4}}{2k^{1/4}} n \frac{F_{Z,\text{radial},1}^2}{t^4} \frac{dW_0(\alpha)}{d\alpha} [\frac{(1-\nu^2)}{E}]^{3/4} \frac{1}{t^{-3/4}} \end{aligned} \tag{48}$$

Rearranging Eq. (48) and solving for $F_{Z,\text{radial},1}/t^2$, we can obtain Eq. (49).

$$\frac{F_{Z,\text{radial},1}}{t^2} = \frac{2^{1/2} k^{1/8}}{12^{3/8}} \sqrt{G_f} [\frac{E}{(1-\nu^2)}]^{3/8} [n \frac{dW_0(\alpha)}{d\alpha}]^{-1/2} t^{-3/8} \tag{49}$$

Thus, Eq. (35) is derived.

References

Anderson, T.L., 2005. Fracture mechanics: fundamentals and applications. CRC press.

API_RP2, 1995. Recommended Practice for Planning, Designing, and Constructing Structures and Pipelines for Arctic Conditions. American Petroleum Institute.

Ashton, G.D., 1986. River and lake ice engineering. Water Resources Publication.

Bažant, Z.P., 1992a. Large-scale fracture of sea ice plates, Proc., 11th IAHR Ice Symposium, Banff, Alberta. Dept. of Civil Engineering, Univ. of Alberta, Edmonton, pp. 991-1005.

Bažant, Z.P., 1992b. Large - scale thermal bending fracture of sea ice plates. Journal of Geophysical Research: Oceans (1978 – 2012), 97(C11): 17739-17751.

Bažant, Z.P., 2002. Scaling of sea ice fracture-Part I: Vertical penetration. Journal of applied mechanics, 69(1): 11-18.

Bažant, Z.P., 2005. Scaling of structural strength. Butterworth-Heinemann.

Bažant, Z.P. and Kim, J., 1998a. Size Effect in Penetration of Sea Ice Plate with Part-Through Cracks.I: Theory. Journal of engineering mechanics, 124(12): 1310-1315.

Bažant, Z.P. and Kim, J., 1998b. Size Effect in Penetration of Sea Ice Plate with Part-Through Cracks.II: Results. Journal of engineering mechanics, 124(12): 1316-1324.

Bažant, Z.P. and Li, Y.N., 1993. Fracture Analysis of Penetration Through Floating Sea Ice Plate and Size Effect. ASME APPLIED MECHANICS DIVISION-PUBLICATIONS-AMD, 163: 131-131.

Bažant, Z.P. and Li, Y.N., 1994. Penetration fracture of sea ice plate: Simplified analysis and size effect. Journal of engineering mechanics, 120(6): 1304-1321.

Bažant, Z.P. and Planas, J., 1998. Fracture and size effect in concrete and other quasibrittle materials. CRC.

Carter, D. and Michel, B., 1971. Lois et mecanismes de l'apparente fracture fragile de la glace de riviere et de lac, University of Laval.

Chen, W.F. and Han, D.J., 1988. Plasticity for structural engineers. Springer-Verlag (New York).

Croasdale, K.R. and Cammaert, A.B., 1994. An improved method for the calculation of ice loads on sloping structures in first-year ice. Power Technology and Engineering (formerly Hydrotechnical Construction), 28(3): 174-179.

DeFranco, S.J. and Dempsey, J.P., 1994. Crack propagation and fracture resistance in saline ice. Journal of Glaciology, 40(136): 451-462.

Dempsey, J.P., DeFranco, S.J., Blanchet, D. and Prodanovic, A., 1994. Mechanisms of fracture of sea ice. Hydrotechnical Construction, 28(3): 164-168.

Dempsey, J.P., Slepyan, L.I. and Shekhtman, I.I., 1995. Radial cracking with closure. International journal of fracture, 73(3): 233-261.

Dempsey, J.P., Sodhi, D.S. and Bažant, Z., 2000. Discussion of "Size Effect in Penetration of Sea Ice Plate with Part-Through Cracks. I: Theory. II: Results" by Devinder S. Sodhi. Journal of engineering mechanics, 126(4): 438-440.

Dempsey, J.P. and Zhao, Z.G., 1993. Elastohydrodynamic response of an ice sheet to forced sub-surface uplift. Journal of the Mechanics and Physics of Solids, 41(3): 487-506.

Gold, L.W., 1971. Use of ice covers for transportation. Canadian Geotechnical Journal, 8(2): 170-181.

Hamilton, J., Holub, C., Blunt, J., Mitchell, D. and Kokkinis, T., 2011. Ice Management for Support of Arctic Floating Operations, OTC Arctic Technology Conference.

Hertz, H., 1884. On the equilibrium of floating elastic plates. Wiedemann's Ann, 22: 449.

Hibbitt, Karlsson and Sorensen, 2013. ABAQUS/Standard user's manual, 1. Hibbitt, Karlsson & Sorensen.

Irgens, F., 2008. Continuum mechanics. Springer Verlag, Berlin Heidelberg.

Irwin, G.R., 1956. Onset of fast crack propagation in High Strength Steel and Aluminum Alloys, Sagamore Research Conference Proceedings, pp. 289-305.

ISO/FDIS/19906, 2010. Petroleum and natural gas industries - Arctic offshore structures,International Standard, International Standardization organization, Geneva, Switzerland,.

Keinonen, A., 2008. Ice Management for Ice Offshore Operations, Proceedings of the Offshore Technology Conference. Houston, TX.

Keinonen, A., Matin, E., Neville, M. and Gudmestad, O.T., 2007. Operability of an Arctic Drill Ship in Ice With and Without Ice Management, Proceedings of the 19th annual Deep Offshore Technology International Conference & Exhibition (DOT).

Keinonen, A., Shirley, M., Liljestrom, G. and Pilkington, R., 2006. Transit and Stationary Coring Operations in the Central Polar Pack. Icetech, Proceedings of the Calgary, Canada.

Kerr, A.D., 1976. The bearing capacity of floating ice plates subjected to static or quasi-static loads. Journal of Glaciology, 17: 229-268.

Kerr, A.D., 1996. Bearing capacity of floating ice covers subjected to static, moving, and oscillatory loads. Applied Mechanics Reviews, 49(11): 463-476.
Kerr, A.D. and Kwak, S.S., 1993. The semi-infinite plate on a Winkler base, free along the edge, and subjected to a vertical force. Archive of Applied Mechanics, 63(3): 210-218.
Kerr, A.D. and Palmer, L.C.W., 1972. The deformations and stresses in floating ice plates. Acta Mechanica, 15(1-2): 57-72.
Kotras, T.V., Baird, A.V. and Naegle, J.N., 1983. Predicting Ship Performance in Level Ice. Transactions - Society of Naval Architects and Marine Engineers, Volume 91, 1983. SNAME, New York, NY, USA, pp. 329-349.
Langhorne, P.J., Stone, K.J.L. and Smith, C.C., 1999. The bearing capacity of saline ice sheets: centrifugal modelling. Canadian Geotechnical Journal, 36(3): 467-481.
Li, Y.N. and Bažant, Z.P., 1994. Penetration fracture of ice plate: 2D analysis and size effect. Journal of engineering mechanics, 120(7): 1481-1498.
Lu, W., 2010. Ice and conical structure interactions. Student thesis Thesis, Norwegian University of Science and Technology, Trondheim, 102-104 pp.
Lu, W., Lubbad, R., Høyland, K.V. and Løset, S., 2014. Physical model and theoretical model study of level ice and wide sloping structure interactions. Cold Regions Science and Technology, 1: 1-33.
Lu, W., Lubbad, R. and Løset, S., (Accepted on November 12th 2014). In-plane fracture of an ice floe: a theoretical study on the splitting failure mode. Cold Regions Science and Technology, DOI: 10.1016/j.coldregions.2014.11.007.
Lu, W., Løset, S. and Lubbad, R., 2012. Ventilation and backfill effect during ice-structure interactions. In: Li and Lu (Editors), The 21st IAHR International Symposium on Ice, Dalian, China, pp. 826-841.
Lubbad, R. and Løset, S., 2011. A numerical model for real-time simulation of ship-ice interaction. Cold Regions Science and Technology, 65(2): 111-127.
Lubbad, R., Moe, G. and Løset, S., 2008. Static and Dynamic Interaction of Floating Wedge-Shaped Ice Beams and Sloping Structures. 19th IAHR Internatioanl Symposium on Ice: 179-189.
Masterson, D.M., 2009. State of the art of ice bearing capacity and ice construction. Cold Regions Science and Technology, 58(3): 99-112.
Mayne, D.C., 2007. Level ice and rubble actions on offshore conical and sloping structures. Doctoral Thesis, University of Calgary, Calgary, Alberta, 190 pp.
Michel, B., 1978. Ice mechanics. LES PRESSES DE L'UNIVERSITE LAVAL, Quebec, 499 pp.
Milano, V.R., 1972. Ship resistance to continuous motion in ice, Stevens Institute of Technology.
Mulmule, S.V. and Dempsey, J.P., 2000. LEFM size requirements for the fracture testing of sea ice. International journal of fracture, 102(1): 85-98.
Nevel, D.E., 1958. The theory of a narrow infinite wedge on an elastic foundation, U. S. Army Snow Ice and Permafrost Research Establishment, Corps of Engineering.
Nevel, D.E., 1961. The narrow free infinite wedge on an elastic foundation, U. S. Army Snow Ice and Permafrost Research Establishment, Corps of Engineering.
Nevel, D.E., 1965. A semi-infinite plate on an elastic foundation, U. S. Army Snow Ice and Permafrost Research Establishment, Corps of Engineering.
Nevel, D.E., 1992. Ice forces on cones from floes, IAHR Symposium, 11th, pp. 1391-1404.
Panfilov, D., 1960. Experimental investigation of the carrying capacity of a floating ice plate. Izvestia Vsesojuznogo Nauchno-Issledovatelsskogo Instituta Gidratekhniki, 64: 80-8.
Sanderson, T.J.O., 1988. Ice mechanics and risks to offshore structures.
Schulson, E.M. and Duval, P., 2009. Creep and fracture of ice, 1. Cambridge University Press, Cambridge, 190-211 pp.
Shkhinek, K. and Uvarova, E., 2001. Dynamics of the ice sheet interaction with the sloping structure.
Sodhi, D.S., 1995. Breakthrough loads of floating ice sheets. Journal of cold regions engineering, 9: 4.
Sodhi, D.S., 1996. Deflection Analysis of Radially Cracked Floating Ice Sheets, OMAE, pp. 97-102.
Sodhi, D.S., 1997. Vertical penetration of floating ice sheets. International Journal of Solids and Structures, 35(31-32): 4275-4294.
Squire, V.A., Hosking, R.J., Kerr, A.D. and Langhorne, P.J., 1996. Moving loads on ice plates, 45. Springer.
Timoshenko, S., Woinowsky-Krieger, S. and Woinowsky, S., 1959. Theory of plates and shells, 580. McGraw-Hill New York.
Ventsel, E. and Krauthammer, T., 2001. Thin plates and shells: theory: analysis, and applications. CRC press, New York.
Wadhams, P. and Horne, R.J., 1980. An analysis of ice profiles obtained by submarine sonar in the Beaufort Sea. Journal of Glaciology, 25: 401-424.
Westergaard, H., 1926. Stresses in concrete pavements computed by theoretical analysis. Public Roads.
Wyman, M., 1950. Deflections of an infinite plate. Canadian Journal of Research, 28(3): 293-302.

Yang, W.Y., Cao, W., Chung, T.S. and Morris, J., 2005. Applied numerical methods using MATLAB. John Wiley & Sons.

Appendix 3 Competition of failure modes

This appendix includes the paper submitted to Journal of Cold Regions Science and Technology (see below). By the time the thesis is submitted, the paper is under review.

- Lu, W., Lubbad, R. and Løset, S., (Submitted in September, 2014). Fracture of an ice floe: Local out-of-plane flexural failures versus Global in-plane splitting failure. Cold Regions Science and Technology.

Appendix III

Fracture of an ice floe: Local out-of-plane flexural failures versus global in-plane splitting failure

Wenjun Lu[1] **Raed Lubbad** **Sveinung Løset** **Marat Kashafutdinov**

Sustainable Arctic Marine and Coastal Technology (SAMCoT), Centre for Research-Based Innovation (CRI)

Norwegian University of Science and Technology (NTNU), Trondheim, Norway

[1] Corresponding author
E-mail address: wenjun.lu@ntnu.no (Wenjun Lu)

Abstract

Sloping structures have gained increasing interests in recent years due to their capability of breaking the incoming level ice in a dominant bending failure mode. However, 'level ice' is a theoretical simplification. A typical ice field in the Arctic is not continuous. Rather, it frequently consists of discontinuous ice features, such as ridges, leads and ice floes of varying sizes, which form a broken ice field. As Arctic exploration and exploitation advance into deeper waters, floating structures are usually employed with support from ice management operations, i.e., these structures primarily operate in a broken ice field. Therefore, a general approach for the evaluation of ice - sloping structure interactions, in which the floe size is considered to be a major variable, is proposed in this paper. Two failure modes have been frequently observed during floe ice - sloping structure interactions, i.e., the local out-of-plane flexural failure mode and the global in-plane splitting failure mode. This paper investigates the two failure modes and develops criteria for their occurrence. The present study assumes that the occurrence of one failure mode alleviates/supresses the occurrence of the other failure mode. Based on theoretical analyses the out-of-plane flexural failure mode can be categorised as: 1) direct rotation of a small ice floe, 2) radial/circumferential cracking of a finite size ice floe, and 3) circumferential crack formation within a semi-infinite ice floe. These categories together with the in-plane failure mode make a total of four possible scenarios for floe ice failures.

The first contribution of this paper is the search for analytical closed-form solutions to evaluate the occurrence of any of the aforementioned scenarios. Substantial efforts have focused on deriving an analytical solution to the deformation of a finite size ice floe with free edges and resting on a Winkler-type elastic foundation. This new solution was employed to attain a conservative estimation of the critical force that causes the radial/circumferential cracking failure scenario. Previously published analytical solutions were compiled to examine the critical force that causes the remaining three failure scenarios, i.e., direct rotation, failure of a semi-infinite ice floe and the splitting failure mode.

With analytical solutions to the critical force that causes the four failure scenarios available, it is therefore at our disposal to quantify their competitions. Within the context of floe ice - sloping structure interactions, it is found that for typical ice material properties, with a fracture energy of 1 N/m, a global splitting crack can travel through nearly square-shaped ice floes which are smaller than 70 m, 300 m, 1.1 km, and 2.5 km for ice thicknesses of 0.5, 1, 2 and 3 m, respectively. In addition to ice material properties, floe size and ice thickness are important for determining the salient failure mode. Therefore, a failure map is quantitatively constructed according to these two variables. Generally, thicker ice has a higher tendency to fail in global splitting failure mode for a given contact property, e.g., thicker ice features demand a significantly larger floe size to maintain the local bending failure mode. Practically, these analytical solutions can be easily implemented within a multi-body dynamic simulator to examine the performance of sloping structures in an ice field covering a large temporal and spatial scale.

Keywords:

Ice structure interactions

Splitting failure mode

Local bending failure

Failure map

1 Introduction

When considering global ice actions on structures, three limiting mechanisms have to be evaluated according to the code (API_RP2, 1995; ISO/FDIS/19906, 2010), including 1) *limit stress*, which denotes the failure of an ice feature in various failure modes; 2) *limit energy*, which characterises the kinetic energy of the ice feature; and 3) *limit force*, which describes the environmental driving force of an ice feature. To obtain a 'rational' estimation of ice loads on structures, these limiting mechanisms, in principal, should be evaluated separately and collectively in combination with probabilistic theory. However, because of the often scarce information and the varying nature of the detailed ice conditions and also to be conservative, most engineering designs directly adopt the 'limit stress' criterion. Utilising this methodology as a theoretical study of the fracture of an ice floe, this paper focuses on cases purely under the 'limit stress' scenarios. Further application of the developed theories with all three limiting mechanisms will be studied in a separate paper with the support of a multi-body dynamics simulator (Lubbad and Løset, 2011).

Within the 'limit stress' mechanism, many failure modes (e.g., crushing, bending, buckling, shearing, spalling and splitting) exist depending on the characteristics of the considered ice feature (e.g., ice thickness, floe size, concentrations and ice material strength), structural characteristics (e.g., sloping, vertical, wide or narrow structures), and interaction details (e.g., aspect ratio, interaction rate and contact properties) (API_RP2, 1995; Hallam, 1986; ISO/FDIS/19906, 2010; Løset et al., 2006; Michel, 1978; Palmer and Croasdale, 2013; Palmer et al., 1983; Sanderson, 1988; Timco, 1987). Historically, it is the failure modes such as crushing, spalling, bending, and buckling that are mostly studied. The reason is partly because these failure modes usually produce higher ice loads compared with global splitting failure and partly due to an implicit priori assumption of a 'level ice' condition, which rules out the splitting failure modes. The term 'level ice' is frequently used to describe a large uniform ice floe, in which global failure is less likely to occur during ice - sloping structure interactions. However, a typical ice field in the Arctic is not continuous, it is typically composed of discontinuous features such as ice ridges, leads and ice floes of various sizes (e.g., 10 m to 10 km according to Leppäranta (2011)), which form a broken ice field. As Arctic exploration and exploitation advance into deeper waters, floating Arctic offshore structures are usually preferred with support from 'ice management' operations due to limitations in mooring lines or dynamic positioning (DP) (Palmer and Croasdale, 2013). This is to say, for most of the time, these structures are operating in a broken ice field with minimal confinement. Therefore, the failure modes of an ice floe, which has a finite size with free boundaries, should be revisited.

Within the context of floe ice - sloping structure interactions, two dominant failure modes from a new perspective are anticipated: the out-of-plane flexural-type failure of an ice floe and the in-plane splitting failure of an ice floe. Based on field observations regarding icebreakers transiting in a broken ice field, these two failure modes are frequently observed. A competing mechanism between these two failure modes is hypothesised, i.e., the occurrence of one failure mode supresses/alleviates the presence of the other failure mode.

The first contribution of this paper is the analytical evaluation of these two frequently observed failures modes to theoretically establish the competing mechanisms. The analytical evaluation is driven by the long-term implementation of the pertinent framework and derived formulas into the multi-body dynamic simulator (Lubbad and Løset, 2011) to assess the performance of a sloping structure that operates in a level/broken ice field covering a large spatial and temporal

scale, e.g., an ice management operation may last for several hours on a spatial scale that extends approximately several kilometres. Among these two frequently observed failure modes, the in-plane splitting failure of an ice floe has been analytically studied in a previous paper (Lu et al., (Accepted on November 12th 2014)). Out-of-plane flexural type failures, however, are further complicated by floe size. Generally, three different failure scenarios can be identified—Scenario #1: direct rotation of a small ice floe without fracture; Scenario #2: radial/circumferential cracking of a finite size ice floe; and Scenario #3: circumferential cracking forming within a semi-infinite ice floe. From numerical studies of radial crack initiation and propagation within a square-shaped finite size ice floe, Lu et al. ((submitted in July, 2014)) have conservatively identified the size border between Scenarios #2 and #3. As an extension, this paper focuses on obtaining the corresponding analytical solutions of Scenario #2 based on relevant studies.

With known analytical solutions for different failure scenarios, the second contribution of this paper is the established framework, in which the competition among different failure scenarios within a relatively 'open' ice condition was investigated. This analytical framework can help us to construct a failure map to determine the corresponding failure patterns and failure loads of an ice floe depending on the floe size, the ice thickness, the material strength, and the contact properties.

To achieve the previously mentioned research goals, we have performed the following tasks: 1) derivation and recommendation of analytical solutions for the out-of-plane flexural failure of a finite size ice floe; 2) compilation of existing analytical solutions for the in-plane-splitting failure of an ice floe, the direct rotation of a small ice floe and the out-of-plane failure of a semi-infinite ice floe; 3) investigation of the competition between out-of-plane flexural failure and in-plane splitting failure for varying floe sizes, ice thicknesses, and contact properties.

2 Problem description

2.1 'Local' out-of-plane flexural failure and 'global' in-plane splitting failures

In the context of a sloping structure interacting with a large ice floe, an ice floe fractures at different scales. In the vicinity of the contact zone, a layer of ice fractures in crushing failure mode. This fracturing process occurs in the order of the grain sizes (e.g., 3-15 mm). Afterwards, proportional to the contact area, an increasing contact force is transferred to the ice floe. This contact force leads to either a local failure mode or a global failure mode. Here, the terms 'local' and 'global' are used to emphasise the spatial variations in an ice floe's fracturing process.

In this paper, 'local failure' is used to describe fracturing processes that occur within a distance that is approximately 30 times the ice thickness (i.e., approximately two times the characteristic length of a plate on an elastic foundation). The majority of the previously mentioned failure modes (i.e., crushing, bending, buckling, shearing, and spalling) occur at this scale. Due to the brittle nature of ice materials at a high loading rate, the traditional strength theory is usually applied to these local failure modes. The considered ice feature fails instantly while the maximum stress within an ice floe attains its material strength. From a fracture mechanics point of view, these local failure modes are controlled by fracture initiation. For sloping structures in this paper, we focus on local bending failure mode, which is considered to be a type of local out-of-plane flexural failure.

The ‘global failure’ of an ice floe is specifically utilised to describe the splitting failure mode in this paper. The splitting failure mode is considered to be an in-plane Mode I fracture, which has been explored in a separate paper (Lu et al., (Accepted on November 12th 2014)). The splitting crack can easily travel an order of magnitude larger than the structural size (Bhat et al., 1991). These large cracks are generally controlled by fracture propagation. A fracture mechanics approach is required to calculate the driving force behind crack propagation (Bhat, 1988; Bhat et al., 1991; Dempsey et al., 1994).

2.2 Observations of two dominant failure modes

During floe ice - sloping structure interactions, both the local bending failure and global splitting failure are frequently observed in physical model tests (refer to Fig. 1a) and in the field (refer to Fig. 1b).

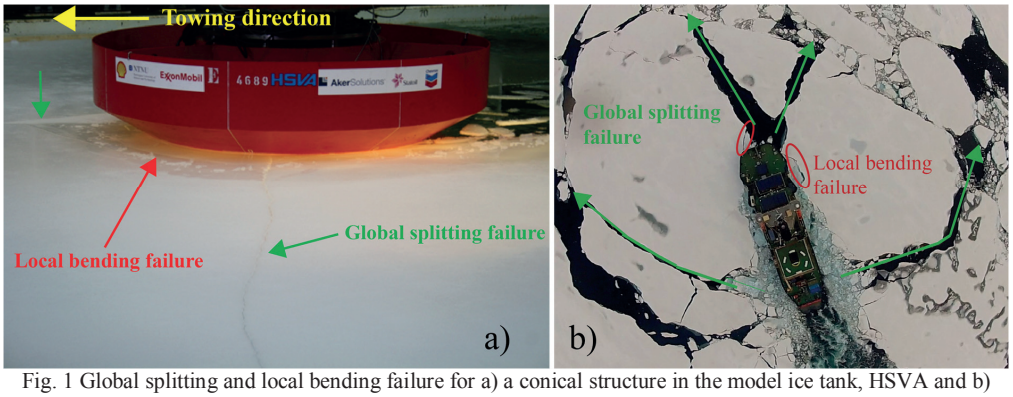

Fig. 1 Global splitting and local bending failure for a) a conical structure in the model ice tank, HSVA and b) Oden in the Greenland Sea (September, 2012).

To model a level ice condition, physical model tests in an ice tank usually strive to supress the splitting failure mode by either tempering the ice (i.e., mainly to scale the flexural strength of the ice and partially to make the model ice easier to fail in local bending failure mode) or adding confinement along the boundaries to suppress global splitting failure. When boundary conditions permit, splitting failure occurs. Aerial photos of the interaction of Oden with finite size ice floes (e.g., in Fig. 1b) highlights the frequent presence of global splitting failure during a voyage into the Greenland Sea between eastern Greenland and Svalbard during the summer (Lubbad et al., 2012; Lubbad et al., 2013).

Competition exists between continuous local bending failure and global splitting failure. This competition is documented by a video camera system installed on the bow of the KV Svalbard in a voyage to the Northern Greenland Sea in March (Lubbad, 2012). During this period of time, first-year sea ice forms a relatively large and uniform ice field. The icebreaker primarily travelled within a large ice floe with continuous local bending failure (refer to Fig. 2a). This dominant flexural failure mode is featured by the initial contact with ice that is crushed and the subsequent formation of cusp- and wedge-shaped ice blocks. When conditions permit (e.g., relatively small ice floe or an ice floe with minimal confinement), the global splitting failure tends to overtake dominant local failure mode. The continuous local bending failures were subsequently alleviated and the structure tended to travel within the ‘lead’ created by the global splitting. The splitting failure was presumed to act as a load-releasing mechanism compared

with continuous local failure. This notion is limited to a relatively 'open' ice condition, e.g., in an ice field with a high ice concentration or ice pressure (Croasdale, 2012), the global ice resistance is not expected to decrease even if the splitting of an ice floe occurs. In this paper, an open and broken ice field with minimal confinement is considered.

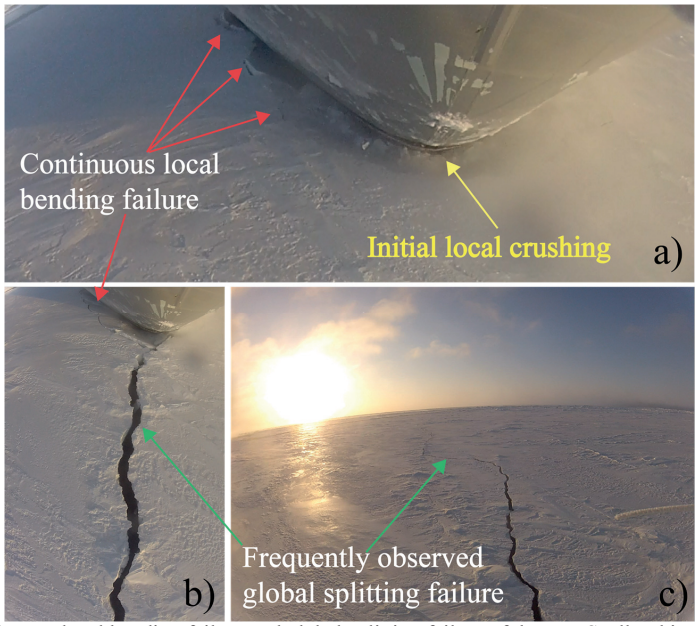

Fig. 2 Continuous local bending failure and global splitting failure of the KV-Svalbard in the Northern Greenland Sea (March, 2012).

2.3 Holistic model for floe ice - sloping structure interactions

As a sloping structure/icebreaker impacts with an ice floe, as shown in Fig. 3(1) to (2), a complicated stress field forms within the contact area. From a global perspective, three different force components can be isolated with the global coordinate system (refer to Fig. 3(3)): the vertical force component F_Z produces a potential out-of-plane flexural failure mode; a pair of horizontal forces F_Y produce a potential in-plane splitting failure; and the in-plane force component F_X increases the compression within the ice floe. The actual failure patterns and failure loads[2] are jointly affected by these global force components and the local stress field. As a simplification, we have decoupled these global force components and separately analysed them in previous relevant publications (Lu et al., (Accepted on November 12th 2014); Lu et al., (submitted in July, 2014)).

In this paper, we focus on the force components F_Z and F_Y, which are considered to be the direct source for the dominant out-of-plane failure and in-plane failure, respectively. This paper focuses on the search for their respective analytical solutions; their potential competition is emphasised, as shown in Fig. 3(4).

[2] The required force component's magnitude, which produces the corresponding failure mode.

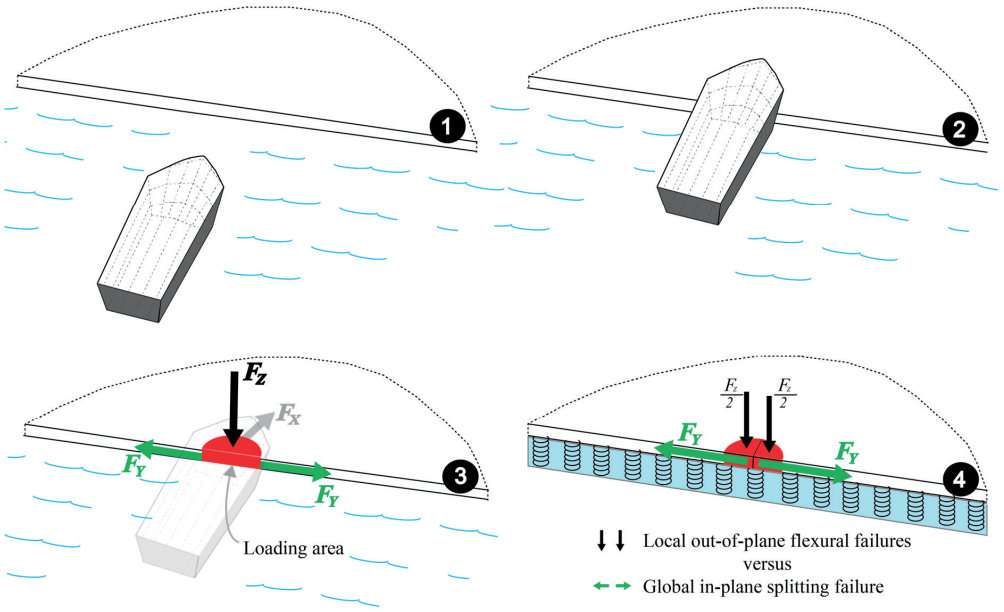

Fig. 3 Simplified global contact force components and their subsequent failures.

If a sloping structure interacts with a relatively large ice floe (e.g., level ice), if an ice floe's lateral boundary confinement is significant, or if ice-structure contact produces a dominant vertical force component, the ice floe's dominant failure mode is expected to be the local out-of-plane flexural-type failure, as shown in Fig. 4. On the other hand, for a relatively small ice floe, a floe with limited/no lateral confinement, or the contact property that induces a significantly large horizontal splitting force pair, the ice floe's dominant failure mode is expected to be in a splitting failure mode, as shown in Fig. 5.

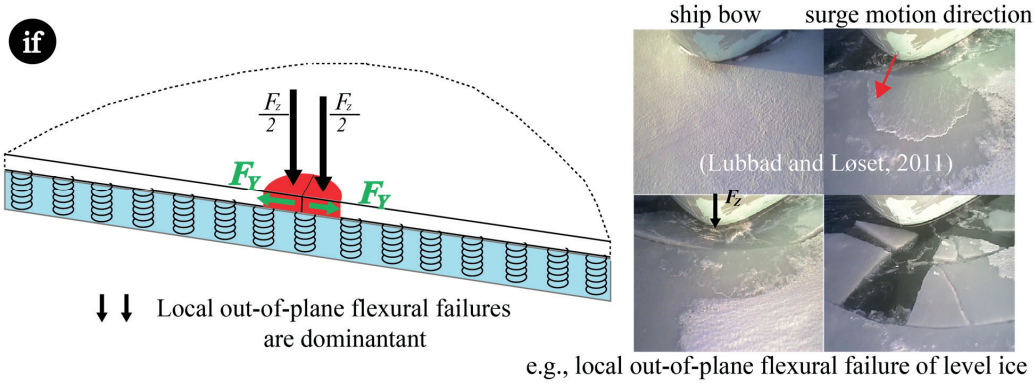

Fig. 4 Dominant local out-of-plane flexural failure.

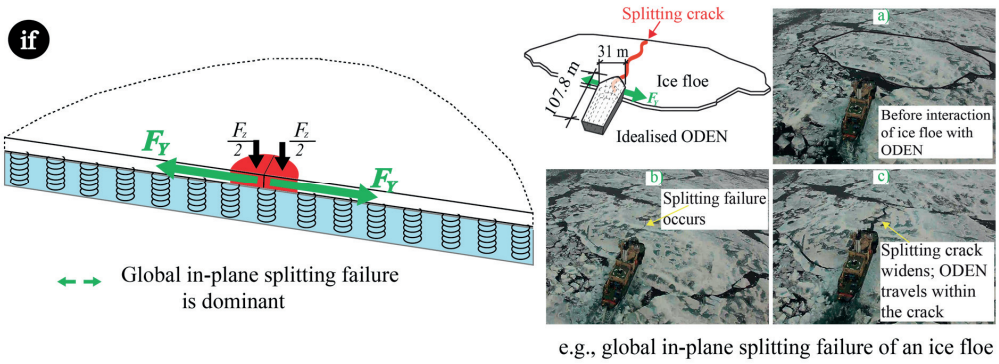

Fig. 5 Dominant global in-plane splitting failure.

However, the local out-of-plane flexural failure is not as straightforward as illustrated in Fig. 4. Depending on the floe size, Fig. 6 illustrates three out-of-plane flexural failure scenarios for a nearly square-shaped ice floe.

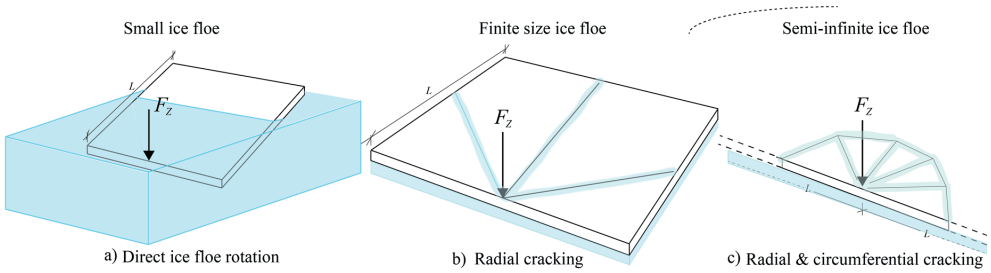

Fig. 6 Conceptual plots of three out-of-plane flexural-type failure scenarios for a square-shaped ice floe.

According to Fig. 6a, a sufficiently small ice floe can be directly tilted by the vertical force F_Z prior to the occurrence of a significant fracture. Strictly speaking, this is not a material failure mechanism. From the perspective of ice load calculations, once the floe rotation process enables the inundation, the vertical force F_Z ceases to increase (if no rubble accumulates beneath the ice floe as assumed in this paper). For theoretical completeness, we consider this situation to be one of the out-of-plane flexural failures. Relevant studies to this scenario have been conducted under the terminology 'ice rotating phase' in several literatures dealing with ice and sloping structure interactions (Lu et al., 2014; Lu et al., 2013; Lu et al., 2012b; Valanto, 2001).

As the floe size continues to increase and if the flexural-type failure is inevitable, the ice floe's failure patterns are significantly influenced by its free boundaries, as demonstrated by the scenario in Fig. 6b for a square-shaped ice floe. Lu et al. ((submitted in July, 2014)) examined a radial crack's initiation and propagation within a square-shaped ice floe (see Fig. 7a). They determined that the failure of a square-shaped ice floe is controlled by radial crack initiation if its size L is less than two times its characteristic length, i.e., 2ℓ (with ℓ defined in Eq. (3)). In this study, this finding for a square-shaped ice floe is extended to a rectangular ice floe with arbitrary width-to-length ratios, i.e., wide and long ice floes shown in Fig. 7b and c. In both

scenarios, either the width or the length of the considered floe is less than 2ℓ and their respective failure is highly influenced by their free boundaries. Wide ice floes with lengths less than 2ℓ and long ice floes with widths less than 2ℓ are assumed to fail at radial crack initiations and circumferential crack initiations, respectively. Analytical solution towards the out-of-plane flexural failure of a finite size ice floe (i.e., with either length or width less than 2ℓ) are pursued in this paper.

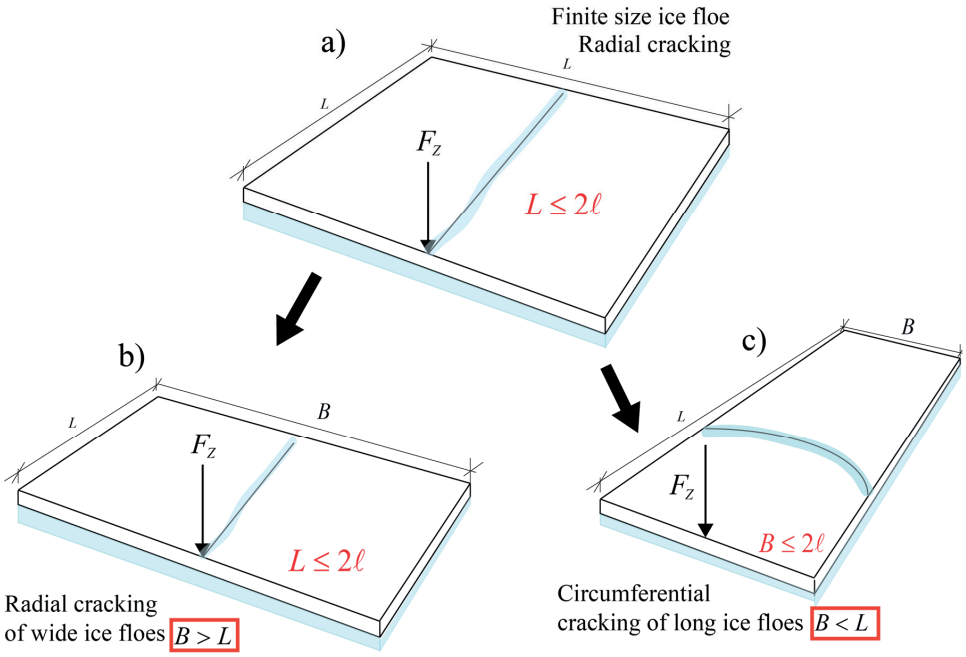

Fig. 7 Out-of-plane flexural failure of a finite size ice floe with a radial or circumferential crack.

As the floe size increases, i.e., both its width and length exceed 2ℓ, it can be conservatively classified as a semi-infinite ice floe (Lu et al., (submitted in July, 2014)). The failure of this ice floe is featured by sequentially forming radial and circumferential cracks, as shown in Fig. 6c. Its eventual failure is assumed to be controlled by circumferential crack initiation.

The structure and flowchart of this study are detailed in Fig. 8. For floe ice - sloping structure interactions, two dominant failure modes are expected: the local out-of-plane flexural failure and the global in-plane splitting failure. Depending on the major variables in this paper, i.e., floe size, ice thickness and contact property, four detailed failure scenarios are anticipated.

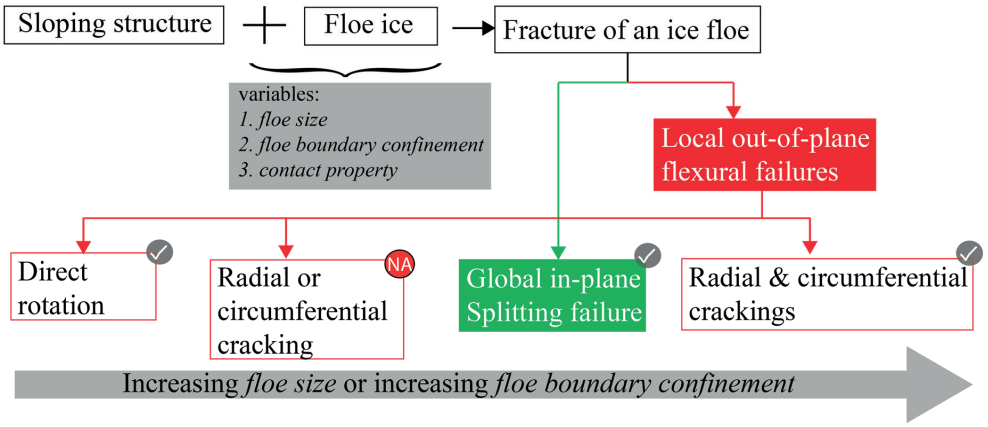

Fig. 8 Structure and flowchart of the study.

To extend previous studies, we seek analytical solutions to the four failure scenarios in Fig. 8. Available analytical solutions from previous studies, which are labelled with a ✓ sign in Fig. 8, comprise analytical solutions for the global splitting failure mode (Dempsey et al., 1993; Lu et al., (Accepted on November 12th 2014)), for the circumferential crack formation within a semi-infinite ice floe (Lubbad and Løset, 2011; Nevel, 1958; Nevel, 1961; Nevel, 1972), and for the direct rigid rotation of a small ice floe (Lindseth, 2013; Lu et al., 2014; Lu et al., 2013). Therefore, we concentrate on deriving relevant formulae to calculate the critical vertical force F_Z that produces the out-of-plane flexural failure of a finite size ice floe with a radial or circumferential crack, as shown in Fig. 7.

3 Research methods and assumptions

The research rationale is straightforward. We decouple the four failure scenarios that are illustrated in Fig. 8. The corresponding failure load F_Z (for 3 different out-of-plane flexural failures) and failure load F_Y (for the in-plane splitting failure mode) are separately analysed. Depending on a simplified ice floe - structure contact relationship, F_Z and F_Y are converted to comparable values to determine which failure mode dominates for certain ice conditions (i.e., floe size, ice thickness, material strength and contact properties).

While studying the competition among the dominant failure modes, which are shown in Fig. 3(4), the following general assumptions are made:

- A relatively open broken ice field is assumed. Within this ice environment, the failure of a single ice floe is explored in this paper. It is admitted that ice concentration and floe-floe interactions generate different boundary conditions. However, we do not further quantify these influences in this paper as they are addressed in a separate paper with the support of a multi-body dynamic simulator (Lubbad and Løset, 2011) and the general solutions obtained in this paper;
- Regarding the interaction depicted in Fig. 3, similar as in early literatures (Bhat, 1988; Bhat et al., 1991), a conservative head-on contact scenario is assumed. However, the

developed formulae can be applied to other general and eccentric contact scenarios by superposing the effects from additional force components;

- Timokhov and Kheysin (1987) (as cited by Leppäranta (2011) on p. 30) pointed out that sea ice floes are convex with a typical rectangular shape during winter and exhibit a rounded shape during the summer. For theoretical simplicity, a rectangular geometric shape is assumed for the ice floe in this study. With a varying width-to-length ratio of a rectangular ice floe, the majority of the ice floes in nature are conservatively approximated;
- The ice material is assumed to be homogeneous, isotropic and response elastically without any creeping effect. The appropriateness of these assumptions has been discussed in a separate paper (Lu et al., (submitted in July, 2014)). For such assumptions to be valid, a fast loading rate is generally required. However, we further neglect any dynamic response from the ice floe and the fluid beneath the ice floe. Although a static approach has been applied to this problem, modifications can be made to the current approach to involve the dynamic effects to certain extend (e.g., Some literatures (Lu et al., 2012a; Lubbad et al., 2008; McKenna and Spencer, 1993) have employed an added mass coefficient to account for the hydrodynamic effect from the fluid foundation);
- While exploring the competition between different failure scenarios, the dominant failure mode is assumed to be the mode that contributes to the smallest ice load (i.e., the smaller value of the comparable[3] F_Z and F_Y values) in Fig. 6;
- The contact property between the ice floe and the structure is highly idealised in this paper. First, we neglect the complicated stress field within the loading area in Fig. 3(3). Only the force components in the global coordinate direction are considered. Second, the subsequent failure mode of an ice floe is assumed to be independently influenced by these corresponding force component, i.e., these force components are decoupled. These different force components (i.e., F_Y and F_Z) are related by a straightforward load ratio. Contact force decomposition in different directions (i.e., X, Y, and Z) is highly dependent on the contact geometry, material and rate. Without using contact mechanics to analyse the stress distribution within the contact zone for specific structure geometries, we circumvent this problem by assuming a series of deterministic load ratios (i.e., β_{XY}, β_{XZ}, and β_{YZ}) in different directions, as shown in Eq. (1).

$$\begin{aligned} \beta_{YX} &= \frac{F_Y}{F_X}; \\ \beta_{XZ} &= \frac{F_X}{F_Z}; \\ \beta_{YZ} &= \beta_{YX}\beta_{XZ} = \frac{F_Y}{F_Z}; \end{aligned} \tag{1}$$

The definitions of different force components are shown in Fig. 9.

These load ratios can be theoretically extracted for a given contact scenario based on contact mechanics or a simple geometric overlapping analysis (Lubbad and Løset, 2011; Su et al., 2010). However, this subject is beyond the scope of this paper. In the specific case in which a vertical cylinder interacts with an ice floe, $\beta_{YX} = 0.5$ has been adopted by Bhat (1988) according to a study of ceramics. To derive the most conservative ice

[3] Note here that these two force components are in different directions. By 'comparable', we mean that these two forces should be projected in the same direction according to the ice-structure contact relationship introduced in the following section.

resistance F_X based on the 'no crack closure' condition and a finite element analysis (FEM), Bhat (1988) calculated the minimum value $\beta_{YX,\min}$, which is a variable of the crack length. In a similar scenario, in which the ice floe's inertia is not considered, Sodhi et al. (1993) attained a value of $\beta_{YX} = 0.3$ based on a FEM analysis. The load ratio β_{YZ} represents the ratio of the loads that cause global splitting failure to the loads that cause local bending failure. As a further simplification and for quantitative comparison purpose, we select $\beta_{YZ} = 0.5$ in most quantitative presentations. However, this specific simplification does not violate the generality of the proposed theoretical framework.

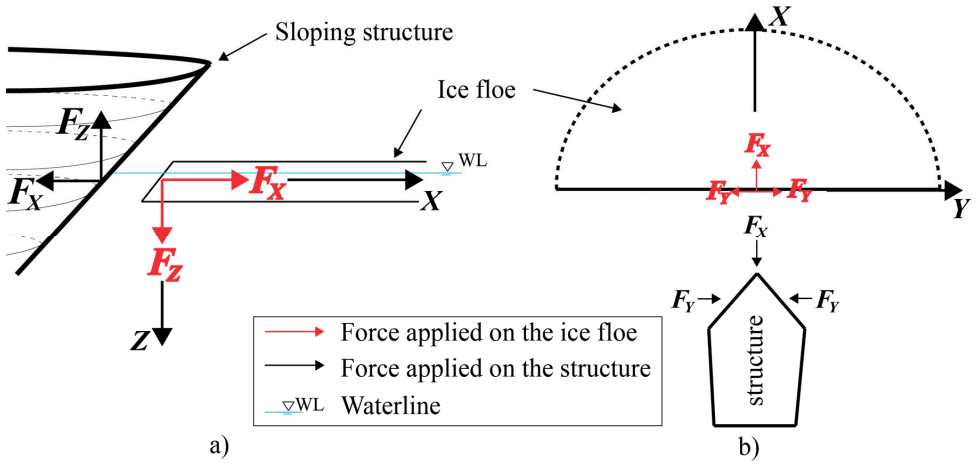

Fig. 9 Illustration of the load ratio and different force components: a) the side view and b) the bird view.

We define in the following the symbols that are utilised throughout this paper:

For the structure (force components in dark colour in Fig. 9):

- Ice resistance F_X: the total ice load in the opposite X direction in the global coordinate system, as shown in Fig. 9;
- F_Z: the ice load in the vertical direction.

For the ice floe (force components in red colour in Fig. 9):

- Ice floe's flexural failure load F_Z: the force required to initiate local bending failure on the ice floe;
- Ice floe's splitting failure load F_Y: appears as pair of force components acting in opposite directions with equal magnitude.

3.1 Out-of-plane flexural failure of a finite size ice floe

The main focus of this study, i.e., analytical solutions towards out-of-plane flexural failure of a finite size ice floe (in Fig. 7), is introduced. In addition to the previous general assumptions, the following assumptions are further made for this failure scenario:

- A finite size ice floe can be idealised as a thin plate on a Winkler-type elastic foundation. To validate the thin plate theory, the characteristic length ℓ of the plate should be more than 10 times the plate thickness t, i.e., $\ell \geq 10t$ (Ventsel and Krauthammer, 2001). Considering that the characteristic length of the sea ice ℓ can be approximated as $\ell = 13.5t^{3/4}$ (Gold, 1971), we can obtain an approximate thickness range in which our developed theory applies, i.e., $t \leq 3.32$ m. This thickness range covers first-year ice (i.e., $30 \text{ cm} \leq t \leq 2$ m) and the majority of multi-year ice (Wadhams and Horne, 1980);
- The thin plate theory also establishes a lower bound requirement for the physical size L of the considered ice floe, i.e., $L \geq \ell$. In a separate study (Lu et al., (submitted in July, 2014)), a conservative size border, i.e., $L \leq 2\ell$, has been drawn between the failure scenarios of Fig. 6 b and c for a nearly square-shaped ice floe. This size border which signifies substantial influence from an ice floe's free boundaries, is extended to arbitrary rectangular ice floes. For arbitrary rectangular ice floes, we primarily consider ice floes with lengths/widths in the range of $\ell \leq L$ or $B \leq 2\ell$ (refer to Fig. 7b and c), i.e., approximately $13.5t^{3/4} \leq L$ or $B \leq 27t^{3/4}$, e.g., for a typical first-year ice floe with thickness $t = 1$ m, we consider a rectangular ice floe with its length or width in the range of 13–27 m;
- While considering the failure pattern of a finite size rectangular ice floe, as previously introduced, a wide ice floe (Fig. 7b) is assumed to fail at radial crack initiation and a long ice floe (Fig. 7c) is assumed to fail at circumferential crack initiation. This assumption is a crude extension of previous numerical studies conducted on a square ice floe (Lu et al., (submitted in July, 2014)). As shall be discussed in Section 3.1.1.3, a conservative failure criterion is introduced for the failure patterns in Fig. 7. There accordingly, even if some inaccuracies were involved regarding the herein assumed potential failure patterns, the final results of the maximum force needed to fail a finite ice floe shall not be jeopardised.

3.1.1 Analytical solutions of rectangular ice floe subjected to a concentrated force

3.1.1.1 Mathematical model

Consider a rectangular plate resting on a Winkler-type elastic foundation with a local coordinate system, as shown in Fig. 10. Based on Kirchhoff's plate bending theory, its formulation is expressed in Eq. (2) as a Partial Differential Equation (PDE) (Nevel, 1965; Timoshenko et al., 1959; Ventsel and Krauthammer, 2001).

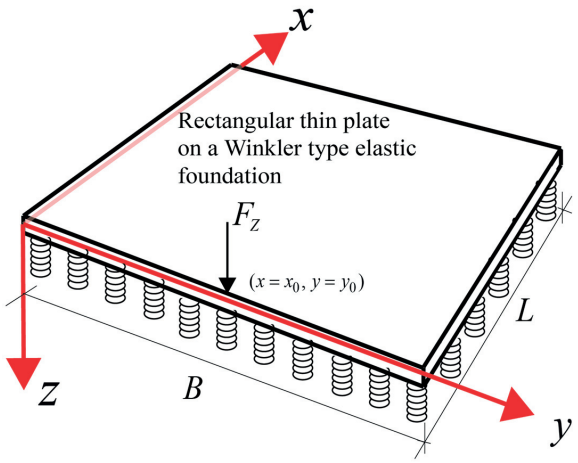

Fig. 10 A finite rectangular thin plate on a Winkler-type elastic foundation and the local coordinate system.

$$D\nabla^4(w) + kw = F_Z\delta(x - x_0)\delta(y - y_0) \tag{2}$$

where

$w(x, y)$	is the lateral deflection of the plate in the z-direction;
$D = \frac{Et^3}{12(1-\nu^2)}$	is the flexural rigidity of the plate;
E	is Young's modulus of the plate;
t	is the thickness of the plate;
ν	is Poisson ratio;
$\nabla^4(\,) = \frac{\partial^4}{\partial x^4} + 2\frac{\partial^4}{\partial x^2 y^2} + \frac{\partial^4}{\partial y^4}$	is the biharmonic operator;
k	is the foundation modulus. For the fluid base $k = \rho_w g$, where ρ_w and g are the fluid density and the gravitational acceleration, respectively;
$\delta(x)$	is a Dirac function.

There are two length scales in Eq. (2):, one is the physical length L of the rectangular ice floe and the other is the characteristic length ℓ as defined in Eq. (3).

$$\ell = \sqrt[4]{\frac{D}{k}} \tag{3}$$

To highlight the influence from the physical length of an ice floe, the PDE in Eq. (2) is normalised by introducing $\xi = x/L$, $\xi_0 = x_0/L$, $\eta = y/L$, $\eta_0 = y_0/L$ and noting that $\delta((\xi - \xi_o)\cdot L) = \delta(\xi - \xi_o)/L$. Eq. (2) is subsequently transformed into Eq. (4).

$$\nabla^4(w) + \frac{kL^4}{D}w = \frac{F_Z L^2}{D}\delta(\xi - \xi_0)\delta(\eta - \eta_0) \tag{4}$$

The new biharmonic operator is defined as $\nabla^4(\,) = \frac{\partial^4}{\partial\xi^4} + 2\frac{\partial^4}{\partial\xi^2\partial\eta^2} + \frac{\partial^4}{\partial\eta^4}$. Introducing the concept of the normalised foundation modulus $K = kL^4/D$ and the normalised deflection $W = (wD)/(F_z L^2)$, the original formulation for a finite size rectangular thin plate on a Winkler-type elastic foundation is transformed into Eq. (5)

$$\nabla^4(W) + KW = \delta(\xi - \xi_0)\delta(\eta - \eta_0) \tag{5}$$

where $0 \le \xi \le 1$ and $0 \le \eta \le \beta$ and β is the width-to-length ratio $\beta = B/L$. Solutions for different sizes of the rectangular plate can be obtained by varying the value of the normalised foundation modulus K. The complexity of the solutions to Eq. (5) is highly dependent on the plate's boundary conditions. Traditionally, a semi-inverse approach is adopted to solve the above PDE, i.e., a trial function that satisfies the boundary condition is inserted into Eq. (5) to simplify the original PDE. For example, in 1820, Navier assumed a double trigonometric series to be the solution to Eq. (5), in which the four boundaries of the rectangular plate are simply supported. In 1900, Levy assumed a single series solution and transformed Eq. (5) into an Ordinary Differential Equation (ODE), in which at least two opposite edges of a rectangular plate are simply supported (Timoshenko et al., 1959). In the next section, a symplectic approach is introduced to solve Eq. (5) with four free edges (i.e., zero moment and shear force distributions along the boundaries of the plate). The normalisation procedure introduced above has been proved efficient in implementing the algorithms.

3.1.1.2 A brief description of a symplectic approach towards analytical solutions

As an idealised mathematical model of a floating rectangular ice floe, the solution to a plate resting on a Winkler-type elastic foundation with four free edges was pursued. This problem has been analytically solved by a symplectic superposition approach (Li et al., 2013). The symplectic methodology is a mathematical approach that has extensive applications in research fields such as relativity, gravitation, and quantum mechanics (Lim and Xu, 2010). Its application in elasticity was proposed in the early 1990s; it has substantially extended analytical solutions within the field of classic mechanics (Yao et al., 2009; Zhong and Williams, 1993; Zhong and Zhong, 1993). In this paper, a general three-step description of the analytical derivations based on the symplectic method is briefly presented. For detailed derivations and formulations, one is refer to the original work of Li et al. (2013).

Step 1: Formulation of the Hamilton canonical equation

Arbitrarily selecting the y (or η) direction as the derivative direction of the basic argument and based on the symplectic approach, Li et al. (2013) formulated the Hamilton canonical equations, as shown in Eq. (6), for the basic plate bending problem on an elastic foundation, as shown in Fig. 10 (equation (2.13) in the original paper).

$$\frac{\partial \mathbf{Z}}{\partial \eta} = \mathbf{H}\mathbf{Z} + \mathbf{f} \tag{6}$$

where $\mathbf{Z} = [W, \theta, -V_\eta, M_\eta]^T$ includes all major unknowns, such as the deflection W, the rotation angle $\theta = \frac{\partial W}{\partial \eta}$, the equivalent shear force $-V_\eta = D[\frac{\partial^3 W}{\partial \eta^3} + \frac{\partial^3 W}{\partial \xi^2 \partial \eta} + (1-\nu)\frac{\partial^3 W}{\partial \xi^2 \partial \eta}]$ and the moment

$M_\eta = -D(\frac{\partial^2 W}{\partial \eta^2} + \nu \frac{\partial^2 W}{\partial \xi^2})$. $\mathbf{H} = \begin{bmatrix} \mathbf{F} & \mathbf{G} \\ \mathbf{Q} & \mathbf{-F^T} \end{bmatrix}$ is a 4×4 Hamiltonian operator matrix with several tempting characteristics (e.g., summarised by Yao et al. (2009) on p.254). These favourable characteristics were utilised in the following derivations (particularly for solving Eq. (8) and deriving Eq. (10)). The components of $\mathbf{H}$ are

$$\mathbf{F} = \begin{bmatrix} 0 & 1 \\ -\nu \frac{\partial^2}{\partial \xi^2} & 0 \end{bmatrix}, \ \mathbf{G} = \begin{bmatrix} 0 & 0 \\ 0 & -\frac{1}{D} \end{bmatrix} \text{ and } \mathbf{Q} = \begin{bmatrix} D\frac{(\nu^2-1)\partial^4}{\partial \xi^4} - K & 0 \\ 0 & 2D\frac{(1-\nu)\partial^2}{\partial \xi^2} \end{bmatrix}.$$

where $\mathbf{f} = [0, 0, \delta(\xi - \xi_0)\delta(\eta - \eta_0), 0]^{\mathrm{T}}$ and $\delta(\xi - \xi_0)\delta(\eta - \eta_0)$ represents the location of a concentrated force, as shown in Eq. (5).

Step 2: Analytical solution to the base case problem

Using the basic Eq. (6), Li et al. (2013) solved a base case with boundary conditions, as shown in Eq. (7) . Referring to the normalised coordinate system in Fig. 11a, the plate's two edges along $\xi = 0$ and $\xi = 1$ are slidingly clamped for the base case problem. The solution serves as a preparation for further development of free-boundary solutions.

$$\left.\frac{\partial W}{\partial \xi}\right|_{\xi=0,1} = 0 \text{ and } V_\xi\big|_{\xi=0,1} = 0 \tag{7}$$

The method involves the separation of variables such as $\mathbf{Z} = \boldsymbol{\chi}(\xi)\Upsilon(\eta)$, which represents the variation in major unknowns in the ξ direction and η direction, respectively. The solution procedures are as follows: First, $\mathbf{Z} = \boldsymbol{\chi}(\xi)\Upsilon(\eta)$ was inserted into the homogeneous equation $\frac{\partial \mathbf{Z}}{\partial \eta} = \mathbf{H}\mathbf{Z}$ to produce two separate equations, in which the eigenvalue in Eq. (8) is a major concern.

$$\mathbf{H}\boldsymbol{\chi}(\xi) = \mu\boldsymbol{\chi}(\xi) \tag{8}$$

where μ is the eigenvalue and $\boldsymbol{\chi}(\xi)$ is the corresponding eigenvector[4]. After solving Eq. (8)'s characteristic equation, and assigning the boundary condition in the base case (i.e., Eq. (7)), $\boldsymbol{\chi}(\xi)$ can be explicitly solved, as shown in Eq. (9), as an ensample of trigonometric functions with $n = 1, 2, 3, \ldots\ldots, N \to \infty$ (Note that the explicit solutions for each component are detailed in equations (3.12) to (3.19) in Li et al. (2013)).

$$\boldsymbol{\chi}(\xi)_{4\times(4+4N)} = [\boldsymbol{\chi}_1(\xi), \boldsymbol{\chi}_2(\xi), \boldsymbol{\chi}_3(\xi), \boldsymbol{\chi}_4(\xi), \ldots\ldots, \boldsymbol{\chi}_{n1}(\xi), \boldsymbol{\chi}_{n2}(\xi), \boldsymbol{\chi}_{n3}(\xi), \boldsymbol{\chi}_{n4}(\xi), \ldots\ldots] \tag{9}$$

Second, $\mathbf{Z} = \boldsymbol{\chi}(\xi)\Upsilon(\eta)$ was inserted into the inhomogeneous Eq. (6). Utilising Eq. (8) and the approach '*expansion by symplectic vectors* $\boldsymbol{\chi}(\xi)$', the original PDE in Eq. (6) was transformed into an ODE as shown in Eq. (10),

$$\frac{d\Upsilon(\eta)}{d\eta} - \mathbf{M}\Upsilon = \mathbf{G} \tag{10}$$

[4] It is also termed as a symplectic eigenvector, which satisfies the symplectic conjugacy and orthogonality (refer to e.g., summarised by Yao et al. (2009) in p.254).

where $\mathbf{M}$ is a $(4+4N)\times(4+4N)$ diagonal matrix in which its elements are the eigenvalues μ_i of Eq. (8) and $\mathbf{G}$ is a $(4+4N)\times 1$ matrix with its components obtained by expanding $\mathbf{f}$ with the symplectic vectors $\boldsymbol{\chi}(\xi)$ as $\int_0^1 \boldsymbol{\chi}^{\mathrm{T}}(\xi)\mathbf{J}\boldsymbol{\chi}(\xi)\mathbf{G}d\xi = \int_0^1 \boldsymbol{\chi}^{\mathrm{T}}(\xi)\mathbf{f}d\xi$, where $\mathbf{J}=\begin{bmatrix} 0 & \mathbf{I}_2 \\ -\mathbf{I}_2 & 0 \end{bmatrix}$ is the unit symplectic matrix with $\mathbf{I}_2$ as a 2×2 unit matrix. The explicit solutions of $\mathbf{G}$ are presented in equation (3.12) of Li et al. (2013). The solutions of $\Upsilon(\eta)$ in Eq. (10) are obtained, as shown in Eq. (11) (Note that the explicit solutions for each component can be obtained from equation (3.30) in Li et al. (2013)).

$$\begin{aligned}\Upsilon(\eta)_{(4+4N)\times 4} = [&\Upsilon_1(c_1,\eta),\ \Upsilon_2(c_2,\eta),\ \Upsilon_3(c_3,\eta),\ \Upsilon_4(c_4,\ \eta),\ \ldots\ldots,\\ &\Upsilon_{n1}(c_{n1},\eta),\ \Upsilon_{n2}(c_{n2},\eta),\ \Upsilon_{n3}(c_{n3},\eta),\ \Upsilon_{n4}(c_{n4},\ \eta),\ \ldots\ldots]^{\mathrm{T}}\end{aligned} \tag{11}$$

As no boundary conditions in the y (or η) direction has been introduced in this derivation, a series of unknowns (i.e., $c_1, c_2, c_3, c_4,\ \ldots\ldots, c_{n1}, c_{n2}, c_{n3}, c_{n4},\ \ldots\ldots$) within $\Upsilon(\eta)$ remain. If known boundary conditions in the y (or η) direction are introduced, $\Upsilon(\eta)$ can be solved and the solution to the original problem in Eq. (6) can be obtained, as shown in Eq. (12).

$$\begin{aligned}\mathbf{Z} = &\boldsymbol{\chi}_1(\xi)\Upsilon_1(\eta)+\boldsymbol{\chi}_2(\xi)\Upsilon_2(\eta)+\boldsymbol{\chi}_3(\xi)\Upsilon_3(\eta)+\boldsymbol{\chi}_4(\xi)\Upsilon_4(\eta)\\ &+\sum_{n=1}^{N\to\infty}[\boldsymbol{\chi}_{n1}(\xi)\Upsilon_{n1}(\eta)+\boldsymbol{\chi}_{n2}(\xi)\Upsilon_{n2}(\eta)+\boldsymbol{\chi}_{n3}(\xi)\Upsilon_{n3}(\eta)+\boldsymbol{\chi}_{n4}(\xi)\Upsilon_{n4}(\eta)]\end{aligned} \tag{12}$$

Additional boundary conditions are introduced in the third step based on the concept of superposition.

Step 3: Superposition of different boundary conditions towards the analytical solution

To obtain the analytical solutions for a rectangular plate with four edges free, the method of superposition has been implemented in Li et al. (2013). Specifically, three sets of different boundary conditions were solved and summed to yield the final free-edge solution shown in Fig. 11.

While deriving analytical solutions for the boundary conditions (BCs) (1), (2) and (3) in Fig. 11, Li et al. (2013) considered the analytical solutions for the base case, as shown in Eqs. (9) and (11), e.g., new boundary conditions along $\eta = 0$ and $\eta = \beta$, as shown in Fig. 11b, can be employed to obtain unknown values within $\Upsilon(\eta)$ of Eq. (11) (i.e., $c_1, c_2, c_3, c_4,\ \ldots\ldots, c_{n1}, c_{n2}, c_{n3}, c_{n4},\ \ldots\ldots$). Therefore, $\mathbf{Z}_1$ with fully slidingly clamped boundary conditions is solved. Similar procedures can be applied to solve $\mathbf{Z}_2$ and $\mathbf{Z}_3$, which correspond to the solution of the BCs (2) and (3) in Fig. 11. However, note that the rotational angle boundary conditions for BCs (2) and (3) in Fig. 11 are unknown. The rotational angle can be expressed as a trigonometric series, as shown in Eq. (13).

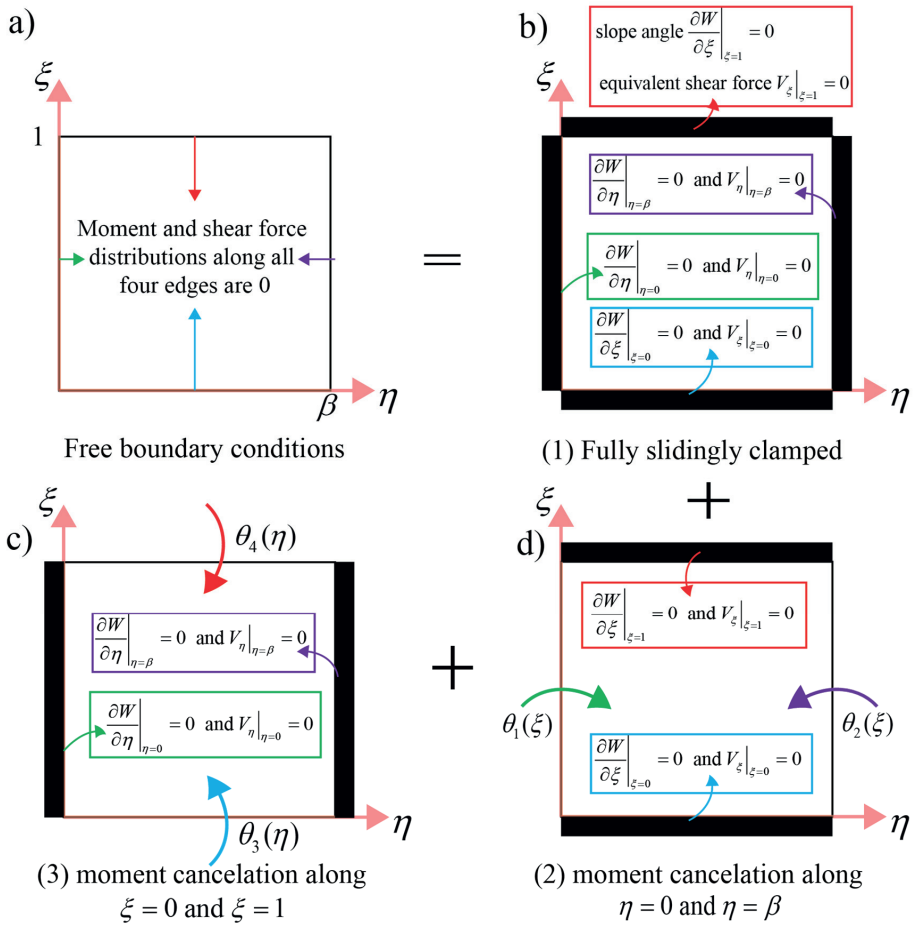

Fig. 11 Superposition of different boundary conditions.

$$\begin{aligned}
\theta_1(\xi) &= E_0 + \sum_{n=1}^{N\to\infty} E_n \cos(\alpha_n \xi), \\
\theta_2(\xi) &= F_0 + \sum_{n=1}^{N\to\infty} F_n \cos(\alpha_n \xi), \\
\theta_3(\eta) &= G_0 + \sum_{n=1}^{N\to\infty} G_n \cos(\beta_n \eta), \\
\theta_4(\eta) &= H_0 + \sum_{n=1}^{N\to\infty} H_n \cos(\beta_n \eta)
\end{aligned} \tag{13}$$

where $\alpha_n = n\pi/1$ and $\beta_n = n\pi/\beta$. The obtained solution of the BCs (2) and (3) are functions with the unknown variables $E_0, F_0, G_0, H_0, E_n, F_n, G_n,$ and H_n. The solutions can be expressed as shown in Eq. (14).

$$\mathbf{Z} = \mathbf{Z}_1 + \mathbf{Z}_2(E_0, F_0, G_0, H_0, E_n, F_n, G_n, H_n) + \mathbf{Z}_3(E_0, F_0, G_0, H_0, E_n, F_n, G_n, H_n) \tag{14}$$

As one of the solutions of $\mathbf{Z}$, the deflection W can be extracted from Eq. (14), as shown in Eq. (15).

$$W = W_1 + W_2(E_0, F_0, G_0, H_0, E_n, F_n, G_n, H_n) + W_3(E_0, F_0, G_0, H_0, E_n, F_n, G_n, H_n) \tag{15}$$

The expressions of $W_1, W_2,$ and W_3 are given in equation (4.2), (4.4) and (4.6), respectively, in Li et al. (2013). However, $4+4N$ unknowns (i.e., $E_0, F_0, G_0, H_0, E_n, F_n, G_n,$ and H_n) remain within Eq. (15). These unknowns can be solved by enforcing the moment distributions along all four boundaries equalling 0. The enforcing equations were obtained from equation (4.7) to (4.14) in Li et al. (2013).

3.1.1.3 Implementation and validation

The previously described formulations have been implemented in a MATLAB script to calculate the deflection W. The calculated results are compared with the relevant Finite Element Method (FEM)-based simulation, as shown in Fig. 12.

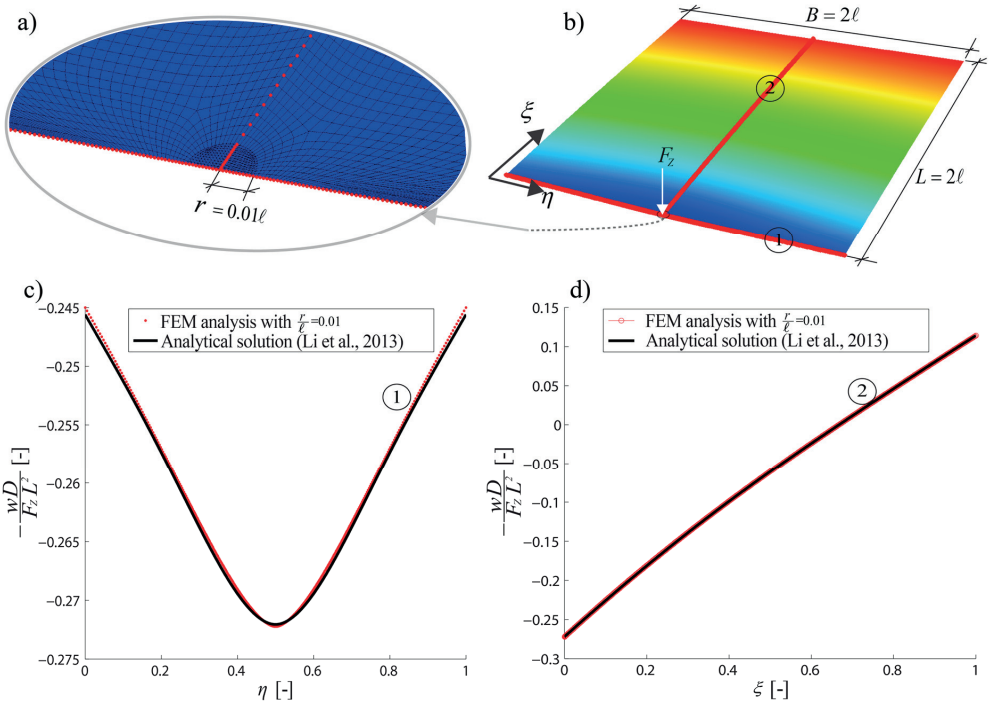

Fig. 12 Validation of the symplectic approach based analytical solutions against the FEM simulations.

Fig. 12a illustrates the mesh pattern at the loading area in the numerical model. As a concentrated load is numerically challenging, a distributed pressure within a small area (i.e.,

the radius[5] of the half-circular load area ($r = 0.01\ell$) is implemented. The same numerical model employed in a separate paper (Lu et al., (submitted in July, 2014)) has been utilised in this paper. Fig. 12b contains the analytical solution obtained based on the symplectic approach described in the previous section. The contour plot represents the deflection of a $2\ell \times 2\ell$ floating ice floe. We are particularly interested in two deflection curves: curve '1' along $\xi = 0$ and curve '2' along $\eta = \beta / 2$. Critical deflection/stress values on curve '1' and curve '2' represent the radial crack initiation and the circumferential crack initiation, respectively. The favourable mutual agreement between the numerical simulation and the analytical solutions in Fig. 12c and d signifies the accuracy of the implementation.

3.1.2 An equivalent loading system and failure criteria

The derivations in Section 3.1.1 were dedicated to a concentrated force acting on an ice floe. For the interaction between a sloping structure and a finite ice floe, a contact force smearing within a loading area should be considered for the following reasons: 1) theoretically, a concentrated load induces infinite stress beneath the loading point and 2) a smeared contact pressure with a specific size is more representative while considering the floe ice-structure contact. Therefore, the original problem in Fig. 13a is replaced with a statically equivalent loading system, as shown in Fig. 13b. The same approach has been implemented in a previous study (Lubbad and Løset, 2011) to obtain analytical solutions of the stress within a semi-infinite ice floe.

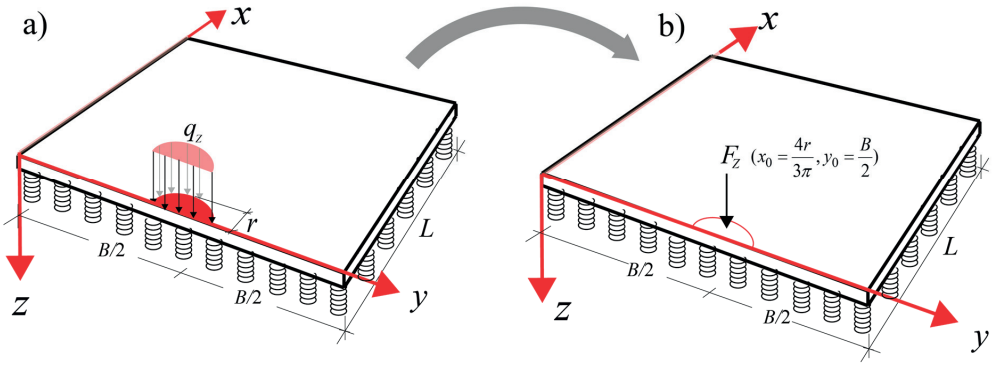

Fig. 13 A statically equivalent loading system.

Despite this equivalent loading system, satisfactory stress calculations can only be obtained if the floe sizes exceed 3ℓ. Relatively large discrepancies regarding stress calculations by the FEM and the symplectic approach are identified for a small ice floe. This large discrepancy is considered due to the slow convergence rate in the stress calculations by this particular symplectic approach. As noted by Li et al. (2013), stress calculation results converge much slower than deflection calculation results. Recalling that our interested application range of floe

[5] In previous relevant publications by the same author, another symbol R has been utilised for the radius of the loading area. However, in the literature of Li et al. (2013), R has been employed for a different purpose. To prevent confusion, this paper utilises r to represent the radius of the assumed half-circular loading area.

size is approximately $\ell < L \le 2\ell$, we abandon the stress criterion and resort to another conservative failure criterion.

As the analytical approach in Section 3.1.1.2 can yield accurate deflection results, a displacement-based criterion is adopted. We have selected the freeboard of an ice floe at point ($x = 0, y = B/2$) as the critical deflection, i.e., the radial or circumferential crack only begins after the deflection at point ($x = 0, y = B/2$) attains the critical value $w_{flood} = (1 - \rho_i / \rho_w)t$, which is induced by the critical vertical force $F_{z\_radial/circumferential\_cracking}$. Note that this displacement-controlled failure criterion is conservative for ice load calculations.

Considering the definition of the normalised displacement in Eq. (5), this failure criterion can be characterised as in Eq. (16); thus, the critical force can be expressed as in Eq. (17) with W calculated by Eq. (15).

$$W = \frac{w_{flood} D}{F_{z\_radial/circumferential\_cracking} L^2} = \frac{D}{F_{z\_radial/circumferential\_cracking} L^2}(1 - \frac{\rho_i}{\rho_w})t \tag{16}$$

where ρ_i is the ice density.

$$F_{z\_radial/circumferential\_cracking} = \frac{D}{WL^2}(1 - \frac{\rho_i}{\rho_w})t \tag{17}$$

The calculated $F_{z\_radial/circumferential\_cracking}$ shall be conservatively utilised for the failure patterns, as shown in Fig. 7, for a rectangular ice floe with its length or width in the range of $\ell < L \le 2\ell$ or $\ell < B \le 2\ell$.

3.2 Methodology and assumptions for the direct rotation of a small ice floe

After introducing the methods utilised to investigate the failure pattern, as shown in Fig. 7, we need to obtain analytical solutions to describe the failure patterns, as shown in Fig. 6a and c. This section presents methods that have been employed to characterise the failure pattern, as shown in Fig. 6a, in which the expected floe size is $L \le \ell$.

Consider a rectangular ice floe with width B and length L , as illustrated in Fig. 14. A sufficiently small ice floe (i.e., $L \le \ell$) can simply be tilted with no significant material failure. To obtain simplified analytical solutions to this type of failure mode based on previous studies, additional assumptions are made as follows:

- It is assumed that the current problem can be described by the two-dimensional theory of a finite beam on a Winkler-type elastic foundation (Hetényi, 1946);
- It has been assumed that the floe length $L \le \ell$ in this failure. According to the literature (Hetényi, 1946, p. 46), if the length of a finite beam $L \le \pi/(4\lambda)$, it can be treated as a short beam and its deflection can be neglected. Recall the definition of λ as in Eq. (18) (Hetényi, 1946, p. 4), in which $I = Bt^3/12$. After some manipulations, considering the expression for flexural rigidity D in Eq. (2) and the expression for ℓ in Eq. (3), the requirement for the short beam theory can be rewritten, as shown in Eq. (19).

$$\lambda = \sqrt[4]{\frac{Bk}{4EI}} \tag{18}$$

$$L \le \pi / (4\lambda) = \frac{\pi}{4}\sqrt[4]{4(1-\nu^2)}\ell \approx 1.08\ell \tag{19}$$

where $\nu = 0.3$ is assumed. Eq. (19) implies that the considered ice floe in Fig. 13a with length $L \le \ell$ can be treated as a short beam with its flexural deflection neglected;

- To apply the short beam theory, the width $B \le \ell$ is assumed such that the deflection in the width direction can be neglected and a two-dimensional treatment is applicable. For the case in which $B > \ell$, the theory introduced in Section 3.1.1 is applicable with Eq. (17);
- When the deflection at the loading end is below the waterline, the required rotation force is assumed to decrease. Potential ventilation effect, which increases the rotating force (Lu et al., 2014; Lu et al., 2013; Valanto, 2001), is not considered in this paper.

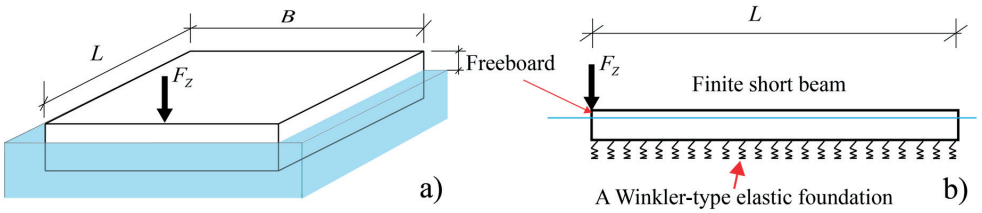

Fig. 14 Direct rotation of a small ice floe and its theoretical simplification.

Based on these assumptions and the selection of the freeboard $(1-\rho_i/\rho_w)t$ as the critical deflection at the loading point, the maximum force that is required to rotate a small ice floe with length $L \le \ell$ is expressed in Eq. (20). This formula is derived from Eq. (65) in the reference (Lu et al., 2014) by changing the 'critical rotation angle' into the 'freeboard divided by rotation length', in which the same short beam theory has been applied under similar assumptions.

$$F_{Z\_direct\_rotation} = \frac{1}{4} w_{flood} \rho_w g B L = (1 - \frac{\rho_i}{\rho_w}) \frac{t}{4} \rho_w g B L \tag{20}$$

3.3 Methodology and assumptions for failures of a semi-infinite ice floe

In terms the failure mode in Fig. 6c, extensive research has been conducted in history. A detailed literature review has been performed in a separate paper (Lu et al., (submitted in July, 2014)). As documented by (Kerr, 1976), the bearing capacity of a semi-infinite ice floe was tested by Panfilov (1960) with varying loading areas. Panfilov (1960) proposed two empirical formulae to calculate the upper and lower bounds of the bearing capacity of a semi-infinite ice floe. The upper-bound empirical formula was recommended for icebreaker designs (Kerr, 1976). Analytically, Nevel's (1958; 1961) solutions regarding infinite wedge beam have been utilised to calculate the local bending failure during level ice - sloping structure interactions (Kotras et al., 1983; Lubbad and Løset, 2011; Milano, 1972; Nevel, 1992). However, a simplified version that approximates the original formulation is employed in this paper, as shown in Eq. (21) (according to equation (1) in Nevel (1972)).

$$F_{Z\_wedge\_bending} = \frac{2m}{6} \tan(\frac{\pi}{2m}) \sigma_f t^2 [1.05 + 2.0(\frac{r}{\ell}) + 0.50(\frac{r}{\ell})^3] \tag{21}$$

where m is the number of wedge beams produced within a semi-infinite ice floe while circumferential crack forms. Note that the coefficient $(2m/6)\tan(\pi/(2m))$ is a monotonically decreasing function and converges to the value $(\pi/6)$ as $m \to \infty$. According to the description of an out-of-plane flexural failure pattern of a semi-infinite ice floe (Kerr, 1976), m exhibits a small value. To be conservative and consistent regarding the experimental description according to Kerr (1976), $m = 2$ is assumed in Eq. (21). Thus, Eq. (22) is obtained to conveniently calculate the critical vertical force $F_{Z\_wedge\_bending}$ to initiate circumferential cracks in a semi-infinite ice floe, as shown in Fig. 15.

$$F_{Z\_wedge\_bending} = \frac{2}{3}\sigma_f t^2[1.05 + 2.0(\frac{R}{\ell}) + 0.50(\frac{R}{\ell})^3] \tag{22}$$

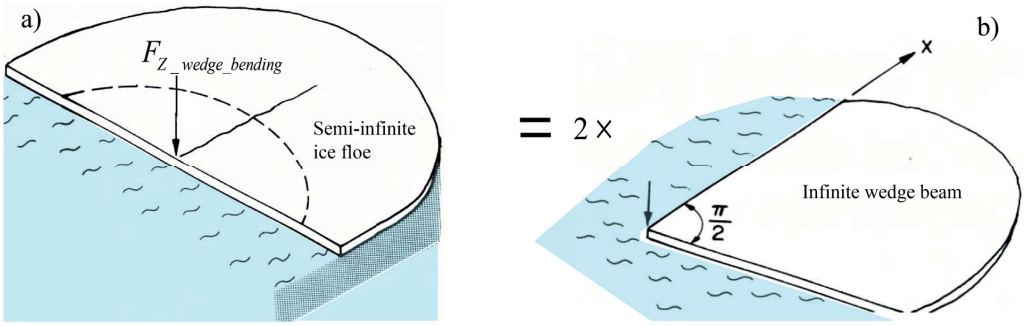

Fig. 15 Failure of a semi-infinite ice floe by forming two independent wedge beams (after Kerr (1976)).

3.4 Methodology and assumptions for global splitting failure

The analytical framework for calculating the ice splitting load has been evaluated in a separate paper (Lu et al., (Accepted on November 12th 2014)). A pre-existing cracked initiated by 'radial cracking' has been assumed in this study. Various methods have been employed to study the force required to propagate this pre-existing crack. A major conclusion from that study is that Linear Elastic Fracture Mechanics (LEFM) is usually sufficient to describe the splitting failure of an ice floe at engineering scales (i.e., approximately larger than 3 m). Therefore, the analytical formula based on LEFM and the weight function method (Bueckner, 1970; Rice, 1972) is presented in Eq. (23) for subsequent comparisons.

$$\frac{F_Y(\alpha)}{tK_{IC}\sqrt{L}} = \frac{1}{H(\alpha,0)} \tag{23}$$

The main symbols are illustrated in Fig. 16 and defined as follows:

$F_Y(\alpha)$ is the ice splitting load with the normalised crack length $\alpha = A/L$;

A is the crack length;

t is the ice floe thickness;

K_{IC} is the fracture toughness of sea ice;

$H(\alpha,0)$ is a weight function for the crack body with the splitting force acting at the crack mouth.

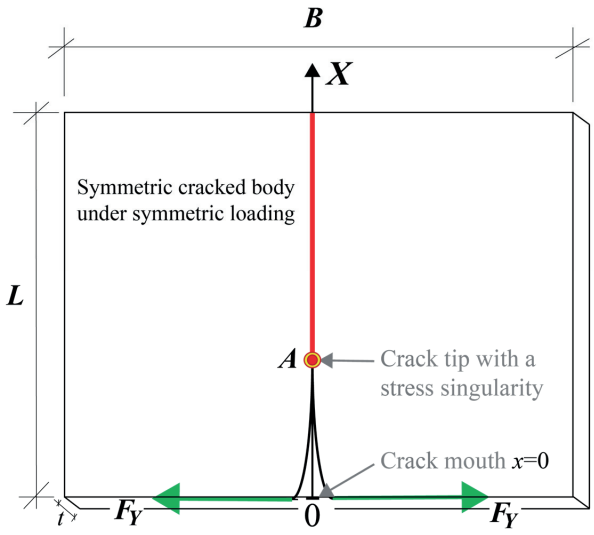

Fig. 16 LEFM-based approach to calculate the global splitting failure of an ice floe.

4 Results and discussions

Analytical solutions for the four failure scenarios in Fig. 8 were introduced in the previous sections, i.e., Eqs. (17), (20), (22), and (23) for radial/circumferential cracking of a finite size ice floe, direct rotation of a small ice floe, circumferential crack formation in a semi-infinite ice plate and global splitting failure of an ice floe, respectively. Now it is at our disposal to evaluate the competition among these different failure scenarios. But before that, out-of-plane flexural failures of rectangular ice floe in Fig. 7 are presented as follows.

4.1 Out-of-plane flexural failure of a finite size ice floe

Although four different failure scenarios' analytical solutions were given in Section 3, the major focused failure scenario of this paper is in Fig. 7. Assuming a conservative failure criterion, i.e., a displacement-controlled criterion, the deflection of a rectangular ice floe for different width-to-length ratios is illustrated in Fig. 17.

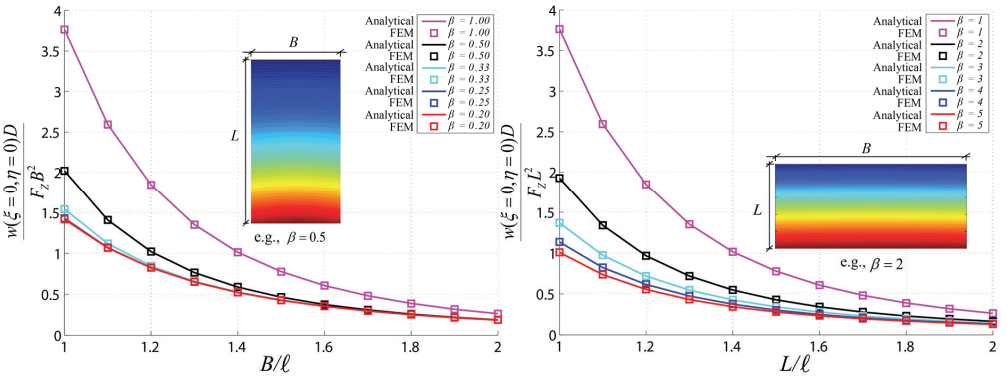

Fig. 17 a) deflections of long ice floes and b) deflections of wide plates.

Fig. 17 illustrates the comparison of the maximum normalised deflection between the numerical results and the analytical solutions for long ice floes and wide ice floes, respectively. Satisfactory agreement is achieved for a rectangular ice floe with various width-to-length ratios.

The calculated defection W in Fig. 17 can be inserted into Eq. (17) to obtain the critical vertical force $F_{z\_radial/circumferential\_cracking}$ for the out-of-plane flexural failure of a finite rectangular ice floe. The rectangular ice floes considered in Fig. 17 are floes with its width or length in the range of ℓ and 2ℓ; the other side varies with different width-to-length ratios. According to the assumptions discussed in Section 3.1, long ice floes in Fig. 17a and wide ice floes in Fig. 17b will fail at circumferential cracking and radial cracking, respectively. Note that this assumption is approximate as neither crack initiation nor propagation has been substantially investigated for arbitrary rectangular ice floes. While calculating the critical failure load $F_{z\_radial/circumferential\_cracking}$, a conservative displacement-controlled criterion was adopted (refer to the discussion in Section 3.1.2). In a separate study (Lu et al., (submitted in July, 2014)), a comparative study of the critical stress criterion and critical deflection criterion on a square shaped ice floe was performed. Based on the stress criterion, radial crack initiation occurs prior to the occurrence of the critical deflection. Similarly, for a beam-like ice floe (e.g., long ice floe in Fig. 17a), previous studies of a beam on a Winkler-type elastic foundation also show that flexural failure occurs much earlier than the inundation of the considered ice floe (Lubbad et al., 2008). In summary, for both potential failure modes in Fig. 7, a displacement control failure criterion is proposed and validated for various width-to-length ratios in Fig. 17.

Fig. 17 also shows that the results begin to converge to certain values for long/wide floes with width-to-length ratios smaller/larger than certain values (e.g., $\beta \le 0.2$ and $\beta \ge 5$ for long and wide rectangular floes, respectively).

4.2 Floe size influences the local out-of-plane flexural failure of an ice floe

After verifying the symplectic approach, Eqs. (17), (20), and (22) can be utilised to quantitatively illustrate the variation in critical vertical force with floe size for different failure scenarios (refer to Fig. 6). Fig. 18 illustrates the normalised critical vertical force $F_Z/(\sigma_f t^2)$ and the corresponding failure scenario for a square ice floe with varying size from 1 m to 10 km. Four curves are plotted in Fig. 18; each represents different ice thicknesses. Within each curve,

three sections can be identified: 1) direct rotation of a small ice floe with $L \le \ell$, 2) radial cracking of a square ice floe with size $\ell < L \le 2\ell$, and 3) failure of semi-infinite ice floes ($L > 2\ell$) with bending of infinite ice wedges. As an example, different sections were applied with transparent colours for the case in which the ice thickness $t = 0.5$ m. As different failure criteria have been assumed for these three failure scenarios, a nonsmooth transition is identified between radial cracking for a finite size ice floe and infinite wedge bending for a semi-infinite ice floe.

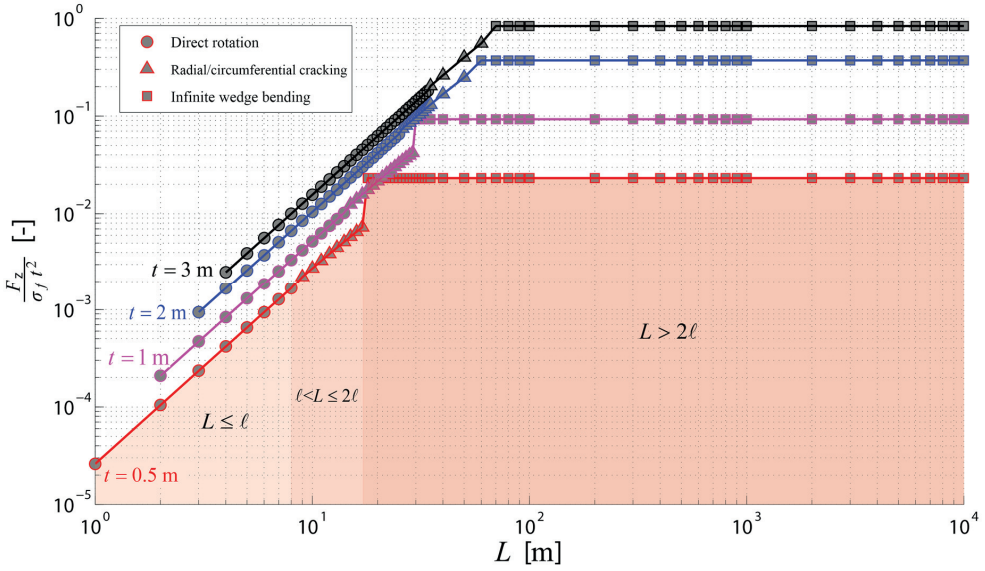

Fig. 18 Out-of-plane flexural failure of square ice floes of varying sizes and thicknesses.

Note that the plots in Fig. 18 only depict square ice floes. If similar plots are constructed for nonsquare-shaped rectangular ice floes, the same relevant formulae can be utilised. However, the failure pattern of a finite size rectangular floe may vary between radial or circumferential cracking depending on the width-to-length ratio (refer to Fig. 7). Using the derived formulae, Fig. 18 quantified critical vertical forces that correspond to different failure scenarios based on two major variables, i.e., the floe size and the ice thickness. Noticeably, even a conservative criterion has been assumed for the radial cracking of a square ice floe, the critical vertical force ($F_{z\_radial/circumferential\_cracking}$) required to initiate failures in a finite size ice floe is still smaller than its counterpart ($F_{Z\_wedge\_bending}$) needed to initiate failures in a semi-infinite ice floe.

4.3 Local out-of-plane flexural failure versus global in-plane splitting failure

With the simplified contact properties assumed in Section 3 with Eq. (1), all developed formulae to calculate different failure scenarios can be plotted in a single figure to quantify the competition. This finding is demonstrated by Fig. 19 for square ice floes of varying size and with a contact property $\beta_{YZ} = 0.5$.

As stated in Section 3, the failure mode is determined by the smaller critical vertical force. Therefore, with all the floe size considered, the dominant failure mode that yields a smaller failure load (i.e., normalised value of $\beta_{YZ}F_Z/(Lt)$ or $F_Y/(Lt)$) can be identified.

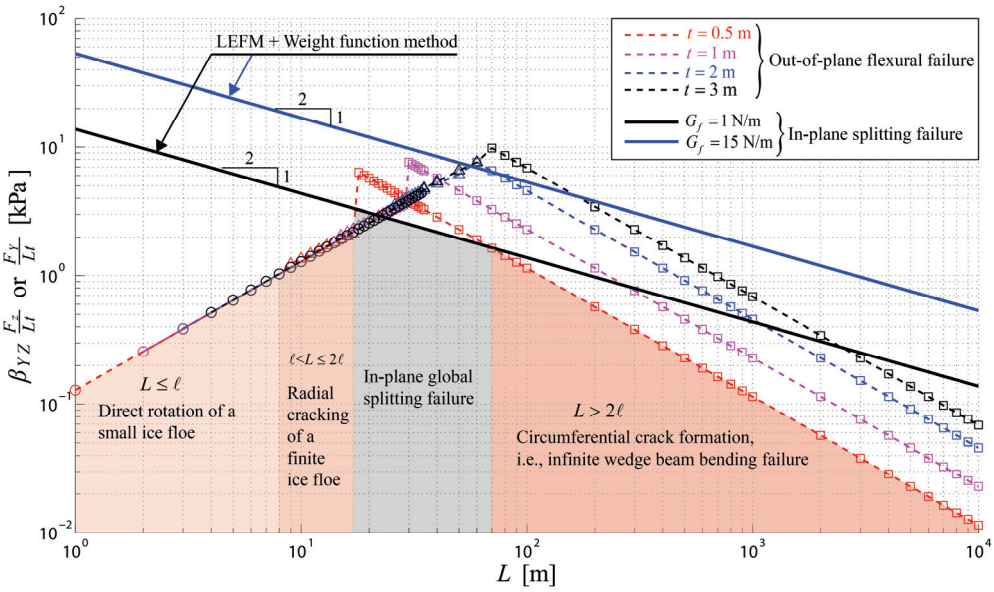

Fig. 19 Competition between different failure modes for a square ice floe of varying sizes and thicknesses ($\beta_{YZ}=0.5$).

As mentioned in Section 3.4, the 'LEFM + weight function' method is applicable for the majority of field-scale engineering applications. Therefore, for the normalised ice splitting load $F_Y/(Lt)$, this method has been employed for the comparison in this study. In Fig. 19, two solid curves (with a slope 1:2) represent plots of the normalised ice splitting load versus floe size. These two curves were calculated with different fracture energy inputs. The lower black solid curve is calculated with the fracture energy $G_f=1$ N/m, which is based on laboratory tests (e.g., (Schulson and Duval, 2009)); and the upper blue solid curve is calculated with the fracture energy $G_f=15$ N/m, which is based on field measurements (Dempsey et al., 1999). Controversies regarding the fracture energy of sea ice exist. Advocates of these two values criticise each other for using an inappropriately subsized test sample in the laboratory to obtain $G_f=1$ N/m or for using a loading rate that is too slow that creep effect was falsely introduced within the large test sample to obtain $G_f=15$ N/m. Testing the validity of these two numbers is beyond the scope of this paper due to scarce test data. However, in utilising the field test data, Mulmule and Dempsey (1998,1999) have indeed accounted for the creeping effect (at least in the bulk material) by applying the viscoelastic fictitious crack model. This model considers the secondary creeping effect in the bulk material (not inside the Fracture Process Zone (FPZ)) by a viscoelastic model. The fracture energy, which is back calculated by their algorithm based on their test data, is anticipated to be minimally influenced by the creep effect of ice. From an engineering application point of view, we present both results here and leave it to the reader's judgment to choose for their specific applications.

In addition, the same four curves that represent out-of-plane flexural failures with different ice thickness $t = 0.5, 1, 2, 3$ m in Fig. 18 are plotted in Fig. 19 by multiplying the load ratio β_{YZ} for comparison. To interpret Fig. 19, the intersections between the black solid curve ($G_f = 1$ N/m) and the red dashed curve with $t = 0.5$ m are highlighted to show the dominant failure scenarios over the considered floe size range (1 m–10 km). In addition, the intersection between the splitting failure curves with the wedge bending curves of the semi-infinite ice floe indicate the size requirement for an ice floe to be considered as level ice at the initial contact (i.e., dominated by local bending failure). Using the black solid curve with $G_f = 1$ N/m as an example, intersections with the wedge bending failure curves occur at the floe sizes of 70 m, 300 m, 1.1 km, and 2.5 km for ice thickness $t = 0.5, 1, 2,$ and 3 m, respectively, i.e., a larger floe is required for thicker ice to be considered as level ice.

Regarding the influences from the idealised contact properties, Fig. 19 demonstrated the competition among different failure scenarios with the deterministic contact forces ratio $\beta_{YZ} = F_Y / F_Z = 0.5$. If a different contact relationship is encountered, the corresponding curves in Fig. 19 can be scaled up and down to reflect the influence of different contact force components, e.g., for contact scenarios that produce a larger β_{YZ}, the floe size range for an in-plane global splitting failure mode in Fig. 19 (in grey colour) is accordingly expanded.

In addition to the material properties (e.g., fracture energy), Fig. 19 shows that the dominant failure mode is significantly influenced by floe size and ice thickness. These two parameters are investigated here to create a failure map with typical material constants in Fig. 20.

First, the border $L_{splitting\_bending}(t)$ between the splitting failure of an ice floe and the circumferential crack formation within a semi-infinite ice floe can be obtained from the equality $\beta_{YZ} F_{Z\_bending} = F_Y$. By inserting relevant formulae from Eqs. (22) and (23) into this equality, $L_{splitting\_bending}$ can be calculated by Eq. (24) and plotted, as shown by the black curves in Fig. 20.

$$L_{splitting\_bending} = \{\frac{2\beta_{YZ}}{3}\sigma_f t[1.05 + 2.0(\frac{r}{\ell}) + 0.50(\frac{r}{\ell})^3]\frac{H(a,0)}{K_{IC}}\}^2 \tag{24}$$

Assuming $\beta_{YZ} F_{Z\_radial\_cracking} = F_Y$ and inserting relevant formulae from Eqs. (17) and (23), the border $L_{splitting\_cracking}(t)$ between the splitting failure and the radial/circumferential cracking of a finite rectangular ice floe can be obtained as demonstrated by Eq. (25) and plotted as red curves in Fig. 20. Note that the solution of $L_{splitting\_cracking}$ is implicitly expressed in Eq. (25), for which a numerical approach is necessary.

$$L_{splitting\_cracking} = [(1 - \frac{\rho_i}{\rho_w})\frac{D\beta_{YZ}}{W(L_{splitting\_cracking})}\frac{H(a,0)}{K_{IC}}]^{2/5} \tag{25}$$

In terms of the border between the direct rotation and radial/circumferential cracking of a finite ice floe, a straightforward criterion, i.e., $L \le \ell$ for direct rotation and $\ell < B \le 2\ell$ or $\ell < L \le 2\ell$ for radial/circumferential cracking, has been adopted to plot the purple curves in Fig. 20.

Fig. 20 entails an ice thickness range of 0.3–3.3 m and a floe size range of 1 m–10 km. A deterministic contact property with $\beta_{YZ} = 0.5$ and two fracture energy input values were employed to create the failure map. For other contact properties and material properties, Eqs. (24) and (25) can be employed for the same purpose. Fig. 20 is plotted at a logarithmic scale and shows that a higher possibility exists for the in-plane global splitting failure mode as the

ice thickness increases. This finding is understandable as the critical vertical force, which produces an out-of-plane flexural failure increases with (thickness)^2, i.e., $\propto t^2$, where the ice splitting force $F_Y \propto t$. Thicker ice has a greater chance of failing in splitting failure mode.

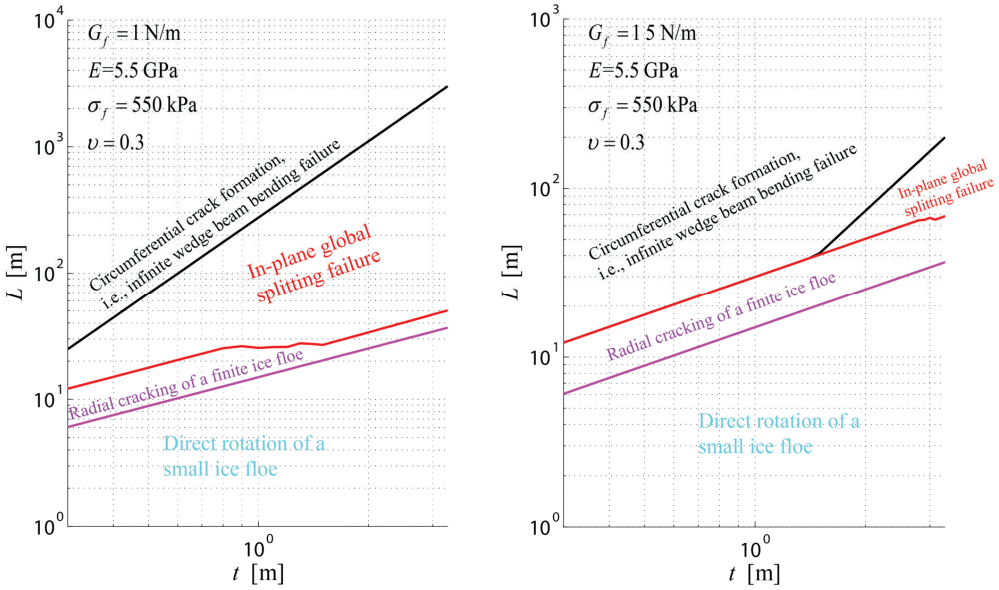

Fig. 20 Failure maps of the interaction of a square ice floe with a sloping structure, where $\beta_{YZ} = 0.5$.

5 Conclusions

This paper examined the fractures of an ice floe on both global and local scales. The effect of floe size on the salient failure modes and failure load is theoretically highlighted. Based on field observations in a relatively 'open' ice condition, e.g., a broken ice field, different failure modes of an ice floe were observed. Specifically, the global in-plane splitting failure and local out-of-plane flexural failures are assumed to be the two primary failure modes within the context of floe ice - sloping structure interactions. In addition, a competing mechanism exists between these two primary failure modes, i.e., the occurrence of one failure mode alleviates/suppresses the occurrence of the other failure mode. This competing mechanism is analytically quantified in this paper by studying each possible failure scenario in a decoupled manner.

Specifically, three different local out-of-plane flexural failure scenarios have been theoretically identified:

- Scenario #1: direct rotation of a small ice floe.
- Scenario #2: radial/circumferential cracking of a finite size ice floe, and
- Scenario #3: circumferential crack formation within a semi-infinite ice floe.

Within these three failure modes, the major focus of this paper is to tender a possible analytical solution towards the second scenario, i.e., radial/circumferential cracking of a finite size ice floe. This task is achieved based on the already available solution of a rectangular plate with

free edges resting on a Winkler-type elastic foundation. This analytical solution is implemented and validated with the current application (i.e., a finite size rectangular ice floe of varying width-to-length ratios). As this method is limited in yielding satisfactory stress calculations for ice floes within the interested floe size range, an alternative failure criterion, i.e., a displacement-controlled failure criterion, is conservatively employed to deduce Eq. (17) for calculating the critical vertical force under which a finite size ice floe fails at radial/circumferential cracking. Based on previous studies, Eqs. (20) and (22) were proposed for failure Scenarios # 1 and # 3. With these analytical formulae, the critical vertical force that produces different types of out-of-plane flexural failures of an ice floe, which encompass a large floe size range (i.e., from 1 m to 10 km), can be calculated. Specifically, the following conclusions for a rectangular ice floe can be formed:

- The direct rotation of an ice floe is anticipated if $\text{floe size} \le 13.5(\text{ice thickness})^{3/4}$. This size border[6] is established mainly for the reason that thin plate theory is not valid within this size range;
- Radial or circumferential cracking of a finite size rectangular ice floe is expected if the floe length or width falls in the range of $(13.5(\text{ice thickness})^{3/4} \sim 27(\text{ice thickness})^{3/4})$. A conservative calculation of the relevant critical vertical force can be obtained with Eq. (17);
- Ice floes with both its length and width larger than $27(\text{ice thickness})^{3/4}$ can be considered as a semi-infinite ice floe; their failure is featured by sequentially forming radial and circumferential cracks. Nevel's (1971) approximate solutions were utilised in this paper; they demonstrate that this failure mode leads to the largest critical vertical force among the previously mentioned out-of-plane flexural failure scenarios.

Afterwards, the known solution (i.e., Eq. (23)) regarding the splitting failure of an ice floe is incorporated into the comparison based on a highly idealised contact relationship. The competition between the out-of-plane failure and the in-plane failure is examined for a large range of floe sizes (i.e., from 1 m to 10 km). This competition reveals when the global splitting failure yields to the local bending failure at the initial contact; it reveals how large an ice floe must be to be considered as level ice. Based on a quantified competition with a fracture energy of 1 N/m and an idealised contact relationship[7] (i.e., $\beta_{YZ} = 0.5$), the size of an ice floe has to exceed 70 m, 300 m, 1.1 km, and 2.5 km for ice thicknesses of $0.5, 1, 2, \text{and } 3$ m, respectively, to be considered as level ice at the initial contact with the sloping structure. Floes less than these sizes with the corresponding thicknesses will fail with global splitting cracks.

In addition to the material properties, two major geometrical inputs (i.e., floe size and ice thickness) serve an important role within this quantified competition. Using typical material properties, a failure map was plotted for an ice floe with varying floe size and ice thickness. The general trend indicates that thicker ice has a greater chance of failure in global splitting failure mode. Detailed quantifications can be achieved with the formulae developed and proposed in this paper.

---

[6] In order to obtain a more sensible understanding, $13.5(\text{ice thickness})^{3/4}$ is utilised herein to approximate the characteristic length ℓ for a floating ice floe according to Gold (1971). However, a detailed formulation of the characteristic length of ℓ is given in Eq. (3).

[7] Please refer to Eq. (1) and Fig. 9 for the physical meaning of the symbol $\beta_{YZ} = 0.5$.

Reference

API_RP2, 1995. Recommended Practice for Planning, Designing, and Constructing Structures and Pipelines for Arctic Conditions. American Petroleum Institute.

Bhat, S.U., 1988. Analysis for splitting of ice floes during summer impact. Cold Regions Science and Technology, 15(1): 53-63.

Bhat, S.U., Choi, S.K., Wierzbicki, T. and Karr, D.G., 1991. Failure analysis of impacting ice floes. Journal of Offshore Mechanics and Arctic Engineering, 113: 171.

Bueckner, H.F., 1970. Novel principle for the computation of stress intensity factors. Zeitschrift fuer Angewandte Mathematik & Mechanik, 50(9).

Croasdale, K.R., 2012. Ice rubbling and ice interaction with offshore facilities. Cold Regions Science and Technology, 76–77(0): 37-43.

Dempsey, J.P., Adamson, R.M. and Mulmule, S.V., 1999. Scale effects on the in-situ tensile strength and fracture of ice. Part II: First-year sea ice at Resolute, NWT. International journal of fracture, 95(1): 347-366.

Dempsey, J.P., DeFranco, S.J., Blanchet, D. and Prodanovic, A., 1993. Splitting of ice floes, 1st International Conference: Development of Russian Arctic Offshore (RAO'93).

Dempsey, J.P., DeFranco, S.J., Blanchet, D. and Prodanovic, A., 1994. Mechanisms of fracture of sea ice. Hydrotechnical Construction, 28(3): 164-168.

Gold, L.W., 1971. Use of ice covers for transportation. Canadian Geotechnical Journal, 8(2): 170-181.

Hallam, S., 1986. The role of fracture in limiting ice forces, Proc. of the IAHR symposium on ice, Iowa City, Iowa, pp. 287-319.

Hetényi, M., 1946. Beams on elastic foundation, 1. University of Michigan Press Ann Arbor, Michigan, USA.

ISO/FDIS/19906, 2010. Petroleum and natural gas industries - Arctic offshore structures,International Standard, International Standardization organization, Geneva, Switzerland,.

Kerr, A.D., 1976. The bearing capacity of floating ice plates subjected to static or quasi-static loads. Journal of Glaciology, 17: 229-268.

Kotras, T.V., Baird, A.V. and Naegle, J.N., 1983. Predicting Ship Performance in Level Ice. Transactions - Society of Naval Architects and Marine Engineers, Volume 91, 1983. SNAME, New York, NY, USA, pp. 329-349.

Leppäranta, M., 2011. The drift of sea ice. Springer, Helsinki.

Li, R., Zhong, Y. and Li, M., 2013. Analytic bending solutions of free rectangular thin plates resting on elastic foundations by a new symplectic superposition method. Proceedings of the Royal Society A: Mathematical, Physical and Engineering Science, 469(2153): 20120681.

Lim, C.W. and Xu, X.S., 2010. Symplectic elasticity: theory and applications. Applied Mechanics Reviews, 63(5): 050802.

Lindseth, S.H., 2013. Splitting as a Load Releasing Mechanism for a Floater in Ice, Norwegian University of Science and Technology, Trondheim, 127 pp.

Lu, W., Lubbad, R., Høyland, K. and Løset, S., 2014. Physical model and theoretical model study of level ice and wide sloping structure interactions. Cold Regions Science and Technology, 101: 40-72.

Lu, W., Lubbad, R. and Løset, S., (Accepted on November 12th 2014). In-plane fracture of an ice floe: a theoretical study on the splitting failure mode. Cold Regions Science and Technology, DOI: 10.1016/j.coldregions.2014.11.007.

Lu, W., Lubbad, R. and Løset, S., (submitted in July, 2014). Out-of-plane failure of an ice floe: radial-crack-initiation-controlled fracture. Cold Regions Science and Technology.

Lu, W., Lubbad, R., Løset, S. and Høyland, K.V., 2012a. Cohesive zone method based simulations of ice wedge bending: a comparative study of element erosion, CEM, DEM and XFEM. In: Li and Lu (Editors), The 21st IAHR International Symposium on Ice, Dalian, China, pp. 920-938.

Lu, W., Lubbad, R., Serré, N. and Løset, S., 2013. A theoretical model investigation of ice and wide sloping structure interactions, Proceedings of the 22nd International Conference on Port and Ocean Engineering under Arctic Conditions, Espoo, Finland, pp. 1-14.

Lu, W., Løset, S. and Lubbad, R., 2012b. Ventilation and backfill effect during ice-structure interactions. In: Li and Lu (Editors), The 21st IAHR International Symposium on Ice, Dalian, China, pp. 826-841.

Lubbad, R., 2012. Data report: KV-Svalbard Survey 2012, Faculty of Engineering Science and Technology (IVT), NTNU, Trondheim.

Lubbad, R., Loset, S. and Lu, W., 2012. Oden Arctic Technology Research Cruise 2012: Data report Part I, SAMCoT report, Norwegian University of Science and Technology, Trondheim.

Lubbad, R. and Løset, S., 2011. A numerical model for real-time simulation of ship-ice interaction. Cold Regions Science and Technology, 65(2): 111-127.
Lubbad, R., Moe, G. and Løset, S., 2008. Static and Dynamic Interaction of Floating Wedge-Shaped Ice Beams and Sloping Structures. 19th IAHR Internatioanl Symposium on Ice: 179-189.
Lubbad, R., Raaij, E.V., Løset, S. and Eik, K.J., 2013. Oden Arctic Technology Rsearch Cruise 2012, Proceedings of the 22nd International Conference on Port and Ocean Engineering under Arctic Conditions, Espoo, Finland.
Løset, S., Shkhinek, K., Gudmestad, O. and Høyland, K., 2006. Actions from Ice on Arctic Offshore and Coastal Structures, Krasnodar, St Petersburg, Russia, 137-148 pp.
McKenna, R. and Spencer, D., 1993. Ice wedge dynamics and local crushing, The 12th International Conference on Port and Ocean Engineering under Arctic Conditions, Hamburg, pp. 85-96.
Michel, B., 1978. Ice mechanics. LES PRESSES DE L'UNIVERSITE LAVAL, Quebec, 499 pp.
Milano, V.R., 1972. Ship resistance to continuous motion in ice, Stevens Institute of Technology.
Nevel, D.E., 1958. The theory of a narrow infinite wedge on an elastic foundation, U. S. Army Snow Ice and Permafrost Research Establishment, Corps of Engineering.
Nevel, D.E., 1961. The narrow free infinite wedge on an elastic foundation, U. S. Army Snow Ice and Permafrost Research Establishment, Corps of Engineering.
Nevel, D.E., 1965. A semi-infinite plate on an elastic foundation, U. S. Army Snow Ice and Permafrost Research Establishment, Corps of Engineering.
Nevel, D.E., 1972. The ultimate failure of a floating ice sheet, International Association for Hydraulic Research, Ice Symposium, pp. 17-22.
Nevel, D.E., 1992. Ice forces on cones from floes, IAHR Symposium, 11th, pp. 1391-1404.
Palmer, A.C. and Croasdale, K.R., 2013. Arctic Offshore Engineering. World Scientific.
Palmer, A.C., Goodman, D.J., Ashby, M.F., Evans, A.G., Hutchinson, J.W. and Ponter, A.R.S., 1983. Fracture and its role in determining ice forces on offshore structures. Annals of glaciology, 4: 216-221.
Panfilov, D., 1960. Experimental investigation of the carrying capacity of a floating ice plate. Izvestia Vsesojuznogo Nauchno-Issledovatelsskogo Instituta Gidratekhniki, 64: 80-8.
Rice, J.R., 1972. Some remarks on elastic crack-tip stress fields. International Journal of Solids and Structures, 8(6): 751-758.
Sanderson, T.J.O., 1988. Ice mechanics and risks to offshore structures.
Schulson, E.M. and Duval, P., 2009. Creep and fracture of ice, 1. Cambridge University Press, Cambridge, 190-211 pp.
Sodhi, D.S., Chin, S.N. and Stanley, J.M., 1993. Indentation and splitting of freshwater ice floes. AMD, 163: 165-175.
Su, B., Riska, K. and Moan, T., 2010. A numerical method for the prediction of ship performance in level ice. Cold Regions Science and Technology, 60(3): 177-188.
Timco, G.W., 1987. Indentation and penetration of edge-loaded freshwater ice sheets in the brittle range. Journal of Offshore Mechanics and Arctic Engineering, 109(3): 287-294.
Timokhov, L.A. and Kheysin, D.Y., 1987. Dynamika Morskikh L'dov. Gidrometeoizdat, Leningrad.
Timoshenko, S., Woinowsky-Krieger, S. and Woinowsky, S., 1959. Theory of plates and shells, 580. McGraw-Hill New York.
Valanto, P., 2001. The resistance of ships in level ice. SNAME, 109: 53-83.
Ventsel, E. and Krauthammer, T., 2001. Thin plates and shells: theory: analysis, and applications. CRC press, New York.
Wadhams, P. and Horne, R.J., 1980. An analysis of ice profiles obtained by submarine sonar in the Beaufort Sea. Journal of Glaciology, 25: 401-424.
Yao, W.A., Zhong, W.X. and Lim, C.W., 2009. Symplectic elasticity. World Scientific.
Zhong, W.X. and Williams, F.W., 1993. Physical interpretation of the symplectic orthogonality of the eigensolutions of a hamiltonian or symplectic matrix. Computers & structures, 49(4): 749-750.
Zhong, W.X. and Zhong, X.X., 1993. Method of separation of variables and Hamiltonian system. Numerical Methods for Partial Differential Equations, 9(1): 63-75.

Appendix 4 Rubble accumulation influences

This appendix includes the paper published in Journal of Cold Regions Science and Technology (see below).

- Lu, W., Lubbad, R., Høyland, K. and Løset, S., 2014. Physical model and theoretical model study of level ice and wide sloping structure interactions. Cold Regions Science and Technology, 101: 40-72.

Appendix IV

Cold Regions Science and Technology 101 (2014) 40–72

Contents lists available at ScienceDirect

Cold Regions Science and Technology

journal homepage: www.elsevier.com/locate/coldregions

Physical model and theoretical model study of level ice and wide sloping structure interactions

Wenjun Lu *, Raed Lubbad, Knut Høyland, Sveinung Løset

Sustainable Arctic Marine and Coastal Technology (SAMCoT), Centre for Research-based Innovation (CRI), Norwegian University of Science and Technology (NTNU), Trondheim, Norway

ARTICLE INFO

Article history:
Received 30 May 2013
Accepted 28 January 2014
Available online 8 February 2014

Keywords:
Physical model test
Theoretical ice load model
Level ice
Downward sloping structure
Rubble accumulation
Interaction mechanism

ABSTRACT

Wide sloping structures have many applications in ice-infested waters because of their ability to fail the incoming ice in a bending failure mode. However, the poor ice clearing ability of such structures could lead to ice rubble accumulation in front of the structure, which subsequently alters the interaction mechanism. In this paper, the mechanism of level ice interacting with wide downward sloping structures was explored through a theoretical model and a series of physical model tests. Emphasis has been placed on the effects of the rubble accumulation. Based on the observations and previous theoretical ice load calculation models, a new theoretical model that couples the rubble accumulation's effects with all of the other interaction processes was proposed in this paper. In addition, this model enables us to effectively construct the ice load's spatial and temporal variations with respect to level ice interacting with downward wide sloping structures. Afterward, the theoretical model was validated by two sets of physical model tests. One of the physical model tests featured a tactile sensor that was installed on a sloping plate, which was pushed through the model level ice. The ice load's spatial and temporal variations were measured and compared to the theoretical predictions. Another physical model test set-up was a wide sloping structure that was equipped with load cells to measure the global ice load. Based on both the experimental results and theoretical model, it was concluded that the rubble accumulation in front of the sloping structure introduces additional pressure on both the incoming ice sheet and the structure itself; this pressure greatly influences the intact level ice's failing mechanism and consequently the ice load. Furthermore, the common results from both the experimental measurements and theoretical model elucidate several important aspects of the interaction mechanisms. For instance, the maximum ice load is detected slightly below the waterline within the undeformed level ice's thickness region; the ice rotating process together with the rubble effects further transmit the ice load downward to a distance of more than three times the ice thickness; and the rubble effects together with possible secondary ice breakings during the ice rotating process were theoretically demonstrated to reduce the eventual ice breaking length.

1. Introduction

Wide sloping structures have many applications in ice-infested waters. Compared to narrow structures, this rather intuitive word 'wide' reflects many different mechanisms that occur during the level ice and sloping structure interactions. Some example mechanisms are a circumferential crack before radial cracks (Løset et al., 2006), rubble accumulation, and scaling effects (Sanderson, 1988). Based on the waterline diameter, Timco et al. (2000) set an order of 100 m and 10 m to separate the wide structures from the narrow structures, respectively, whereas Yue et al. (2007) refer to a narrow cone as a structure without rubble accumulation. However, insufficient data are available for a precise structure classification (Løset et al., 2006). In the current paper, the term 'wide structure' is used to highlight the rubble-accumulation effects. In addition, the sloping surface of the structure can be conical, multifaceted, or flat (ISO/FDIS/19906, 2010), and the structure can have either downward or upward sloping surfaces. As fundamental research to investigate the rubble accumulation's effect on the overall interaction mechanism, the current study is simply confined to a fixed two-dimensional wide structure with downward, flat sloping surfaces.

In the development of theoretical models regarding the interaction between level ice and a sloping structure, it has long been recognised that the ice load comprises at least two components, namely, the ice-breaking component and the ice ride-up/down component (termed as rubble accumulation in this paper) (Ralston, 1981). The maximum load that a sloping structure encounters could even be due to the rubble-accumulation part rather than the ice breaking part (Määttänen and Hoikkanen, 1990; Paavilainen and Tuhkuri, 2013). Because of the relatively limited clearing capability of a wide sloping structure, the presence of rubble greatly influences the entire interaction mechanism. However, in the current ISO standard (ISO/FDIS/19906, 2010), such an influence is merely mentioned, whereas the recommended principal methods (Croasdale and Cammaert, 1994; Ralston, 1980) treat the rubble accumulation load and ice breaking load separately without explicitly

* Corresponding author.
E-mail address: wenjun.lu@ntnu.no (W. Lu).

0165-232X/$ – see front matter © 2014 Elsevier B.V. All rights reserved.
http://dx.doi.org/10.1016/j.coldregions.2014.01.007

accounting for their possible coupling in the bending failure. To account for the fact that the piled rubble rests on both the sloping structure and intact incoming ice, Määttänen and Hoikkanen (1990) introduced additional rubble pressure in their elastic-foundation beam formulation, which was solved with the finite element method (FEM). Mayne (2007) derived analytical formulas to consider the rubble pressure's influence on the ice breaking process for two basic cases, namely, the triangle-shaped rubble pressure distribution and the uniform rubble pressure distribution. The presence of rubble alters the location of the maximum bending moment and thus changes the ice breaking load and ice breaking length. Most of these efforts have been dedicated to identifying the maximum ice load that the relevant structure would encounter.

From a different approach, sophisticated numerical theories and tools have been developed to study the interaction in a procedural manner. These tools include the combined finite element and discrete element method (DEM) (Paavilainen et al., 2009), the cohesive element method (CEM) (Gürtner et al., 2008; Lu et al., 2012a), continuum damage mechanic (CDM) based method (Kolari et al., 2009), etc. In contrast to the abovementioned theoretical methods, these numerical methods allow the progressive failure of the ice to be simulated. The major interaction processes are simulated with the ice load history calculated in the time domain. The rubble accumulation and its effects become a natural output from the simulations. In these simulations, different processes are typically difficult to quantify separately. Furthermore, these tools are computationally exhaustive compared to simplified theoretical models.

In parallel to studying the interaction mechanism with the presence of rubble accumulation, the current paper also seeks to tender a theoretical model that is situated between the above two approaches (i.e., the conventional theoretical models that focus on the single design ice load and the sophisticated numerical methods that simulate the process as a whole to account for the ice load history). This theoretical model is capable of predicting both the spatial and temporal variation of the ice load in a two-dimensional setting. It is also efficient because of its theoretical simplifications. However, the interaction between the level ice and sloping structures is rather complicated because of the presence of rubble accumulation. Different assumptions and formulas are applicable only at certain interaction stages. For example, Croasdale (2012) identified three different stages and proposed different ice load prediction formulas for different interaction scenarios. Thus, one of the goals for the current paper is to adapt the new theoretical model to different interaction stages that has been observed in the physical model tests.

The current paper is composed of three major parts. In the first part, the theoretical model is proposed and derived in detail. In the second part, physical model studies to validate this theoretical model are introduced and the results are compared to the theoretical predictions. Finally, in the third part, the important findings based on both the theoretical model and physical model are discussed and conclusions are drawn.

2. A theoretical model for level ice interacting with wide sloping structures

The developed theoretical model is presented in this section. First, the interaction mechanism is developed based on previous knowledge and observations. Then, the derivation of the theoretical model within each of the interaction processes is described. Lastly, how different interaction processes are linked to construct the ice load's spatial and temporal variations are elucidated.

2.1. The interaction mechanism

Frederking and Timco (1985) discerned three different ice load components for level ice interacting with sloping structures (i.e., breaking, rotating, and sliding) and proposed formulas to calculate them. These components were conservatively added up to obtain the maximum design ice load.

With respect to the interaction process, Croasdale (2011, 2012) identified three stages. In the first two stages, the incoming level ice fails against the sloping structure, and in the third stage, the incoming ice fails against the accumulated ice rubble. The ISO 19906 (2010) recommended formulas (Croasdale and Cammaert, 1994) are valid only for the first two stages. The third stage is analogous to the ridge building process; and the ice load on the structure can be calculated with the recommended ridging load (Croasdale, 2009; Palmer and Croasdale, 2013). Based on the physical model test observations, the above mentioned two different cases (i.e., incoming ice, case 1: fails against the inclined structure; and case 2: fails against the accumulated rubble) are included in the current theoretical model. However, the possibility of grounding the accumulated ice rubble is excluded from the initial assumption.

With similar definitions for the above-mentioned load components and interaction processes, and in analogy to the research on ship and level ice interactions (Kotras, 1983; Lindqvist, 1989; Valanto, 2001), in the current paper, the interaction processes are categorised into the ice breaking process (i.e., the process in which the intact level ice breaks in bending failure mode), ice rotating process (i.e., the already-broken ice block is further rotated until it becomes parallel to the sloping surface), and rubble accumulation process (i.e., instead of being cleared, part of the ice rubble accumulates in front of the structure, leading to an additional ice load).

Based on the ice basin and field[1] observations and the above classification, the interaction process can be simplified, as shown in Fig. 1. The interaction sequence is assumed to be the following: ❶, ❷, ❸ and ❹, as shown in an anticlockwise sequence in Fig. 1.

The incoming level ice first failed against the sloping structure in a bending failure mode under the influence of rubble pressure (i.e., buoyancy) from beneath, as shown in Fig. 1❶.

Then, in the ice rotating process, the ice started to be gradually rotated downwards. The recorded ice load slides down along the sloping plate. This process is illustrated in Fig. 1❷. Note here that the rotating ice block is 'jumping' out of the water during the rotating process. This phenomenon has been observed both in the current physical model test (see the left figure in Fig. 2) and in the field (see the right figure in Fig. 2). A similar field observation has also been stated by Valanto (2001).

Previous studies have noted that elastic-foundation beam or plate theory tends to over-predict the ice breaking length than the lengths that have actually been observed (Michel, 1978). Some investigators attribute the shorter ice breaking length to a dynamic effect (Lubbad et al., 2008), and others propose that other failure modes play a role, such as shearing failure with thicker ice (Lau et al., 1999; Määttänen et al., 1996). In the current paper, another possibility is introduced: the rubble pressure influence and possible secondary breaking of an ice block in the ice rotating phase, as shown in Fig. 1❸. First, as will be shown later, the presence of rubble accumulation would lead to a shorter ice breaking length. Moreover, depending

[1] Mainly based on observations on the icebreaker ODEN, which has a rather flat downward sloping bow (with a 31 m beam width) interacting with ice at a rather low speed (e.g., 1–2 knots).

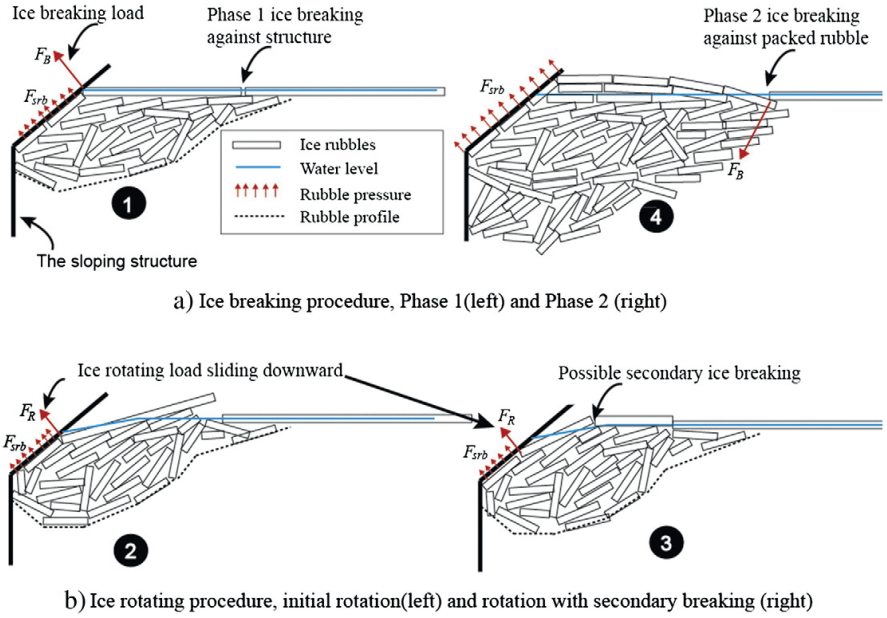

Fig. 1. Level ice and wide sloping structure interaction mechanism (refer to Table 1: F_B denotes the ice breaking load; F_R represents the ice rotating load; F_{srb} stands for the load due to the rubble pressure).

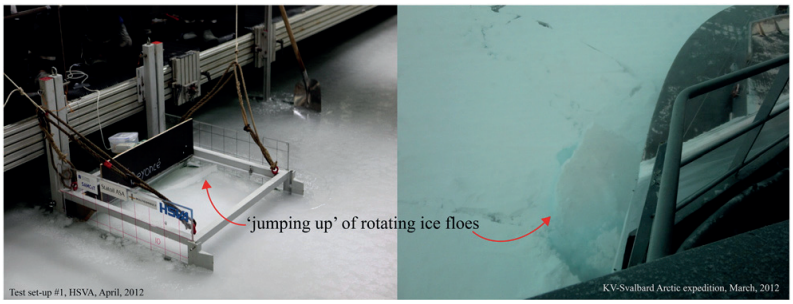

Fig. 2. The observed rotating ice floes are jumping up (left: the physical model test set-up #1 in the current paper[2], and right; field observation.

on the length of the rotating ice block, the amount of rubble accumulation, and the ventilation phenomena (Lu et al., 2012b), a secondary ice breaking phenomenon can be expected theoretically. Such secondary ice breaking during the ice rotating phase has been observed by Timco (1984) during model tests with an upward sloping plate. It is difficult to observe such phenomena in the current test set-up with the downward sloping plate which has a rather limited size. However, as shown in Fig. 3, the secondary ice breakings are frequently observed when the icebreaker ODEN transits in level ice. Furthermore, with the same algorithm for ice rotating process, it has been shown by Lu et al. (2013a) that there is a high possibility for such phenomena to occur under the influence of rather high rubble pressure for typical ice properties.

As more ice rubble accumulates in front of the structure, the ice fails onto the rubble instead of onto the sloping structure. This phenomenon is shown in Fig. 1❹. This process was referred to as a 'rubbling' failure mode by Croasdale (2011), and it was categorised in the third stage of interaction based on Croasdale (2012). Croasdale further discerned three different cases with respect to the rubbling failure mode (i.e., footing failure, ride up, and ride down). In the current test set-up, however, only the ride-up failure mode was observed (i.e., the incoming level ice fails against the accumulated rubble by bending and is further pushed upward, as shown in Fig. 1❹). Such an observation is illustrated in Fig. 4.

By assuming that the ice fails in bending against the rubble with a random rubble sloping angle, Kry (1980) derived a formula to calculate the ice load during rubble formation as a fraction of the ice load required to buckle or crush an incoming ice beam. However, during the current test set-up,

[2] In the second part of this paper, two test set-ups (test set-ups #1 and #2) will be introduced in detail. Both test set-ups are considered to be wide sloping structures. For the discussion in this section, because the focus is on the interaction mechanisms, the test set-up details were not introduced beforehand. However, interested readers are referred to the details in the second part of this paper.

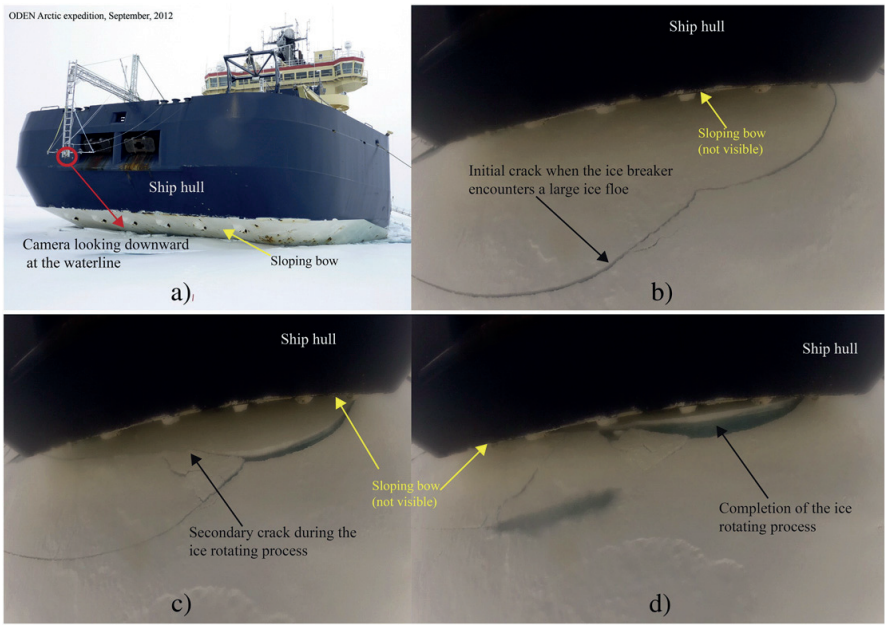

Fig. 3. One of the often-observed secondary ice breakings near the bow of the icebreaker.

the upper part of the rubble is quite compact, and the sloping angle of the rubble is rather stable. Therefore, in the current study, when deriving the bending failure of the incoming level ice against the accumulated ice rubble, a deterministic rubble sloping angle was calculated based on static analysis.

2.2. The overall structure and basic assumptions of the theoretical model

Fig. 5a illustrates that the theoretical model is composed of three modules, namely, the ice breaking module, ice rotating module, and rubble accumulation module. Among these modules, depending on the amount of rubble accumulation, the ice breaking module is further classified into phase 1 and phase 2 ice breaking stages (see also Figs. 1❶, ❹ and 4). Possible secondary ice breaking is considered in the ice rotating module (see Fig. 1❸).

Within each module, considerable attention has been paid to the importance of the rubble accumulation's effects. Based on the current physical model test observations (Lu et al., 2013b; Serré et al., 2013b), and also the observation made by Timco (1991), the accumulated rubble has been found to influence the failing mechanism significantly. Thus, a coupled description of the rubble accumulation and intact ice interaction is essential during the level ice and wide sloping structure interactions.

From a temporal perspective, the current theoretical model situates between those conventional theoretical models which calculate one single design ice load irrespective of its temporal information; and those sophisticated numerical models which simulate the global ice load at each time step so as to construct the ice load history. The current theoretical model does not solve any dynamic equation to advance the solution in time. Instead, in analogy to the methods used by the ice–ship interaction researchers (Kotras, 1983; Valanto, 2001), we split the interaction into different procedures (i.e., different modules) and solve corresponding governing equations in a sequential manner to construct the ice load history. Fig. 5b

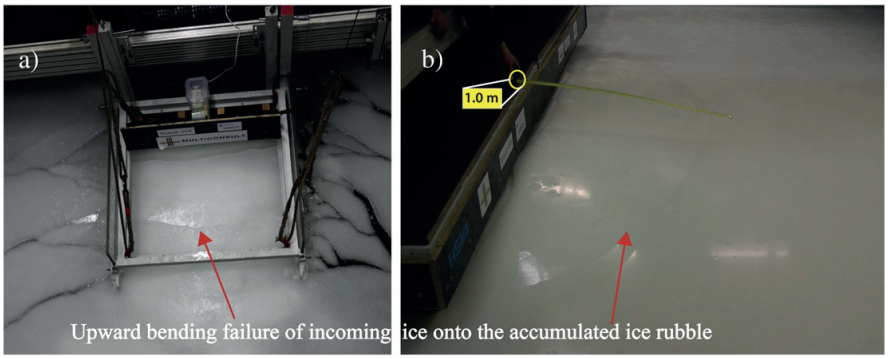

Fig. 4. The phase 2 ice breaking scenario: the incoming ice sheet fails in upward bending before reaching the sloping structure (a) physical model test set-up #1; (b) physical model test set-up #2.

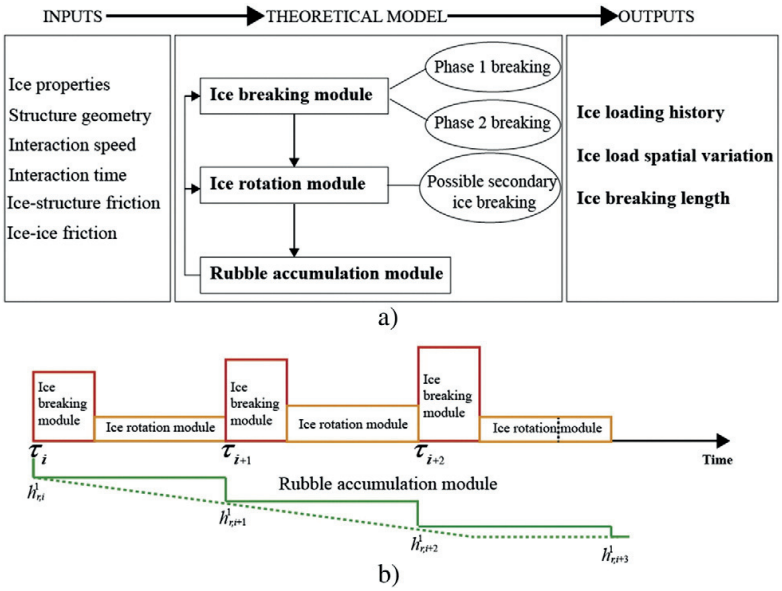

Fig. 5. (a) The overall structure of the current theoretical model; (b) the time domain activation/deactivation of each module.

schematically illustrates how different modules are activated at a particular time point τ_i in order to obtain the corresponding ice load in the time domain. Here an important reference time point τ_i has been introduced (see Fig. 5b). It can be understood as a reference time point τ_i at which the rubble height had a step wise change into $h^1_{r,i}$ (i.e., the boundary conditions of each module). From τ_i to τ_{i+1}, the physical processes are the breaking off of an ice block from the intact ice sheet and also the rotation of this broken ice block. During this period, it is simply assumed that the rubble height is a constant value $h^1_{r,i}$. From τ_i to τ_{i+1}, the ice breaking module and ice rotation module are activated sequentially to calculate the corresponding ice load history to fill up this time gap. In Section 2.3, formulas to calculate the changing rubble height $h^1_{r,i}$ will be given. Afterwards, the detailed algorithm to calculate the ice load based on each module at a reference time point τ_i will be introduced. Then in Section 2.4, how these calculated ice loads can be generalised at arbitrary time t is given. Finally, these different load components' spatial variation is also introduced.

In developing this theoretical model, the following assumptions have been made:

- The theoretical model is developed in a two-dimensional space (see Fig. 1). In the structure's width direction, the ice is assumed to fail simultaneously (i.e., non-simultaneous contact is not considered; potential size effect in the width direction is not considered);
- Due to the relatively low interaction speed in most tested cases (i.e., around 0.2 m/s in full scale), this theoretical model is based on quasi-static mechanics;
- Only the bending failure mode is considered in the current theoretical model. Other possible failure modes, such as shearing and buckling failures are not considered. However, as illustrated by the numerical simulation of Paavilainen et al. (2010), the major failure modes are dominated by bending failure during ice and wide sloping structure interactions. Nevertheless, caution should be made when applying this model to thick ice conditions since shearing failure was not included. The current bending failure assumption would over-predict the ice breaking load and ice breaking length for thick ice conditions. This will further increase the ice rotating load and eventually the global ice load. Caution should also be made for the application of the current model to structures with rather steep sloping angle due to the possible events of buckling failures. The underlying assumption of this theoretical model is that bending failure is the dominant failure modes. Once other failure modes (crushing, shearing or buckling) start to override, modifications to the current model are necessary;
- The intact ice is assumed to fail instantly when the tensile stress in the upper surface reaches the flexural strength of the ice. The progressive fracturing process (Lu et al., 2012c) is not considered here;
- During the formulation of the bending failure problem, the axial force is not considered. The presence of axial force would increase the ice breaking load. However, as demonstrated by a detailed study in Appendix A.3, the simplification made to neglect the axial force in most cases (i.e., structure's sloping angle smaller than 60° and ice–structure friction coefficient less than 0.3) would not under-predict the calculated ice breaking load by more than 10%;
- Within the ice rotation module, it is assumed that there is no contact between the rotating ice block and the intact level ice sheet (as shown in Fig. 1❷);
- Upon the completion of the ice rotation, it has been assumed that a new contact with the intact ice sheet occurs immediately and the ice breaking module is activated (see Fig. 5b);
- A continuum assumption is made for the accumulated ice rubble. Therefore, the ice rubble's influence is considered by adding additional pressure in the formulation of the ice breaking and ice rotation modules. The porosity of the rubble is taken from the measurements conducted in the same test (Serré et al., 2013b). Although the rubble's discrete nature is lost by assuming that it is a continuum, this approach avoids the low-porosity problem that is created by a two-dimensional DEM simulation, as mentioned by Paavilainen et al. (2010);
- A bilinear rubble profile with constant repose angle has been assumed during the whole rubble accumulation phase.(details of the rubble profile are presented in the next section).

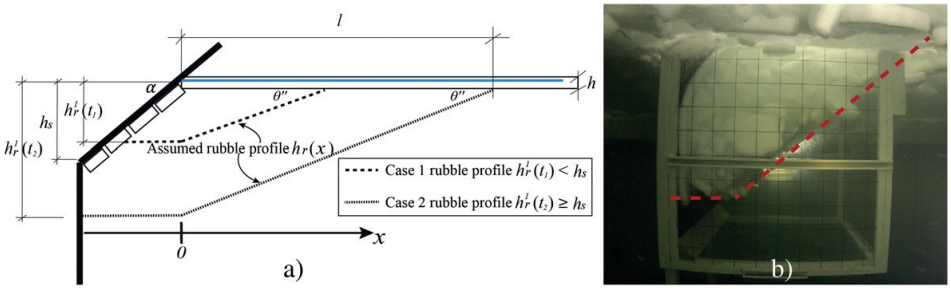

Fig. 6. Simplified bilinear rubble profile: (a) theoretical idealisation; (b) physical test observation.

- There is no grounding effect for the accumulated rubble because the grounding rubble typically lowers the ice load (Palmer and Croasdale, 2013).
- The rubble clearing effect is considered only by setting a maximum rubble height $h_{r,max}$ as a threshold beyond which the ice rubble is assumed to be cleared instantly. The maximum rubble height $h_{r,max}$ in the current study is chosen based on the structure's geometry (e.g., distance from waterline to the location where the rubble deflecting skirt is located).

2.3. The geometry of the rubble accumulation profile

Instead of simulating the rubbling process and predicting the rubble profile's history as Paavilainen et al. (2010), the current paper focuses mainly on the overall effects of rubble accumulation. Therefore, the rubble profile is simply assumed to be a bilinear shape (see Fig. 6) based on the observations in the current test campaign (Lu et al., 2013b). The bilinear rubble profile is also proposed by Mayne (2007) based on observations from the confederation bridge pier. Furthermore, it is also assumed that the repose angle θ'' remains unchanged when the rubble volume is growing due to rubble accumulation (e.g., see the two different rubble profiles (i.e., case 1 and case 2) at different times in Fig. 6).

Although the shape of the rubble profile has been largely simplified by assumption, it should be noted here that the appropriate choice of a constant slope to approximate the rubble volume works well irrespective of its actual rubble profile (Palmer and Croasdale, 2013). Based on the rubbling process's simplification, the volume change $V(t)$ in the ice rubble accumulation is described by Eq. (1).

$$V(t) = \max\left(vt - \frac{h_s}{\sin(\alpha)}, 0\right) h \frac{1}{(1-\eta)} \tag{1}$$

where

vt is the ice penetration; v is the interaction velocity; and t is the interaction duration;
h_s is the height of the underwater part of the sloping surface and is a constant for a specific sloping structure;
α is the sloping angle of the structure;
$\frac{h_s}{\sin(\alpha)}$ is the length of the sloping surface. Based on experimental observations, the broken ice usually slides further along the sloping surface before they rotate upwards to form the rubble accumulation. Therefore, this length is subtracted from the ice penetration vt. In another word, the first $\frac{h_s}{\sin(\alpha)}$ length of the ice sheet is not considered a part of the ice rubble;
h is the thickness of the incoming level ice;
$\eta = \frac{V_{sea\_water}}{V_{sea\_water}+V_{pure\_ice}+V_{brine\_pockets}}$ is the rubble's macro porosity V_{sea_water}, V_{pure_ice} and $V_{brine\_pockets}$ are the volume of sea water, pure ice and brine pockets respectively. In this paper, the calculation of the macro porosity is calculated based on Serré et al. (2013b).

The rubble height at the level ice and structure's contact point is denoted as h_r^1, in which the index 1 represents the first value in the spatial discretisation of the rubble profile $h_r(x)$ (see Fig. 6). In Fig. 6, two different cases can be discerned depending on the rubble volume. Moreover, based on assumption, there is a threshold value $h_{r,max}$ to account for the rubble clearing efficient. The rubble height h_r^1 can be expressed by Eq. (2) for three different cases.

$$\begin{aligned} h_r^1(t) &= \sqrt{2V(t)/\left(\frac{1}{\tan\theta''}+\frac{1}{\tan\alpha}\right)} \quad h_r^1 < h_s \\ h_r^1(t) &= \sqrt{h_s^2\left[\left(\frac{\tan\theta''}{\tan\alpha}\right)^2 + \frac{\tan\theta''}{\tan\alpha}\right] + 2V(t)\tan\theta''} - h_s\frac{\tan\theta''}{\tan\alpha} \quad h_r^1 \geq h_s \\ h_r^1(t) &= h_{r,max} \quad h_r^1 \geq h_{r,max} \end{aligned} \tag{2}$$

θ'' is the repose angle of the ice rubble.

The rubble profile $h_r(x)$ can be expressed by Eq. (3):

$$h_r(x,t) = h_r^1(t)\frac{(l-x)}{l} \tag{3}$$

x is the coordinate system of the rubble profile, $0 \leq x \leq l$ (see Fig. 6).
l is the rubble span (see Fig. 6).

Table 1
Expressions for the different load components.

F_x	General format of the different total ice load component expressions
F_B	Total ice breaking load in the ice breaking module
F_R	Total ice rotating load in the ice rotation module
F_p	Total load that is required to push the ice movements toward the structure in the ice accumulation module
F_{srb}	Total load due to the rubble accumulation's stationary buoyancy pressure against the structure in the ice accumulation module

Eqs. (2) and (3) above are continuous in time. The green dashed curve in Fig. 5b illustrates the rubble height $h_r^1(t)$ ' s variation. However, the rubble is assumed to increase in a stepwise manner in the calculations. The actual rubble height that was involved in the calculation remains constant from $t = \tau_i$ until $t = \tau_{i+1}$. This leads to the value of $h_r^1(\tau_i) = h_{r,i}^1$ (see the solid green curve in Fig. 5b).

After introducing the assumption made for the rubble profile, different load components are introduced separately in the following sections. Before entering the following sections, it is helpful to introduce some general conventions that are used throughout the remainder of this paper.

- Different ice load components are expressed in a general form as F_X, in which X can be replaced to obtain the different load contributors, as in Table 1;
- The different load components, F_{XH} and F_{XV}, represent the horizontal and vertical components of F_X, respectively. The positive direction of each load components together with the contact normal and shear for both the structure and the ice beam area shown in Fig. 7. Considering the relative motion between the incoming level ice, accumulated ice rubble, and structure, these three load components can be related, as in Eqs. (4) and (5). Note here that with the different considered bodies, structure or ice, the load has a same magnitude but opposite direction according to Newton's 3rd law.

$$\frac{F_{XH}}{F_{XV}} = \frac{\sin\alpha + \mu_s \cos\alpha}{\cos\alpha - \mu_s \sin\alpha} \tag{4}$$

$$F_X = \frac{F_{XH}}{\sin\alpha + \mu_s \cos\alpha} = \frac{F_{XV}}{\cos\alpha - \mu_s \sin\alpha} \tag{5}$$

μ_s is the ice–structure friction coefficient.
$\boldsymbol{s}$ (in Fig. 7) is the positive shear direction in the ice–structure contact interface.
$\boldsymbol{n}$ (in Fig. 7) is the positive normal direction in the ice–structure contact interface.

When any one of these three load components is known, the other two can be derived based on Eqs. (4) and (5). In the following model development, the focus will be placed on calculating only one of the load components without elaborating on how each of the other load components is obtained.

- In this paper, discrete values in the spatial domain are distinctively written in index form with an upper index (e.g., the rubble profile at a certain time, i.e., $h_r(x, t = 0) = h_{r,1}^k$. k is a spatial discretising index);
- Values in time domain are written in vector form with bold letters (e.g., the load history $\boldsymbol{F_X}$ and ice beam's tip deflection $\boldsymbol{Z_B}$). If the time domain value has to be written with index notation, lower index is utilised (e.g., $F_X(t = t_j) = F_{X,j}$, with j being a temporal discretising index).

2.3.1. The ice breaking module

The ice breaking module is further separated into two phases. The load components on the structure considered in each phase are illustrated in Fig. 8.

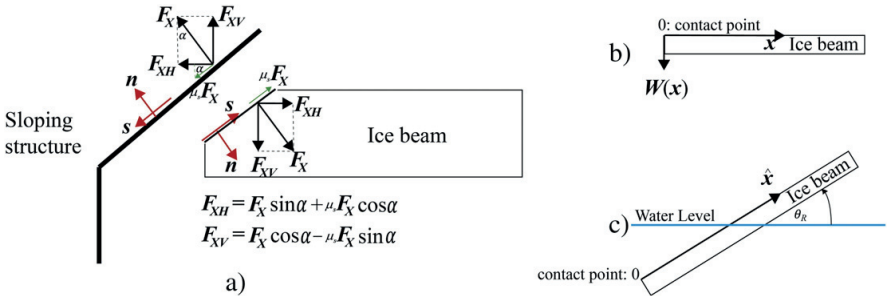

Fig. 7. (a) Positive contact force components, contact normal and shear direction for both the structure and the ice; (b) positive kinematic terms in the ice breaking module in a fixed Cartesian coordinate system ($W(x)$ is the vertical ice beam deflection); (c) positive kinematic terms in the ice rotation module in a co-rotational coordinate system (θ_R is the angle of the ice beam's rotation).

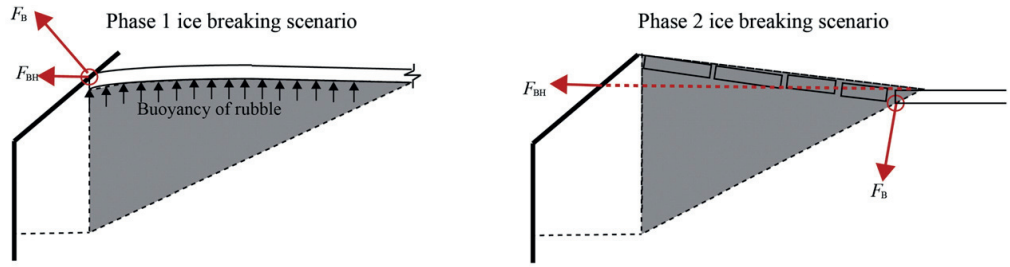

Fig. 8. The two different phases of the ice breaking module: (a) phase 1 ice breaking scenario; (b) phase 2 ice breaking scenario.

Fig. 8a illustrates that the rubble pressure (in the shaded area) introduces an additional bending moment in the incoming ice sheet. The ice breaking load F_{BV} in the phase 1 ice breaking scenario represents the load that is required to fail the incoming ice sheet in bending with the presence of additional rubble pressure beneath it.

When formulating the ordinary differential equation (ODE) for the phase 1 ice bending scenario, F_{BV} can be obtained by solving Eq. (6) at a reference time point τ_i.

$$EI\frac{d^4W(x)}{dx^4}+\rho_w gDW(x)=-Dq_r(x,\tau_i)_{0\le x\le l}+F_{BV}(\tau_i)\cdot\delta(x) \tag{6}$$

E is Young's modulus of the ice;
I is the area moment of the ice beam cross section;
x is the coordinate of the ice beam, see Fig. 6;
$W(x)$ is the vertical deflection of the beam;
D is the width of the considered ice beam and is taken to be one here to calculate a line load;
$q_r(x, \tau_i)$ is the rubble pressure profile and can be expressed as in Eq. (7).

$$q_r(x,\tau_i)=(\rho_w-\rho_i)gh_r(x,\tau_i)(1-\eta) \tag{7}$$

ρ_w and ρ_i are the water density and ice density, respectively;
g is the gravitational acceleration;
$\delta(x)$ is a delta function with $\delta(x=0)=1$ and $\delta(x\neq 0)=0$.

The value of τ_i and further temporal evolution of F_{BV} is addressed in Section 2.4.1. The detailed solution methods and procedures of Eq. (6) are provided in Appendix A. In general, the solutions of the beam deflection are obtained by superimpositions as in Eqs. (60) and (61). The value for $F_{BV}(\tau_i)$ is solved through Eq. (62) in an iterative manner (see the numerical scheme in Appendix A.3).

When solving Eq. (6), if the rubble pressure alone can already break the ice (see Fig. 4), then the phase 2 ice breaking scenario is activated, as shown in Fig. 1❹ and Fig. 8b. In this situation, Eq. (8) is utilised to extract the ice breaking load. In Eq. (8), the influence from the rubble pressure (i.e., the additional bending moment) is neglected (see Fig. 8b). The problem reduces to the conventional semi-infinite beam on the Winkler foundation under a free-end point load $F_{BV}\delta(x)$.

$$EI\frac{d^4W(x)}{dx^4}+\rho_w gDW(x)=F_{BV}\delta(x). \tag{8}$$

To calculate the ice breaking load in phase 2, the key value to determine is the angle of the rubble's upward slope θ'. In the current paper, a simple localised static balance calculation is performed to determine this angle (see Fig. 9). Along the rubble profile, the keel depth of the rubble $h_r^k(\tau_i)$ is known (e.g., it can be discretised from Eq. (3)); a search is made to find the point (i.e., the value of X_r^k) where $\left(1-\frac{\rho_r}{\rho_w}\right)h_r^k(\tau_i)=X_r^k\tan(\alpha)$. Once this point is found, the rubble profile's upward sloping angle $\theta'(\tau_i)$ is calculated, as in Eq. (9).

$$\theta'(\tau_i)=\tan^{-1}\left[\frac{\left(1-\frac{\rho_r}{\rho_w}\right)h_r^k(\tau_i)}{(l-X_r^k)}\right] \tag{9}$$

where ρ_r is the density of the ice rubble. For a downward sloping structure it can be calculated as in Eq. (10).

$$\rho_r=(1-\eta)\rho_i+\eta\rho_w. \tag{10}$$

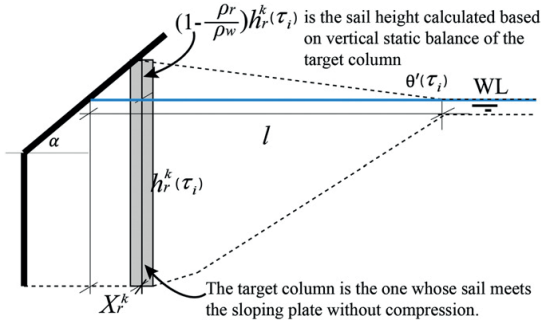

Fig. 9. A simple search to find the rubble profile's upward slope angle (the dashed line represents the rubble profile).

The horizontal ice load based on the solution of Eq. (8) is shown in Eq. (11) (Croasdale and Cammaert, 1994). The load action point of this load is assumed to be at the water line area (see Fig. 8b).

$$F_{BH}(\tau_i) = 0.68D\sigma_f\xi(\tau_i)\left(\frac{\rho_w g h^5}{E}\right)^{0.25} \tag{11}$$

$\theta'(\tau_i)$ is the angle of the rubble profile above water, see Fig. 9;
$\xi(\tau_i) = \frac{\sin\theta' + \mu_s\cos\theta'}{\cos\theta' - \mu_s\sin\theta'}$ is the ratio between the horizontal and vertical loads on the upward rubble slope.

2.3.2. Outputs and discussion of the ice breaking module

In the above developed ice breaking module formulations, the axial force was not included. The presence of the axial force (see Fig. A.1) could change the ODE as in Eq. (12) with an additional term $N_H = F_{BH} = F_{BV}\cdot\frac{\sin\alpha+\mu_s\cos\alpha}{\cos\alpha-\mu_s\sin\alpha}$ representing the axial compression:

$$EI\frac{d^4W(x)}{dx^4} + N_H\frac{d^2W(x)}{dx^2} + \rho_w gDW(x) = -Dq_r(x,\tau_i)_{0\le x\le l} + F_{BV}\cdot\delta(x). \tag{12}$$

If coupling the axial force in the beam bending formulation as in Eq. (12), an additional bending moment was introduced. Furthermore, the presence of the axial force N_H would alter the tensile stress within the ice beam as in Eq. (13)

$$\begin{aligned}\sigma_{flexural} &= EI\frac{d^2W(x)}{dx^2}\cdot\frac{6}{Dh^2}\\ \sigma_{compressive} &= \frac{N_H}{Dh} = \frac{F_{BH}}{Dh}\\ \sigma_{tensile} &= \sigma_{flexural} - \sigma_{compressive}.\end{aligned} \tag{13}$$

The additional compressive stress to alleviate the flexural stress in Eq. (13) was considered in the current ISO/FDIS/19906 (2010) in an iterative manner to obtain the ice breaking load with the presence of axial force.

In the current paper, the effect of both Eqs. (12) and (13) are not included in the formulation for the purpose of obtaining closed form solutions for beam deflections under triangular distributed rubble pressure (see Eqs. (54) and (55) in Appendix A). However, Eqs. (12) and (13) are studied in Appendix A.4 to justify and caution the negligence of axial force in the current paper.

Based on all the assumptions made and also the proposed formulations, applying the ice breaking module calculations at a reference time τ_i, the ice breaking load $F_B(\tau_i)$ and ice breaking length $L_B(\tau_i)$ can be constructed. Additionally, the ice breaking location $Z_B(\tau_i)$ (which is the value of W^1 in at the instance of bending failure) is also calculated and stored.

2.3.3. The ice rotation module

The ice rotation module denotes the process of rotating the already-broken ice block until it becomes parallel to the sloping surface. This process has been analytically described in several papers in the literature, with different complexities (Aksnes, 2011; Frederking and Timco, 1985; Kotras, 1983; Naegle, 1980; Valanto, 2001). Compared with these models, the current ice rotation module is characterised by the following features:

- During the rotation process, the ice block tends to 'jump' out of the water (see Fig. 2). The rotating centre of the ice block can be moving during the rotation process[3];
- By utilising the concept of elastic–plastic foundation, both the ventilation and backfill effect are considered in the formulation;
- The rubble accumulation's effects are considered in the ice rotating process;
- The tensile stress inside the rotating ice block is examined to produce possible secondary ice breakings.

[3] As will be shown later, the rotating process was further separated into the rotation with elastic foundation and rotation with elastic–plastic foundation. The centre of rotation was found to be fixed based on the elastic foundation assumption and moving with the elastic–plastic foundation assumption.

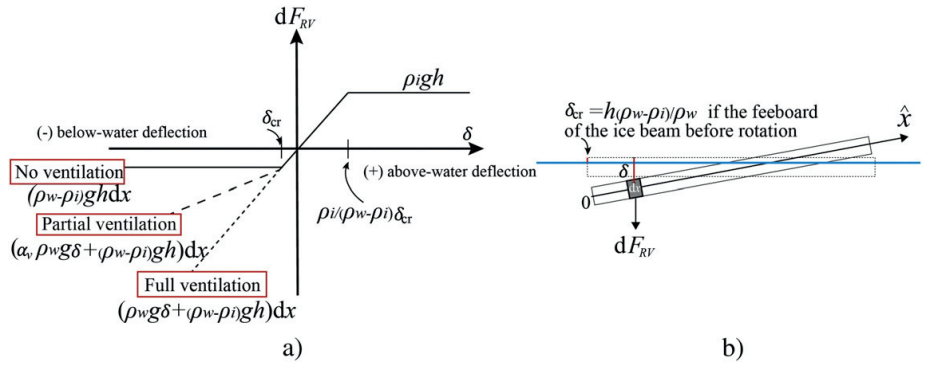

Fig. 10. The ice rotation module with elastic–plastic foundation.

The ice rotation module follows immediately after the ice breaking module to rotate the already-broken ice block. Lu et al. (2013a) have shown that in the phase 1 ice breaking scenario, the ice breaking length decreases with increasing rubble accumulation. Therefore, the longest ice breaking length that would be encountered theoretically is predicted by Eq. (14). Its derivation is given in Appendix A.3.

$$L_{B,max} = \frac{\sqrt{2}\pi}{4}\sqrt[4]{\frac{EI}{\rho_w g D}}. \tag{14}$$

Because $\lambda L_{B,max} = \pi/4$ (see Eqs. (48) and (49)'s symbol explanations for the expression of λ); and $L_{B,max}$ is the longest ice breaking length that can be expected, we shall have $\lambda L_B < \pi/4$ for typical sea ice properties. Therefore, the short beam classification applies here (Hetényi, 1946). The already-broken ice block's rotating motion can be treated as rigid body motion due to limited flexural deflections even at the instance of the secondary ice breakings.

The ice rotation module is further separated into the initial ice rotation with an elastic foundation and subsequent ice rotation with elastic–plastic foundation. This separation is illustrated in Fig. 10 for a unit width ice block.

Fig. 10a assumed that the fluid foundation behaves elastically both under and above water before the broken ice block's critical deflection δ_{cr} is reached. However, when the broken ice block's below-water deflection exceeds the critical value δ_{cr}, different scenarios were encountered depending on the degree of the ventilation and the backfill effect (Lu et al., 2012b). The ventilation and backfill phenomena denote how much water is on top of the rotating ice block (see the waterline in Fig. 11). A lowered water level above the rotating ice block leads to large pressure differences above and below the rotating ice block. This phenomenon in turn influences the ice rotating load. In reality, this water level is not stationary; it depends largely on the interaction speed and ice concentration. For the current simplified analysis and for theoretical completeness, a ventilation factor α_v is introduced to account for different scenarios.

If the full ventilation scenario (i.e., there is no water on top of the rotating ice block) is assumed, then $\alpha_v = 1$ and the fluid's resistance continues to increase with increasing underwater deflection. Full ventilation typically occurs at rather high interaction speeds (e.g., higher than 0.8 m/s) such that the water does not have sufficient time to backfill the ventilated area. This situation is typically the case for icebreakers that interact with level ice at high speeds (Valanto, 2001). However, for level ice interacting with fixed sloping structures, the ventilation phenomenon is combined with a backfill process to alleviate the pressure difference. Such a combined effect is accounted for by the ventilation factor $0 \le \alpha_v \le 1$ in the current study. When $\alpha_v = 0$, the resistance is left only with a constant static buoyancy, as $(\rho_w - \rho_i)ghD$ (see Fig. 10).

Meanwhile, the above-water deflection might become sufficiently large to reach the gravity load intensity $\rho_i gh$. Here, h is the thickness of the ice.

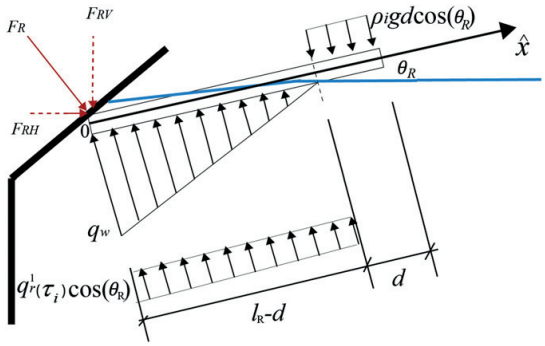

Fig. 11. Free-body diagram of the ice rotating process.

Fig. 10b shows that $\delta_{cr} = \frac{(\rho_w - \rho_i)}{\rho_w} h$ is the freeboard of the floating ice block. Before this critical deflection is reached, the ice rotating process is within the elastic foundation range. Based on static mechanics, the ice rotating load in the vertical direction F_{RV} can be calculated by Eq. (15). Relevant derivations are presented in Appendix B.1.

$$F_{RV} = \frac{1}{6}\theta_R l_R^2 \rho_w g D \tag{15}$$

θ_R is the broken ice block's rotating angle, as shown in Fig. 11;
l_R is the general expression of the length of the broken ice block.

The temporal information in Eq. (15) is included in θ_R and l_R. These two values change with varying time. This will be further discussed in Section 2.4.2. The maximum moment can be calculated by Eq. (16).

$$M_{Rotation\_max} = \frac{2}{81}\theta_R \rho_w g l_R^3 D \quad \theta_R \le \theta_{cr}. \tag{16}$$

Maximum flexural stress can be accordingly derived through Eq. (16) based on simple beam theory; and the possibility of secondary ice breaking can be evaluated.

When the ice block's rotation angle $\theta_R > \theta_{cr}$, a new formulation is required to account for the possible 'plastic region' above and below the water level. Fig. 11 illustrates the situation in which the ice block's rotation enters the 'plastic foundation region'. In this case, the far end part of the ice block tends to jump out of water. Due to this observation, the current theoretical model has assumed no contact between the intact level ice and the rotating ice block. Similarly, though Valanto (2001) pointed out such possible contact, his formulation neglected this contact force. However, it should be borne in mind that there are at least two force components which results in such rotating motion. One is the possible contact force F_c between the incoming intact level ice and the rotating ice block; another is the friction F_f between the accumulated rubble (with a rolling motion) and the rotating ice block (see Fig. B.2). However, these two undetermined force components were all neglected in the free body diagram in Fig. 11 in order to estimate a reasonably conservative ice rotation load. The justification of such assumption is validated in Appendix B.2.

In Fig. 11, d denotes the length of the beam that is above the water level. Additionally, q_w and $q_r^1(\tau_i)$ represent the water pressure and rubble pressure at the contact point with the structure. These variables can be expressed by using Eqs. (17) and (18) when $\theta_R \ge \theta_{cr}$, $0 \le \hat{x} \le l_R - d$ and $0 \le \alpha_v \le 1$ (i.e., the top area of the rotating ice block can be partially ventilated):

$$q_w(\hat{x}) = \alpha_v \rho_w g (l_R - d - \hat{x}) \sin\theta_R D \tag{17}$$

and

$$q_r^1(\tau_i) = (\rho_w - \rho_i)(1-\eta) g h_r^1(\tau_i) D. \tag{18}$$

Based on the drawing in Fig. 11, the force in the vertical direction and the momentum balance can be written as in Eq. (19), respectively.

$$\begin{aligned} &\frac{\alpha_v}{2}\rho_w g (l_R-d)^2 \sin(\theta_R)\cos(\theta_R) D + (\rho_w - \rho_i) g h (l_R - d) D + q_r^1 (l_R - d)\cos(\theta_R)^2 D = F_{RV} + \rho_i g h d D \\ &\frac{\alpha_v}{6}\rho_w g (l_R-d)^3 \sin(\theta_R) D + (\rho_w - \rho_i) g h \frac{(l_R-d)^2}{2}\cos(\theta_R) D + q_r^1 \frac{(l_R-d)^2}{2}\cos(\theta_R) D = \rho_i g h d \left(l_R - \frac{d}{2}\right)\cos(\theta_R) D. \end{aligned} \tag{19}$$

There are two unknowns in Eq. (19): F_{RV} (i.e., the ice rotating force projected in the vertical direction) and d (i.e., the length of the rotating ice block that 'jumps' out of the water). The rotation angle θ_R varies from θ_{cr} to the sloping angle of the structure, α. A relatively conservative solution for F_{RV} can be obtained by assuming a static equilibrium for the rotation process, as illustrated in Fig. 11. Analytical solutions for F_{RV} and d within Eq. (19) are possible; however, they are too lengthy. Instead, from an engineering point of view and without worrying too much about efficiency, in the current theoretical model development, a search algorithm[4] is adopted to identify the value of d and the corresponding F_{RV} under each rotation angle θ_R based on Eq. (19). Consequently, the relationships of $F_{RV,j}$ and d_j in correspondence to $\theta_{R,j}$ are constructed. Here the index j is a discretization in the time domain. It describes the process of the rotation. Thereafter, the moment distribution of $M_{rotation,j}(\hat{x})$ can be obtained with Eqs. (20) and (21).

$$M_{rotation,j}(\hat{x}) = \rho_i g h \frac{(l_R - \hat{x})^2}{2}\cos\left(\theta_{R,j}\right) D \quad \hat{x} \ge l_R - d_j \tag{20}$$

$$\begin{aligned} M_{rotation,j}(\hat{x}) = {} & \rho_i g h d_j \left(l_R - \hat{x} - \frac{d_j}{2}\right)\cos\left(\theta_{R,j}\right) D - \frac{q_r^1 \cos\left(\theta_{R,j}\right)\left(l_R - \hat{x} - d_j\right)^2}{2} \\ & D - \int_{\hat{x}}^{l_R - d_j} (x' - \hat{x}) q_w(x') dx' D - \frac{(\rho_w - \rho_i) g h}{2}\left(l_R - \hat{x} - d_j\right)^2 \cos\left(\theta_{R,j}\right) D \end{aligned} \tag{21}$$

when $0 \le \hat{x} \le l_R - d_j$.

When the momentum distribution along the rotating beam is known, the tensile stress distribution can be correspondingly constructed. During the course of rotation, it is assumed that a secondary ice breaking occurs once the maximum stress reaches the flexural strength of the beam. The general procedures of using the above equations to construct the ice rotating load history involving secondary ice breakings are detailed in Appendix C.

[4] Specifically, we utilized a MATLAB command 'fminbnd' which is based on golden section search algorithm to solve the unknowns in the equation. However, other search algorithm method in solving nonlinear equations would be equally well here.

If we neglect the additional rubble pressure term and assume full ventilation (i.e., setting $q_r^1 = 0$ and $\alpha_v = 1$), the formulation in Eq. (19) reduces to Valanto's (2001) solution without axial force in the rotating ice block.

Based on the formulations, a parameter study was conducted by Lu et al. (2013a) to study the influence of the ventilation effects and additional rubble pressure on the ice rotation module. It was found that both the ventilation and rubble accumulation increase the ice rotating load and the possibility of secondary ice breakings. During the rotating process, the value of d increases initially and then decreases. These changes correspond to the observation that the rotating ice block tends to 'jump' out of the water (i.e., d increases) before it submerges (i.e., d decreases). This process is in line with the interaction mechanism drawing in Fig. 1❷.

2.3.4. Outputs of the ice rotation module

For a fixed reference time point τ_i, running the ice rotation module will help to construct the vectors $F_{RV}(\tau_i, \theta_{R,j})$ and $F_{RH}(\tau_i, \theta_{R,j})$, which denote the vertical and horizontal ice rotating load history (i.e., from $\theta_{R,0} = 0$ to $\theta_{R,m} = \alpha$), respectively.

Based on Appendix C, the updated ice breaking length vector $\boldsymbol{L_R}$ (with its element $L_{R,i}$ having a general expression form l_R in the current paper, $i = 1, 2, 3, \ldots, M$ and M is the number of broken blocks) after a possible secondary breaking is obtained based on the original ice breaking length vector $\boldsymbol{L_B}$. These values are further clarified regarding its temporal evolution in Section 2.4.2.

The rotating ice block's deflection at the contact point with the structure $Z_R(\tau_i, \theta_{R,j})$ is also constructed. This value carries the information on the ice rotating load's action location, which will be utilised to construct the ice rotating load's spatial variation in Section 2.5.

2.3.5. The rubble accumulation module

In the previous sections, when discussing the ice breaking and ice rotation modules at a reference time τ_i, the rubble effect in the shaded area in Fig. 8 has been explicitly considered by the value $q_r^k(\tau_i)$ (i.e., the rubble pressure profile) and $h_r^k(\tau_i)$ (i.e., the rubble's geometric profile) in discrete forms in the spatial domain. In addition, the rubble's direct pressure on the structure, as shown in Fig. 12 (i.e., the rubble profile under Area 1), should also be considered. This load is denoted as $\boldsymbol{F_{srb}}$, where '*srb*' stands for the stationary rubble pressure. The amount of rubble that rests directly on the structure is initially large when the broken ice is about to be rotated (see the size of Area 1 in Fig. 12a) and starts to decrease during the ice rotating process (see Fig. 12b). It can be assumed that the size of Area 1 is minimal when the rotating ice rubble becomes parallel to the sloping surface (see Fig. 12c) and is then maximised immediately when a new rotating process begins.

To obtain analytical formulas for the rubble's pressure on the structure, it is assumed here that the rubble profile's evolution is the same as the red dashed line in Fig. 12. The size of Area 1 becomes minimal in Fig. 12c. It is assumed here that the size of Area 1 changes linearly between the maximum (i.e., Fig. 12a) and minimum values (i.e., Fig. 12c) during each single ice rotating cycle. Therefore, only two values (i.e., the maximum and minimum values of the size of Area 1) are to be identified within each ice rotating process to construct the temporal variation of Area 1.

Under the current assumption, the width $W_b^1(\tau_i)$ while Area 1 is maximum in Fig. 12a; and the width $W_b^2(\tau_i + \Delta\tau_i)$ while Area 1 is minimum in Fig. 12c can be written by Eq. (22).

$$\begin{aligned} W_b^1(\tau_i) &= \frac{\min\left(h_r^1(\tau_i), h_s\right)}{\tan(\alpha)} \\ W_b^2(\tau_i + \Delta\tau_i) &= \max\left(W_b^1(\tau_i) - l_R\cos(\alpha), 0\right) \end{aligned} \tag{22}$$

in which $\Delta\tau_i = l_R/v$, and it has been implicitly assumed in these formulations that during $\Delta\tau_i$, the rubble height $h_r^1(\tau_i)$ remain unchanged.

During the very initial stage of rubble accumulation, a situation could arise in which the rubble depth $h_r^1(\tau_i)$ is smaller than h_s (see the dashed rubble profile in Fig. 6). In such situations, $W_b^1(\tau_i)$ is calculated with the smaller value between $h_r^1(\tau_i)$ and h_s as in the first equation of Eq. (22).

Having obtained the values of $W_b^1(\tau_i)$ and $W_b^2(\tau_i + \Delta\tau_i)$, the size of Area 1 in these two cases are expressed in Eq. (23).

$$\begin{aligned} S_b^1(\tau_i) &= \max\left(\left(h_r^1(\tau_i) - \frac{h_s}{2}\right), \frac{h_r^1(\tau_i)}{2}\right) W_b^1(\tau_i) \\ S_b^2(\tau_i + \Delta\tau_i) &= \max\left(\left(h_r^1(\tau_i) - l_R\sin(\alpha) - \frac{h_s - l_R\sin(\alpha)}{2}\right), \frac{h_r^1(\tau_i) - l_R\sin(\alpha)}{2}, 0\right) W_b^2(\tau_i + \Delta\tau_i). \end{aligned} \tag{23}$$

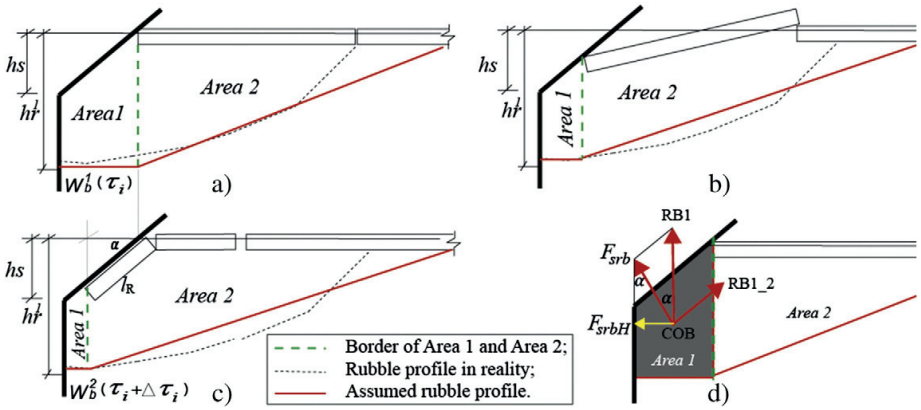

Fig. 12. Panels (a), (b), and (c) illustrate the rubble profile's evolution; panel (d) illustrates the ice rubble's load components with several abbreviations (COB stands for the centre of buoyancy; RB1 stands for the rubble buoyancy in Area 1; and RB1_2 stands for the rubble buoyancy component that is transferred from Area 1 to Area 2).

Based on the above area calculations, the corresponding rubble accumulation load can be obtained and projected in the horizontal and vertical directions, respectively. Fig. 12d illustrates how the load components are related. The load component RB1_2 represents the rubble buoyancy that has transferred from Area 1 to Area 2. This load does not act on the structure directly. If we view the ice rubble as a whole, this load component is an internal load within the ice rubble.

In Eq. (24), the maximum and minimum horizontal rubble-accumulation load is presented separately.

$$\begin{aligned} F^1_{srbH}(\tau_i) &= (\rho_w - \rho_i) g (1-\eta) S^1_b(\tau_i) \cos(\alpha) \sin(\alpha) D \\ F^2_{srbH}(\tau_i + \Delta\tau_i) &= (\rho_w - \rho_i) g (1-\eta) S^2_b(\tau_i + \Delta\tau_i) \cos(\alpha) \sin(\alpha) D. \end{aligned} \tag{24}$$

As already assumed, the corresponding direct rubble pressure loading history can be attained by simple linear interpolation between the maximum and minimum values as in Eq. (25).

$$F_{srbH}(t) = F^1_{srbH}(\tau_i) + \frac{F^2_{srbH}(\tau_i + \Delta\tau_i) - F^1_{srbH}(\tau_i)}{l_R} v(t - \tau_i) \quad \tau_i \le t < \tau_i + \Delta\tau_i. \tag{25}$$

Moreover, because of the motion of the incoming level ice, the ice rubble beneath (i.e., Area 2) is pushed against the structure resulting in an additional horizontal force, which is termed as $\boldsymbol{F_{PH}}$ in this paper. This load is mainly due to the friction between the incoming ice sheet and ice rubble (see the green arrows in Fig. 13a and b). This load is thought to be the source of the observed rubble motion (see Fig. 13c), and it is assumed here that this load is eventually transferred onto the structure.

Initially, the frictional resistance is caused by the rubble buoyancy from beneath (see Fig. 13a). In this case, the horizontal ice pushing load $F_{PH}(t)$ shares the same physical meaning as H_P in Croasdale and Cammaert's (1994) model. However, as the rubble accumulation increases, the ice blocks' gravity on top of the ice rubble becomes the normal force that leads to frictional resistance (see Fig. 13b). Considering the fact that an upper limit exists for this pushing load, a cut-off is made for this load, as shown in Eq. (26).

$$F_{PH}(t) = \min(H_P(t), \mu_i \rho_i g h l(t)). \tag{26}$$

$H_P(t)$ is the ice pushing load, which shares a same physical meaning as in Croasdale's model (Croasdale and Cammaert, 1994) and can be calculated by Eq. (27). $l(t)$ represents the rubble span and increases monotonically with time.

$$\begin{aligned} H_P(t) &= \frac{\mu_i D}{2} h^1_r(t) l(t) (\rho_w - \rho_i) g (1-\eta) \\ l(t) &= \frac{h^1_r(t)}{\tan\theta''} \end{aligned} \tag{27}$$

in which θ'' is the repose angle of the rubble profile, as shown in Fig. 6.

2.3.6. Outputs of the rubble accumulation module

The rubble accumulation module constructs a load history that is induced by the direct rubble pressure $F_{srbH}(t)$ onto the structure. The action location of this load is assumed to be evenly distributed between 'the rotating block's contact point with the structure' and 'the bottom of the sloping surface'. Moreover, a load history that denotes the ice pushing load $F_{PH}(t)$ is also constructed. The spatial distribution of this load is discussed in Section 2.5.

2.4. Construction of the ice load's temporal variation

In this section, we illustrate how the global ice load is constructed in the time domain based on the theoretical assumptions and calculated results from different modules (see Fig. 14). This figure is partly reproduced from Fig. 5b, however, with more details regarding how the time evolution is made for each different calculation module.

The algorithm regarding how the calculated ice load is distributed in the time domain is introduced herein.

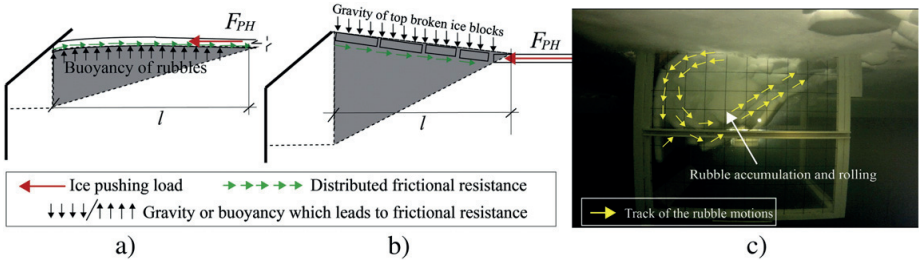

Fig. 13. The ice pushing load and its effect.

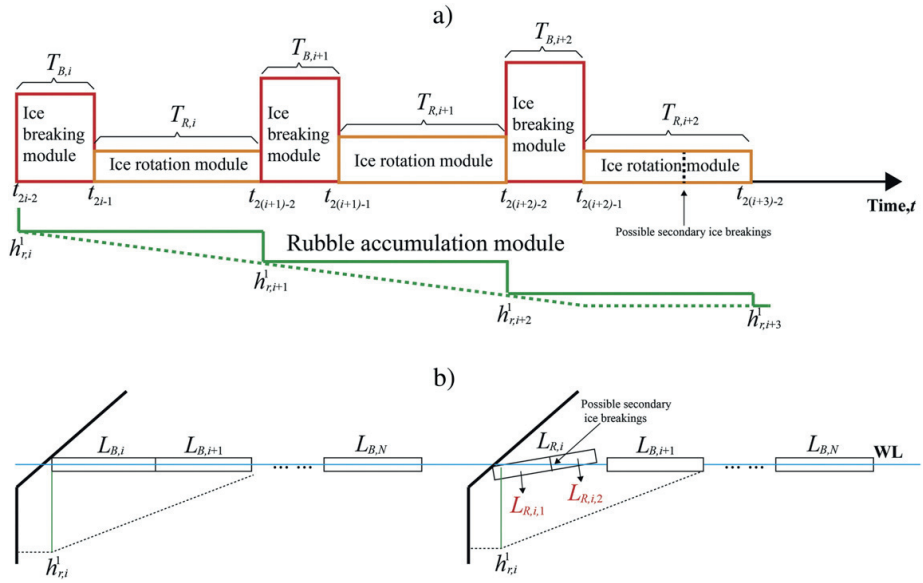

Fig. 14. Illustration of the global ice load's time domain construction.

2.4.1. Ice breaking module

For the ice breaking module, in the time domain, the value for the reference time τ_i is expressed as in Eq. (28).

$$\tau_i = t_{2i-2} = \sum_{a=1}^{i-1} L_{B,a}/v \quad (i = 1,\ 2,\ 3\ \ldots,\ N;\ \text{and}\ t_0 = 0,\ a\ \text{is a dummy index}) \tag{28}$$

with known τ_i, the value for $h_r^1(\tau_i)$ and $q_r(x, \tau_i)$ can be calculated by Eqs. (3) and (7). Inserting the results into Eq. (6) or (8) to obtain the value for $F_B(\tau_i)$, $L_B(\tau_i)$, and $Z_B(\tau_i)$. Further simplifying these notations as $F_{B,i}$, $L_{B,i}$ (see left of Fig. 14b), and $Z_{B,i}$. In the next reference time station τ_{i+1}, according to Eq. (28), with known $L_{B,i}$, we have:

$$\tau_{i+1} = t_{2(i+1)-2} = \sum_{a=1}^{(i+1)-1} L_{B,a}/v. \tag{29}$$

This leads to known $F_{B,i+1}$, $L_{B,i+1}$, and $Z_{B,i+1}$ with Eq. (6) or (8). Eventually, we obtain vectors $\boldsymbol{F_B}$, $\boldsymbol{L_B}$, and $\boldsymbol{Z_B}$. These discrete values need further be distributed in the time domain. Supposing the total ice penetration distance is L and there are in total N times of bending failures. According to Fig. 14, the following relationships apply.

$$\sum_{i=1}^{N}\left(T_{B,i} + T_{R,i}\right) = L/v \tag{30}$$

$$T_{B,i} + T_{R,i} = L_{B,i}/v \tag{31}$$

$$T_{B,i} = \frac{Z_{B,i}}{v\sin\alpha} \tag{32}$$

where $v\sin\alpha$ is assumed to be the deflection speed of the ice beam in the vertical direction.

$$t_{2i-1} = t_{2i-2} + T_{B,i} \quad i = 1,\ 2,\ 3\ \ldots,\ N;\ \text{and}\ t_0 = 0,\ t_{2i-2} = \sum_{a=1}^{i-1} L_{B,a}/v \tag{33}$$

$$F_{B\_temporal}(t) = \begin{cases} F_{B,i} \cdot \dfrac{t - t_{2i-2}}{T_{B,i}} & t_{2i-2} \le t < t_{2i-1} \\ 0 & t_{2i-1} \le t < t_{2(i+1)-1} \end{cases}. \tag{34}$$

A schematic illustration of the results of the ice breaking load in the time domain is given with the red curve in Fig. 15. Thus far, the discrete values within $\boldsymbol{F_B}$ have been distribute continuously in a time with function $F_{B\_temporal}$.

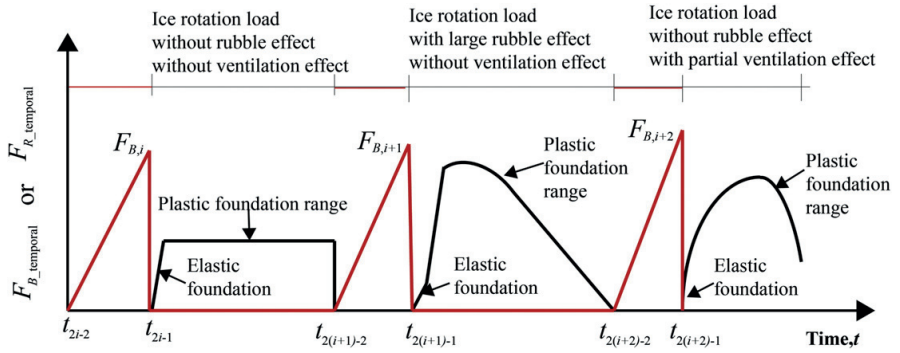

Fig. 15. Schematic illustration of the ice breaking load (red) and ice rotating load (black) in the time domain (note that the curves are not in scale).

2.4.2. Ice rotation module

The ice rotation module results' temporal distribution is more complex than the ice breaking module. Here we first consider the case without secondary ice breakings. The case with secondary breakings will be detailed in Appendix C, the principles behind which are similar. With the previous ice breaking module, in each interaction process i, an broken ice block $L_{B,i}$ is produced. The length $L_{B,i}$ is the initial ice rotating block's length. If there are no secondary ice breakings taking place, we have $L_{R,i} = L_{B,i}$ (also $\boldsymbol{L_R} = \boldsymbol{L_B}$, see right of Fig. 14b and assuming no secondary ice breaking takes place). Thereafter, the following equations can be obtained as inputs to Eqs. (15) and (19).

$$l_R = L_{R,i} \tag{35}$$

$$\theta_{R,j} = \theta_{R,j-1} + \Delta\theta_R \quad j = 1,\ 2,\ 3,\ \ldots,\ m;\ \text{and}\ \theta_{R,0} = 0,\ \theta_{R,m} = \alpha \tag{36}$$

in which m is an integer related to the step size of rotation angle $\Delta\theta_R$ as $m = \frac{\alpha}{\Delta\theta_R}$

$$\tau_i = \sum_{a=1}^{i-1} L_{R,a}/v \quad \left(L_{R,0} = 0;\ i = 1,\ 2,\ 3,\ \ldots,\ M\right) \tag{37}$$

in which, M is the number of broken blocks after the ice rotation process. If there is no secondary breakings, Eq. (37) is identical to Eq. (28) and $M = N$. Inserting Eqs. (35), (36), and (37) to Eqs. (15) and (19), $F_{RV}(\tau_i, \theta_{R,j})$ and $Z_R(\tau_i, \theta_{R,j})$ can be obtained. Using $L_{R,i}$ as the initial value together with Eq. (37) to obtain the next reference time τ_{i+1} leads to $F_{RV}(\tau_{i+1}, \theta_{R,j})$ and $Z_R(\tau_{i+1}, \theta_{R,j})$. Converting $F_{RV}(\tau_{i+1}, \theta_{R,j})$ into $F_R(\tau_{i+1}, \theta_{R,j})$ according to Eq. (5) and running the ice rotation module, the final output $\boldsymbol{F_R}$ is obtained with its elements shown in Eq. (38).

$$\boldsymbol{F_R} = [\ldots,\ F_{R,i,1},\ F_{R,i,2},\ F_{R,i,3},\ \ldots F_{R,i,m},\ F_{R,i+1,1},\ F_{R,i+1,2},\ F_{R,i+1,3},\ \ldots F_{R,i+1,m},\ \ldots F_{R,M,1},\ F_{R,M,2},\ F_{R,M,3},\ \ldots F_{R,M,m}]. \tag{38}$$

The index notation here for the element of $\boldsymbol{F_R}$ has a matrix flavour. However, for the convenience of describing the temporal evolution and also in the numerical storage implementation it is treated as a vector as in Eq. (38). This vector is to be further distributed in the time domain as in Fig. 14.

In the time domain, note that Eqs. (31) and (32) lead to:

$$T_{R,i} = L_{B,i}/v - \frac{Z_{B,i}}{v\sin\alpha} \tag{39}$$

$$t_{2(i+1)-2} = t_{2i-1} + T_{R,i} \quad (i = 1,\ 2,3\ \ldots N;\ \text{and}\ t_1 = T_{B,1},\ t_{2i-1} = \sum_{a=1}^{i-1} L_{B,a}/v + T_{B,i}). \tag{40}$$

It has been assumed a stable ice rotation process and also that while the ice rotation process terminates, the structure has a new contact with the intact ice sheet. Therefore, we can further separate $T_{R,i}$ into m sections and introduce a time step $\Delta t_i = T_{R,i}/m$. This leads to the expression for $F_{R\_temporal}$ as in Eq. (41).

$$F_{R\_temporal}(t) = \begin{cases} F_{R,i,j} + \dfrac{F_{R,i,j+1} - F_{R,i,j}}{\Delta t_i} \cdot [t - (t_{2i-1} + (j-1)\Delta t_i)] & t_{2i-1} + (j-1)\Delta t_i \le t < t_{2i-1} + j\Delta t_i \\ 0 & t_{2i-2} \le t < t_{2i-1} \end{cases}. \tag{41}$$

Eq. (41) is a linear interpolation between those obtained m values for each rotation of an ice block $L_{R,i}$. A schematic illustration of the above calculation results in the time domain is shown with the dark curves in Fig. 15. Furthermore, the typical shapes of the load curve for three different cases

are also illustrated. If there is no ventilation effect and no rubble influence, after $\theta_R \geq \theta_{cr}$, $F_{R\_temporal}$ becomes a constant value (in analogy to perfect plastic foundation). For a more detailed quantitative comparison of these three different cases, please refer to Lu et al. (2013a). In the current paper's validation against the experimental results (see the following Sections 4.1 and 4.2), only the first two cases in Fig. 15 were utilised.

2.4.3. Ice accumulation module

The outputs from the ice accumulation module $F_{srbH}(t)$ and $F_{PH}(t)$ have already been distributed in the time domain and will not further described herein.

2.5. Construction of the ice load's spatial variation

The presence of rubble accumulation complicates the ice load's spatial distribution. It has been observed that the majority of particles in a granular material carry less than average load (Peters et al., 2005; Radjai et al., 1998). Under the context of ice rubble, Palmer and Croasdale (2013) stated that within loaded particulate materials (i.e., ice rubble), the load is far from evenly distributed. Most of the load is transmitted by a small number of loaded particles that form a chain. The ice load's spatial distribution was studied by Paavilainen and Tuhkuri (2013) through the force chain concept. In their study, the ice rubble was treated as a collection of discrete elements. The major ice load is carried by the force chain that branches onto the structure. Typically, the maximum load occurs during the buckling of the force chain (Radjai et al., 1998).

However, in the current study, the rubble has been assumed to be a continuum. Focus has been placed on the overall influence of the rubble instead of on its internal structure. Accordingly, the following idealisations have been adopted to identify the ice load's spatial variation.

First, the load history components of $\boldsymbol{F_B}$, $\boldsymbol{F_R}$, $\boldsymbol{F_{srb}}$, and $\boldsymbol{F_P}$ are constructed. Naturally, the spatial variation of $\boldsymbol{F_B}$ is based purely on the corresponding ice action location vector $\boldsymbol{Z_B}$ (i.e., the contact point at the instance of ice breaking); $\boldsymbol{F_R}$, and $\boldsymbol{F_{srb}}$ are based on the value of $\boldsymbol{Z_R}$ (i.e., the contact point during the ice rotating process). This process is visualised in the schematic drawing in Fig. 16.

With a known ice breaking load F_B and ice beam's tip deflection Z_B, the red curve in Fig. 16 illustrates how the ice breaking load $\boldsymbol{F_B}$ develops both in time and space. When the ice breaking process steps into the phase 2 ice breaking scenario, the ice breaking load that acts far away is assumed to be transferred to the structure at the water line (see Fig. 8b).

For the ice rotating process, a one-to-one relationship can be constructed between the ice rotating load F_R and corresponding broken ice block's deflection Z_R. The orange curve in Fig. 16 depicts their evolution.

With respect to the accumulated rubble's static pressure $\boldsymbol{F_{srb}}$, the green solid line illustrates its distribution and how it develops over time. The static pressure is assumed to act evenly in a region that is below the rotating ice block (i.e., below Z_R, shown with the solid green line). As the ice block is rotating downwards, the static pressure $\boldsymbol{F_{srb}}$ on the area above Z_R becomes zero due to loss of contact (i.e., the dashed green line). Instead, the rubble pressure above Z_R (i.e., the dashed green line) is transferred to the rotating ice block and is calculated in the ice rotating load component $\boldsymbol{F_R}$.

Moreover, when seeding these spatial loads into pressure, the centre of the contact area is assumed to be at the load action point. The size of the contact area is determined by the ratio of contact force and crushing strength of ice. This is to say, the local pressure cannot exceed the crushing strength of the ice. Once the pressure is found to be larger than the crushing strength, the ice is assumed to be crushed, and thus, the contact area is increased. The additional part of the pressure is smeared in the neighbouring areas to keep the total force in balance.

Seeding the ice pushing load $\boldsymbol{F_P}$ into space is not as straightforward as the other three load components due to the continuum assumption for the ice rubble. During the experiments, the ice rubble was observed to roll around a centre, as shown in Fig. 13c and illustrated in Fig. 17a. A similar rubble rolling observation was made in the physical model tests by Timco (1991) and the numerical simulations of Paavilainen et al. (2010). As discussed above, the ice load is not evenly distributed spatially. The existence of a force chain to transfer the ice load onto the sloping surface has been suggested (Paavilainen and Tuhkuri, 2013; Palmer and Croasdale, 2013). Furthermore, Paavilainen and Tuhkuri (2013) concluded that the peak ice load resides near the waterline for steep slopes and beneath the waterline as the slopes become milder. Based on the description of force chain method (Peters et al., 2005; Radjai et al., 1998) and basic buckling theory, it is noted that particles on either side of the force chains should carry relatively smaller forces, but their presence stabilises the chains. This point has also been mentioned in Palmer and Croasdale (2013) under the context of ice rubble load. Therefore, it can be reasonably inferred that the ice pushing load has a peak near the waterline and gradually becomes attenuated in the downward direction.

Based on both the observations made in Fig. 17a and the information regarding the force chain concept and also in analogy to the shear stress profile of a Newtonian fluid between two oppositely moving plates (Irgens, 2008), it is ideally assumed here that the ice pushing load is linearly distributed over half of the rubble height h_r^1 in the vertical direction, as shown in Fig. 17b.

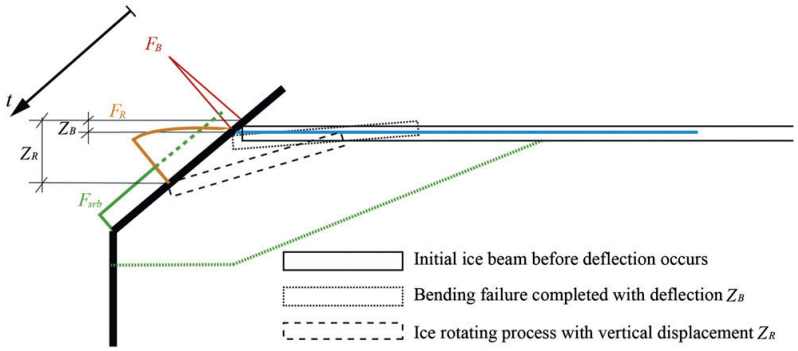

Fig. 16. Different ice load's spatial distributions based on one complete interaction procedure (without secondary breakings).

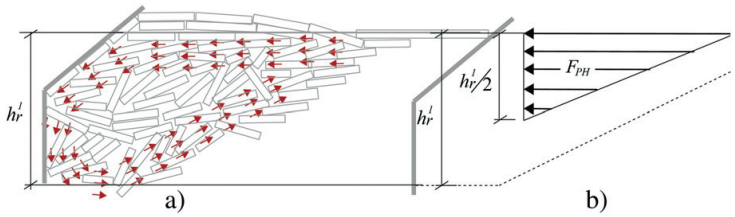

Fig. 17. Spatial distribution of the ice pushing load F_{PH}.

The theoretical model used to predict the ice load's spatial and temporal distribution has been described in the previous sections, together with detailed implementations suggested in Appendices A–C. In the following, two types of physical model tests conducted in the Hamburg Ship Model Basin (HSVA), Germany, are introduced. The measurements from these physical model tests are utilised to validate the above-derived theoretical model.

3. Physical model tests

The physical model tests conducted in this test campaign aimed to study the mechanisms through which level ice interacts with a downward sloping structure in the presence of rubble accumulation. Two different test set-ups were utilised in the current study (Serré et al., 2013a, 2013b). The first set-up (i.e., test set-up #1) is a box-shaped structure that has a sloping plate installed within the box. This structure is featured by the utilisation of a tactile sensor to measure the local ice pressure. Another test set-up (i.e., test set-up #2) is a wide sloping structure with load cells to measure the ice load on the inclined plate. The tests are introduced separately below.

As a common practice, both the Cauchy and the Froude scaling laws were maintained throughout the experiments to scale the physical model test results to full scale (Schwarz, 1977) with a geometrical scale-factor of 20. Although there are controversies with and objections against the concept of the current model test with weakened ice and the pertinent similitude law (Atkins and Caddell, 1974; Palmer and Dempsey, 2009), it is not the intention of the current paper to test the validity of the utilised model ice and scaling law. Lau et al. (2007) reported that most of the model ice typically has a higher fracture toughness. This might lead to certain error in scaling the ice breaking load. However, as introduced previously, the ice breaking load is only one part of the total ice load. Other interaction processes, such as the ice block rotation and rubble accumulation processes, are more dominated by the effects of the inertia, gravity, and buoyancy forces. These effects can be well characterised by the Froude scaling law. Therefore, it is thought that one load component's (i.e., the ice breaking load) possible inaccurate estimation would not ruin the validity of the full-scale load based on the current model ice and scaling law. Croasdale also tends to agree with the usefulness of model tests for sloping sided structures in which bending and clearing (or accumulation) processes are dominant (Palmer and Croasdale, 2013).

In this paper, unless otherwise stated, all of the numbers are given in full scale based on a combination of Cauchy and Froude scaling laws.

3.1. Test set-up #1: sloping plate with a tactile sensor to measure the local ice track

Timco (1991) studied the ice pressure's distribution upon a segmented plate with several load cells instrumented separately in the vertical direction. This study shows that for a downward sloping structure, the maximum ice load occurs slightly lower than the waterline (i.e. in segment 3 in the original paper). In order to achieve higher resolution in ice load's spatial distribution, Izumiyama et al. (1998, 1999) pioneered the application of tactile sensor measuring system in ice engineering. The measurement conducted upon an icebreaker showed that a line-like ice pressure can travel down below water level for approximately 30% of the ship draft (Izumiyama et al., 1999). An examination of the same work shows that the maximum ice load locates at about 10% of the ship draft below water. Izumiyama et al. (1999) schematically attribute this measurement to the ice rotation process. Later tactile sensor applications were mainly conducted in ice crushing scenarios (Määttänen et al., 2012; Sodhi, 2001; Sodhi et al., 1998). With tactile sensor, the present study aims to measure the ice load's spatial and temporal variations on a sloping plate to shed light on the interaction mechanisms.

This test set-up involves a sloping flat plate that is mounted with a tactile sensor. Moreover, this sloping plate is confined within two transparent vertical walls to mimic a two-dimensional scenario by restricting the horizontal movements. These two vertical walls are also equipped with cleavage cutters to alleviate the boundary effects on the incoming ice. By pushing this 'box' through the level ice, the rubble was perfectly trapped in the box and accumulated gradually. The geometry of the test set-up and the tactile sensor's location are shown in Fig. 18. In the current test, the tactile sensor was mounted in the centre of the sloping plate. Due to the limited size of the sensor, the plate was only partially covered (44% of the plate in the vertical direction), as shown in Fig. 18b. Vertically, the plate is positioned such that two thirds of the tactile sensor was below the waterline. The tactile sensor is composed of 44 × 55 sensels, which are used to measure the local ice pressure. The ice load's spatial resolution is determined by the size of each sensel, as shown in Fig. 18b. Temporally, the sensor scans at a frequency of 10 Hz during each experiment. This frequency is adopted due to the consideration of both the storage capacity and test purpose. In ice crushing research, a rather high scanning frequency is required to capture the randomly developed hot spots. In contrast, the purpose of the current test is to identify different ice load components (i.e., the ice breaking load, ice rotating load, and rubble-accumulation load) in different interaction processes. Such a complete interaction process requires a much larger time scale to develop; therefore, we adopted a lower scanning frequency.

The installation and calibration of the tactile sensor has been detailed in Lu et al. (2013b). The tactile sensor does not have the same accuracy in the entire pressure range (Tekscan, 2003). This nonlinear nature has been discussed in Izumiyama et al. (1998). In his work the measured data was only qualitatively analysed. Due to the complexity of the ice and structure interactions, the ice pressure in nature covers a very wide range of possible values. In the current tests, based on the chosen sensitivity and saturation pressure, the tactile sensor tends to capture the ice pressure that repeats most often (i.e. to more accurately report a pressure in a range that would be around the mean ice pressure). However, the tactile sensor's accuracy is questionable for extreme values. Nevertheless, the merits of using a tactile sensor in the current mission should not be discredited because the tactile sensor will output the contact area (i.e., the load's spatial variation) and the comparative

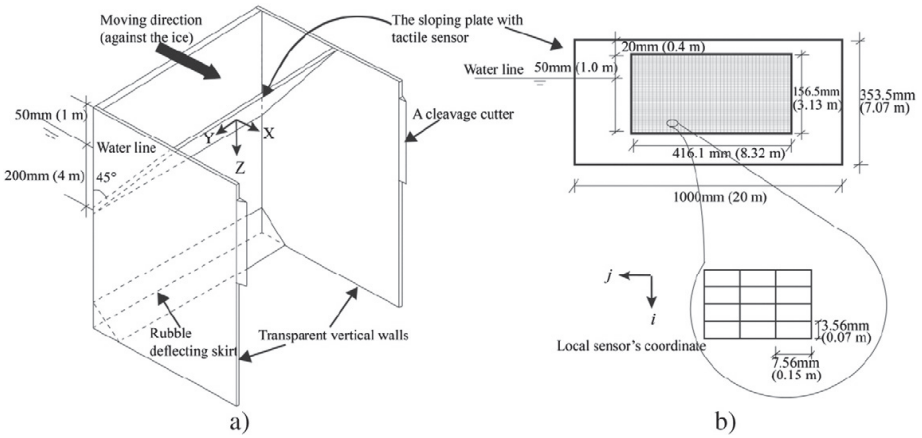

Fig. 18. (a) Schematic drawing of the test set-up and (b) geometrical details of the tactile sensor.
The drawing is not according to scale, and a full-scale size is labelled in brackets after the model scale size, other detailed geometric information can be found in Serré et al. (2013b).

pressures regardless of the possible errors within its measured maximum values (Sodhi et al., 1998). However, the measured mean value should be given a higher degree of confidence compared with measurements of the extreme values.

3.2. Test set-up #2: sloping plate with load cells

The above tests were based only on the tactile sensor's measurements. However, the tactile sensor's results are not accurate in all of the possible load ranges, especially at a high load range, due to the current calibration. Therefore, it is necessary to introduce a test in which the ice load is measured with a more mature technique. Because of their versatility, load cells are frequently used in various ice load measurements (Palmer and Croasdale, 2013). This section introduces the test set-up that utilised load cells to measure the ice load.

In the second set-up, the ice was allowed to flow around the structure (an aspect ratio of approximately 50, see Fig. 19), and the forces on the two individual sloping panels were measured with load cells. The load cells did not provide the spatial pressure variation, but they do provide a more precise load estimate than the tactile sensor. An underwater video demonstrated that the rubble accumulation reached the rubble deflection skirt without a considerable amount of rubble flowing around the structure. Thus, we also consider these experiments to be two-dimensional (or at least semi-two-dimensional).

3.3. Test matrix

There were five ice sheets prepared in HSVA. The first digit in the test series number denotes the number of the ice sheet. The ice properties of the different ice sheets are listed in Table 2.

The test matrices for both test set-ups are provided in Table 3.

4. Validation of the theoretical model with the physical model tests

In the previous two sections, the development of the theoretical model and the physical model test set-ups were described in detail. In this section, the theoretical model is validated by comparing the physical model test results with the predictions of the theoretical model. Specifically, the horizontal load components (i.e., the *X* direction, see Fig. 18) of both the measured ice loads and the predicted ice load were extracted for comparison. In the following, unless otherwise stated, the ice load refers to the load in the horizontal direction. The ice load in the vertical direction follows a similar trend.

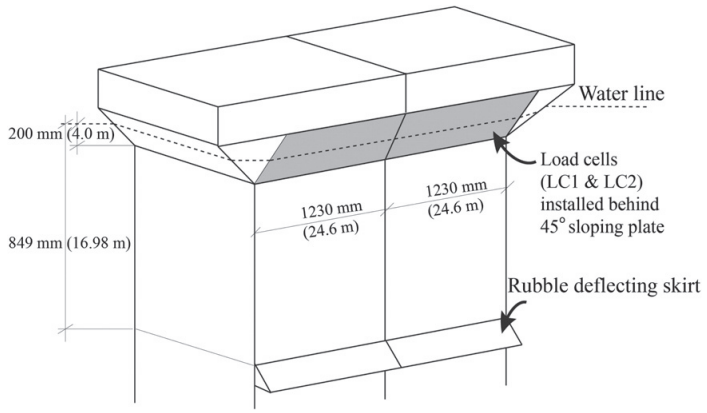

Fig. 19. Geometry of a wide sloping structure.
Model scale size and full-scale size in brackets, other detailed geometric information can be found in Serré et al. (2013a).

Table 2
Ice properties in the different tests (FS: full scale; MS: model scale).

Test series	Flexural strength		Ice thickness		Young's modulus		Ice density
	FS	MS	FS	MS	FS	MS	FS,MS
	[kPa]	[kPa]	[m]	[mm]	[MPa]	[MPa]	[kg/m^3]
1000	1060	53	0.86	43	1220	61	906
2000	1164	58.2	0.86	43	1060	53	902
3000	1092	54.6	0.94	47	1760	88	806
4000	914	45.7	1.22	61	2060	103	928
5000	942	47.1	0.82	41	620	31	894

Two groups of validation were developed. First, the theoretical model's results are compared to the measurements by the tactile sensor (i.e., in test set-up #1) to verify the theoretical model's capability in constructing the ice load's spatial and temporal variation. Afterwards, the current theoretical model's global load prediction capability is compared with the load cell's measurements in test set-up #2.

4.1. Spatial and temporal load prediction versus measurements by the tactile sensor

The inputs for the current theoretical model are shown in Table 4. The unspecified values in Table 4 can be found in Tables 2 and 3, or in the references. The rubble profile is expressed separately in Eq. (3).

For the tactile sensor measurements, all of the recorded normal pressures by each sensel were later multiplied by the sensel's area and projected in the horizontal direction (opposite of the X direction, see Fig. 18). These measurements were stored as a third-order tensor $\mathbf{M}$ with components M_{ijk}. Here, i and j represent the row and column numbers of the tactile sensor's sensel, respectively, and k is the number of scans, representing the recording time. This ice load tensor $\mathbf{M}$ is summed in the horizontal j direction to highlight the ice load variation in the vertical direction (i.e., the z direction) (see Eq. (42)).

$$F_H^m(z,t) = \sum_{j=1}^{n_j} M_{ijk} \tag{42}$$

where

$F_H^m(z,t)$ is the measured horizontal ice load at time t and at the vertical location z [kN];
n_j is the number of recordings in the horizontal direction, $n_j = 55$.

The result of the current theoretical model is written as $F_H^p(z,t)$ which is the horizontal ice load at time t and at the vertical location z [kN].

Table 3
Test matrices for test set-up #1 and test set-up #2 (FS: full scale; MS: model scale).

	Speed		Travelling distance	
	FS: [m/s]	MS:[mm/s]	FS: [m]	MS: [m]
Test series with test set-up #1 (measured by a tactile sensor)				
1210	0.2	44.7	200	10
2210	0.89	199.0	400	20
3210	0.2	44.7	200	10
4210	0.09	20.1	200	10
5210	0.2	44.7	200	10
Test series with test set-up #2 (measured by load cells)				
3130	0.2	44.7	240	12
4140	0.29	64.8	200	10
5130	0.2	44.7	200	10

In the following comparisons, the above two ice loads $F_H^m(z,t)$ and $F_H^p(z,t)$ are written indiscriminately as $F_H(z,t)$ when they are under the same manipulations.

- Ice load's spatial variation comparisons.

To highlight the spatial variation, at a specific location z, the mean ice load $\overline{F_H(z,t)}$ and maximum ice load $\max(F_H(z,t))$ in the time domain were calculated. Then, the corresponding mean and maximum ice load measured or calculated at each of the vertical locations were plotted in Figs. 20 and 21. The shaded area in these two figures represents the location of the undeformed level ice. The tactile sensor covered only a part of the sloping plate; therefore, the theoretical predictions have a larger vertical coverage than the measurements.

- Temporal variation comparison.

To highlight the ice load's time domain variation, $F_H(z,t)$ is summed in the z direction to obtain an ice load history $F_H(t)$ that represents the total horizontal ice load in the range of the size of a tactile sensor. $F_H^p(z,t)$ has not been summed over all of the calculated values in the z direction. Only those values within the height of a tactile sensor were summed for comparison purposes.

Instead of showing the entire measured and calculated ice load history, for illustration purposes, the obtained ice load histories were sectionalised by a characteristic length (Lu et al., 2013b). Within each section, the ice load's mean and maximum values were calculated as in Eqs. (43) and (44) to illustrate their respective temporal variations (see Fig. 22). This characteristic length is chosen to be L_B, as in Eq. (14), because this length is expected to be sufficiently long to encapsulate the main interaction procedures (i.e., breaking, rotating, and sliding) during each interaction cycle.

$$\overline{F_H(t,n)} = \overline{F_H\left((n-1)\frac{L_B}{v} \le t \le (n)\frac{L_B}{v}\right)} = \frac{\Delta t \cdot v}{L_B} \sum_{t=(n-1)L_B/v}^{t=nL_B/v} F_H(t) \tag{43}$$

$$\max(F_H(t,n)) = \max_{(n-1)L_B/v \le t \le nL_B/v}(F_H(t)) \tag{44}$$

where $n = 1, 2, 3, \ldots, \lceil L/L_B \rceil$; $\lceil L/L_B \rceil$ is the rounded-up integer value of L/L_B, which represents the number of the section; and L is the total ice penetration during the interaction. Since both the experimental measurements and the current theoretical model yields load history in discrete format, Δt represents time interval between theoretical ice load calculations and $1/\Delta t$ represents the sampling frequency during the experimental measurements.

4.2. Global ice load prediction versus measurements by the load cells

The inputs of the current calculation include the geometry of the structure (shown in Fig. 19). In addition to the inputs provided in Table 4, some additional inputs are listed in Table 5.

The theoretical model's prediction and actual load cell's measurements are compared in Fig. 23 for Test 3140. The mean and maximum loads are compared in Table 6. Except for test #4140, the current

Table 4
Inputs for the theoretical model calculation (e.g., in test #3210).

σ_f	Flexural strength of the ice in full scale [kPa] obtained by standard test procedures in HSVA (Schwarz et al., 1981)
σ_c	Crushing strength of the ice, which is assumed to be twice the flexural strength due to a lack of measured data [kPa]
h	Thickness of the ice in full scale [m]
$h_s = 4$	Height of the underwater portion of the sloping surface [m]
P_i	Density of the ice [kg/m^3]
$P_w = 1006$	Density of the water [kg/m^3]
E	Young's modulus of the model ice [MPa]
$\mu_s = 0.027$	Ice structure friction coefficient [–] obtained by standard test procedures in HSVA (Schwarz et al., 1981)
$\mu_i = 0.3$	Ice–ice friction coefficient [–] taken from Paavilainen et al. (2011) and Sukhorukov et al. (2012)
$D_T = 8.32$	Width of the tactile sensor's measuring range in the horizontal direction [m]
$h_{r,max}$	Maximum rubble height during the accumulation stage [m]; this value is determined by the structure's geometry and ice clearing efficiency. Based on the geometry of the above two test set-ups, this value was chosen to be 21 m and 16.98 m for test set-ups #1 and #2, respectively
$\alpha_v = 0$	No ventilation is considered here because the interaction speed is low
η	Rubble porosity taken from Serré et al. (2013a,b) (e.g., in Test 3210, $v = 021$)
θ''	Repose angle of the accumulated rubble taken from (Kulyakhtin et al., 2013) (e.g., in Test 3210, $9'' = 36$) [°]
v	Interaction speed [m/s]
L	Ice penetration length [m]. In all of the test designs, this final penetration length is often 200 m because $h_{r,max}$ was expected to have reached with such a penetration distance

theoretical model appears to slightly underestimate the mean load (i.e., within 1.0% for test #3140 and 10.6% for test #5130), whereas it is relatively conservative for the maximum ice load predictions.

5. Discussion

The validation results of the theoretical model were presented in the previous section. In this section, we discuss the capability of the theoretical model to predict the ice load. We also elaborate on the interaction mechanism illustrated by the common results obtained from both the theoretical model and physical model tests.

5.1. Spatial and temporal predictions of the ice load

Fig. 20 illustrates that in general, the current theoretical model's predictions regarding the mean ice load's spatial distribution are in agreement with the measurements (i.e., they agree well with each other in terms of both the load magnitude and spatial variation). However, differences do exist between the results from the theoretical model and physical model tests. First, the theoretical model fails to predict any load above the shaded area (i.e., the thickness region of the undeformed level ice). This is due to the simplification that the rubble sail's effect was not considered. Second, a further observation in the detailed differences in each test indicates the following:

(a) For test #2210, the overall load was tested at a higher interaction speed (i.e., 0.89 m/s). Because the dynamic effects were not considered in the theoretical model, the mean ice load is considerably underestimated below the shaded area. This underestimation implies that the dynamic effects during the ice rotating and ice accumulation process require further study;
(b) For test #4210, compared to the measurements, the theoretical prediction also underestimates the measurements. In test #4210, the ice is relatively thick (i.e., 1.22 m). Thicker ice requires more energy to propagate the tensile crack through the ice thickness direction, and the ice block's rotating process might be confined because of this thickness. However, in the current theoretical model, the manner in which the ice thickness influences each interaction module was not considered. This difference might be the reason for the difference between the theoretical predictions and measurements;
(c) For tests #1210, #3210 and #5210, better predictions are shown in Fig. 20. Although there is some underestimation of the ice load below the shaded area, the difference is relatively small. Such a small difference might be due to the estimated assumption of the ice pushing load F_P's spatial distribution (see Fig. 17).

With respect to the maximum ice load's spatial distribution, as shown in Fig. 21, the theoretical model tends to overestimate the maximum ice load compared to the tactile sensor's measurements. However, this overestimation is speculative because of the inaccuracy of the tactile sensor in measuring the peak loads with the current calibration. However, the general trend and maximum ice load's location for both the theoretical prediction and experimental measurements are similar.

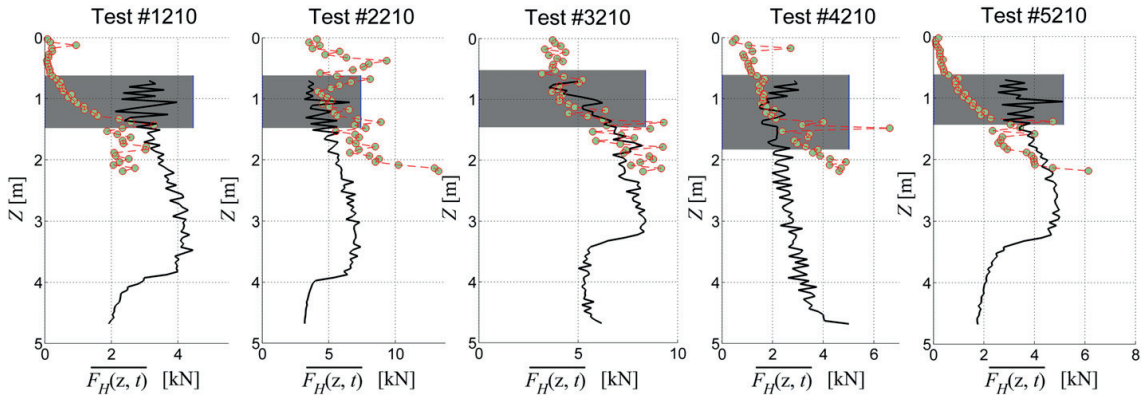

Fig. 20. Spatial variation of the mean ice load (theoretical prediction: solid line; measurements: circles with dashed line).

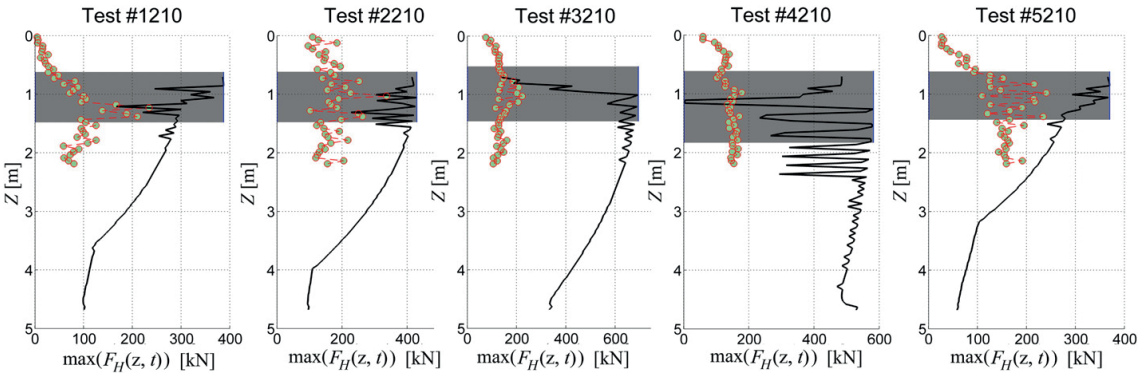

Fig. 21. Spatial variation of the maximum ice load (theoretical prediction: solid line; measurements: circles with dashed line).

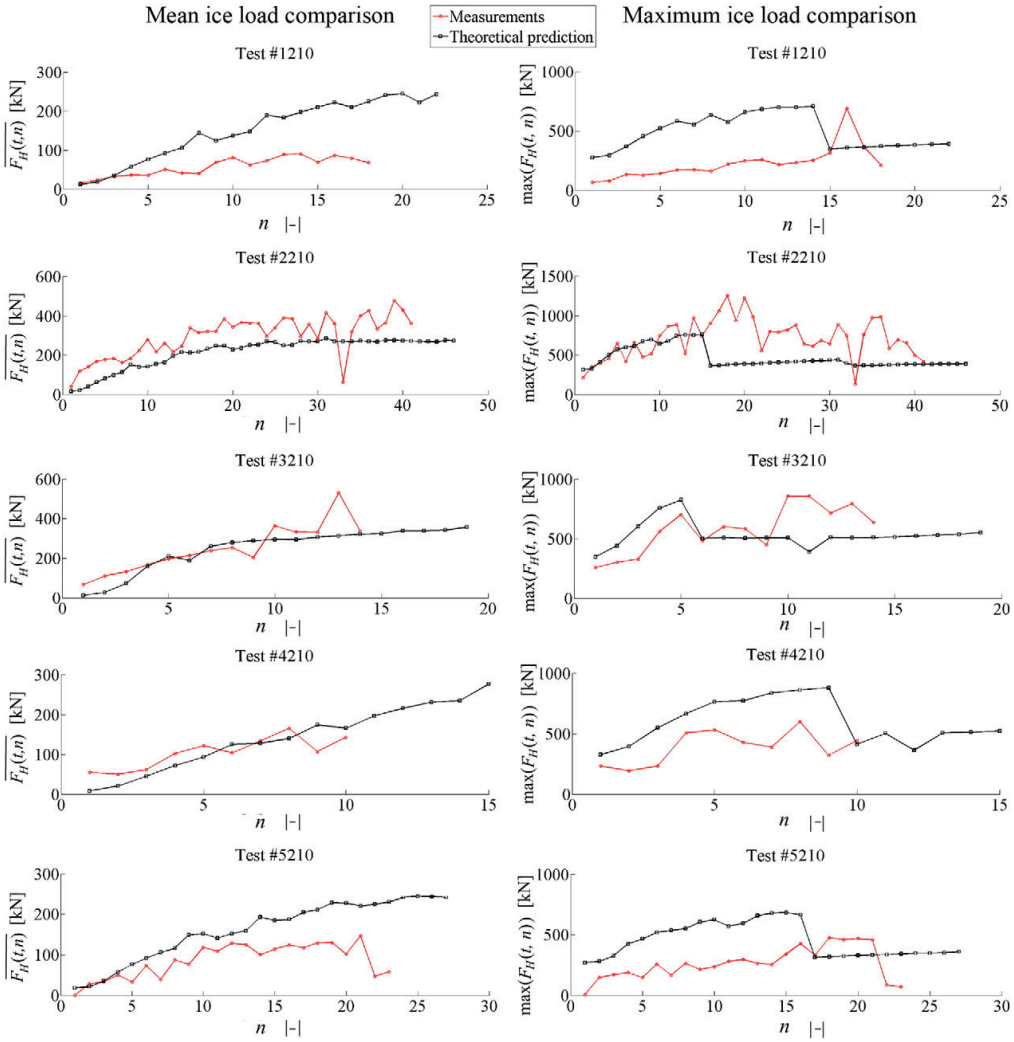

Fig. 22. Temporal variation of the ice load (theory versus measurements).

Table 5
Additional inputs for the ice load calculation of test set-up #2.

$D_S = 52.2$	Width of the structure at the water line in the horizontal direction [m]
$h_{r,max} = 1698$	Maximum rubble height [m]
$\eta = 0.3$	Rubble porosity [–]; this parameter is not measured during the test; it is assumed to be 0.3
$\theta'' = 45$	Repose angle of the accumulated rubble [°], which is assumed to be 45° due to a lack of measurements

Temporally, the mean global ice load's history has been sectionalised and compared between the theoretical predictions and measurements in the left column in Fig. 22. The left column of Fig. 22 illustrates that the theoretical model captures the ice load's increasing trend over time. Such an increase is due to the presence of the volume-growing rubble accumulation. The same underestimation in tests #2210 and #4210 is also visible in the left column of Fig. 22. The same explanation as above can also be applied to these discrepancies. The mean ice load's temporal trend has been satisfactorily captured in the other tests, which signifies the applicability of the current theoretical model.

In terms of the temporal evolution of the maximum ice load, as shown in the right column of Fig. 22, the theoretical predictions are not in agreement with the measurements. As discussed previously, this difference is partially due to the inaccuracy of the tactile sensor when measuring the peak loads. Furthermore, the occurrences of the maximum ice loads tend to be rather random. Therefore, it might be difficult, if not impossible, to illustrate the temporal evolution of the maximum ice load. Consequently, large discrepancies are observed in the right column of Fig. 22.

5.2. Prediction of the global ice load

It has been attempted to compensate for the inaccuracy in the tactile sensor's measurements of the maximum ice load by using load cells in test set-up #2. A comparison regarding the global ice load history for test #3140 was made in Fig. 23. The results demonstrate that, in general, the theoretical model predicts less frequent ice loading events than do the measurements. Such a discrepancy might be due to the two-dimensional assumption of the theoretical model in which the incoming ice fails in the width direction simultaneously. In reality, imperfect contact between the level ice and sloping structure occurs frequently. This imperfect contact leads to frequent non-simultaneous bending failure of the level ice in the width direction and thus leads to more frequently measured ice loading events that have relatively lower magnitude.

In the entire interaction process, the load trends (see the smoothed load history comparison in Fig. 23), load magnitude, and cyclic pattern of the load appear to have been captured by the theoretical model.

Similar satisfactory comparisons can also be found for tests #4140 and #5130, as shown in Table 6. However, for test #4140, similar to the validations made against the tactile sensor, the theoretical model underestimated both the mean and maximum ice loads measured by the load cell. The same explanation given previously for such underestimation is expected to be applied here (i.e., the effect from the ice thickness). For other two tests #3140 and #5130 the current theoretical model predicts a relatively conservative maximum ice load. They also predict rather close mean ice load, as shown in Table 6. The slight difference may be due to the limitation in the current two-dimensional theory and the oversimplification of the rubble profiles. The comparisons made here further validate the ability of the current theoretical model to capture the ice load history (including the maximum ice load), which is blurred by the inaccurate measurements of the tactile sensor in the previous physical tests.

5.3. The interaction mechanism

In this section, the interaction mechanism of the level ice and the wide sloping structure are discussed based on the common results obtained from both the theoretical model and physical model tests.

As observed from both the experimental measurements and theoretical predictions in Fig. 20, the largest mean ice loads in all of the tests continue to increase in the vertical downward direction until even beyond the undeformed level ice's thickness region (i.e., the shaded area). Similar measurements as in Izumiyama et al. (1999) and Timco (1991) show the same ice load's spatial variation on sloping structures/ship hull. As is known, when bending failure occurs, the tip deflection of an ice beam on an elastic foundation is minimal compared to its thickness (Lubbad et al., 2008). Therefore, the ice breaking load is not expected to be transferred below the undeformed ice thickness region. In contrast, according to the theoretical model, the ice rotating load F_R together with the rubble accumulation load F_{srb} are able to transfer the ice load below the undeformed level ice's thickness region (see Fig. 16). Therefore, this largest mean ice load is considered to be a result of the effects from the ice rotating load together with the rubble accumulation load. This consideration is a further theoretical support of Izumiyama et al.'s (1999) schematic illustration in explaining the observed 'line-like' ice pressure travelling further below the waterline.

However, as observed from Fig. 21, although they have different magnitudes, both the theoretical model predictions and experimental measurements indicate that the maximum ice load locates within the undeformed level ice's thickness region. According to the theoretical

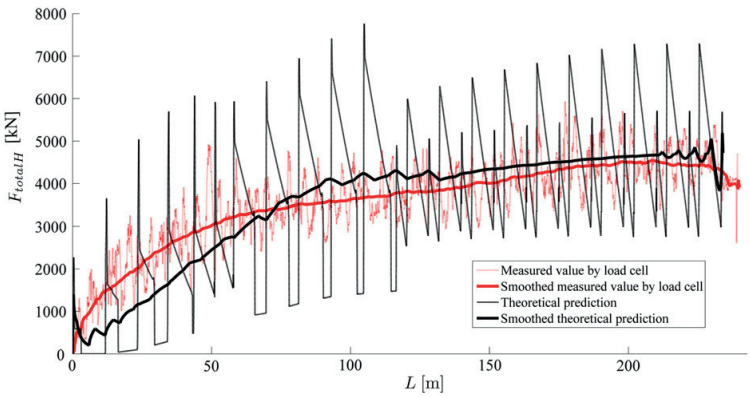

Fig. 23. Global load comparison between the theoretical model and load cells for test #3140.

Table 6
Comparison of the mean and maximum loads.

Test series	Measured mean value	Calculated mean value	Measured maximum value	Calculated maximum value
#	kN	kN	kN	kN
3140	3586	3550.4	7624.0	7767.1
4140	2345.3	1413.2	7064.4	6628.5
5130	1961.6	1752.8	4872.0	5438.4

model, all of the load components ($\boldsymbol{F_B}$, $\boldsymbol{F_R}$, $\boldsymbol{F_{srb}}$,and $\boldsymbol{F_P}$) are active in this region. The maximum ice load's contributions from these different components are discussed in the following section.

The effects of rubble accumulation are highlighted in the mean ice load's temporal variation in the left column of Fig. 22 and the global ice load's history in Fig. 23. As the rubble accumulation increases, the mean ice load tends to increase gradually. According to the theoretical model, the rubble accumulation tends to increase the ice breaking load in the phase 1 ice breaking scenario and tends to increase the ice rotating load and ice accumulation load. Thereafter, the measured ice load increases.

5.4. Load contribution and eventual ice breaking length

In this section, the theoretical model is further explored to obtain information that cannot be directly measured in the current test set-up.

First, the load contributions from different interaction processes are illustrated. Different components of the ice load's time history are constructed in Fig. 24 based on the theoretical model and using inputs from test #3210. In the design of test set-up #1, it was assumed that the maximum rubble height was $h_{r,max} = 21$ m. In other words, when the accumulated ice rubble beneath the waterline reaches a depth of 21 m, further incoming ice rubble starts to overflow and be cleared away. Therefore, this depth (i.e. maximum rubble height) determines the stationary ice loading history. In the current theoretical calculations, based on the assumed rubble volume calculations (i.e., Eqs. (1), and (2)), it is found that the maximum rubble height was reached when the ice penetration $L = 300$ m with the assumed bilinear rubble profile and measured rubble porosity. In the current trial calculation, $L = 400$ m was chosen as the maximum ice penetration to demonstrate the ice load contribution from the different ice load components.

Fig. 24 shows that the ice breaking load F_B is decisive initially and increases with the rubble accumulation. However, when reaching the phase 2 ice breaking stage, the ice breaking load suddenly decreases due to the assumption (i.e., the incoming ice no longer has direct contact with the structure) made in the theoretical model. Furthermore, the dominant ice load shifts to the ice rotating load F_R. Its peak values may become even larger than the ice breaking loads. The load F_P that is required to push the ice through the rubble becomes significant as the ice penetration increases. However, in test #3210, the model ice's density is rather low and the rubble effects have been amplified. The rubble accumulation load F_{srb} also contributes an important portion to the global ice load. The general trend of each load component is: in the phase 1 ice breaking scenario, all these load components increase with the amount of rubble accumulation; in the phase 2 ice breaking scenario, except the ice breaking load, all the other load components keep increasing until the maximum rubble height was reached.

Due to the low ice density in test #3210, the incoming level ice starts to fail against the accumulated rubble at a rather early stage (i.e., with an ice penetration of approximately 50 m). Following this stage, are the interactions in the rubbling process. It has been implicitly assumed that Croasdale's model is valid only while the ice fails against the structure (Croasdale and Cammaert, 1994). After the ice starts to fail against the accumulated rubble, new formulations are required to calculate the rubbling load.

In Fig. 25, the global ice load history of the current theoretical model prediction is compared with the maximum ice load obtained by several other methods for test #3210. Because the current model is a two-dimensional model, the two-dimensional formulas proposed by Croasdale (2012) in Eq. (45) and Comfort et al. (1998) in Eq. (46) were utilised for comparison purposes. A further comparison is also made against the secant formula (Bažant and Cedolin, 2010), as in

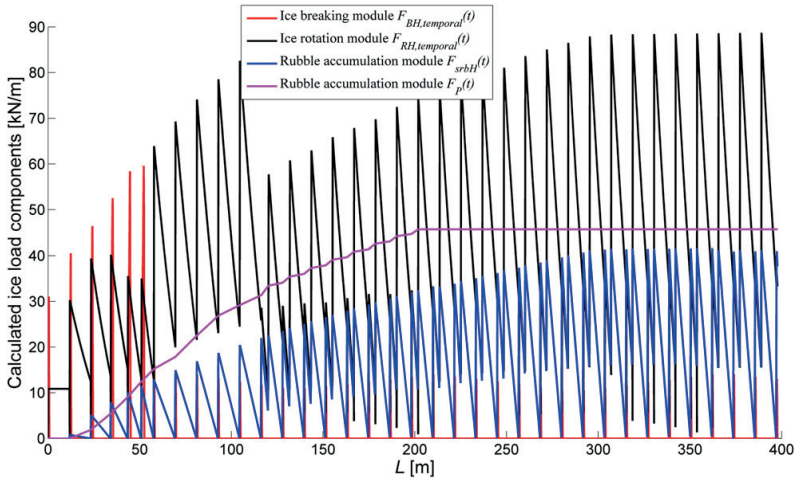

Fig. 24. Load contribution from the different load components.

Eq. (47), to extract the maximum rubbling load (Paavilainen and Tuhkuri, 2013).

$$F_{\text{ridging\_Croasdale}} = 105.3h^{1.104} \tag{45}$$

$$F_{\text{ridging\_Comfort}} = 100h^{1.25} \tag{46}$$

$$F_{\text{forcechain}} = \frac{\sigma_c Dh}{\left[1 + \frac{ey_c}{r^2}\sec\left(\frac{l}{2r}\sqrt{\frac{F_{\text{forcechain}}}{EDh}}\right)\right]} \tag{47}$$

where

$F_{\text{ridging\_Croasdale}}$ is the two-dimensional ridge building line load based on Croasdale (2012) [kN/m]; the unit for h in the equation is [m];

$F_{\text{ridging\_Comfort}}$ is the two-dimensional ridge building line load based on Comfort et al. (1998) when the ice thickness is smaller than 2 m, in [kN/m], and the unit for h in the equation is [m];

$F_{\text{forcechain}}$ is the maximum rubbling load due to the buckling of the force chain within the rubble [kN];

e is the eccentricity [m];

y_c is the largest distance from the neutral axis of the force chain to a fibre that is in compression [m];

r is the radius of gyration of the considered beam profile [m].

In general, Fig. 25 illustrates that the current theoretical model predicts a rather close ice load in comparison to the other methods. With the ridge building load, the current theoretical model predicts a relatively conservative maximum ice load with a maximum rubble height of 21 m. As discussed by Palmer and Croasdale (2013), Eq. (45) is more influenced by the ice–ice friction, gravity and buoyancy terms rather than the bending failure terms. Judging from the ice properties' inputs to the current theoretical model (e.g., ice–ice friction is 0.3 and low ice density), the agreement between the current theoretical model and Eq. (45) in reality would be better than it appears in Fig. 25.

The calculation of the secant formula (i.e., Eq. (47)) is largely influenced by the chosen values of e and y_c. As discussed by Paavilainen and Tuhkuri (2013), the eccentricity e typically increases with the sloping angle. In the current calculation with a 45° slope, it is assumed that $e = 2.5$ m. This assumption is in line with the value of 2.0 m used for a 30° slope angle in the same reference. The value of y_c is conservatively assumed to be half of the ice thickness. Moreover, the force chain length is chosen as the length of the rubble span expressed as l in Eq. (47). A relatively smaller variation on $F_{\text{forcechain}}$ is induced by the value of l. As it can be observed in Fig. 25 that the current theoretical model predicts closer results with the secant formula while the rubble amount is not significant. While more ice rubble is present, the secant formula appears to be less conservative. Paavilainen and Tuhkuri (2013) discussed the applicability of the secant formula in describing the buckling of force chain. In the current calculation, it has been assumed that an intact 'ice beam' is eccentrically loaded. And the support from the ice rubble is not considered in the secant formula. The additional rubble support would strengthen the eccentrically loaded 'ice beam' and hence increase the ice load. If this effect can be added into the secant formula, the current theoretical model's prediction could be closer with the force chain concept's prediction.

Furthermore, it should bear in mind that the formulas used in the current comparisons are all two dimensional. When extending the line load in the width direction, the size effect should be cautioned. However, this consideration is not covered in the current paper because of the two-dimensional assumption.

The variation of the ice breaking length in the presence of secondary ice breaking is illustrated in Fig. 26 for test #3210. This figure illustrates that the secondary ice breakings occurred when the ice penetration reaches approximately 110 m. The presence of secondary breaking breaks an initially long ice block into two smaller pieces. This finding agrees with the model tests conducted by Timco (1984), who observed that the ice breaks into two or three smaller pieces during the rotating process. Rubble accumulation increases the likelihood of secondary ice breaking and leads to a shorter eventual ice breaking length.

With the influence from additional rubble pressure, secondary ice breaking takes place in test #3210. For other tests, even without the occurrence of secondary ice breakings, shorter ice breaking lengths were also observed with the increasing amount of rubble accumulation, as shown in Fig. 27. Fig. 27 is in line with the field observation that the eventual ice breaking length tends to be approximately three to six times the ice thickness (Michel, 1978). However, the theoretically predicted range (i.e., three to nine times) is relatively larger than the field observation (i.e., three to six times). Such discrepancy may due to the assumed perfect contact in the width direction in the current two-dimensional setting. Nevertheless, the current secondary ice breaking theory and rubble accumulation effects offer another explanation for the observed shorter ice breaking length than that predicted by elastic-foundation beam theory. This explanation is also in line with the simulation results obtained by Paavilainen et al. (2010), who calculated a short eventual ice breaking length even when the bending failure mode is dominant.

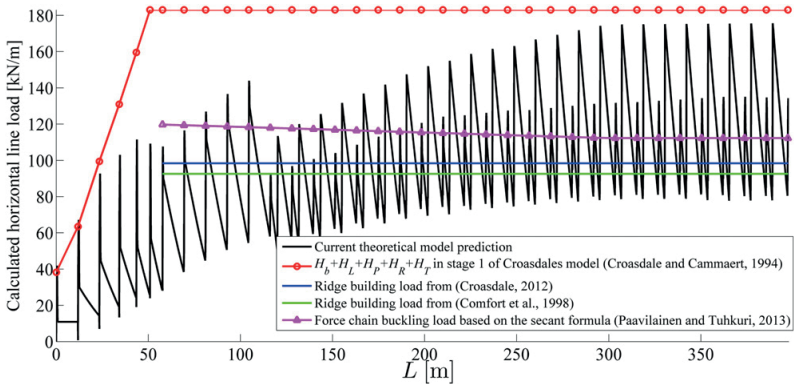

Fig. 25. Total load history of test #3210 in comparison with other existing theoretical models.

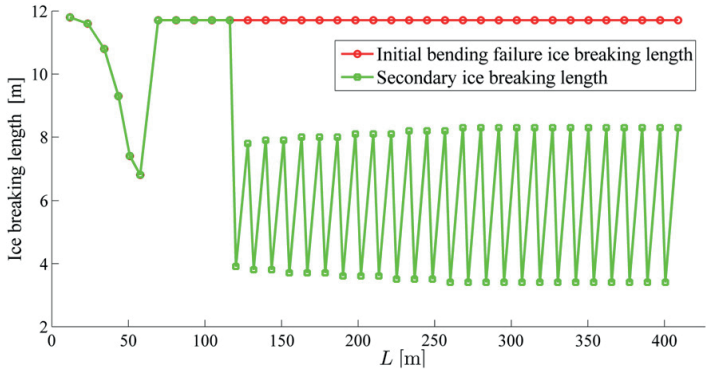

Fig. 26. Illustration of secondary ice breaking and ice breaking length evolution during the ice rotating phase (based on numerical simulations).

Moreover, this result further indicates that the ice rotating load could be further transmitted downwards below the waterline for more than three times of the ice thickness.

6. Conclusions

Based on previous theoretical models and observations, a quasi-static 2D theoretical model was developed to describe the interaction process between level ice and wide sloping structures. This theoretical model has the following features:

- Different interactions are treated separately in a procedural manner in the time domain;
- The rubble accumulation effect is coupled with all of the important interaction processes;
- The theoretical model is designed to predict the spatial and temporal variations of the ice load.

The implemented theoretical model is compared with the measurements from both a tactile sensor and load cells. Based on the above comparisons of the available test data against the theoretical prediction, it can be concluded that:

- The current theoretical model can satisfactorily predict the spatial and temporal variation of the ice load when the interaction speed is low (i.e., approximately 0.2 m/s) and when the ice thickness is smaller than 1 m.
- Further study is still required to clarify the dynamic influence in the ice rotating process and rubble-accumulation process; further study is also needed to consider the influence of the ice thickness in different interaction processes.

The following conclusions can be drawn from the shared results from both the tactile sensor measurements and theoretical predictions:

- The largest mean ice load typically occurs below the undeformed level ice's thickness region. This arrangement indicates the importance of the ice accumulation load and ice rotating load when considering the largest mean ice load;
- The maximum ice load's location is found to be within the undeformed level ice's thickness region. Based on the load distribution assumption and load component analysis, the major contributor to the maximum load can be due to either the ice breaking load, ice rotating load, or ice pushing load. This offers an alternative explanation to the peak ice load's location as opposed to other method (e.g., the buckling of force chain method). Further research is needed to clarify the connections between these explanations;
- Compared with other two-dimensional theories (i.e., the ridge building load), the current theoretical model yields relatively conservative but similar predictions regarding the maximum ice load during the rubbling process. However, as one of the anonymous reviewers pointed out that the validity of the physical model tests and accordingly the theoretical model's application in the context of full scale need further more rigorous validations;
- Secondary ice breakings occur frequently, especially in the presence of a large pressure induced by the rubble accumulation (e.g. test #3210). The secondary ice breaking causes the eventual ice breaking length to be approximately three to eight times the ice thickness. Even without

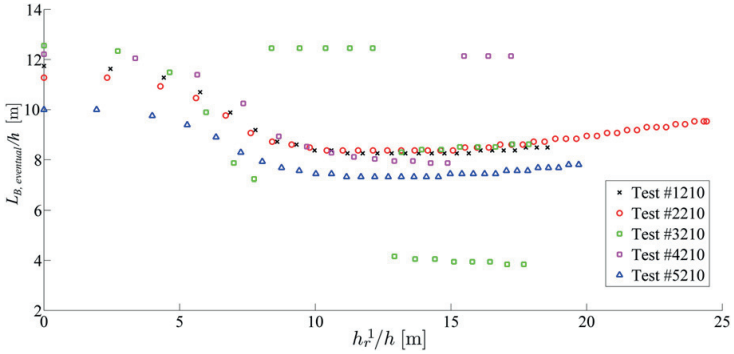

Fig. 27. Calculated eventual ice breaking length with possible secondary ice breakings versus the rubble height (note here that the rubble height is calculated according to Eq. (3), with $\theta'' = 45\ ^\circ$).

the secondary ice breakings, the presence of rubble accumulation also tends to decrease the eventual ice breaking length (i.e. around six to nine times the ice thickness). This theory offers another explanation for the often-observed shorter ice breaking length compared to the elastic-foundation beam theory's prediction.

In summary, mutual support has been attained from both the test results of the physical models and the predictions of the theoretical model to reveal some important aspects regarding the level ice interaction with wide sloping structures. Special attention has been placed on the importance of the rubble accumulation's effects. Based on the physical model's measured results, the currently developed theoretical model can serve as a preliminary yet useful prediction and investigation tool to harvest the spatial and temporal variation of the ice load.

Acknowledgements

The authors would like to thank the Norwegian Research Council through the project 200618/S60-PetroRisk and the SAMCoT CRI for financial support. Additionally, the work described in this publication was supported by the European Community's 7th Framework Programme through the grant to the budget of the Integrated Infrastructure Initiative HYDRALAB-IV, Contract no. 261520. Furthermore, financial contribution from Statoil to construct the experimental setups and the initiation of the test campaign by Multiconsult are appreciated.

The authors are sincerely grateful to Professor Mauri Määttänen, Dr. Karl-Ulrich Evers, Dr. Nicolas Serre, and Dr. Basile Bonnemaire and Ph.D. students Sergey Kulyakhtin, Ivan Metrikin, Marat Kashafutdinov, Torodd Nord, Sergiy Sukhorukov, and Anton Kulyakhtin for their valuable discussions and suggestions. The authors would also like to thank the Hamburg Ship Model Basin (HSVA), especially the ice tank crew, for the hospitality, technical and scientific support and the professional execution of the test programme in the Research Infrastructure ARCTECLAB.

Appendix A. Vertical ice breaking load with the presence of a triangular rubble profile

As is shown in Fig. A.1, in order to determine F_{BV} with the presence of a triangular rubble profile beneath, the method of superimposition is utilised herein. At first, the ice beam's deflection $W_{rubble}(x)$ and moment distribution $M_{rubble}(x)$ are calculated. Then it is possible to calculate the flexural stress distribution $\sigma_{rubble}(x)$ induced by rubble pressure alone. It is firstly checked whether or not the rubble pressure alone can already break the ice. If yes, then the phase 2 ice breaking scenario is activated; if not, we need to further superimpose the effect of F_{BV} (to be calculated) to meet the ice bending failure criteria.

A.1. Infinite beam on elastic foundation under triangular distributed load

In order to calculate the triangular distributed load's effect on a semi-infinite beam, the method of end conditioning force (Hetenyi, 1946) is utilised. The same approach has been adopted by Mayne (2007). However, his derivation suffers from a minor error. Therefore, the derivation is repeated here with constant references back to the results of Hetenyi (1946) and Mayne (2007).

It is important to define in the very beginning the sign of different force terms. We adopt here the same convention that has been utilised by both Hetenyi (1946, p. 3) and Mayne (2007, p. 83) (see Fig. A.2). Furthermore, in order to take advantage of the already available solutions and also in order to make less confusion, the original problem has been equivalently transformed as in Fig. A.2.

The solution for this case has been given in Hetenyi (1946, p. 17). By changing variables in the original solution, we obtain the infinite beam's deflection, shear force, and moment distribution as in the following:

For $0 \le x \le l$ (changing $a = l - x$ and $b = x$):

$$\begin{aligned} W(x) &= \frac{q_0}{4\lambda k'}\frac{1}{l}\left[C_{\lambda(l-x)} - C_{\lambda x} - 2\lambda l D_{\lambda x} + 4\lambda(l-x)\right] \\ M(x) &= -\frac{q_0}{8\lambda^3}\frac{1}{l}\left(A_{\lambda(l-x)} - A_{\lambda x} - 2\lambda l B_{\lambda x}\right) \\ Q(x) &= -\frac{q_0}{4\lambda^2}\frac{1}{l}\left(B_{\lambda(l-x)} + B_{\lambda x} - \lambda l C_{\lambda x}\right). \end{aligned} \tag{48}$$

For $x > l$ (changing $a = x - l$ and $b = x$):

$$\begin{aligned} W(x) &= \frac{q_0}{4\lambda k'}\frac{1}{l}\left[C_{\lambda(x-l)} - C_{\lambda x} - 2\lambda l D_{\lambda x}\right] \\ M(x) &= -\frac{q_0}{8\lambda^3}\frac{1}{l}\left(A_{\lambda(x-l)} - A_{\lambda x} - 2\lambda l B_{\lambda x}\right) \\ Q(x) &= \frac{q_0}{4\lambda^2}\frac{1}{l}\left(B_{\lambda(x-l)} - B_{\lambda x} + \lambda l C_{\lambda x}\right) \end{aligned} \tag{49}$$

with the definition of variables as in the following: $\lambda = \sqrt[4]{\frac{\rho_w g D}{4EI}}$, $k' = \rho_w g D$, $q_0 = -q_r^0 = -(\rho_w - \rho_i) g h_r^1 (1 - \eta)$, $A_{\lambda x} = e^{-\lambda x}(\cos \lambda x + \sin \lambda x)$, $B_{\lambda x} = e^{-\lambda x} \sin \lambda x$, $C_{\lambda x} = e^{-\lambda x}(\cos \lambda x - \sin \lambda x)$, and $D_{\lambda x} = e^{-\lambda x} \cos \lambda x$.

Note that in the above equations, the sign of $Q(x)$ is opposite to the original solution in Hetenyi (1946, p.17). This is because in the original solution of Hetenyi (1946, p. 17), the triangular distributed load is sloped in an opposite manner. Imagining setting $x = 0$ (i.e., setting $a = l$ and $b = 0$ in the original work of Fig. 9 in Hetenyi

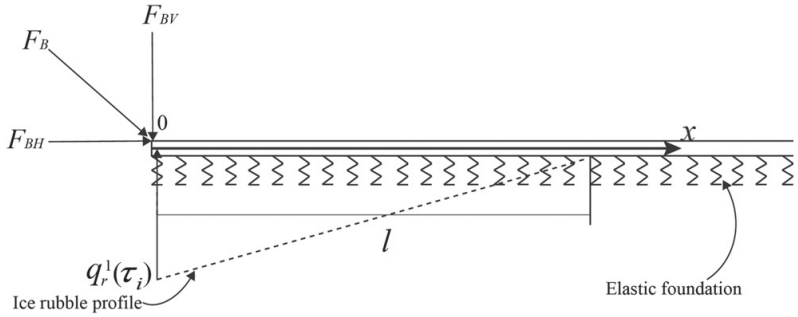

Fig. A.1. Illustration of different loads on the assumed semi-infinite elastic-foundation ice beam.

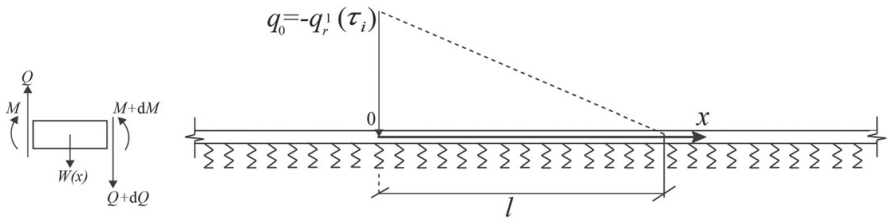

Fig. A.2. Positive directions and triangular distributed load on infinite beam on elastic foundation.

(1946, p. 17), a shear force component can be obtained on the right-hand side of the truncated beam; while setting $x = 0$ in the current case (Eq. (49)), we can obtain a same shear force component having the same magnitude and pointing direction, but on the left-hand side of the truncated beam (see Fig. A.2). This leads to an opposite sign according to the sign convention in Fig. A.2. This is a fast check to see that the shear force component in the current case is supposed to have a negative sign in comparison to Hetenyi's solution. In the work of Mayne (2007, p. 92), all the terms in Eqs. (48) and (49) are the same, except the expression for $Q(x)$ in Eq. (48). This is the small mistake we have mentioned.

A.2. Semi-infinite beam on elastic foundation under triangular distributed load

With the solution of infinite beam on elastic foundation, the solution for semi-infinite beam under the same external loadings can be obtained by applying the end conditioning force P_0 and moment M_0 at the truncation point ($x = 0$) such that they can cancel out the existing moment and shearing force at $x = 0$. According to Hetenyi (1946, p. 23), the expression for P_0 and M_0 can be written as:

$$\begin{aligned} P_0 &= 4[\lambda M(x=0) + Q(x=0)] \\ M_0 &= -\frac{2}{\lambda}[2\lambda M(x=0) + Q(x=0)]. \end{aligned} \tag{50}$$

Inserting Eq. (48) into Eq. (50) with $x = 0$, we obtain the expression for P_0 and M_0 respectively as:

$$\begin{aligned} M(x=0) &= \frac{q_0}{8\lambda^3}\frac{1}{l}(1-A_{\lambda l}) \\ Q(x=0) &= \frac{q_0}{4\lambda^2}\frac{1}{l}(\lambda l - B_{\lambda l}) \\ P_0 &= \frac{q_0}{2\lambda^2 l}(1-A_{\lambda l} + 2\lambda l - 2B_{\lambda l}) \\ M_0 &= -\frac{q_0}{2\lambda^3 l}(1-A_{\lambda l} + \lambda l - B_{\lambda l}). \end{aligned} \tag{51}$$

Defining $\omega = (1 - A_{\lambda l} + 2\lambda l - 2B_{\lambda l})$ and $\psi = (1 - A_{\lambda l} + \lambda l - B_{\lambda l})$, the end conditioning forces will convert the solution for an infinite beam into a semi-infinite beam. These end conditioning forces also introduce additional beam deflection, shearing force and moment distribution along the beam length. According to Hetenyi (1946, p. 12 & p. 14), the solutions for an infinite beam under point load or a concentrated moment have been explicitly given. This leads to the expression for different terms as in the following:

For the point load P_0:

$$\begin{aligned} W_{P_0}(x) &= \frac{P_0\lambda}{2k'}A_{\lambda x} = \frac{q_0}{4k'\lambda l}\omega A_{\lambda x} \\ M_{P_0}(x) &= \frac{P_0}{4\lambda}C_{\lambda x} = \frac{q_0}{8\lambda^3 l}\omega C_{\lambda x}. \end{aligned} \tag{52}$$

For the moment M_0:

$$\begin{aligned} W_{M_0}(x) &= \frac{M_0\lambda^2}{k'}B_{\lambda x} = -\frac{q_0}{2\lambda k' l}\psi B_{\lambda x} \\ M_{M_0}(x) &= \frac{M_0}{2}D_{\lambda x} = -\frac{q_0}{4\lambda^3 l}\psi D_{\lambda x}. \end{aligned} \tag{53}$$

Applying the principle of superimposition, the deflection and moment of a semi-infinite beam under triangular distributed load can be written as:

For $0 \le x \le l$:

$$\begin{aligned} W_{rubble}(x) &= W_{P_0}(x) + W_{M_0}(x) + W(x) \\ &= \frac{q_0}{4\lambda k' l}\left(\omega A_{\lambda x} - 2\psi B_{\lambda x} + C_{\lambda(l-x)} - C_{\lambda x} - 2\lambda l D_{\lambda x} + 4\lambda(l-x)\right) \\ M_{rubble}(x) &= M_{P_0}(x) + M_{M_0}(x) + M(x) \\ &= -\frac{q_0}{8\lambda^3 l}\left(-\omega C_{\lambda x} + 2\psi D_{\lambda x} + A_{\lambda(l-x)} - A_{\lambda x} - 2\lambda l B_{\lambda x}\right) \end{aligned} \tag{54}$$

For $x > l$:

$$\begin{aligned} W_{rubble}(x) &= W_{P_0}(x) + W_{M_0}(x) + W(x) \\ &= \frac{q_0}{4\lambda k' l}\left(\omega A_{\lambda x} - 2\psi B_{\lambda x} + C_{\lambda(x-l)} - C_{\lambda x} - 2\lambda l D_{\lambda x}\right) \\ M_{rubble}(x) &= M_{P_0}(x) + M_{M_0}(x) + M(x) \\ &= -\frac{q_0}{8\lambda^3 l}\left(-\omega C_{\lambda x} + 2\psi D_{\lambda x} + A_{\lambda(x-l)} - A_{\lambda x} - 2\lambda l B_{\lambda x}\right). \end{aligned} \tag{55}$$

Note here the expressions in Eqs. (54) and (55) are identical to the results of Mayne (2007, p. 94) except that the definition of ω and ψ are different. This is due to different results on the end conditioning force. A quick way of disproving Mayne's (2007) results is to check the expression of end deflection $W_{rubble}(x = 0)$ according to Eq. (54) as in the following:

$$\begin{aligned} W_{rubble}(0) &= \frac{q_0}{4\lambda k' l}(\omega A_{\lambda 0} - 2\psi B_{\lambda 0} + C_{\lambda l} - C_{\lambda 0} + 2\lambda l D_{\lambda 0}) \\ &= \frac{q_0}{4\lambda k' l}(\omega + C_{\lambda l} - 1 + 2\lambda l). \end{aligned} \tag{56}$$

In the original work of Mayne (2007, p. 94), $\omega = (1 - A_{\lambda l} + 2B_{\lambda l} + 2\lambda l)$. Inserting this expression into Eq. (56), it turns out:

$$\begin{aligned} W_{rubble}(0) &= \frac{q_0}{4\lambda k' l}[(1-A_{\lambda l} + 2B_{\lambda l} + 2\lambda l) + C_{\lambda l} - 1 + 2\lambda l] \\ &= \frac{q_0}{4\lambda k' l}(2B_{\lambda l} + C_{\lambda l} - A_{\lambda l} + 4\lambda l) = \frac{q_0}{k'}. \end{aligned}$$

This expression is to say, the end point deflection of a semi-infinite beam under triangular distributed load is independent of l. This is physically untrue.

A.3. Semi-infinite beam on elastic foundation under vertical point load F_{BV} at the free end

Applying a point load at the free end of a semi-infinite beam on elastic foundation, the corresponding solutions are given in Hetenyi (1946, p. 24) as in the following:

$$\begin{aligned} W_{F_{BV}}(x) &= \frac{2F_{BV}\lambda}{k'} D_{\lambda x} \\ M_{F_{BV}}(x) &= -\frac{F_{BV}}{\lambda} B_{\lambda x} \end{aligned} \tag{57}$$

Before continuing with the superimposition to solve the problem, it is worthwhile to explore Eq. (57)'s moment distribution $M_{F_{BV}}(x)$ in this loading case (i.e., without the rubble influence). Based on the assumption of pure bending, it can be calculated the location of ice breaking by setting $\frac{dM_{F_{BV}}(x)}{dx} = 0$ and solve for x. This leads to:

$$\frac{dM_{F_{BV}}(x)}{dx} = -\frac{F_{BV}}{\lambda}\frac{dB_{\lambda x}}{dx} = -\frac{F_{BV}}{\lambda}\left(-\lambda e^{-\lambda x}\cos\lambda x + \lambda e^{-\lambda x}\sin\lambda x\right) = 0. \tag{58}$$

The solution for the above Eq. (58) leads to:

$$\lambda x = n\pi + \frac{\pi}{4} \quad n = 0,\ 1,\ 2.... \tag{59}$$

Eq. (59) indicates that the closest bending point is at $x = \frac{\pi}{4\lambda} \quad = \frac{\pi}{4}/\sqrt[4]{\frac{\rho_w g D}{4EI}} = \frac{\sqrt{2}\pi}{4}\sqrt[4]{\frac{EI}{\rho_w g D}}$. This static solution can be considered as the longest ice breaking length encountered if bending failure dominates (see Eq. (14)).

Utilising the principle of superimposition again, the final beam deflection and moment distribution can be obtained as following:

For $0 \le x \le l$:

$$\begin{aligned} W_{total}(x) &= W_{rubble}(x) + W_{F_{BV}}(x) \\ &= \frac{q_0}{4\lambda k' l}\left(\omega A_{\lambda x} - 2\psi B_{\lambda x} + C_{\lambda(l-x)} - C_{\lambda x} - 2\lambda l D_{\lambda x} + 4\lambda(l-x)\right) \\ &\quad + \frac{2F_{BV}\lambda}{k'} D_{\lambda x} \\ M_{total}(x) &= M_{rubble}(x) + M_{F_{BV}}(x) \\ &= -\frac{q_0}{8\lambda^3 l}\left(-\omega C_{\lambda x} + 2\psi D_{\lambda x} + A_{\lambda(l-x)} - A_{\lambda x} - 2\lambda l B_{\lambda x}\right) - \frac{F_{BV}}{\lambda} B_{\lambda x}. \end{aligned} \tag{60}$$

For $x > l$:

$$\begin{aligned} W_{total}(x) &= W_{rubble}(x) + W_{F_{BV}}(x) \\ &= \frac{q_0}{4\lambda k' l}\left(\omega A_{\lambda x} - 2\psi B_{\lambda x} + C_{\lambda(x-l)} - C_{\lambda x} - 2\lambda l D_{\lambda x}\right) + \frac{2F_{BV}\lambda}{k'} D_{\lambda x} \\ M_{total}(x) &= M_{rubble}(x) + M_{F_{BV}}(x) \\ &= -\frac{q_0}{8\lambda^3 l}\left(-\omega C_{\lambda x} + 2\psi D_{\lambda x} + A_{\lambda(x-l)} - A_{\lambda x} - 2\lambda l B_{\lambda x}\right) - \frac{F_{BV}}{\lambda} B_{\lambda x}. \end{aligned} \tag{61}$$

Eqs. (60) and (61) are used to calculate the ice breaking load F_{BV} and ice breaking length L_B by equating the following terms:

$$\mathrm{Max}(|M_{total}(x)|) = \frac{\sigma_f D h^2}{6}. \tag{62}$$

Eq. (62) is a nonlinear equation and its closed-form solution for F_{BV} is difficult to obtain. Simple search algorithms can be implemented to calculate the ice breaking load F_{BV} and ice breaking length L_B. In the current paper, the following steps are implemented:

1) Discretize the ice beam in the length direction (x domain);
2) Assigning a trial value to $F_{BV} = F_{BV}^{trial} = F_{BV}(q_r^1 = 0)$ (This is the critical ice breaking load without the presence of ice rubble. See Eqs. (57), (59) and (62));

$$F_{BV}^{trial} = F_{BV}\left(q_r^1 = 0\right) = \frac{\sigma_f D h^2}{6}\lambda / B_{\lambda x}\left(\lambda x = \frac{\pi}{4}\right) = \frac{\sigma_f D h^2}{6}\frac{\lambda}{e^{-\frac{\pi}{4}}\sin\frac{\pi}{4}}. \tag{63}$$

3) Evaluate the error ratio between the calculated maximum trial moment and the critical ice bending moment as $R = \left[\mathrm{Max}(|M_{total}(x)|) - \frac{\sigma_f D h^2}{6}\right] / \left(\frac{\sigma_f D h^2}{6}\right)$;
4) Update the a new trial ice breaking load as $F_{BV}^{trial,new} = F_{BV}^{trial,old} - RF_{BV}^{trial,old}$;
5) Define the force error as $\Delta = |F_{BV}^{trial,new} - F_{BV}^{trial,old}|$, if $\Delta > \Delta_{cr}$, step (3)–(5) are repeated. If the error is within the chosen limit Δ_{cr} (e.g., 1 N), the iteration stops and $F_{BV} = F_{BV}^{trial,new}$, the corresponding location where the maximum moment takes place can be easily identified and it is the location where L_B can be calculated.
6) If the F_{BV} was found to be negative, this means that the rubble pressure alone can already break the ice. Then phase 2 ice breaking scenario is activated and a different formula need to be used to calculate the ice breaking load as in Eq. (8).

This algorithm has been implemented and studied in details in Lu et al. (2013a,b) regarding the influence of different parameters.

A.4. The influence of the axial force

In the current model, the axial force was not considered. This section demonstrates the consequence of this simplification. There are three different cases should be identified:

Case 1. F_{BV} (without axial compression)

This is the basic assumption of the current paper. This is to say, setting $N_H = 0$ in Eqs. (12) and (13) are not considered.

Case 2. F_{BV} (with axial compression, coupling axial force with the beam bending formulation)

In this case, $N_H \neq 0$ in Eqs. (12) and (13) are utilised to iteratively obtain the ice breaking load F_{BV}.

Case 3. F_{BV} (with axial compression, decoupling axial force from the beam bending formulation)

In this case, $N_H = 0$ in Eqs. (12) and (13) are utilised to iteratively obtain the ice breaking load F_{BV}. For instance, the current ISO/FDIS/19906 (2010) is not coupling the axial force in the beam bending formulation.

These relationships between these 3 cases are studied with different parameters. For the coupled bending Case 2, the formulation and relevant solutions are well treated in Hetenyi (1946, p. 135). Based on the same theory, we briefly present how the presence of additional compressive load F_{BH} would alter the vertical ice breaking load F_{BV}. Utilising the relationship between F_{BH} and F_{BV}, we can construct the relationship between F_{BV} (with axial compression) and F_{BV} (without axial compression) as in Fig. A.3. Based on the calculated results, the

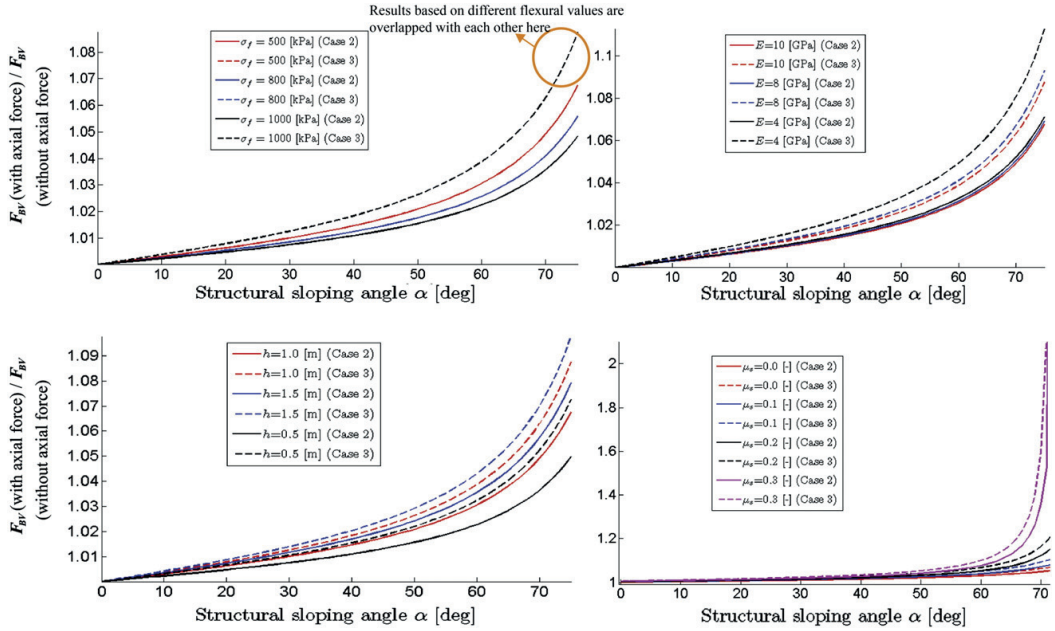

Fig. A.3. The effect of axial force with different mechanical parameters. (Note that the red-coloured lines are the base case in all the comparisons with inputs: $\sigma_f = 500$ kPa, $E = 10$ GPa, $h = 1.0$ m, and $\mu_i = 0.0$).

following conclusion can be made regarding the axial force's influence:

- For most engineering structures, while the sloping angle is between 30 and 60 (i.e., dominated by ice bending failure), based on all the calculated cases, the inclusion of the axial force (i.e., in Cases 2 and 3) will increase the vertical direction ice breaking load not more than 10%;
- Neglecting the axial compression's contribution to the additional bending moment (i.e., setting $N_H = 0$ in Eq. (12) in Case 3) would lead to more conservative estimation of the vertical direction ice breaking load;
- Among all studied parameters (i.e., flexural strength, Young's modulus, ice thickness and ice–structure friction coefficient), the ice–structure friction coefficient can significantly magnify the horizontal load which in turn significantly increase the vertical direction ice breaking load;
- Caution should be made and modification should be taken to the current developed ice breaking module once the structure's sloping angle (e.g., larger than 60°) and the ice–structure friction coefficient (e.g., larger than 0.2) was large.

Appendix B. Ice rotation module: derivation and model development

B.1. Derivation of the ice rotating load F_{BV} within the elastic foundation range

The vertical direction ice rotating load F_{BV} is calculated in two different regions. The free body diagram and corresponding derivation within the elastic foundation range are shown as in the following:

Elastic foundation range: $\theta_R \le \theta_{cr}$.
In this case, the ice block's rotation angle θ_R is very small and the fluid base behaves elastically. Furthermore, due to the rather small rotation, ice rubble's pressure is neglected. Based on these idealizations, the free body diagram can be illustrated as in Fig. B.1.

The force balance in the vertical direction and the moment balance around the rotation centre (unknown) could be written as:

$$\begin{aligned} &F_{RV} + \frac{1}{2}\rho_w g D d^2 \theta_R = \frac{1}{2}\rho_w g D (l_R - d)^2 \theta_R \\ &F_{RV}(l_R - d) = \frac{1}{3}\rho_w g D d^3 \theta_R + \frac{1}{3}\rho_w g D (l_R - d)^3 \theta_R. \end{aligned} \tag{64}$$

The solutions of the above Eq. (64) are:

$$\begin{aligned} &d = \frac{1}{3} l_R \\ &F_{RV} = \frac{1}{6}\theta_R l_R^2 \rho_w g D \quad \textit{a repetition of} \text{ Eq. (15)}. \end{aligned} \tag{65}$$

It turns out that d is a constant as long as l_R given. This is to say that within the assumed elastic rotation range, the rotation centre is always 2/3 of the length away from the contact point. Moreover, the maximum moment along the beam can be identified at the location where shear

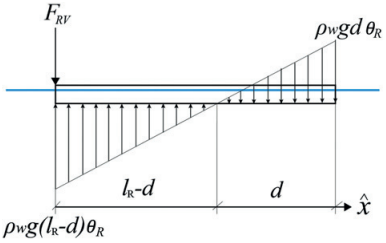

Fig. B.1. Free body diagram of ice rotation in the elastic foundation range (note here that l_R is a general expression for the length of the rotating ice block).

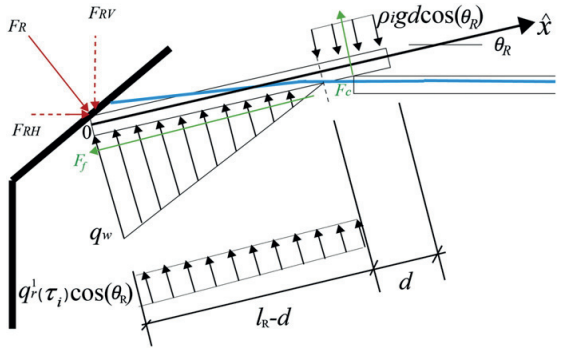

Fig. B.2. Ice rotation module with undetermined contact forces.

force becomes 0. i.e., $\hat{x} = \frac{1}{3}l$ and the corresponding maximum moment can be obtained as:

$$M_{Rotation\_max} = \max(|M(\hat{x})|) = \frac{2}{81}\theta_R \rho_w g l_R^3 D \quad a\ repetition\ of\ Eq.\ (16). \tag{66}$$

B.2. Model development of the ice rotation module in the plastic range

During the rotation of the ice block, it is interesting to identify the driving force to construct the free body diagram. A complete illustration of different force components is illustrated as in Fig. B.2. In comparison to the assumed free body diagram in Fig. 11, there are two additional force components, F_f and F_c, in green coloured arrows. F_f stands for the friction between the rotating ice block and the rolling ice rubble beneath; F_c is the possible contact force between the intact ice sheet and the rotating ice block. Both of these force components are undetermined and further information is needed to back calculate them.

For F_f, the relative motion between the rotating ice block and the rolling rubble beneath is needed. Without such information, it can be any value between 0 and a critical value $F_{f,cr} = \mu_i q_r^1 \cos(\theta_R)$ (i.e., the dynamic friction induced by the rubble pressure). Regarding F_c, depending on if there will be contact or not, it can vary between 0 and a critical value $F_{c,cr}$ limited by the bending failure of the incoming ice sheet. Based on Eq. (63), it can be expressed as in Eq. (67) as a conservative estimation.

$$F_{c,cr} = \frac{F_{BV}\left(q_r^1 = 0\right)}{\cos(\theta_R)}. \tag{67}$$

It is easy to include these two undetermined force components in Eq. (19) to evaluate their respective influences. In this section, a conservative trial simulation is made to justify the assumed free body diagram in Fig. 11. A conservative trial simulation here means that a relatively long ice block is rotating upon a large amount of rubbles without secondary breakings (i.e., $l_R = 10$ m; $h_r^1 = 20$ m; $\mu_i = 0.3$). The results are presented in Fig. B.3.

Fig. B.3 shows that neglecting these two undetermined terms yield relatively conservative results on the ice rotating load. Notably, the influence from the rubble friction force F_f has higher influence on the ice rotating load. Even though, the overestimation (less than 30 kN) takes place at relatively large ice rotation angle. Knowing that most of the peak ice rotating load occurs at small ice rotation angle (e.g., see the ice rotating load trend in Fig. 15), the influence from the neglect of F_f is thus minimal.

Therefore, it can be concluded that neglecting these two undetermined force components in Eq. (19) leads to reasonably conservative estimation of the ice rotation load and the utilisation of Fig. 11 is thus justified.

Appendix C. Numerical scheme for constructing the ice rotating load history with secondary ice breakings

The process of ice rotation with secondary ice breakings can be illustrated in Fig. C.1. The first peak ❶ is due to rotating a relatively large ice block. The load peak drops due to the presence of secondary breakings. After a sudden load decrease (but not dropping until zero), the ice rotating load starts to increase again in ❷ by rotating a newly formed ice block. Then the second newly formed ice block starts to rotate in ❸ and❹. However, this process is rather complex to be casted into simple formulations, especially the transition from ❶ to ❷.

To simplify this process and make it theoretically easy to implement, the process between ❶ to ❷ is 'decoupled' as in Fig. C.2. The continuous process from ❶ to ❹ in Fig. C.1 has been replaced by two independent processes from ① to ② in Fig. C.2. In process ① the initial ice block was rotated until its failure (i.e., secondary ice breakings), the corresponding ice rotating load F_{RV}^0 keeps calculating values with Eqs. (15) and (19) before the secondary ice breakings, after which, its value was set to be zero. In process ②, two independent new ice blocks are rotated from $\theta_1 = 0$ until $\theta_m = \alpha$. The ice rotating load is recorded as F_{RV}^1. The final ice rotating load is assumed to be $\max(F_{RV}^0, F_{RV}^1)$. The eventual ice rotating load curve would appear similar to that in Fig. C.1. The detailed algorithm of the current conceptual description is further explored in the following.

In Section 2.3.2, the length information of a series of broken ice blocks that failed by bending failure is stored in a vector $\boldsymbol{L_B}$. Each element (i.e., the initial broken ice blocks) within $\boldsymbol{L_B}$ is corresponding to a reference time point τ_i and is about to be rotated. The following described procedure should be applied to each element within $\boldsymbol{L_B}$ to obtain the ice rotating load history with the presence of secondary ice breakings. This section supposes that an element $L_{B,i}$ within $\boldsymbol{L_B}$ is under consideration.

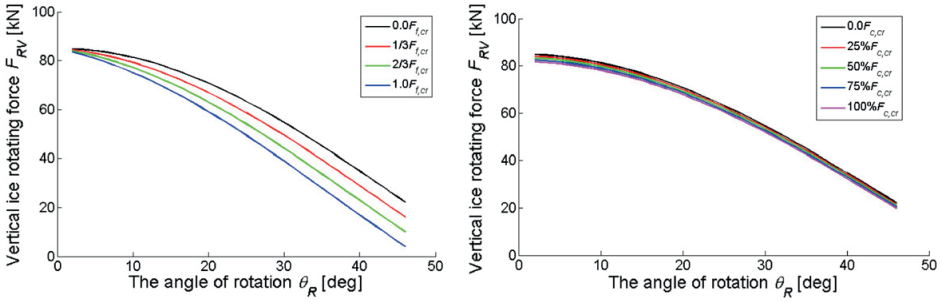

Fig. B.3. Influences of the undetermined force on the ice rotation module.

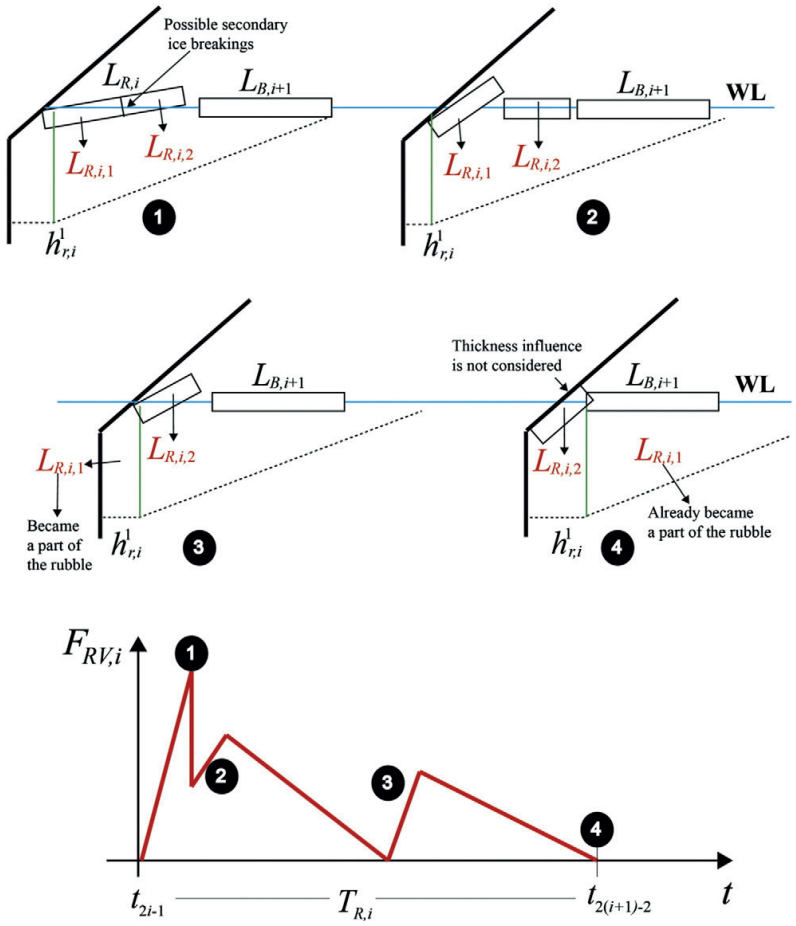

Fig. C.1. Schematic illustration of ice rotation process and ice rotating load with the presence of secondary ice breakings (please refer to Section 2.4.2 for the explanations of different symbols).

Without secondary ice breakings, we simply have $l_R = L_{R,i} = L_{B,i}$. The ice rotation load's temporal distribution has been described in Section 2.4.2. However, if secondary ice breaking takes place, in most cases $l_R \neq L_{R,i} \neq L_{B,i}$. Here we introduce the notation $L^k_{R,i}$ $k = 0, 1, 2, 3, \ldots, N_{\text{secondary}}$ ($N_{\text{secondary}}$ is the number of secondary breakings for each ice block with an initial length of $L^0_{R,i} = L_{B,i}$. Since it has a flavour of spatial distribution, an upper index is assigned to it herein). The algorithms for the calculations are as in the following:

1) For a particular time reference point τ_i, assigning the ice breaking length to the initial ice rotation length $L^0_{R,i} = L_{B,i}$ and denoting $l_R = L^0_{R,i}$;
2) Inserting l_R into Eqs. (15) and (19) to calculate $F^0_{RV,i,j}$, and in the meantime monitoring the flexural stress inside the rotating ice block with Eqs. (16), (20) and (21) to calculate the moment distribution;
3) Once the maximum flexural stress exceeds the ice flexural strength, secondary ice breaking occurs. Numerically, we replace $L^0_{R,i}$ with two new ice blocks $L^1_{R,i} = [L^0_{R,i,1}\ L^0_{R,i,2}]$; correspondingly, the initial ice rotating load is considered as following:

$$F^0_{RV,i,j} = \begin{cases} F^0_{RV,i,j} & \text{before secondary ice breaking} \\ 0 & \text{after secondary ice breaking} \end{cases} \quad \text{For } L^0_{R,i}: 0 \le \theta_j \le \alpha. \tag{68}$$

4) Iterating within the new elements of $L^1_{R,i}$: i.e., assigning firstly $l_R = L^0_{R,i,1}$ and running through the above 2) to 3) to construct the new ice rotating load for the first new ice block $F^1_{RV,i,j}$ (for $L^0_{R,i,1}$: $0 \le \theta_j \le \alpha$); assigning secondly $l_R = L^0_{R,i,2}$ to obtain the second new ice block's rotating load $F^1_{RV,i,j}$ (for $L^0_{R,i,2}$: $0 \le \theta_j \le \alpha$); These two sequential load together composed of the new ice rotating load $F^1_{RV,i,j} = [F^1_{RV,i,j}(for\ L^0_{R,i,1})\ F^1_{RV,i,j}(for\ L^0_{R,i,2})]$ (e.g., see the two dashed triangle curves in Fig. C.2);
5) If Further secondary ice breakings took place for any of the above new ice block $L^0_{R,i,1}$ or $L^0_{R,i,2}$, step 4) is repeated until no further secondary ice breakings take place. This leads to the final ice block length vector for the reference time τ_i as $L^{N_{\text{secondary}}}_{R,i}$, and also the ice rotating load history $F^{N_{\text{secondary}}}_{RV,i}$;
6) Moving to the next reference time station τ_{i+1} and repeat 1) to 6). Eventually, the following ice breaking length vectors $\boldsymbol{L}^{N_{\text{secondary}}}_{\boldsymbol{R}}$ and ice rotating load vectors $\boldsymbol{F}^{N_{\text{secondary}}}_{\boldsymbol{RV}}$ are constructed;
7) As an example, $\boldsymbol{L}^0_{\boldsymbol{R}}$ and $\boldsymbol{L}^1_{\boldsymbol{R}}$ are shown in Fig. 26 (i.e., in this figure, $N_{\text{secondary}} = 1$); The final ice rotating load is constructed as in Eq. (69);

$$\boldsymbol{F}_{\boldsymbol{RV}} = \max\left(\boldsymbol{F}^0_{\boldsymbol{RV}}, \boldsymbol{F}^1_{\boldsymbol{RV}}, \boldsymbol{F}^2_{\boldsymbol{RV}}, \ldots, \boldsymbol{F}^{N_{\text{secondary}}}_{\boldsymbol{RV}}\right). \tag{69}$$

8) Converting $\boldsymbol{F}_{\boldsymbol{RV}}$ into $\boldsymbol{F}_{\boldsymbol{R}}$ according to Eq. (5) leads to Eq. (38);

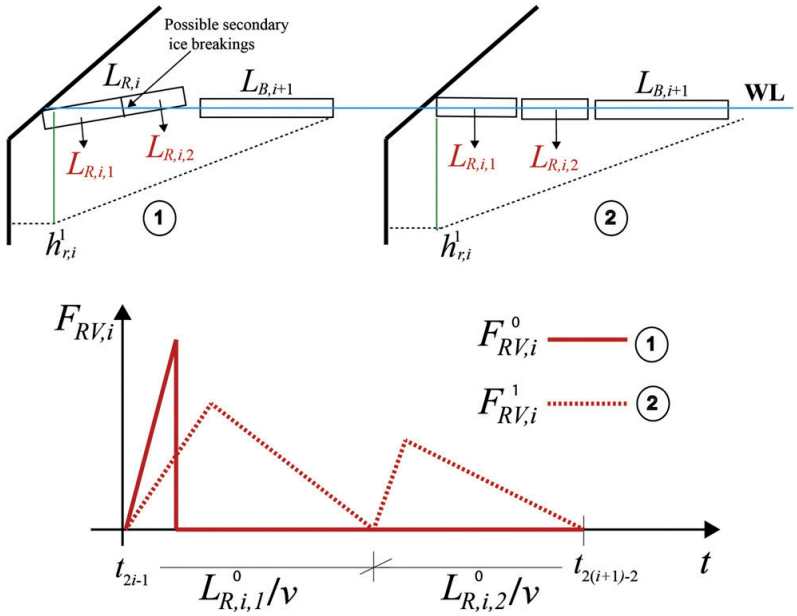

Fig. C.2. Theoretically idealised secondary ice breaking process.

9) The same procedure as described in Section 2.4.2 can be utilised to construct the temporal evolution of the ice rotation load $F_{R\_temporal}$.

References

Aksnes, V., 2011. A panel method for modelling level ice actions on moored ships. Part 1: local ice force formulation. Cold Reg. Sci. Technol. 65 (2), 128–136.

Atkins, A.G., Caddell, R.M., 1974. The laws of similitude and crack propagation. Int. J. Mech. Sci. 16 (8), 541–548.

Bažant, Z., Cedolin, L., 2010. Stability of structures: elastic, inelastic, fracture and damage theories. World Sci., 22–24.

Comfort, G., Singh, S., Dinovitzer, A., 1998. Limit-force ice loads and their significance to offshore structures in the Beaufort Sea. Int. J. Offshore Polar Eng. 8 (1).

Croasdale, K., 2009. Limit force ice loads—an update. Proceedings of the 20th International Conference on Port and Ocean Engineering Under Arctic Conditions Luleå, Sweden, pp. 9–12.

Croasdale, K., 2011. Platform shape and ice interaction: a review. Proceedings of the 21st International Conference on Port and Ocean under Arctic Conditions, Montreal, Canada.

Croasdale, K., 2012. Ice rubbling and ice interaction with offshore facilities. Cold Reg. Sci. Technol. 76–77, 37–43.

Croasdale, K., Cammaert, A., 1994. An improved method for the calculation of ice loads on sloping structures in first-year ice. Power Technol. Eng. formerly Hydrotech. Constr 28 (3), 174–179.

Frederking, R.M.W., Timco, G.W., 1985. Quantitative analysis of ice sheet failure against an inclined plane. J. Energy Resour. Technol. 107 (3) (United States).

Gürtner, A., Konuk, I., Gudmestad, O., Liferov, P., 2008. Innovative ice protection for shallow water drilling: part III—finite element modelling of ice rubble accumulation. Proceedings of the ASME 27th International Conference on Offshore Mechanics and Arctic Engineering. ASME, Estoril, Portugal.

Hetényi, M., 1946. Beams on elastic foundation, 1. University of Michigan Press Ann Arbor. Michigan, USA.

Irgens, F., 2008. Continuum MechanicsSpringer Verlag, Berlin Heidelberg.

ISO/FDIS/19906, 2010. Petroleum and Natural Gas Industries — Arctic Offshore StructuresInternational Standard, International Standardization organization, Geneva, Switzerland.

Izumiyama, K., Wako, D., Uto, S., 1998. Ice force distribution on a flat indentor. In: Shen, T. (Ed.), Proceedings of the 14th International Symposium on Ice, Potsdam, New York, USA.

Izumiyama, K., Wako, D., Uto, S., 1999. Ice force distribution around a ship hull. Proc. of the 15th Int. Conf. on Port and Ocean Eng. Under Arctic Conditions, Espoo, Finland, pp. 707–716.

Kolari, K., Kuutti, J., Kurkela, J., 2009. Fe-simulation of continuous ice failure based on model update technique. Proceedings of the 20th International Conference on Port and Ocean Engineering under Arctic Conditions, Luleå, Sweden.

Kotras, T.V., 1983. Predicting ship performance in level ice. Soc. Nav. Architects Mar. Eng. Trans. 91, 329–349.

Kry, P., 1980. Third Canadian Geotechnical Colloquium: ice forces on wide structures. Can. Geotech. J. 17 (1), 97–113.

Kulyakhtin, S., Høyland, K.V., Astrup, O., Evers, K.-U., 2013. Rubble ice transport on arctic offshore structures (RITAS), Part III: Analysis of model scale rubble ice stability, Proceedings of the 22nd International Conference on Port and Ocean Engineering under Arctic Conditions. Espoo, Finland.

Lau, M., Molgaard, J., Williams, F., ASJ, S., 1999. An analysis of ice breaking pattern and ice piece size around sloping structures. Proceedings of the 18th International Conference on Offshore Mechanics and Arctic Engineering, St. John's, Newfoundland, Canada.

Lau, M., Wang, J., Lee, C., 2007. Review of ice modeling methodology. Proceedings, 19th International Conference on Port and Ocean Engineering under Arctic Conditions, Dalian, China, pp. 350–361.

Lindqvist, G., 1989. A straightforward method for calculation of ice resistance of ships. Proceedings of POAC 1989, pp. 722–735.

Løset, S., Shkhinek, K., Gudmestad, O., Høyland, K., 2006. Actions from Ice on Arctic Offshore and Coastal Structures, Krasnodar, St Petersburg, Russia 137–148.

Lu, W., Løset, S., Lubbad, R., 2012a. Simulating ice-sloping structure interactions with the cohesive element method. International Conference on Ocean, Offshore and Arctic Engineering, Rio de Janeiro, Brazil.

Lu, W., Løset, S., Lubbad, R., 2012b. Ventilation and backfill effect during ice–structure interactions. The 21st IAHR International Symposium on Ice.

Lu, W., Lubbad, R., Løset, S., Høyland, K.V., 2012c. Cohesive zone method based simulations of ice wedge bending: a comparative study of element erosion, CEM, DEM and XFEM. The 21st IAHR International Symposium on Ice.

Lu, W., Lubbad, R., Serré, N., Løset, S., 2013a. A theoretical model investigation of ice and wide sloping structure interactions. Proceedings of the 22nd International Conference on Port and Ocean Engineering Under Arctic Conditions, Espoo, Finland.

Lu, W., Serré, N., Høyland, K.V., Evers, K.-U., 2013b. Rubble Ice transport on Arctic Offshore Structures (RITAS), part IV tactile sensor measurement of the level ice load on inclined plate. Proceedings of the 22nd International Conference Port and Ocean Engineering Under Arctic Conditions, Espoo, Finland, p. 87.

Lubbad, R., Moe, G., Løset, S., 2008. Static and dynamic interaction of floating wedge-shaped ice beams and sloping structures. 19th IAHR International Symposium on Ice, pp. 179–189.

Määttänen, M., Hoikkanen, A., Avis, J., 1996. Ice failure and ice loads on a conical structure-Kemi-1 cone full-scale ice force measurement data analysis. Proceedings of the 13th International Symposium on Ice (IAHR), Beijing, China, pp. 8–17.

Määttänen, M., Hoikkanen, J., 1990. The effect of ice pile-up on the ice force of a conical structure. Proceedings of IAHR Symposium on Ice, Helsinki.

Määttänen, M., Løset, S., Metrikine, A., Evers, K.-U., Hendrikse, H., Lønøy, C., Metrikin, I., Torodd, N., Sergiy, S., 2012. Novel ice induced vibration testing in a large-scale facility: deciphering ice induced vibrations, part 1. 21st IAHR International Symposium on Ice. Dalian University of Technology, Dalian, China, pp. 946–958.

Mayne, D.C., 2007. Level Ice and Rubble Actions on Offshore Conical and Sloping Structures. (Doctoral Thesis) University of Calgary, Calgary, Alberta 190.

Michel, B., 1978. Ice MechanicsLes Presses de l'Universite Laval, Quebec 499.

Naegle, J.N., 1980. Ice-resistance Prediction and Motion Simulation for Ships Operating in the Continuous Mode of IcebreakingThe University of Michigan.
Paavilainen, J., Tuhkuri, J., 2013. Pressure distributions and force chains during simulated ice rubbling against sloped structures. Cold Reg. Sci. Technol. 85, 157–174.
Paavilainen, J., Tuhkuri, J., Polojärvi, A., 2009. 2D combined finite–discrete element method to model multi-fracture of beam structures. Eng. Comput. 26 (6), 578–598.
Paavilainen, J., Tuhkuri, J., Polojarvi, A., 2010. Rubble pile formation against an inclined structure analysis of simulation results. IAHR International Symposium on Ice.
Paavilainen, J., Tuhkuri, J., Polojärvi, A., 2011. 2D numerical simulations of ice rubble formation process against an inclined structure. Cold Regions Science and Technology 68 (1–2), 20–34.
Palmer, A., Croasdale, K., 2013. Arctic Offshore EngineeringWorld Scientific, New Jersey (London. Singapore. Beijing. Shanghai. Hongkong. Taipei. Chennai).
Palmer, A., Dempsey, J., 2009. Model tests in ice. Proceedings, Twentieth International Conference on Port and Ocean Engineering Under Arctic Conditions, Luleå.
Peters, J., Muthuswamy, M., Wibowo, J., Tordesillas, A., 2005. Characterization of force chains in granular material. Phys. Rev. E 72 (4), 041307.
Radjai, F., Wolf, D.E., Jean, M., Moreau, J.-J., 1998. Bimodal character of stress transmission in granular packings. Phys. Rev. Lett. 80 (1), 61–64.
Ralston, T., 1980. Plastic limit analysis of sheet ice loads on conical structures. Physics and Mechanics of IceSpringer-Verlag, New York, USA 289–308.
Ralston, T., 1981. Plastic limit analysis of ice splitting failure. Proc. 6th POAC, Quebec. , 1, pp. 205–215.
Sanderson, T.J.O., 1988. Ice Mechanics and Risks to Offshore Structures.
Schwarz, J., 1977. New developments in modeling ice problems. Proc. 4th International Conference on Port and Ocean Engineering Under Arctic Conditions, pp. 45–61.
Schwarz, J., Frederking, R., Gavrillo, V., Petrov, I., Hirayama, K.I., Mellor, M., Tryde, P., Vaudrey, K., 1981. Standardized testing methods for measuring mechanical properties of ice. Cold Regions Science and Technology 4 (3), 245–253.
Serré, N., Høyland, K.V., Lundamo, T., Bonnemaire, B., Evers, K.-U., Gürtner, A., 2013a. Rubble Ice transport on Arctic Offshore Structures (RITAS), part I: scale-model investigations of level ice action mechanisms. Proceedings of the 22nd International Conference on Port and Ocean Engineering under Arctic Conditions, Espoo, Finland.
Serré, N., Lu, W., Høyland, K.V., Bonnemaire, B., Borge, J., Evers, K.-U., 2013b. Rubble Ice Transport on Arctic Offshore Structures (RITAS), part II: 2D scale-model study of the level ice action. Proceedings of the 22nd International Conference on Port and Ocean Engineering Under Arctic Conditions, Espoo, Finland.
Sodhi, D.S., 2001. Crushing failure during ice–structure interaction. Eng. Fract. Mech. 68 (17–18), 1889–1921.
Sodhi, D.S., Takeuchi, T., Nakazawa, N., Akagawa, S., Saeki, H., 1998. Medium-scale indentation tests on sea ice at various speeds. Cold Reg. Sci. Technol. 28 (3), 161–182.
Sukhorukov, S., Maattanen, M., Løset, S., 2012. Field Experiments on the Friction Coefficient of Sea Ice on Sea Ice. In: Lu, L.a. (Editor), 21st IAHR International Symposium on Ice. Dalian University of Technology, Dalian, China.
Tekscan, I., 2003. I-can Equilibration and Calibration Practical SuggestionsTekscan, Inc, South Boston, MA.
Timco, G., 1984. Ice forces on structures: physical modelling techniques. Proceedings of the 7th IAHR Symposium on Ice, Hamburg, pp. 27–31.
Timco, G., 1991. The vertical pressure distribution on structures subjected to rubble forming ice. 11th International Conference on Port and Ocean Engineering Under Arctic Conditions, St. John's, Canada, pp. 185–197.
Timco, G., Croasdale, K., Wright, B., 2000. An Overview of First-year Sea Ice RidgesCanadian Hydraulics Centre.
Valanto, P., 2001. The resistance of ships in level ice. Soc. Nav. Architects Mar. Eng. 109, 53–83.
Yue, Q., Qu, Y., Bi, X., Tuomo, K., 2007. Ice force spectrum on narrow conical structures. Cold Reg. Sci. Technol. 49 (2), 161–169.

Appendix 5 Explorations into the Cohesive Element Method

This appendix includes the paper published in Journal Offshore Mechanics and Arctic Engineering (see below).

- Lu, W., Lubbad, R. and Løset, S., 2014. Simulating Ice - sloping Structure Interactions With the Cohesive Element Method. Journal of Offshore Mechanics and Arctic Engineering, 136(3): 031501-031501.

Appendix V

Is not included due to copyright

Appendix 6 Ice load measurement by tactile sensor

This appendix includes the conference paper published in the Proceedings of the 22nd International Conference on Port and Ocean Engineering under Arctic Conditions (see below).

- Lu, W., Serré, N., Høyland, K.V. and Evers, K.-U., 2013. Rubble Ice transport on Arctic Offshore Structures (RITAS), part IV Tactile sensor measurement of the level ice load on inclined plate, Proceedings of the 22nd International Conference Port and Ocean Engineering under Arctic Conditions, Espoo, Finland.

Appendix VI

POAC'13
Espoo, Finland

Proceedings of the 22nd International Conference on
Port and Ocean Engineering under Arctic Conditions
June 9-13, 2013
Espoo, Finland

Rubble Ice Transport on Arctic Offshore Structures (RITAS), part IV: Tactile sensor measurement of the level ice load on inclined plate

Wenjun Lu[1], Nicolas Serre[2], Knut Høyland[1] and Karl-Ulrich Evers[3]

[1)]*SAMCoT, NTNU, Trondheim, Norway*

[2)]*Multiconsult, Tromsø, Norway*

[3)]*Hamburg Ship Model Basin (HSVA), Hamburg, Germany*

wenjun.lu@ntnu.no

ABSTRACT

When level ice interacts with downward wide sloping structures, the incoming level ice usually fails in bending failure mode. As the failed rubble accumulates, the bending process is influenced by the rubble beneath. An experimental investigation of the effect from the volume-growing rubble field in front of a sloping structure is described in the present paper. It is completed by 3 associated papers: "*Rubble Ice Transport on Arctic Offshore Structures (RITAS), part I: Model scale investigation of level ice action mechanisms"*, "*Part II: 2D model scale study of the level ice action*", and "*part III: Analysis of model scale rubble ice stability*". The present paper describes an experiment where we have mounted a tactile sensor on the sloping surface of a structure measuring the ice pressure's spatial and temporal variation. As oppose to the ice load measured at the waterline, it is found out that equally large ice load was also detected below waterline region. This is postulated due to the contribution from the ice rotating process. Especially, as the accumulated rubble's volume grows, the load induced by the ice rotating process and static rubble pressure increase significantly and eventually changes the ice bending process.

Introduction

Wide sloping structures have many applications in the ice infested waters. Due to the relatively limited ice clearing capability of a wide sloping structure, the presence of rubble greatly influences the whole interaction mechanism (Serré et al., 2013a). The significance of the rubble accumulation has been investigated in the current test set-up as a preparation for a new theoretical model. The current paper focuses on the test set-up and results. Its layouts are as in the following: First, the test set-up and test matrix are briefly introduced. Additional information is given in (Serré et al., 2013a). Following this, the installation and calibration of the tactile sensor are presented into detail. Then the ice load's spatial and temporal variations during ice structure interaction and rubble accumulation are presented. Lastly, based on the discussion made on the measured data, the interaction mechanisms are discussed and important findings are concluded.

Test set-up

The physical tests are conducted in the ice tank at the Hamburg Ship Model Basin (HSVA). The geometry of the test set-up and the location where the tactile sensor is mounted are shown in Figure 1. During the tests, the Tekscan sensor #5513 was utilized. It has an operating temperature ranging from -9 ^{o}C to 60 ^{o}C; the pressure measuring range was claimed to be within 0 to 175 MPa. All these specifications are compatible with the current application. Most importantly, this sensor has a rather long tail. This ensures that the handle which connects the tail to the computer can be positioned far away from the water.

The tactile sensor is mounted in the center of the sloping plate. Due to limited size of the sensor, the plate is only partially covered, as shown in Figure 1 (c). The sensor was positioned in the upper middle part of the sloping plate. It is positioned in such a way that 1/3 of the measuring area is above the waterline while the remaining 2/3 of the measuring area is below the waterline. The tactile sensor is composed of 44×55 sensels which are used to measure the local load and averaged into each small sensel as pressure. The ice load's spatial resolution is determined by the size of each sensel as shown in Figure 1 (c). Temporally, the sensor is scanning at a frequency of 10 Hz during each experiment. There are two reasons for using this scanning frequency. For one reason, the interaction speed is usually very low. The main focus of this research is the bending failure of ice and also the rubble accumulation load. Both of them are of rather low frequency in comparison to the continuous crushing process. Therefore a 10 Hz scanning frequency is considered enough to capture the concerned load information; for another reason, utilization of such a lowered frequency is mainly to ensure that the storage capacity during each measurements campaign.

Test matrix

There are in total 5 ice sheets prepared and the box is pushed within each ice sheet with different speeds. The test matrix is shown in Table 1 together with the ice properties in model scale.

Tactile sensor installation

As recommended in the manual (Tekscan, 2011), during the installation, great attention has been paid to make sure the tactile sensor is waterproof and protected from ice abrasion during the test.

With respect to the waterproof issue, similar as previous experimental practices (Määttänen et al., 2012), the tactile sensor is protected by two waterproof layers (plastic film) adhered by

silicone gel. However, during the experiment, a small amount of water eventually entered into the plastic film bag and had contact with the sensor. After each test, the sloping plate is dismantled, cleaned with fresh water and dried under room temperature.

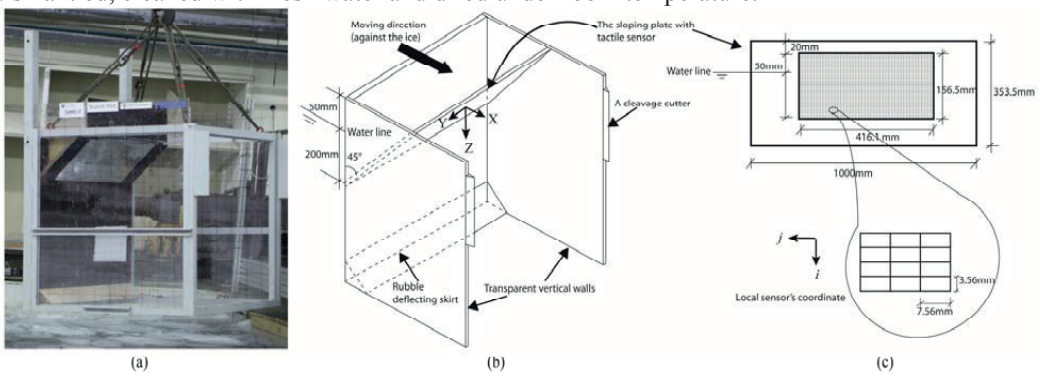

Figure 1 (a) The buoyancy box (b) The schematic drawing of the test set-up with geometry (N.B, drawing not in scale) (c) The tactile sensor.

Table 1 The test matrix

Test series	flexural strength	Ice thickness	Young's Modulus	Speed	Travelling distance
1210	53 kPa	0.043 m	61 MPa	0.045 m/s	10 m
2210	58.2 kPa	0.043 m	53 MPa	0.2 m/s	20 m
3210	54.6 kPa	0.047 m	88 MPa	0.045 m/s	10 m
3211	54.6 kPa	0.047 m	88 MPa	0.2 m/s	10 m
3212	54.6 kPa	0.047 m	88 MPa	0.045 m/s	10 m
4210	45.7 kPa	0.061 m	103 MPa	0.02 m/s	10 m
4211	45.7 kPa	0.061 m	103 MPa	0.2 m/s	10 m
4212	45.7 kPa	0.061 m	103 MPa	0.045 m/s	10 m
5210	47.1 kPa	0.041 m	31 MPa	0.045 m/s	10 m

Table 2 Validation of the tactile sensor with known weights before each test

	Validation weight [kg]	Measured weight [N]	Error
Test 2210	25	260	4%
	25	280	12%
	25	272	8%
Test 321x (x=0,1,2)	20	198-200	1%
	25	265	4%
	10	105	5%
Test 421x (x=0,1,2) and 5210	5	54	8%
	10	100	0%
	15	142	5%
	20	222	11%

Before each test, the tactile sensor is again validated against several known weights so as to confirm its functionality (the detailed procedures and methods are introduced in the next

section). In all the validations, the errors between the measured results and the known weights were all within 15% as shown in Table 2. In terms of the ice abrasion protection, a thin adhesive metallic foil was selected. This metallic foil is 0.15 mm thick and its strength was tested by crushing several cold fresh water ice blocks onto it without causing visual damage.

In conclusion, the installation of the tactile sensor on the sloping plate includes the following important steps corresponding to Figure 2:

(1) The sensor was first put in between two plastic films adhered by silicone gel so as to make it waterproof.

(2) The metallic adhesive layer was applied above the sensor serving as the abrasion protection.

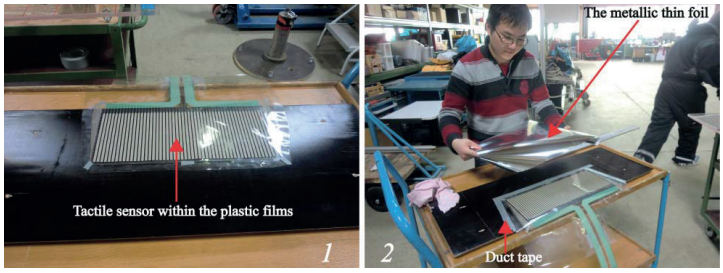

Figure 2 Installation of the tactile sensor on the sloping plate.

Tactile sensor calibration

After the installation of the tactile sensor, a 2 point method was utilized to calibrate the tactile sensor with different sensitivities (Tekscan, 2003). The calibrations and also the above mentioned validations were all conducted in the cold room with temperature around 0 ^{o}C which is rather close to the ice temperature (e.g. -0.6 ~ -0.8 ^{o}C). During the calibration/validation[1], a rubber pad (150 mm × 100 mm × 5 mm, with negligible weight) was utilized to transfer the deadweight to the tactile sensor. This rubber pad usually is randomly placed within the tactile sensor to make a location-blind calibration/validation. Due to the surface roughness both on the rubber pad, on the deadweight, and also on the wooden plate onto which the tactile sensor was attached, the contact area varies slightly in each calibration/validation. It is worth noting here that since the equilibrator with which to eliminate the tactile sensor measurement's spatial errors was unavailable, no further effort was made to confirm the tactile sensor's accuracies in spatial measurement in all the calibrations/validations. It was simply assumed here that the measured load's spatial variation is trustworthy.

The outputs of the ice pressure contour are illustrated by different color bands. A proper saturation pressure is such that the ice pressure contour covers as much color band as possible (see Figure 3 (c)) without exceeding the measuring range (e.g. Figure 3 (a) and Figure 3 (b)). However, in the current test, the interest lies in the local ice pressure for the bending failure mode of ice sheets. Previous applications of tactile sensor in ice load measurements were mainly conducted in ice crushing scenarios (Määttänen et al., 2012; Sodhi, 2001; Sodhi et al.,

[1] This section is dedicated to the calibration method of the tactile sensor used in this test. However, its procedure and methods share several commons with the previously mentioned validation of the tactile sensor (see Table 2). They are introduced here together with the expression 'calibration/validation' if they share a common feature.

1998). The potential local ice pressure in the current test setting is therefore not known a priori. Accordingly, several rounds of trial and errors were made to make sure the chosen sensitivity and saturation pressure can properly yield a 'colorful' output of the ice load pressures as shown in a sample ice pressure outputs in Figure 3 (d)). Eventually, a much lower saturation pressure is adopted in the current test comparing to previous applications as shown in Table 3.

However, it is worth noting that the tactile sensor does not have the same accuracy in all the pressure range (Tekscan, 2003). This can also be seen from the validation measurements shown in Table 2. This nonlinear nature has been discussed in (Izumiyama et al., 1999). Due to the complexity of ice and structure interactions, the ice pressure covers a very wide range of possible values. In the current tests, based on the chosen sensitivity and saturation pressure, the tactile sensor tends to capture the ice pressure that repeats most often, saying the pressure that would be around the mean ice pressure. However, for extreme values, the sensor is prone to underestimate the extreme values. It is not possible now to quantify how much the extreme values have been underestimated. Even though, the merits of using tactile sensor in the current test should not be degraded. The tactile sensor will anyhow output the contact area (i.e. the load's spatial variation) and comparative pressure irrespective of possible errors within its measured maximum values.

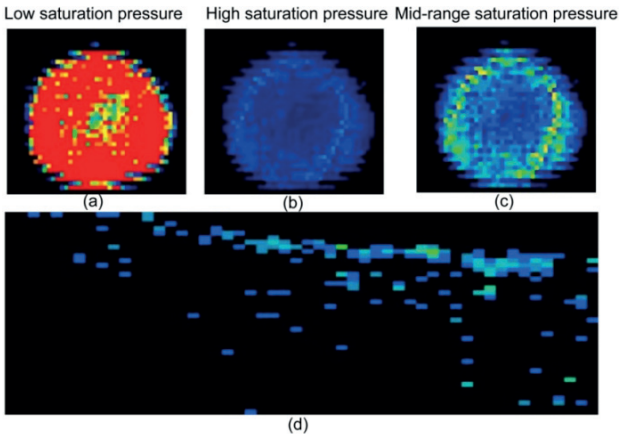

Figure 3 Measurements with different saturations (a),(b)and (c); and a sample of current ice pressure measurements(d). (figures (a),(b) and (c) are from user's manual of Tekscan (2003)).

Table 3 Sensitivity and saturation pressure of the tactile sensor

	Saturation pressure	Sensitivity	Application
(Sodhi et al., 1998)	6.86 MPa	unknown	sea ice crushing failure (full scale)
(Määttänen et al., 2012)	1.6 Mpa 4.5 Mpa	30 23	Salty ice crushing failure (not scaled)
(Kim, 2012)	20 Mpa 6 Mpa 8-10 Mpa	13 13 13	Fresh water ice crushing failure (model scale)
Current test	125 kPa	40	Salty ice bending failure (model scale)

Experimental observation

The visual observations are introduced here as a preparation for future discussion. The general interaction procedure can be illustrated as in Figure 4 (a), (b) and (c). Initially the incoming ice fails in bending against the downward sloping plate (see Figure 4 (a)). Afterwards, this broken ice piece is further rotated downwards (Figure 4 (b)). This ice rotating process is further illustrated in Figure 4 (d) from a side view. It can be seen that there leaves a gap between the sloping plate and the incoming ice. This rotating ice is supposed to transfer the ice load downwards lower than the waterline. As the interaction proceeds, more ice rubbles accumulate beneath the incoming ice (see Figure 4 (e)). The rubble accumulation's track is illustrated by the arrows in Figure 4 (e). This volume-growing ice rubble tends to shift the failing mechanism of the incoming ice sheet from 'bending downwards by the structure' to 'bending upwards by the accumulated rubbles' as shown in Figure 4 (c).

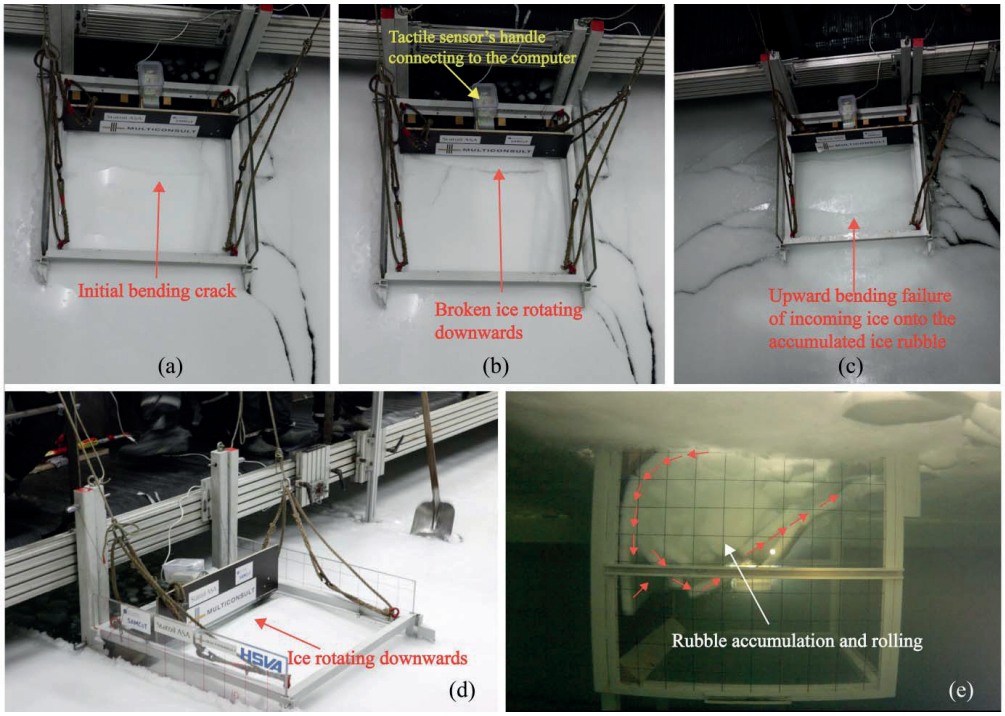

Figure 4 (a), (b) and (c) the interaction procedures; (d) the ice rotating side view; (e) the rubble accumulation.

Experimental results

An example of the measured local normal pressure is shown in Figure 5 (different colors represent different pressure magnitude). This measurement illustrates one circle of the ice load development (i.e. ice breaks at the waterline and slides downwards afterwards). It takes approximately 3 seconds for such cycle to develop in Test 1210. It can be seen that the pressures are not uniform in the lateral Y direction, meaning that non-uniform contact is taking place[2]. Furthermore, after the initial breaking of the incoming ice, the local pressure

[2] Since this is just a random case illustrating the visualization of the ice load development, dissimilar trend in comparison to Figure 6 is possible.

did not diminish instantly. Instead, the pressure keeps travelling down at a relatively smaller yet comparable magnitude.

All these recorded normal pressures are later multiplied with the sensel's area and projected in the horizontal direction (opposite of X direction). They were stored as a third order tensor **M** with components $M_{ijk.}$ Here i and j represent the row and column numbers of the tactile sensor's sensel. And k is the number of scans, representing the recording time.

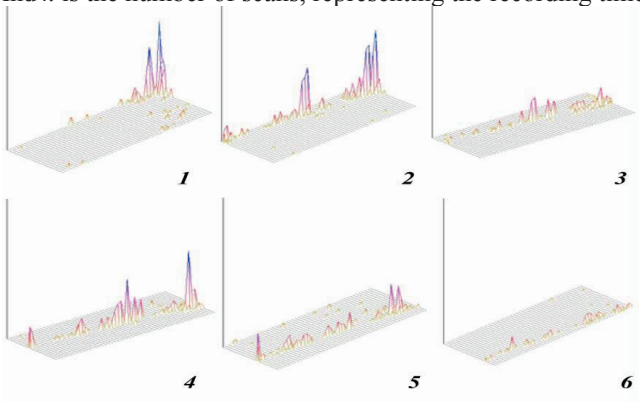

Figure 5 A real time display of the pressure evolution.

Measurements of ice load's spatial variation

It is firstly decided to show how the load varies in the lateral direction (Y or j direction). Therefore, M_{ijk} is processed as in the following:

$$\bar{H}_j = \frac{1}{n_k}\sum_{k=1}^{n_k}[\frac{1}{n_i}(\sum_{i=1}^{n_i} M_{ijk})] \qquad [\,1\,]$$

$$H_{j,max} = \max_{1\le k\le n_k}[\frac{1}{n_i}(\sum_{i=1}^{n_i} M_{ijk})] \qquad [\,2\,]$$

In the previous two equations [1] and [2], the recorded value M_{ijk} is first averaged in the vertical i direction, and then the corresponding time domain (i.e. k direction) averaged lateral load distribution $\bar{H}_j$ and maximum value $H_{j,max}$ are obtained as shown in Figure 6.

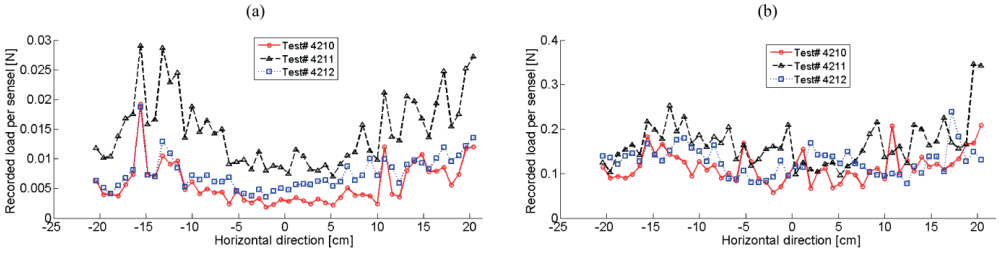

Figure 6 (a) Mean ice load (in time history) and (b) Max ice load (in time history) in the lateral directions of the sensor.

Then the load variation in the vertical direction is investigated with the following equation

$$\bar{V}_j = \frac{1}{n_k}\sum_{k=1}^{n_k}\left(\sum_{j=1}^{n_j} M_{ijk}\right) \qquad [3]$$

$$V_{j,max} = \max_{1\le k\le n_k}\left[\left(\sum_{j=1}^{n_j} M_{ijk}\right)\right] \qquad [4]$$

The comparison of $\bar{V}_j$ and $V_{j,max}$ in different location Z (the distance from the upper side of the tactile sensor) for test 1210 are shown in Figure 7's left column and right column respectively. Together shown in the figure is also the location of the un-deformed level ice. The results in other tests show similar variation trend in the vertical direction (Lu et al., 2013a).

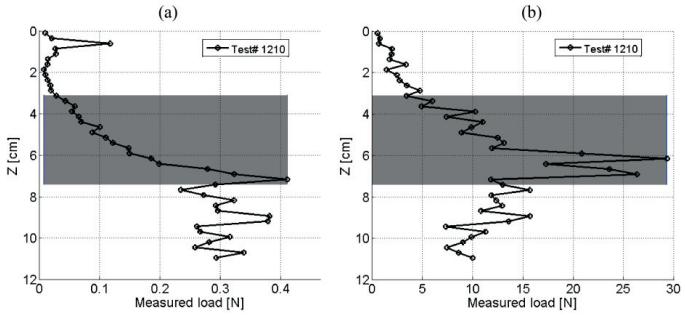

Figure 7 (a) The mean ice load (in time history) and (b) the maximum ice load (in time history) variation in the vertical direction of the sensor (the shaded area is the location of the un-deformed level ice).

Discussions about ice load's spatial variation

It can be seen from the Figure 6 that in the lateral direction, comparing to the maximum load, the mean load varies significantly in different lateral locations. The recorded mean loads are always larger in both lateral sides of the sloping plate (i.e. lateral location around -15.0 cm and 15.0 cm) than in the middle (i.e. lateral location around 0.0 cm). There might be two explanations to such uneven lateral mean load distribution. First, this is due to the non-uniform contact between the incoming level ice and the sloping plate (also can be seen in Figure 5); Secondly, this is due to the tactile sensor's measuring error under the possibilities that the tactile sensor does not have the same sensitivity in all its sensels. The equilibration procedure (Tekscan, 2003) to ensure all the sensels having the same sensitivity was not conducted in the current test due to the lack of equipment. However, the user's manual claims that there exists only slight variations within individual sensels (Tekscan, 2011).

Between the above mentioned two explanations, the authors are prone to adopt the first non-uniform contact explanation for the following three reasons. Firstly, non-uniform contact is taking place throughout the whole experiment as shown by the measurements in Figure 4 (a), (b), and Figure 5. Secondly, in the lateral direction, during the bending process, the incoming ice suffers more boundary confinement on both lateral sides. This can lead to more frequent larger bending force on both lateral sides than in the middle. Though it might be argued that the sensor covers only a small portion of the inclined plate situating in the centre; therefore the boundary effects are negligibly influencing the shoulders of the sensor. However, as can be seen from Figure 4 (a) and (b), the boundary effects really leads to additional 'radial' cracks which locate rather close to the centre. This illustrates how much the boundary effects can propagate inward and eventually influence the ice bending load. Thirdly, if there are large

differences in the sensitivity of sensels in the lateral direction, both the maximum and mean load should be amplified at the same sensitive locations. On the contrary here, the maximum recorded load shows less lateral location variation as shown in the lower figure of Figure 6. This helps to exclude the existence of large difference in the sensels' sensitivity.

Based on the above discussion, in order to quantify the influence of the non-uniform contact, a variation factor is defined here as:

$$k_v = \frac{\sigma}{\mu} \qquad [5]$$

σ is the standard deviation of the measurements of $\overline{H}_j$ or $H_{j,max}$

μ is the mean value of $\overline{H}_j$ or $H_{j,max}$

Perfectly even contact and uniform breaking of homogeneous ice would yield $k_v = 0$. However, the presence of non-uniform contact in all the experiments leads to the value of k_v as shown in Table 4.

Table 4 Variation factor of different test series

Test series	k_v of $\overline{H}_j$	k_v of $H_{j,max}$
1210	0.54	0.42
2210	0.45	0.31
3210	0.65	0.39
3211	0.35	0.25
3212	0.37	0.30
4210	0.60	0.29
4211	0.40	0.31
4212	0.39	0.25
5210	0.53	0.34

It can be seen from Table 4 that non-uniform contact takes place for all experiments. And as discussed before, the maximum values are not as much influenced by non-uniform breaking as those of mean values.

With respect to the ice load's vertical direction variations, both elastic foundation beam and plate theory suggest that the tip deflection at flexural failure (see Figure 4 (a)) is minimal comparing to the thickness of the ice. Therefore, it would be reasonable to assume the ice breaking load (i.e. the load required to bend the incoming intact ice) is within the un-deformed level ice's thickness region (i.e. the shaded area in Figure 7). Note that inside this region, other interaction mechanisms such as the initial ice rotating and rubble effect also exit (Lu et al., 2013a).

It is observed in Figure 7 (b) that the maximum load of $V_{j,max}$ are mainly found within such shaded area. This agrees with our common sense and previous research assumptions that the ice breaking load is one of the decisive components of the ice load. However, as it is shown in the theoretical model (Lu et al., 2013a; Lu et al., 2013b), the ice rotating load would also become decisive when there is sufficient rubble accumulated in front of the structure. For the time being, it can be simply concluded that based on the tactile sensor's measurement, the maximum load often takes place around the un-deformed level ice's thickness region. This is

in agreement with the measurements conducted by Timco (1991) with a similar test set-up within broken ice field. The numerical simulation conducted by Paavilainen and Tuhkuri (2013) also detected the maximum ice load slightly below the waterline for gentle sloping angles.

On the other hand, it is shown in Figure 7 (a) that, the mean load $\bar{V}_j$ usually keeps increasing, or at least stays in a same level, even after passing the shaded area. This is to say, some other equally profound interaction mechanisms other than ice breaking process are taking place below the shaded area. If categorizing the ice sloping structure interaction process as those in ice ship interactions (Kotras, 1983; Lindqvist, 1989; Valanto, 2001), it is speculated that the ice rotating load (i.e. the load required to rotate the already broken ice rubble paralleling to the sloping surface) is the reason for such undiminishing mean load on the sensor below the shaded area. This ice rotating load is introduced by the ice rotating process as shown in Figure 4 (b) and (d). Additional ice load is needed to rotate the already broken ice downwards. This rotating process further transferred the ice load beneath the shaded area (i.e. the un-deformed level ice thickness region) in Figure 7.

Results of ice load's temporal variation

The measured local ice load is summed in both *i* and *j* directions as in equation [6] and displayed in Figure 8. The whole loading histories of all tests presents a cyclic pattern. In order to identify the ice load's temporal variation, the loading history (i.e. ice penetration) is sectionalized by the ice breaking length L_B (see equation [7]). This ice breaking length can be determined by the static solutions of an elastic-foundation beam. Afterwards the mean load and maximum load measured inside each of such section is calculated so as to identify the ice load's temporal evolution (e.g. as illustrated in Figure 8 (a)).

$$F_{k,total} = \sum_{i=1}^{n_i} \sum_{j=1}^{n_j} M_{ijk} \qquad [6]$$

$$L_B = \frac{\sqrt{2}\pi}{4} \sqrt[4]{\frac{EI}{\rho_w g D}} \qquad [7]$$

L_B	Ice breaking length that is predicted by the static solution of beam on elastic foundations
E	Young's modulus of the ice
I	Area moment of the beam's cross sectional area
ρ_w	Water density
g	Gravitational acceleration
D	is the width of the beam, taken as 1 here

The mean value and maximum value of each section in the ice penetration domain is separated and illustrated in Figure 9.

The temporal evolution trend of the mean ice load is shown in Figure 9 (a). The general trend of the mean load is increasing from an initially very small load to remaining at a certain higher load level. The mean load may decrease during the interaction, but it can travel back to its previously maintained level immediately. However, for the maximum load in each section, as shown in Figure 9 (b), apart from an initially increasing trend, some decrease of maximum load are also frequently observed. Especially for test 2210 where the 'box' has been pushed through an exceptionally longer distance (20 metres) comparing to all the other experiments

(10 metres), the maximum load increases before the first 20 times the ice breaking length, and then starts to decrease gradually.

Discussions about ice load's temporal variation

As the ice penetration length increases, greater amount of rubble is accumulated in front of the structure (Serré et al., 2013b). Therefore higher ice rotating load and rubble buoyancy would be applied onto the sloping surface. This might be the reason that the mean load is increasing gradually from an initially smaller load value. On the other hand, quite often the maximum load is related to the ice breaking load, which also increases with the rubble accumulation (Lu et al., 2013b). However, when there is sufficient amount of rubble accumulated in front of the structure, the incoming level ice will fail against the piled rubble instead of onto the structure (see Figure 4 (c)). This will bring a decrease on the ice breaking load and hence the recorded maximum load might start to decrease when the ice penetration reaches certain values as shown in Figure 9 (b).

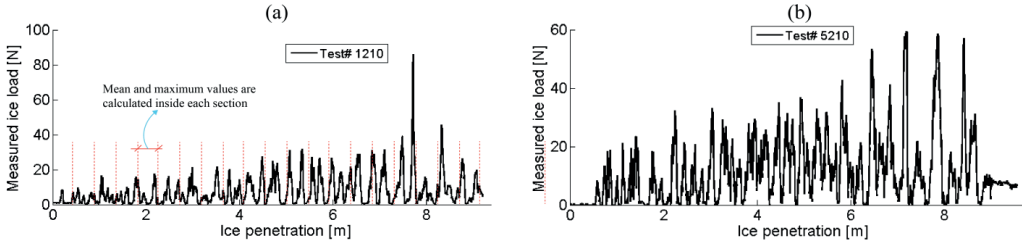

Figure 8 Total measured loading history on the tactile sensor in (a) test1210 and (b) test 5210

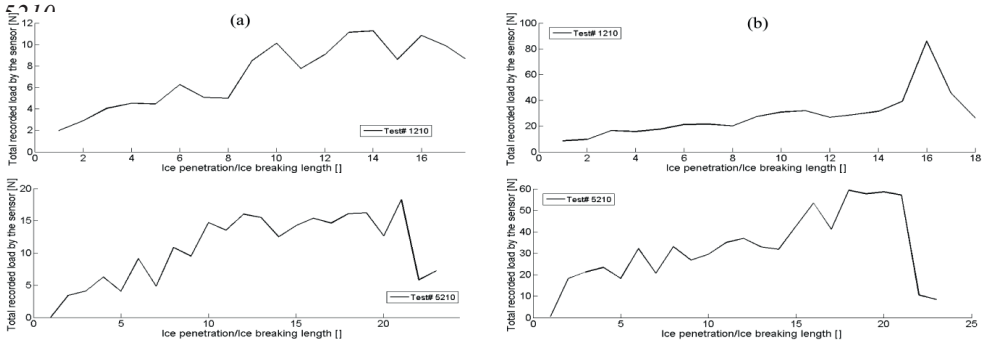

Figure 9 (a) Mean load (left column) and (b) maximum load (right column) of each section in the ice penetration domain.

The above discussion is based on the mean and maximum values within each section of the total ice load history. And the size of each section is chosen as the ice breaking length L_B. The reason that this calculated ice breaking length is chosen as the basis value for separating the ice penetration domain is due to the assumption that a complete interaction procedure can be capsulated in the structure's travelling distance of an ice breaking length. This is to say, as the structure penetrated into the ice for the distance of one ice breaking length, the process of breaking the ice and rotating the broken ice would be complete. In reality the ice breaking length is much smaller than the static prediction of an elastic-foundation beam. A theoretical study in (Lu et al., 2013a) shows that the actual ice breaking length is approximately 1/3 of the static prediction made in Equation [7]. The selected bin length as L_B therefore ensures more than one loading events taking place in each separated section. Choosing a smaller section length would lead to more load history variation in the ice penetration domain and

hence the comparisons become less illustrative. Although the above observation and explanation are rather qualitative, it can help to understand the interaction mechanisms.

Ice load's spatial and temporal variation

In the previous two sections, the measured ice load's spatial and temporal variations were presented and discussed separately. In this section, both the spatial and temporal variation will be presented in a similar fashion. Spatially, the vertical (Z or *i*) direction variation of the load will be accounted for. In the vertical direction, a total of 44 measured values are available in each scan. However, for illustrating purpose, these 44 values are averaged into 11 bins representing the load variation in the vertical direction. Temporally, similarly as in the previous section, the ice penetration history is separated into sections with the length of an ice breaking length L_B. The mean ice loads in different vertical locations were calculated within each section. Thereafter, the spatial and temporal variations of ice load are condensed in the following Figure 10 for test 1210 and test 5210 as an example.

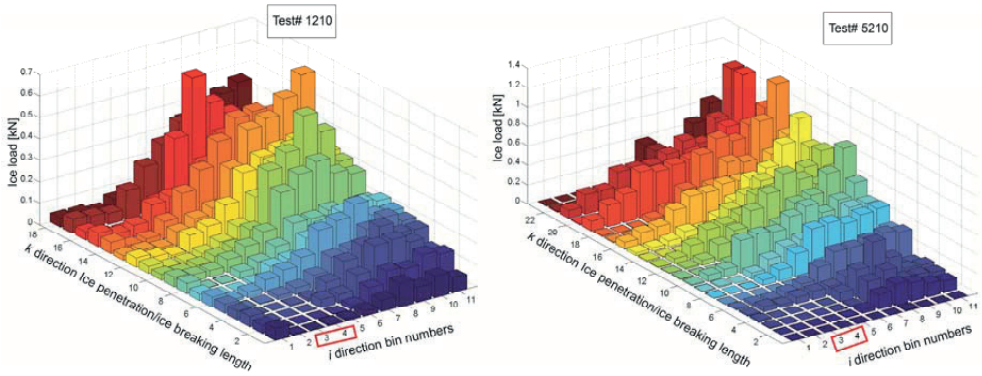

Figure 10 Vertically spatial and temporal distribution of ice load (bins 3 and 4 in the red square is appoximately where the undeformed level ice is).

It can be seen from Figure 10 that generally most of the recorded loads in the vertical *i* direction increase with the ice penetration in *k* direction. This signifies the importance of rubble accumulation. Moreover, below the un-deformed level ice's thickness region (i.e. below bin number 3 and 4 in the *i* direction), the recorded ice load also increases with time and may become even more significant than the process that occur at the un-deformed level ice's thickness region. This further strengthens the point made in the previous section that the accumulated rubble together with the ice rotating process intensifies the ice load under the un-deformed level ice's thickness region.

Conclusion

In this paper, experiments are described to explore the mechanism of level ice interacting with wide sloping structures. In the tests, the tactile sensor has been utilized to measure the spatial and temporal variation of ice load.

Based on the measured load's spatial and temporal analysis, the following conclusion can be made.

- During the interaction, after the breaking of an initially intact ice, the recorded ice load does not diminish instantly. Instead, the ice moves down continuously with a relatively lower load magnitude. This is considered due to the effect of ice rotating load in combination of the accumulated rubble effects;

- Non-uniform contact during ice and wide sloping structure interactions are a rule rather than an exception. This is speculated mainly due to the boundary effects from the confining vertical wall. In reality, the boundary condition may be more complicated and non-stationary (i.e. different boundary conditions in different time). Therefore, different from the current tests where the large loads were deterministically determined at the same place (i.e. both sides in the lateral direction), in reality, the non-uniform lateral load might be randomly non-uniform;
- Based on the mean ice load's (i.e. averaged in time) vertical variation, it is found out that equally large ice load can be detected beneath the un-deformed level ice's thickness region. As discussed above, the contribution of this large ice load is mainly due to the combined effects of ice rotating load and the rubble accumulation;
- Generally the recorded maximum load acts at the un-deformed level ice's thickness region. The ice breaking occurs mainly at the waterline region. This is in line with previous experiments and assumptions that the ice breaking load is one of the decisive loads during design. However, it should bear in mind that that such maximum load detected at the un-deformed may not 100% due to the ice breaking load.

Acknowledgement

The authors would like to acknowledge the Norwegian Research Council through the project 200618/S60-PetroRisk and the SAMCoT CRI for financial support and all the SAMCoT partners. The work described in this publication was supported by the European Community's 7th Framework Programme through the grant to the budget of the Integrated Infrastructure Initiative HYDRALAB-IV, Contract no. 261520. The financial support from Statoil AS and the experimetenal designs of MultiConsult are also greatly acknolwedged. The authors would like to thank Dr. Basile Bonnemaire, Mrs, Oda S. Astrup, Mr. Henning Helgøy, Mr. Sergey A. Kulyakhtin, Mrs Juliane Borge and Mrs Trine Lundamo for great help during the experiments. The authors would also like to thank the Hamburg Ship Model Basin (HSVA), especially the ice tank crew, for the hospitality, technical and scientific support and the professional execution of the test programme in the Research Infrastructure ARCTECLAB.

Reference

Izumiyama, K., Wako, D. and Uto, S., 1999. Ice force distribution on a flat indentor, Proc. of the 14 th Int. Symp. on Ice, Edited by T. Shen, pp. 917-922.

Kim, E., 2012. Personal communication: Saturation pressure. In: w. Lu (Editor), Trondheim.

Kotras, T.V., 1983. Predicting ship performance in level ice. SNAME Trans, 91: 329-349.

Lindqvist, G., 1989. A straightforward method for calculation of ice resistance of ships, Proceedings of POAC 1989, pp. 722-735.

Lu, W., Lubbad, R., Hoyland, K. and Løset, S., 2013a. Physical and theoretical model to study level ice and wide sloping structure interactions (in press). Cold Regions Science and Technology.

Lu, W., Lubbad, R., Serré, N. and Løset, S., 2013b. A theoretical model investigation of ice and wide sloping structure interactions, Proceedings of the 22nd International Conference on Port and Ocean Engineering under Arctic Conditions, Espoo, Finland.

Määttänen, M., Løset, S., Metrikine, A., Evers, K.-U., Hendrikse, H., H, H., Lønøy, C., Metrikin, I., Torodd, N. and Sergiy, S., 2012. Novel Ice Induced Vibration Testing in a Large-scale Facility: Deciphering Ice Induced Vibrations, Part 1, 21st IAHR

International Symposium on Ice. Dalian University of Technology, Dalian, China, pp. 946-958.

Paavilainen, J. and Tuhkuri, J., 2013. Pressure distributions and force chains during simulated ice rubbling against sloped structures. Cold Regions Science and Technology, 85(0): 157-174.

Serré, N., Høyland, K.V., Lundamo, T., Bonnemaire, B., Evers, K.-U. and Gürtner, A., 2013a. Rubble Ice transport on Arctic Offshore Structures (RITAS), part I: Scale-model investigations of level ice action mechanisms, Proceedings of the 22nd International Conference on Port and Ocean Engineering under Arctic Conditions, Espoo, Finland.

Serré, N., Lu, W., Høyland, K.V., Bonnemaire, B., Borge, J. and Evers, K.-U., 2013b. Rubble Ice Transport on Arctic Offshore Structures (RITAS), part II: 2D model scale study of the level ice action, Proceedings of the 22nd International Conference on Port and Ocean Engineering under Arctic Conditions, Espoo, Finland.

Sodhi, D.S., 2001. Crushing failure during ice–structure interaction. Engineering Fracture Mechanics, 68(17–18): 1889-1921.

Sodhi, D.S., Takeuchi, T., Nakazawa, N., Akagawa, S. and Saeki, H., 1998. Medium-scale indentation tests on sea ice at various speeds. Cold Regions Science and Technology, 28(3): 161-182.

Tekscan, I., 2003. I-can Equilibration and Calibration Practical Suggestions. Tekscan, Inc, South Boston, MA.

Tekscan, I., 2011. I-Scan User Manual. Tekscan Inc, South Boston, MA.

Timco, G., 1991. The vertical pressure distribution on structures subjected to rubble forming ice, 11th International Conference on Port and Ocean Engineering under Arctic Conditions, St.John's, Canada, pp. 185-197.

Valanto, P., 2001. The resistance of ships in level ice. SNAME, 109: 53-83.